DOE/PC/91008-22
Distribution Category UC-122

Fractured Reservoir Discrete Feature Network Technologies

By
William S. Dershowitz
Herbert H. Einstein
Paul R. LaPointe
Thorsten Eiben
Eugene Wadleigh
Violeta Ivanova

December 1998

Work Performed Under Subcontract No. G4S51728 Contract DE-AC22-94PC91008

Prepared for
U.S. Department of Energy
Assistant Secretary for Fossil Energy

Robert E. Lemmon, Technology Manager
National Petroleum Technology Office
P.O. Box 3628
Tulsa, OK 74101

Prepared by:
Golder Associates,Inc.
4104 – 148th Avenue, N.E.
Redmond, WA 98052

DISCLAIMER

TABLE OF CONTENTS Page No.

LIST OF TABLES

LIST OF FIGURES

EXECUTIVE SUMMARY

This report describes research carried out for the project, "Fractured Reservoir Discrete Feature Network Technologies," a project of Fundamental Geoscience Research and Development, sponsored by the U.S. Department of Energy National Oil and Related Programs through BDM-OK/NIPER. The report summarizes project research in five areas:

- development of hierarchical fracture models, which provide a flexible framework for geologically realistic, discrete-fracture network generation;
- fractured reservoir compartmentalization, block size, and tributary volume analysis, which provides quantitative evaluation of fracture network connectivity effects on oil production;
- development of fractured reservoir discrete feature data analysis tools, and demonstration of those tools through application to the Yates, Texas Tract 49 and Tract 17 study sites;
- development of tools for data integration and reservoir simulation through application of discrete feature network technologies for tertiary oil production, and demonstration of those tools at project study sites; and
- quantitative evaluation of the economic value of the discrete feature analysis approach based on the project study site application.

Detailed descriptions are provided in project research reports cited in the report. Reports, algorithms, software, and data referenced in the text are currently maintained on the web site *http:\\www.golder.com\niper\niprhome.htm*.

ACKNOWLEDGEMENTS

The authors would like to thank the U.S. Department of Energy, National Oil and Related Programs for sponsoring the research described in this report, though the National Institute for Petroleum Energy Research (NIPER), management by BDM-OK. In additional to the authors listed on the report, we would like to thank other contributors including:

Anna Burago, Golder Associates Inc.

Trenton Cladouhos, Golder Associates Inc.

Thomas W Doe, Golder Associates Inc.

Glori Lee, Golder Associates Inc.

Aaron Fox, Golder Associates Inc.

Dawn Shuttle, Golder Associates Inc.

Jon Snell, Marathon Oil Company

Joan Tilden, Marathon Oil Company, Petroleum Technology Center

Daniele Veneziano, Massachusetts Institute of Technology

This project would not have been possible without the generous support of Marathon Oil Company, Midland Texas, which donated data, analyses, and field activities which formed the basis for this research.

In addition, we would like to thank Min Tham of BDM-OK, our Project Technical Officer for his support.

1. INTRODUCTION

1.1 Project Overview

This report describes research and technology development for the project, "Fractured Reservoir Discrete Feature Network Technologies," a project of Fundamental Geoscience Research and Development, sponsored by the U.S. Department of Energy National Oil and Related Programs through BDM-OK/NIPER. This project was carried out by Golder Associates (Seattle, WA) together with Marathon Oil Company (Midland, Texas) and the Massachusetts Institute of Technology (Cambridge, Massachusetts). Golder Associates was the project lead, and carried out the primary research, technology development, management, and technology transfer activities. Marathon Oil Company (Midland, Texas) carried out field tests and contributed project data for the project study at the Yates Field in Iraan, TX (Tracts 17 and 49). Marathon also participated in the research applications. Marathon's participation was contributed to the project. Theoretical development of the Hierarchical Fracture Model (HFM) and implementation of the HFM model for Tracts 17 and 49 were carried out by the Massachusetts Institute of Technology.

The project combined theoretical research into discrete fracture network models, technology development, and technology demonstration.

Theoretical research focused on the development of the hierarchical fracture model (HFM), a new discrete feature network (DFN) model designed to provide a more realistic representation of reservoir geology. The model uses a cell-based approach to describe fracture properties, and supports rotations, translations, and correlation between geological structures. The model was verified by application at the project study site.

Technology development was carried out in two areas: discrete feature network (DFN) data analysis procedures and fractured reservoir analysis procedures. DFN data analysis procedures were developed to increase the amount of value, which can be extracted from existing well test, geological, and geophysical data. DFN analysis technologies were developed for set definition, orientation distributions, spatial pattern analysis, and well test interpretation. Well test analyses methods are based on the "fractional dimension" flow approximation.

Technology development for fractured reservoir analysis included the development of procedures for analysis of reservoir compartmentalization, rock block volumes, and tributary drainage volume. In addition, technologies were developed to link the DFN approach and conventional cell-based stratigraphy models and flow simulators.

Technologies developed during the project were demonstrated and evaluated using data from the project study sites. Particular attention was devoted to the application of the thermally assisted gravity segregation (TAGS) technique. The TAGS process is an innovative approach to steam-flooding which utilizes discrete fracture networks to provide simultaneous pathways for steam flow and oil production. The project carried out analyses of pathways based on tracer tests. The TAGS process was simulated using a

conventional dual porosity approach with parameters derived from DFN models, based on the DFN/continuum integration approaches developed as part of this project.

Technology transfer included 4 research reports, 19 professional papers published or submitted for publication, 15 presentations to conferences and workshops, and over 17,000 hits to the project web site.

This report is organized according to the project task numbering. Table 1-1 provides a cross-reference between project tasks and the corresponding sections in this report. Detailed information about project research can be found in the following technical reports:

Ivanova, V. 1998. Research Report, 3D Hierarchical Fracture Model Prepared for BDM/OK NIPER under contract G4S51728. Massachusetts Institute of Technology, Cambridge.

Dershowitz, W., T. Foxford, and T. Doe, 1998. Research Report, Fracture Data Analysis Technology. Prepared for BDM/OK NIPER under contract G4S51728. Golder Associates Inc., Seattle.

Dershowitz, W., T. Foxford, and P. LaPointe, 1997. Research Report, Fractured Reservoir Compartmentalization. Prepared for BDM/OK NIPER under contract G4S51728. Golder Associates Inc., Seattle.

Dershowitz, W., T. Foxford, and A. Burrago, 1998. Research Report, Linking Discrete Fracture Network and Reservoir Geo-cellular Models. Prepared for BDM/OK NIPER under contract G4S51728. Golder Associates Inc., Seattle.

See the project web page for access to project reports, databases, and software. The project web page was developed and maintained under the scope of project tasks 5.1.1 and 5.1.2.

http://www.golder.com/niper/niprhome.htm.

Table 1-1 Project Tasks

Section	Task	Task Description
2	1.1.1	Initial Data Warehouse
2	1.1.2	Data Updates
3	1.2.1	3D Hierarchical Fracture Model
4	1.3.1	Improved Matrix Block Analysis
4	1.3.2	Drainage Volume Analysis
5	2.1.1	Fracture Set Analysis
5	2.1.2	Spatial Location Analysis
5	2.1.3	Hydraulic Parameter Analysis
5	2.1.4	Compartmentalization Analysis
6	3.1.1	Linkage to Reservoir Model/Software Development
7	3.2.1	MS Windows 95 Fracture Data Analysis System
7	3.2.2	Discrete Fracture Analysis for the TAGS Process
7	3.2.3	Software Linking
8	4.1.1	Fracture Image Data Acquisition
8	4.1.2	Well Testing Data Acquisition
1,2	5.1.1	WWW Server Development
1,2	5.1.2	WWW Site Updates

2. TASK 1.1: FRACTURED RESERVOIR SITE CHARACTERIZATION DATA

2.1.1 Task 1.1.1: Initial Data Warehouse

Figure 2-1 shows the location of the project study site, tracts 17 and 49 within the Yates fractured reservoir field in Iraan, Texas. At project initiation, Marathon Oil Company collected fracture and production data from the project study site and provided this data to Golder Associates for distribution through the project web site. The following data was donated to the project to form the initial data warehouse:

- core analysis,
- geophysical logs,
- structural analyses,
- well performance histories,
- lineament maps,
- production data related to TAGS, and
- well adjustment and response monitoring.

This data was assembled and processed into an information warehouse within the World-Wide-Web (WWW) server application (Task 5.1.1). Figures 2-2 through 2-7 present examples of the data from the initial data warehouse.

The WWW server organizes the Technology Transfer Database into the following categories:

- **Progress Reports:** An annotated list of project progress reports. By selecting a report from the list, site visitors may view an HTML version of the document within the browser.
- **Peer Reviewed Papers:** An annotated list of peer reviewed papers produced within the project. By selecting a report from the list, site visitors may download the selected file.
- **Professional Meeting Presentations:** A list of presentations.
- **Site Characterization Data:** An annotated list of site characterization data files. Selecting a file from the list begins downloading.
- **Algorithms and Software:** An annotated list of software and algorithms developed within the project. Selecting a file from the list begins downloading.

Marathon Oil Company
Mid-Continent Region

YATES FIELD UNIT
Pecos & Crockett Counties, Texas

Approximate boundary for areas of investigation

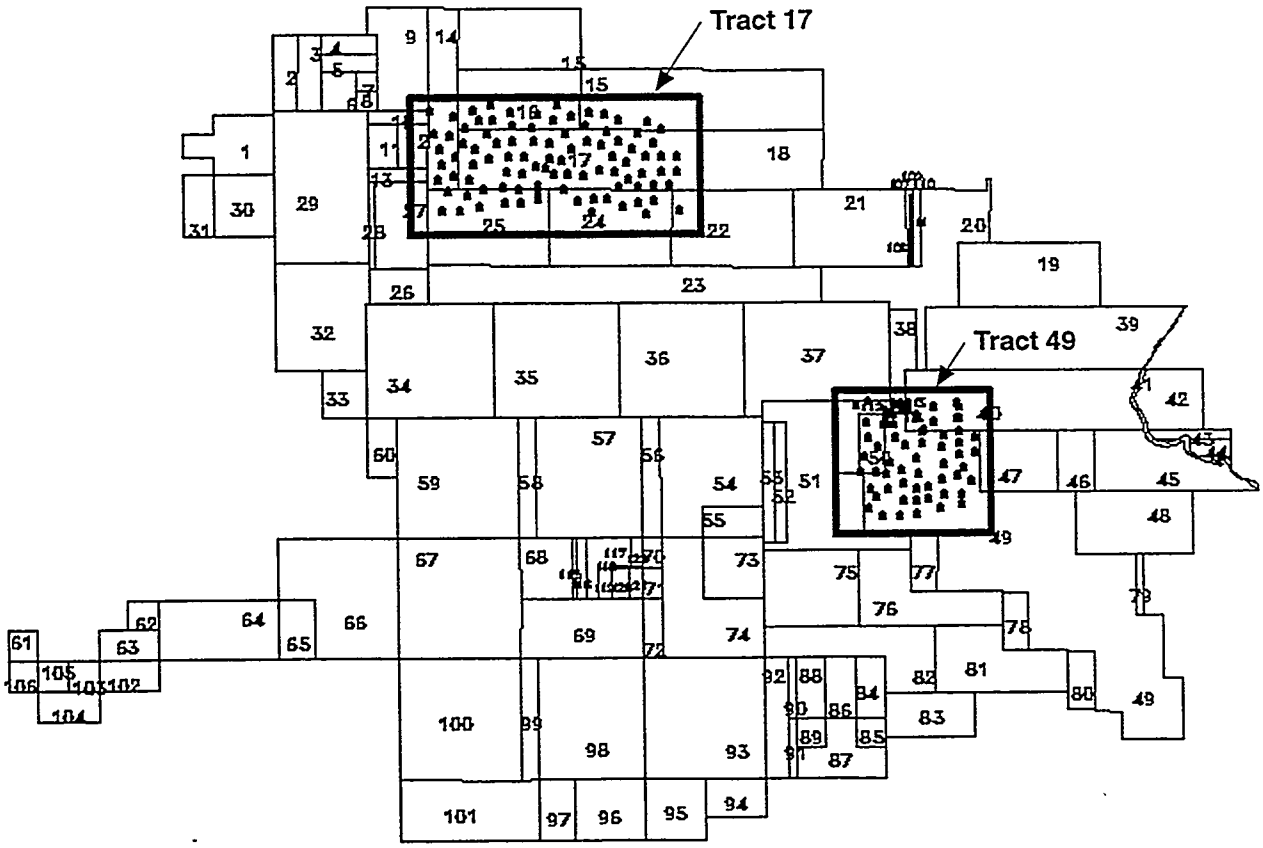

FIGURE **2-1**
PROJECT STUDY SITE
NIPER/FINAL REPORT/WA

PROJECT NO. 963 1357.521 DRAWING NO. 80665 DATE 9/29/98 DRAWN BY EA

Golder Associates

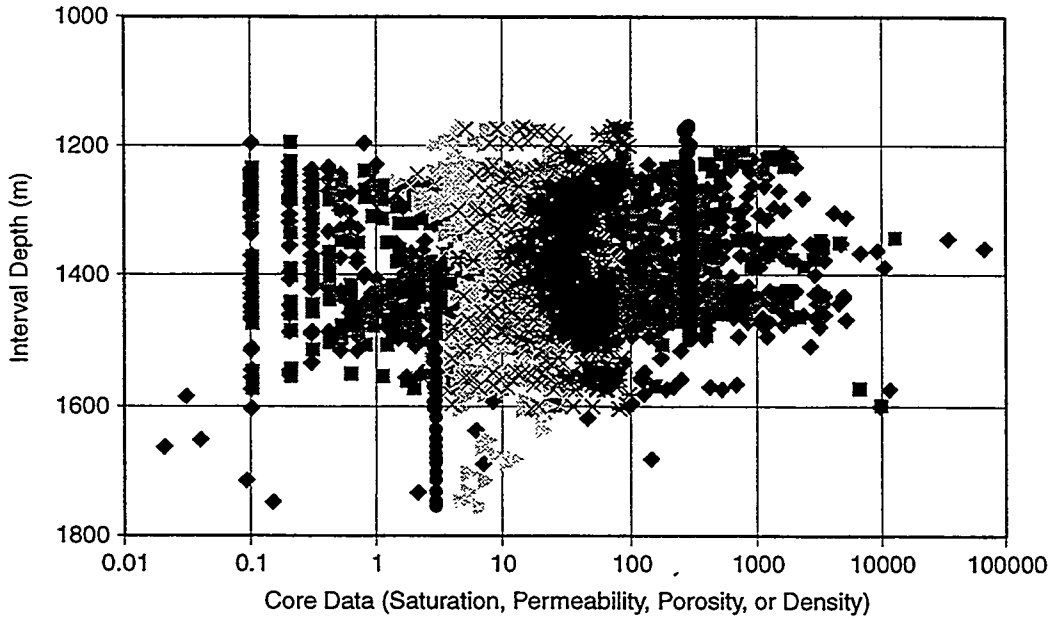

FIGURE **2-2**
CORE LOG ANALYSIS
BH-17, WELL 11
NIPER/FINAL REPORT/WA

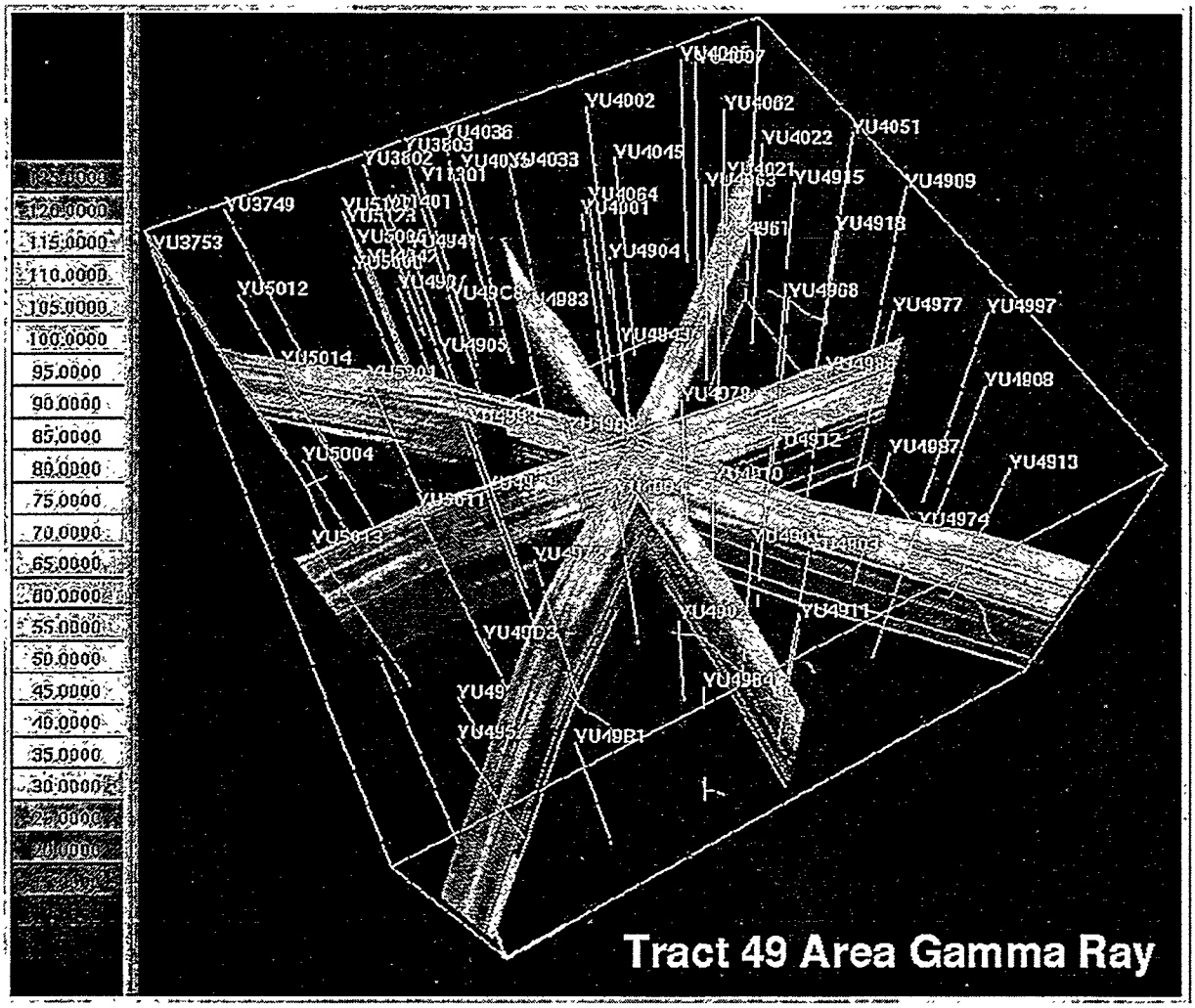

FIGURE **2-3**
FENCE DIAGRAM OF GAMMA RAY LOGS FOR RESERVOIR TRACT 49
NIPER/FINAL REPORT/WA

PROJECT NO. 963 1357.521 DRAWING NO. 80667 DATE 9/25/98 DRAWN BY EA

Golder Associates

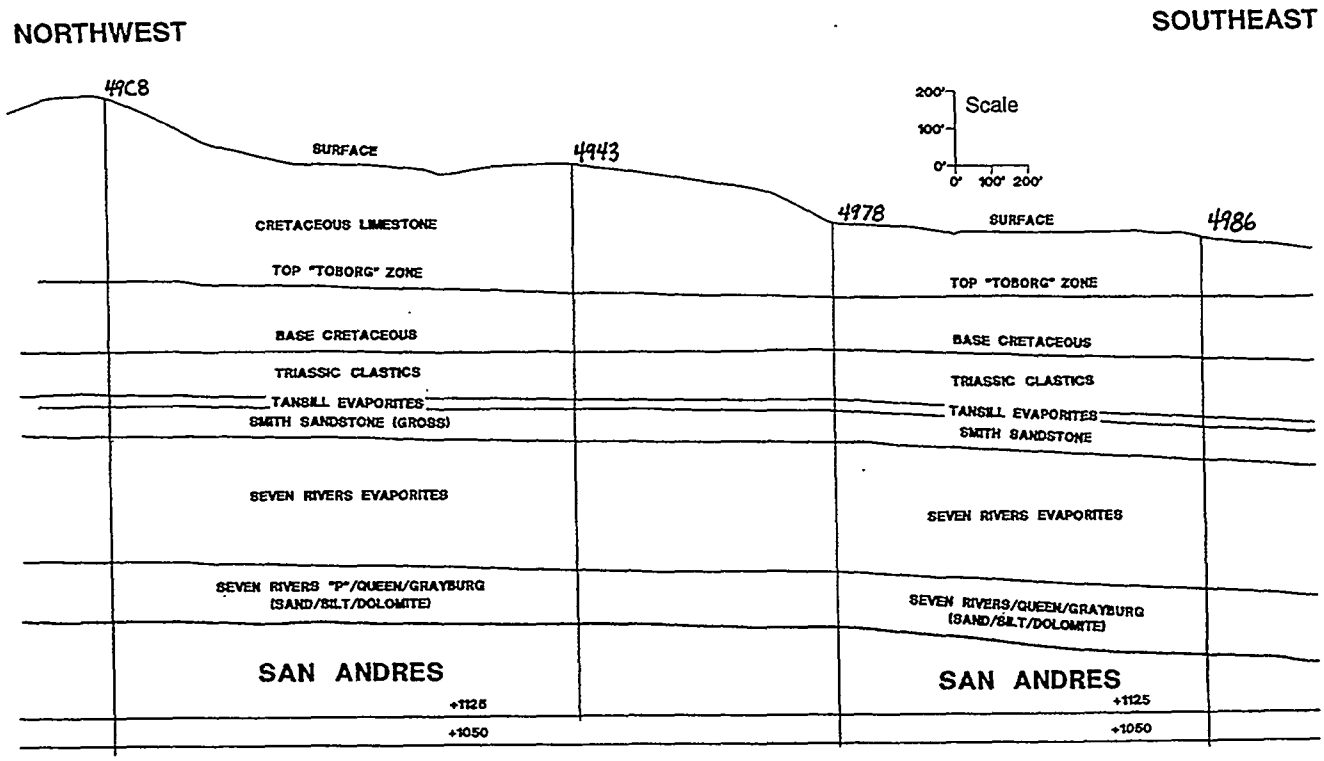

FIGURE **2-4**
CROSS SECTION THROUGH YATES FIELD STUDY SITE
NIPER/FINAL REPORT/WA

PROJECT NO. 963 1357.521 DRAWING NO. 80668 DATE 9/25/98 DRAWN BY EA

Golder Associates

YATES FIELD UNIT
Observation Well GOC & WOC
Tract = 049 Well = 56

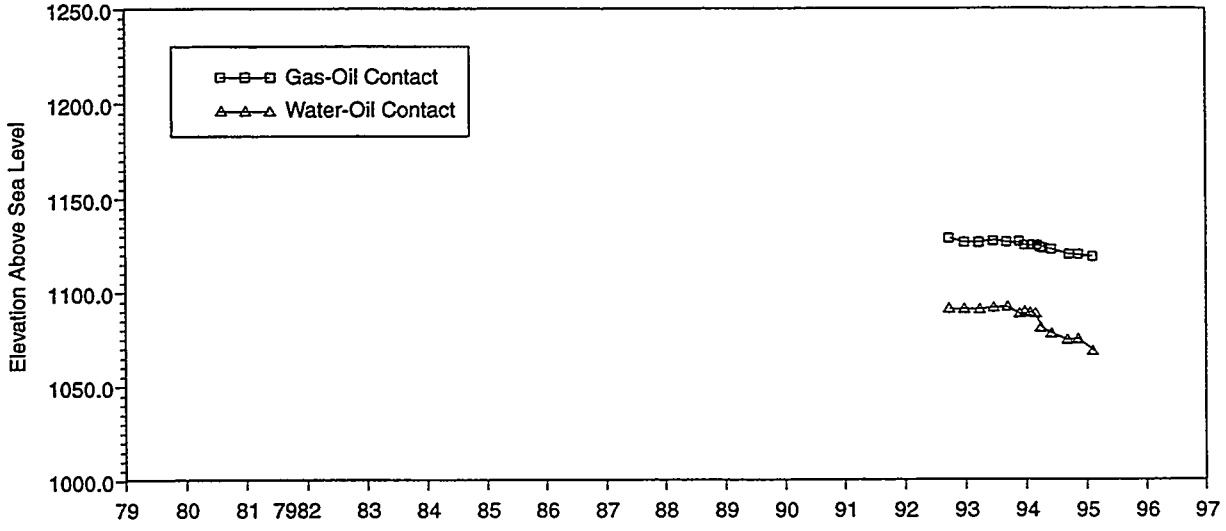

FIGURE **2-5**
FLUID CONTACT HISTORIES
NIPER/FINAL REPORT/WA

PROJECT NO. 963 1357.521 DRAWING NO. 80669 DATE 9/25/98 DRAWN BY EA

Golder Associates

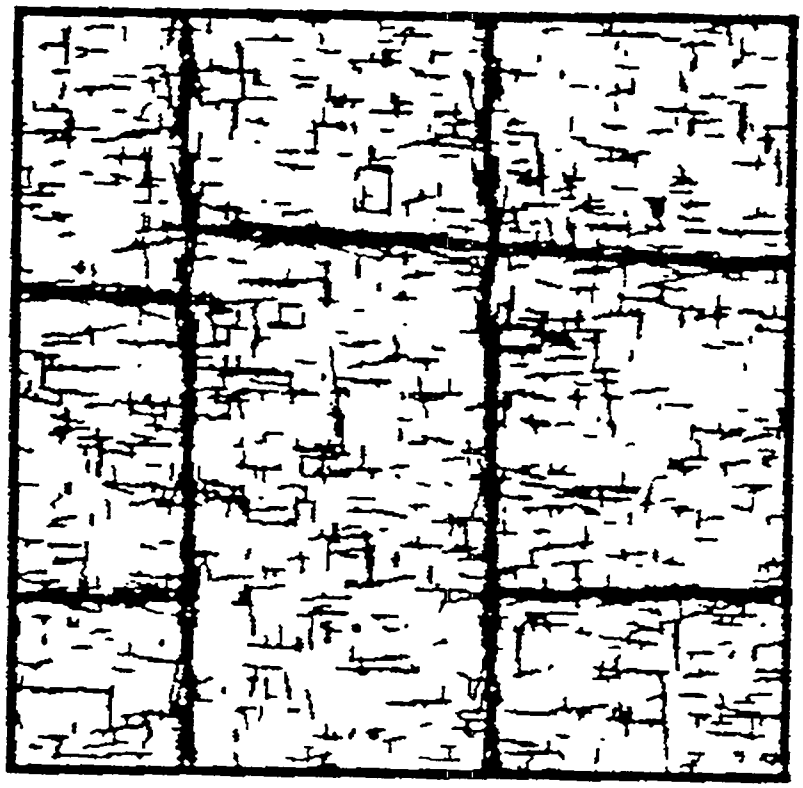

- Tract 17 area
- Incorporates local large-scale features

FIGURE **2-6**
SYNTHETIC LINEAMENT MAP FOR TRACT 17 AREA
NIPER/FINAL REPORT/WA

PROJECT NO. 963 1357.521 DRAWING NO. 80670 DATE 9/25/98 DRAWN BY EA

Golder Associates

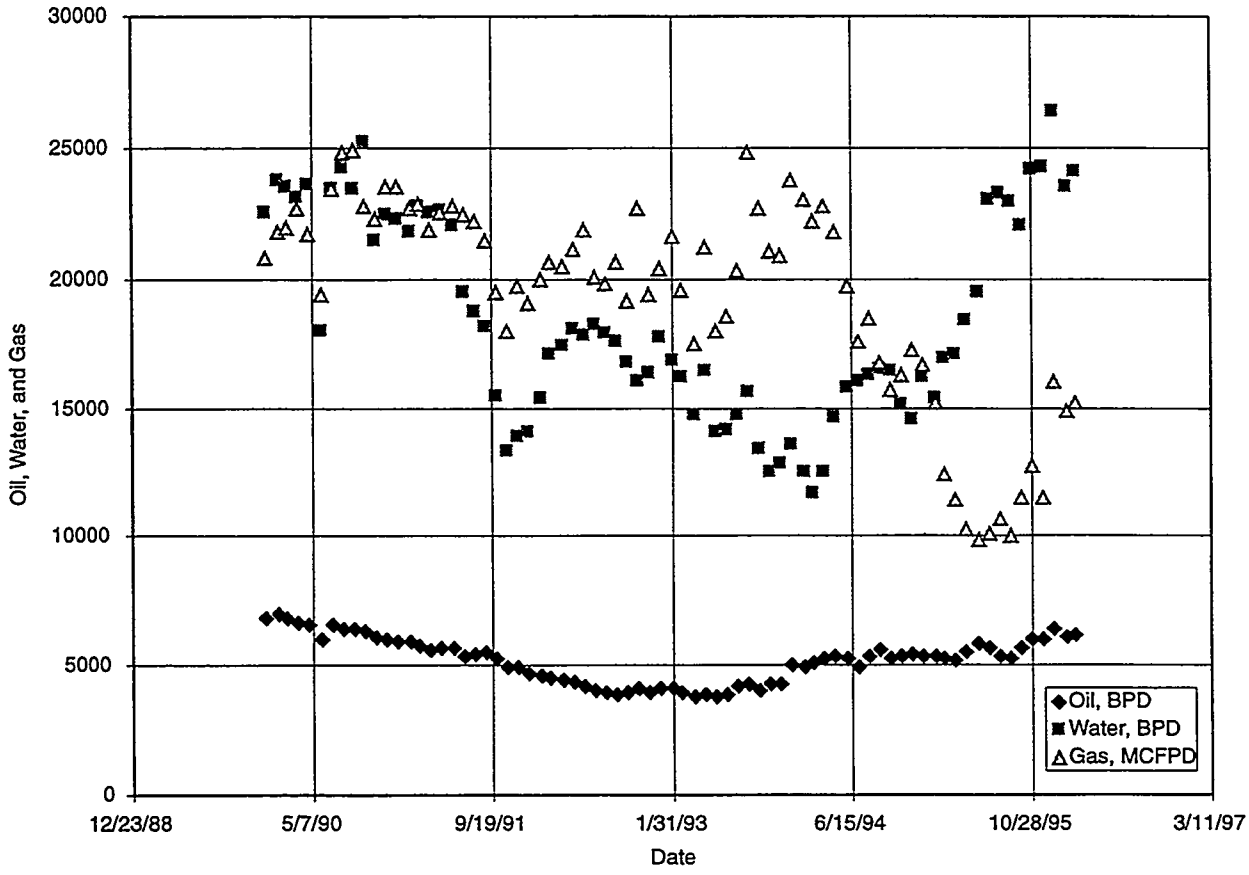

FIGURE **2-7**
YATES AREA 17 PRODUCTION DATA
NIPER/FINAL REPORT/WA

PROJECT NO. 963 1357.521 DRAWING NO. 80671 DATE 9/25/98 DRAWN BY EA

Golder Associates

- **Reservoir Data and Simulations**: An annotated list of reservoir data and simulation files saved as compressed (.ZIP) files. Selecting a file from the list begins downloading.

- **Technology Transfer Workshop Information**: Schedule and registration information for technology transfer workshops.

2.1.2 Task 1.1.2: Data Updates

Throughout the project, Marathon Oil Company regularly collected fracture and production data from the project study site and provided these data to Golder Associates to update the online data warehouse. The following data were donated to the project during the project:

- FMI Geophysical logs
- Geophysical logs from selected wells
- Well performance histories
- Production data related to TAGS
- Well adjustment and response monitoring
- 3D geologic reservoir characterization data (StrataModel)
- Core data on lithology, fracturing, and rock properties
- Additional log interpretations from Tract 17 and 49
- Material properties and boundary condition assumptions for THERM/DK and ECLIPSE reservoir simulations

These data were assembled and incorporated into the project World-Wide-Web (WWW) site (Task 5.1.2). Figures 2-8 through 2-10 present additional examples of the data provided by Marathon during the project.

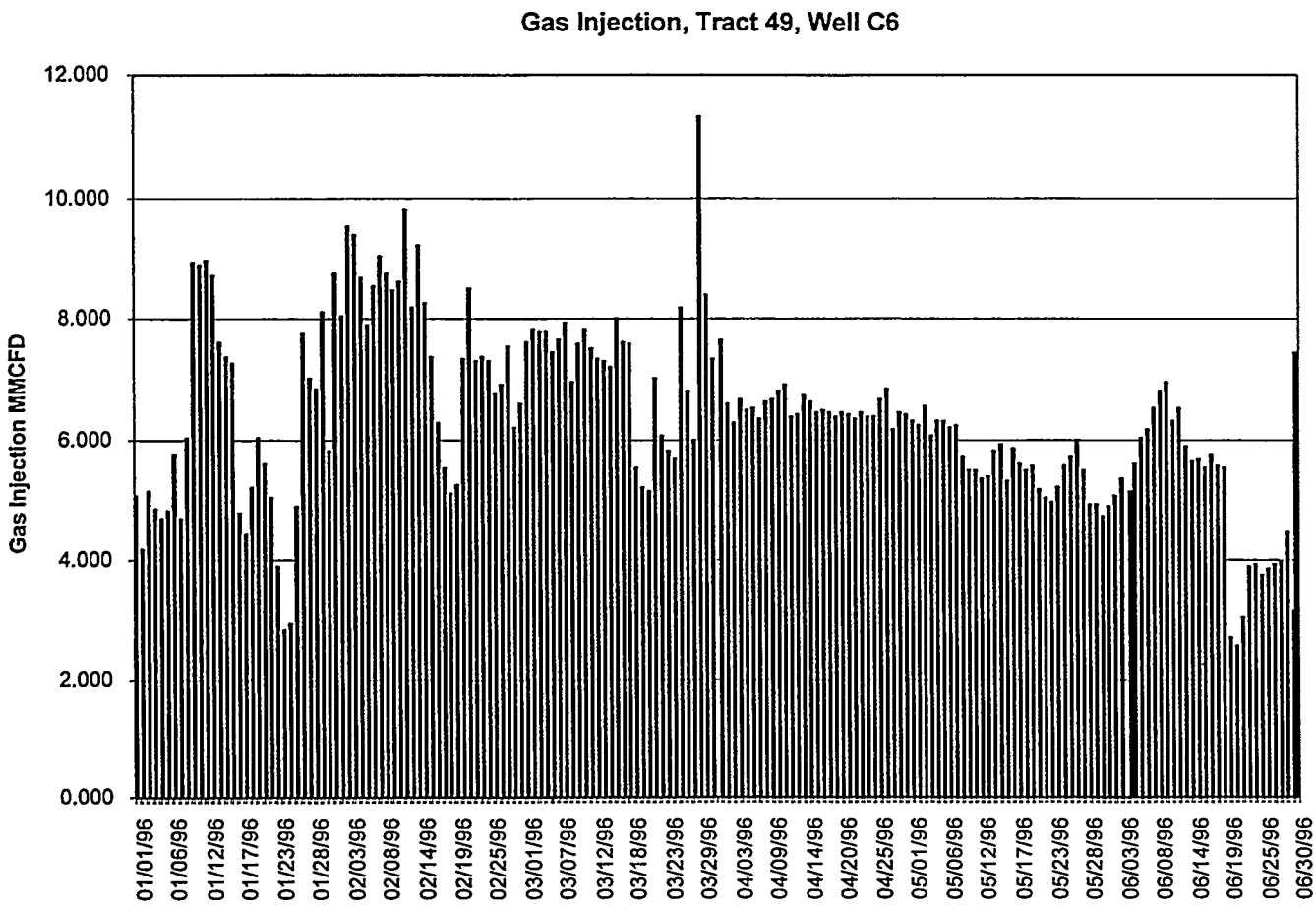

FIGURE **2-8**
GAS INJECTION HISTORIES
UNIT 49, WELL C6
NIPER/FINAL REPORT/WA

PROJECT NO. 963 1357.521 DRAWING NO. 80791 DATE 9/28/98 DRAWN BY EA

Golder Associates

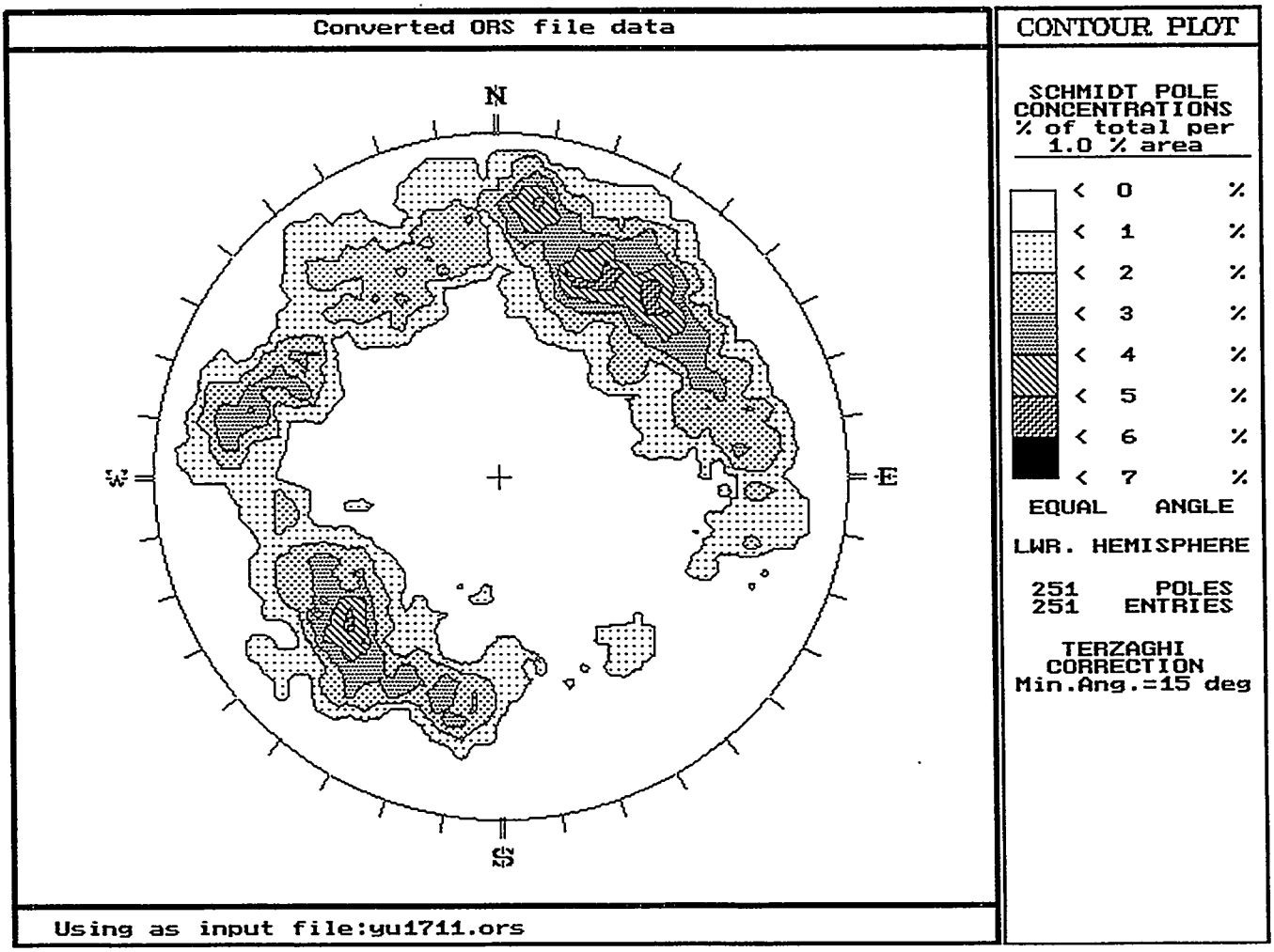

FIGURE **2-9**
FRACTURE ORIENTATIONS
YFU1711
NIPER/FINAL REPORT/WA

PROJECT NO. 963 1357.521 DRAWING NO. 80792 DATE 9/28/98 DRAWN BY EA

Golder Associates

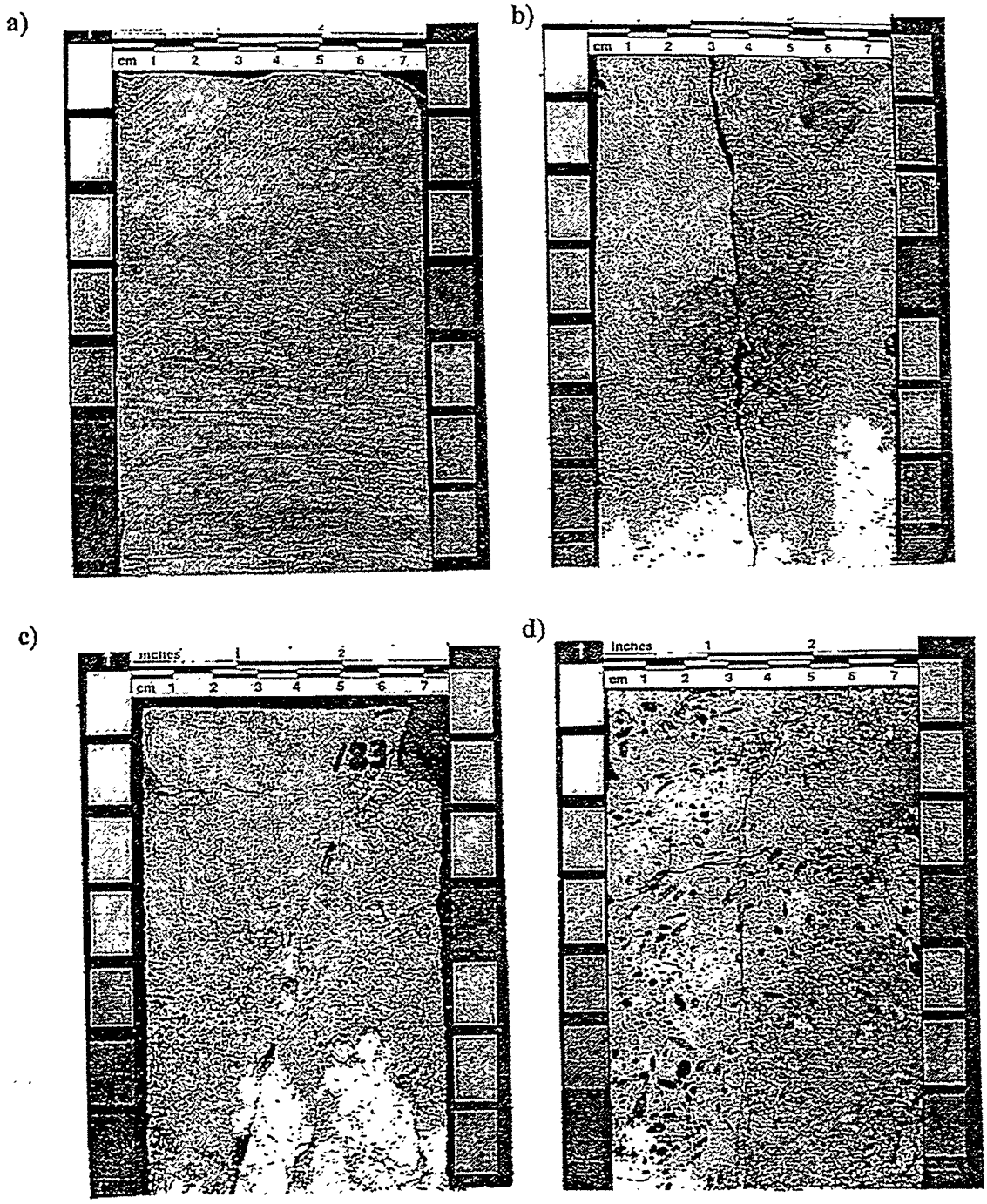

Texture and fracturing of the San Andres formation (core photographs): a) dense, dolomitic shale mudstone; b) dolomitic grainstone cut by a totally open penetrating (TOPN) oil-stained fracture; c) dolomitic packstone/grainstone cut by a partially filled with calcite penetrating (FILO) fracture; d) dolomitic packstone with fusumoldic porosity, cut by a vertical calcite-filled (FILL) fracture (stained red), and a horizontal drilling-induced (INDU) fracture.

FIGURE **2-10**
SAN ANDRES CORE PHOTOGRAPHY
NIPER/FINAL REPORT/WA

PROJECT NO. 963 1357.521 DRAWING NO. 80793 DATE 9/28/98 DRAWN BY EA

Golder Associates

3. TASK 1.2: 3D HIERARCHICAL FRACTURE MODEL

The 3D Hierarchical Fracture Model (HFM) is a new discrete feature network (DFN) model developed and applied for the project by the Massachusetts Institute of Technology. HFM was designed to provide an efficient numerical tool for generation of realistic geologically-conditioned fracture patterns. HFM generates fractures by superposition of hierarchical fracture sets, using three stochastic processes that reflect inherent relationships between the fracture system geometry and the underlying mechanics. HFM combines Poisson plane processes, Poisson line tessellation, and 3D rotation and translation to generate orientations of potential fracture planes, fracture intensity, and relationships between fracture geometry and known geological structures. The development of the HFM is described in Section 3.1 below. The HFM model was verified through application to the project study site, Tracts 17 and 49 of the Yates, Texas fractured Permian sedimentary oil reservoir. Section 3.2 below describes development of a conceptual model for the geologic evolution of the fracture system in the reservoir formations of the Yates oil field. Numerical simulations are described for generation of fracture sets related to the regional stresses and depositional trends and to the asymmetric anticlinal structure of reservoir strata. A comparison of the HFM synthetic fracture system to field data shows a good match between measured and simulated fracture orientation and intensity as measured in wells.

3.1 Task 1.2.1: Hierarchical Model Development

During the year, the 3D Hierarchical Model (Ivanova, 1995; Ivanova et al., 1995), model was enhanced with some new procedures, the most important being the Fractal Line Tessellation. This is expected to be particularly useful for modeling the San Andres formation and similar fractured reservoirs because it reproduces the clustering of fractures into zones.

3.1.1 Basic Concepts of the 3D Hierarchical Fracture Model

The HFM combines a series simple geometric procedures to reproduce the 3D geometry of fracture systems, created by complex mechanical processes, on the basis of inherent relationships between mechanics and geometry. Thus, the model combines the advantages of the purely geometric and the purely mechanical models. On the one hand, it has the capability of geometric models to reproduce complex fracture systems in 3D space by using various statistical and geometric methods. On the other hand, geology-based geometric algorithms provide a realistic representation of natural fracture systems, similar to mechanical models that reproduce the true mechanisms of fracture initiation and propagation.

In the HFM, fractures are convex polygons (Figure 3-1), randomly oriented and randomly located in three-dimensional space. The pole orientation and the coordinates of the center and the vertices of an individual fracture are determined indirectly when the fracture is generated as a member of a set (details follow in Section 3.1.2). The model incorporates Poisson plane and line stochastic processes, and is thus related to earlier 3D fracture network models (Veneziano, 1978; Dershowitz, 1979). Good references on the

fundamental theory of Poisson point, line, and plane processes are Diggle (1983), Stoyan et al. (1987), Upton and Fingleton (1985), and Miles (1969 and 1973).

Figure 3-1 Dimensions and Shape of an Individual Fracture in the 3D Model

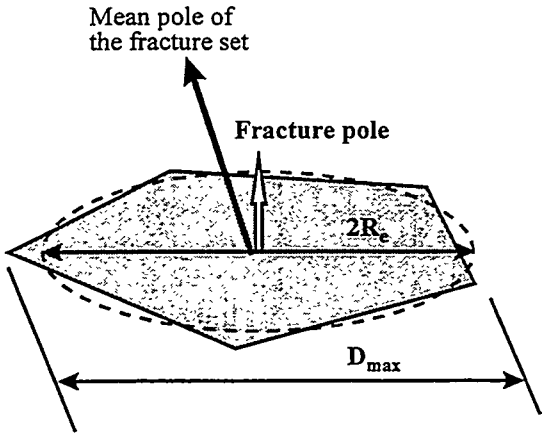

Elongation:

$$e = \frac{D_{max}}{2R_e}$$

Figure 3-2 illustrates the three major stochastic processes of the conceptual model. The primary process (Figure 3-2a), a random plane network, models the orientation of the stress field which creates fractures along planes of maximum shear and tension in rocks. The secondary process (Figure 3-2b), subdivision of the potential fracture planes into intact and fractured regions, is accomplished through a line tessellation and a polygon marking procedure. The combined primary and secondary processes reproduce fracture intensity. The tertiary process (Figure 3-2c), random translation and rotation of polygon-fractures, represents the relationship of fracture intensity and orientation to local structures that modify the general stress field. The three stochastic processes are explained in Section 3.1.2 in the context of fracture set generation with the 3D HFM.

3.1.2 HFM Fracture Set Algorithm

Geometrically, a fracture set is a collection of fractures with related orientations, sizes, and locations. A fracture set is characterized by two parameters:

- probability density function (PDF) describing the variation of fracture plane orientations;
- intensity of fracturing as it varies in space.

The geometry of a fracture set is reproduced though the three stochastic processes defined in Section 3.1.1.

a) Primary process: Poisson Plane Network

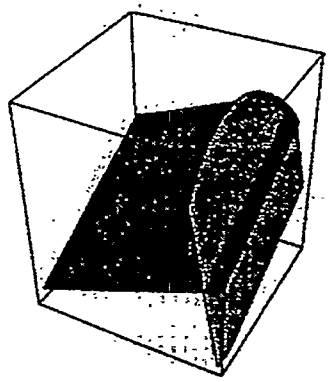

b) Secondary process: Poisson Line Tessellation and Polygon Marking

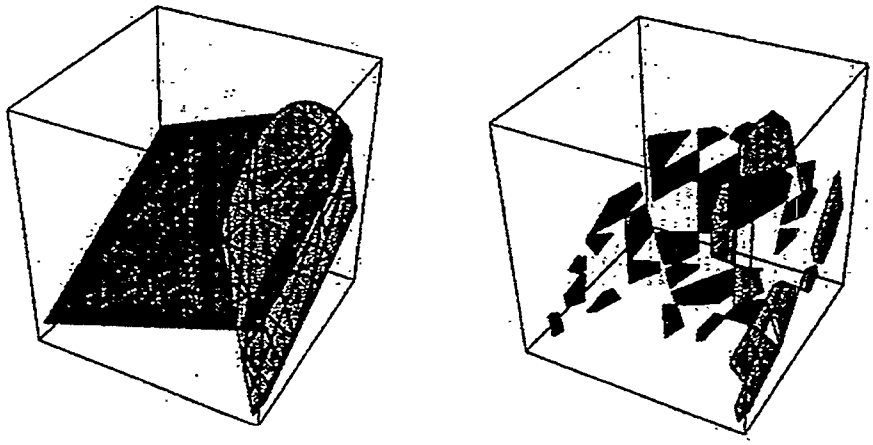

c) Tertiary process: Random Polygon Translation/Rotation

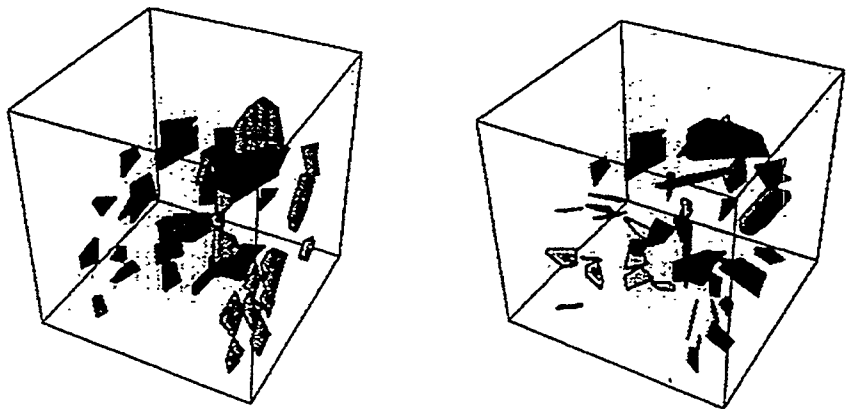

FIGURE **3-2**
STOCHASTIC PROCESSES OF THE 3-D FRACTURE SYSTEM MODEL
NIPER/FINAL REPORT/WA

PROJECT NO. 963 1357.521 DRAWING NO. 80687 DATE 9/25/98 DRAWN BY EA

Golder Associates

3.1.2.1 Modeling of Stress Field Orientation: Primary Stochastic Process

Stress field orientation is defined as the orientations of planes of maximum shear and tension that are related to fracture plane orientations. The orientations of the potential fracture planes are represented by the primary stochastic process: a homogeneous, anisotropic, Poisson plane network (Figure 3-2a).

Frame of Reference and Orientations of Potential Fracture Planes

The mean orientation of a fracture set is specified in polar coordinates in terms of an azimuth Θ and a latitude Φ (Figure 3-3) in a global frame of reference (OXYZ). The axes of the global coordinate system coincide with some relevant global directions; usually the positive directions of OX and OY are east and north, respectively, and OZ is vertical.

In the frame of reference of a fracture set (Oxyz in Figure 3-3) a plane is defined by the equation:

$$x \sin\theta \sin\varphi + y \cos\theta \sin\varphi + z \cos\varphi = d \qquad (3\text{-}1)$$

where d is the distance from the global origin O to the plane, and θ and ϕ are the azimuth and latitude of the normal vector (pole Oz' in Figure 3-3), respectively. The orientations of potential fracture planes are randomly generated as pairs of polar coordinates (θ, ϕ) in the frame of reference of the fracture set (Oxyz in Figure 3-3). The directional pairs (θ, ϕ) follow a spherical PDF, inferred from the measured data. Possible probability density functions (PDFs), illustrated in Figure 3-4, include uniform or partial uniform, one-parameter or two-parameter Fisher, and Bingham. In some cases all fracture planes may be assumed parallel and deterministically assigned the same orientation. The application of the distributions illustrated in Figure 3-4 for generation of directional data is reviewed in more detail in Dershowitz (1979), Dershowitz et al. (1996), and Ivanova (1995).

Modeling Volume of a Fracture Set

The Poisson plane network is generated in a modeling volume that represents the rock mass where the fracture network of interest develops. A generic modeling volume is bound by several planes and surfaces in 3D space. For example, the modeling volumes of independent sets are defined by the boundaries of geologic structures (such as the topographic surface, bedding planes, fold surfaces, or datum planes) over a certain area. The boundaries of the modeling volumes of dependent fracture sets are usually defined by previously generated independent sets. An example of a possible modeling volume for independent fracture sets is shown in Figure 3-5. The volume in Figure 3-5 is enclosed between four vertical planes at $X=X_m$, $X=-X_m$, $Y=Y_m$, $Y=-Y_m$, one horizontal plane at Z=0, and a top surface described by a quadratic function:

$$Z = C_1 X^2 + C_2 XY + C_3 Y^2 + C_4 X + C_5 Y + C_6 \qquad (3\text{-}2)$$

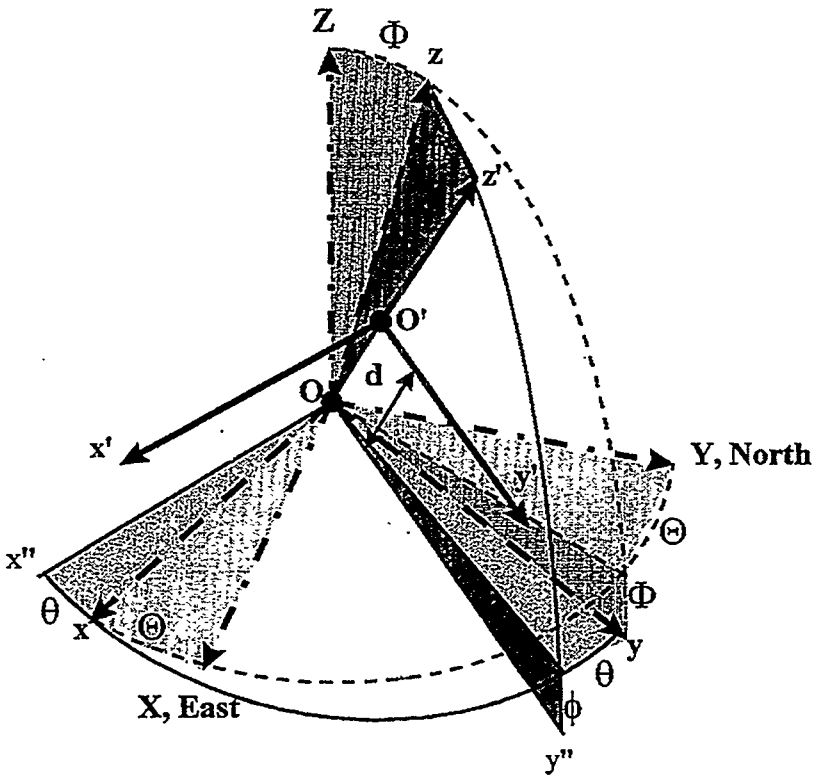

LEGEND

OSYZ	Global frame of reference (f.o.r.)
Oz	Mean pole direction of the fracture set, defined by global azimuth Θ and global latitude Φ
Oxyz	f.o.r. of the fracture set
Oz'	pole (normal vector) of a (potential) fracture plane, defined by local azimut θ and local latitude ϕ
d = OO'	Orthogonal distance of the fracture plane from the global origin O
O'x'y'z'	f.o.r. of the fracture plane (O'x' is parallel to Ox", and O'y' is parallel to Oy")

FIGURE **3-3**
PRIMARY STOCHASTIC PROCESS: FRAMES OF REFERENCE OF A FRACTURE SET
NIPER/FINAL REPORT/WA

PROJECT NO. 963 1357.521 DRAWING NO. 80688 DATE 9/25/98 DRAWN BY EA

Golder Associates

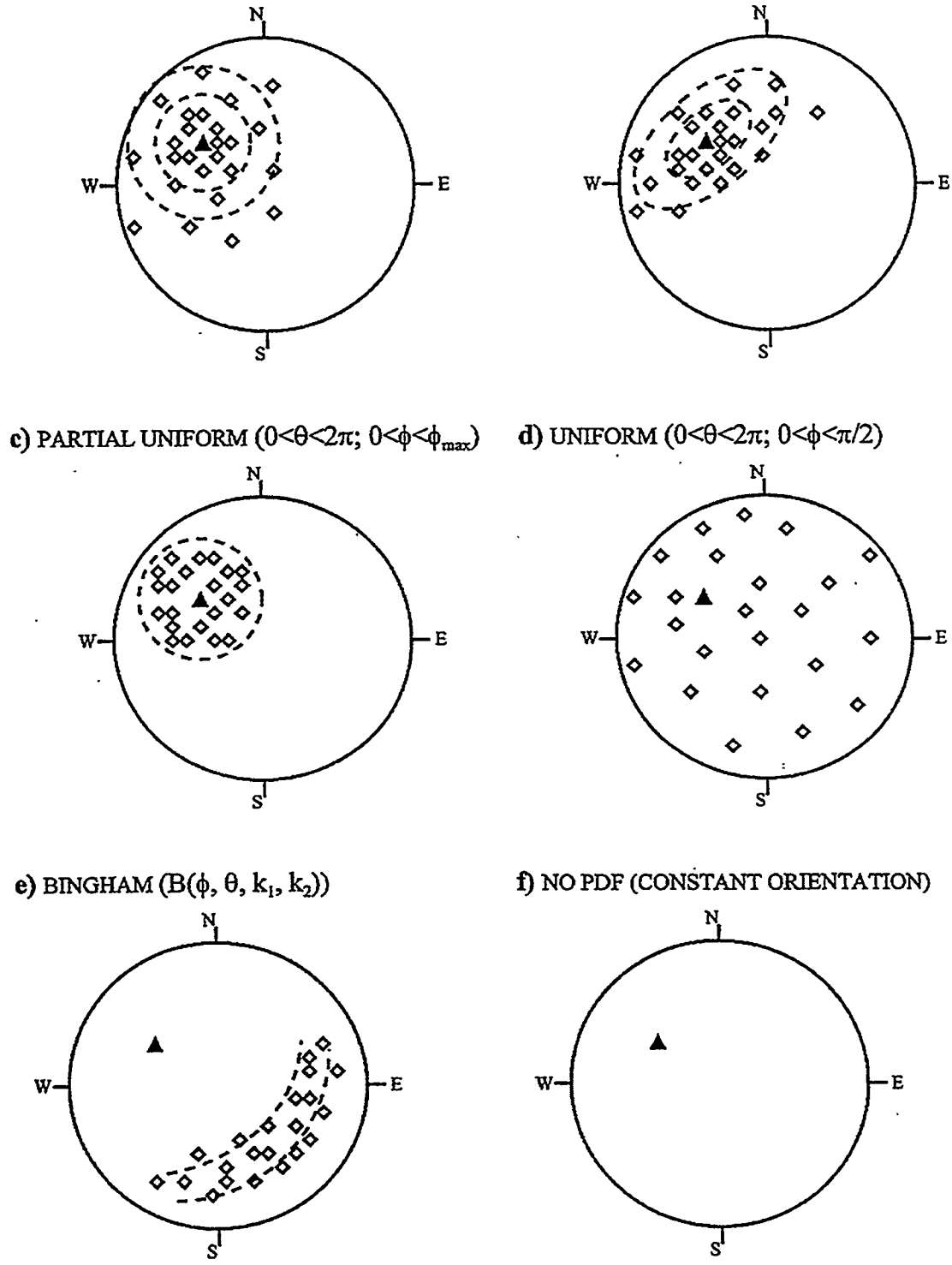

LEGEND

A	One-parameter Fisher
B	Two-parameter Fisher
C	Partial uniform
D	Uniform
E	Bingham (girdle)
F	Constant orientation of all planes

FIGURE **3-4**
SPHERICAL PDFS OF FRACTURE PLANE ORIENTATIONS
NIPER/FINAL REPORT/WA

Figure 3-5 Primary Stochastic Process: Example of a Modeling Volume for Independent Fracture Sets

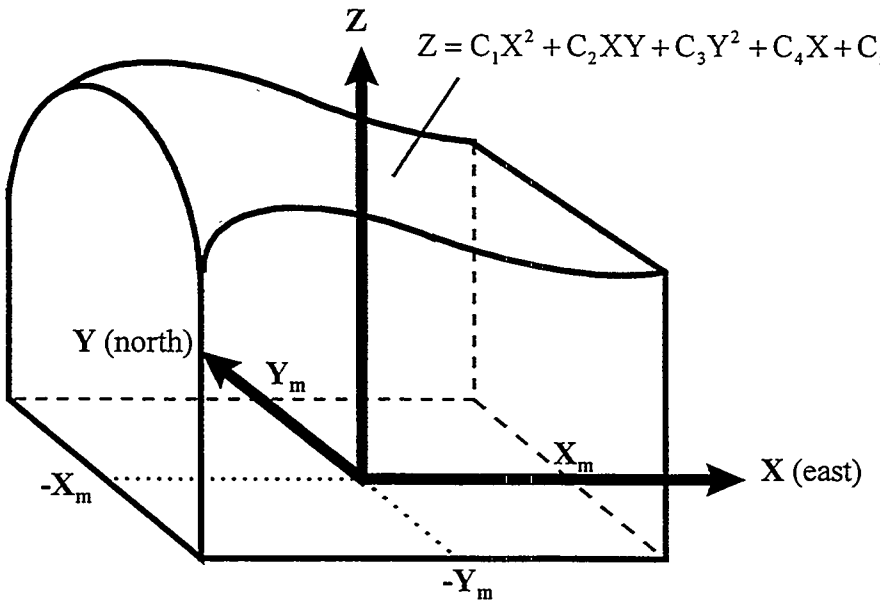

The top boundary may represent, for example, the topographic surface.

Intensity of the Poisson Plane Network

The number of planes in the primary process is a Poisson number which is related to the modeled fracture intensity (discussed in more detail in Section 3.1.2.2). In summary, a homogeneous Poisson plane network of intensity μ corresponds to a Poisson point process in the region:

$$\{(d,\theta,\phi): -\infty < d < \infty, 0 \le \theta \le \pi, 0 \le \phi \le \pi\} \tag{3-3}$$

with non-homogeneous intensity function of the type:

$$\mu(d,\theta,\phi) = \mu f_{\theta,\phi}(\theta,\phi) \tag{3-4}$$

where $f_{\theta,\phi}$ is the joint PDF of θ and ϕ and μ is a positive constant (Veneziano, 1978).

The ordered distances from an arbitrary point to the planes of a Poisson network with intensity μ define a Poisson point process on a line with intensity 2μ (Miles 1969; Veneziano, 1978). The expected number of planes, $E(N_p)$ that intersect a sphere of radius R is therefore:

$$E[N_p] = 2\mu R = 2\mu R \tag{3-5}$$

The expected number of Poisson planes that intersect a 3D region of irregular shape is theoretically expressed by Miles (1969) as a function of the surface area of the region.

3.1.2.2 Modeling of Fracture Intensity: Primary and Secondary Stochastic Processes

In the model, fracture intensity is defined as the cumulative fractured area per unit volume of rock:

$$P_{32} = \frac{\sum_{i=1}^{N} A_{f,i}}{V} \tag{3-6}$$

where N is the total number of fractures and $A_{f,i}$ is the area of an individual fracture inside the volume V (P_{32} is notation after Dershowitz and Herda 1992 who defined various measures of fracture intensity). For statistical modeling of a system that consists of a large number of fractures, P_{32} is the best intensity measure for two reasons: (1) it represents the two-dimensional nature of fractures, and (2) it does not depend on the size and shape of the region (as long as the fractures are smaller than the region itself). Fracture intensity, modeled by the combined primary and secondary processes, incorporates fracture size distribution and cumulative fracture area.

A random subdivision of the planes, generated by the primary process, into a fractured region and its complementary region of intact rock constitutes the basis of the secondary process. This subdivision is accomplished by a Poisson line tessellation on every plane and a process of marking the so-created polygons as fractured or intact rock (Figure 3-2b). The secondary process produces sets of fractures that have a certain size and shape variation and are arranged in clusters.

The model incorporates fracture intensity algorithms that are based on previously published second and first moments of Poisson plane and line processes (Miles 1973; Veneziano, 1978), and some geometric properties of the population of polygons, established by numerical simulations. The rest of Section 3.1.2.2 presents in detail the application of Poisson point, line and plane processes for modeling of fracture intensity (defined by Equation 3-6) through generation of populations of polygon-fractures with desired size and shape variation.

Poisson Line Tessellation

In the local 2D frame of reference O'x'y' on a plane, a line from the Poisson network is defined as:

$$x'\cos\alpha + y'\sin\alpha = D \tag{3-7}$$

in terms of an angle α on A, measured counterclockwise from the axis O'x', and a distance D from the origin O' to the line (Figure 3-6).

Figure 3-6 Secondary Stochastic Process: Generation of a Poisson Line

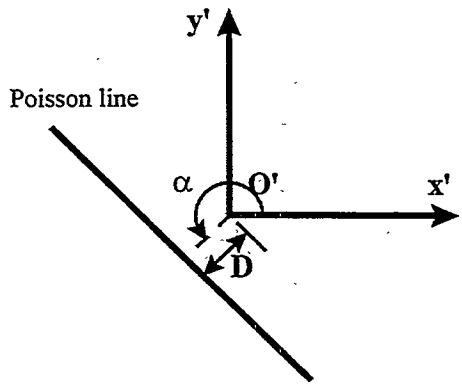

A homogeneous Poisson line network with intensity λ corresponds to a Poisson point process in the region:

$$\{(D,\alpha): 0 \le D \le \infty, 0 \le \alpha \le 2\pi\} \tag{3-8}$$

with intensity function of the points of the type:

$$\lambda(D,\alpha) = \lambda f_\alpha(\alpha) \tag{3-9}$$

where λ is a positive constant and $f_\alpha(\alpha)$ is the PDF of α in (0, 2π). The ordered distances from an arbitrary point on the plane to the lines of a Poisson line network with intensity λ form a Poisson point process with intensity 2λ (Miles, 1973; Veneziano, 1978). The expected number of lines that intersect a circle of radius R is 2λR. The expected number of Poisson lines that intersect a 2D region of irregular shape is theoretically expressed by Miles (1973) as a function of the perimeter of the region.

The points of intersection of all pairs of lines determine the vertices of polygonal tiles. First and second moments of the polygons created by a Poisson line tessellation of intensity λ are summarized in Table 3-1.

Table 3-1 Theoretical Statistics of Polygons Obtained Through a Poisson Line Tessellation with Intensity λ (after Miles 1973, and Veneziano, 1978)

Geometric Property	Mean	Variance, covariance	
		N	A
Number of vertices, N	4	$\frac{(\pi^2-8)}{2}$	$\frac{\pi(\pi^2-8)}{2\lambda^2}$
Polygon area, A	$\frac{\pi}{\lambda^2}$	$\frac{\pi(\pi^2-8)}{2\lambda^2}$	$\frac{\pi^2(\pi^2-2)}{2\lambda^4}$

The standard deviation of polygon areas can be calculated as:

$$\sigma_A = \sqrt{\text{var}[A]} = \sqrt{\frac{\pi^2(\pi^2-2)}{2\lambda^4}} = \sqrt{\frac{\pi^2-2}{2}}\left(\frac{\pi}{\lambda^2}\right) \approx 1.98E[A] \tag{3-10}$$

Polygon marking procedure and distribution of fracture sizes and shapes

The process of dividing each plane into a fractured region and its complementary region of intact rock is homogeneous in a statistical sense. The probability of marking a polygon as fractured, P_f, is calculated individually for every polygon:

$$P_f = P_f(size, shape, location) \tag{3-11}$$

It can be expected that, if only polygons with certain shapes are retained as possible fractures, the mean and variance of their areas will be different from those of the entire population of polygons created by a Poisson line tessellation. For example, analysis according to the Best Linear Unbiased Estimation (BLUE) theory calculates conditional mean and variance of the areas, A, of polygons that have a certain number of vertices, N=n, as:

$$\begin{aligned} E[A|N=n] &\cong E[A] + \frac{\text{cov}[A,N]}{\text{var}[N]}(n - E[N]) \\ \text{var}[A \mid N=n] &\cong \text{var}[A]\left(1 - \frac{(\text{cov}[A,N])^2}{\text{var}[N]\text{var}[A]}\right) \end{aligned} \tag{3-12}$$

According to the BLUE formula, the mean area of the polygons with five vertices, created by a Poisson line tessellation of intensity λ, is:

$$E[A \mid N=5] \approx \frac{\pi}{\lambda^2} + \frac{\frac{\pi(\pi^2-8)}{2\lambda^2}}{\frac{(\pi^2-8)}{2}}(5-4) = \frac{\pi}{\lambda^2} + \frac{\pi}{\lambda^2} = 2\frac{\pi}{\lambda^2} = 2E[A] \tag{3-13}$$

Similarly, E(A|N=6)=3E(A), E(A|N=7)=4E(A), etc. Although the analysis is approximate, it illustrates an important characteristic of the polygonal shapes created by a Poisson line tessellation: that larger polygons tend to have more vertices. Larger polygons also tend to have larger angles, since the mean angle of an n-sided polygon is $\pi(n-2)/n$.

In the 3D model, only polygons that have shapes similar to that of natural fractures are retained from the population of polygons created by a Poisson line tessellation. The shape of a "good" polygon is that of a typical non-elongated natural fracture which is here defined as follows:

- the polygon is convex and has at least four vertices;
- all angles are at least $\pi/3$ (60°);
- the polygon elongation (as defined in Figure 3-1) is not more than 1.6 (modeling of elongated shapes is discussed by Ivanova, 1995).

Based on the BLUE analysis above, one can conclude that larger polygons are more likely than smaller ones to be retained as potential fractures. Figure 3-7 compares the size distribution of 84191 polygons obtained by a Poisson line tessellation, to the size distribution of 14378 polygons marked as "good" in the simulation. The Poisson line tessellation creates a large number of small polygons. The polygon size PDF has a "long tail": a small number of polygons with large areas are widely spread in the range above the mean E(A). The PDF of the sizes of "good" polygons has a similar shape, but a much lower peak in the range of the smallest polygon sizes. The polygon size distributions in Figure 3-7 were obtained through numerical simulations of the Poisson line tessellation, in which the desired mean area E(A) of all polygons was given as input and the line intensity λ was calculated as:

$$\lambda = \sqrt{\frac{\pi}{E[A]}} \tag{3-14}$$

Since most of the polygons, discarded in the shape marking process have small sizes, the expected area of "good" polygons is larger than the expected area of the entire population of polygons created by a Poisson line network. Table 3-2 summarizes the relationship of the sizes of "good" polygons (including mean, standard deviation, median, and cumulative area) to the intensity λ of the Poisson line tessellation.

Two correction coefficients best express the relationship of the areas of "good" polygons to the intensity of the underlying Poisson line tessellation:

the ratio C_A of the mean area of "good" polygons to the mean area of all polygons produced by a tessellation with intensity λ;

the ratio $\gamma = A'_T / AT$, where A'_T is the sum of the areas of all "good" polygons that are created within a finite region of total area AT by a Poisson line tessellation of intensity λ.

a) Number of plygons vs. normalized polygon area

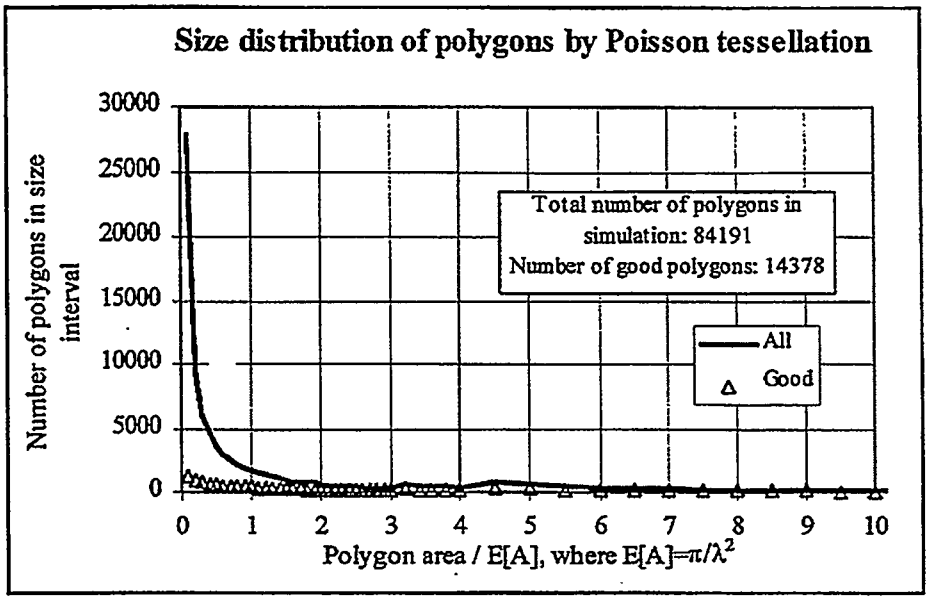

b) Normalized number of polygons vs. normalized polygon area

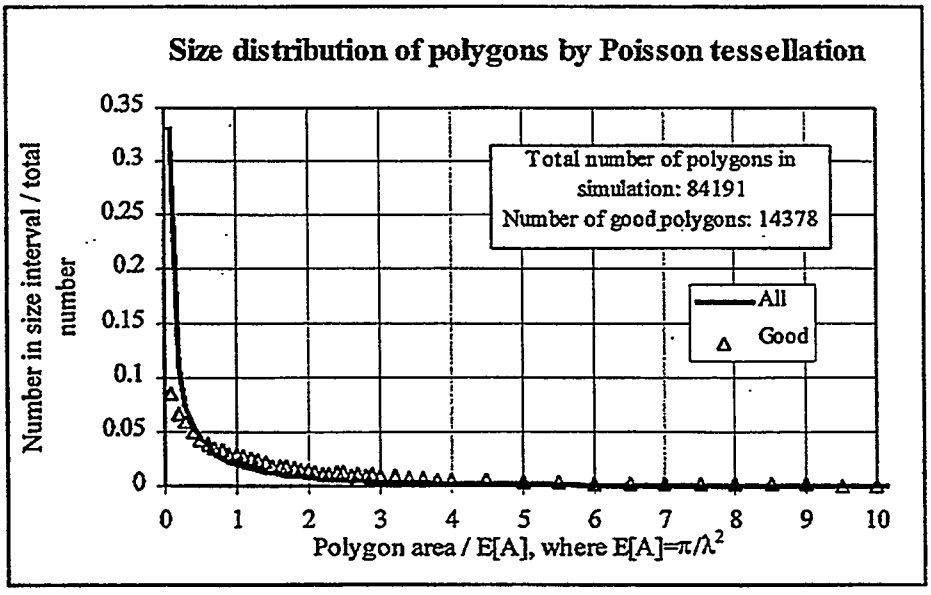

FIGURE **3-7**
DISTRIBUTIONS OF AREAS OF ALL POLYGONS AND "GOOD" POLYGONS OBTAINED THROUGH A POISSON LINE TESSELLATION OF INTENSITY λ
NIPER/FINAL REPORT/WA

Table 3-2 Statistics of the Distribution of Areas of "Good" Polygons (i.e., polygons with fracture-like shapes), Produced by a Poisson Line Tessellation of Intensity λ in a Region With Total Area A_T

Statistical Property	Value Based on Simulations
Mean fracture area, $E[A']$	$E[A'] = C_A \frac{\pi}{\lambda^2}$, where C_A=2.2
Standard deviation of fracture area, $\sigma_{A'}$	$\sigma_{A'} = 1.4E[A']$
Median of fracture area, $M_{A'}$	$M_{A'} = 0.5E[A']$
Cumulative fracture area, A'_T	$A'_T = \gamma A_T$, where γ=0.4

Theoretically, the coefficients C_A and γ do not depend on the intensity λ of the Poisson line network but only on the rule by which polygons are marked as "good" (Veneziano, pers. Comm.). Therefore, the coefficients C_A=2.2 and γ=0.4, given in Table 3-2, are valid for any intensity λ of the Poisson lines, as long as "good" polygons are marked according to the three rules listed above.

Figure 3-8 illustrates the fit of a Gamma distribution, $\Gamma(\alpha, \beta)$, to the distribution of sizes (areas) of "good" polygons generated with a Poisson line tessellation. In the empirical PDF, the polygon size intervals on the abscissa are normalized by the mean area of "good" polygons, whereas on the ordinate the number of polygons in each size interval is normalized by the total number of "good" polygons in the simulation. The coefficients α and β of the Gamma distribution are calculated so that the mean, m_Γ, and variance, σ_Γ^2, are equal to the mean and variance of the empirically obtained normalized PDF of "good" polygon areas (see Table 3-2):

$$\left.\begin{aligned} m_\Gamma &= \alpha\beta = 1.0 \\ \sigma_\Gamma^{\,2} &= \alpha\beta^2 = (1.4)^2 \end{aligned}\right\} \Rightarrow \begin{aligned} \alpha &= 0.51 \\ \beta &= 1.96 \end{aligned} \qquad (3\text{-}15)$$

The distribution of polygon sizes, illustrated in Figure 3-8 and described in Table 3-2, is representative of natural fracture systems in the sense that they usually include few large fractures and many small fractures. However, in many cases one may want to represent a smaller variation of fracture sizes (i.e., a smaller standard deviation $\sigma_{A'}$ of sizes of "good" polygons). In order to do so, the model currently implements a simple procedure of marking "good' polygons not only by shape, but also according to their size relative to the mean equivalent radius of "good" polygons $E[R'_e]$, and relative to the mean polygon area E[A] of the underlying Poisson line tessellation. Table 3-3 summarizes statistics of the PDF of areas of "good" polygons obtained through a Poisson line tessellation and different shape-and-relative-size marking processes (for comparison, the characteristic values for the marking process only by shape are also shown).

a) PDF of polygon areas

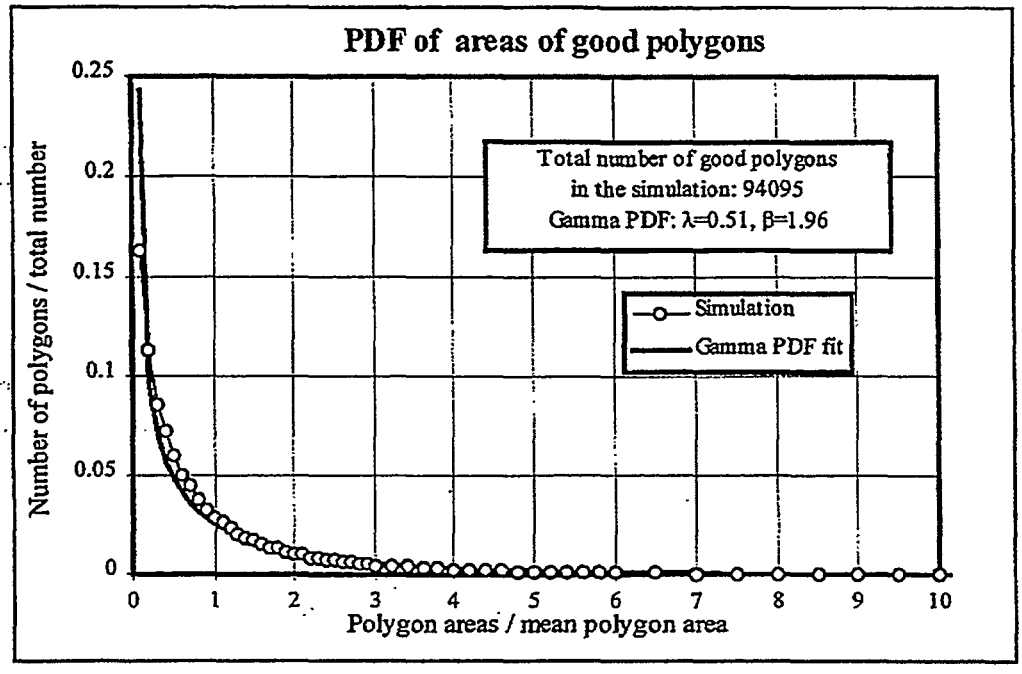

b) Cumulative PDF of polygon areas

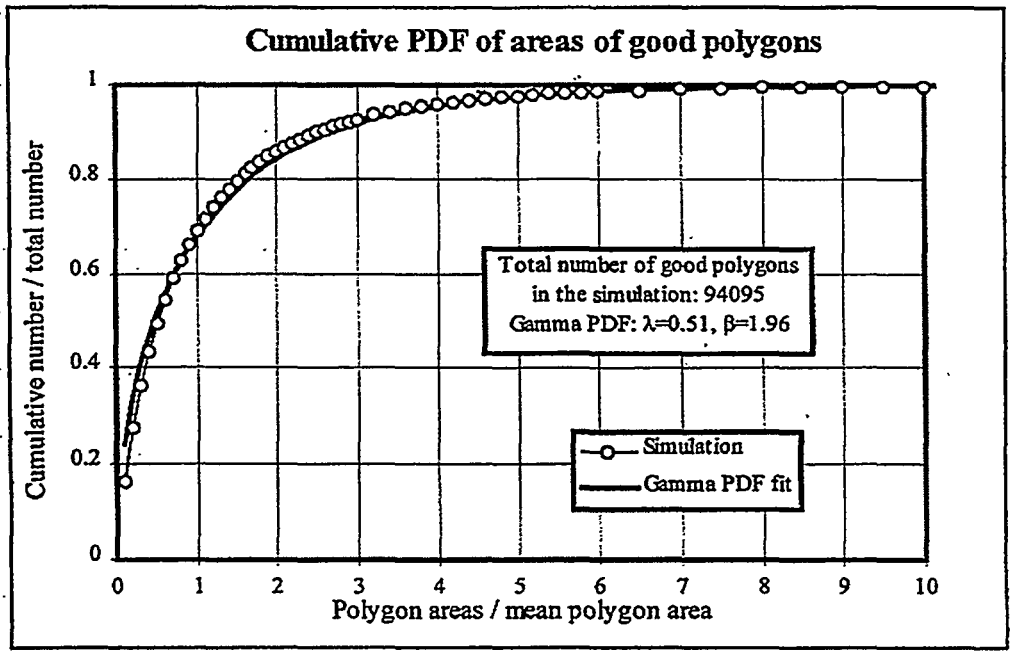

FIGURE **3-8**
EMPIRICAL DISTRIBUTION OF AREAS OF "GOOD" POLYGONS OBTAINED THROUGH A POISSON LINE TESSELLATION, AND A FIT OF GAMMA PDF
NIPER/FINAL REPORT/WA

PROJECT NO. 963 1357.521 DRAWING NO. 80691 DATE 9/25/98 DRAWN BY EA

Golder Associates

Applying a marking rule according to relative polygon size essentially leads to truncation of the size PDF, hence to a decrease in the spread of sizes of the remaining polygons, i.e., to a smaller $\sigma_{A'}$. As Table 3-3 shows, the correction coefficients C_A and γ are different for different marking rules. Theoretically, as long as the marking is only according to shape and relative size, the coefficients C_A and γ are independent of the intensity λ of the Poisson line tessellation. A marking process according to relative size of polygons leads to decrease of the cumulative fractured area on a plane (i.e., a smaller coefficient γ). The maximum possible value in the current version of the model is $\gamma = 0.4$ (corresponding to marking of all "good" polygons). This value of γ represents the maximum possible intensity of coplanar fractures on a given plane that can be reproduced with the model.

Table 3-3 Statistics of "Good" Polygons, Marked by Shape and Relative Size, Obtained Through a Poisson Line Tessellation of Intensity λ in a Finite Region With Total Area A_T

Marking Rule	$C_A = \frac{E[A']}{E[A]}$	$\gamma = \frac{\sum_{i=1}^{N} A'_i}{A_T}$	$\frac{\sigma_{A'}}{E[A']}$	$\frac{M_{A'}}{E[A']}$
All with good shape	2.2	0.4	1.4	0.5
$A'_i > E[A]$	3.6	0.36	0.93	0.7
$A'_i > 2E[A]$	5.0	0.30	0.74	0.75
$R'_{e,i} < 3E[R'_e]$	1.8	0.38	1.26	0.6
$R'_{e,i} < 2E[R'_e]$	1.4	0.23	0.96	0.7
$A'_i > E[A]$, $R'_{e,i} < 3E[R'_e]$	3.6	0.36	0.90	0.8
$A'_i > E[A]$, $R'_{e,i} < 2E[R'_e]$	3.4	0.36	0.72	0.75

E(A)=$\pi/\lambda 2$: theoretical mean area of all polygons; N: total number of "good" polygons; $E[A']$, $\sigma_{A'}$, and $M_{A'}$: expected value, standard deviation, and median, respectively, of the areas of "good" polygons; A'_i and $R'_{e,i}$: area and equivalent radius (radius of a circle with area equal to A'_i) of the I-th "good" polygon; $E[R'_e]$: expected value of the equivalent radius of "good" polygons.

Poisson Plane Network Intensity and Total Fracture Area in the Modeling Volume

In order to obtain the expected value of fracture intensity P_{32} (Equation 3-6), one needs to know not only γ but also the expected value of the cumulative total area $\sum A_{T,i}$ that is cut from a volume V by a Poisson network of planes with intensity μ. Figure 3-9 illustrates the derivation of the $\sum A_{T,i}$ for a sphere. The plane at a random distance d_i cuts from the sphere with radius R a circle with radius:

$$r_i = \sqrt{R^2 - d_i^2} \qquad (3\text{-}16)$$

and area:

$$A_{T,i} = \pi r_i^2 = \pi\left(R^2 - d_i^2\right) \tag{3-17}$$

The expected area $E(A_T)$ of a circle cut by a Poisson plane from a sphere of radius R can be calculated as:

$$E[A_T] = \int_0^R pdf(d)\pi\left(R^2 - d^2\right)dd = \int_0^R \frac{1}{R}\pi\left(R^2 - d^2\right)dd = \pi\frac{1}{R}\frac{2}{3}R^3 = \frac{2}{3}\pi R^2 \tag{3-18}$$

Figure 3-9 Derivation of Total Fractured Area in a Sphere

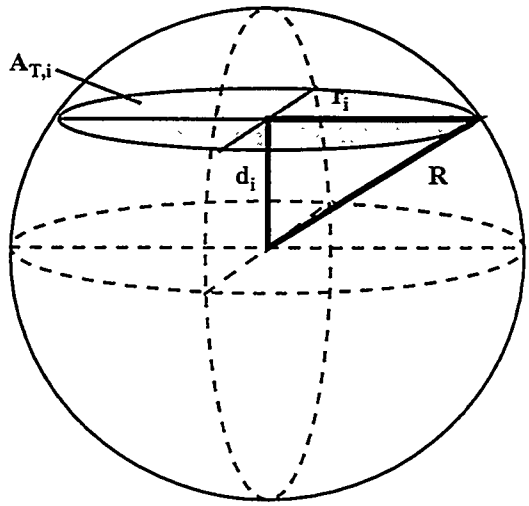

where pdf(d)=1/R is the probability density function of d. Using Equations 3-5, 3-6, and 3-18, the expected cumulative area of potential fractures per unit volume (equal to the fracture intensity P_{32}) is:

$$E\left[\frac{\sum A_{f,i}}{V}\right] = P_{32} = \frac{E[N_p]\gamma E[A_T]}{V} = \frac{2\mu R\gamma E[A_T]}{V} = \frac{2\mu R\gamma\frac{2}{3}\pi R^2}{\frac{4}{3}\pi R^3} = \gamma\mu \tag{3-19}$$

The expected cumulative area of polygon-fractures per unit volume does not depend on R, i.e., it is independent of the shape and size of the total volume in which the Poisson plane process is generated. Therefore the modeled fracture intensity P_{32} only depends on the intensity of the Poisson line network μ and on the rule by which polygons are marked as potential fractures.

If the fracture sizes are comparable to the size of the region of interest, truncations of fractures by the boundaries of the region would affect the coefficient γ, and hence the

geometric property described by Equation 3-19. In such a case, if one uses this stochastic model, the fracture system needs to be generated in a modeling volume much larger than the region of interest. However, it is important to know the exact locations of fractures as large as or larger than the region of interest. Therefore, it is recommended that they are not stochastically generated, but deterministically established if at all possible.

Zone Marking of Polygons and Varying Fracture Intensity in Space

There are two ways to obtain a smaller percentage γ^* of the potentially fractured planes (i.e., a lower percent of coplanar fractures). One can either use the tertiary stochastic process (Section 3.1.2.3), or mark the "good polygons" with a probability P such that:

$$\gamma^* = P\gamma \tag{3-20}$$

where $0<P<1$.

Then a Poisson plane network with intensity $\mu^*=\mu/P$ preserves the fracture intensity:

$$E\left[\frac{A_{Tf}}{V}\right] = \gamma\mu = \gamma P\frac{\mu}{P} = \gamma^*\mu^* \tag{3-21}$$

In the model, the probability of marking a polygon as fractured can be a function of the distance to some specified cluster centers, for example, other fractures or local faults (Figure 3-10). A zone is defined by the maximum and minimum value of the distance from the face of a polygon-fracture to the face of another polygonal feature. Within every zone j the zone probability P_j is constant, but that constant is generally different in different zones. Polygons in zone j are retained with probability P_j and discarded with probability $1- P_j$. To obtain different fracture intensity within the same fracture set in different portions V_1, V_2, etc. of the volume V, one has to calculate the different probabilities P_1, P_2, etc. for polygon marking in the different regions. Volume V_i does not have to be continuous; it can be defined as a function of any continuous rock property. For example, V_i may be defined as "the regions where the fractures of the set are at a distance not more than L" from the fractures of a primary set or from a fault face. Alternatively, V_i can be defined as "the regions where the rock is dolomite" or "the regions where the porosity of the rock is not more than n%", etc. It is only the intensity of fractures, and not the orientation that can be controlled by the marking probability process. Any marking according to polygon orientation would affect the function $f_{\theta,\phi}(\theta,\phi)$ in Equation 3-4 and the constant μ itself.

Figure 3-10 Secondary Stochastic Process: Definition of Fracture Zones and Zone Marking Probability

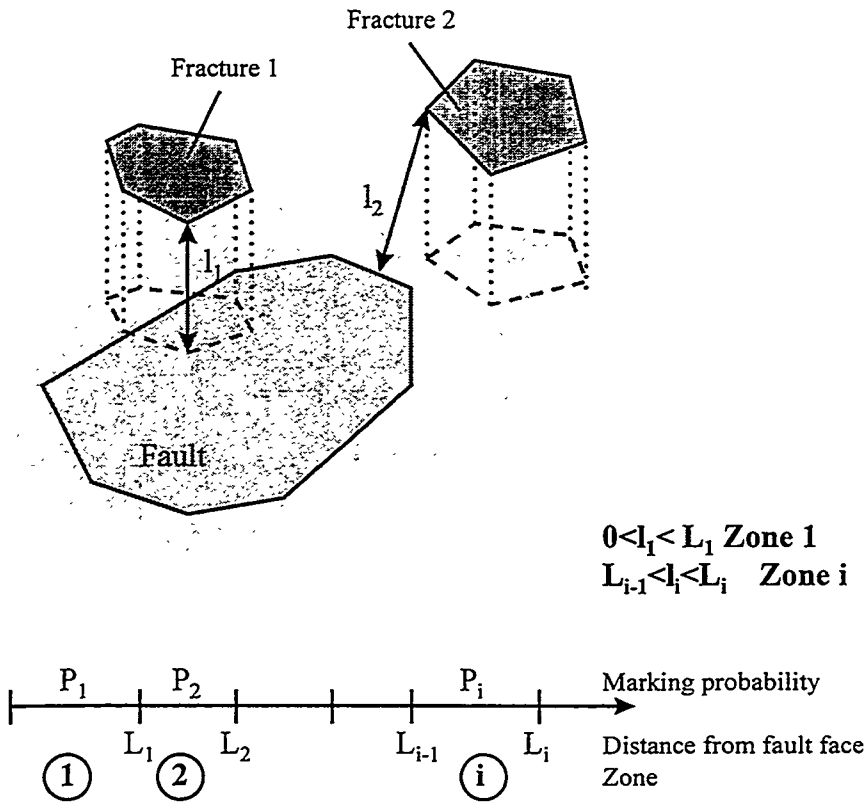

Figures 3-11 and 3-12 illustrate examples of varying fracture intensity in space, generated using the 3D hierarchical model. Figure 3-11a illustrates a fracture network with higher intensity in the vicinity of a fault. Figure 3-11b shows the relative locations of the fault, and two outcrop planes: vertical and horizontal. Figures 3-11c and d depict the trace outcrops of the fracture network on the horizontal and vertical outcrop planes, respectively. Figure 3-12 illustrates the trace outcrops of two fracture systems: one exists only in a layer enclosed between two bedding surfaces but not in the surrounding rock (Figure 3-12a); the other one has higher intensity in the rock below a bedding plane than above it (Figure 3-12b).

Summary of Fracture Intensity Modeling

In summary, desired fracture intensity is modeled in the following order:

1. Desired mean fracture size $E[A']$, fracture intensity $P_{32,i}$ in various regions V_i and the extent of those regions are given as input.

2. The intensity of the Poisson plane process is calculated as $\mu = P_{32,max}/\gamma$.

a) 3D fracture system

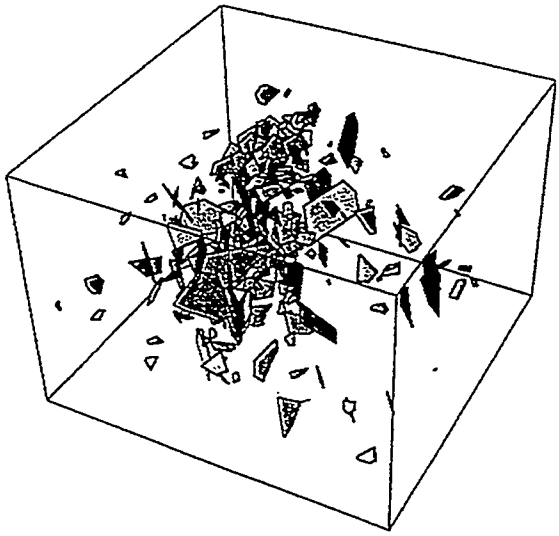

b) Fault and outcrop

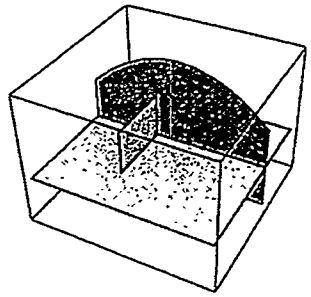

c) Horizontal trace outcrop

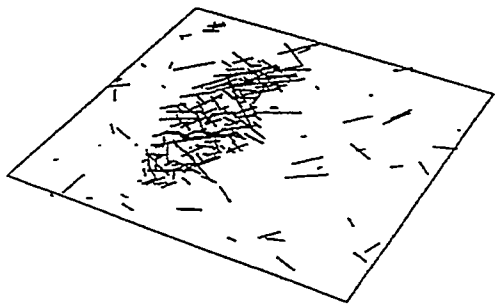

d) Vertical trace outcrop

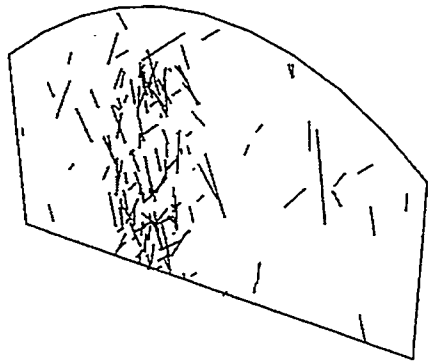

FIGURE **3-11**
FRACTURE SYSTEM WITH HIGHEST INTENSITY NEAR A FAULT
NIPER/FINAL REPORT/WA

PROJECT NO. 963 1357.521 DRAWING NO. 80692 DATE 9/25/98 DRAWN BY EA

Golder Associates

a) 3D view and vertical outcrop of a fracture system that exists only in one layer

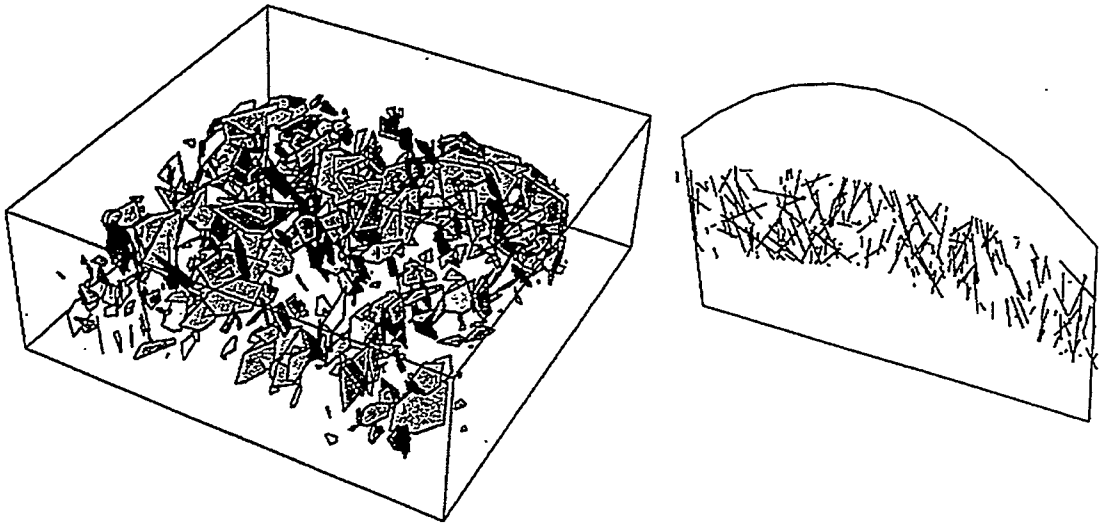

b) Vertical outcrop of a fracture system with intensity increasing with depth

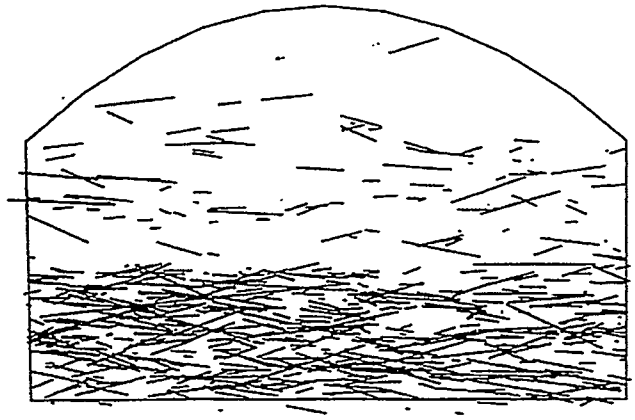

FIGURE **3-12**
FRACTURE SYSTEM WITH DIFFERENT INTENSITY IN DIFFERENT LAYERS
NIPER/FINAL REPORT/WA

PROJECT NO. 963 1357.521 DRAWING NO. 80693 DATE 9/25/98 DRAWN BY EA

Golder Associates

3. Poisson planes are generated in the total volume V.

4. The expected polygon area of the Poisson line network is calculated as $E[A] = E[A'] / C_A$.

5. Poisson line tessellation with intensity $\lambda=(\pi/E[A])^{1/2}$ is generated on the planes.

6. The probability of marking "good polygons" is calculated as $P_i=P_{32,i}/P_{32,max}$.

7. Polygons with bad shapes are discarded and polygons with good shapes are marked as fractures (with probability P_i in region V_i).

The above algorithm ensures that the expected value of the intensity of the fracture set will be the desired intensity P_{32} (or $P_{32,i}$ in regions V_i, respectively).

3.1.2.3 Modeling of Stress Field Variation: Tertiary Stochastic Process

The translation procedure of the tertiary stochastic process (Figure 3-2c) controls the ratio of coplanar fractures and fractures that are parallel but not coplanar. The rotation algorithm (Figure 3-2c) represents possible deviations of fracture orientations from the regional directions due to variations of the stress field near local geologic structures.

Random Polygon Translation

In the tertiary stochastic process translation is performed in the frame of reference of the fracture plane (O'x'y'z' in Figure 3-3). Translation is accomplished by assigning a non-zero coordinate z'_i to the center and the vertices of a polygon and hence to the entire polygon. The algorithm, currently implemented in the model, allows for translation of a polygon at a maximum distance:

$$dz'_{max} = C \frac{E[R'_e]}{R'_e} E[R'_e] \qquad (3\text{-}22)$$

where R'_e is the equivalent radius of a "good" polygon, and $E[R'_e]$ is the expected value of that radius. Thus larger polygons are shifted closer to their original positions than smaller polygons. C in Equation 3-22 is a coefficient of fracture coplanarity: the smaller C, the more coplanar fractures can be expected. Figure 3-13 illustrates the effect of increasing C to decrease the coplanarity of fractures. The fracture systems shown on horizontal outcrops in Figure 3-13a and b are statistically the same (in terms of P_{32}, mean size, orientation, etc.); only C in Figure 3-13b is higher, hence there are fewer coplanar fractures.

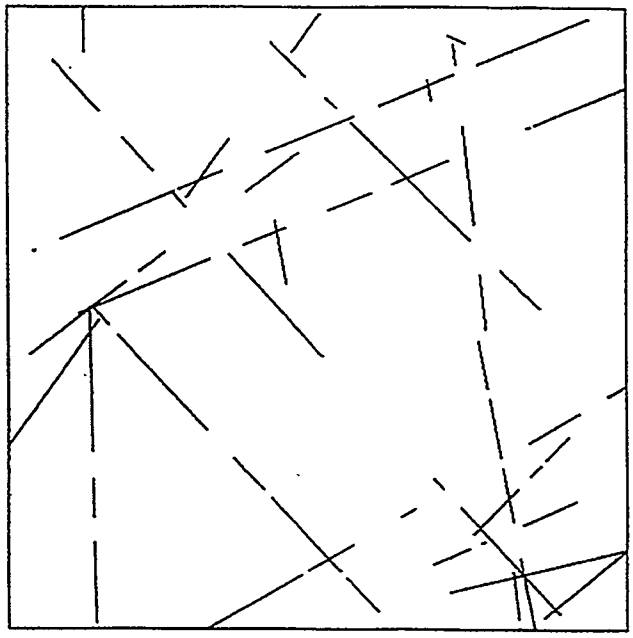

a) Trace outcrop of coplanar fractures, C = 0

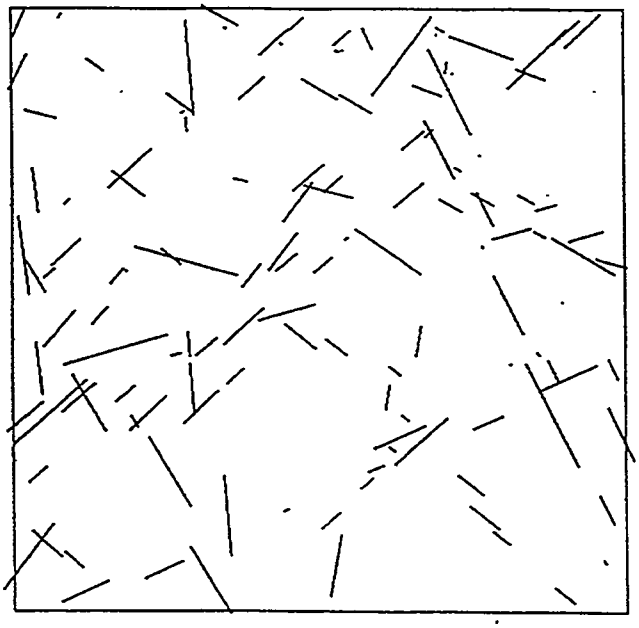

b) Trace outcrop of non-coplanar fractures,
C = 0.5, coefficient of coplanarity

FIGURE **3-13**
TERTIARY STOCHASTIC PROCESS, TRANSLATION OF POLYGONS
NIPER/FINAL REPORT/WA

PROJECT NO. 963 1357.521 DRAWING NO. 80694 DATE 9/25/98 DRAWN BY EA

Golder Associates

Random polygon rotation

The random rotation of polygons in the tertiary process is used for cases when the local conditions modify the stress field so much that the most likely fracture orientation deviates from the most likely orientation defined by the general stress field. The algorithm, currently implemented in the model, checks the orientations of numerically generated polygons against a specified relation of the real fracture orientations to the geologic structures, bedding planes, or other features that may influence the direction of fracture propagation. Figure 3-14 illustrates the rotation process. In Figure 3-14a the fracture system is generated with intensity P_{32} through superposition of two sub-vertical sets: one striking NW, and another one striking NE. In Figure 3-14b, after rotation, the fractures strikes are concentric or radial to a circular dome with apex in the center of the rectangular area. Rotation preserves the fracture intensity P_{32} of the set. The rotation process is discussed in detail in Section 3.1.3.2 in the context of fold-related fractures.

3.1.3 Fracture System Modeling

3.1.3.1 General HFM Model Algorithm

In the HFM, a fracture system is reproduced by superposition of independent and dependent fracture sets. Two fracture sets can be considered independent of one another and reproduced as such if the inferred statistics of the first set are not related to the statistics of the second set. Each independent set is modeled with the stochastic sequence, described in the previous section (therefore there is a correlation between the geometric characteristics of its members). The same three stochastic processes generate a dependent fracture set. Dependence on previously generated sets can be obtained in many ways; for example, the zone probability can be defined as a function of the distance to primary fractures. Also, dependence can be obtained by defining a function for termination of fractured polygons from the secondary set at the intersections with fractures from the primary set.

Figure 3-15 shows a fracture system, generated by superposition of two sets: Set 1 (blue), an independent set of large, sub-horizontal primary fractures, and Set 2 (yellow), a dependent set of smaller, sub vertical secondary fractures, produced in the vicinity of Set 1. Figure 3-15 illustrates the capability of the model to represent fracture clustering by assigning appropriate zone probabilities. In the generation of Set 2, a zone function has been defined so that the closer a polygon is to a fracture from Set 1, the higher the probability is that the polygon will be marked as fractured.

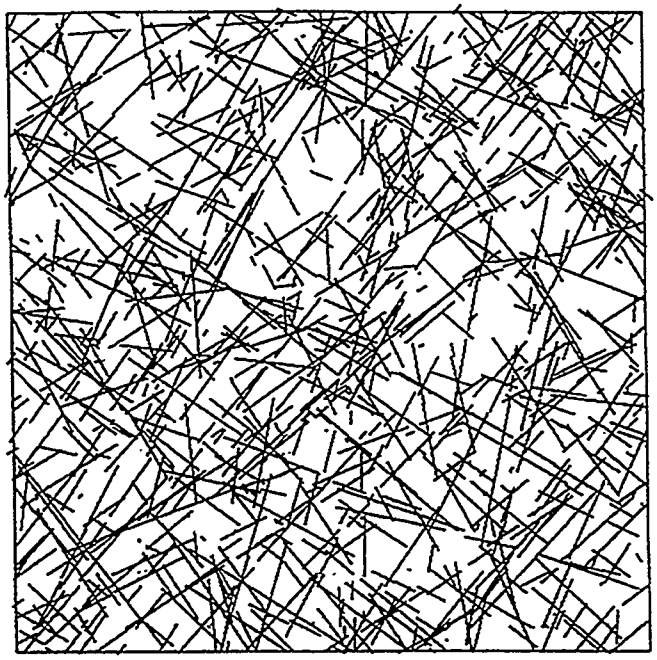

a) Trace outcrop of fractures with orientations related to the general stress field directions

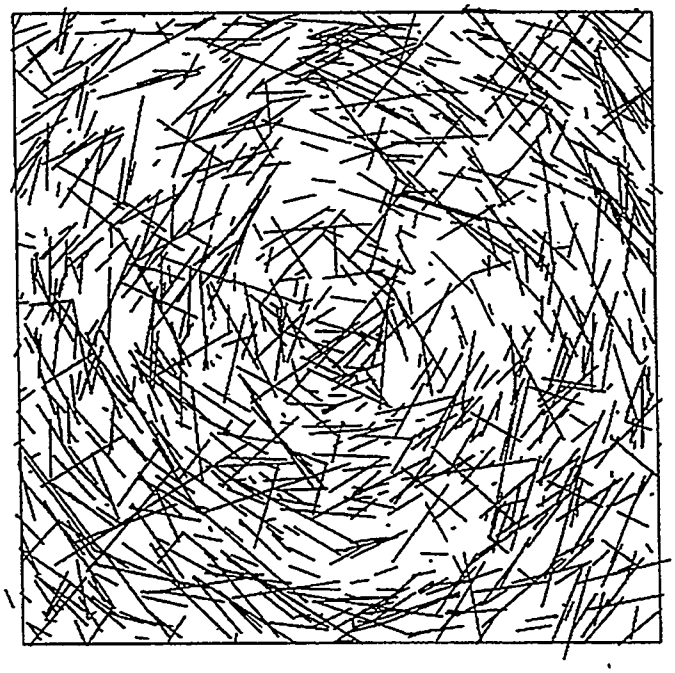

b) Trace outcrop of the fractures from (a) with their orientations related also to a circular dome

FIGURE **3-14**
TERTIARY STOCHASTIC PROCESS, ROTATION OF POLYGONS
NIPER/FINAL REPORT/WA

PROJECT NO. 963 1357.521 DRAWING NO. 80695 DATE 9/25/98 DRAWN BY EA

Golder Associates

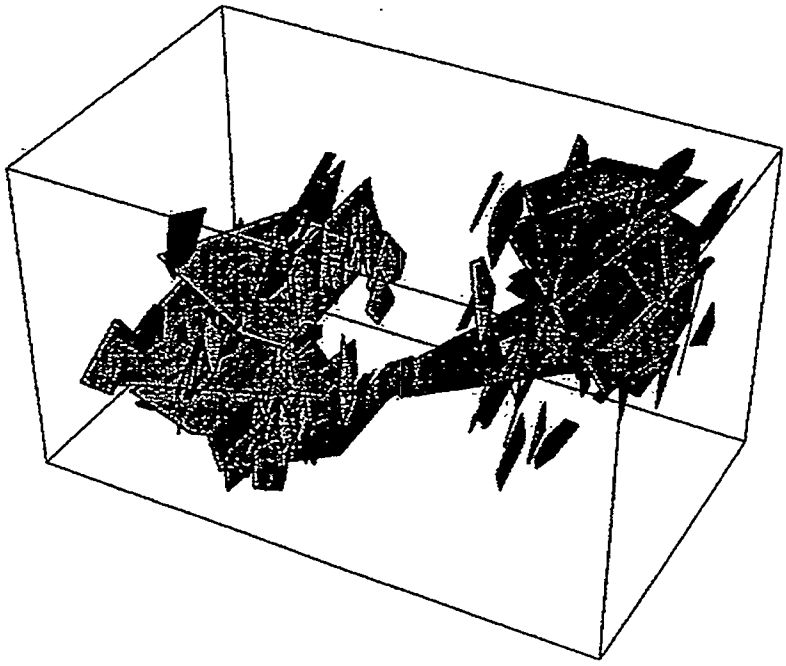

FIGURE **3-15**
FRACTURE SYSTEM MODELING VIA SUPERPOSITION OF HIERARCHICALLY RELATED FRACTURE SETS
NIPER/FINAL REPORT/WA

PROJECT NO. 963 1357.521 DRAWING NO. 80696 DATE 9/25/98 DRAWN BY EA

Golder Associates

The rest of Section 3.1.3 presents specific algorithms that can be used for representation of rock fracture systems in the major geologic environments: folds (Section 3.1.3.2), crustal faults (Section 3.1.3.3), remote tension (Section 3.1.3.4), and central structures (Section 3.1.3.5). The recommended methods for representation of the orientation variation of potential fracture planes include application of theoretical PDFs on a unit hemisphere (schematically illustrated in Figure 3-4). Sections 3.1.3.2 to 3.1.3.5 also contain suggested procedures for modeling of fracture intensity in the different geologic settings.

3.1.3.2 Fracture Systems Related to Folds

All fracture sets that form during folding are related to the curved fold surface in terms of both orientation and intensity. Therefore, the first step in modeling a fold-related fracture system is representation of the geometry of the fold itself. Currently in the 3D hierarchical model fold geometry is described by a cubic function of the type:

$$Z = c_1X^3 + c_2X^2Y + c_3XY^2 + c_4Y^3 + c_5X^2 + c_6XY + c_7Y^2 + c_8X + c_9Y + c_{10} \qquad (3\text{-}23)$$

The coefficients c_i can be derived through a polynomial fit to elevations of formation contacts of folded strata. Such elevations may be obtained, for example, from log data or from mapped exposures of folds on outcrop planes. By varying the coefficients c_i in Equation 3-23 one can represent various fold shapes. For example, if all coefficients except c_{10} and c_5 are zero, Equation 3-23 represents a cylindrical fold with vertical axial plane parallel to the global axis OY (a syncline if $c_5>0$, or an anticline if $c_5<0$).

The orientations of fractures in folded strata are related to the varying strike and dip of the fold surface. Figure 3-16 illustrates the calculation of strike and dip at a given point $P_0(X_0, Y_0, Z_0)$ on the fold surface. The coordinates of the normal vector N_f are defined by the directional first derivatives of the function F(X,Y,Z)=0, describing the fold surface:

$$\vec{N}_f = \begin{pmatrix} F_X \\ F_Y \\ F_Z \end{pmatrix} = \left.\begin{pmatrix} \frac{\partial F}{\partial X} \\ \frac{\partial F}{\partial Y} \\ \frac{\partial F}{\partial Z} \end{pmatrix}\right|_{\substack{X=X_0 \\ Y=Y_0}} = \left.\begin{pmatrix} -3c_1X^2 - 2c_2XY - c_3Y^2 - 2c_5X - c_6Y - c_8 \\ -c_2X^2 - 2c_3XY - 3c_4Y^2 - c_6X - 2c_7Y - c_9 \\ 1 \end{pmatrix}\right|_{\substack{X=X_0 \\ Y=Y_0}} \qquad (3\text{-}24)$$

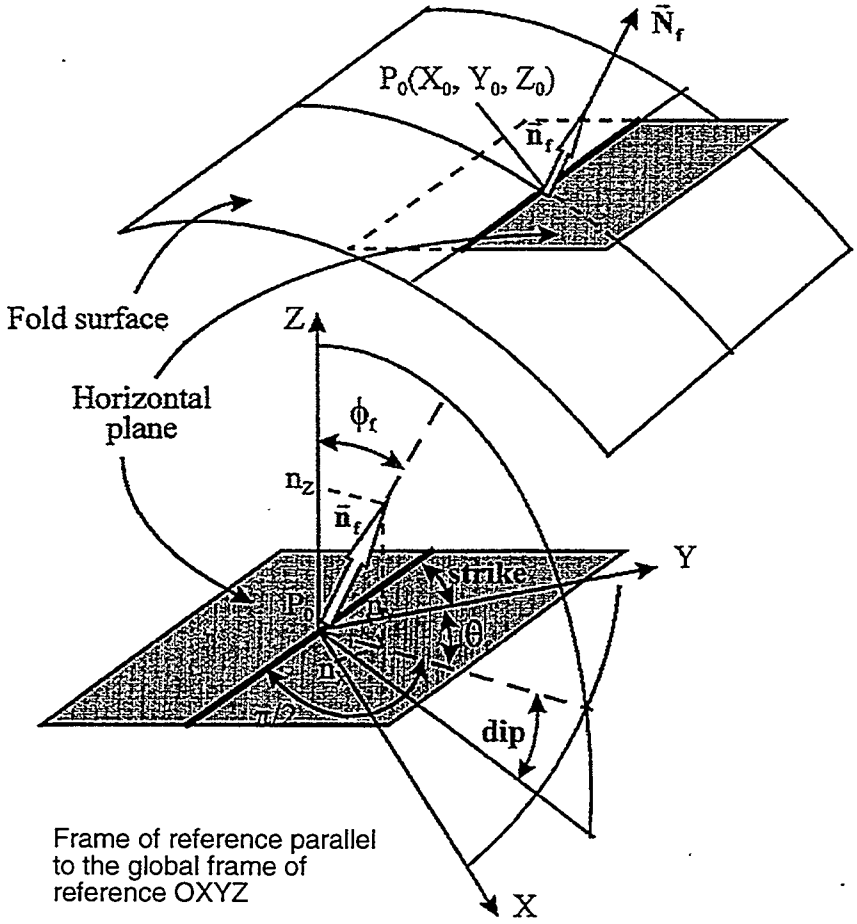

FIGURE **3-16**
CALCULATION OF LOCAL DIP AND STRIKE OF FOLD
NIPER/FINAL REPORT/WA

PROJECT NO. 963 1357.521 DRAWING NO. 80697 DATE 9/30/98 DRAWN BY EA

Golder Associates

The unit normal vector n_f at the point P_0 has coordinates:

$$\vec{n}_f = \begin{pmatrix} n_X \\ n_Y \\ n_Z \end{pmatrix} = \begin{pmatrix} \dfrac{F_X}{\sqrt{F_X{}^2 + F_Y{}^2 + F_Z{}^2}} \\ \dfrac{F_Y}{\sqrt{F_X{}^2 + F_Y{}^2 + F_Z{}^2}} \\ \dfrac{1}{\sqrt{F_X{}^2 + F_Y{}^2 + F_Z{}^2}} \end{pmatrix} \tag{3-25}$$

The strike and dip of the fold surface at point P_0 (illustrated in Figure 3-16) can be calculated as:

$$\begin{aligned} strike &= \theta_f - \frac{\pi}{2} = Arc\tan\left(\frac{n_Y}{n_X}\right) - \frac{\pi}{2} \\ dip &= \phi_f = Arc\cos(n_Z) \end{aligned} \tag{3-26}$$

To compare the orientation of a fracture-polygon to that of a fold, one can calculate the angle α between the unit normal vector of the fracture plane, $n_p = (n_{X,p}, n_{Y,p}, n_{Z,p})$, and the unit normal vector of the surface that describes the fold curvature at the polygon center, $n_f = (n_X, n_Y, n_Z)$. This angle can be calculated from the dot product of the two vectors:

$$\begin{aligned} \vec{n}_p \bullet \vec{n}_f &= \left|\vec{n}_p\right|\left|\vec{n}_f\right|\cos\alpha = (1)(1)\cos\alpha = n_{X,p}n_X + n_{Y,p}n_Y + n_{Z,p}n_Z \\ \alpha &= Arc\cos\left(n_{X,p}n_X + n_{Y,p}n_Y + n_{Z,p}n_Z\right) \end{aligned} \tag{3-27}$$

To compare the strike of a fracture-polygon to the local strike of a fold, one can calculate the difference α_{strike} between the angle of azimuth of the polygon, θ_p, and the angle of azimuth of the fold surface at the polygon center (θ_f in Figure 3-16):

$$\alpha_{strike} = \left|\theta_p - \theta_f\right| \tag{3-28}$$

To compare the dip of a fracture-polygon to the local dip of a fold, one can calculate the difference α_{dip} between the angle of latitude of the polygon, ϕ_p, and the angle of latitude of the fold surface at the polygon center (ϕ_f in Figure 3-16):

$$\alpha_{dip} = \left|\phi_p - \phi_f\right| \tag{3-29}$$

Once these angles are calculated, they need to be checked against the specified relationships of the fractures to the fold. For example, a small angle α in Equation 3-27 indicates that the fracture is subparallel to the fold surface. An angle α_{strike} close to 90° in Equation 3-28 means that the fracture strikes approximately orthogonal to the local fold strike (i.e., parallel to the local slope of the fold surface). An angle α_{strike} close to zero or

180° in Equation 3-28 means that the fracture strikes approximately parallel to the local fold strike (i.e., orthogonal to the local slope of the fold surface). A small angle α_{dip} in Equation 3-29 indicates that the fracture has approximately the same dip as the fold at that location.

If the orientation of a fracture-polygon does not conform to the specified relationships between fractures and fold, the polygon is rotated. For example, rotation by dip (so that the new fracture dip is subparallel to the local fold dip) is performed by assigning a new latitude angle ϕ_{new} to the polygon:

$$\phi_{new} \propto U\left[\phi_f - \delta\alpha_{dip}, \phi_f + \delta\alpha_{dip}\right] \tag{3-30}$$

where $\delta\alpha_{dip}$ is a small angle of allowed deviation of the fracture dip from the local dip of the fold. Rotation by strike is performed by assigning a new azimuth angle θ_{new} to the polygon:

$$\theta_{new} \propto U\left[\theta_f - \delta\alpha_{strike}, \theta_f + \delta\alpha_{strike}\right] + C_s \frac{\pi}{2} \tag{3-31}$$

where $\delta\alpha_{strike}$ is a small angle of allowed deviation of the fracture strike from the local strike of the fold, or from the horizontal direction orthogonal to the local strike of the fold. The coefficient C_s is either $C_s=0$ or $C_s=1.0$, depending on whether the fracture is rotated to be concentric or radial to the fold, respectively. If necessary, a completely new orientation of the fracture can be generated (in a frame of reference where the local normal vector to the fold is assumed to be the mean polar direction). After calculating the new dip or/and strike, the fracture-polygon is rotated. Rotation of a polygon means that new 3D coordinates are calculated for every vertex (formulas for rotation in the global frame of reference of the model are given in Ivanova, 1995).

In summary, the following algorithm for generation of a fracture set related to a fold by strike and/or dip is currently implemented in the model:

Primary stochastic process: fracture planes are generated according to a spherical PDF around a mean pole direction related to the fold axial plane. For example, the mean direction of tensile joints is either orthogonal to the axial plane, or parallel to the fold hinge. The mean orientation of a set of strike-slip faults is oblique to the fold axial plane. Fracture orientation variation can be modeled with Fisher PDF (assuming a large coefficient κ for subparallel fractures) or partial uniform PDF (assuming small angle ϕ_{max} for subparallel fractures). The fracture planes generated in this way are related to the general stress field: compression orthogonal to the fold axial plane.

Secondary stochastic process: the fracture planes generated with the primary process are subdivided into polygons via the tessellation and marking procedures. Different fracture intensity (hence different zone marking probability of polygons) can be assigned in strata bounded by curved surfaces which represent formation contacts. For example, in the generation of the fracture system illustrated in Figure 3-17 only polygons between two bounding surfaces have been retained. Also, the polygons that intersect either surface have been truncated and only the portions above the underlying and below the overlying surface have been retained.

Tertiary stochastic process: the strike and dip of every polygon-fracture produced with the primary and secondary processes are compared to the strike and dip of the fold surface at the center of the polygon. Fractures with orientations that do not conform to the specified relationship between the fracture set and the fold are assigned new strikes and/or dips and are rotated.

Figure 3-17 shows an example of a set of tensile joints parallel to the hinge of a cylindrical fold. Figure 3-17a illustrates the initial step in which the polygons were generated following a partial uniform PDF with mean pole orientation orthogonal to the fold axial plane. The horizontal cross section shows that the fractures strike parallel to the fold axial plane. The vertical cross section shows that the fractures are very steeply dipping. Figure 3-17b depicts the system from Figure 3-17a after rotation has been applied. The horizontal cross section has not changed much: the traces still strike parallel to the fold axial plane. However, the vertical cross section shows that the fractures are not only steeply-dipping, but also approximately orthogonal to the fold surface.

Figure 3-17 illustrates the importance of correct identification of the geologic setting before fracture modeling. The two horizontal cross sections are very similar, but the three-dimensional geometry of the systems in Figure 3-17a and b is different. If the inference procedure were based only on horizontal trace outcrops without considering the existence of a fold, it could be incorrectly assumed that all fractures were vertical and did not intersect at depth.

Because of the great variety of fracture sets related to folds, many geometric algorithms, other than the rotation described above, can be incorporated in the 3D model. Figure 3-18 schematically illustrates a simple geometric procedure for generating bedding-plane fractures in flexural folds. The contact surfaces between the beds are described by 3D functions of the type of Equation 3-23. All bedding surfaces are "unfolded" to planar polygonal regions. Then every planar region is subdivided into fractured polygons and intact zones by a Poisson line tessellation. Finally, all planar regions are transformed back to their folded shapes and the fracture centers are automatically located along the bedding surfaces.

a) Initial fractures related to the general stress field

Horizontal Cross Section

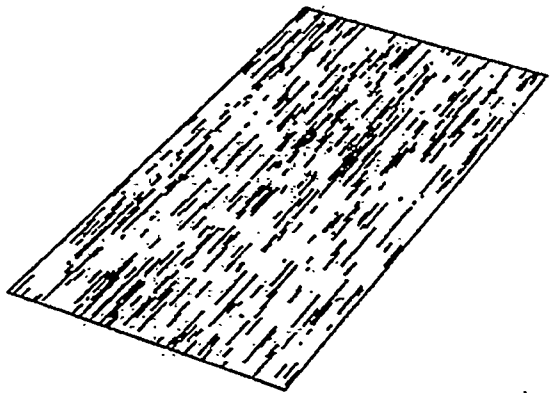

Vertical Cross Section

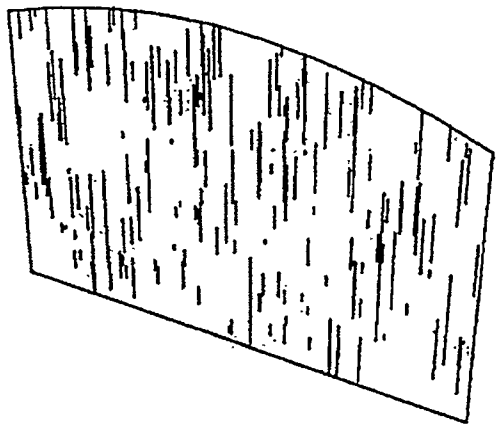

b) Rotation of fractures by dip

Horizontal Cross Section

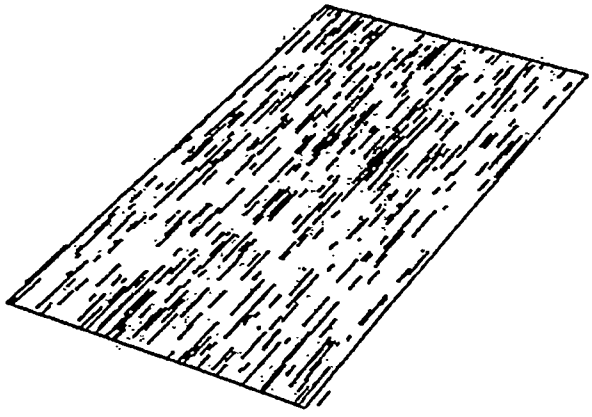

Vertical Cross Section

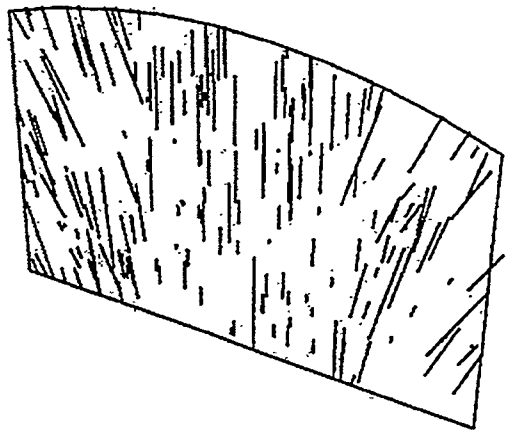

FIGURE **3-17**

SIMULATION OF A SET OF TENSILE FRACTURES PARALLEL TO THE AXIAL PLANE OF A FOLD

NIPER/FINAL REPORT/WA

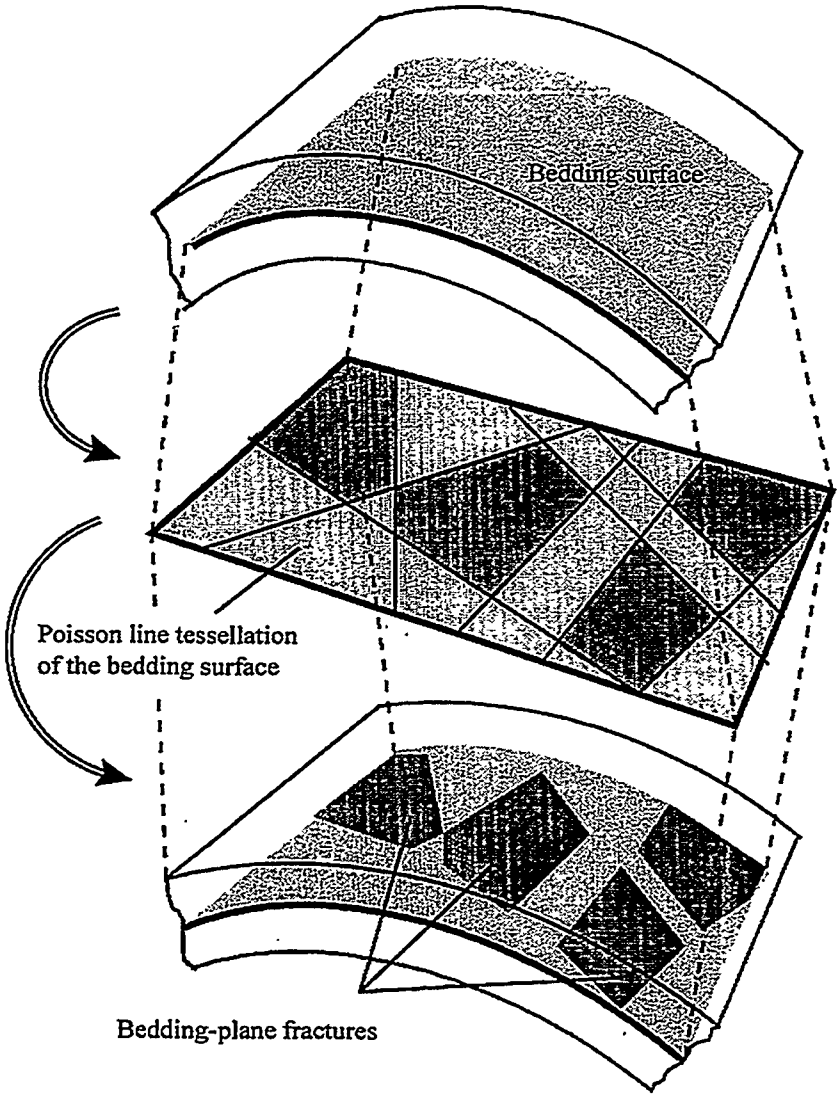

FIGURE **3-18**
GENERATION OF BEDDING-PLANE FRACTURES IN FLEXURAL FOLDS
NIPER/FINAL REPORT/WA

PROJECT NO. 963 1357.521 DRAWING NO. 80699 DATE 9/25/98 DRAWN BY EA

Golder Associates

3.1.3.3 Fracture systems Associated with Crustal Faults

Fracture systems associated with crustal faults include primary faults and numerous secondary fracture sets. Modeling of the geometry of sets of primary faults (normal, strike-slip, or thrust) is relatively easy. Usually there are one or two sets that form angles of less than 45° with the direction of the maximum compressive stress. Commonly, one of the sets is major and the other one is minor. The faults in a set are subparallel to one another and usually do not intersect the faults from the other set. The variation of orientations in a primary fault set can be described by Fisher PDF (with a high coefficient κ) or by partial uniform PDF (with a small angle ϕ_{max}). The mean pole orientation is orthogonal to the planes of maximum shear (Figure 3-19). When modeling the minor set, one should also apply a procedure to check fault intersections with the primary set. This procedure involves a termination probability, and high probability of rejection of minor faults that intersect major faults.

Figure 3-19 Mean Pole Orientation of Primary Fault Sets Related to the Directions of Maximum Compression and Maximum Shear

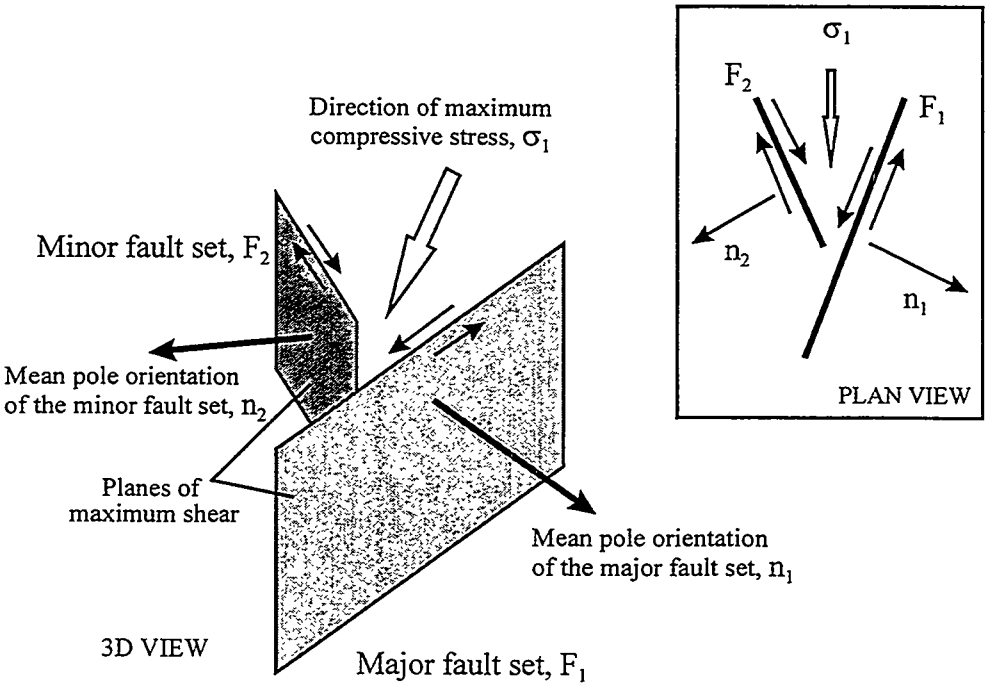

The stress field associated with crustal faults usually varies with time. Creation of new fractures often changes the local principal stress directions in the vicinity of primary faults, although the general shear direction along them remains the same. Numerous secondary, tertiary, etc. fault and joint sets form between and near primary faults. Therefore, the first important step in modeling the secondary and younger sets is to determine their hierarchy, i.e., the sequence of their formation.

Once the hierarchy of fracture genesis is established, the modeling volume and the mean orientation of a fracture set is defined by the fractures of older sets, including the primary faults. Figure 3-20 illustrates this process with two examples.

Figure 3-20a depicts the modeling volumes and mean pole orientations of a set of secondary antithetic faults, dependent on a set of primary normal faults. The secondary faults form inside the blocks enclosed between the primary faults. The intensity of the antithetic fault set is highest immediately above the normal faults. Most antithetic faults terminate at an underlying normal fault. Figure 3-20b illustrates the modeling volumes and mean pole orientations for secondary and tertiary fractures in strike-slip fault zones. The modeling volumes of secondary and tertiary fractures are enclosed between the primary and secondary ones, respectively.

After determining the modeling volume and the mean pole orientation, the variation of fracture orientations in a dependent set can be modeled with Fisher or partial uniform PDF. The fracture intensity is generally highest in the regions adjacent to older fractures. The translation procedure of the tertiary process of the model can be applied to avoid coplanarity of fractures. Rotation is usually not necessary since the fractures are not related to any other structures except to the older faults (which is accounted for by choosing the correct mean pole orientation of the set).

The main emphasis in modeling fracture systems related to crustal faults has to be placed on calculating modeling volumes of various 3D shapes. The currently implemented modeling volume (Figure 3-5) has a fixed shape: it is bounded by a horizontal (datum) plane, four vertical planes, and a cubic top surface. The next step should be to develop a generic modeling volume, enclosed between surfaces of any shape.

3.1.3.4 Fracture Systems in Remote Tension

The fracture systems, typical for remote tension, consist of numerous subparallel joints, orthogonal to the direction of the least principal stress σ_3. Therefore, the mean pole orientation of fracture sets can be assumed to coincide with the direction of σ_3. The orientations of all fracture planes in the primary stochastic process can be assumed to be the same (orthogonal to σ_3). More realistically, however, the variation of fracture plane orientations can be described by a spherical PDF that produces clustering of the poles close to the mean pole direction, for example:

- One-parameter Fisher PDF with a high value of the coefficient κ (e.g., $\kappa>20$);
- Partial uniform PDF where the latitude angle ϕ varies between 0 and a small value ϕ_{max}.

Both spherical PDFs generate fracture plane normal vectors that form small angles with the mean pole direction. The one-parameter Fisher PDF is the best option: when the coefficient κ is high, the probability of generating orientations that are very close to the mean direction is much higher than the probability of generating orientations that deviate by a larger angle from the mean.

a) Normal faults and secondary antithetic faults

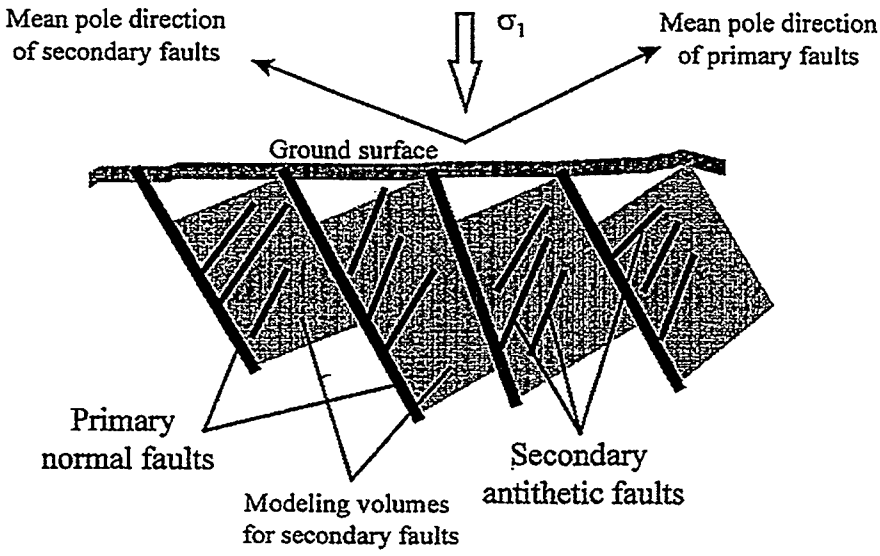

b) Strike-slip faults, secondary and tertiary fractures

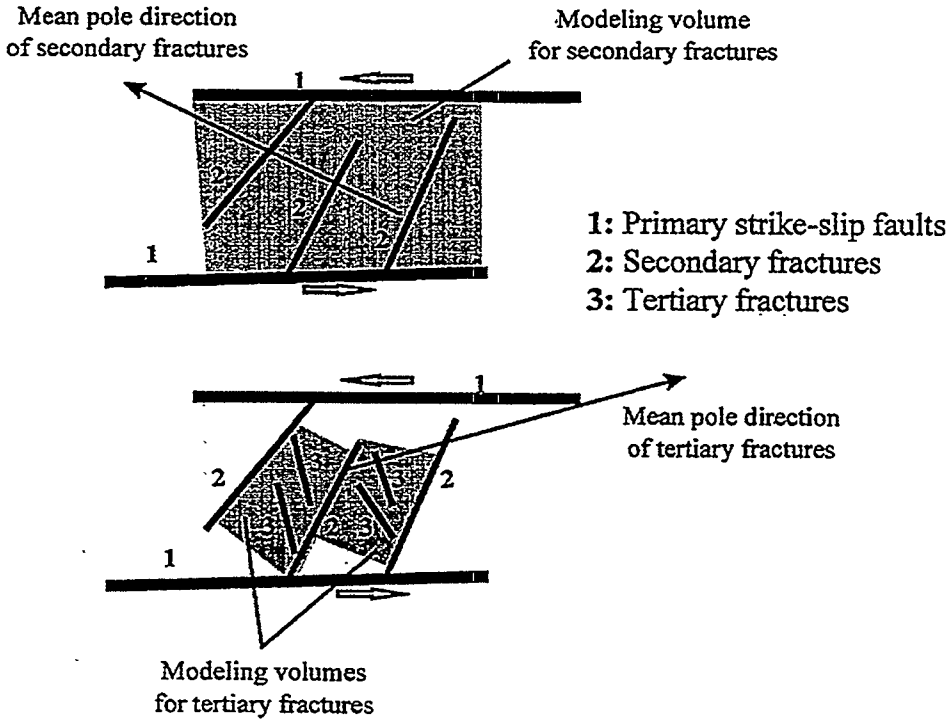

FIGURE **3-20**
DETERMINATION OF MODELING VOLUMES AND MEAN ORIENTATIONS FOR FRACTURE SETS DEPENDENT ON PRIMARY FAULTS
NIPER/FINAL REPORT/WA

During modeling of fracture intensity it is important to take into account the lithology of the rock. For example, typical tensile fracture systems in igneous rocks contain a few widely-spaced large joints and numerous smaller joints and extension cracks clustered around them. In sedimentary rocks, both the extent of tensile fractures and their spacing are often approximately equal to the bedding thickness. Two algorithms are suggested in the next two paragraphs in order to realistically represent the intensity of fractures in remote tension.

First, when modeling large primary fractures which inhibit the development of other large fractures in their vicinity, one can apply zone marking probability as defined in Figure 3-10. In the generation of new fractures, low probability should be assigned to the zones immediately surrounding already generated fractures. Thus it is ensured that the distances between large primary fractures are not smaller than a specified value (for example, equal to the bedding thickness in sedimentary rocks).

Second, small cracks and secondary fractures, clustered around the large primary fractures, can be reproduced according to the procedure illustrated in Figure 3-21. Once the primary fractures are generated, new modeling volumes are calculated adjacent to them, and the secondary fractures are generated only in these secondary volumes. Figure 3-22 illustrates the cross section of a tensile fracture system produced according to this algorithm. Figure 3-22a shows the outcrop traces of relatively large primary fractures. Figure 3-22b shows the outcrop traces of all fractures, after generation of secondary, relatively small, fractures in secondary volumes adjacent to the fractures in Figure 3-22a. The cross section in Figure 3-22b is very similar to horizontal outcrop traces of vertical joints observed in igneous rocks.

Figure 3-21 Modeling of Fracture Intensity in Remote Tension: Primary and Secondary Modeling Volumes

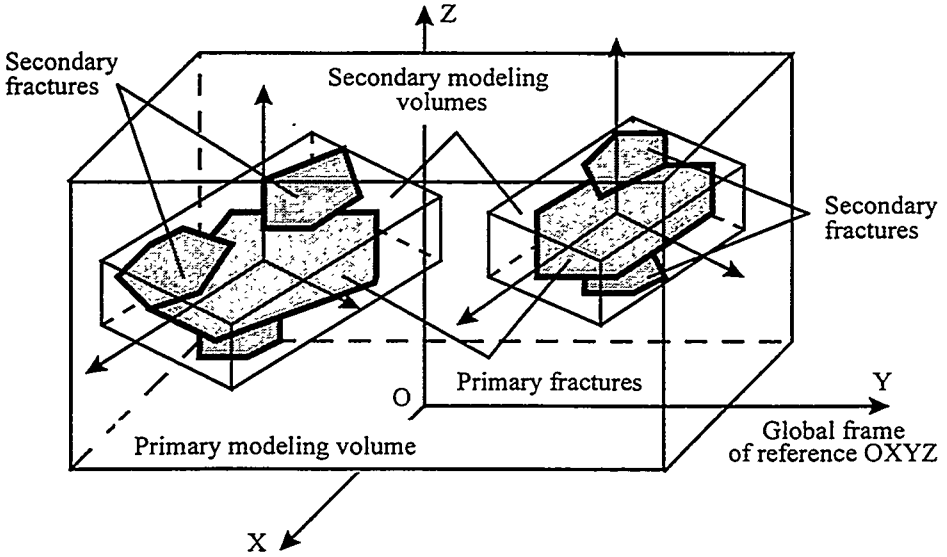

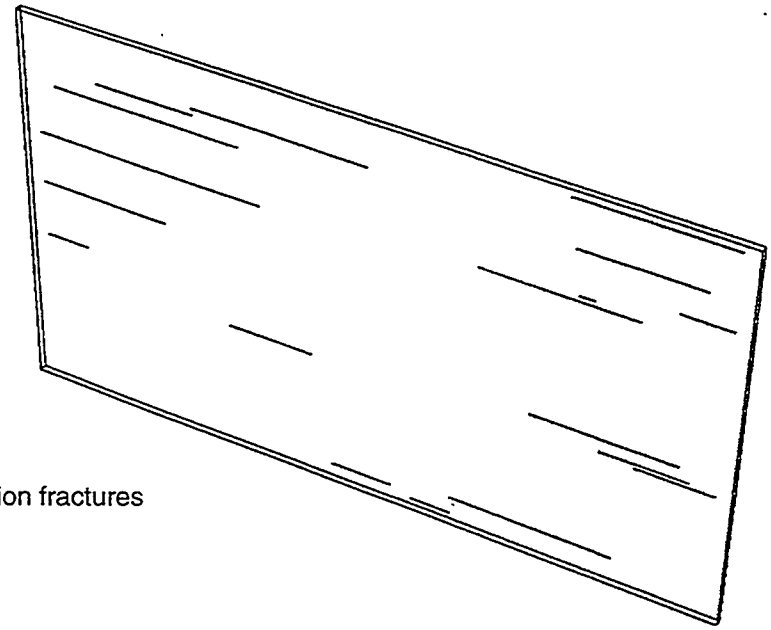

a) Original tension fractures

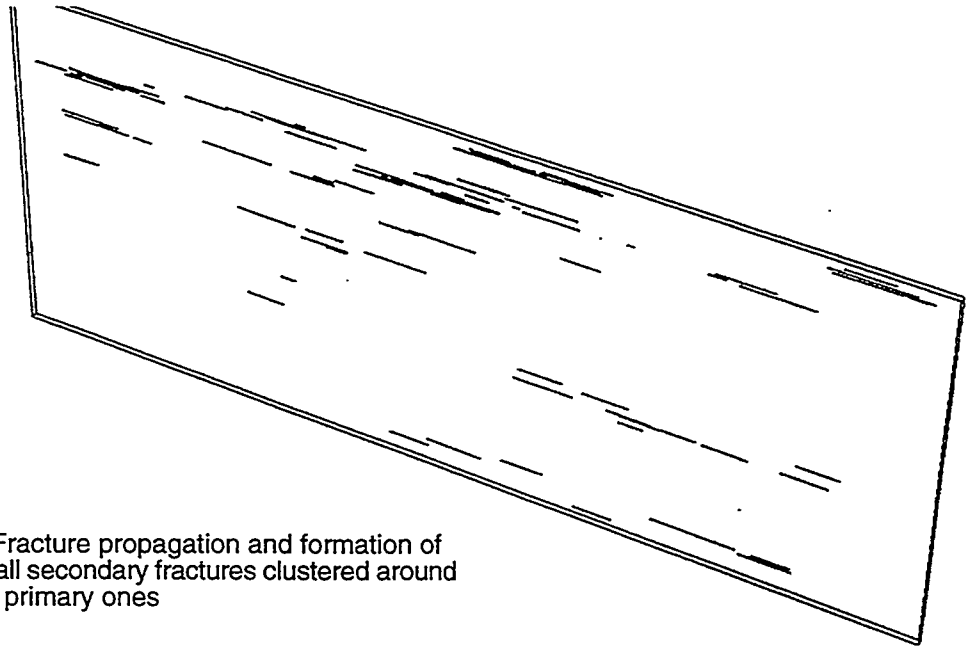

b) Fracture propagation and formation of small secondary fractures clustered around the primary ones

FIGURE **3-22**

TRACE OUTCROPS OF A TENSILE FRACTURE SYSTEM, GENERATED ACCORDING TO THE ALGORITHM IN FIGURE 3-21

NIPER/FINAL REPORT/WA

3.1.3.5 Fracture Systems in Central Structures

Fracture systems in and around central intrusive and extrusive structures include various sets of joints and faults (some of them are observed in other geologic environments as well). Some algorithms, developed in the context of geologic settings such as folds, faults, and remote tension, can be applied for modeling of specific fracture sets related to central structures. For example, the 3D shape of a dome can be described by a function of the type of Equation 3-23. Rotation algorithms developed for folds (Section 3.1.3.2) can be successfully applied for generation of radial and concentric fractures (dipping outwards or inwards toward the center) around a dome. Figure 3-23 illustrates horizontal cross sections of computer-generated fractures related to a dome: a radial pattern (Figure 3-23a), and a concentric pattern (Figure 3-23b).

In Figure 3-23, the dome surface is part of a hemisphere, centered in the middle of the horizontal area. The surface is described by Equation 3-23 using coefficients $c_5 = c_7$, and $c_1 = c_2 = c_3 = c_4 = c_6 = c_8 = c_9 = 0$. The synthetic systems in Figure 3.3.10a and b are similar to natural systems of radial dikes and ring dikes, respectively.

Doming creates numerous intersecting normal and reverse faults in the strata overlying the intrusion. Therefore algorithms designed for fracture systems associated with crustal faults (Section 3.1.3.3) can be applied for generation of fracture systems related to central structures. Also, the algorithms designed for fractures in remote tension (Section 3.1.3.4) can be used for modeling of tension joint sets associated with sheet intrusions.

Figure 3-24 depicts two algorithms, suggested for modeling of fracture sets typical for large igneous intrusions. For example, the orientations of tension joints in the host rock, created by upward pressure of expanding magma, can be modeled with Bingham PDF (Figure 3-24a). On the other hand, cooling of the magma creates several sets of fractures, including flat-lying joints inside the igneous intrusion. The variation of pole orientations of flat-lying joints can be described with Fisher PDF (Figure 3-24b).

3.2 Task 1.2.2: HFM Model Verification: Yates Field

This section describes the application and verification of the 3D HFM, using data from the Yates, Texas study site, Tracts 17 and 49. The modeled fracture system includes fractures that are subparallel to the inferred paleostress directions (System 1), and fractures that are related to both inferred paleostress directions and field anticlinal structure (System 2). Section 3.2.1 and Section 3.2.2 contain the results from the numerical simulations of the fracture system in Tract 49 and Tract 17, respectively. Presentation of the numerical modeling for each area includes the following:

- Inference of the model parameters from geology and field data, namely inference of number of fracture sets, fracture intensity P_{32}, fracture plane orientation PDF, fracture size variation, and relation of fractures to the field structure.

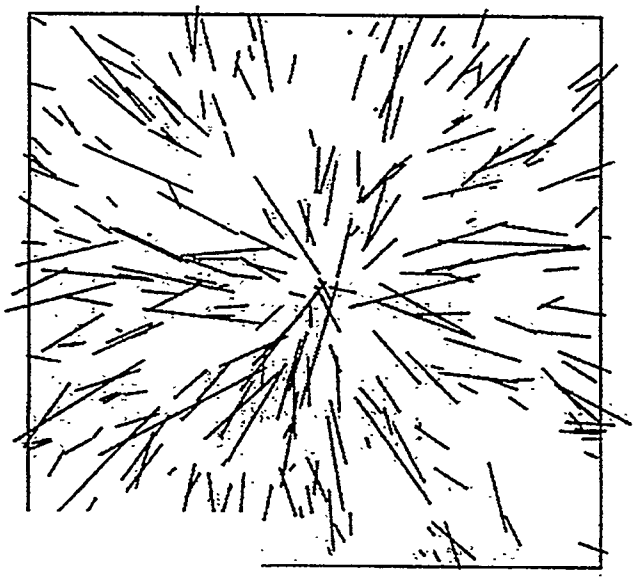

a) Radial fractures

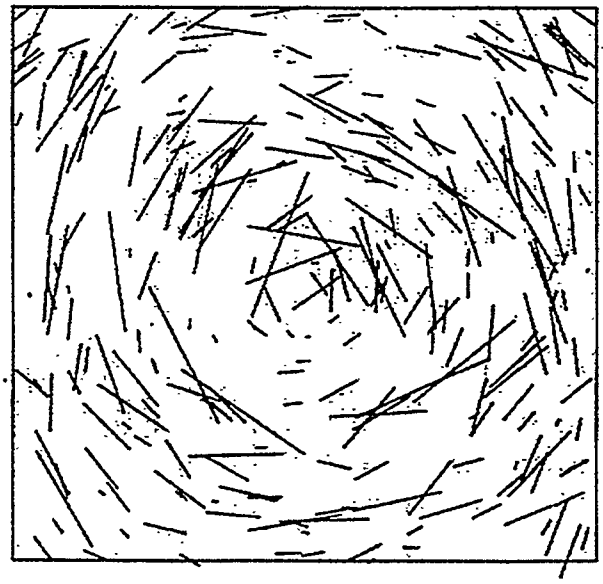

b) Concentric fractures

FIGURE **3-23**
HORIZONTAL OUTCROPS OF FRACTURE SYSTEMS RELATED TO A CIRCULAR DOME
NIPER/FINAL REPORT/WA

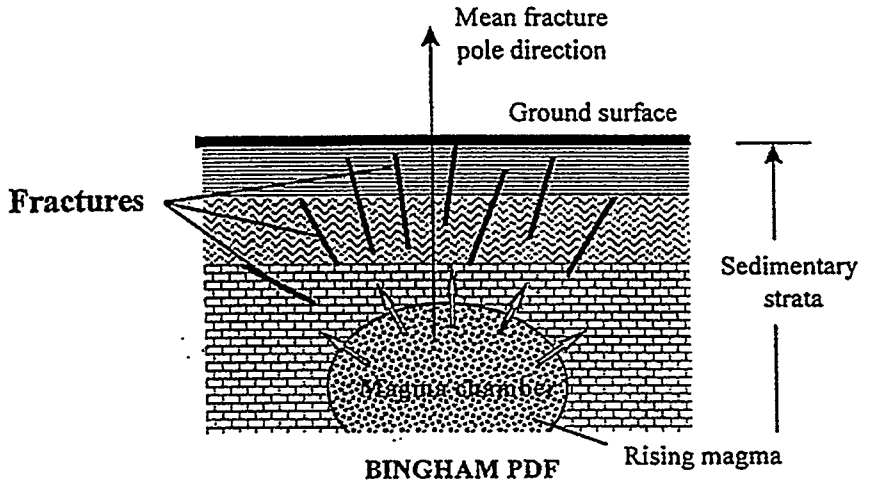

a) Bingham PDF: Steep fractures in overlying sediments due to rising of magma

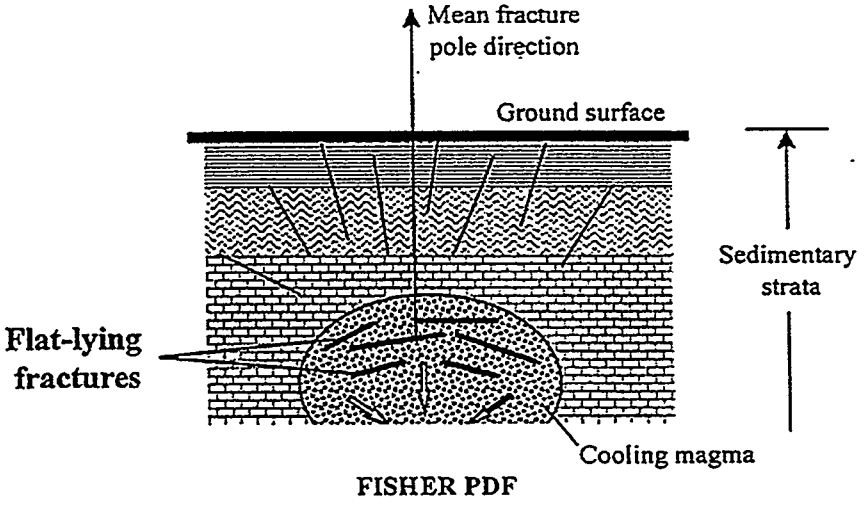

b) Fisher PDF: Flat-lying joints in the intrusion due to cooling of magma

FIGURE **3-24**
ORIENTATION DISTRIBUTIONS FOR FRACTURES RELATED TO CENTRAL STRUCTURES
NIPER/FINAL REPORT/WA

PROJECT NO. 963 1357.521 DRAWING NO. 80703 DATE 9/25/98 DRAWN BY EA

Golder Associates

- Development of specific algorithms
- Results from numerical generations and comparison to field data.

Mean and PDF of Fracture Plane Orientations

The number of fracture sets, and their mean orientations, defined by the regional stresses, are the same in Tract 17 and Tract 49. Throughout the Yates field, field data consistently show that there are two major fracture sets. One set strikes to the northwest and the other one strikes to the northeast. The expected value for the strike of the northwest set is N50°W, and for the northeast set is N40°E (parallel to the two major regional depositional trends on the Central Basin Platform). Both fracture sets are composed of vertical or steeply dipping fractures. In the primary process of the numerical model, the mean pole direction (θ, ϕ) of fracture planes that belong to the first set is defined as (40°, 90°), i.e., orthogonal to a vertical plane striking N50°W. The mean pole direction of fracture planes in the second set is defined as (-50°, 90°), i.e., orthogonal to a vertical plane striking N40°E. Fisher distribution with Fisher constant κ=20 is used for the generation of fracture planes in each set. This spherical PDF (with the relatively high κ=20) preferentially produces planes with poles at small angles with the specified mean pole orientation, as they occur in reality (mostly steep fractures in a narrow dip range).

Relation of Fractures to the Field Structure

At different locations in the Yates field, the predominant fracture strikes often deviate from the two regional directions, since the majority of the fractures are also related to the curvature of the reservoir structure. The structure-defined variation of fracture orientations around the mean directions of the two major sets is relatively simple in Tract 49 (discussed in Section 3.2.1), and quite complex in Tract 17 (Section 3.2.2).

Fracture Size Variation and P_{32}

The inference of size variation and P_{32} from geologic data is discussed in Section 3.2.1 for Tract 49, and in Section 3.2.2 for Tract 17. In general, the estimation of the fracture size distribution from the available field data is imprecise since fractures are sampled only by one-dimensional field tests: logs and cores. For preliminary evaluation of the HFM model, fracture size is assumed solely on the basis of known relationships of fracture sizes to layers in sedimentary rocks.

In the 3D geometric-mechanical model, fracture intensity P_{32} should be inferred from the magnitude of geologic stresses and strains, and from the mechanical properties (strength, deformation moduli) of the host rock. However, since this information is not available, P_{32} is inferred from field data (i.e., following a procedure that is typical for a geometric, rather than for a geometric-mechanical, model). Inference of cumulative fracture intensity (Equation 3-6) from logs and cores is straightforward since P_{32} (as long as it is not too low) is linearly related to the mean spacing of fracture intersections in boreholes (Dershowitz, 1984; Dershowitz and Herda, 1992; Low, 1986). In the inference procedure, the emphasis is placed on making assumptions about which field-sampled fractures are

significant and which ones are not. Table 3-4 summarizes advantages and drawbacks of the field sampling methods, used in the Yates field, in terms of the information which they provide on fracture intensity.

Well water injection and monitoring gives very good, direct evidence of where the conductive fractures are (Figure 3-25). The shape of the water dissipation profile indicates if a major conductive fracture exists at a given elevation, or if numerous conductive fractures intersect the well along a certain depth interval. However, since only sparse data is available from water injection tests in the Yates field, one cannot rely on this information alone for inference of fracture intensity.

Table 3-4 Field Tests and Their Limitations as Indicators of Fracture Intensity in the Yates Reservoir

Field Test	Advantages	Drawbacks
Water injection	Gives direct indication of where the major conductive features are.	Very limited testing, not enough data to form a representative field sample.
Continuous cores	Fractures, as well as rock lithology, porosity, calcite filling, etc. are directly observed and measured.	Core description (available only in electronic form) includes numerous minor fractures and microcracks, difficult to distinguish from major conductive fractures.
FMS/FMI logs	Logs penetrate almost the entire thickness of the San Andres formation.	Fractures are not directly observed, but identified (possibly very subjectively) on resistivity profiles of the logged wells.

There is a dramatic difference between the intensity of conductive fractures, suggested by water injection tests, and the intensity of fractures identified on log profiles or observed in cores. For example, Figure 3-25b shows that there are only two large conductive features (possibly fractures) in a 50 ft. water profile at well YU4903.

Figure 3-26 shows the rosette diagrams of fracture strikes at one well in Tract 17 (YU1711) and two wells in Tract 49 (YU4007, YU5127), determined from two independent analyses of the same FMS/FMI logs.

a) TRACT 17

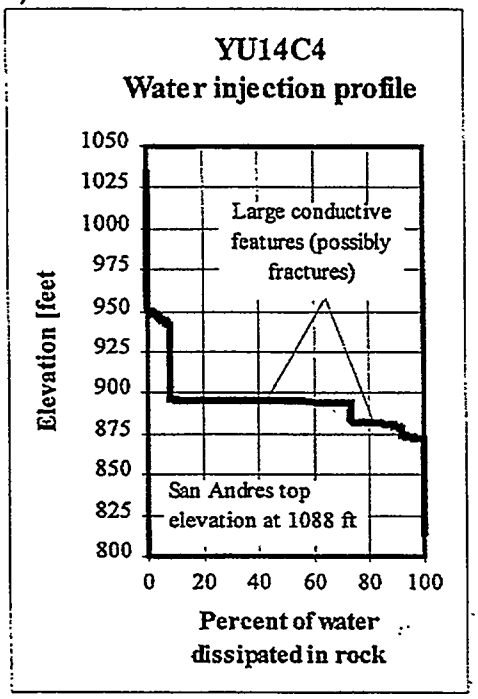

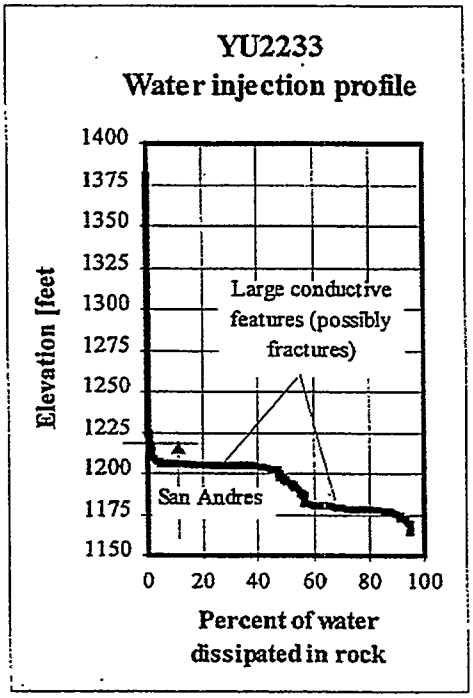

b) TRACT 49

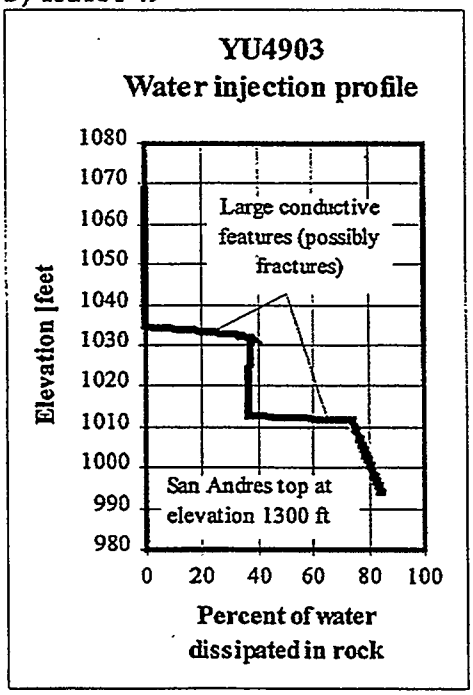

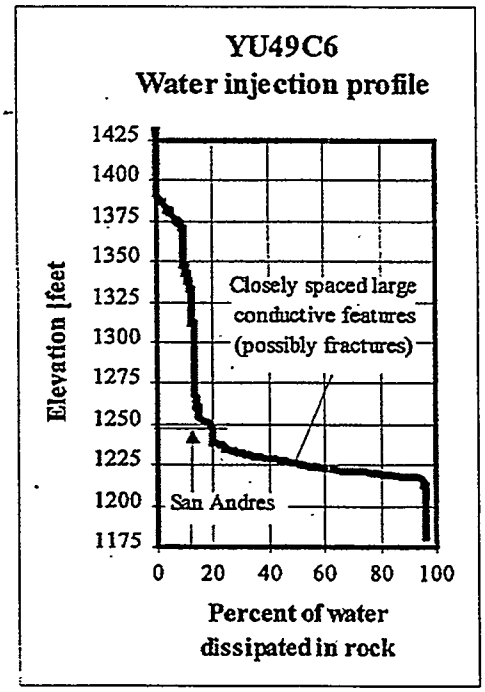

FIGURE **3-25**
WATER INJECTION PROFILES
NIPER/FINAL REPORT/WA

LOG ANALYSIS 1

YU1711
124 log fractures

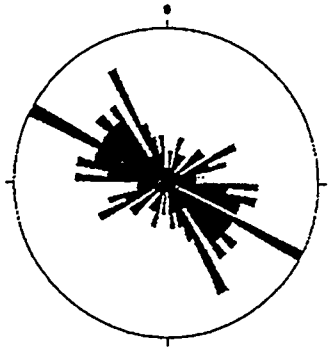

YU4007
105 log fractures

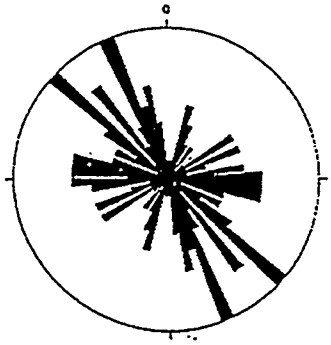

YU5127
122 log fractures

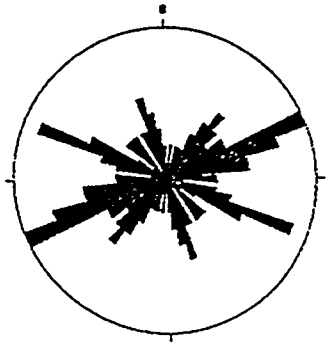

LOG ANALYSIS 2

YU1711
20 log fractures

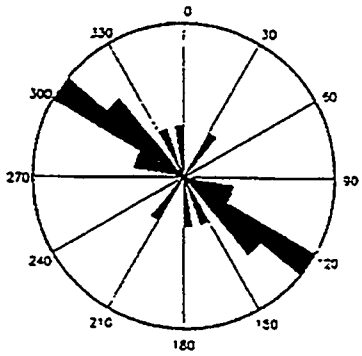

YU4007
71 log fractures

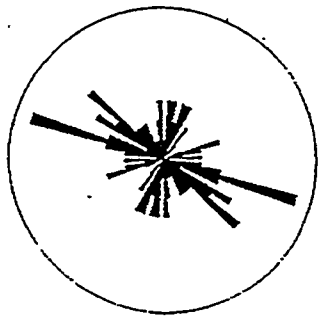

YU5127
47 log fractures

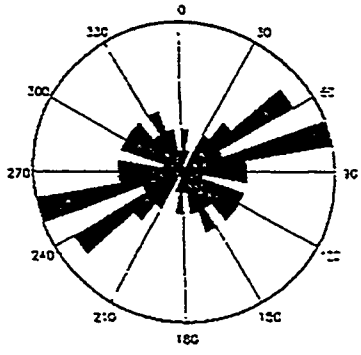

FIGURE **3-26**
COMPARISON OF NUMBER AND STRIKES OF FRACTURES; IDENTIFIED ON FMS/FMI PROFILES DURING TWO INDEPENDENT LOG ANALYSES
NIPER/FINAL REPORT/WA

Core description is the only test where fractures are actually observed and not assumed based on other data. Since there are not enough water injection tests, whereas the log analyses give ambiguous information on the number of intersected fractures, fracture intensity P_{32} is determined through analysis of core data from the Tract 17 and Tract 49 areas. Locations in and near the two tracts where continuous cores were taken are indicated in Figure 3-27. However, only a computer database (not the actual cores) is available to the case study. The database includes description of every available foot of core, including fracture count and comment on whether the fractures penetrate or not across the entire cored foot. Inference of fracture intensity from the core database is discussed in Section 3.2.1 for Tract 49 and in Section 3.2.2 for Tract 17. Also, Section 3.2.1 and Section 3.2.2 present some specific algorithms, implemented in the 3D fracture system model, which enable reading of StrataModel porosity and shale data in order to account for their effect on fracture intensity in Tract 49 and Tract 17, respectively.

3.2.1 Numerical Simulation of the Fracture System in Tract 49

Inference of Model Parameters

Fracture intensity P_{32} is inferred from the mean spacing of large significant fractures intersected by continuous cores (core locations are shown in Figure 3-27b). Table 3-5 illustrates the types of fractures, defined as "significant" in the inference procedure, through examples from the core database of Tract 49.

Fracture 1 in Table 3-5 is totally open, and penetrates more than one cored foot (type TOPN). It is stained by oil, which indicates that it is conductive. This fracture is of the type shown in Figure 3-28b. Fracture 2 in Table 3-5 is partially filled with calcite and has aperture of 5 mm which is much larger than that of similar fractures. The large aperture is due to solution enhancement. This fracture, which penetrates the entire core diameter, is of the type FILO shown in Figure 3-28c. It very likely belongs to System 1 fractures, created prior to folding of the reservoir strata, and affected by solution enhancement and calcite precipitation. Fracture 3 in Table 3-5 is filled with calcite (type FILL). Even though at its intersection with the core this fracture is not conductive, the fact that its aperture (thickness) is so large (4 mm) and its dip is so steep (80°) indicates that it probably extends to elevations above and below the local level of calcite precipitation. Therefore, this fracture is considered significant since portions of it are likely to be conductive. Fractures of type FILL with smaller thickness or flatter dips are not considered significant. Fractures of types PONP (non penetrating the entire thickness of the core) and INDU (drilling-induced) are ignored in the inference procedure.

In order to gather information on fracture size, vertical fractures in cores were specifically described during the inference procedure. Table 3-6 shows two examples of "vertical fractures" identified in continuous core.

a) TRACT 17

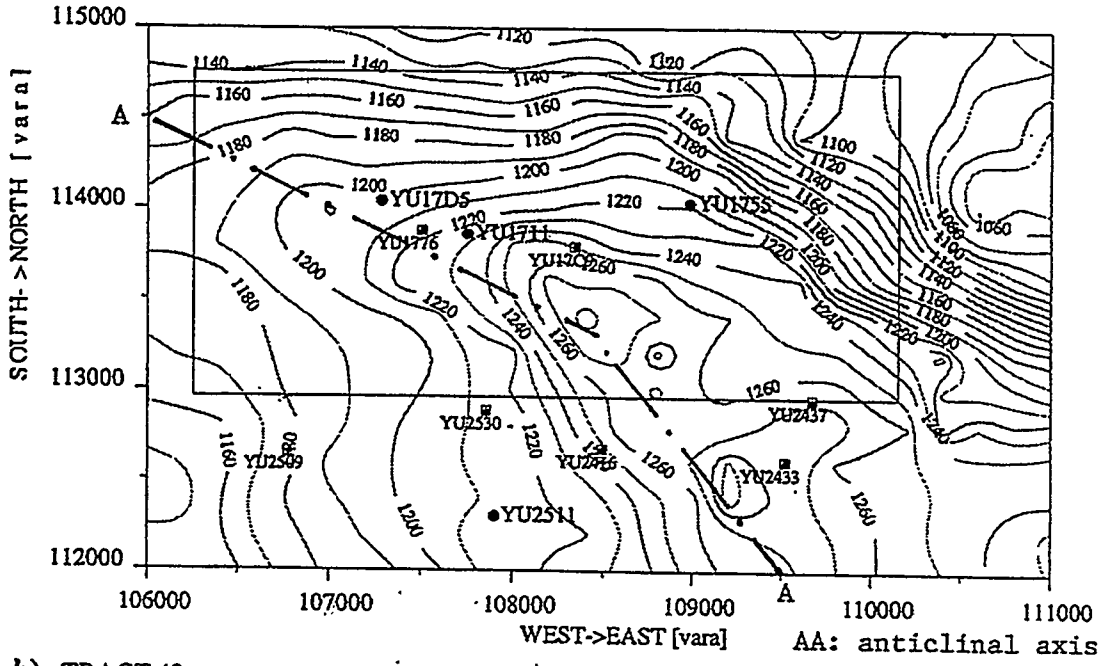

b) TRACT 49

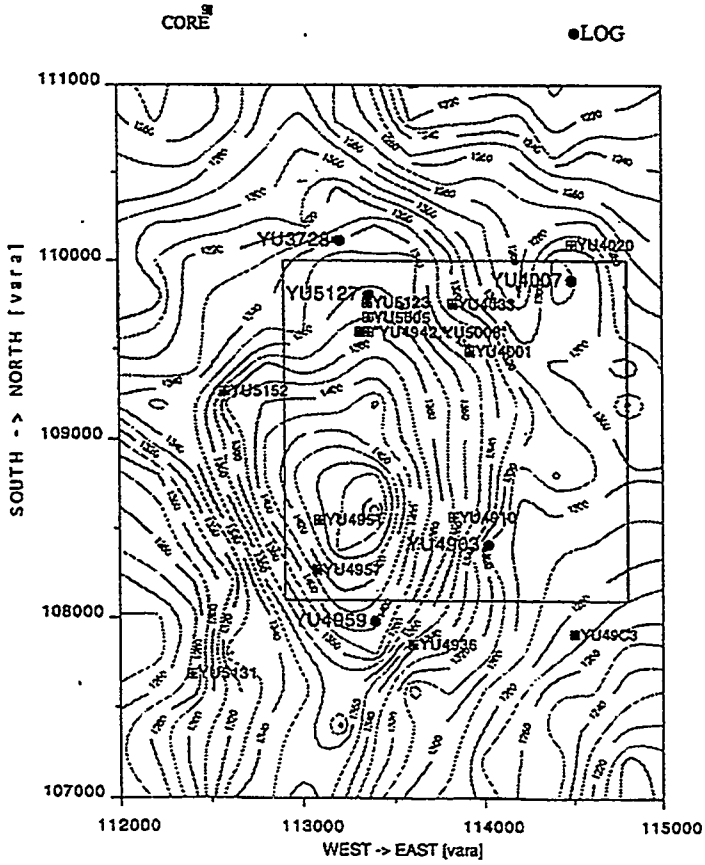

FIGURE **3-27**
LOCATIONS OF LOGGED AND CORED WELLS, SUPERIMPOSED ON STRUCTURE MAPS OF THE SAN ANDRES TOP
NIPER/FINAL REPORT/WA

PROJECT NO. 963 1357.521 DRAWING NO. 80728 DATE 9/29/98 DRAWN BY EA

Golder Associates

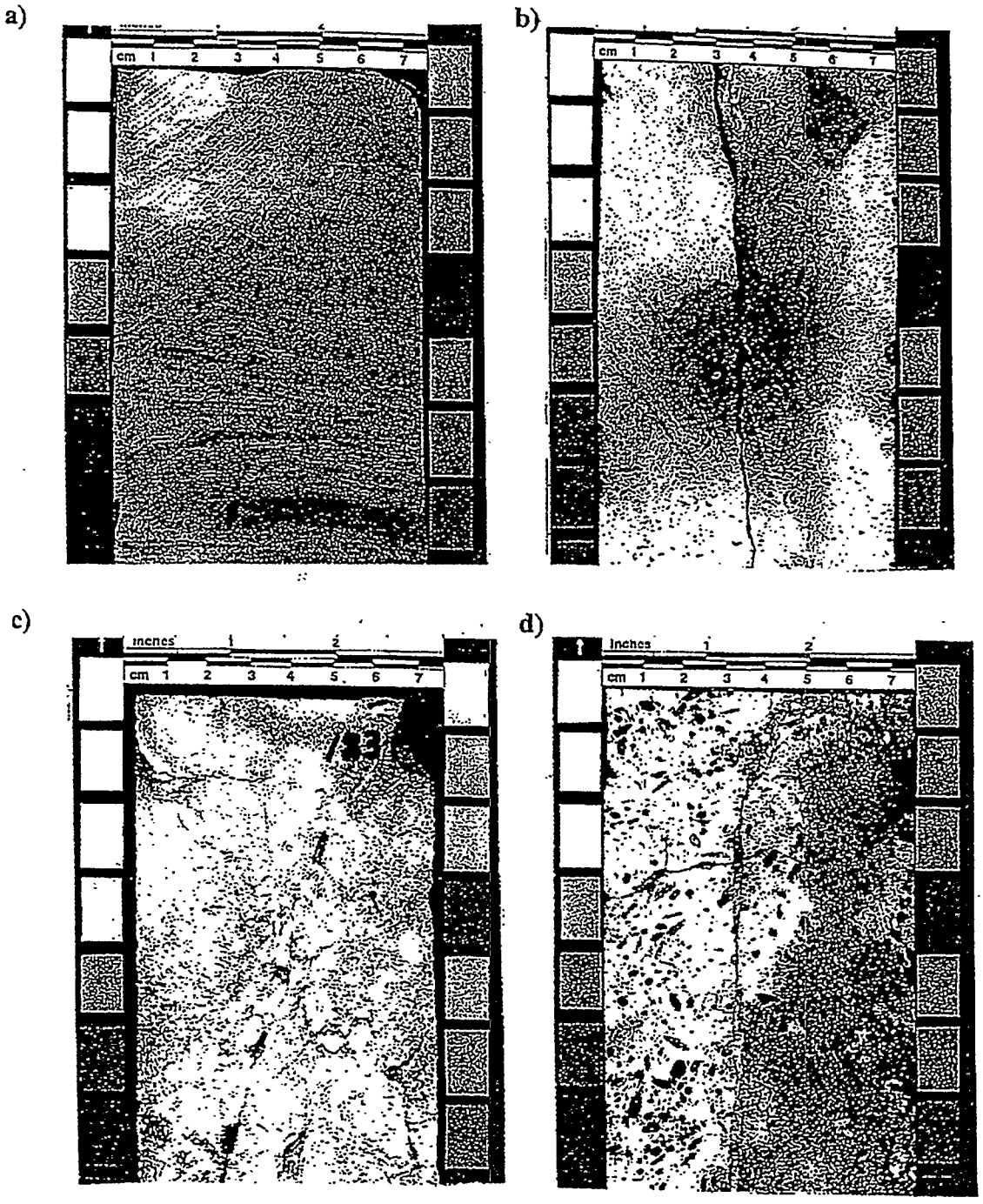

LEGEND

A Dense, dolomitic shale mudstone

B Dolomitic grainstone cut by a totally open penetrating (TOPN) oil-stained fracture

C Dolomitic packstone/grainstone cut by a partially filled with calcite penetrating (FILO) fracture

D Dolomitic packstone with fusumoldic porosity, cut by a vertical calcite filled (FILL) fracture (stained red), and a horizontal drilling-induced (INDU) fracture

FIGURE **3-28**
TEXTURE AND FRACTURING OF THE SAN ANDRES FORMATION (CORE PHOTOGRAPHS)
NIPER/FINAL REPORT/WA

Figure 3-29 Dip Distribution of 135 Fractures, Identified As "Significant" on Cores From Twelve Wells in the Tract 49 Area

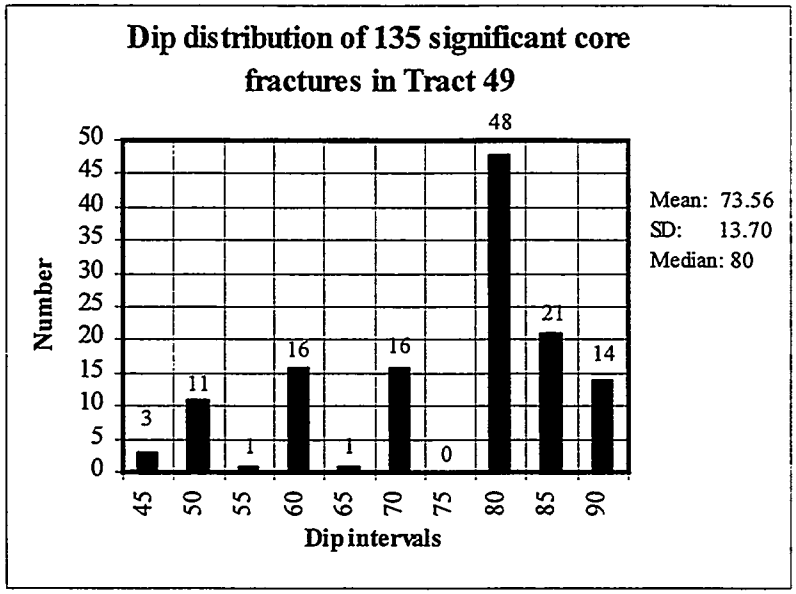

Table 3-5 Significant Fractures identified on Cores From Tract 49

WELL	DEPTH	ELEV.	POROS.	APER.	DIP	TYPE	COMMENT	FRACTURE
FRACTURE 1								
YU5005	1425	1157	9.7	N/A	80	TOPN	Light oil stain	
YU5005	1426	1156	12.2	N/A	85	TOPN	TOPN continues	BIG TOPN 85
YU5005	1427	1155	14.3	N/A	85	TOPN	TOPN continues	
YU5005	1428	1154	10.7	N/A			Light oil stain	
FRACTURE 2								
YU4936	1536	1035	5.6	5	50	FILO	Calcite; cont. below	BIG FILO 50-70
YU4936	1537	1034	6.5	5	70	FILO	Solution; calcite	
FRACTURE 3								
YU5008	1508	1118	9.6	4	80	FILL	Calcite filling	
YU5008	1509	1117	N/A	4	80	FILL	FILL continues	BIG FILL 80

a) totally open, penetrating fracture (type TOPN); b) solution-enhanced, partially filled with calcite fracture (type FILO); c) steep fracture filled with calcite at its intersection with the well (type FILL). The shaded column includes the interpretation of significant fractures in the current case study. The rest of the table presents data from the core database of the Yates field

Table 3-6 Vertical Fractures, Identified on Continuous Core

WELL	DEPTH	ELEV.	POROS.	APER.	DIP	TYPE	COMMENT	FRACTURE
YU4936	1433	1138	25.7	0.2	90	POPN		start POPN 90
YU4936	1434	1137	24	0.4	90	POPN		8 ft long
YU4936	1435	1136	12.6	.	.		Microfractures	
YU4936	1436	1135	10.6	.	.		Microfractures	
YU4936	1437	1134	10	.	90		Solution	
YU4936	1438	1133	19.2	0.4	90	POPN		
YU4936	1439	1132	22.9	0.4	90	POPN		
YU4936	1440	1131	24.2	.	90	POPN		end POPN 90
YU4936	1565	1006	18.9	.	90	TOPN	Rubble; cont. below	start TOPN 90
YU4936	1566	1005	16.3	.	90	TOPN		8 ft long
YU4936	1567	1004	19.1	.	.	TOPN	Rubble; cont. below	
YU4936	1568	1003	14.1	.	.	TOPN	As above	
YU4936	1569	1002	11.9	.	90	TOPN	Some calcite fill	
YU4936	1570	1001	11.1	.	90	TOPN	Microfractures	
YU4936	1571	1000	10.8	.	90	TOPN		
YU4936	1572	999	12.1	.	70	TOPN		end TOPN 90

The shaded column includes interpretation of vertical fractures in the current case study. The rest of the table presents data from the core database of Tract 49.

Table 3-7 summarizes the spacing of significant fractures, identified in cores available from twelve wells located inside or in the vicinity of Tract 49. The average spacing of significant fractures varies from 6.5 ft to 14.9 ft (2-4.5 m) in dolomite that has porosity 6.9-20.4% (excluding the two extreme values for wells YU4910 and YU4957). There is a tendency of fewer well fracture intersections where the porosity of the rock is higher than 20% (see data for wells YU4910, YU4951, YU4936), although sometimes many intersections are observed in high-porosity rock (well YU5152). Nine vertical fracture intersections have heights from 4 ft to 40 ft (1.2-12 m), with all but two having heights less than 10 ft (3 m). It has to be noted that the real "diameter" of a vertical fracture is usually larger than the height of its well intersection. The dip distribution of significant fractures, intersected by cores in Tract 49, is shown in Figure 3-29.

The fact that some vertical fractures have been intersected at all indicates that the intensity of significant fractures in the Yates reservoir is very high. However, the probability of intersection of a large vertical fracture by coring is extremely low. Because of the great number of smaller fractures, some of the vertical ones have been intersected by the well. Therefore, the heights of vertical fractures intersected by cores mark the lower end of size variation of significant fractures. The upper end (largest sizes) can be estimated through analysis of the thickness of dolomite cycles in the San Andres formation (summarized in Table 3-8). In the middle and upper portions of the San Andres formation, there are three layers of similar thickness that could have acted as mechanical units during folding when the San Andres dolomite strata bent over compacted underlying muds. The three mechanical units are: the relatively thick second

dolomite cycle, combined with two very thin cycles above it (Unit 1 in Table 3-8); three cycles of approximately the same thickness combined together (Unit 2 in Table 3-8); and the top portion of the San Andres dolomite (Unit 3 in Table 3-8). The average thickness of the three units is about 60 ft (18 m) which can be assumed as an approximation for the average diameter of the largest fractures in Tract 49. Fractures of that size and larger possibly exist in the Yates reservoir, and, even if they are not too many, because of their large sizes, they may provide for significant reservoir conductivity.

Table 3-7 Spacing of Significant Fractures, Identified in Cores From Tract 49

Well	n_{ave} (%)	N	s_{ave} (ft)	Comment
YU4001	12.54	13	7.27	SD=2.82 ft.
YU4033	18.85	4	13	
YU4910	20.52	3	25.5	No fractures in zone with n_{ave}=27.4%.
YU4951	12.27	3	12	No big fractures in zone with n_{ave}=21.5%.
YU4957	5.85	2	2	Spacing of smaller fractures s_{ave}=13 ft.
YU5005	8.05	3	7	All big fractures are in zone with n_{ave}=11.46%. Smaller fractures with s_{ave}=8.5 ft in n_{ave}=6.03%.
YU5008	6.9	6	13.6	SD=6.19 ft. Mostly calcite-filled.
YU5123	8.83	9	6.5	SD=5.85 ft. No big fractures below elevation 1150 ft.
YU4936	12.03	11	14.90	SD=10.32 ft. Spacing varies: s_{ave}=5.67-10.7 ft in zones with n_{ave}=10.10-12.6%; no big fractures in high porosity n_{ave} >20%. Vertical fractures: 4 ft in n_{ave}=9.73%; 7 ft in n_{ave}=18.65%; 40 ft in n_{ave}=10.1%.
YU49C3	18.24	9	12	SD=7.59 ft. Spacing varies: s_{ave}=8-8.5 ft in zones where n_{ave}=13.2-18.23%; s_{ave}=21.5 ft in n_{ave}=21.5%. Vertical fractures: 7 ft in n_{ave}=13.2%; 21 ft in n_{ave}=14.3%; 8 ft in n_{ave}=18.23%; 9 ft in n_{ave}=21.5%.
YU5131	11.51	4	9	No natural fractures below elevation 1191 ft.
YU5152	20.37	9	12.5	SD=11.90 ft. Spacing varies: s_{ave}=5.5-6.6 ft in n_{ave}= 18.72-25.75%; s_{ave}=12.67 ft in n_{ave}=18.76%. Vertical fractures: 4 ft in n_{ave}=21.82%; 6 ft in n_{ave}=18.72%.

n_{ave}: average core porosity; N: number of significant fractures identified at the given well; s_{ave}: average spacing of significant fractures; SD: standard deviation of spacing between significant fractures (given only where N>5).

Table 3-8 Thickness of Dolomite Cycles in the San Andres Formation

	THICKNESS			
	MIN	AVERAGE	MAX	STRATIGRAPHIC LAYER
	250.35	309.1012	347.05	Cycle 1 dolomite
UNIT 1	38.1	51.7887	64.5	Dolomite layer 2
	1	5.9067	18.1	Dolomite layer 3
	1	3.3237	5.2	Dolomite layer 4
	40.1	61.0191	87.8	Total Unit 1
UNIT 2	10.6	19.2643	28	Dolomite layer 5
	9.4	17.4586	26.7	Dolomite layer 6
	7.9	17.6432	32	Dolomite layer 7
	27.9	54.3661	86.7	Total Unit 2
UNIT 3	29.4	71.6617	113	Dolomite to San Andres top
	6	34.3345	58.4	Greyburg
	19.3	24.4931	36.1	Queen

In Tract 49 the relationship of the fractures to the field anticlinal structure is relatively simple: fractures are predominantly concentric. This is not only suggested by rosette diagrams of log fracture strikes (Figure 3-30b), but, more important, results from simple mechanical analysis. The San Andres formation in Tract 49 includes the apex of the field anticlinal dome. This indicates that during folding the reservoir strata in Tract 49 experienced radial extension which defined tangentially striking planes of maximum tension. The two regional fracture sets (striking to the northwest and northeast) exist in Tract 49, but which one of them is locally the major set depends on which one is "more concentric" to the dome.

Numerical Algorithms

Most of the algorithms for generation of fold-related fracture sets, implemented in the 3D model, were developed in the context of the Yates field case study. The methods for generation of fracture sets related to a curved surface (fold) were presented in detail in Section 3.3.2.

An additional algorithm reads porosity values from the StrataModel and calculates the average porosity of the host rock that surrounds a numerically generated polygon. Then the polygon is retained as a fracture with probability P_f as a function of the average porosity:

$$P_f = f_n\left[\frac{1}{N}\sum_{i=1}^{N} n_i\right] \tag{3-32}$$

a) TRACT 17

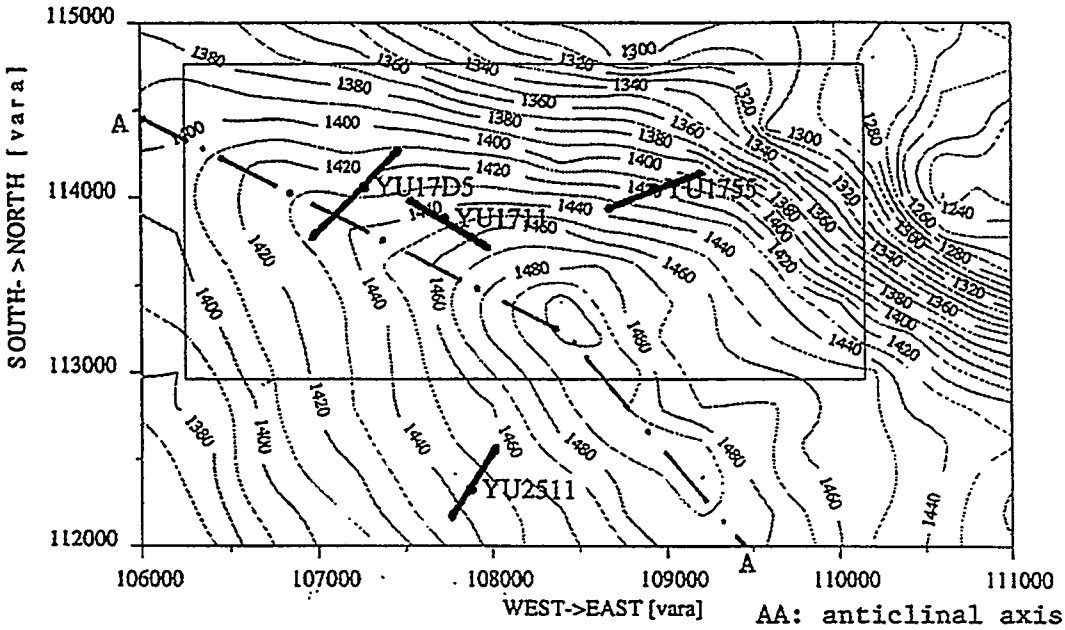

b) TRACT 49

•LOG

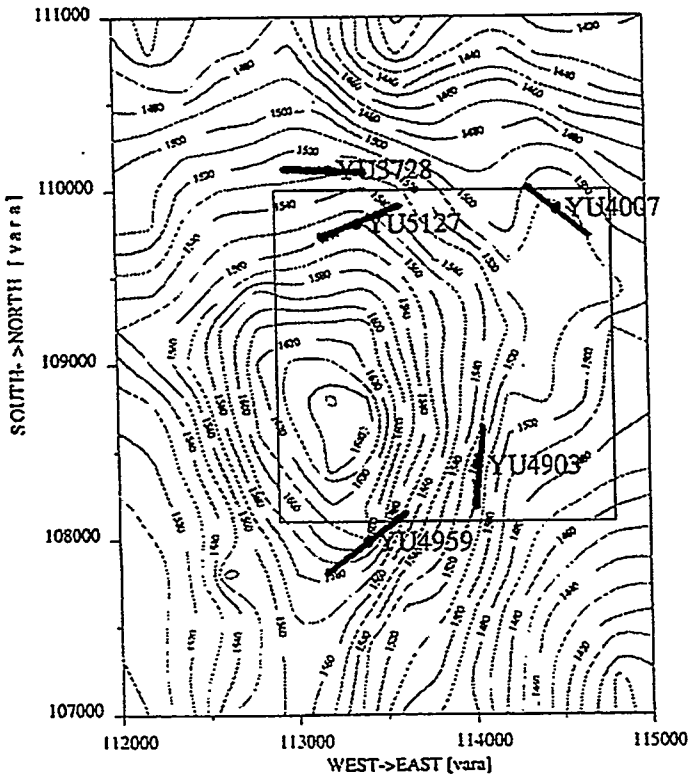

FIGURE **3-30**

PREDOMINANT STRIKE OF FRACTURES IN THE SAN ANDRES FORMATION IDENTIFIED ON WELL LOG PROFILES, SUPERIMPOSED ON STRUCTURE MAP OF THE SEVEN RIVERS M DATUM

NIPER/FINAL REPORT/WA

where N is the number of geocells from the reservoir StrataModel intersected by the polygon, and n_i is the porosity of the i-th intersected cell.

Numerical simulations

Based on the inference procedure, presented above, the following parameters of the 3D fracture system model are selected for the simulations in Tract 49:

- Mean orientations of two fracture sets (inferred from regional geology): vertical planes, striking N50°W and N40°E.

- PDF of fracture plane orientations: Fisher (κ=20) which produces close clustering of plane pole orientations around the mean pole.

- Modeling volumes: five modeling volumes for the five logged wells: YU4007, YU4903 and YU5127 inside Tract 49, and YU3728 and YU4959 in the vicinity of Tract 49. Each modeling volume is defined by the following boundaries: a horizontal datum surface at 700 ft above sea level; four vertical planes (two striking south-north and two striking east-west), each at a horizontal distance of 300 ft (91 m) from the vertical well; a quadratic upper surface, parallel to the San Andres top and located 100 ft (30 m) above it. The coefficients of the quadratic function are calculated through a polynomial fit with matlab to the elevations of the San Andres top at the wells in the Tract 49 area.

- Fracture intensity (inferred from field data, since the stress and strain magnitudes, and the mechanical properties of the San Andres dolomite are not known yet): 0.3 (ft^2/ft^3) for each set, i.e., the total P_{32}=2(0.3)=0.6 (ft-1), established through simulations to produce expected spacing in vertical boreholes E[s]=10 ft (3 m).

- Fracture size distribution (approximate procedure, since field sampling of fracture sizes is not available): the mean of the equivalent radius is assumed $E[R'_e] = 30$ft (9 m; equal to half the average thickness of mechanical units in the San Andres formation). Marking in terms of relative size is assumed of the type $A'_i > E[A]$, $R'_{e,i} < 3E[R'_e]$, where $E[A'] = \pi(30)2 = 2827$ (ft^2) is the expected area of fractures. This type of marking (see Section 3.2) eliminates the polygons with extremely small and extremely large sizes, and produces fracture areas that have a standard deviation $\sigma_{A'} = 0.9E[A']$ and median $M[A'] = 0.8E[A']$. 70% of the produced fractures have areas smaller than the average area.

- Effect of porosity (approximate procedure since the exact effect of high porosity on fracture intensity has not been studied yet): fracture intensity in areas with porosity n>20% is assumed to be half of the fracture intensity where n<20%, i.e., $P_{32}|n>20\% = 50\% P_{32} = 0.5(0.6) = 0.3$ (ft^{-1}). A fracture is discarded with probability Pf=0.5 if the average porosity of the dolomite matrix around the fracture is n_{ave}>20%. This method results in discarding fractures with relatively small sizes,

since they are the most likely to be located entirely in an area of high porosity. Thus in high porosity dolomite only relatively large fractures are retained which results in larger spacing of fractures intersected by a vertical well.

- Relationship to the anticlinal structure (inferred from local geology): fractures are predominantly concentric to the field dome. The shape of the field anticline is approximated by a cubic surface, fit to the shape of the Seven Rivers M horizon in Tract 49 (illustrated in Figure 3-31). The coefficients of the cubic surface are calculated through a polynomial fit with matlab to the elevations of the Seven Rivers M horizon in the wells in Tract 49. The strike of every fracture is compared to the strike of the cubic surface at the center of the fracture. If the fracture strike deviates more than 30° from the local fold strike, the fracture is rotated with a probability P=0.6. A smaller percent of fractures (P=0.2) are rotated to be orthogonal to the structure strike (and to the major concentric fracture set). The remaining fractures (P=0.2) retain their orientations defined by the regional stress. Rotation is not applied to the largest numerically generated fractures ($A'_i > 2E[A']$; 10% of the total number of fractures), since they possibly belong to System 1 which was formed prior to folding; hence they are related only to the regional depositional trends (this algorithm is approximate and can be modified when more detailed information is available on the intensities of System 1 and System 2 fractures).

Table 3-9 summarizes results from numerical simulations of the fracture system around the three logged wells in Tract 49. These results are the last step in the simulations which established the correct fracture intensity P_{32} of the system in Tract 49. There is a linear relationship between the fracture intensity P_{32} and the fracture spacing in boreholes (similar to the linear relationships established by Dershowitz, 1984 and Low, 1986). The horizontal sections in Figures 3-32a - 3-34a illustrate the shape of the field anticlinal structure in the vicinity of the logged wells in Tract 49. Fracture traces on hypothetical horizontal outcrops in Figures 3-32b - 3-34b show how the numerically generated fracture system in Tract 49 relates to the field structure in the vicinity of the three logged wells in Tract 49 (YU4007, YU4903, and YU5127).

Figure 3-35 illustrates an example of fractures intersected by a simulated borehole at well YU4007. The simulated boreholes intersect mostly large fractures, therefore the average size of fractures intersected by a borehole is larger than the mean size of the entire population of fractures in a given simulation.

a) ACTUAL FOLD SHAPE IN TRACT 49: SEVEN RIVERS M HORIZON

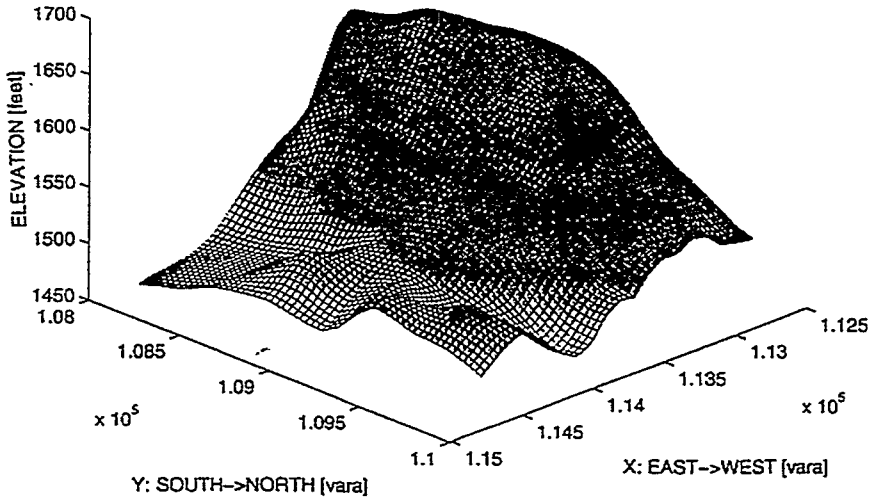

b) REPRESENTATION OF SEVEN RIVERS M BY A CUBIC SURFACE

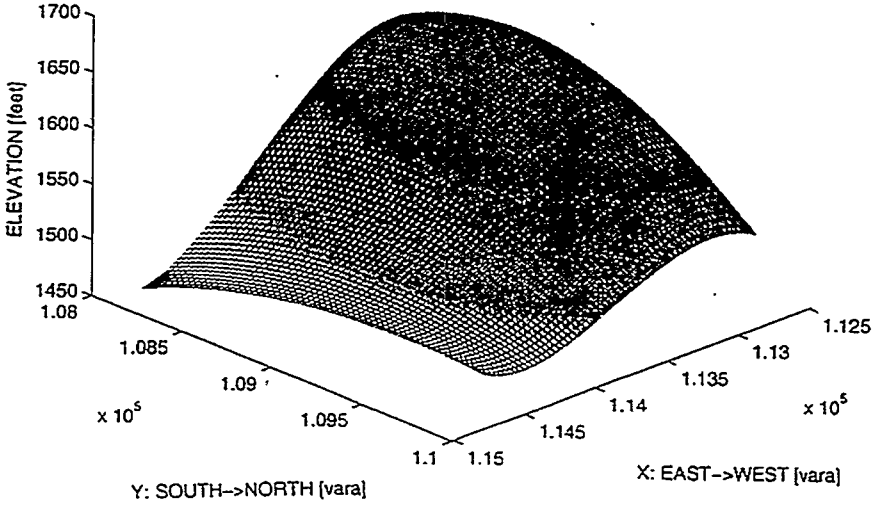

FIGURE **3-31**

FIT OF A CUBIC SURFACE TO REPRESENT THE FOLD IN TRACT 49: ACTUAL SHAPE AND CUBIC APPROXIMATION OF THE SEVEN RIVERS M HORIZON

NIPER/FINAL REPORT/WA

PROJECT NO. 963 1357.521 DRAWING NO. 80706 DATE 9/28/98 DRAWN BY EA

Golder Associates

a) Fold structure map

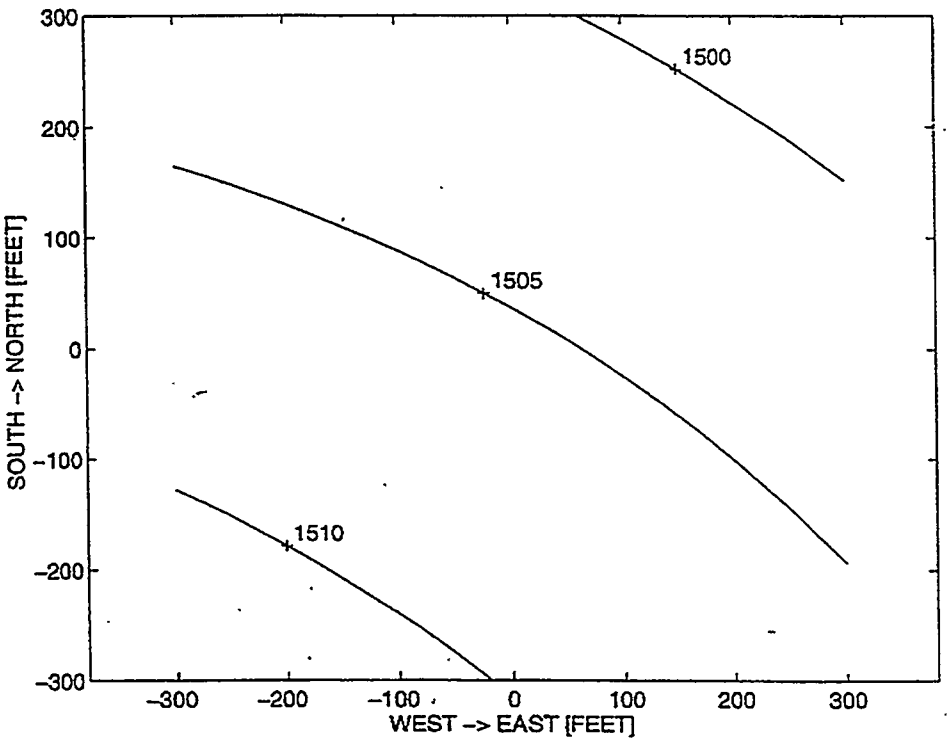

b) Traces of fold-related fractures on a hypothetical horizontal outcrop plane

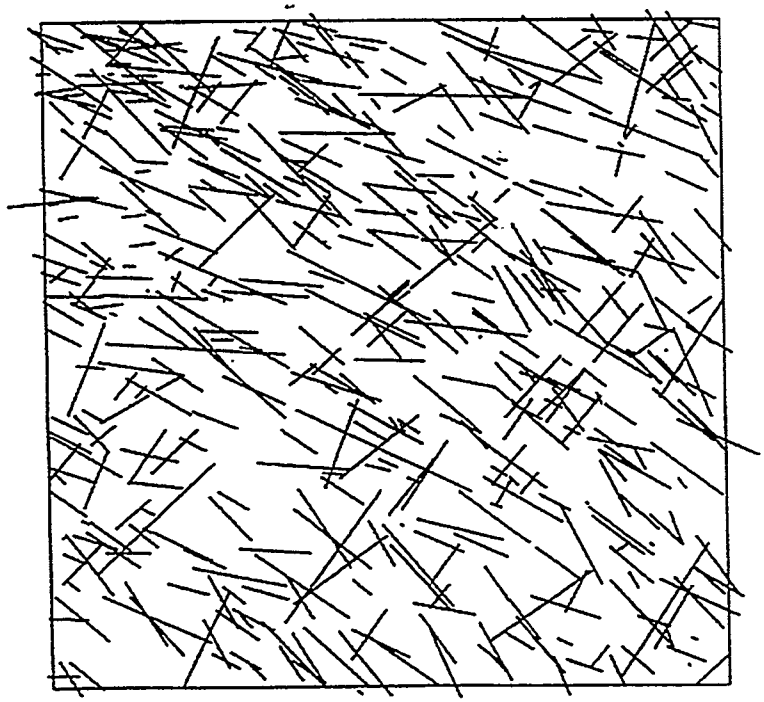

FIGURE **3-32**
RELATIONSHIP OF THE FRACTURE SYSTEM IN THE VICINITY OF WELL YU4007 TO THE LOCAL SHAPE OF THE FOLD
NIPER/FINAL REPORT/WA

a) Fold structure map

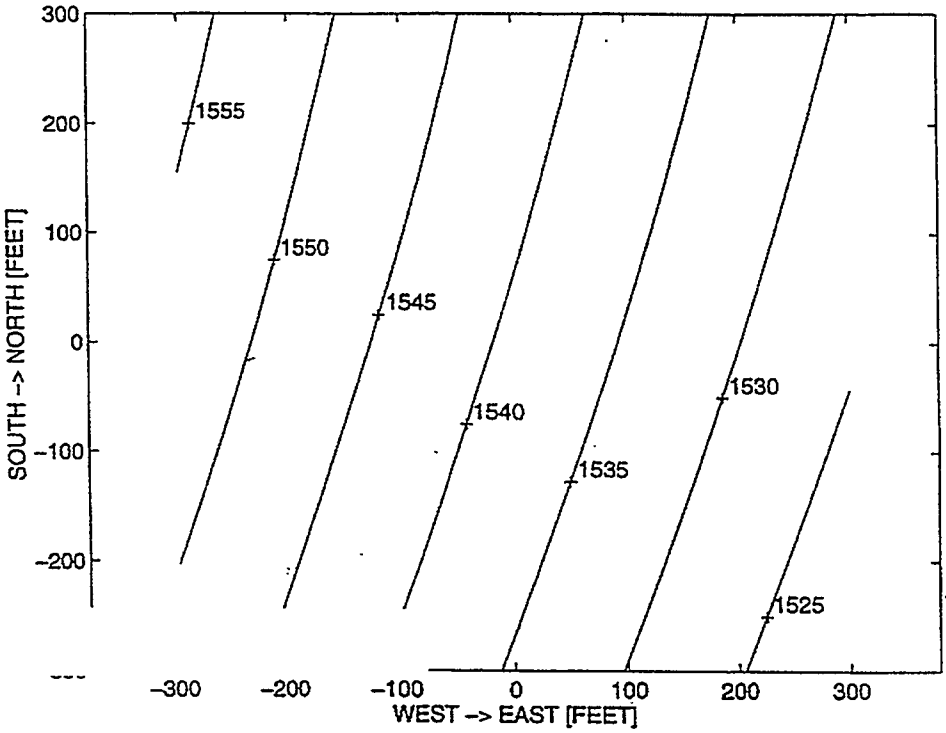

b) Traces of fold-related fractures on a hypothetical horizontal outcrop plane

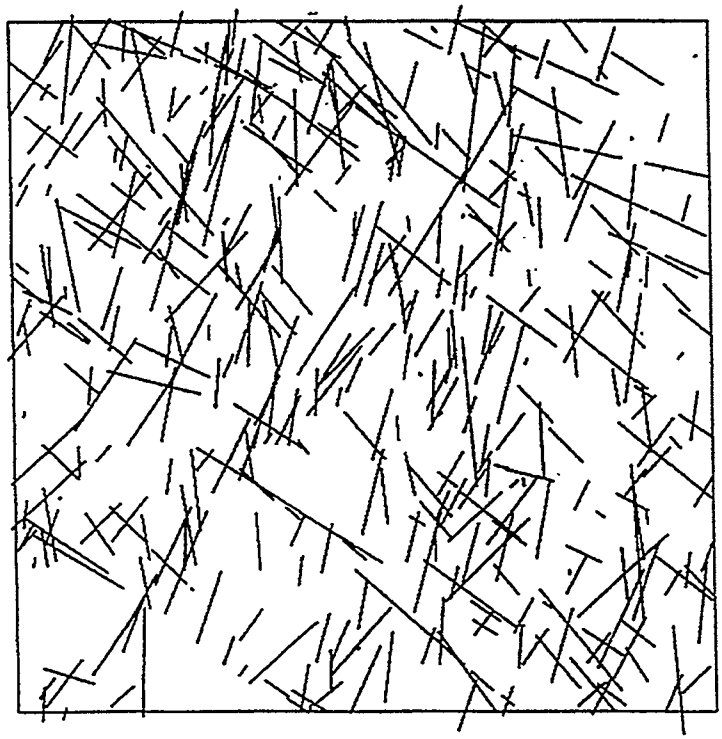

FIGURE **3-33**
RELATIONSHIP OF THE FRACTURE SYSTEM IN THE VICINITY OF WELL YU4903 TO THE LOCAL SHAPE OF THE FOLD
NIPER/FINAL REPORT/WA

a) Fold structure map

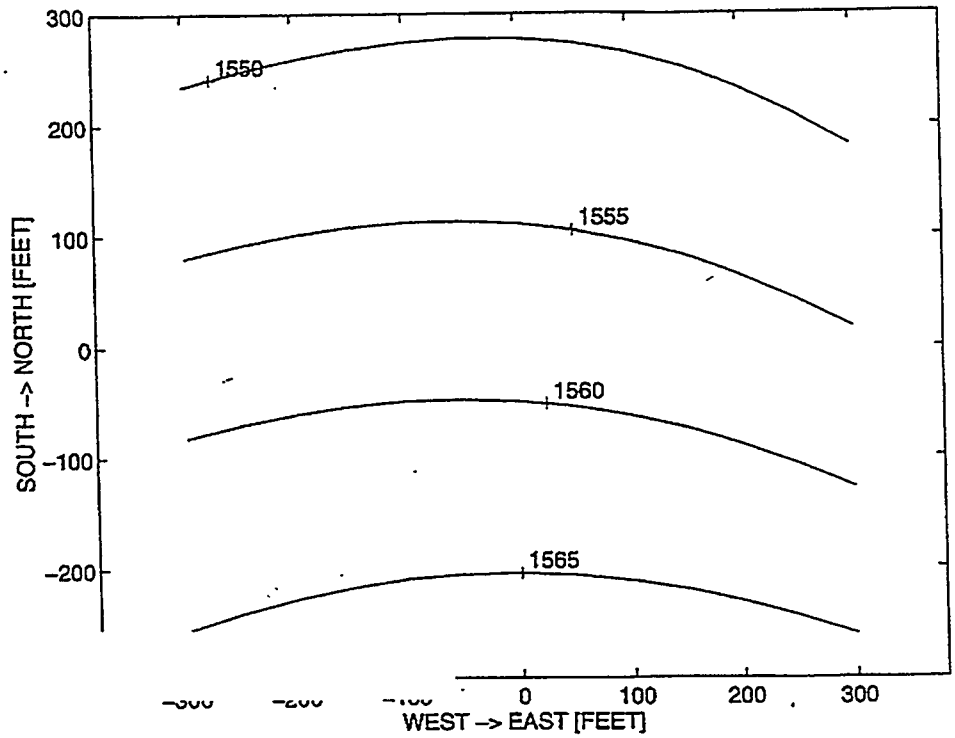

b) Traces of fold-related fractures on a hypothetical horizontal outcrop plane

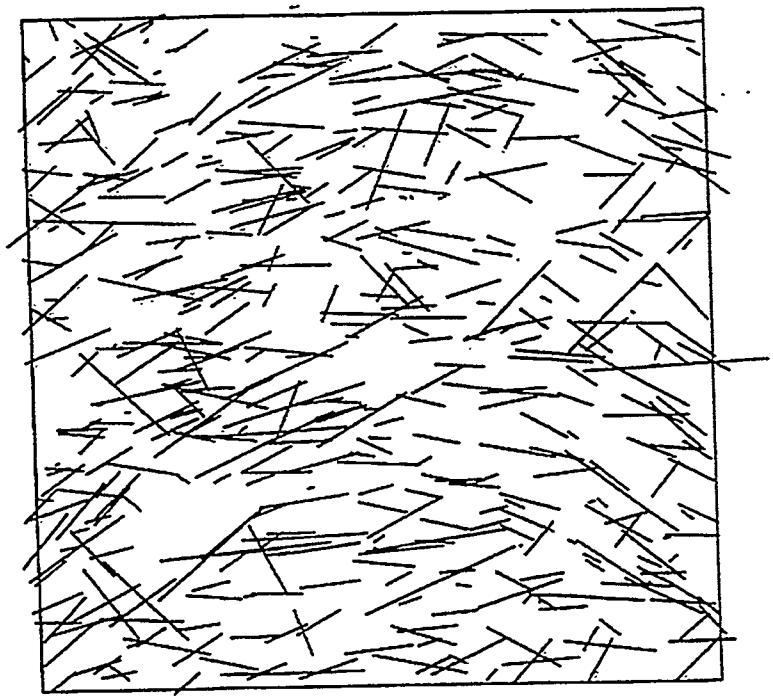

FIGURE **3-34**

RELATIONSHIP OF THE FRACTURE SYSTEM IN THE VICINITY OF WELL YU5127 TO THE LOCAL SHAPE OF THE FOLD

NIPER/FINAL REPORT/WA

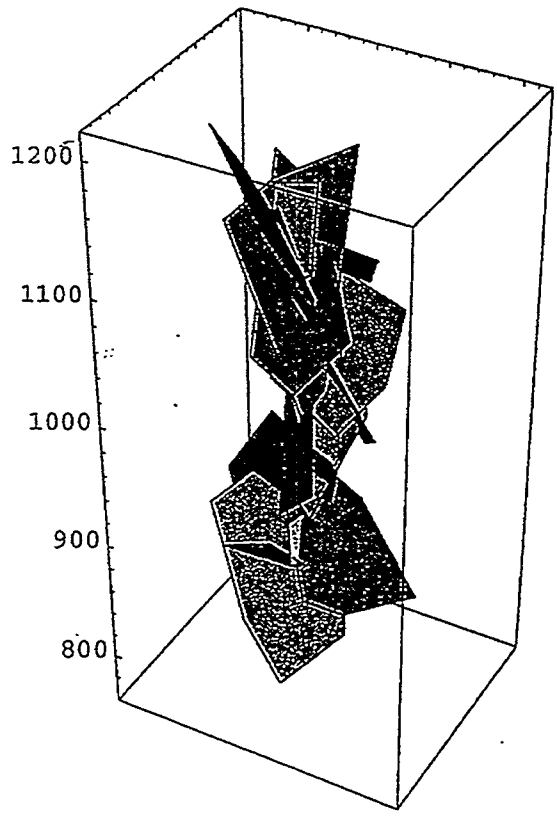

FIGURE **3-35**
NUMERICALLY GENERATED FRACTURES INTERSECTED BY A SIMULATED BOREHOLE AT WELL YU4007
NIPER/FINAL REPORT/WA

PROJECT NO. 963 1357.521 DRAWING NO. 80710 DATE 9/28/98 DRAWN BY EA

Golder Associates

Table 3-9 Results From Numerical Simulations of the Fracture System in the Vicinity of Wells YU4007, YU4903, and YU5127 in Tract 49

#	N	P_{32} (ft^{-1})	Simulated Vertical Borehole		
			S_{ave} (ft)	σ_s (ft)	N_b
well YU4007: input P_{32}=2(0.3)=0.6 ft-1, $E[R'_e]$ =30 ft, 150 ft borehole					
1	45684	0.593718	7.42	7.45	17
2	45641	0.602779	6.88	6.59	20
3	45454	0.607149	10.13	5.62	14
4	45169	0.603828	12.84	10.43	10
5	48273	0.599406	9.68	10.04	12
6	46740	0.604518	6.47	4.48	19
7	43844	0.583571	7.41	6.45	13
8	44299	0.581402	9.39	8.02	14
9	43475	0.578401	10.20	7.84	14
10	46953	0.602952	11.66	11.02	13
well YU4903: input P_{32}=2(0.3)=0.6 ft-1, $E[R'_e]$ =30 ft, 200 ft borehole					
1	50321	0.592024	8.34	8.55	24
2	47780	0.571936	11.60	9.25	18
3	49854	0.601455	12.37	11.68	16
4	51041	0.611094	11.60	7.83	16
5	49802	0.600112	11.31	8.46	17
6	53181	0.604869	8.78	6.96	23
7	51964	0.610513	6.22	6.45	29
8	50520	0.606669	7.46	5.58	24
9	48544	0.583886	10.65	14.52	15
10	51105	0.589622	9.81	10.25	21
well YU5127: input P_{32}=2(0.3)=0.6 ft-1, $E[R'_e]$ =30 ft, 200 ft borehole					
1	49106	0.589063	10.64	10.64	19
2	48274	0.579433	9.22	9.12	21
3	48708	0.58493	14.05	12.89	15
4	51585	0.587576	8.11	6.29	21
5	47071	0.546611	11.86	7.29	17
6	48965	0.58914	8.75	7.09	22
7	49046	0.583544	10.48	13.12	18
8	45983	0.555588	12.75	9.49	15
9	48174	0.575173	10.3	5.18	18
10	49459	0.592878	10.71	7.53	18

P_{32}: fracture intensity defined as cumulative fracture area per unit volume; $E[R'_e]$: expected value of fracture equivalent radius; N: total number of fractures generated in a simulation; N_b: fractures intersected by a simulated borehole; s_{ave} and σ_s: average value and standard deviation of fracture spacing in the simulated borehole. Dip distributions of the fractures in the shaded rows are shown in Figure 3-39.

Figures 3-36 through 3-38 show rosette diagrams of fracture strikes in simulated boreholes at wells YU4007, YU4903, and YU5127. The strikes of numerically generated fracture well intersections match well the strikes of fractures, identified on the log profiles of the wells in Tract 49. Figure 3-39 illustrates the normalized dip distribution of numerically generated fractures compared to the normalized dip distribution of significant fractures identified in cores in Tract 49. The figure shows three examples of fracture dip distribution in simulations of borehole intersections with wells YU4007, YU4903, and YU5127 (the three simulations correspond to the shaded rows in Table 3-9).

Table 3-10 shows results from simulations in which, after generating the population of fractures, they were also marked as a function of the porosity of the surrounding rock. As a result, in parts of the modeling volumes around the wells, the simulated fracture intensity is lower due to high porosity of the dolomite matrix which makes the material relatively ductile. The distinction between "low" and "high" porosity has been assumed to be at n=20%. Numerically generated fractures which lie entirely in regions with average porosity $n \geq 20\%$ are discarded with probability $P_f=0.5$. Thus, in the high-porosity dolomite the fracture system includes only relatively large fractures, whereas in dolomite with lower porosity both large and smaller fractures exist. The simulations in Table 3-10 were performed for illustration of the capability of the model to reproduce fracture intensity as a function of rock properties. Since the exact effect of the porosity of San Andres dolomite on the fracture intensity in the formation has not been studied yet, more precise simulations cannot be done at this stage of the Yates case study.

As Table 3-10 shows, due to high porosity, the total fracture number N of fractures decreases within the modeling volumes surrounding wells YU4007, YU4903, and YU5127, hence the fracture intensity P_{32} also decreases. The fracture spacing in the simulated boreholes is larger when porosity is accounted for in cases when the well cuts across some regions of high porosity (see data for wells YU4903 and YU5127). In the case when the well does not cut across high-porosity regions (YU4007) there is no change in the spacing of fractures in simulated boreholes before and after the porosity effect has been accounted for. However, the fracture number and the overall fracture intensity P_{32} in the entire modeling volume are smaller if the porosity is considered.

The results from the modeling of fracture intensity as a function of porosity once again confirms the importance of inferring model parameters from the entire geologic environment of a fracture system, rather than assuming geometric characteristics of the 3D system based on intersections by boreholes (or surface outcrops). Figure 3-40 shows rosette diagrams of strikes of the numerically generated fractures intersected by simulated boreholes at wells YU4903 and YU5127 (a) before, and (b) after porosity effect has been considered.

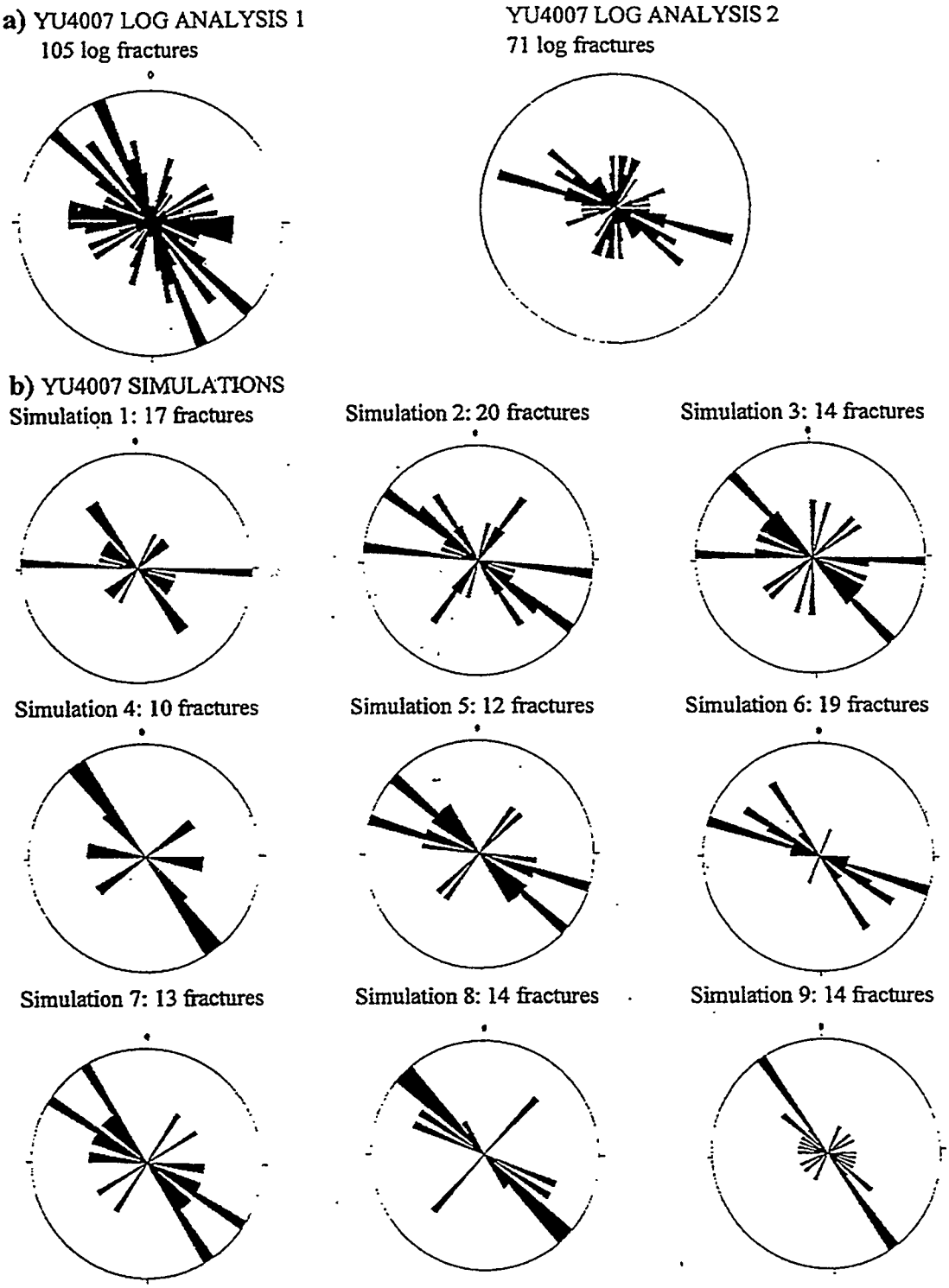

FIGURE **3-36**

ROSETTE DIAGRAMS OF MEASURED AND SIMULATED FRACTURE STRIKES AT WELL YU4007

NIPER/FINAL REPORT/WA

PROJECT NO. 963 1357.521 DRAWING NO. 80711 DATE 9/28/98 DRAWN BY EA

Golder Associates

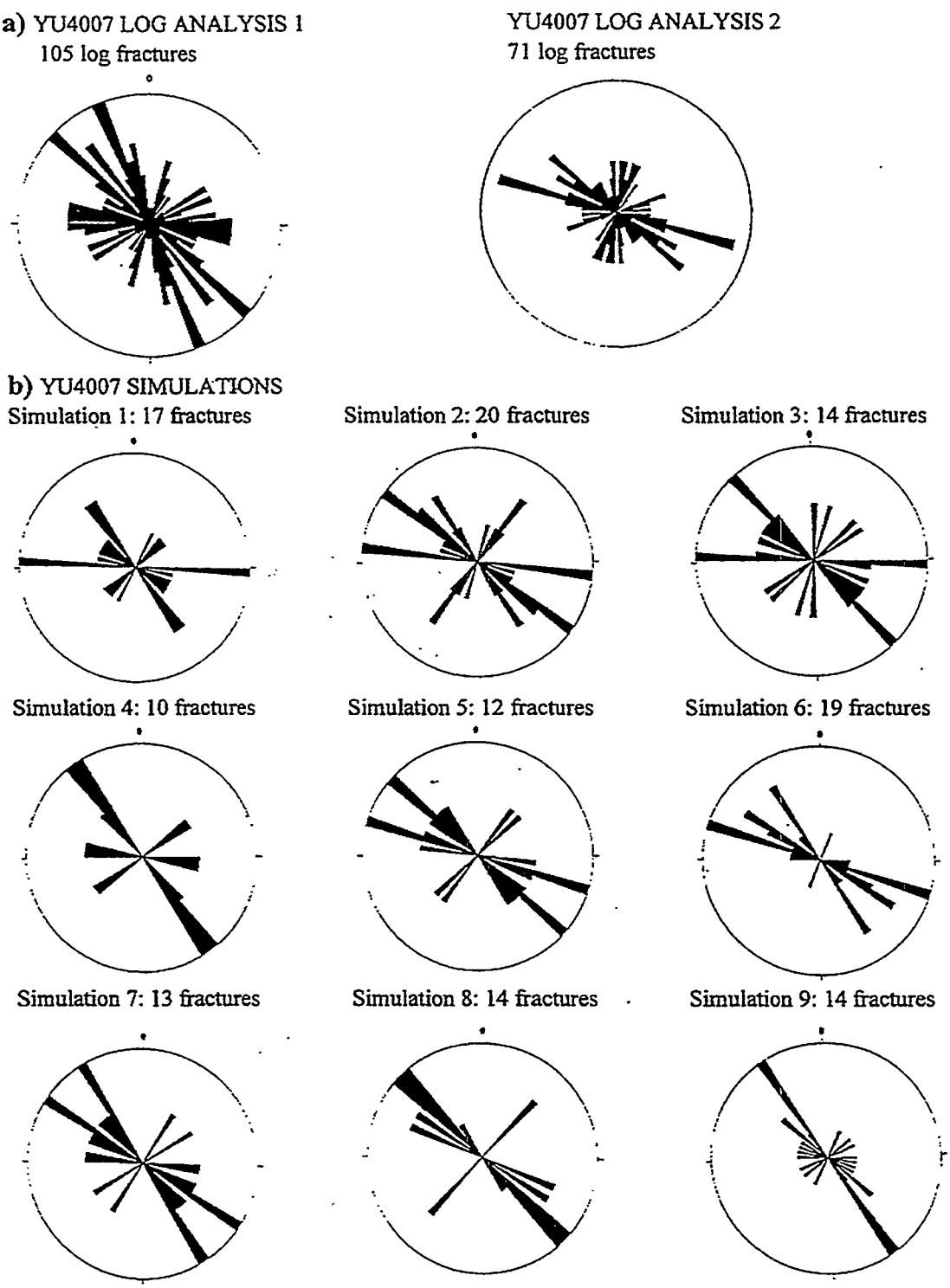

FIGURE **3-37**

ROSETTE DIAGRAMS OF MEASURED AND SIMULATED FRACTURE STRIKES AT WELL YU4903

NIPER/FINAL REPORT/WA

PROJECT NO. 963 1357.521 DRAWING NO. 80712 DATE 9/28/98 DRAWN BY EA

Golder Associates

a) YU5127 LOG ANALYSIS 1
122 log fractures

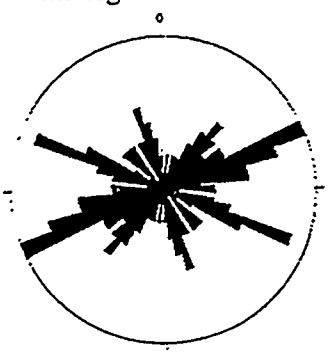

YU5127 LOG ANALYSIS 2
47 log fractures

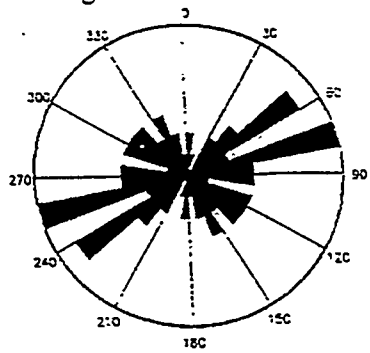

b) YU5127 SIMULATIONS

Simulation 1: 19 fractures

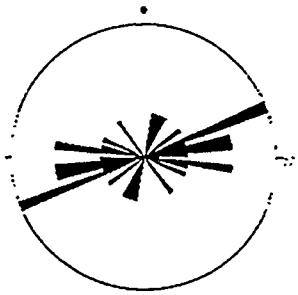

Simulation 2: 21 fractures

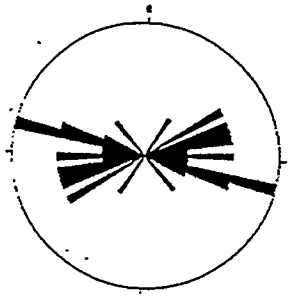

Simulation 3: 15 fractures

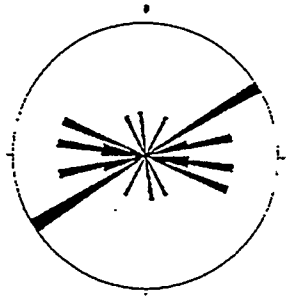

Simulation 4: 21 fractures

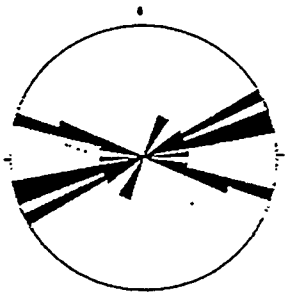

Simulation 5: 17 fractures

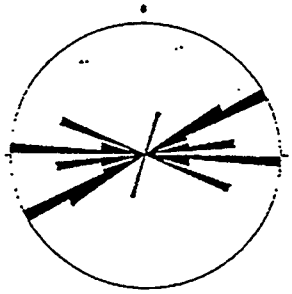

Simulation 6: 22 fractures

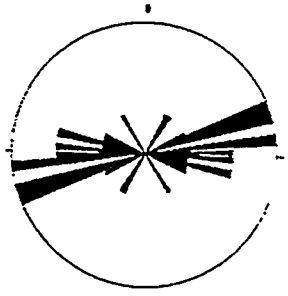

Simulation 7: 18 fractures

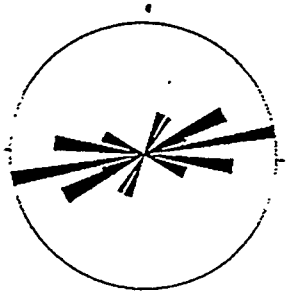

Simulation 8: 15 fractures

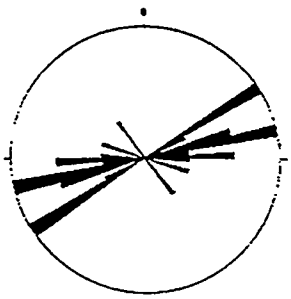

Simulation 9: 18 fractures

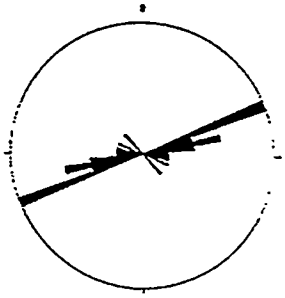

FIGURE **3-38**
ROSETTE DIAGRAMS OF MEASURED AND SIMULATED FRACTURE STRIKES AT WELL YU5127 IN TRACT 49
NIPER/FINAL REPORT/WA

SIMULATION 1

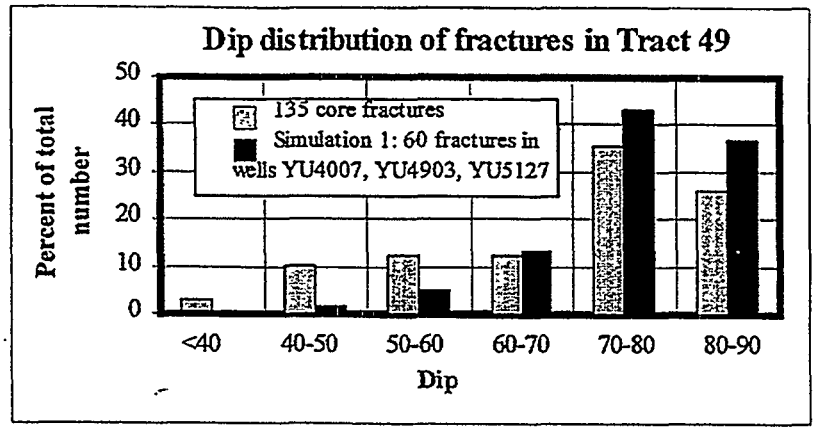

SIMULATION 3

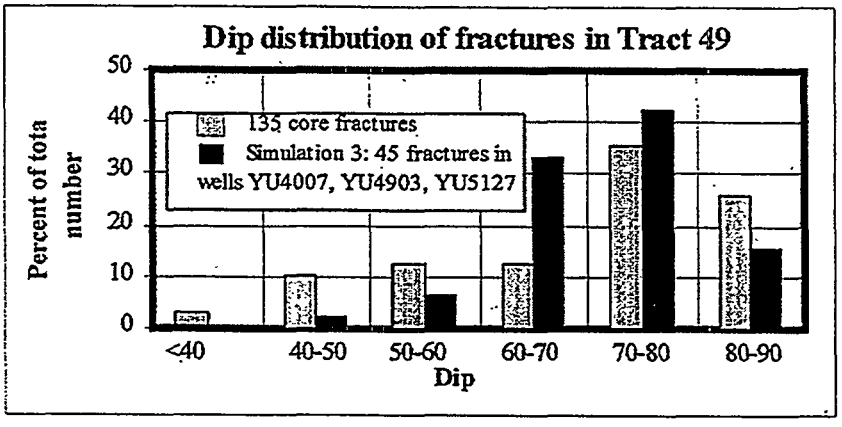

SIMULATION 8

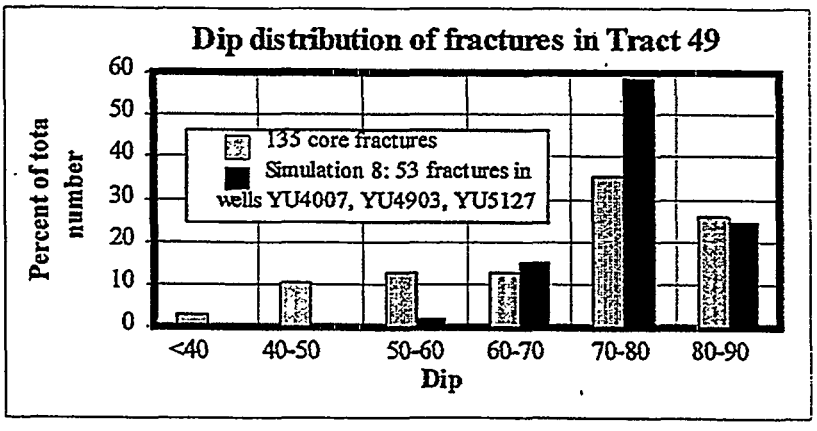

FIGURE **3-39**

COMPARISON OF FRACTURE DIP DISTRIBUTION FROM SIMULATIONS TO DIP DISTRIBUTION OF SIGNIFICANT FRACTURES IN CORES IN TRACT 49

NIPER/FINAL REPORT/WA

Figure 3-40 Rosette Diagrams of Strikes of Numerically Generated Fractures Intersected by Simulated Boreholes at Wells YU4903 and YU5127

a) without considering porosity

YU4903: 19 fractures

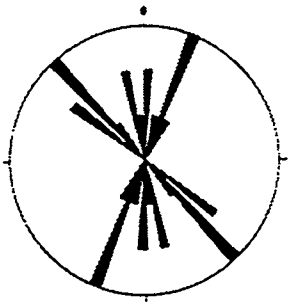

YU5127: 17 fractures

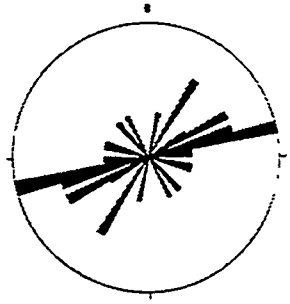

b) after accounting for porosity effect

YU4903: 17 fractures

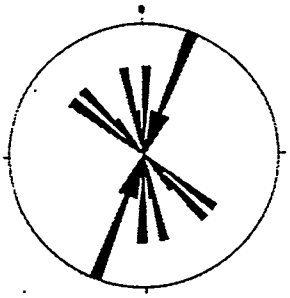

YU5127: 13 fractures

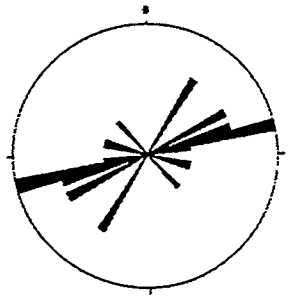

Table 3-10 Results From Numerical Simulations of Fracture Intensity as a Function of Porosity in Tract 49

Well	N	P_{32} (ft^{-1})	N_b	s_{ave} (ft)
YU4007				
Simulation 1				
Before porosity marking	46887	0.623321	12	12.24
After porosity marking	43405	0.587105	12	12.24
Simulation 2				
Before porosity marking	46581	0.618255	10	6.58
After porosity marking	43062	0.580815	10	6.58
YU4903				
Simulation 1				
Before porosity marking	52823	0.626901	17	11.80
After porosity marking	37678	0.458482	15	13.48
Simulation 2				
Before porosity marking	50785	0.610058	19	10.28
After porosity marking	36071	0.444844	17	11.52
YU5127				
Simulation 1				
Before porosity marking	49080	0.592736	18	11.18
After porosity marking	43330	0.533109	17	11.34
Simulation 2				
Before porosity marking	48201	0.577111	17	11.90
After porosity marking	42682	0.518546	13	14.03

After generation of the fracture system, P_{32} in porous dolomite (n>20%) is reduced to half of P_{32} in dense dolomite. N: total number of fractures generated in the modeling volume; P_{32}: fracture intensity (averaged for the entire modeling volume); N_b: number of fractures intersected by a simulated borehole; s_{ave}: average spacing between fractures in the simulated borehole.

3.2.2 Numerical Simulation of the Fracture System in Tract 17

Inference of Model Parameters

Similar to the inference procedure for Tract 49, fracture intensity P_{32} in Tract 17 is determined from the mean spacing of significant fractures intersected by cores. Table 3-11 summarizes the spacing of significant fractures, identified in cores available from eight wells located inside or in the vicinity of Tract 17. Significant fractures are determined from core analysis according to the method described in Section 3.2.1 for Tract 49 (see Table 3-5). However, while in Tract 49 the distinction between significant and insignificant fractures is relatively clear, in Tract 17 there are numerous fractures that cannot be ignored even if they are not of the type illustrated in Table 3-5. For example, there are numerous vertical TOPN fractures which are relatively small (having 1 ft or 2 ft intersections with the core). Also, there are numerous TOPN or POPN fractures of large aperture that cut wall to wall only one cored foot. In Table 3-11 such fractures are referred to as "smaller significant fractures".

Table 3-11 Spacing of Significant Fractures, Identified in Cores in Tract 17

Well	n_{ave} (%)	N	s_{ave} (ft)	Comment
YU1776	13.2	13	7.50	SD=6.87 ft. Numerous smaller fractures. Alternating zones of low and high porosity. Spacing of all (not only the largest) significant fractures: s_{ave}=5.5-6.5 ft. Vertical fractures (from top to bottom): 4 ft in n_{ave}=7.9%; 44 ft in zones with n_{ave}=7.9%, 10.9% and 19.5%; 2 ft in n_{ave}=19.5%; 8 ft and 19 ft in n_{ave} =20.7%.
YU17C9	6.9	4	11.33	Spacing between all significant fractures: s_{ave}=7 ft.
YU2530	N/A	2	7	Only 15 ft of core recovered.
YU2437	19.4	8	4.5	SD=2.07 ft. Zones with very high porosity ϕ_{ave}=20-30%. Vertical fractures: 13 ft in n_{ave}=17.82%; 7 ft in n_{ave} =21.28%.
YU2416	21.62	6	13.8	SD=14.48 ft. Numerous smaller fractures. No fractures in zone with very high porosity n_{ave}=29.28%. Some thin layers of low porosity n_{ave}=7.87%. Spacing s_{ave}= 4.5 ft in n_{ave}=17.05%. No fractures below elevation 1098 ft (in 87 ft of core).
YU2433	19.4	36	6.4	SD=5.36 ft. Longest continuous core: 318 ft. Mostly high porosity n>20%. Spacing increasing with depth (from top to bottom): s_{ave}=3.25 ft in n_{ave}=7.81% (27 ft top zone); s_{ave}=3 ft in n_{ave}=21%; thin zone (4 ft) with n_{ave}=5.3%; s_{ave}=3.43 ft in n_{ave}=22.5%; s_{ave}=5 ft in n_{ave}=11.6%; s_{ave}=8.2 ft in n_{ave}=22.5%; s_{ave}=9 ft in n_{ave}=20.9%. Vertical fractures: 7 ft and 2 ft in n_{ave}= 7.81%; 7 ft start in n_{ave}=21%, terminate at n_{ave}=5.3%; 4 ft in n_{ave}=22.1%; 4 ft and 2 ft in n_{ave}=22.5%; 4, 1, 1, 1, 3, 2, 2, 5, 12 ft in n_{ave}= 20.9% (bottom zone).
YU2509	20.9	12	17.09	SD=9.43 ft. Numerous smaller significant fractures. Spacing including smaller significant fractures s_{ave}= 7.48 ft. In upper layers spacing s_{ave}=4.77 ft in n_{ave}= 5.07-14.7%; in lower layers s_{ave}=8.82 ft in n_{ave}=20.8%. Almost all vertical fractures: 3, 5, 11, 4, 15, 1, 2, 3, 4, 1, 2, 4, 6, 1, 2, 1, 2, 2 ft (top to bottom).
YU14D4	4.9	11	7.18	SD=7.36 ft. Well is located in the far west side of field.

n_{ave}: average core porosity; N: number of large significant fractures identified at the given well; s_{ave}: average spacing of large significant fractures; SD: standard deviation of spacing between large significant fractures (given only where N>5).

As Table 3-11 shows, the average spacing of intersections of significant fractures with the vertical wells in Tract 17 varies between 4.5 ft and 11.3 ft (1.4-3.4 m) where the rock porosity is n_{ave}<20%. The spacing increases where the rock porosity is n_{ave}>20% (see data for wells YU2416 and YU2509). When the smaller significant fractures are also considered, the average spacing is between 4.5 ft and 7.5 ft (1.4-2.3 m). There may be a tendency of increasing spacing with depth, suggested by the longest available continuous core (318 ft; 97 m) at well YU2433. Forty vertical fracture intersections in Tract 17 cores have heights from 1 ft to 44 ft (0.3-13 m), with all but five having heights less than 10 ft (3 m).

The dip distribution of significant fractures, intersected by cores in Tract 49, is shown in Figure 3-41. Compared to Tract 49, there are more vertical or nearly vertical fractures in Tract 17. Dip distribution similar to that shown in Figure 3-41 has also been determined from the log analysis of the only horizontal well in the study area: well YU17D5 in Tract 17 (Figure 3-42). According to Tinker and Mruk (1995), "the quality of the data in this well and the confidence in the fracture picks are very high". The average spacing of 671 fractures intersections in the 1550 ft (472 m) long horizontal well is s_{ave}= 2.31 ft (0.7 m). Since the fractures in the Yates reservoir rocks are nearly vertical, they are much more easily intersected by the horizontal well than by the vertical wells.

In Tract 17 the relationship of the fractures to the field anticlinal structure is more complex than that in Tract 49 (Figure 3-30). Tract 17 is on the peri-anticline of the reservoir dome: a zone of transition from uncompactible grainstones on the east side toward compacted mudstones to the west. In Tract 17, the northwest striking regional fracture set is sub-parallel to the major hinge of the peri-anticline and to a set of drape folds / faults. The northeast striking regional set is sub-parallel to the minor hinge of the peri-anticline (which defines the so called cross-curvature of the fold) and to a second set of drape folds / faults.

Numerical Algorithms

In Tract 17, the algorithm defined in Section 3.2.1 to read porosity data from the Yates field StrataModel, and to mark polygons as a function of the porosity of the surrounding rock, is used in the numerical generation of the fracture system. In Tract 17, there is an additional influence of the rock lithology on the fracture intensity: "shales" are considered to be more ductile (hence less fractured) than the brittle dolomite between them. An algorithm reads from the StrataModel not only porosity values, but also gamma ray (GR) data (indicator of shale content), and calculates the average porosity and the average GR of the host rock surrounding a given polygon. Then a polygon is retained as a fracture with probability P_f as a function of the average porosity and the average GR of the surrounding rock:

$$P_f = P_f\left(\frac{1}{N}\sum_{i=1}^{N} n_i, \frac{1}{N}\sum_{i=1}^{N} GR_i\right) \tag{3-33}$$

where N is the number of geocells from the reservoir StrataModel intersected by the polygon, n_i is the porosity and GR_i is the gamma ray response in the i-th intersected cell.

Numerical Simulations

Based on the inference procedure, presented above, the following parameters of the 3D HFM are selected for the simulations in Tract 17:

- Mean orientations of two fracture sets (inferred from regional geology): vertical planes, striking N50°W and N40°E.

Figure 3-41 Dip Distribution of 93 Fractures, Identified as "Significant" on Cores From Eight Wells in the Tract 17 Area

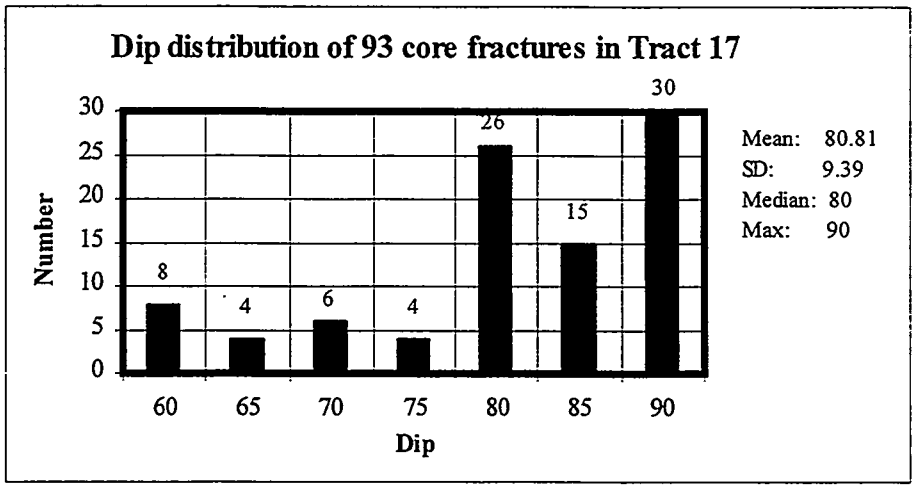

YU1711

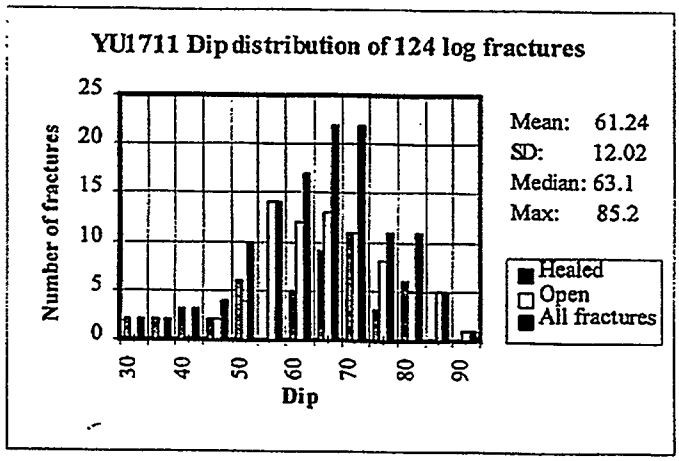

YU1755

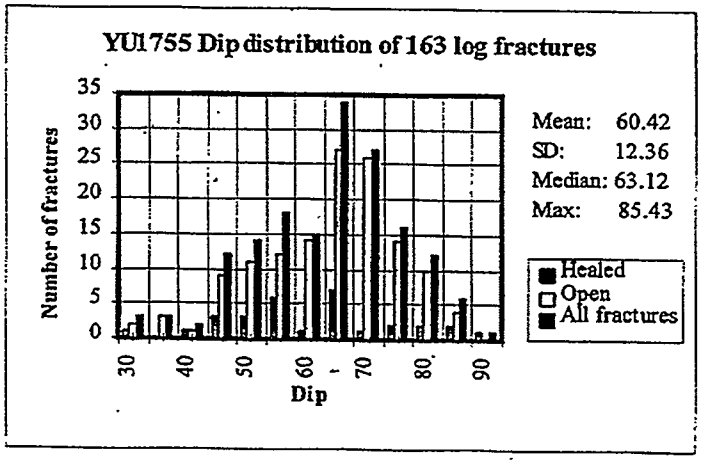

YU17D5

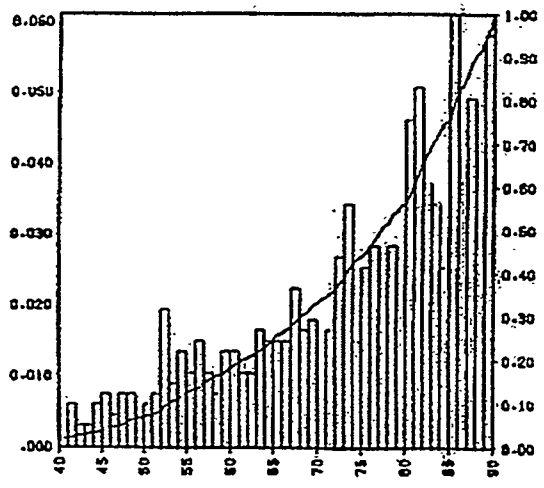

Number of fractures: 671
Mean fracture dip: 73.57
Standard deviation: 13.38
Median of dip: 77.18
Mode of dip: 85.5
Maximum dip: 90

FIGURE **3-42**
DISTRIBUTION OF FRACTURE DIPS AT LOGGED WELLS IN TRACT 17
NIPER/FINAL REPORT/WA

PROJECT NO. 963 1357.521 DRAWING NO. 80730 DATE 9/28/98 DRAWN BY EA

Golder Associates

- PDF of fracture plane orientations: Fisher (κ=20) which produces close clustering of plane pole orientations around the mean pole.

- Modeling volumes:

  - Vertical logged wells: YU1711 and YU1755 inside Tract 17, and YU2511 in the vicinity of Tract 17. The modeling volume for a vertical well is defined by the following boundaries: a horizontal datum surface at 700 ft above sea level; four vertical planes (two striking south-north and two striking east-west), each at a horizontal distance of 300 ft (91 m) from the vertical well; a quadratic upper surface, parallel to the San Andres top and located 100 ft (30 m) above it. The coefficients of the quadratic function are calculated through a polynomial fit with matlab to the elevations of the San Andres top at the wells in the Tract 17 area.

  - Horizontal logged well: YU17D5 in Tract 17 (north-south trend). The modeling volume for the horizontal well is defined by the following boundaries: a horizontal datum surface at 800 ft above sea level (about 200 ft, 61 m, below the elevation of the well); two vertical planes, striking south-north, at a horizontal distance of 200 ft (61 m) from the well; two vertical planes, striking east-west, at a horizontal distance of 800 ft (244 m) from the midpoint of the well (i.e., 50 ft, 15 m, from the two ends of the well); a quadratic upper surface, parallel to the San Andres top and located 100 ft (30 m) below it (i.e., at least 200 ft, 61 m, above the elevation of the well). The coefficients of the quadratic function are calculated through a polynomial fit with matlab to the elevations of the San Andres top.

- Fracture intensity (inferred from field data, since the stress and strain magnitudes, and the mechanical properties of the San Andres dolomite, are not known yet): total P_{32}=0.8 (ft^2/ft^3), established through simulations to produce expected spacing in vertical boreholes E(s)=7 ft (2.1 m). The intensities of two fracture sets contribute to the total P_{32}: a major set with assumed intensity $P_{32}1$=0.6 (ft-1), and a minor set with intensity $P_{32}2$=0.2 (ft^{-1}). The N50°W regional set is major in the vicinity of well YU1711 which is located on the crest of the major northwest striking anticlinal axis (Figure 3-30a). The N40°E regional set is major in the vicinity of the other three wells: YU17D5, YU1755, and YU2511, which are located in more peripheral areas of the peri-anticline.

- Fracture size distribution (approximate procedure, since field sampling of fracture sizes is not available): similar to Tract 49, the mean of the equivalent radius is assumed $E[R'_e]$=30 ft (9 m; related to the thickness of mechanical units in the San Andres formation). Marking in terms of relative size is assumed of the type $A'_i < E[A']$, where $E[A']=\pi(30)2=2827$ (ft^2) is the expected area of fractures. This type of marking (see Section 3.2) eliminates the polygons with extremely large sizes, and produces fracture areas that have a standard deviation $\sigma_{A'} = 1.26E[A']$ and median $M[A'] = 0.6E[A']$. 65% of the produced fractures have areas smaller than the average area.

- Effect of porosity (approximate procedure since the exact effect of high porosity on fracture intensity has not been studied yet): fracture intensity in areas with porosity n>20% is assumed to be half of the fracture intensity where n<20%, i.e., $P_{32}|n>20\% = 50\% P_{32} = 0.5(0.8) = 0.4$ (ft^{-1}). A fracture is discarded with probability Pf=0.5 if the average porosity of the dolomite matrix around the fracture is $n_{ave}>20\%$. This method results in discarding fractures with relatively small sizes, since they are the most likely to be located entirely in an area of high porosity. Thus in high porosity dolomite only relatively large fractures are retained which results in larger spacing of fractures intersected by the wells.

- Effect of shale (approximate procedure since the exact effect of high shale content on fracture intensity has not been studied yet): fracture intensity in areas with high shale content is assumed to be half of the fracture intensity in clean dolomite, i.e., P_{32}, shale $= 50\% P_{32} = 0.5(0.8) = 0.4$ (ft^{-1}). Rock with high shale content ($\geq$10%) is defined to be the one where the porosity $n_{ave}<20\%$, and the gamma ray response $GR_{ave}>40$ API. Thus a fracture is discarded with probability $P_f=0.5$ if the average porosity of the dolomite matrix around the fracture is $n_{ave}<20\%$ and the average gamma ray response is $GR_{ave}>40$ API. This methods results in discarding fractures with relatively small sizes, since they are the most likely to be located entirely in the relatively thin shale layers. Thus the clean dolomite in Tract 17 includes numerous small and fewer large fractures, but only the relatively large ones cut across the thin shale layers.

- Relationship to the anticlinal structure (inferred from local geology): in Tract 17, where the slope of field anticline is very gentle, the relationship of fractures to the local slope of the structure is not as pronounced as it is in Tract 49. The shape of the field anticline is approximated by a cubic surface, fit to the shape of the Seven Rivers M horizon in Tract 17 (illustrated in Figure 3-43). The coefficients of the cubic surface are calculated through a polynomial fit with matlab to the elevations of the Seven Rivers M horizon in the wells in Tract 17. The relation of fracture orientation to the reservoir structure is more complex than it is in Tract 49: predominant fracture orientations in Tract 17 are related to the shape of the entire peri-anticline rather than only to the local slope of the structure. This relationship is accounted for by choosing which one of the regional sets (related to the shape of the peri-anticline) is dominant in the vicinity of different wells. Only a small percent of fractures in Tract 17 are related to the local strike of the fold structure at their centers. In the numerical generation, such fractures are rotated to be predominantly parallel to the slope of the cubic surface near wells YU1711, YU1755, and YU2511, and predominantly orthogonal to the slope (i.e., parallel to the structure itself) in the vicinity of the horizontal well YU17D5.

a) ACTUAL FOLD SHAPE IN TRACT 17: SEVEN RIVERS M HORIZON

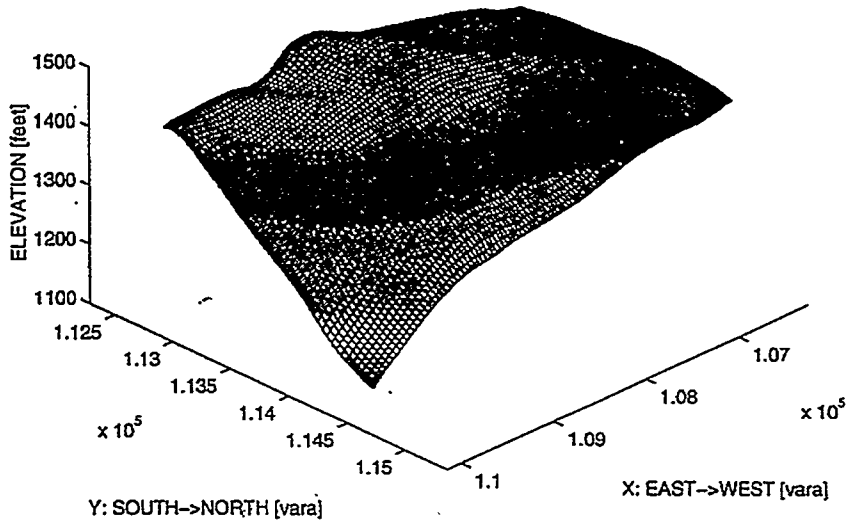

b) REPRESENTATION OF SEVEN RIVERS M BY A CUBIC SURFACE

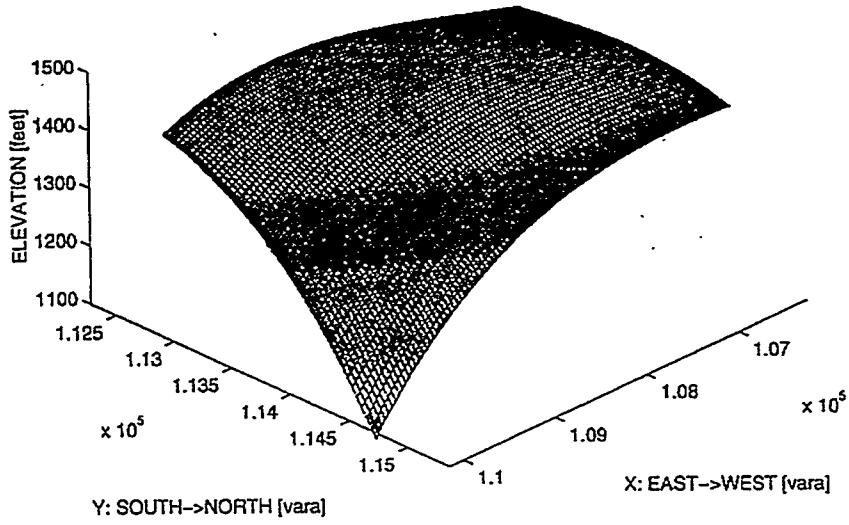

FIGURE **3-43**

FIT OF A CUBIC SURFACE TO REPRESENT A FOLD IN TRACT 17: ACTUAL SHAPE AND CUBIC APPROXIMATION OF THE SEVEN RIVERS M HORIZON

NIPER/FINAL REPORT/WA

PROJECT NO. 963 1357.521 DRAWING NO. 80733 DATE 9/29/98 DRAWN BY EA

Golder Associates

Table 3-12 summarizes results from numerical simulations of the fracture system around the three logged wells in Tract 17 (YU1711, YU1755, and YU17D5). These results reflect the last step of the simulations that established the correct fracture intensity P_{32} of the system in Tract 17. The spacing of fracture intersections in the simulated horizontal well YU17D5 (shaded column in Table 3-12), which is essentially equal to the known actual spacing of 2.31 ft, confirms that the fracture intensity P_{32} used in the simulations (based on fracture intersections with vertical wells) has been assumed correctly.

Table 3-12 Results from numerical simulations of the fracture system in the vicinity of wells YU1711, YU1755, and YU17D5 in Tract 17

#	N	P_{32} (ft^{-1})	Simulated Vertical Borehole		
			s_{ave} (ft)	σ_s (ft)	N_b
well YU1711: input P_{32}=0.8 ft-1 $E[R'_e]$=30 ft, 250 ft borehole					
1	52456	0.779530	7.51	8.51	33
2	52995	0.786830	7.95	7.59	32
3	53475	0.802514	6.10	5.95	40
4	53865	0.836727	8.06	12.29	30
5	52005	0.820035	7.96	6.03	31
6	53222	0.823912	4.65	4.83	54
well YU1755: input P_{32}=0.8 ft-1, $E[R'_e]$=30 ft, 300 ft borehole					
1	49776	0.820790	7.24	10.65	41
2	50009	0.829751	9.26	7.60	32
3	49632	0.802260	5.99	5.27	50
4	48966	0.811473	5.95	5.27	49
5	49333	0.816772	7.93	6.83	38
6	49349	0.807361	7.18	6.41	42
Well YU17D5: input P_{32}=0.8 ft-1, $E[R'_e]$=30 ft, 1500 ft borehole					
1	77743	0.805955	2.23	2.49	672
2	75648	0.830260	2.14	2.42	696
3	76732	0.833689	2.19	2.60	682
4	74975	0.810587	2.19	2.54	686
5	74593	0.780934	2.44	2.77	613
6	74938	0.804766	2.37	2.95	632

P_{32}: fracture intensity defined as cumulative fracture area per unit volume; $E[R'_e]$: expected value of fracture equivalent radius; N: total number of fractures generated in a simulation; N_b: fractures intersected by the simulated borehole; s_{ave} and σ_s: average value and standard deviation of fracture spacing in the simulated borehole. Dip distribution of the fractures in the shaded row is shown in Figure 3-50. The shaded column represents a test of P_{32} (assumed on the basis of spacing of fracture intersections with vertical wells): compare to the actual spacing of 2.31 ft determined from log analysis of the horizontal well YU17D5.

The horizontal sections in Figures 3-44a through 3-46a illustrate the shape of the field anticlinal structure in the vicinity of the logged wells inside and near Tract 17. Fracture traces on hypothetical horizontal outcrops in Figures 3-44b through 3-46b show how the numerically generated fracture system in Tract 17 relates to the field structure in the vicinity of the three logged wells in Tract 17 (YU1711, YU1755, and YU17D5).

Figures 3-47 through 3-49 show rosette diagrams of measured and simulated fracture strikes in simulated boreholes at wells YU1711, YU1755, and YU17D5. The strikes of numerically generated fracture well intersections are compared to the strikes of fractures, identified on the log profiles of the wells in Tract 17. Figure 3-50 illustrates the normalized dip distribution of numerically generated fractures compared to the normalized dip distribution of significant fractures identified in cores in Tract 17. The figure shows the fracture dip distribution in a simulation of borehole intersections with wells YU1711, YU1755, and YU17D5 (corresponding to the shaded row in Table 3-12).

Table 3-13 shows results from simulations in which the effect of high porosity and shale content on fracture intensity was also considered. In parts of the modeling volumes around the wells, the fracture intensity is lower due to either high porosity or high shale content of the dolomite matrix, both of which make the material relatively ductile. The distinction between "low" and "high" porosity has been assumed to be at n=20%. The distinction between "low" and "high" shale content has been assumed to be at 10% (GR=40 API). Numerically generated fractures which lie entirely in regions with either average porosity $n \geq 20\%$ or with average shale content of more than 10% are discarded with probability Pf=0.5. Thus, in the high-porosity dolomite the fracture system includes only relatively large fractures, whereas in dolomite with lower porosity both large and smaller fractures exist. Only the relatively large fractures cut across the thin layers with high shale content, whereas the intensity of small fractures in the shales is much lower than it is in the clean dolomite. The simulations in Table 3-15 were performed for illustration of the capability of the model to reproduce fracture intensity as a function of rock properties. Since the exact effect of the porosity and shale content of San Andres dolomite on the fracture intensity in the formation has not been studied yet, more precise simulations cannot be done at this stage of the Yates case study.

3.2.3 Evaluation of 3D HFM Application to Tracts 17 and 49

The model for the development of the fracture system in the Yates reservoir is based on the depositional model of prograding and aggrading carbonate shoals, published data on the regional tectonic history of the Permian Basin, and other geologic information (including field data) provided by Marathon Oil Company. The model for fracture system development and the proposed algorithms of the 3D hierarchical model best suit the geological information available from the Yates field. Should any additional field data significantly differ from the data available so far, the model for fracture system evolution and the numerical hierarchical model may have to be modified. With this in mind, the following conclusions can be drawn regarding the modeling of the fracture system in the Yates reservoir rocks, presented in the preceding sections of this chapter.

a) Fold structure map

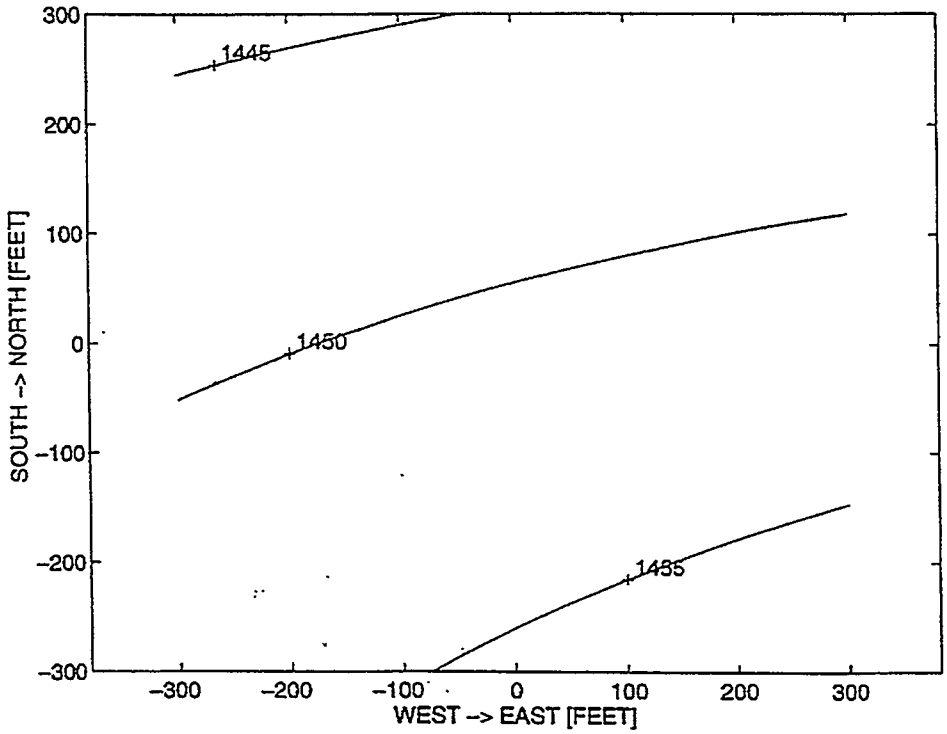

b) Traces of fold-related fractures on a hypothetical horizontal outcrop plane

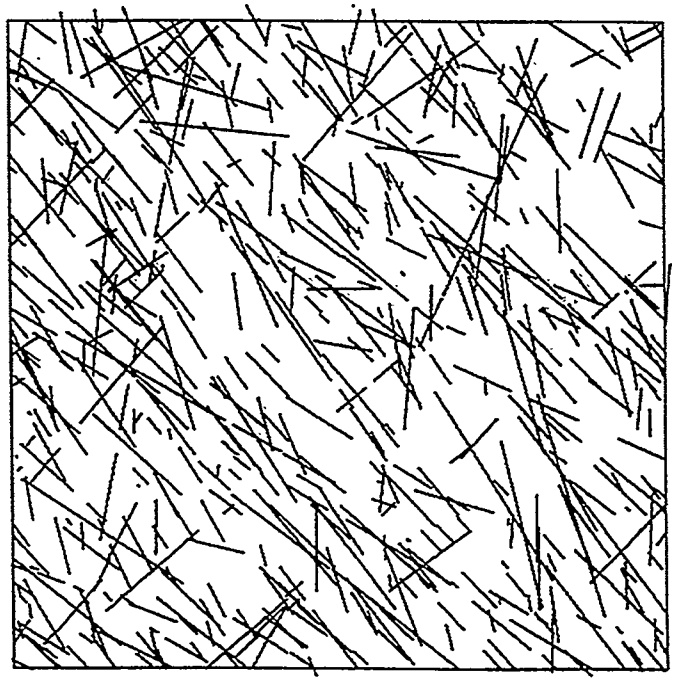

FIGURE **3-44**
RELATIONSHIP OF THE FRACTURE SYSTEM IN THE VICINITY OF WELL YU 1711 TO THE LOCAL SHAPE OF THE FOLD
NIPER/FINAL REPORT/WA

a) Fold structure map

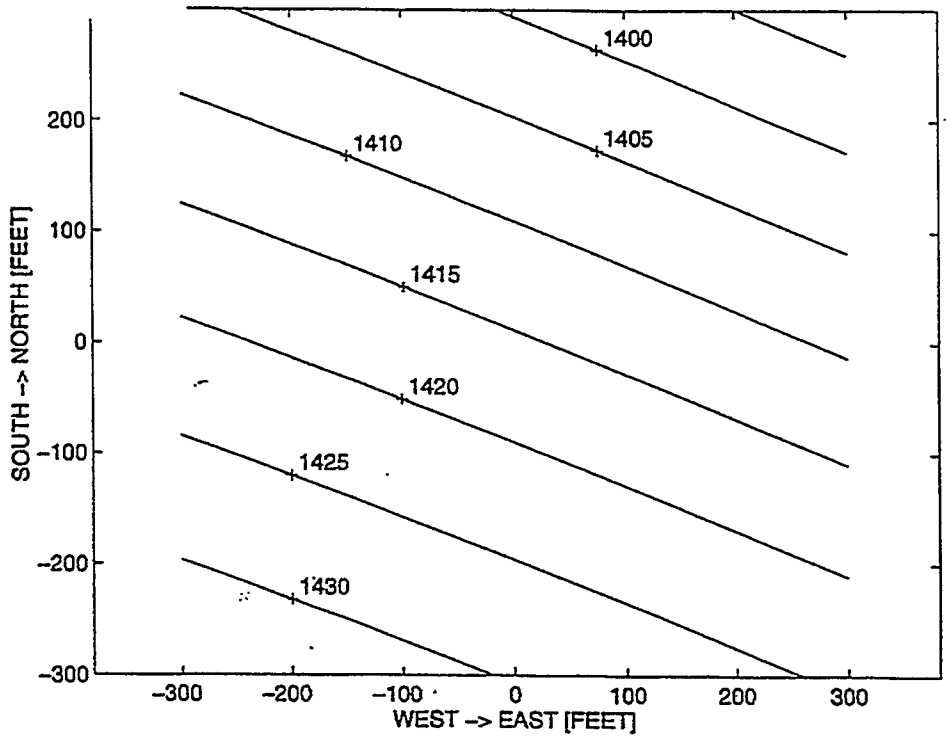

b) Traces of fold-related fractures on a hypothetical horizontal outcrop plane

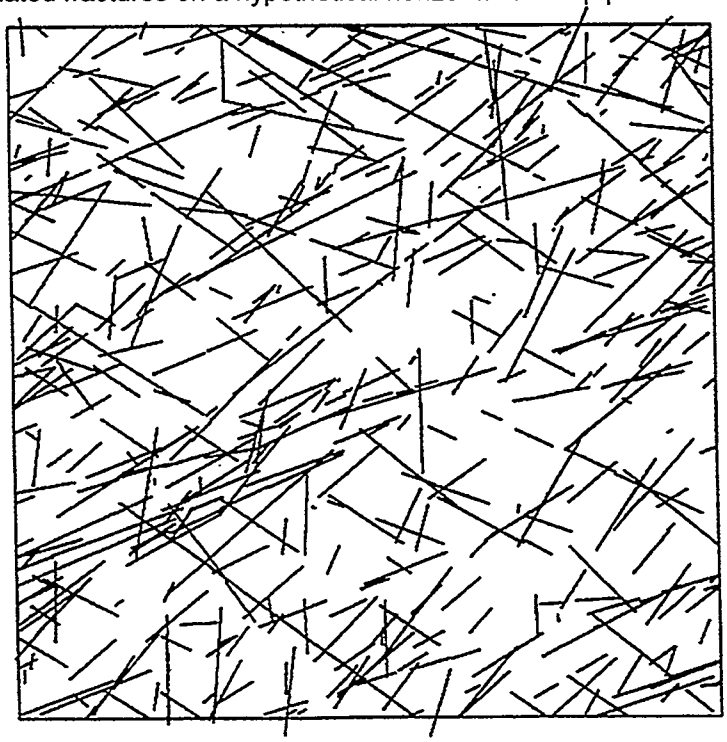

FIGURE **3-45**
RELATIONSHIP OF THE FRACTURE SYSTEM IN THE VICINITY OF WELL YU 1755 TO THE LOCAL SHAPE OF THE FOLD
NIPER/FINAL REPORT/WA

a) Fold structure map

b) Traces of fold-related fractures on a hypothetical horizontal outcrop plane

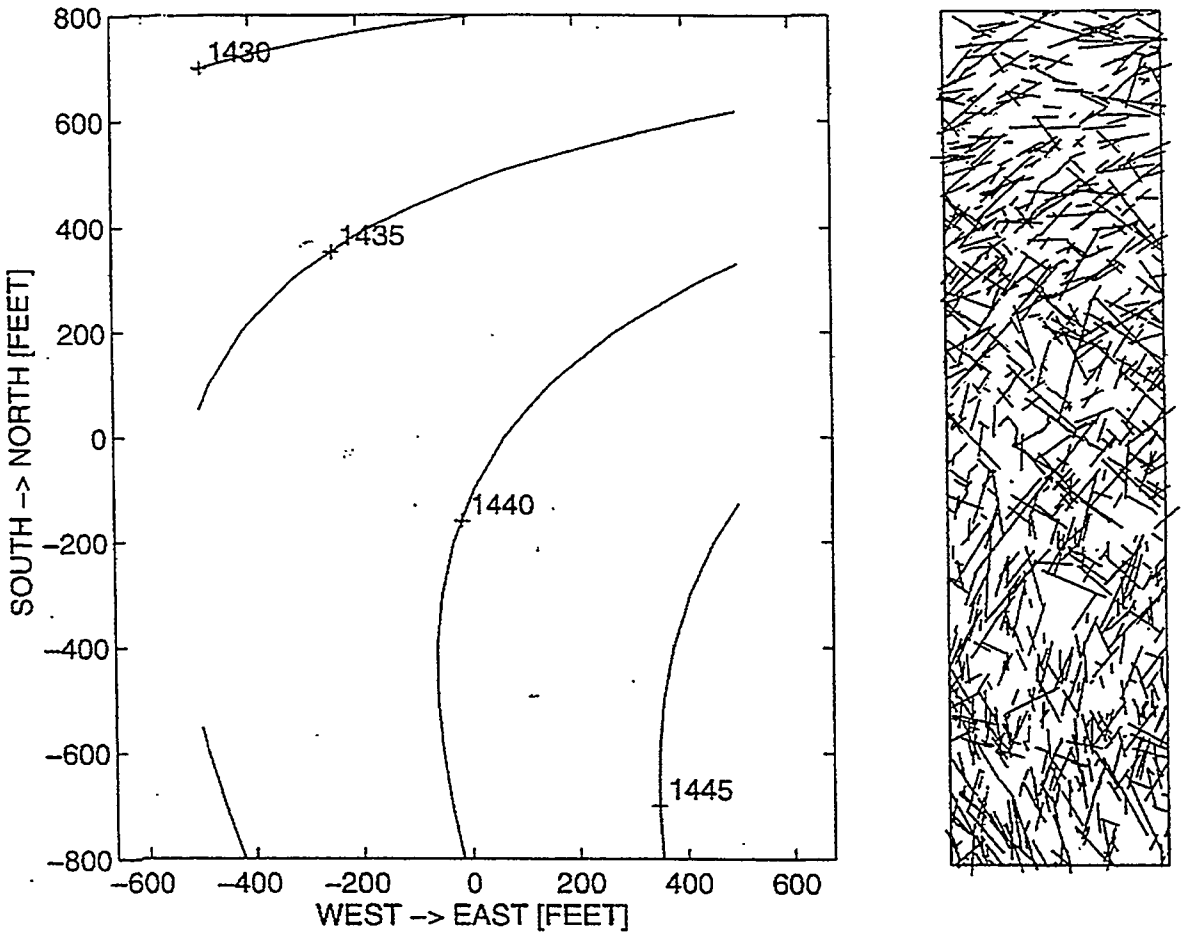

FIGURE **3-46**

RELATIONSHIP OF THE FRACTURE SYSTEM IN THE VICINITY OF WELL YU 17D5 TO THE LOCAL SHAPE OF THE FOLD

NIPER/FINAL REPORT/WA

YU1711 LOG ANALYSIS 1
124 log fractures

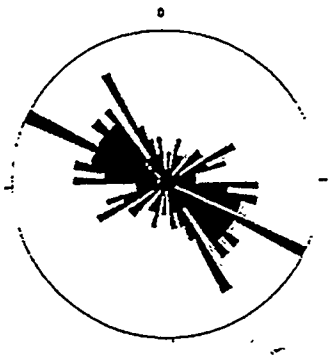

YU1711 LOG ANALYSIS 2
20 log fractures

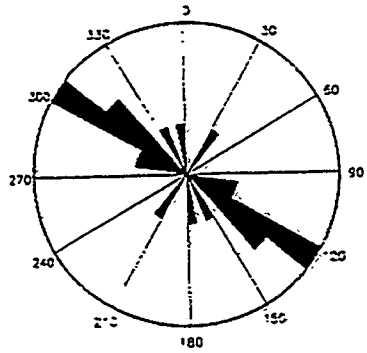

b) YU1711 SIMULATIONS

Simulation 1: 33 fractures

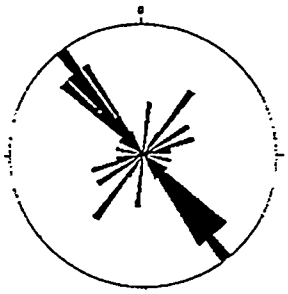

Simulation 2: 32 fractures

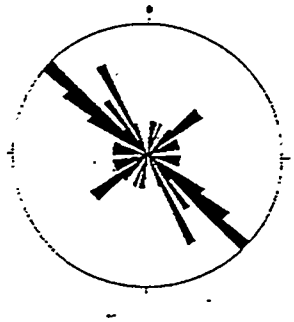

Simulation 3: 40 fractures

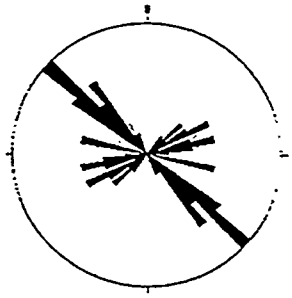

Simulation 4: 30 fractures

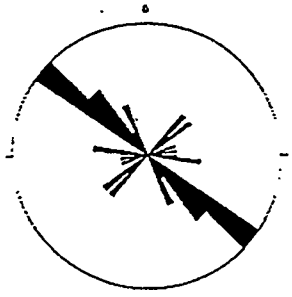

Simulation 5: 31 fractures

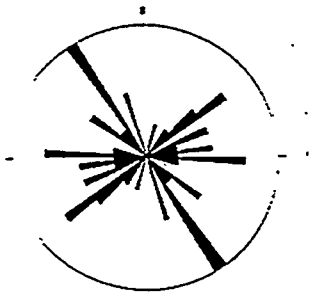

Simulation 6: 54 fractures

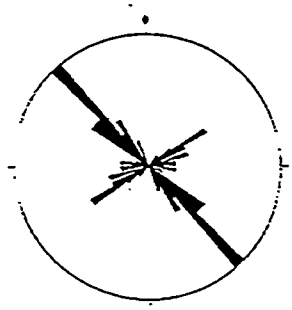

FIGURE **3-47**
ROSETTE DIAGRAMS OF MEASURED AND SIMULATED FRACTURE STRIKES AT WELL YU1711 IN TRACT 17
NIPER/FINAL REPORT/WA

PROJECT NO. 963 1357.521 DRAWING NO. 80737 DATE 9/28/98 DRAWN BY EA

Golder Associates

a) YU1755 LOG ANALYSIS
163 log fractures

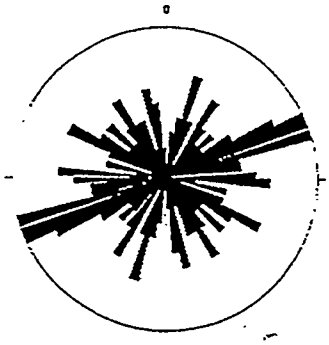

b) YU1755 SIMULATIONS

Simulation 1: 41 fractures

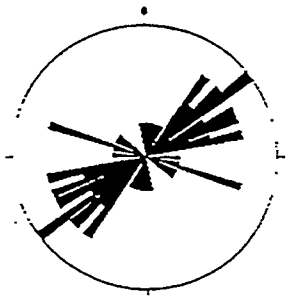

Simulation 2: 32 fractures

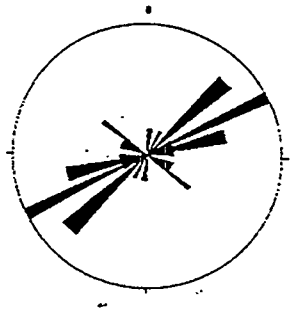

Simulation 3: 50 fractures

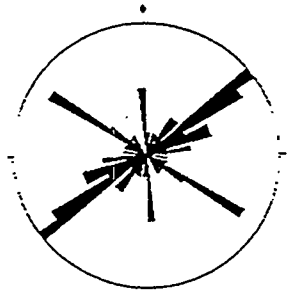

Simulation 4: 49 fractures

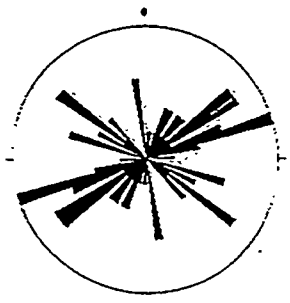

Simulation 5: 38 fractures

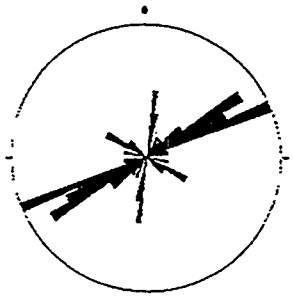

Simulation 6: 42 fractures

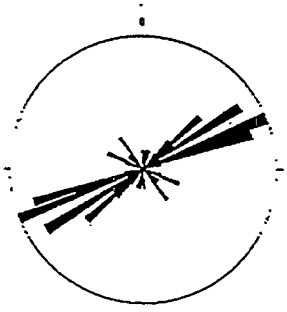

FIGURE **3-48**
ROSETTE DIAGRAMS OF MEASURED AND SIMULATED FRACTURE STRIKES AT WELL YU1755 IN TRACT 17
NIPER/FINAL REPORT/WA

a) YU17D5 LOG ANALYSIS
671 log fractures

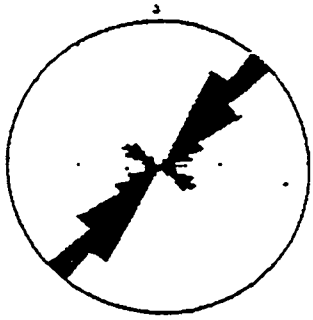

b) YU17D5 SIMULATIONS

Simulation 1: 672 fractures

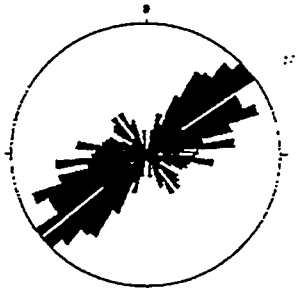

Simulation 2: 696 fractures

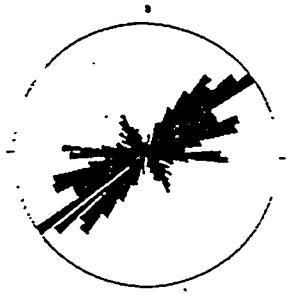

Simulation 3: 682 fractures

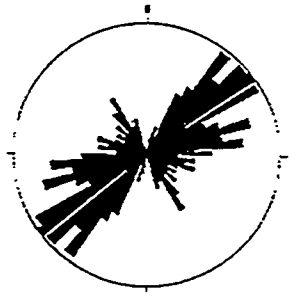

Simulation 4: 686 fractures

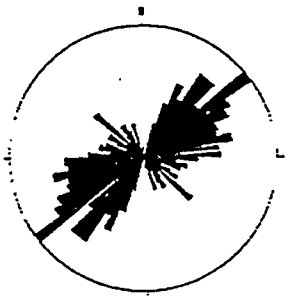

Simulation 5: 613 fractures

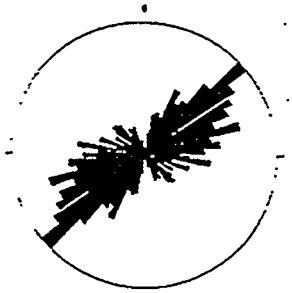

Simulation 6: 632 fractures

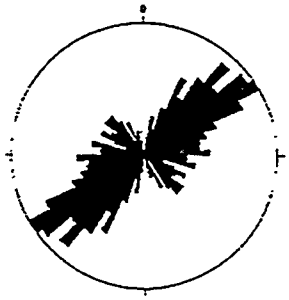

FIGURE **3-49**
ROSETTE DIAGRAMS OF MEASURED AND SIMULATED FRACTURE STRIKES AT WELL YU17D5 IN TRACT 17
NIPER/FINAL REPORT/WA

PROJECT NO. 963 1357.521 DRAWING NO. 80739 DATE 9/28/98 DRAWN BY EA

Golder Associates

Figure 3-50 Comparison of Fracture Dip Distribution From Simulations to Dip Distribution of Significant Fractures in Cores in Tract 17

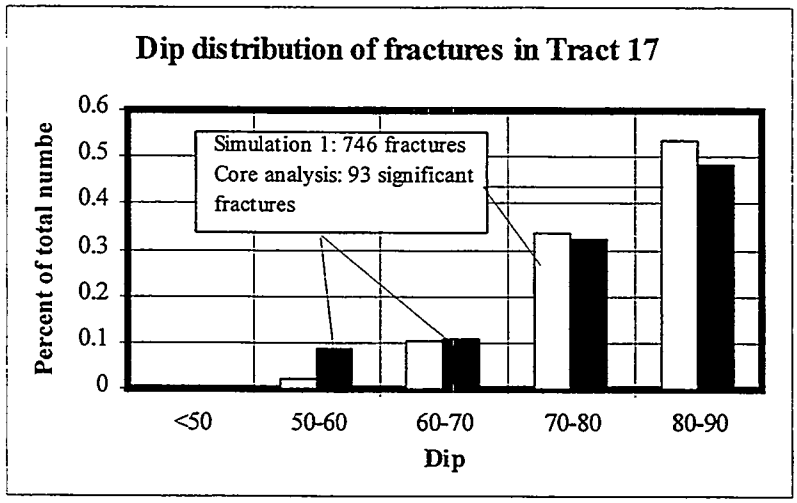

Table 3-13 Results From Numerical Simulations of Fracture Intensity as a Function of Lithology (Including Effect of Porosity and Shale Content) in the Vicinity of Three Wells in Tract 17

Well	N	P_{32} (ft-1)	N_b	s_{ave} (ft)
YU1711				
Before lithology marking	52736	0.788880	30	8.08
After lithology marking	33101	0.531829	20	11.39
YU1755				
Before lithology marking	51409	0.837606	49	6.02
After lithology marking	34771	0.62375	36	8.26
YU17D5				
Before lithology marking	74663	0.809764	639	2.34
After lithology marking	41600	0.494508	575	2.60

After generation of the fracture system, P_{32} in dolomite of high porosity (n>20%) is reduced to half of P_{32} in lower-porosity dolomite, and P_{32} in "shales" (shale content>10%) is reduced to half of P_{32} in clean dolomite. N: total number of fractures generated in the modeling volume; P_{32}: fracture intensity in the modeling volume; N_b: number of fractures intersected by a simulated borehole; s_{ave}: average spacing between fracture intersections with the simulated borehole.

Fracture Orientations

In the case study, a model of the geologic genesis of the reservoir fracture system in the Yates field was developed. This model accounted for regional and local geologic mechanisms that determined the fracture orientations. The assumed variation of fracture orientations includes subvertical joints, related by strike to regional depositional trends and to the reservoir anticlinal structure. The fracture orientations are confirmed by the intersections in cored and logged wells in the Yates field. Since the geology has been considered in detail, there is great confidence that the assumptions regarding fracture orientations away from the wells are correct. The results from the numerical simulations show that the proposed 3D model has the capability of realistically reproducing various fracture orientation distributions, including relationships to both regional stress directions and local structures (folds).

In the light of a future study, one has to remember that besides the steeply-dipping fractures, flat-lying bedding boundaries most likely also contribute to the reservoir conductivity (possibly even more than the fractures themselves). Bedding-planes have not been modeled in this case study; however, their orientations should not be ignored in a study of flow though the fractured reservoir.

Fracture Intensity: P_{32}

In the case study, fracture intensity P_{32}, expressed as cumulative fractured area per unit rock volume, has been assumed on the basis of field data (e.g., fracture core intersections), since field data on geologic stress and strain magnitudes, and experimental data on mechanical properties (strength, deformation moduli) of the

reservoir formations, are not available yet. The effect of rock lithology (porosity and shale content) on fracture intensity has also been considered in some simulations. Given the available data, the general method of inference of fracture intensity is correct. Also, the results from the numerical simulations show that the 3D model has the capability of reproducing desired fracture intensity such as P_{32}, including its 3D variation as a function of rock properties. However, in terms of the exact values of P_{32} used in the simulations, there is more to be desired. The following recommendations should be incorporated in a future study of the fracture system intensity in the Yates reservoir.

The fracture system modeling, presented in this chapter, included inference and numerical simulation of a "total" fracture intensity P_{32}. All fractures which were considered "significant" (i.e., totally open, having a large aperture, etc.), were reproduced. However, in reality it is possible that certain major (possibly the largest) fractures control the flow in the reservoir. If one is interested in the reservoir conductivity, a "conductive" P_{32} should be used in the simulations (Dershowitz, 1993). The field data available to the case study so far was not sufficient for inference of the conductive P_{32}. However, a limited number of water profiles from Tract 17 and Tract 49 suggest that fluid injection field tests can be a good method to determine the conductive P_{32} which is likely to be lower than the total P_{32}. Also, numerical simulations of flow through the fracture system, generated with the 3D fracture system model, can be a good way to establish which fractures in the Yates field reservoir are conductive and which are not.

In the Yates field case study, rock lithology is considered to affect the "ductility" or "brittleness" of the reservoir rocks, and hence the fracture intensity P_{32}. This is mostly based on assumptions by geologists and engineers: for example, since fewer fractures are observed in very porous dolomite in the San Andres formation, high porosity is considered to "increase rock ductility". Similarly, dolomites with high shale content on the west side of the field are considered more ductile (hence less fractured). It would be much better if the assumptions about the lithology effect were based on laboratory tests of the mechanical properties of the Yates reservoir rocks. If specimens with different porosity and shale content are tested for tensile and shear strength, and for deformability, more reliable assumptions can be made about which lithological characteristics really affect the mechanical properties of the San Andres dolomite and the other reservoir formations.

The core database, used in the inference of total P_{32}, has been available to the case study only in electronic form (the actual cores are at MOC PTC in Littleton, Colorado). In a future study, it would be better to identify significant fractures on the actual continuous cores.

In general, the extensive database available from the Yates field includes very detailed information on depositional sequences, rock lithology, porosity, and other reservoir properties that are traditionally of interest to the oil industry. However, since fractures are subject of a more recent interest, far less information has been collected on the mechanical properties of the reservoir formations. It would be good to develop a procedure for recording field information on the fracture system from a "more

mechanical" point of view (for example, taking samples for laboratory experiments, etc.), rather than describing fractures by number or lithology of the mineral filling. The intersections of fractures by cores and logs do not necessarily indicate what fractures exist away from the wells; whereas a depositional model, combined with a database on the mechanical properties of the various formations, can enable one to make a good estimate of the variation of fracture intensity in the reservoir.

Lastly, only P_{32} of vertical fractures was the subject of this case study. In a future study of flow through the reservoir, intensity of conductive features along flatly-lying bedding boundaries (fractures or not) should be considered as well.

Fracture Intensity: Size Variation

Fracture size distribution in the case study was assumed on the basis of limited exposures of vertical fractures in cores and a simplified analysis of major mechanical units in the reservoir. This procedure is approximate and does not give a precise estimate for distribution of fracture sizes in the Yates reservoir. Sizes are not considered in more detail since at this stage it is more important to first make a correct estimate of the fracture intensity P_{32}.

In a future study, fracture size distribution, if desired, can be correlated to distribution of bedding thicknesses or thicknesses of depositional sequences behaving as mechanical units in the reservoir formations. In sedimentary rocks, fractures usually propagate to the extent of the thickness of the beds, and align in-plane and out-of-plane across bedding boundaries. Therefore, fracture sizes in the Yates reservoir most likely vary as a function of the variation of the bed of mechanical layer thickness, being larger in massive dolomite, and smaller and more closely spaced in thin-bedded dolomite. However, smaller fractures may not be conductive at all; hence a reliable estimate of the conductive P_{32} of the reservoir formations remains of primary importance.

Fracture Intensity: Zone Variation

There is field evidence that suggests that field scale faults bounded carbonate blocks that moved relative to one another during drape folding of the reservoir strata. If such faults exist, it is important to know their exact locations, since they very likely affect the intensity of the fracture system. The "faults" themselves may be actually fault zones which consist of numerous interconnected fractures. The field-scale system of faults/drape folds in the Yates reservoir is currently being studied by Marathon Oil geologists (Wadleigh, pers. comm.).

The field-scale faults were not included in the numerical generation of the fracture system in the Yates reservoir in this HFM study. However, the 3D model incorporates algorithms for modeling of fracture intensity in zones defined according to distances from primary faults. In a future study, if the locations of the field scale faults/drape folds are known, they can easily be incorporated in the numerical generation of the Yates fracture system.

4. TASK 1.3: RESERVOIR COMPARTMENTALIZATION

In a fractured reservoir, a well produces from the fracture network intersecting the well, and from the matrix that feeds into the fracture system. Many, if not most, fractured reservoirs contain fracture networks that are compartmentalized to some extent. This compartmentalization is due to both the geometry of the fractures, and to the fluid flow properties of individual fractures. As a result, production from a well or zone in a well is limited to the fracture network(s) to which it is connected, and to the matrix that can feed into the fracture system by means of pressure-depletion or gravity drainage.

This chapter describes research on the development of quantitative measures of reservoir compartmentalization in terms of parameters which can be readily applied to reservoir engineering. The measures developed address:

- **Matrix Block Geometry**: The size and shape distribution of matrix blocks defined by fractures and fracture networks (Section 4.1), and

- **Tributary Volume**: The volume of hydrocarbon that can be produced by specific wells (Section 4.2).

Further research described in Section 5.5 below addresses

- **Compartmentalization**: The large-scale geometric pattern of accessible reservoir regions defined by isolated fracture network clusters,

These quantitative measures of reservoir compartmentalization have the potential to provide significant improvements to fractured reservoir production. For example, estimating the horizontal cross-section of reservoir compartments is useful for

- optimizing well spacings,

- assessing the likelihood that infill drilling will tap into new oil compartments, and

- evaluating the sweep efficiency obtained by flooding or similar processes.

However, measures such as the horizontal cross-section of reservoir compartments do not directly describe how much hydrocarbon might be produced. For example, in a fractured reservoir in which oil flows from the matrix into the fractures by means of pressure-depletion, the volume of oil is related to the pressure differential, the surface area of the fracture network, and the volume of matrix accessed by this network. During steam injection, the movement of the condensation front through time, which describes how effectively the matrix is being heated by the injected steam, is both a function of the network connectivity and the multiphase fluid properties of the fractures in the network.

All of these three aspects of fracture network compartmentalization share the need to quantify fracture network connectivity and the amount of matrix "accessed" by the fracture network.

4.1 Task 1.3.1: Improved Matrix Block Size Estimation

The project developed a range of new algorithms which were implemented and evaluated for estimation of rock block volume. The assessment of rock block volume is essential for efficient development and production of fractured reservoirs.

4.1.1 Alternative Block Size Algorithms

Reservoir simulation in dual porosity systems requires calculation of several parameters related to matrix block shape and size. The fracture surface area of matrix blocks within a cell influences the rate and quantity of fluids that can move between the matrix and the fracture system. The Z-dimension of matrix blocks influences gravity drainage mechanisms. The shape of the matrix blocks influences the choice of sugar cube, matchstick or slab idealization. A realistic description of block size and shape that can be implemented in existing dual porosity simulators will benefit not only the thermal simulation for TAGS processes, but also non-thermal simulation of injection or production in fractured reservoirs. Two algorithms have been developed and tested to compute matrix block shape and size. Both are based on geologically realistic three-dimensional fracture systems, and provide output in the form required by conventional dual-porosity simulators.

The first algorithm is a fast computational method to compute blocks based upon fracture spacing distributions in several directions. Its main advantage is the speed of calculation. Its disadvantage is that it assumes that block dimensions are uncorrelated. This algorithm is referred to as the *multi-directional spacing (MDS) algorithm.*

The second algorithm is based upon graph theory. Because the convex hull of points lying on fractures bounding or partially bounding a matrix block is computed, this algorithm is referred to as the *convex hull (CH) algorithm.*

4.1.1.1 Multi-Directional Spacing Distribution Algorithm

Figure 4-1 illustrates the multi-directional spacing algorithm. For each realization of the discrete fracture model, a series of randomly-located lines in user-specified directions are generated. The location of fractures intersected by each line is recorded. This leads to a spacing frequency distribution in several directions. Typically, the directions include the vertical direction, in order to calculate the vertical dimension of blocks for gravity drainage considerations, and in two or three orthogonal directions that relate to simulator grid layering geometry and the fracture system.

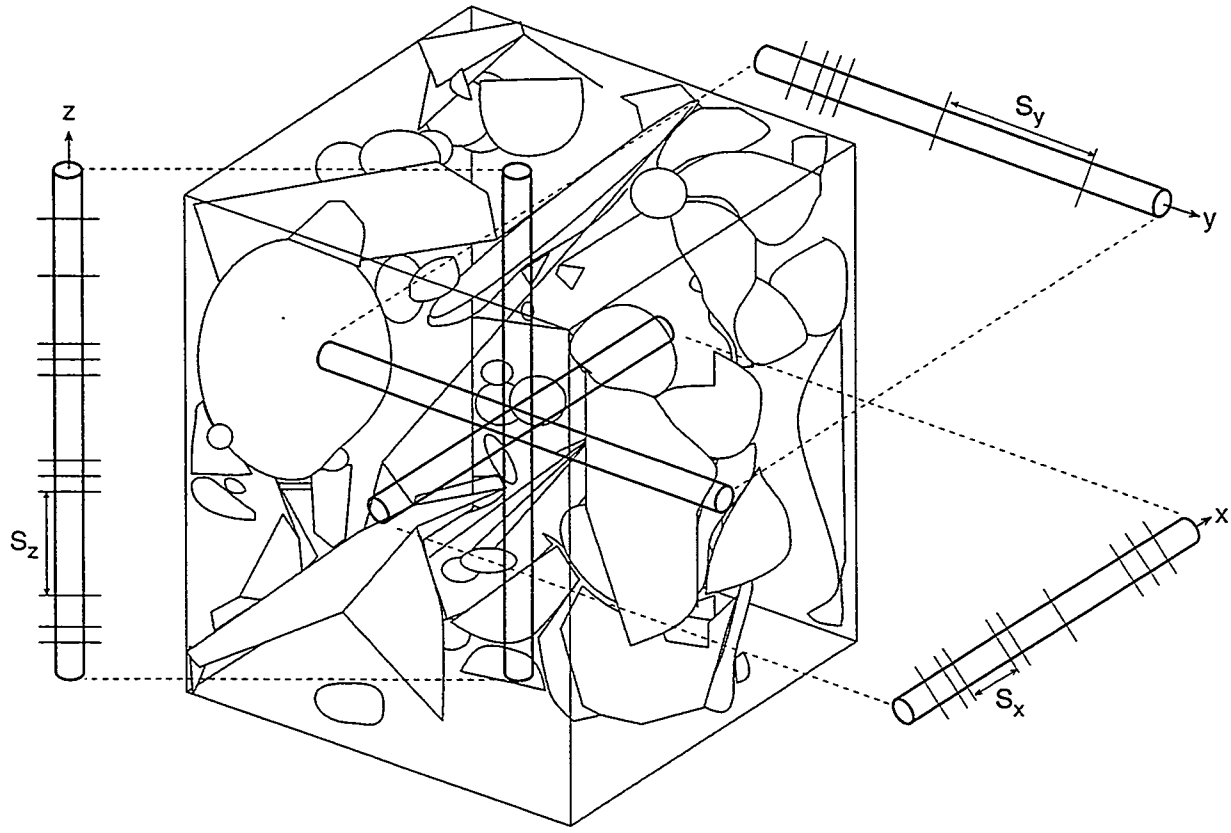

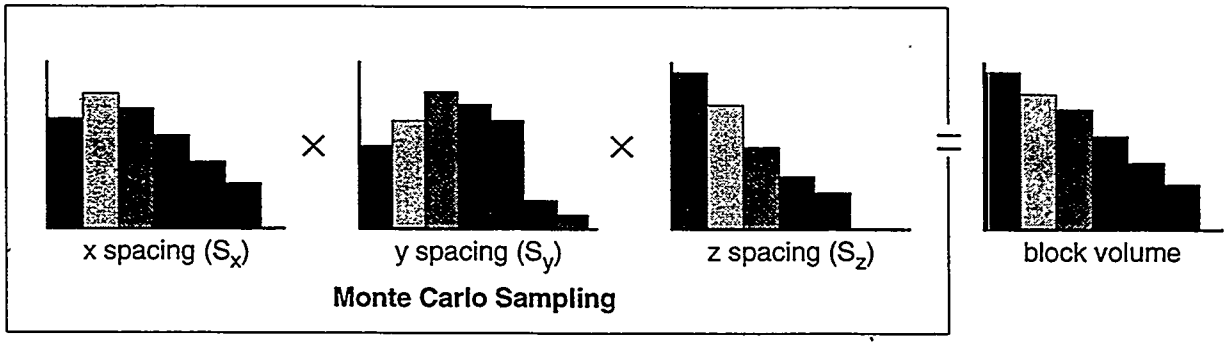

FIGURE **4-1**
MULTI-DIRECTIONAL SPACING ALGORITHM
NIPER/FINAL REPORT/WA

The spacing probability distributions are multiplied together using Monte Carlo sampling techniques to produce a frequency distribution of block volumes and surface areas. This is carried out by selecting X, Y and Z spacing values at random with selection probability proportional to their frequency, and multiplying them together to create a prismatic block.

The volume of the block for the i-th Monte Carlo computation is the product of the spacing values:

$$Volume_i = X_i * Y_i * Z_i \tag{4-1}$$

The surface area of the i-th block is given by:

$$SA_i = 2*(X_i * Y_i + Z_i * Y_i + X_i * Z_i) \tag{4-2}$$

The block shape is given by the ratios of the mean X, Y and Z spacings:

$$\overline{X}:\overline{Y}:\overline{Z} \tag{4-3}$$

The vertical dimension of the blocks is taken as the mean value of the Z spacing distribution:

$$Vertical\ Dimension = \overline{Z} \tag{4-4}$$

4.1.1.2 Convex Hull Algorithm

The convex hull algorithm is more computationally intensive, but measures the actual dimensions of the blocks, rather than reconstructing blocks stochastically from spacing frequencies. Thus, any correlations among block dimensions or non-prismatic block shapes do not present problems. The algorithm's accuracy is governed by two factors: whether in fact the matrix blocks are convex; and how many points are required to accurately characterize the convex block. The algorithm as implemented allows the user to specify the number of points for characterizing the convex block, but computation time increases as the number of points increases.

Figure 4-2 illustrates the CH algorithm. From a random point within a discrete fracture model, lines are projected out in user-specified directions until they intersect a fracture. The intersection point coordinates for all of the line intersections constitutes a sample of the matrix block. As is shown in the 2D illustration (Figure 4-2a), some of these intersection points may not all be on the block exterior. Next, a convex hull (Figure 4-2b) is calculated for the set of points. A convex hull has the property that it includes all of the points, and that it is convex. In two dimensions, the hull is a convex polygon. A convex polygon has the property that any line joining two arbitrary points within or on the boundaries of the polygon lies entirely on the boundary or in the interior of the polygon. In practice, this means that the polygon has no "holes" or embayments, and it is a single polygon, not several isolated ones. In three dimensions, the polygon is a polyhedron.

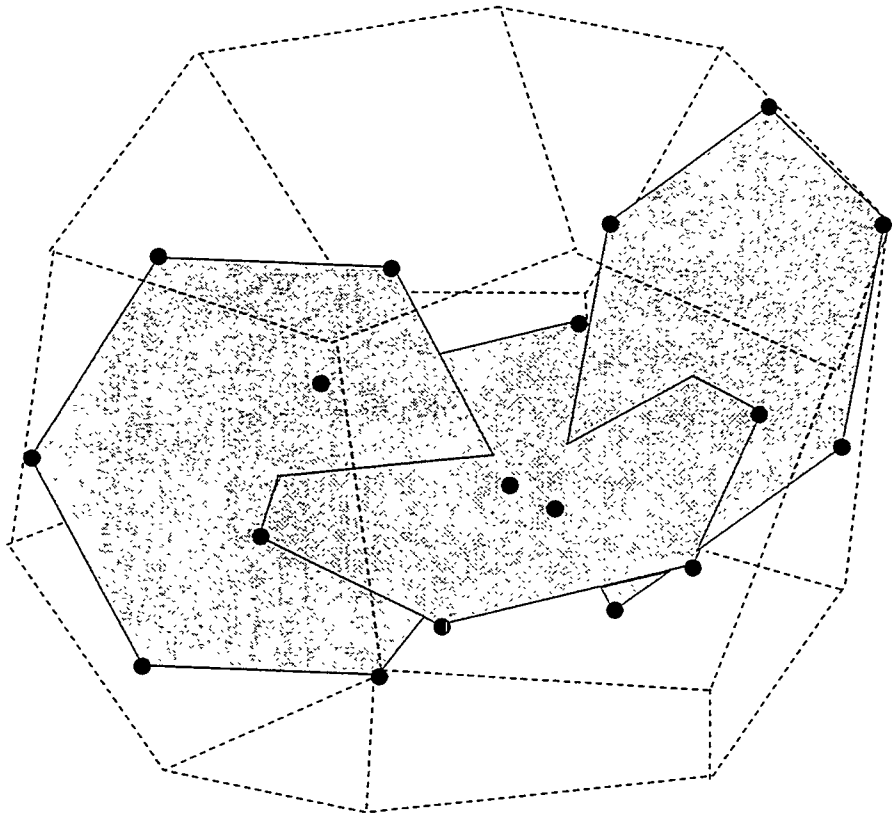

(a) Points

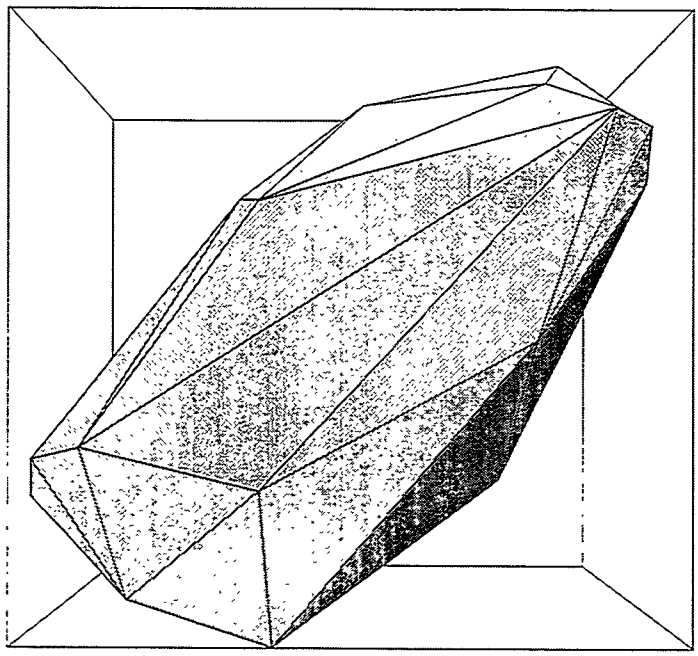

(b) Convex Hull

FIGURE **4-2**
CONVEX HULL BLOCK SIZE ALGORITHM
NIPER/FINAL REPORT/WA

It is a simple matter to compute the volume and the surface area of the convex hull. The vertical dimension of the matrix block is taken to be the difference between the minimum and maximum Z coordinate of the convex hull. The shape of the matrix blocks approximated as convex hulls can be determined by visually displaying the hulls, or by computing the aspect ratios for the X, Y and Z directions from the hull coordinates.

The convex blocks to be analyzed are identified by projecting rays from randomly selected points within the model. Since a larger block has a proportionately greater probability of having a randomly located point within it, the algorithm overestimates the number of large blocks and underestimates the number of small blocks, particularly if multiple points are selected in the same block. The current algorithm checks to see if each new block has previously been estimated, and if so, it retains the block with the larger volume. This is because a convex hull estimate of a convex block is always equal to or less than the volume of the actual block.

4.1.2 Test Cases

Three test cases were devised to assess how well these two algorithms correctly estimated the matrix block size distribution. Cases 1 and 2, which are not geologically realistic, serve as verification and evaluation cases for the algorithms. It is not possible to calculate the true block volume distribution for Case 3, but this case illustrates how the algorithms might be applied in more realistic DFN models. Case 1 (Figure 4-3a) consists of a 202 m by 202 m by 202 m cube dissected into 8000 10 m cubes. Each cube is a matrix block, and is completely bounded by fractures. Case 2 (Figure 4-3b) consists of slabs and cubes, but of varying sizes and with dimensions that are partially correlated. The distribution of block volumes is bi-modal. These two test cases are geologically unrealistic, but clearly illustrate how well the algorithms perform. Case 3 (Figure 4-3c) is more geologically realistic. In this model, fractures do not completely isolate blocks. There are three sets in approximately three orthogonal orientations, much like the fracture pattern that develops in carbonates or other layered rocks.

Table 4-1 summarizes the values for Z dimension, specific surface area, P_{32} and volume for the three test cases. Both the specific surface area and P_{32} quantify how much fracture surface area per volume of rock there is in the model. The specific surface area is calculated by summing all of the surface area for all of the identified blocks, and dividing by the total volume. In test cases 1 and 2, this means that almost every fracture will be part of two blocks. P_{32} on the other hand, is the total amount of fracture area divided by the volume of rock, and is independent as to whether these fractures form blocks. For test cases 1 and 2, the specific fracture surface area should be approximately twice the value of P_{32}. For simulation purposes, it is necessary to use the surface area that relates to the matrix block idealization, rather than the absolute P_{32} value.

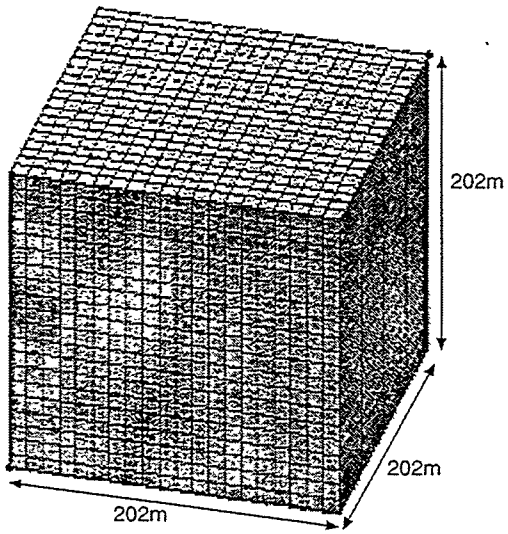

(a) Test Case 1

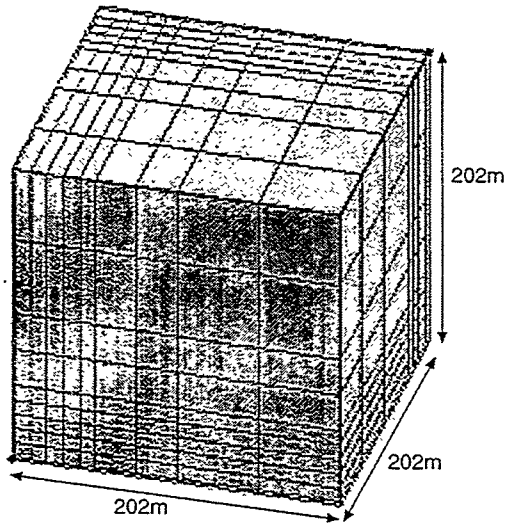

(b) Test Case 2

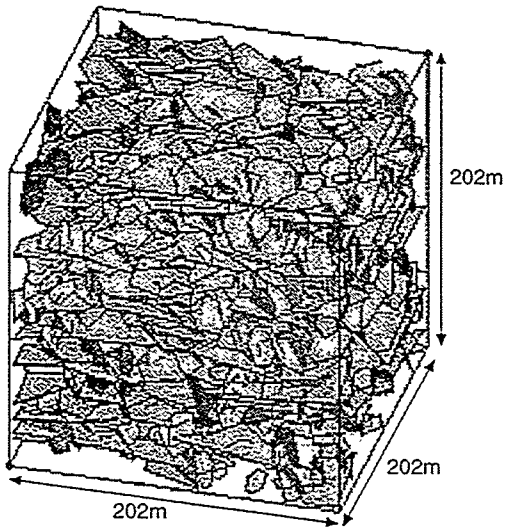

(c) Test Case 3

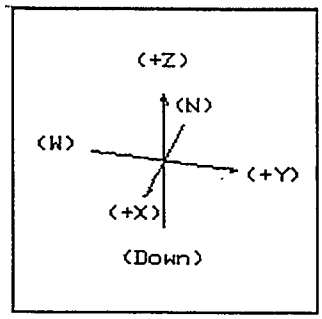

FIGURE **4-3**
BLOCK SIZE TEST CASES
NIPER/FINAL REPORT/WA

Table 4-1 Block Size Algorithm Test Case Expected Values

Test Case	Z Dimension (m)	Surface Area/Rock Volume (m^2/m^3)	P_{32} (m^2/m^3)	Volume (m^3)
Case 1	10.0	0.6	0.312	1,000
Case 2	mean = 22.22	0.27	0.146	mean = 10,974
Case 3	not calculated	not calculated	0.112	not calculated

Table 4-2 presents the results for MDS and CH analysis of Test Cases 1, 2, and 3. The MDS algorithm matches the correct block dimensions exactly for Case 1 when the sampling directions were chosen to be perpendicular to the block faces. In many situations involving fracturing of layered rocks, principal fracture orientations should be parallel and perpendicular to bedding, so it may be possible to choose sampling orientations that give very good matrix block volume estimates. The MDS algorithm produces reasonable estimates for Case 2, but has a tendency to somewhat overestimate the number of very small matrix blocks. Nevertheless, the MDS algorithm reproduces the shape and bimodality of the correct distribution reasonably well (Figure 4-4).

Table 4-2 MDS and CH Block Size Algorithms

Test Case	Z Dimension (m)	Surface Area/Rock Volume (m^2/m^3)	P_{32} (m^2/m^3)	Volume
Case 1 - MDS	10.0 (constant)	0.60	0.312	1,000 (constant)
Case 1 - CH	14.1 (mean)	0.63	0.312	823 (mean)
Case 2 - MDS	23.4 (mean)	0.25	0.146	6,653 (mean)
Case 2 - CH	29.3 (mean)	0.32	0.146	9,154 (mean)
Case 3 - MDS	11.1 (mean)	0.36	0.112	5,484 (mean)
Case 3 - CH	43.0 (mean)	0.36	0.112	10,642 (mean)

The CH algorithm provides better results for Case 2 and worse results for Case 1. For Case 1, most convex hulls will contain a smaller volume than the cubes in which they are calculated. This is due to the fact that the convex hull is based upon a finite number of points lying on the edge surfaces of the cubes. This means that corners of the cube may be effectively "trimmed off" by calculating the hull, which in turns leads to an underestimate of block volumes. For Case 2, the median and mean block volumes are more accurately estimated by the CH algorithm than by the MDS algorithm. The inherent ability of the CH algorithm to account for the correlation in block dimensions appears to offset the tendency to underestimate the volume of cubical matrix blocks.

Case 3 is a more realistic DFN model. As horizontal and vertical cross-sections through one DFN model realization illustrate (Figure 4-5), blocks are not completely isolated on all faces by fractures. There are blocks of many different sizes, but in horizontal cross-section, the blocks are on the order of 40 m, and in vertical cross-section blocks are on the order of 10 m.

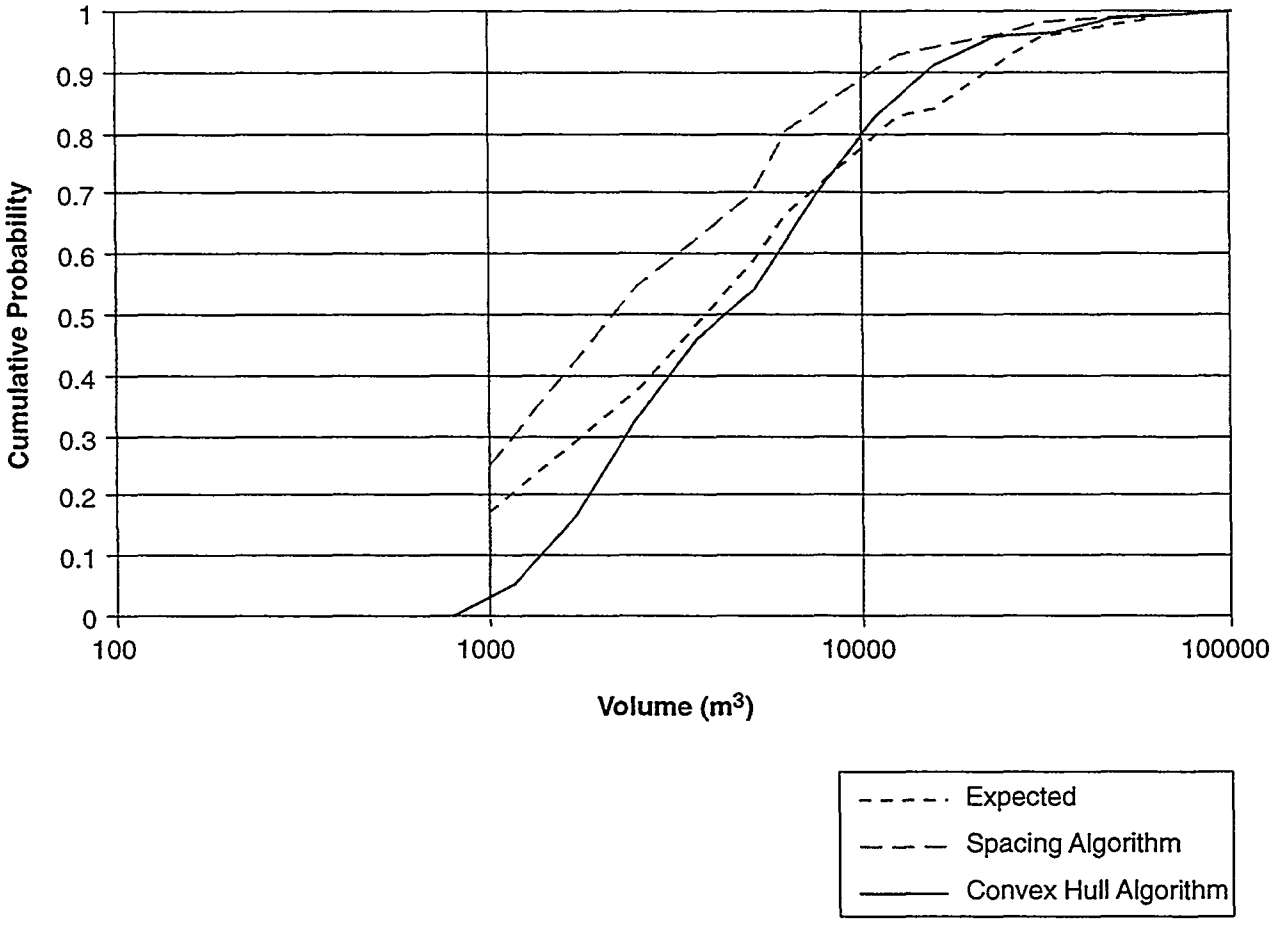

FIGURE **4-4**
BLOCK SIZE DISTRIBUTION FOR TEST CASE 2
NIPER/FINAL REPORT/WA

PROJECT NO. 963 1357.521 DRAWING NO. 80675 DATE 9/25/98 DRAWN BY EA

Golder Associates

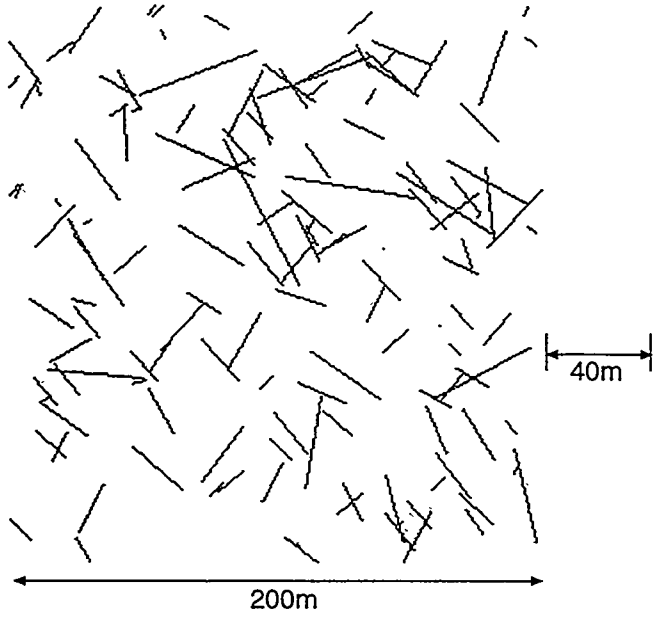

(a) Horizontal Cross Section

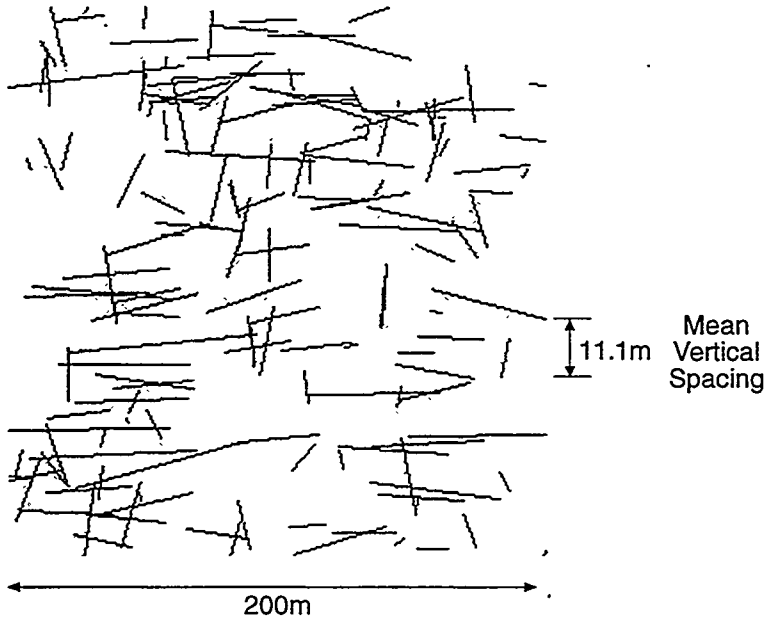

(b) Vertical Cross Section

FIGURE **4-5**
CROSS SECTION THROUGH TEST CASE 3
NIPER/FINAL REPORT/WA

PROJECT NO. 963 1357.521 DRAWING NO. 80676 DATE 9/25/98 DRAWN BY EA

Golder Associates

In summary, the three test cases suggest that both the MDS and CH algorithms provide reliable and consistent estimates of fracture surface area, at least for simple fracture geometries. The CH algorithm appears to provide better estimates of the mean volume of matrix blocks when block dimensions are partially correlated. Since jointing in many sedimentary rocks is characterized by pseudo-periodic spacings (e.g., La Pointe and Hudson, 1985), it may be preferable to use the CH algorithm to estimate block volumes. On the other hand, the geometric construction of a convex hull from a sparse data set creates hulls with slightly greater average Z-dimensions than the MDS algorithm. In both test cases 1 and 2 the MDS algorithm provided more accurate estimates of the Z-dimension. Thus, both algorithms have proven useful and necessary to provide estimates of matrix block parameters, and neither alone is completely satisfactory.

4.2 Task 1.3.2: Drainage Volume Analysis

Tributary drainage volume is related to both block size and compartmentalization. Tributary drainage volume is the estimated volume of matrix that a fracture system intersected by a well or perforated zone can access. In those reservoirs in which the matrix provides the storage, and the fracture system the reservoir permeability, the amount of hydrocarbon that can be produced is a function of the fracture network connectivity and geometry.

Nonetheless, the mobilization and drainage of oil due to pressure depletion occurs in many fractured reservoirs. Improving forecasts of the potential volume of reservoir that a well can drain through the connected fracture system is useful for planning field development in many fractured reservoirs.

4.2.1 Algorithm

The algorithm developed to compute the tributary drainage volume is divided into two steps:

Step 1. Identify the fracture networks connected to a well or perforated zone of interest

Step 2. Estimate the volume of matrix within that could be produced

Step 1 utilizes the algorithm developed for compartmentalization analysis, as described in Section 5.4 below. As in the compartmentalization algorithms, it is possible to process the fractures in a DFN model to identify those fractures which are connected to a well or a portion of a well.

There are different ways that might be used to accomplish Step 2. If the fracture network were very dense, then the volume of the matrix accessed by the fracture network will be closely approximated by the volume of the convex hull enclosing the network. In essence, this means that the compartment volume is equal to the tributary volume. However, there is no reason to expect that all fracture networks will be sufficiently dense that the convex hull method produces the best estimate. In less dense

fracture networks, some or maybe a significant portion of the volume inside the convex hull will be too far from any of the fractures to be easily produced (Figure 4-6).

A better estimate of tributary drainage volume would not include matrix that might not be efficiently produced through pressure depletion drainage. Figure 4-7 illustrates a possible alternative algorithm to achieve this. In this algorithm, each fracture is circumscribed by a prism that is calculated from the area of the fracture and the distance away from the fracture over which drainage might be effective. For pressure depletion mechanisms, the fracture forms the midplane of the prism.

An obvious problem with this algorithm is to avoid double-counting the volume of overlap between prisms. Volume calculations based upon solid geometry which account for the overlap are time-consuming for the number of fractures that might commonly be encountered in a fracture network. A simpler, more efficient method has been devised, although it is not as numerically exact.

An approach based on the use of grid cells is illustrated in Figure 4-8. The prism enclosing each fracture is approximated by a series of cells that are referenced to a global origin. All of the cells whose centers lie within the prism are said to belong to the prism. Initially, all cells have the value of "0". Each fracture is processed in turn, and all cells belonging to the fracture prism are incremented by the value "1". If a cell belongs to more than one fracture prism, then its counter is incremented to a number equal to the number of prisms it belongs to. After all of the fractures are processed, the total number of non-zero cells multiplied by the cell volume is taken as the estimate of the tributary volume, or:

$$Volume = \sum_{i=1}^{n} \delta(i) dx dy dz \qquad (4\text{-}5)$$

where δ(i) is the Dirac function which is equal to 1.0 if the cell has a value greater than 0.0, and is set to 0.0 if the value in the cell is 0.0,

n is the number of cells, and

dx, dy, dz are the cell dimensions.

4.2.2 Test Cases

An example of this calculation for a simple, verifiable test case is shown in Figure 4-9. The model consists of three horizontal fractures with partial horizontal overlap. Expected and actual results for Test Case 1 are shown in Table 4-3.

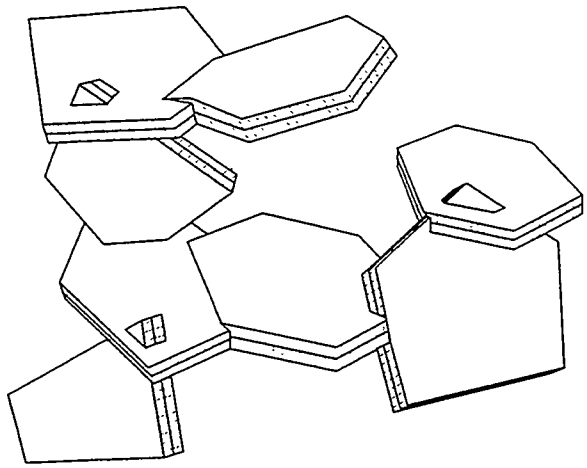

Fracture Network

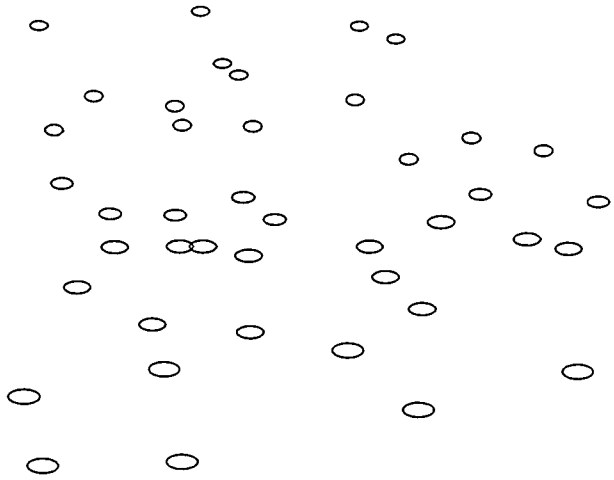

Network Converted to 3D
Set of Points (Vertices)

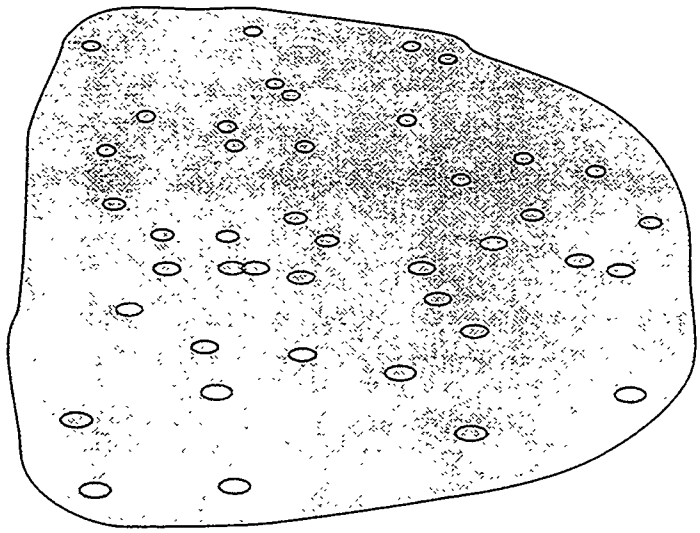

Convex Hull

FIGURE **4-6**
TRIBUTARY DRAINAGE VOLUME BY CONVEX HULL
NIPER/FINAL REPORT/WA

PROJECT NO. 963 1357.521 DRAWING NO. 80677 DATE 9/25/98 DRAWN BY EA

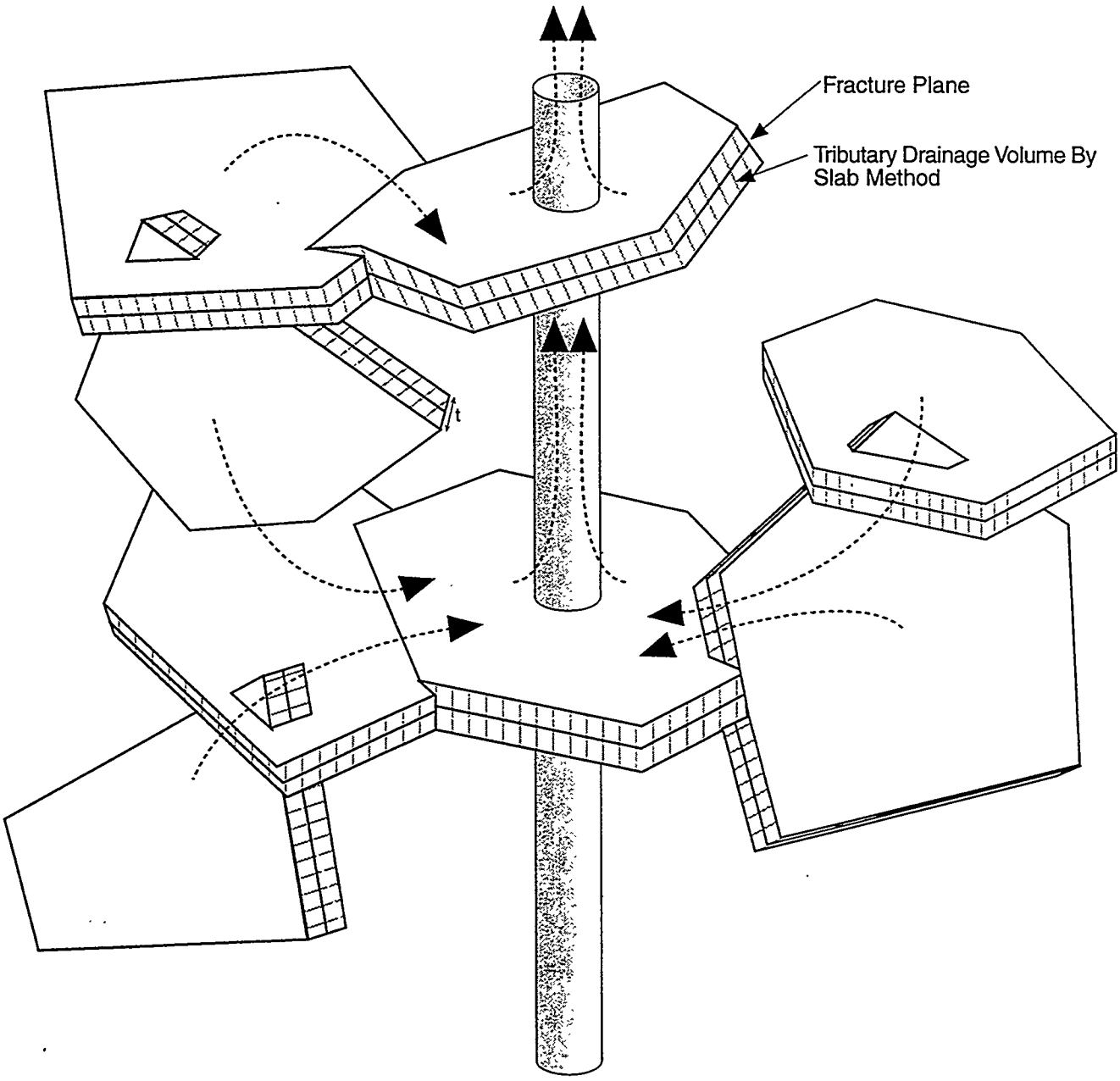

FIGURE **4-7**
TRIBUTARY DRAINAGE VOLUME BY SLAB ALGORITHM
NIPER/FINAL REPORT/WA

PROJECT NO. 963 1357.521 DRAWING NO. 80678 DATE 9/25/98 DRAWN BY EA

Golder Associates

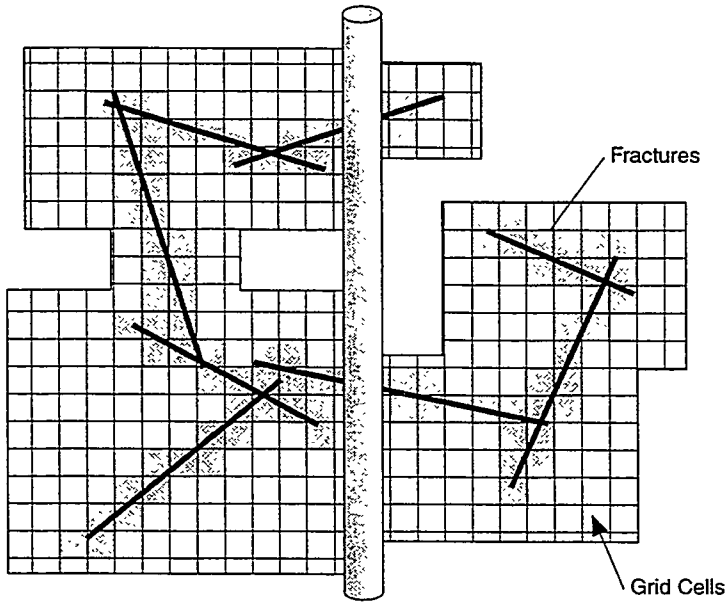

(a) 2D Visualization

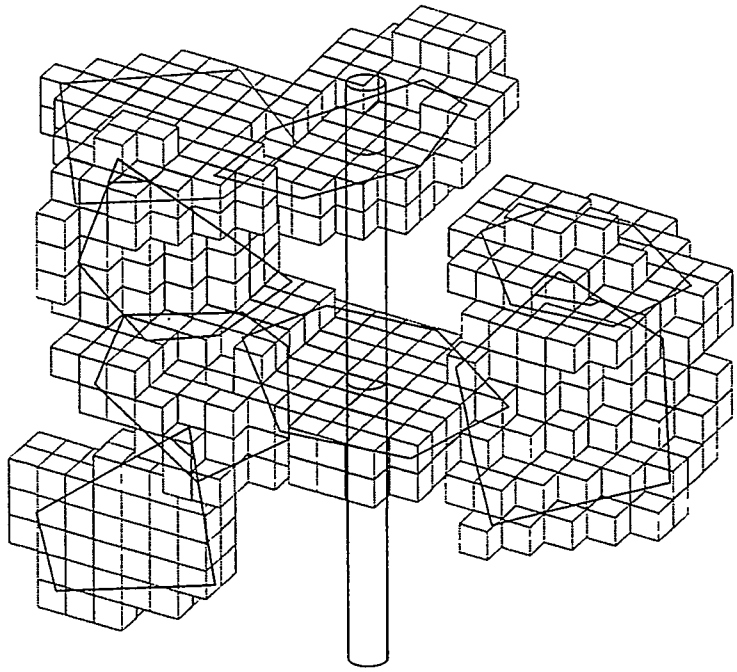

(a) 3D Visualization

FIGURE **4-8**
GRID CELL ALGORITHM
NIPER/FINAL REPORT/WA

PROJECT NO. 963 1357.521 DRAWING NO. 80679 DATE 9/25/98 DRAWN BY EA

Golder Associates

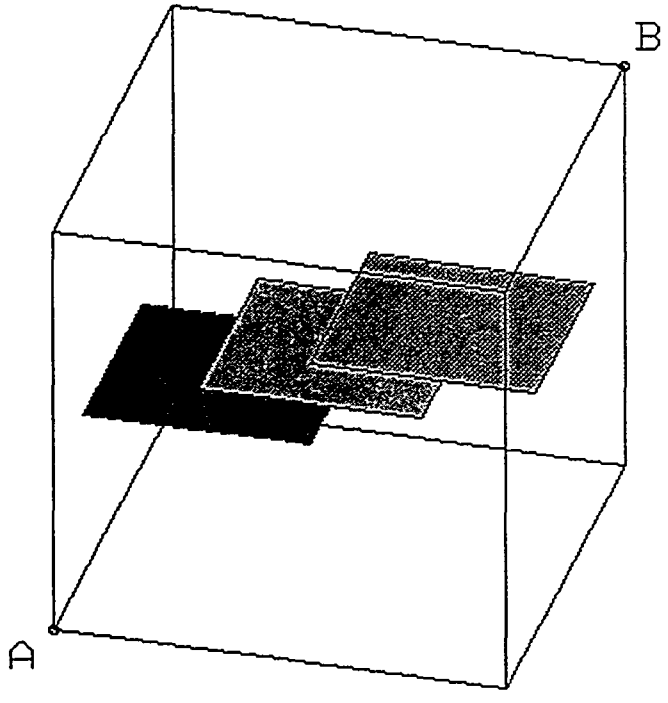

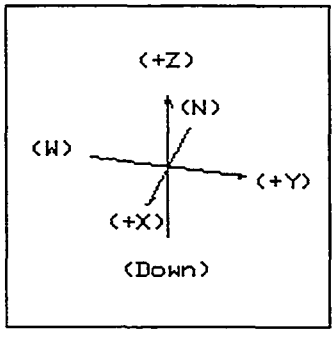

A: (10.0, -10.0, -10.0)
B: (-10.0, 10.0, 10.0)
C:\FM251\TEST1.FDT

FIGURE **4-9**
DRAINAGE VOLUME TEST CASE 1
NIPER/FINAL REPORT/WA

PROJECT NO. 963 1357.521 DRAWING NO. 80680 DATE 9/25/98 DRAWN BY EA

Golder Associates

Table 4-3 Drainage Volume Algorithm, Test Case 1

Case 1 (half-thicknesses, in meters)	Expected Volume (m^3)	Estimated Volume (m^3)	Percent Difference
1.0	600	600	0.0%
2.0	1000	1000	0.0%
8.0	3400	3400	0.0%

These series of verification cases are simplistic, but demonstrate that the algorithm correctly computes the volume and does not double-count when the tributary fracture volumes overlap. The reason for the exact match between expected and predicted volumes is that the fractures are horizontal, making the prisms exactly approximated by a series of stacked cells, and the cell size (1.0 m cubes) were evenly divisible into the prism thickness. For example, if a cell size of 3 m were used, then the algorithm would underestimate the volume. The predicted underestimated volumes and the actual results are shown in Table 4-4.

Table 4-4 Expected Errors for Drainage Volume Algorithm, Test Case 1

Case 1 (half-thicknesses, in meters)	Expected Underestimated Volume (m^3)	Estimated Volume (m^3)	Percent Difference with True Volume
1.0	567	567	-5.5%
2.0	972	972	-2.8%
8.0	3240	3240	-4.7%

These cases verify that the algorithm functions as intended, and shows that a poorly chosen cell size can lead to a mis-estimation on the order of 5%.

Test Case 2 is designed for demonstration purposes, because there is no analytical solution for the case of incompletely constrained blocks in discrete fracture networks. Test Case 2 is defined using the fracture geometry for fractures connected to a vertical well drilled in the center of Block Size Test Case 3 (Figure 4-3). For this analysis we assume that the prism surrounding the fracture is of variable thickness, similar to the increasing volume of matrix produced through time as the reservoir is depleted. The measuring cells are cubes with edges of length 1.0 m. Results are shown in Table 4-5.

Table 4-5 Drainage Volume Algorithm, Test Case 2

Case 2 (half-thicknesses, in meters)	Volume from Drainage Volume Algorithm (m^3)
1.0	2908
2.0	5735
8.0	21840

Table 4-5 shows that the tributary volume does not scale linearly with increasing prism thickness, due to the overlap of the drainage regions for each fracture.

5. TASK 2.1: TECHNOLOGY DEVELOPMENT

5.1 Task 2.1.1: Fracture Set Analysis

During the year, we developed a neural net technology for fracture set analysis. This section describes this technology development.

5.1.1 Background

Neural networks are a sophisticated form of non-linear pattern recognition that are used in such diverse areas as stock market analysis, loan application screening, diseases diagnosis, and medical expert systems (Eberhart and Dobbins, 1993). They are particularly well-suited for problems in which the input and output variables vary spatially and in scale of importance, are of different mathematical types (e.g., class, ordinal, and continuous variables) and are complexly interrelated. Neural network have found geologic application in a variety of areas including slope stability analysis (Xu et al., 1994), rock and soil mechanics (Ellis et al., 1995; Feng, 1995; Lee and Sterling, 1992), fracture network hydrology (La Pointe et al., 1995; Thomas and La Pointe, 1995) and prediction of earthquake intensity and liquefaction (Goh, 1994; Tung et al., 1994).

There are many types of neural networks, but all share a common architecture consisting of *neurons* and *synapses* (Figure 5-1). A neuron is simply a node in the network which uses a non-linear transfer function to convert an input signal (value) to an output signal. Neurons are connected by synapses. A synapse takes the output signal from one neuron, multiplies it by a *synaptic weight*, and passes the modified signal to an adjacent neuron as input. Depending on the number of incoming and outgoing synapses connected to it, a neuron can be classified into one of three categories:

1. *Input neurons* have zero incoming synapses and one or more outgoing synapses. They are used to represent input variables, and take the variable value as their output.
2. *Output neurons* have one or more incoming synapses and zero outgoing synapses. They are used to represent output variables, and produce an output signal which equals the predicted variable value.
3. *Hidden neurons* have one or more incoming synapses and one or more outgoing synapses. They sit between the input and output neurons and pass signals through the network.

A distinct advantage of neural networks over other classification methods is their ability to learn the relative importance and complex interrelations among input and output variables. By changing the neuron transfer functions, the synaptic weights, or the network connectivity, a neural network can be conditioned to provide the expected response for a given input pattern. Once trained, a neural network can then be used to make predictions for input patterns whose correct classification is unknown.

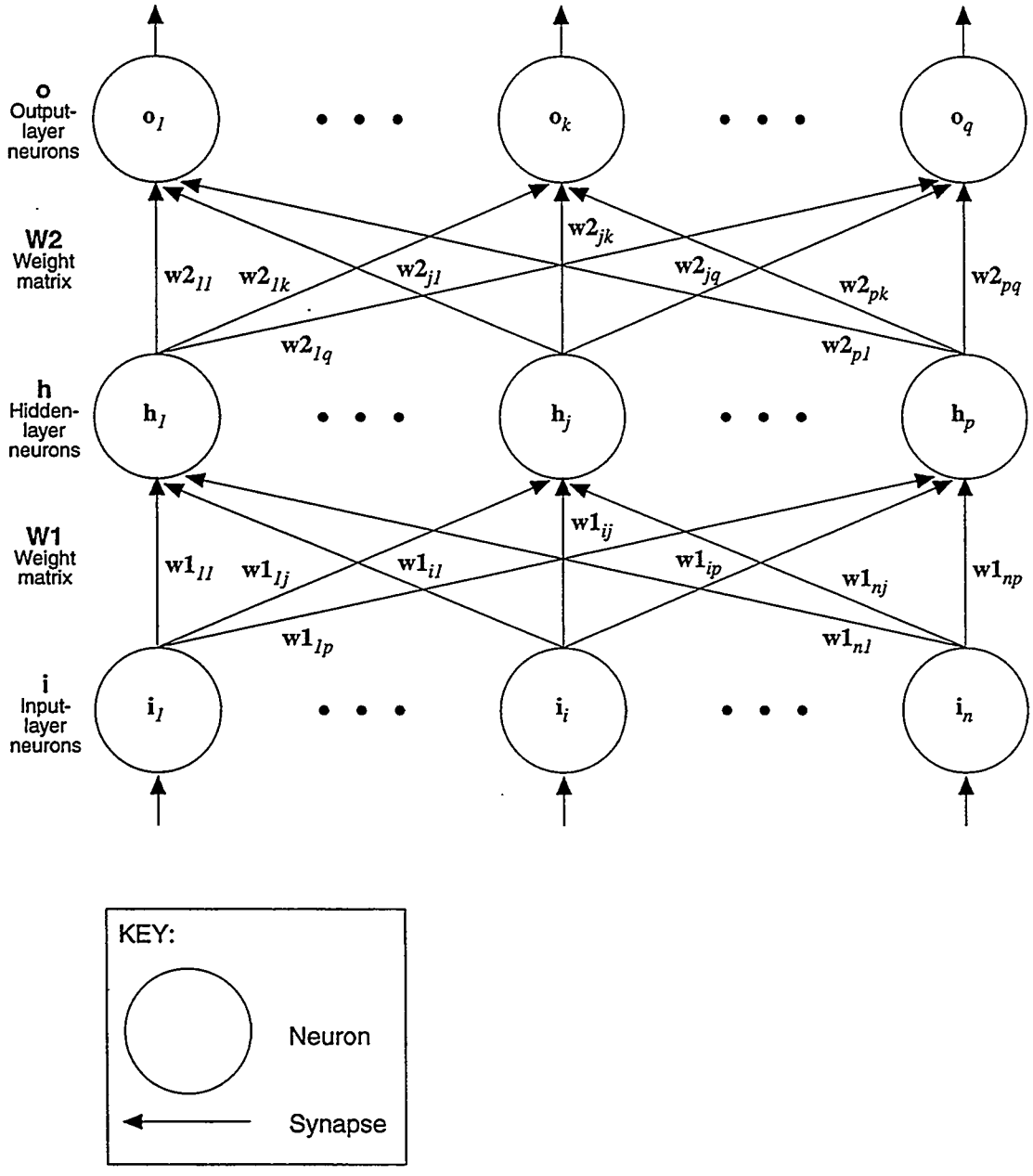

FIGURE **5-1**
NEURAL NETWORK TOPOLOGY
NIPER/FINAL REPORT/WA

Fracture conductivity studies may be considered an exercise in discriminant analysis: given a variety of geological and environmental parameters, is a particular fracture likely to be conductive or not? Backpropagation neural networks are well-suited for this purpose. In a backpropagation neural network, the input, hidden, and output nodes are arranged in layers. A single *input layer*, consisting only of input neurons, is connected to an *output layer*, consisting only of output neurons, through one or more *hidden layers*, consisting only of hidden neurons (Figure 5-1). Each neuron in a given layer is connected to all neurons in the preceding and following layers by synapses, which are characterized by their *synaptic weight*.

As an example, consider a fracture conductivity dataset consisting of the input and output parameters listed in Table 5-1. Of the five input variables, three are continuous, one is of class type, and the remaining one is boolean. The single output parameters is of class type, indicating the fracture set. A backpropagation neural network constructed for this problem would require at least five input nodes, one output node, and perhaps a single hidden layer containing three or so hidden nodes (Figure 5-2).

Table 5-1 Input and Output Parameters for Fracture Conductivity Study

Parameter	Type	Range	Units
Input Parameters			
Strike	Continuous	0 - 360	degrees
Dip	Continuous	0-90	degrees
Mineralization	Class	Calcite, quartz, epidote, ...	N/A
Aperture	Continuous	≥ 0	mm
Open (or closed)?	Boolean	true, false	N/A
Output *Parameters*			
Fracture Set?	Class	Set Number	N/A

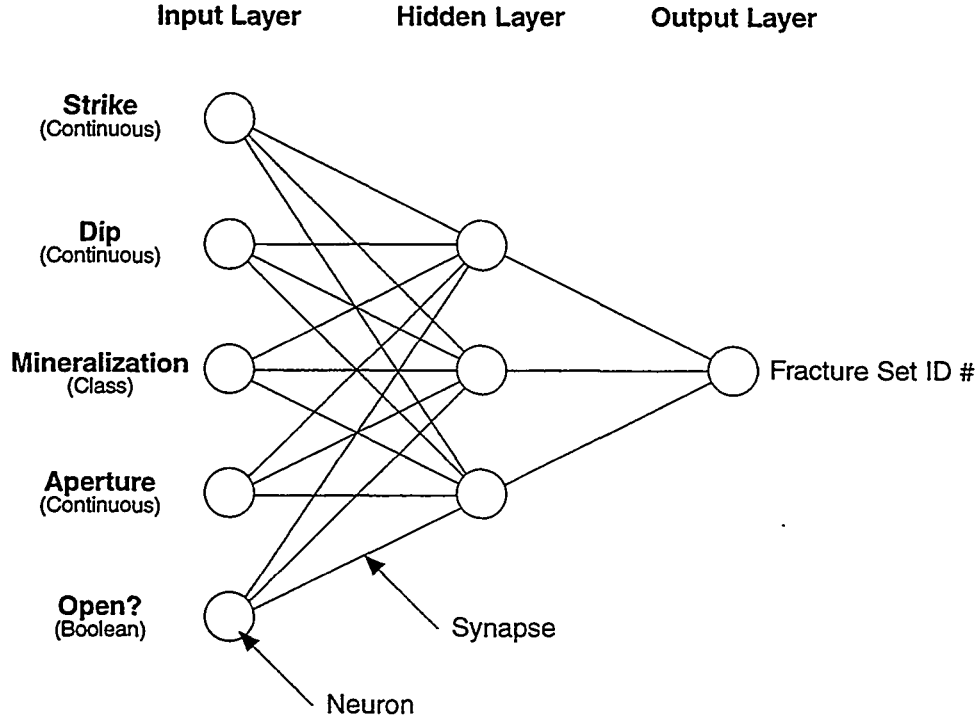

FIGURE **5-2**
EXAMPLE NEURAL NETWORK FOR FRACTURE SET ASSIGNMENT
NIPER/FINAL REPORT/WA

In a backpropagation network, the network connectivity and the neuron transfer function are held constant, and network behavior is modified by adjusting synaptic weights. Initial synaptic weights are assigned from a random distribution. The neural network is then presented with a series of training patterns, and an error signal is computed from the difference between the network's output signal and the desired output signal. In an iterative procedure known as back propagation of errors, the synaptic weights connecting each layer are modified so as to reduce the output error. In this way, the network is trained to successfully classify the training data. Any backpropagation network with one or more hidden layers using a non-linear neuron transfer function is capable of learning complex non-linear mappings (Eberhart and Dobbins, 1990). Once trained, a neural network can be used to make predictions for data sample whose output parameters are unknown (e.g., assignment of additional fractures to sets).

Additional information can be obtained by examining the synaptic weights of a trained neural network. These weights provide a record of the network's classification strategy and of the input parameters most important for classification. Synaptic weights can be viewed graphically using a Hinton diagram (Figure 5-3), or examined quantitatively by computing the neural network's relation factors. Of these, the simplest is *relation factor one*, which indicates the strength of the output signal produced by a single neuron.

The probabilistic neural network (Specht, 1990) is based on a combination of probability theory and Bayesian statistics, and was developed primarily for solving multivariate classification problems (Masters, 1993). The definition of fracture sets can be considered a classical classification problem, with the following special attributes:

- The combination of diverse data types, including orientations, vectors, real, integer, and ordinal values, and classes
- The need to consider both upper and lower hemisphere orientation vectors when defining distances between orientation values
- The bias toward definition of sets with distinctive mean orientations and minimized dispersion
- The need to consider geologists judgment for definition of prior distribution assumptions

The probabilistic neural network algorithm is designed to provide a classification which minimizes misclassification of fractures to the wrong set. The classification system which has the minimum "cost" of misclassification is termed "Bayes Optimal" (Parzan, 1962).

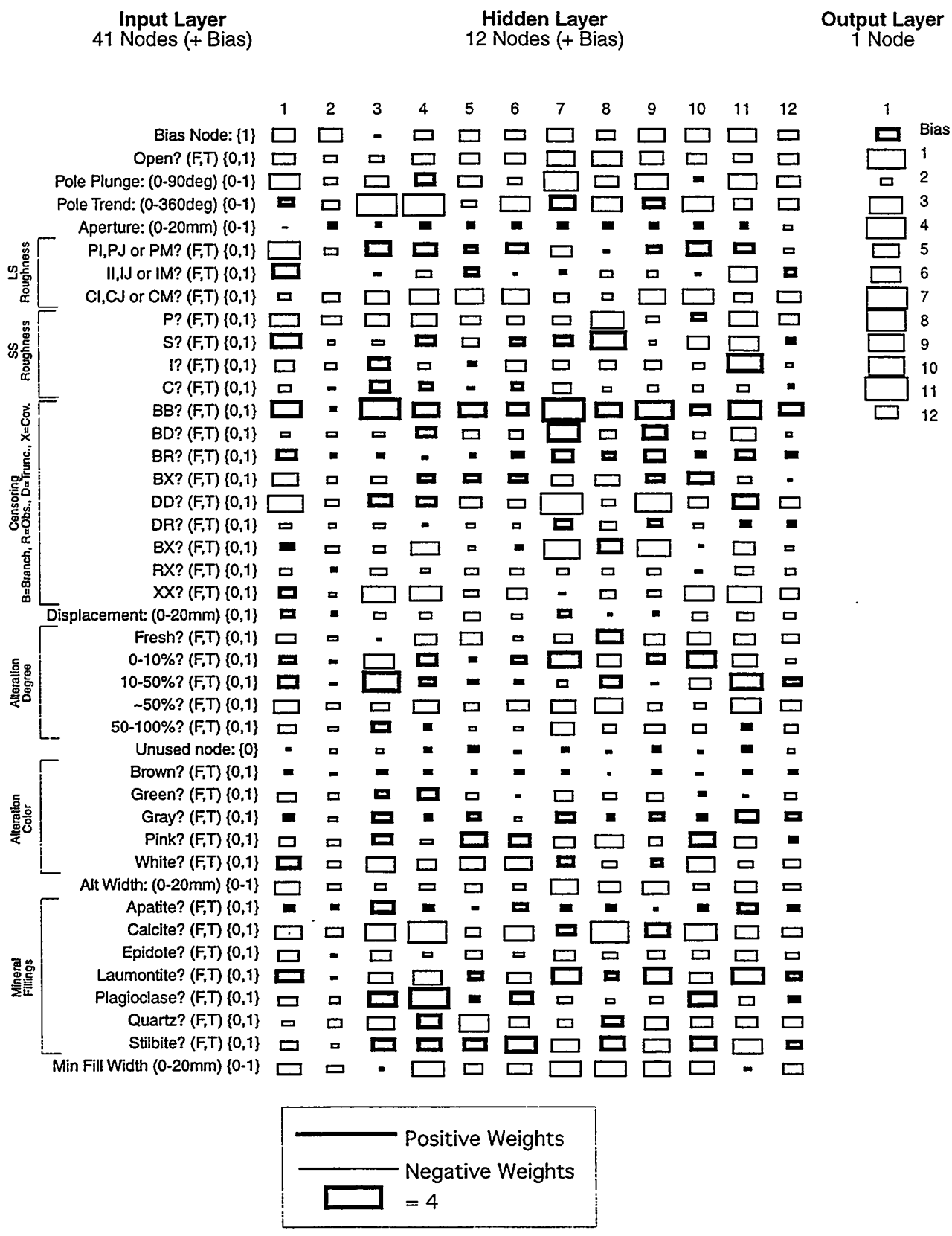

FIGURE **5-3**
HINTON DIAGRAM USING CONTINUOUS VARIABLES
NIPER/FINAL REPORT/WA

PROJECT NO. 963 1357.521 DRAWING NO. 80683 DATE 9/25/98 DRAWN BY EA

Golder Associates

5.1.2 Algorithm

The algorithm for the implemented probabilistic neural network is illustrated in Figure 5-4. The algorithm proceeds as follows.

1. The user evaluates the data to define the variables to be considered in set classification.
2. The user evaluates the data to define prior distributions for each of the sets. Fractures with these distributions of properties are then generated to constitute the "training set".
3. The user specifies weightings w_i for each of the classification variables, for use in the utility function for evaluation of set classification.

   $$V(c) = \sum W_i \sum D_i(j|c)$$

   where V(c) is the utility for classification c, W_i is the weighting for variable i, and $D_i(j|c)$ is the euclidian distance from the data point j for its classification c,
4. The neural network algorithm uses the minimum distance V(c) for each data point to determine which set it should be assigned to. Each fracture is evaluated for its probability of membership in each of the defined sets, and is assigned to those sets.
5. The statistics for each set are reported based on the fractures assigned to each set.
6. Set statistics and graphical displays are provided.

The classes of fracture properties which can be used in this algorithm are provided in Table 5-2. Implementation and verification of this algorithm are described in Section 7.1.1.2 below.

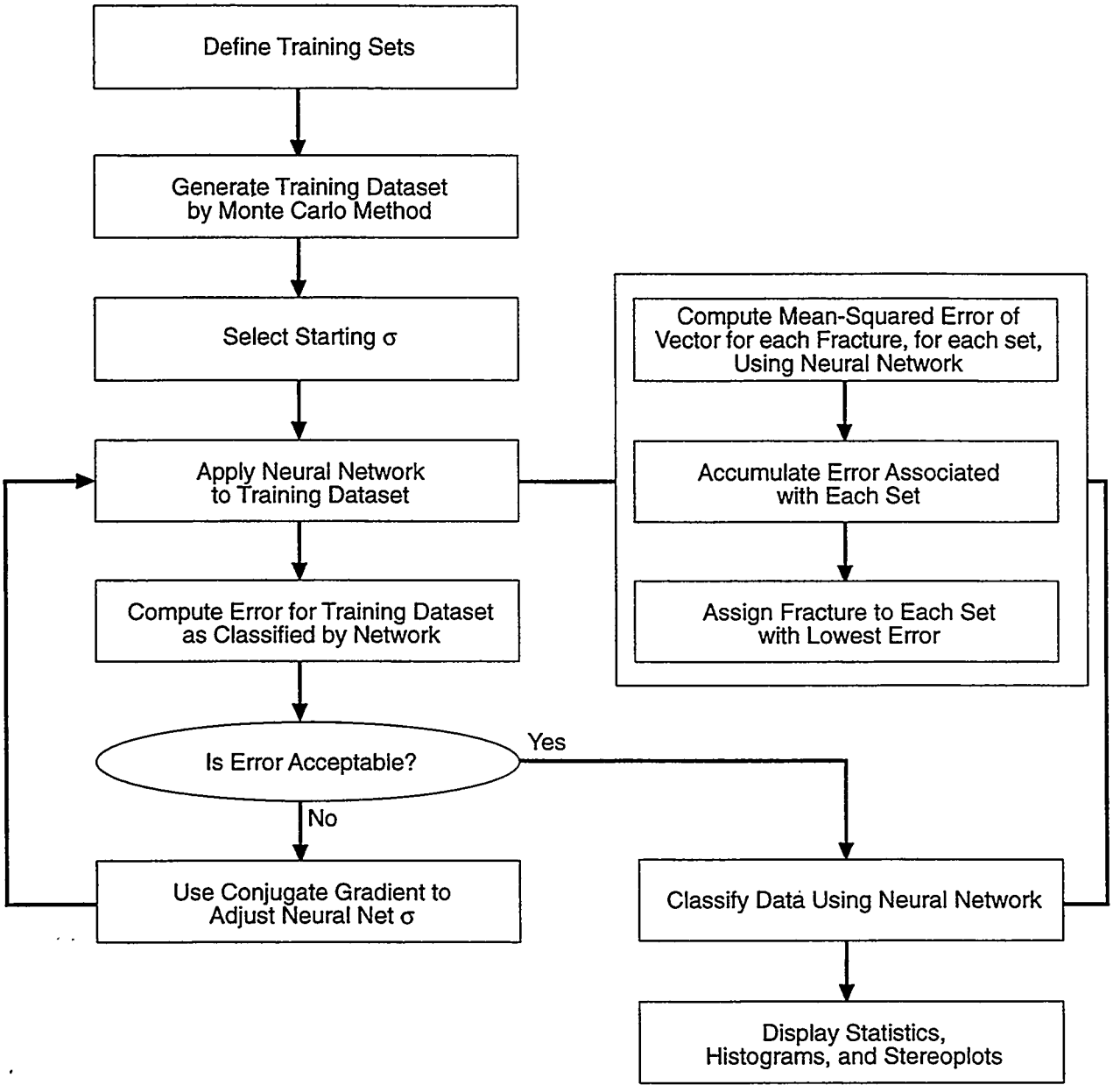

NOTE: Weighting uses the Kernal $W(Z) = e^{-Z^2}$ where Z is the "difference between data vectors. "Difference" is defined appropriately for each data type.

FIGURE **5-4**
PROBABILISTIC NEURAL NETWORK ALGORITHM
NIPER/FINAL REPORT/WA

PROJECT NO. 963 1357.521 DRAWING NO. 80684 DATE 9/25/98 DRAWN BY EA

Golder Associates

Table 5-2 Fracture Property Classes

Property Class	Description	Example
Real	Real valued number	Trace length, aperture
Integer	Integer valued number	JRC, RQD
Orientation	Trend (θ)on (0,360) and Dip (ϕ) on (0,90) for the dip vector (D) or pole vector (P). For calculation of sperical angles the minimum angle of either the upper or lower hemisphere orientation vector is used. The default is lower hemisphere	Fracture orientation, striation orientation, foliation orientation.
Vector	Similar to orientation, but uses only lower hemisphere values	
Class	Membership in a group, as a logical (0,1) cvalue	Rock type, fracture termination mode
Ordinal	Positive, integer value	Fracture Set Number

5.2 Task 2.1.2: Spatial Location Analysis

Spatial analysis of fracture patterns is an essential aspect of the discrete feature network modeling processes. Current spatial analysis methods include geostatistical (Isaaks and Srivastava, 1985), spatial statistics (Ripley, 1988), and fractal (La Pointe and Barton, 1995). Rule-based methods developed within the scope of this project provide an important additional tool for use in defining structural patterns.

5.2.1 Background

The key to spatial fracture analysis of discrete features is the recognition that fracture formation is not a purely stochastic process. Rather, there is a physical, mechanical basis for every fracture's location and geometry. While it is frequently not productive to attempt to understand the entire stress-strain and material property history related to each fracture, the basic rules of fracture formation can be used to derive more realistic DFN model spatial location processes.

Spatial pattern analysis is looking for correlation structures which can be used to explain the location, size, and orientation of discrete features. In a rule-based approach, we rely on geologically based correlations rather than on purely statistical or stochastic/fractal process based correlations. The geological correlations behind fracture spatial patterns can be expressed quantitatively as (Figure 5-5):

- precedence: the relative order in the sequence of fracture creation
- intensity trends: the variation of fracture intensity with distance from specific types of pre-existing features, or in a specific direction
- orientation trends: the variation of orientation with distance from specific types of pre-existing features, or in a specific direction

(a) Precedence

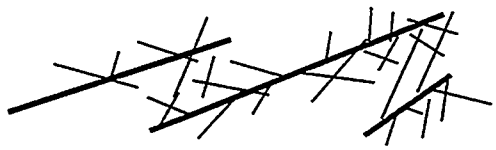

(b) Intensity Trends

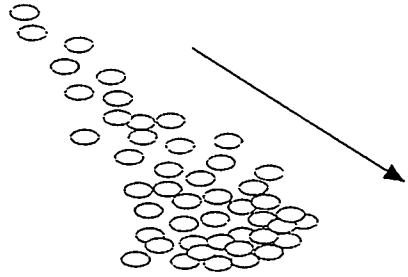

(c) Orientation Trends

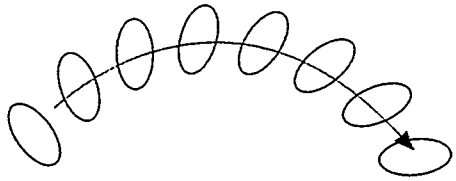

(d) Size Trends

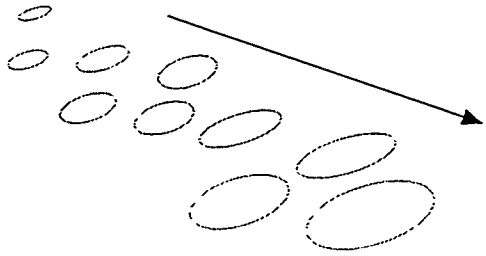

FIGURE **5-5**
SPATIAL CORRELATIONS
NIPER/FINAL REPORT/WA

PROJECT NO. 963 1357.521 DRAWING NO. 80740 DATE 9/28/98 DRAWN BY EA

Golder Associates

- size trends: the variation of orientation with distance from specific types of pre-existing features, or in a specific direction

These correlation structures provide the underlying underpinings for the Hierarchical Fracture Model (see Chapter 3). The rule-based spatial analysis approach quantifies spatial trends and correlations to provide input parameters for hierarchical fracture models.

5.2.2 Algorithm

The rule-based algorithm developed for analysis of spatial fracture patterns is illustrated in Figure 5-6. The algorithm starts with digitized fracture spatial data from wells or outcrops (Figure 5-7). The analysis proceeds as follows. Verification of this algorithm is described in Section 7.1.2.2 below.

1. **Set Definition**: The first step in the algorithm is to preprocess fractures into sets using a method which allows definition of fracture sets in terms of precedence and geological characteristics as well as orientation. Examples of these algorithms include the Neural network (see Section 3), and stochastic/probabilistic methods (Figure 5-8; Dershowitz et al, 1996).

2. **Data Gridding:** Data is gridded by defining a grid over the data and marking cells (a) (0,1) fractured/unfractured; (b) number of fractures; or (c) intensity P_{21} (tracemeters/meters squared), as illustrated in Figure 5-9.

3. **Same-Set Trends**: The second step in the algorithm is to identify possible spatial trends in intensity, size, and orientation for each set. This is done by calculating the statistics for the set on a grid (Figure 5-10).

4. **Prior Set Correlations**: Once a list of possible spatial trends have been established, the algorithm looks for prior-set features which could explain the trends. Examples of prior set correlation include, for example, decreases in intensity away from identified "fracture zones", and increased intensity within identified "fracture zones" (Figure 5-11).

5. **Between Set Correlations**: The fourth step is to determine whether there are correlations between the trends observed for different sets. For example, the spatial variation in intensity or orientation should correlate strongly for conjugate shears (Figure 5-12).

6. **Statistical Probabilities**: For each of the possible correlations, and trends identified in (2), (3), and (4) above, the algorithm calculates the probability that the correlation will apply for a particular fracture generation. The rules and statistical probabilities are then reported.

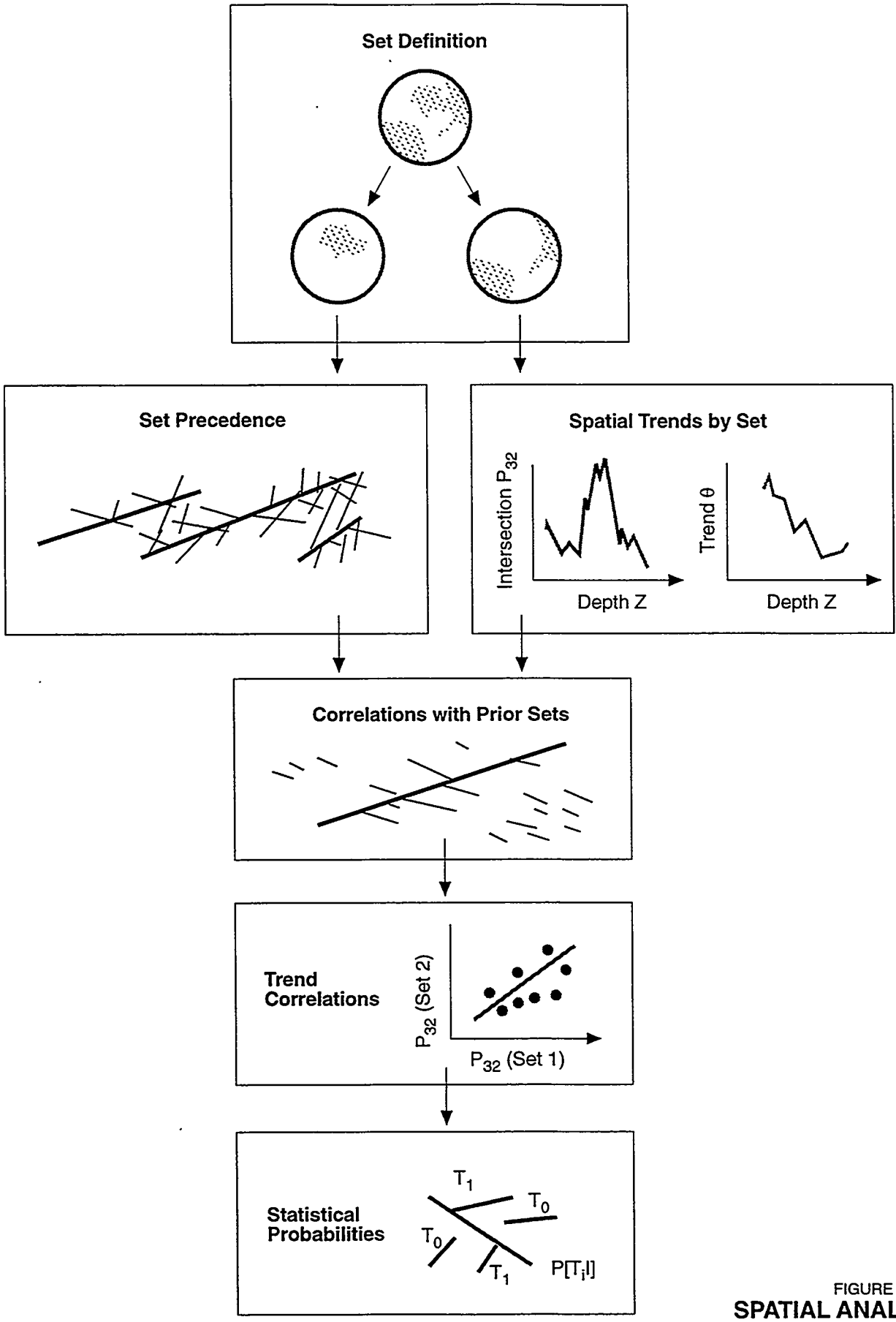

FIGURE **5-6**
SPATIAL ANALYSIS ALGORITHM
NIPER/FINAL REPORT/WA

PROJECT NO. 963 1357.521 DRAWING NO. 80741 DATE 9/28/98 DRAWN BY EA

Golder Associates

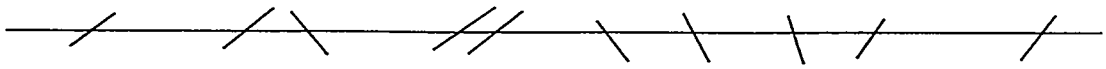

A. Scan line or borehole data

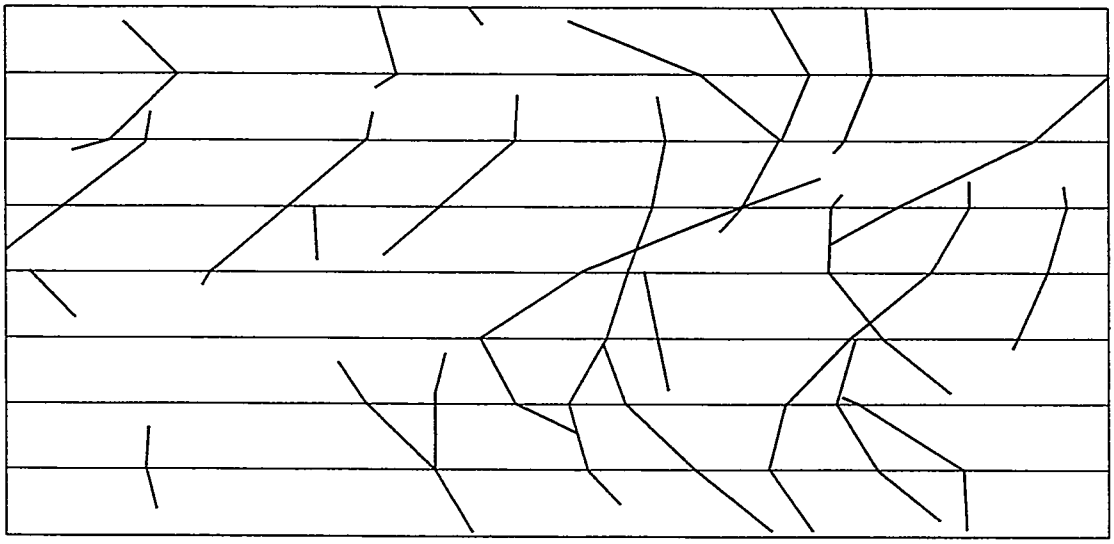

B. FMS/FMI borehole data

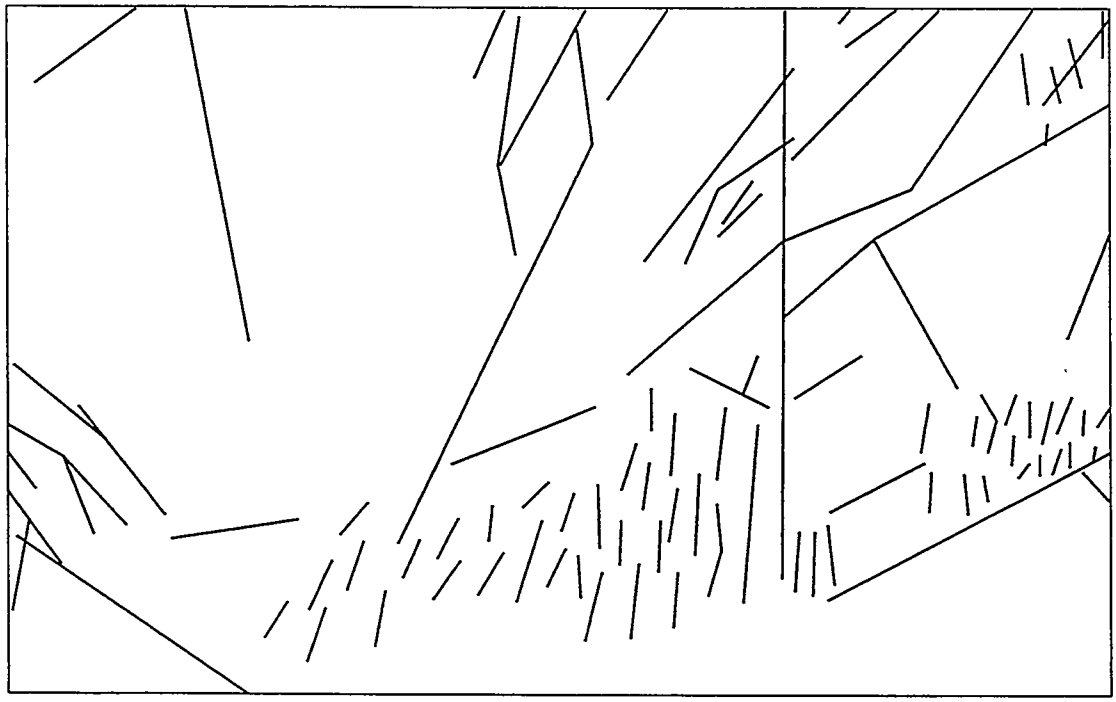

C. Trace map data

FIGURE **5-7**
EXAMPLES OF SCAN LINE, BOREHOLE, AND TRACE MAP DATA
NIPER/FINAL REPORT/WA

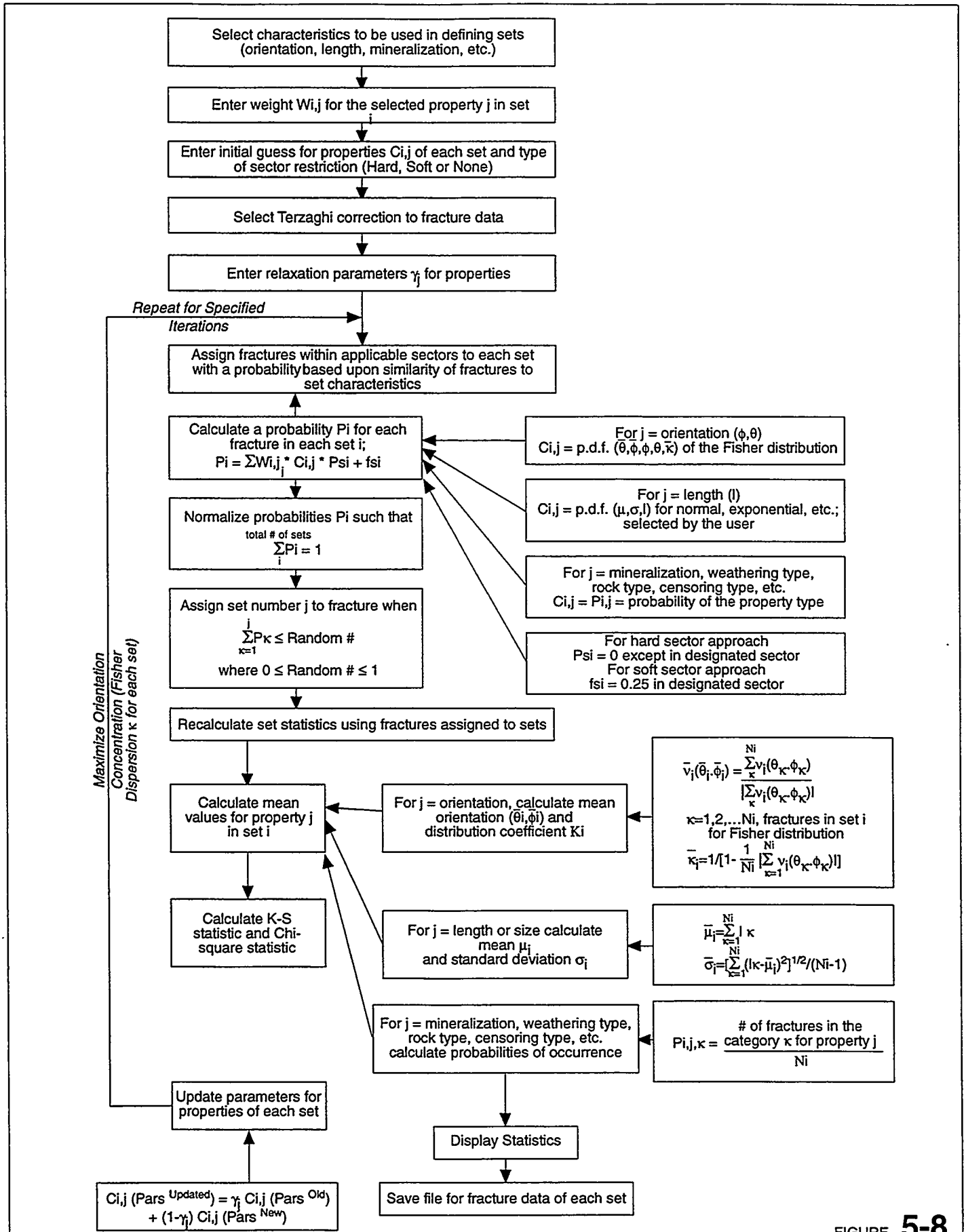

FIGURE **5-8**

STOCHASTIC/PROBABILISTIC SET DEFINITIONS

NIPER/FINAL REPORT/WA

PROJECT NO. 963 1357.521 DRAWING NO. 80742 DATE 9/28/98 DRAWN BY EA

Golder Associates

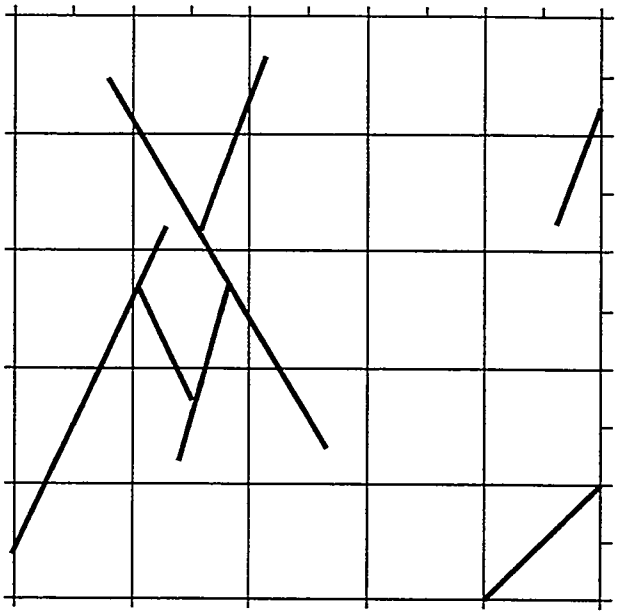

A. DFN Input

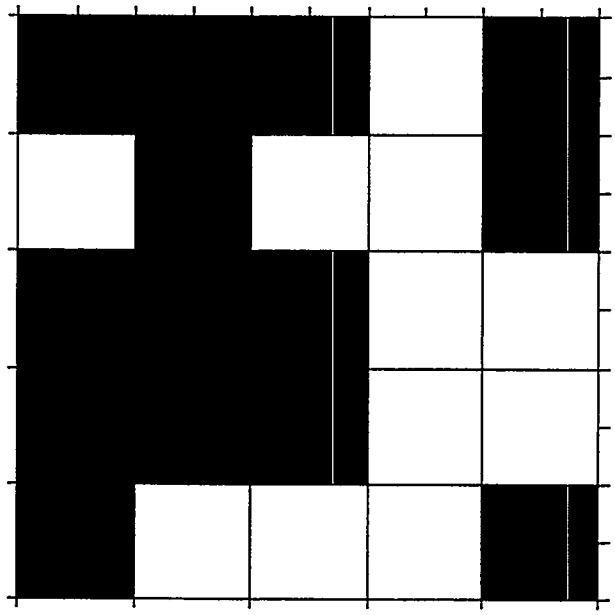

B. Fractured or Unfractured

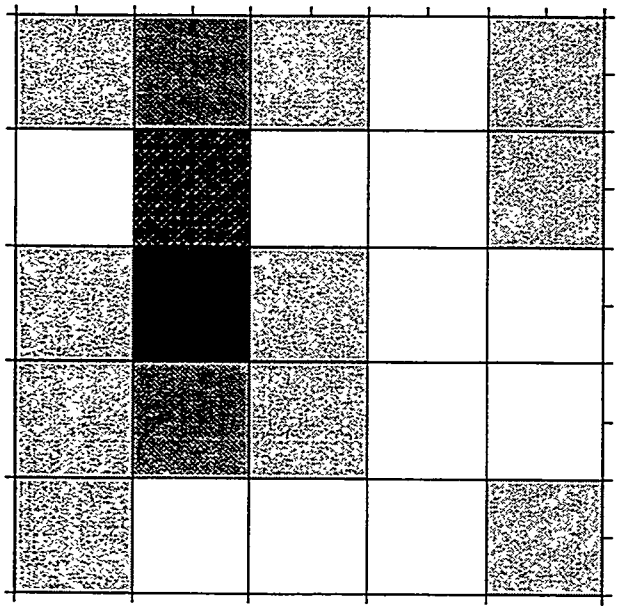

C. Number of Fractures

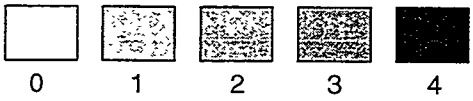

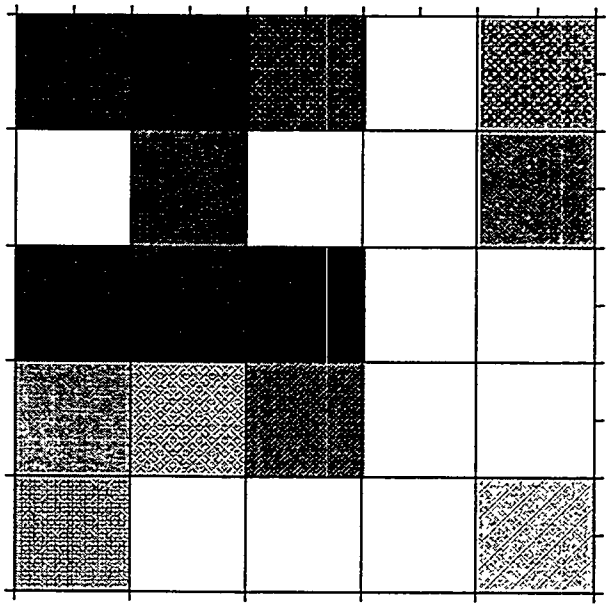

D. Intensity, P21

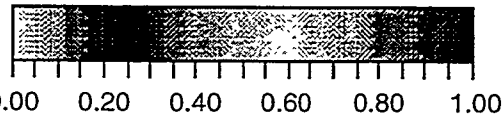

FIGURE **5-9**
GRIDDING ALGORITHMS
NIPER/FINAL REPORT/WA

PROJECT NO. 963 1357.521 DRAWING NO. 80761 DATE 9/28/98 DRAWN BY EA

Golder Associates

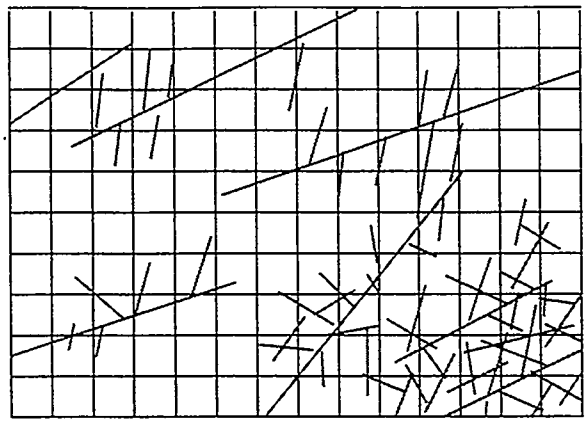

(a) Gridded Fracture Data

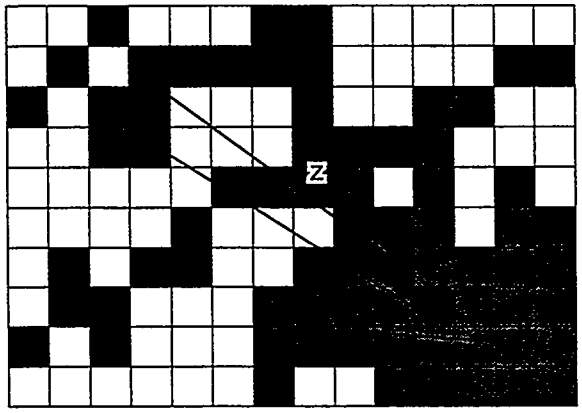

(b) Intensity Values on Grid

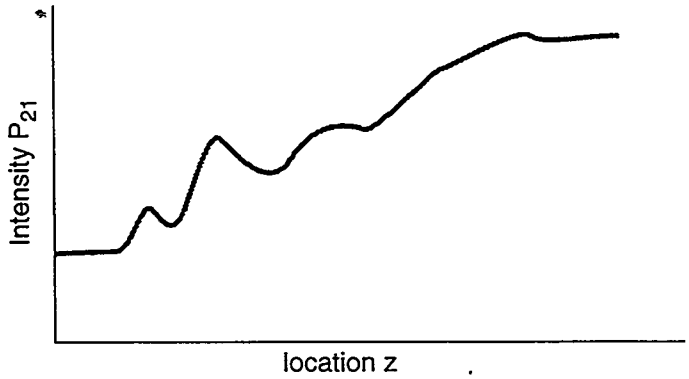

(c) Spatial Trends

FIGURE **5-10**
INTENSITY TREND ON GRID
NIPER/FINAL REPORT/WA

PROJECT NO. 963 1357.521 DRAWING NO. 80743 DATE 9/28/98 DRAWN BY EA

Golder Associates

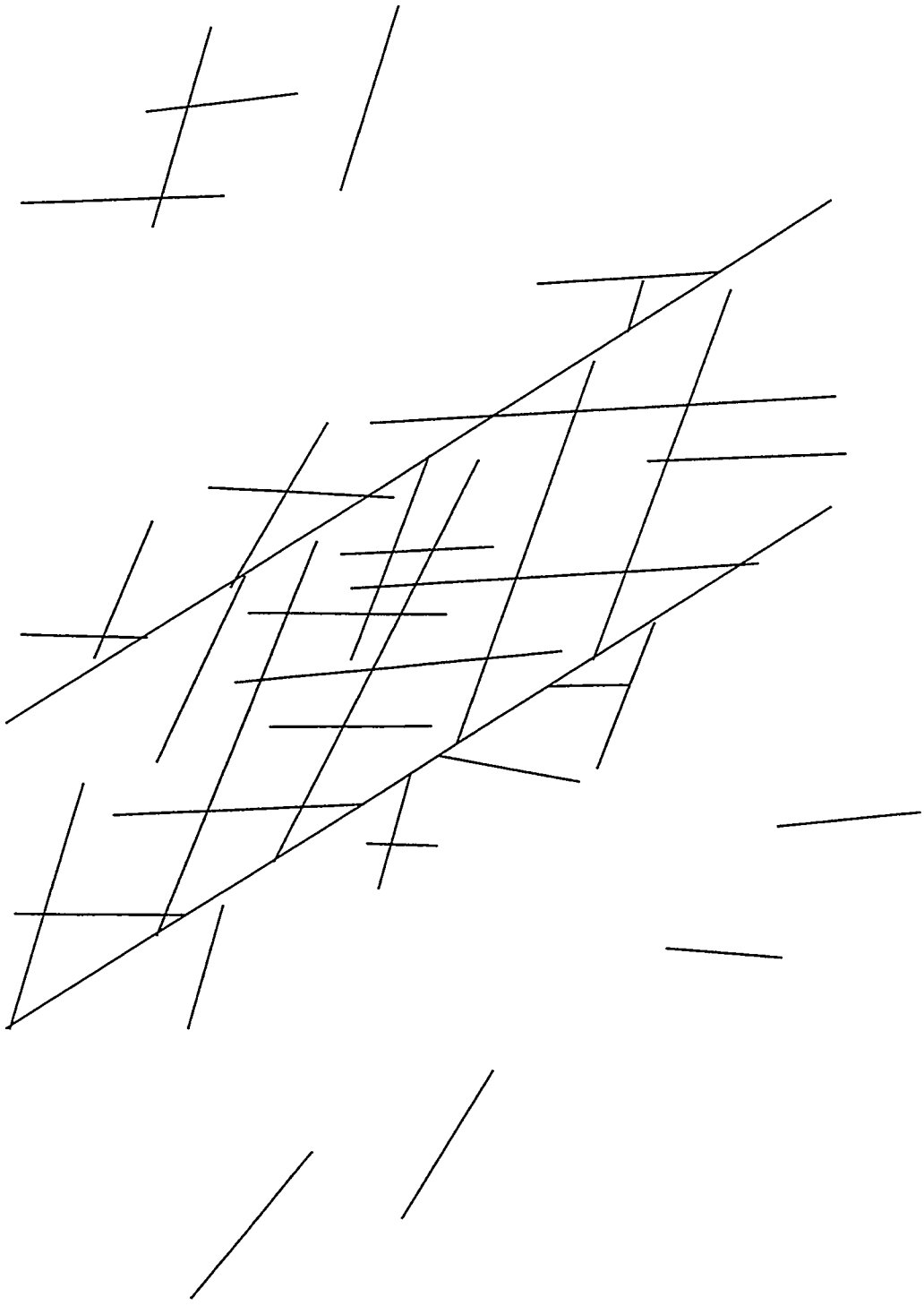

FIGURE **5-11**
PRIOR SET CORRELATION
NIPER/FINAL REPORT/WA

PROJECT NO. 963 1357.521 DRAWING NO. 80744 DATE 9/28/98 DRAWN BY EA

Golder Associates

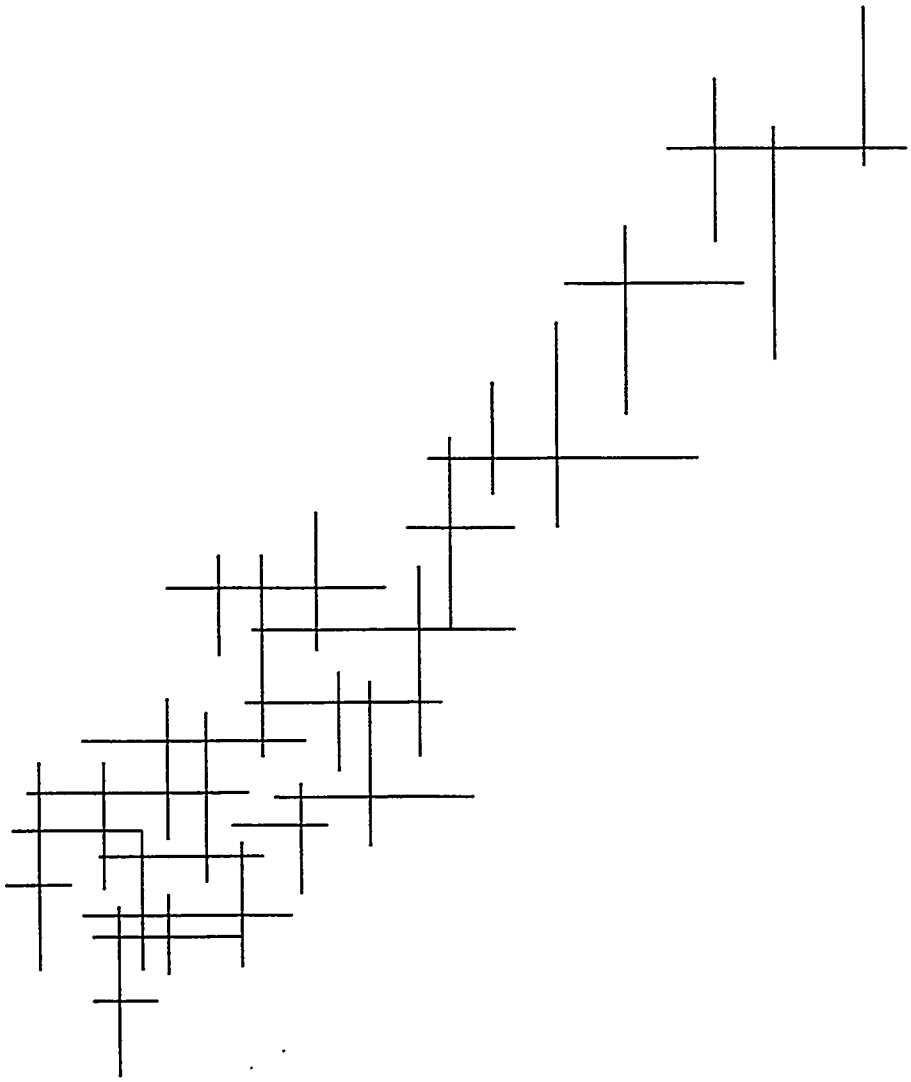

FIGURE **5-12**
CORRELATION BETWEEN CONJUGATE SHEARS
NIPER/FINAL REPORT/WA

PROJECT NO. 963 1357.521 DRAWING NO. 80745 DATE 9/28/98 DRAWN BY EA

Golder Associates

5.3 Task 2.1.3: Hydraulic Parameter Analysis

Hydraulic pathways through fractured rock are frequently formed by a combination of matrix permeability, flow in planar features such as fractures and fracture zones, and flow through one-dimensional channels such as those formed by selective mineralization, dissolution, and fracture intersection processes (Figure 5-13). This combination of flowing features of different dimensionality is referred to as "fractional dimension response" (Barker, 1988; Doe and Chakrabarty, 1996), as illustrated in Figure 5-14.

An approach was developed for analysis of DFN models to obtain simulated distributions of flow dimension to ensure that the simulated DFN has the same connectivity and heterogeneity structure as the in situ reservoir rock. This method provides an integrated approach to analysis of hydraulic tests in fractured rocks exhibiting this type of "fractional dimension" (Barker, 1988) and heterogeneously connected behavior.

The approach developed combines fractional dimension type curve analysis (Doe and Chakrabarty, 1996) with discrete fracture network simulation (Dershowitz et al, 1996). Implementation and verification of this algorithm are described in Section 7.1.3 below.

5.3.1 Background

The main geometric feature which distinguishes different flow dimensions is the power law change in flow area with radial distance. There is a second-power relationship for spherical flow, first power relationship for cylindrical flow, and zero power (or constant) for linear flow. The dimension is simply the power of the radial variation plus one. As pointed out by Doe and Geier (1991), power law variability of hydraulic properties can also produce dimensional behavior. The combined effects of area and property variation define a conductance, which is the product of area and hydraulic conductivity.

The dimension of the well test contains very fundamental and useful information about the hydraulic geometry of fracture networks. One-dimensional flow may indicate a single channel within a fracture, or a chain of channels forming a linear network. Two-dimensional flow may indicate a single fracture normal to the borehole, or a network of fractures that is confined to a planar zone, such as a fracture zone or a highly fractured sedimentary bed. Three-dimensional flow may indicate a well-connected, space-filling network of discrete fractures or channels. Finally, non-integer dimensions will appear between these cases where the fracture pattern does not fill a particular space, as in a fractal or power-law network geometry.

Differently dimensioned flow systems have significantly different behavior. In addition, since the systems are fractured, they can be both scale dependent and heterogeneously connected. Research was carried out toward development of procedures for analysis of fractional dimension type curve responses, using Laplace transform solutions for the equation of fractional dimensional flow.

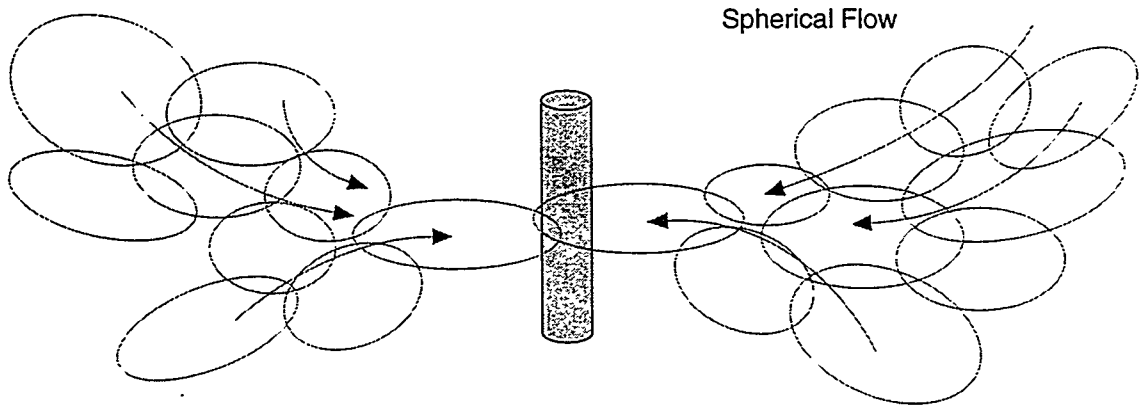

(a) Dimension 3

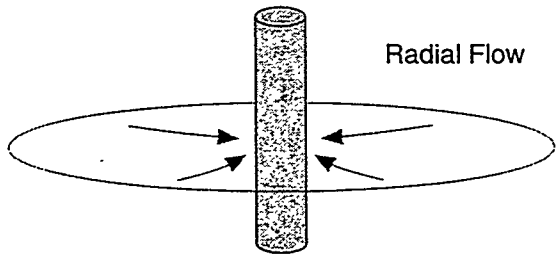

(b) Dimension 2

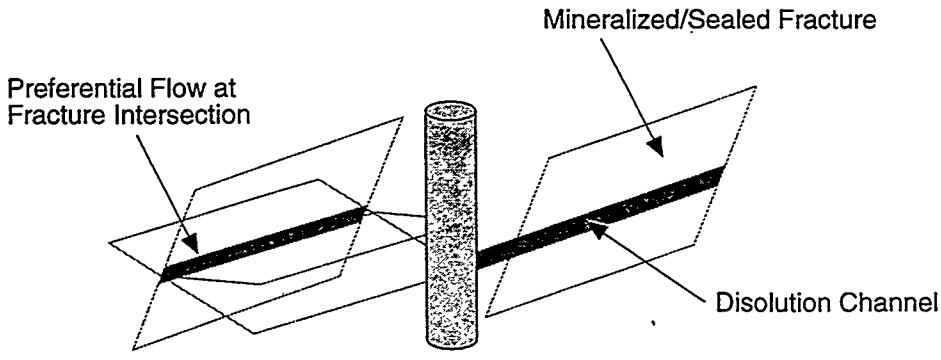

(c) Dimension 1

FIGURE **5-13**
HYDRAULIC PATHWAY FLOW DIMENSION
NIPER/FINAL REPORT/WA

PROJECT NO. 963 1357.521 DRAWING NO. 80746 DATE 9/28/98 DRAWN BY EA

Golder Associates

Porous Continuum

Fractured and/or
Channeled Discontinuum

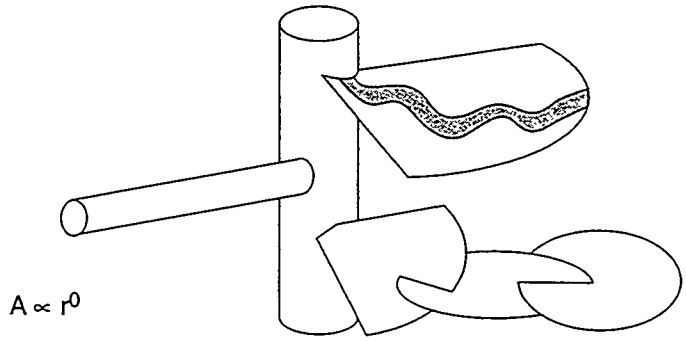

$A \propto r^0$

a) Linear

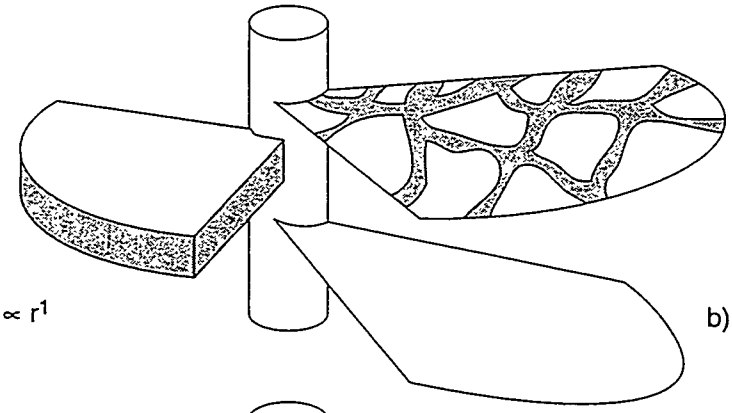

$A \propto r^1$

b) Radial

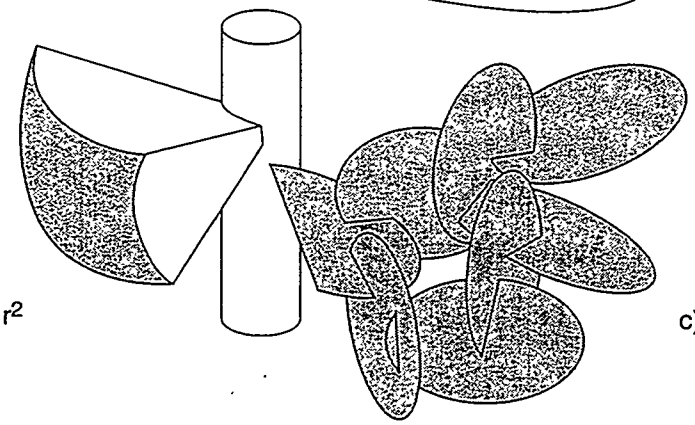

$A \propto r^2$

c) Spherical

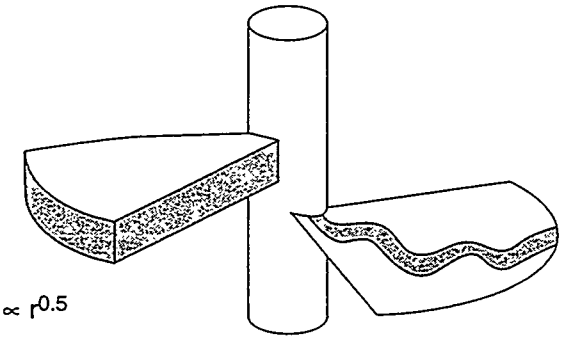

$A \propto r^{0.5}$

d) Fractional Dimension

FIGURE **5-14**
FRACTIONAL DIMENSION FLOW
NIPER/FINAL REPORT/WA

PROJECT NO. 963 1357.521 DRAWING NO. 80830 DATE 9/30/98 DRAWN BY EA

Golder Associates

5.3.2 Algorithm

The main assumptions made in the course of developing the models for transient rate and pressure behavior in a two-zone composite system are as follows:

1. Transient Darcian flow takes place in the system, and the near-well flow direction is radial
2. The i^{th} zone is characterized by flow dimension n_i (i = 1 for the inner zone and i = 2 for the outer zone), where n_i is not necessarily an integer; the source well is an n_1-dimensional "sphere" projected through three-dimensional space
3. The i^{th} zone is characterized by hydraulic conductivity and specific storage K_i and S_{si}, respectively
4. The system is infinite, and either a constant-rate or a constant-pressure condition is imposed at the source well
5. Wellbore/source storage capacity is non-negligible

The radial flow behavior of water in a two-zone composite system is governed by the following equations (Barker, 1988):

$$\frac{\partial^2 h_{D1}}{\partial r_D^2}+\left(\frac{n_1-1}{r_D}\right)\frac{\partial h_{D1}}{\partial r_D}=\frac{\partial h_{D1}}{\partial t_D},\ 1 \le r_D \le r_{D1} \tag{5-1a}$$

and

$$\frac{\partial^2 h_{D2}}{\partial r_D^2}+\left(\frac{n_2-1}{r_D}\right)\frac{\partial h_{D2}}{\partial r_D}= D_r \frac{\partial h_{D2}}{\partial t_D},\ r_{D1} \le r_D < \infty \tag{5-1b}$$

respectively, where

$$D_r = \frac{K_1/S_{s1}}{K_2/S_{s2}}. \tag{5-1c}$$

In terms of the dimensionless variables, the initial and boundary conditions become

$$h_{D1}(r_D,0)=h_{D2}(r_D,0)=H_D(0)=0, \tag{5-2a}$$

$$S_{wD}\frac{dH_D}{dt_D}=1+\frac{\partial h_{D1}}{\partial r_D}\Big|_{r_D=1}, \tag{5-2b}$$

$$h_{D2}(r_D \to \infty, t_D)=0, \tag{5-2c}$$

$$h_{D1}(r_{D1},t_D) = h_{D2}(r_{D1},t_D), \tag{5-2d}$$

and

$$\sigma \frac{\partial h_{D1}}{\partial r_D}\Big|_{r_{D1}} = \frac{\partial h_{D2}}{\partial r_D}\Big|_{r_{D1}} \tag{5-2e}$$

where

$$S_{wD} = \frac{S_w}{S_{s1}\, b^{3-n_1}\, \alpha_{n_1}\, r_w^{n_1}}, \tag{5-2f}$$

$$\sigma = \frac{K_1\,(b/r_1)^{n_2-n_1}}{K_2}\frac{\alpha_{n_1}}{\alpha_{n_2}}, \tag{5-2g}$$

and

$$r_{D1} = r_1 / r_w. \tag{5-2h}$$

Laplace transforms can be used to solve the system of partial differential equations. The subsidiary equations are

$$\frac{d^2\,\bar{h}_{D1}}{d\,r_D^2} + \frac{n_1-1}{r_D}\frac{d\,\bar{h}_{D1}}{d\,r_D} = p\,\bar{h}_{D1},\ 1 \le r_D \le r_{D1} \tag{5-3a}$$

and

$$\frac{d^2\,\bar{h}_{D2}}{d\,r_D^2} + \frac{n_2-1}{r_D}\frac{d\,\bar{h}_{D2}}{d\,r_D} = p\,D_r\,\bar{h}_{D2},\ r_{D1} \le r_D < \infty \tag{5-3b}$$

After transforming the boundary conditions, Equations 5-3a and 5-3b are solved simultaneously. The solutions in Laplace space are

$$\bar{h}_{D1}(r_D,p) = \frac{\Delta_2\, K_{v_1}(r_D\sqrt{p}) + \Delta_1\, I_{v_1}(r_D\sqrt{p})}{p\,(\Delta_1\,\lambda_2 + \Delta_2\,\lambda_1)} \tag{5-4a}$$

$$1 \le r_D \le r_{DI}$$

and

$$\bar{h}_{D2}(r_D,p) = \frac{\left[\Delta_2 K_{v_1}(r_{D1}\sqrt{p}) + \Delta_1 I_{v_1}(r_{D1}\sqrt{p})\right] K_{v_2}(r_D\sqrt{D_r\,p})\; r_{D1}^{v_1-v_2}\; r_D^{v2}}{p\,K_{v_2}(r_{D1}\sqrt{D_r\,p})\,(\Delta_1\lambda_2 + \Delta_2\lambda_1)}$$

$$r_{D1} \le r_D < \infty \tag{5-4b}$$

where

$$\Delta_1 = \frac{\sigma}{\sqrt{D_r}} K_{v_1-1}(r_{D1}\sqrt{p})\, K_{v_2}(r_{D1}\sqrt{D_r\, p}) -$$

$$K_{v_2-1}(r_{D1}\sqrt{D_r\, p})\, K_{v_1}(r_{D1}\sqrt{p}), \quad \text{(5-5a)}$$

$$\Delta_2 = \frac{\sigma}{\sqrt{D_r}} I_{v_1-1}(r_{D1}\sqrt{p})\, K_{v_2}(r_{D1}\sqrt{D_r\, p}) +$$

$$K_{v_2-1}(r_{D1}\sqrt{D_r\, p})\, I_{v_1}(r_{D1}\sqrt{p}), \quad \text{(5-5b)}$$

$$\lambda_1 = p\, S_{wD}\, K_{v_1}(\sqrt{p}) + \sqrt{p}\, K_{v_1-1}(\sqrt{p}), \quad \text{(5-5c)}$$

$$\lambda_2 = p\, S_{wD}\, I_{v_1}(\sqrt{p}) - \sqrt{p}\, I_{v_1-1}(\sqrt{p}), \quad \text{(5-5d)}$$

and

$$v_i = 1 - \frac{n_i}{2},\ i = 1, 2 \quad \text{(5-5e)}$$

Using Equations 5-1 through 5-5 and the related type curves of Figures 5-15 through 5-17, it is possible to derive both transmissivity, storativity, and flow dimension as a function of distance from the well bore from well tests. Of these, the flow dimension as a function of distance may prove to be the most important for reservoir design, since lower flow dimensions indicate that only a small portion of the reservoir is being accessed.

5.4 Integration of DFN and Fractional Dimension Flow Approaches

Just as heterogeneous fractured rock masses are not limited to integer flow dimensions, a series of well tests from different locations in a fracture networks may exhibit a distribution of flow dimensions rather than a single, characteristic flow dimension. This distribution of flow dimensions is thus a valuable measure of rock mass heterogeneity and connectivity. Flow dimension distributions from well test analyses of large data sets from Japan and Sweden (Geier et al., 1995; Winberg , 1996) are shown in Figure 5-18. Each of these sites shows a unique distribution of transmission and flow dimension which is indicative of the rock mass heterogeneity and connectivity.

5.4.1 Background

Figure 5-19 illustrates the approach developed by the project to use well test results in terms of transmissivities and flow dimension distributions to develop DFN models with consistent fracture network connectivity and hydraulic properties.

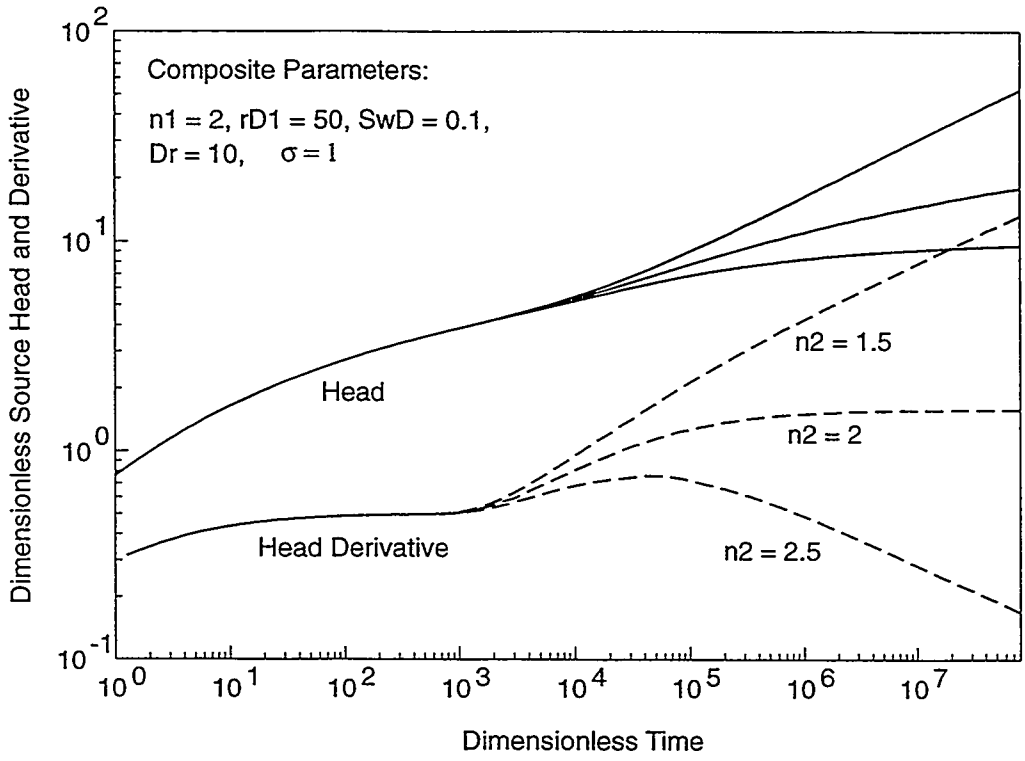

a) Dimensionless head and head derivative in source well vs. time with different outer zone flow dimensions

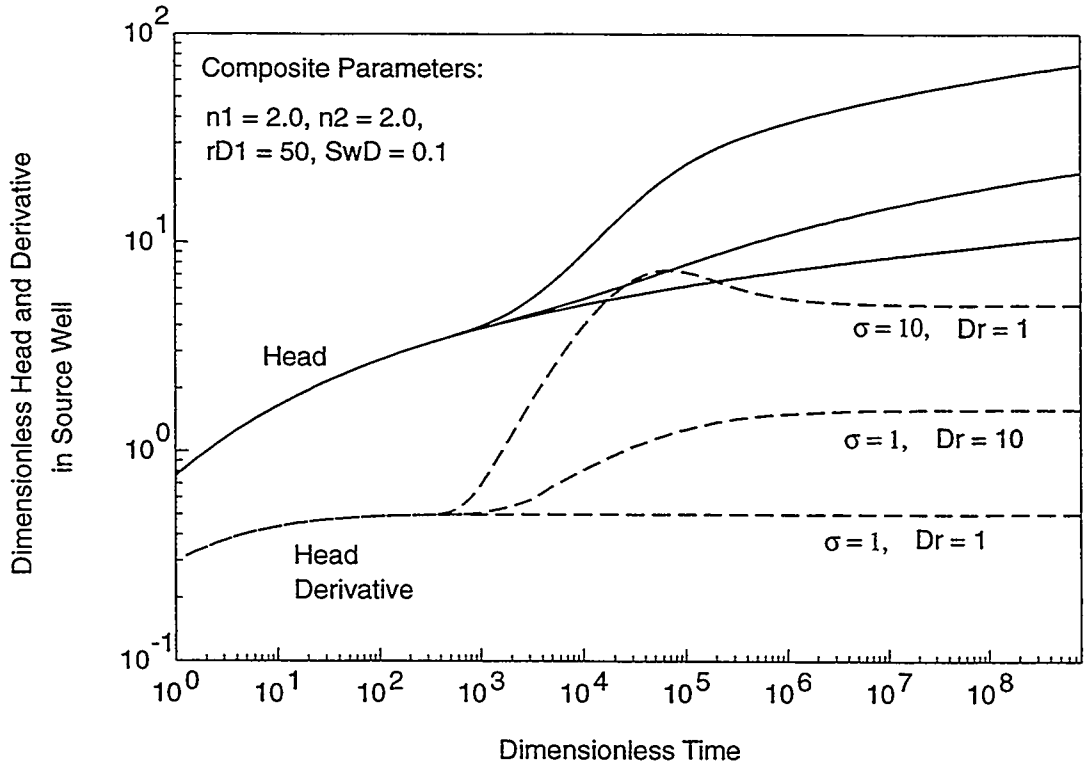

b) Dimensionless plot of head and head derivative in source well vs. time for different values of σ and Dr: n1 = n2 = 2

FIGURE **5-15**
FRACTIONAL DIMENSION TYPE CURVES
NIPER/FINAL REPORT/WA

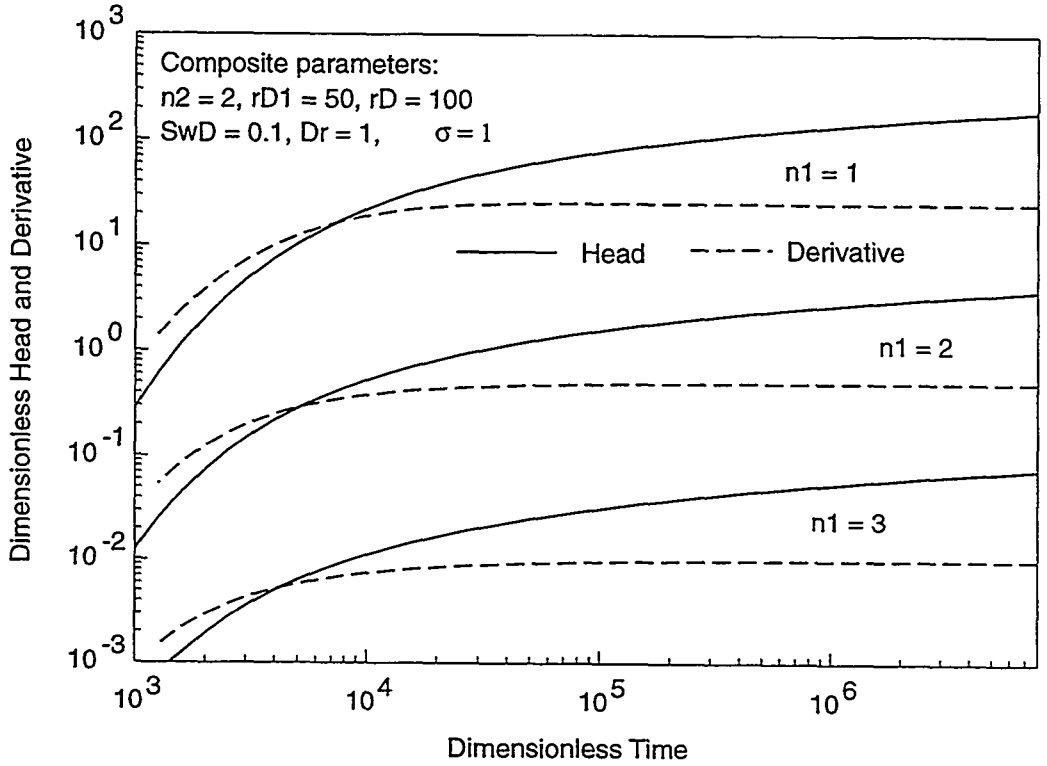

Constant rate interference test solution with varying inner zone flow dimension: observation well in outer zone

FIGURE **5-16**
FRACTIONAL DIMENSION TYPE CURVES
NIPER/FINAL REPORT/WA

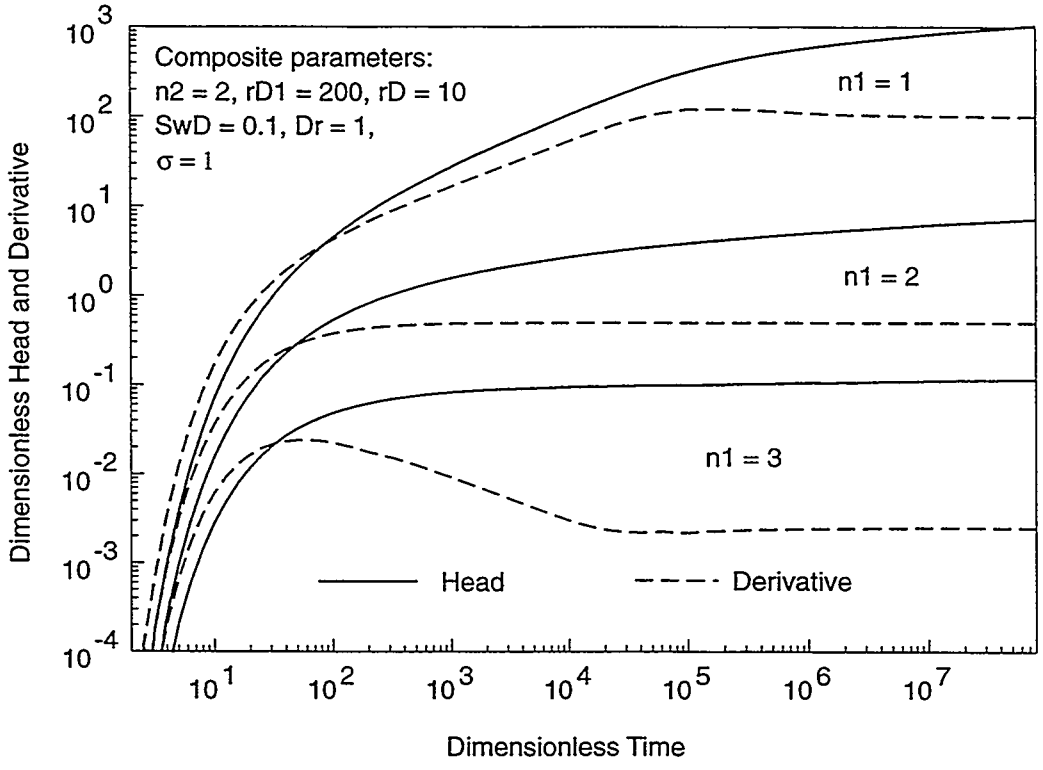

Constant rate interference test solution with varying inner zone flow dimension: observation well in inner zone

FIGURE **5-17**
FRACTIONAL DIMENSION TYPE CURVES
NIPER/FINAL REPORT/WA

PROJECT NO. 963 1357.521 DRAWING NO. 80831 DATE 9/29/98 DRAWN BY EA

Golder Associates

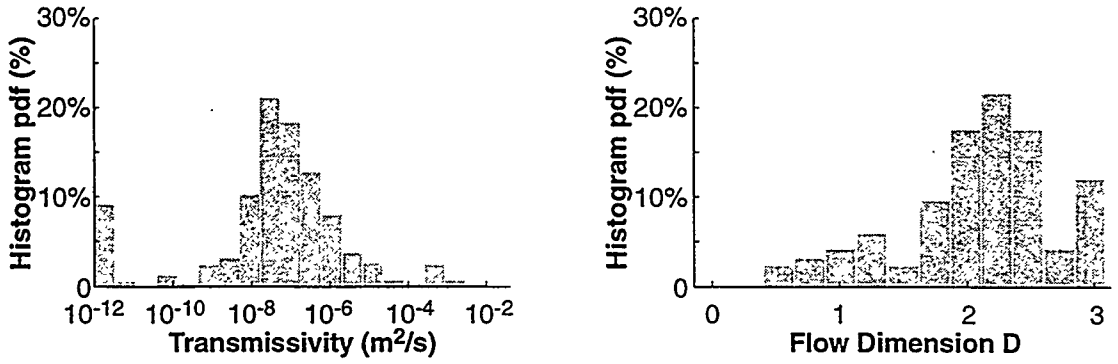

(a) Finnsjon, Sweden (after Geier et al., 1995)

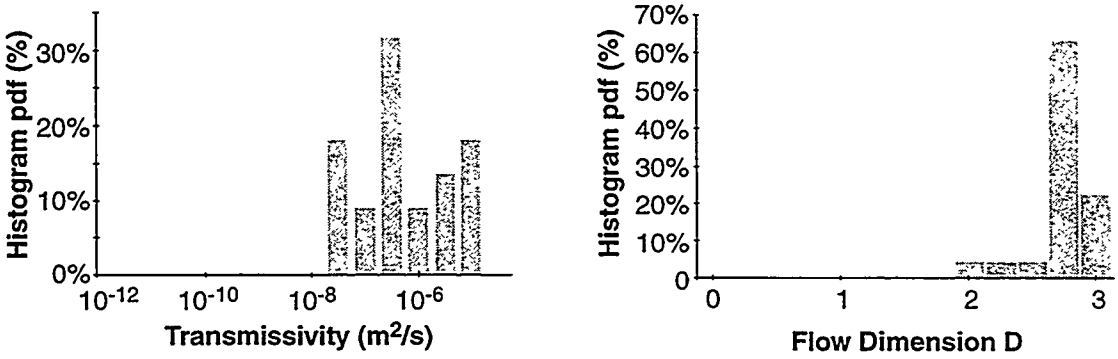

(b) Äspö "TRUE-1" Block (after Winberg et al., 1996)

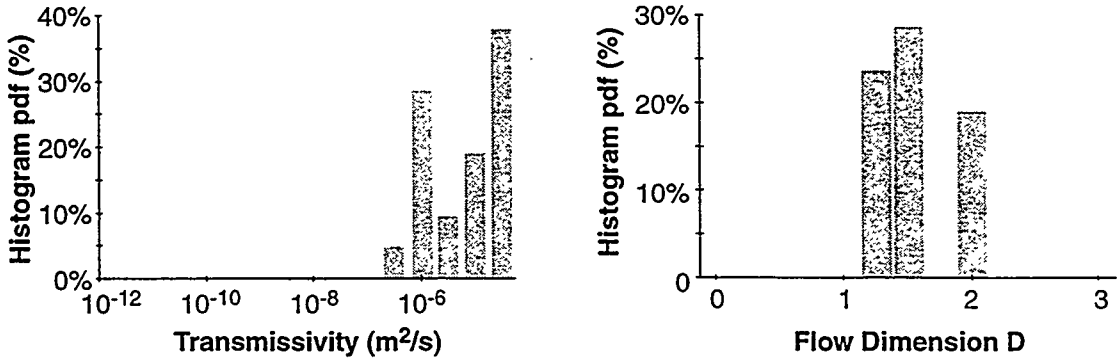

(c) Kamaishi KD-90 Area

FIGURE **5-18**

DISTRIBUTION OF FLOW DIMENSION, FINNSJON AND ÄSPÖ, SWEDEN AND KAMAISHI, JAPAN

NIPER/FINAL REPORT/WA

PROJECT NO. 963 1357.521 DRAWING NO. 80751 DATE 9/28/98 DRAWN BY EA

Golder Associates

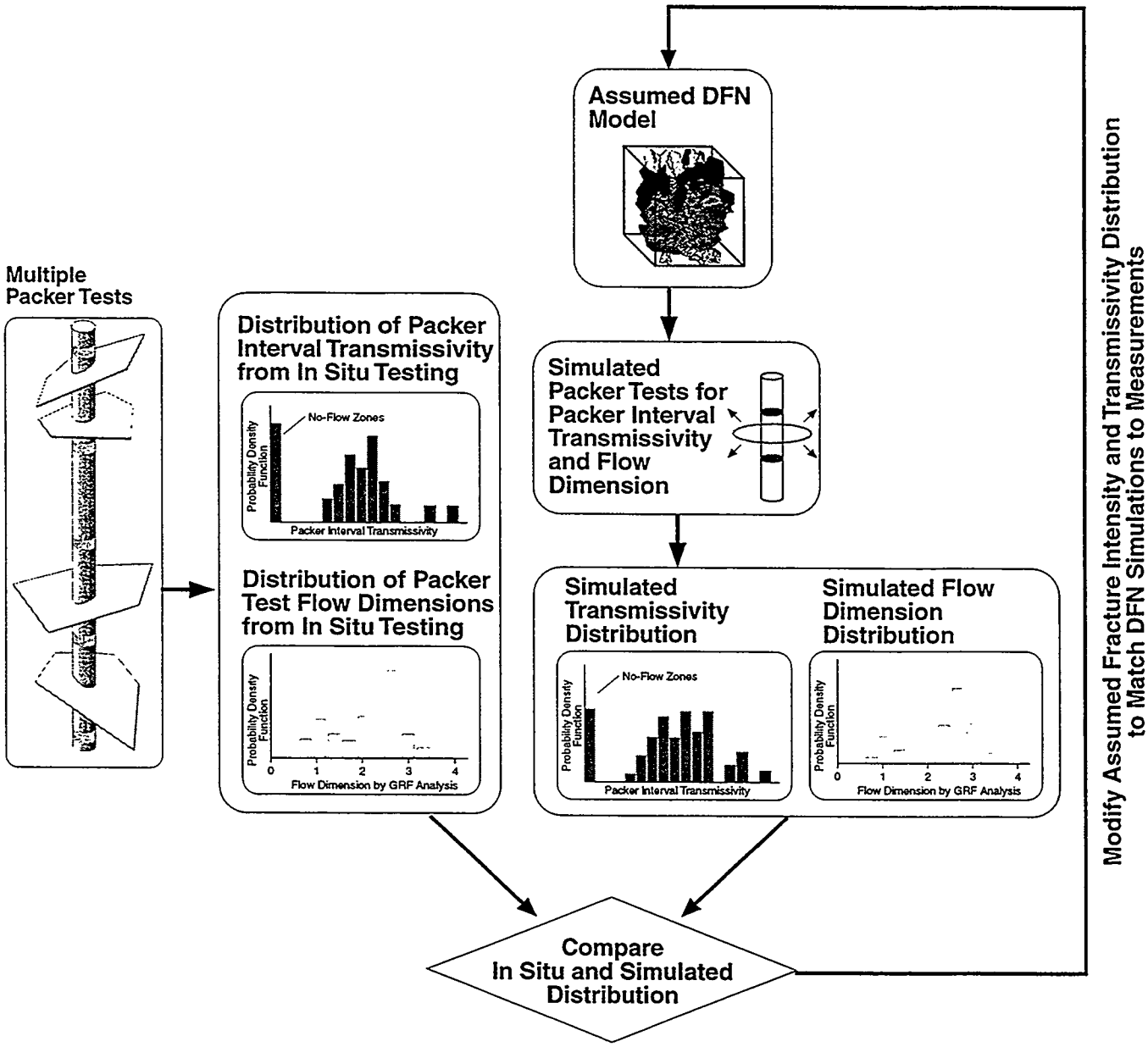

FIGURE **5-19**
CALIBRATION OF DFN TO HYDRAULIC TESTS
NIPER/FINAL REPORT/WA

PROJECT NO. 963 1357.521 DRAWING NO. 80752 DATE 9/28/98 DRAWN BY EA

Golder Associates

The analysis starts with:

1. **Hydraulic Test Results:** A file containing the results of transient packer test or drill-stem hydraulic test results, expressed as distributions of interval transmissivity and flow dimension, similar to those illustrated in Figure 5-18. These are derived from packer test transient results using fractional dimensional type curve analyses (Doe, 1991).

2. **DFN Model:** A discrete fracture network (DFN) conceptual model implemented as a spatial location model, distributions for orientation, intensity, size, and shape, and analysis of any correlations between these.

The forward modeling approach presented here attempts to reduce the effort required to get the distribution of dimensions from the DFN model. The approach concentrates on the variation in the flow path conductance as a function of radial distance, rather than using simulated hydraulic tests.

As discussed above and by consequence of Equations 5-1 through 5-5, the flow dimension is a measure of the power law variation of flow area or conductance with radial distance. The relationship between the variation in flow path area, (which is an analog for conductance) with radial distance and the flow dimension is illustrated in Figure 5-20.

For linear (1D) flow, the area (conductance) is constant with radial distance

- For radial (2D) flow, the area (conductance) increases linearly with radial distance

- For spherical (3D) flow, the area (conductance) increases as radial distance squared

- For generalized radial flow (nD), the flow area A_f (as an analog of conductance C) increases as a power of radius R equal to the one less than the flow dimension, according to

$$C \propto A_f \propto R^{D-1} \tag{5-6}$$

5.4.2 Algorithm

In the forward simulation approach, a graph theory search is used to work out from the borehole into the fracture network to calculate the variation in conductance with distance from the borehole. This search is carried out as follows:

1. **DFN Simulation:** A series of realizations of a discrete fracture network model are generated, using assumed distributions for parameters based on initial data analysis. The same wells used in the field testing are "completed" into each of the DFN simulations.

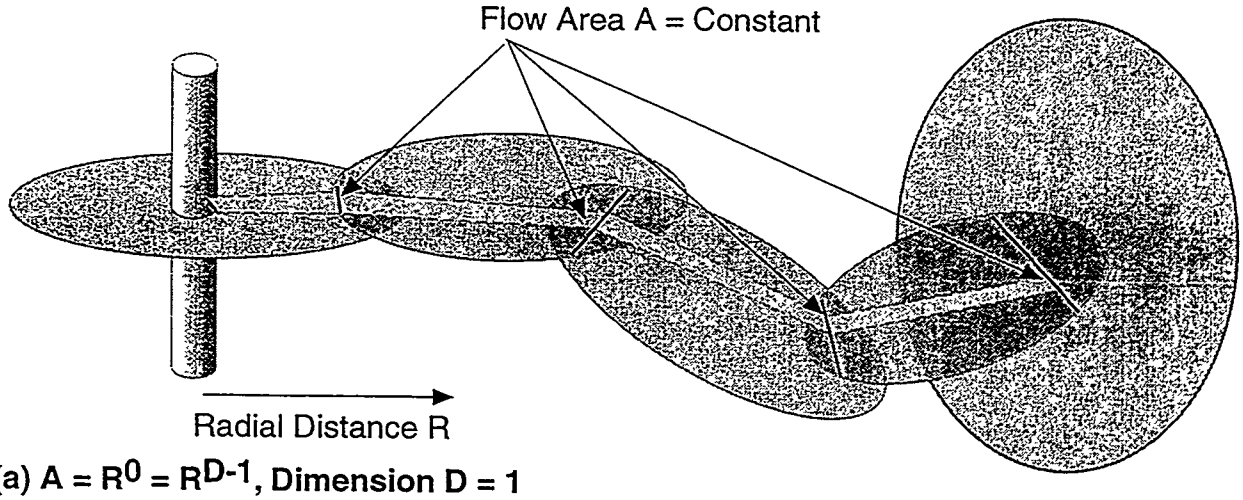

(a) $A = R^0 = R^{D-1}$, Dimension D = 1

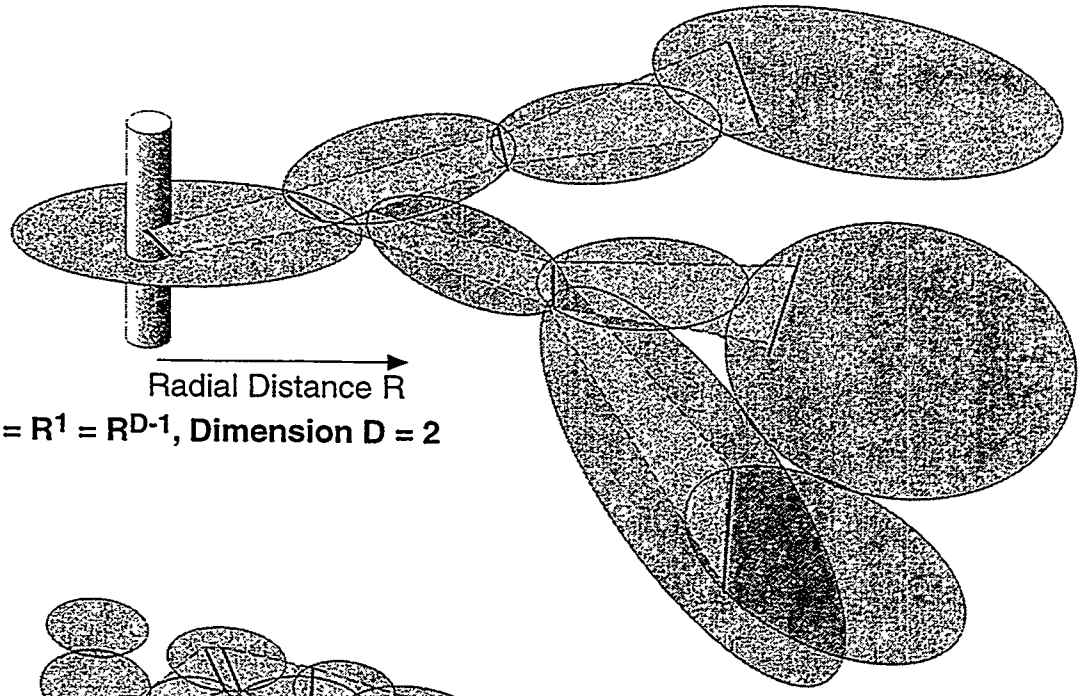

(b) $A = R^1 = R^{D-1}$, Dimension D = 2

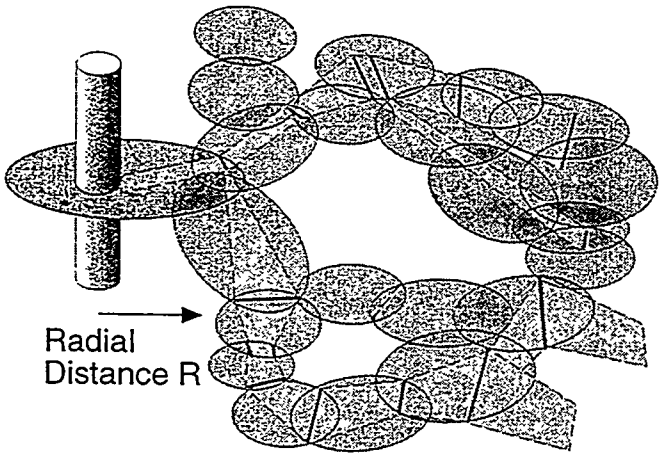

(c) $A = R^2 = R^{D-1}$, Dimension D = 3

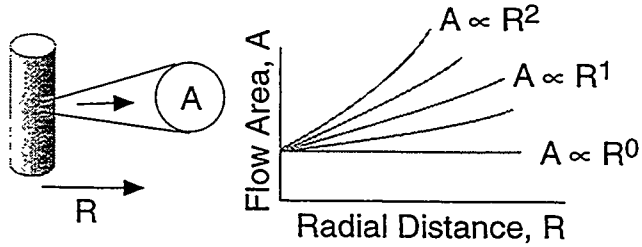

(d) Flow Area Function

FIGURE **5-20**
FLOW AREA VS. RADIAL DISTANCE
NIPER/FINAL REPORT/WA

2. **Cluster Analysis:** A cluster analysis is used to identify all the fractures which exceed a specified size or transmissivity threshold and which are connected to well test interval in the simulated well. The result of the cluster analysis may contain the entire network or it may be only a few fractures depending on the connectivity of the fracture network.

3. **Graph Analysis:** The fracture pattern is converted to a pipe network graph, with each graph element i assigned a length L_i and pipe conductance C_i. The pipe conductance is calculated as

$$C_i = W_i T_i \tag{5-7}$$

where W_i is the flow width achieved in the fracture, and T_i is the transmissivity of the fracture containing the pipe.

A number of algorithms are available to calculate the flowing width in the fracture from the geometry of fractures and fracture intersections. For the present demonstration, the width is calculated based on the geometry of the traces formed by fracture intersections, with an applied channeling factor F_i,

$$W_i = \tfrac{1}{2} F_i (L_{1i} + L_{2i}) \tag{5-8}$$

L_{1i} and L_{2i} are the lengths of the two traces which define the fracture intersections (Figure 5-21).

4. **Flow Dimension:** Using this approach, a plot of radial distance from the well against conductance can be derived for any borehole configuration and DFN model. The slope S of this relationship on a log-log plot provides an estimate of the flow dimension as,

$$D = 1+S \tag{5-9}$$

where S is the non-linear regression fit to the radial distance vs. conductance plot.

By carrying out this analysis on a series of stochastic realizations of the DFN model, one can obtain a distribution of packer test flow dimension.

5. **Packer Test Transmissivity:** The packer test transmissivity T_{pi} for each network realization can be approximated by,

$$T_{pi} = f(\Sigma T_{fj}, D_i) \tag{5-10}$$

where T_{fj} is the transmissivity of each fracture intersecting the interval and D_i is the packer interval flow dimension calculated by Equation 5-9 above.

6. **Comparison and Optimization:** The distributions of simulated and measured packer test transmissivity and flow dimension can then be compared to determine the match between the hydrogeological heterogeneity and connectivity of the simulated DFN and the *in situ* rock mass. The DFN can then be calibrated or conditioned to match the observed behavior.

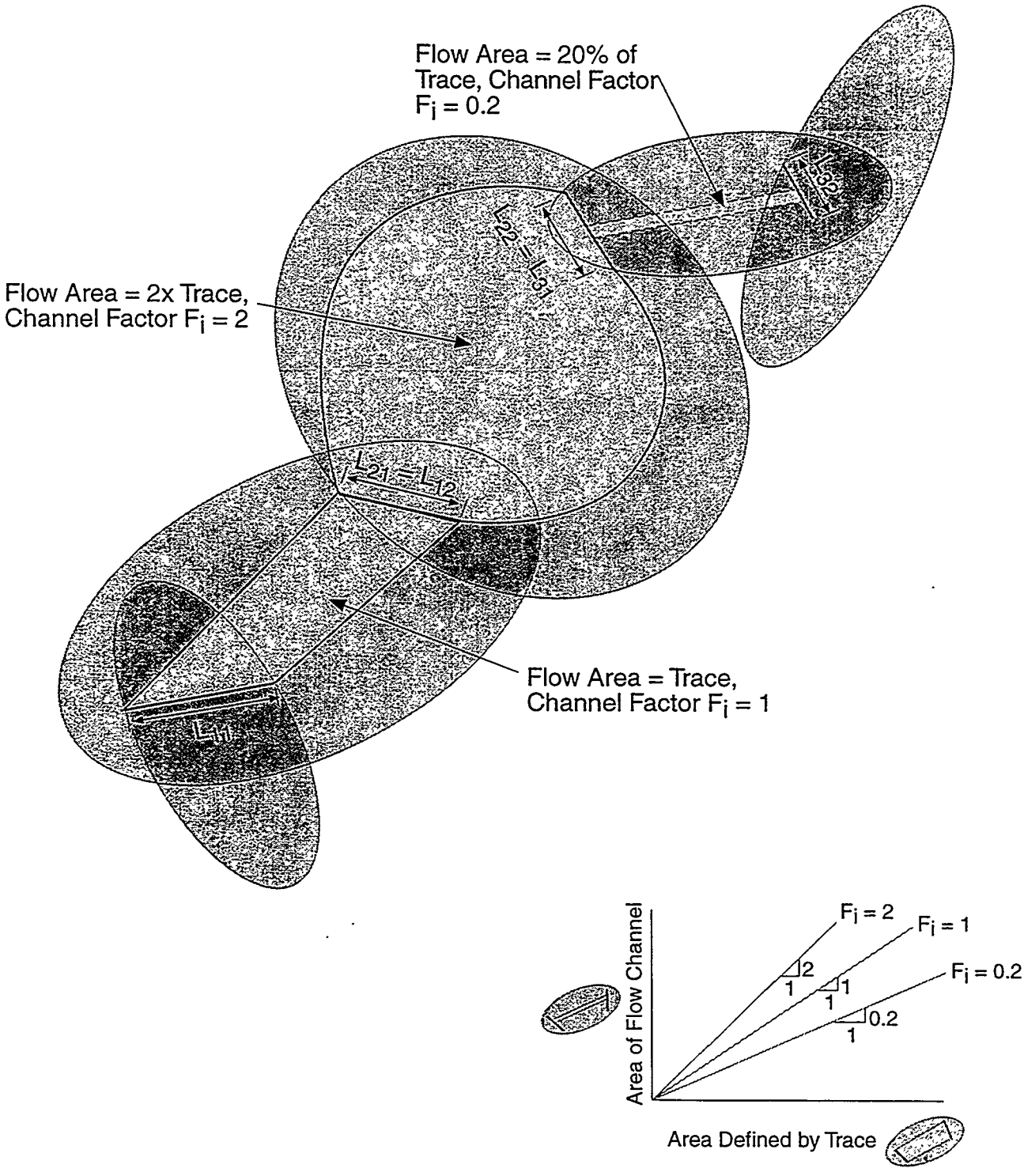

FIGURE **5-21**
FLOW WIDTH CHANNELING FACTOR F_i
NIPER/FINAL REPORT/WA

PROJECT NO. 963 1357.521 DRAWING NO. 80754 DATE 9/29/98 DRAWN BY EA

Golder Associates

5.5 Task 2.1.4: Compartmentalization Analysis

Compartmentalization in reservoirs where fractures dominate permeability often leads to wells that produce at different rates and volumes than expected (Figure 5-22). This section describes compartmentalization analysis algorithms and algorithm verification. Application is described in Section 7.2.2 below.

5.5.1 Background

Within compartments, pressure communication can be nearly instantaneous, while nearby wells in different compartments may have very little communication. This situation can lead to several undesired consequences, among them, unanticipated interference among wells, reduced recovery efficiency, and increased production uncertainty. Estimating the degree of compartmentalization is important at all stages of field development in order to properly engineer the field and to provide realistic recovery estimates and rates for financial decisions.

Compartmentalization may be due to several factors: fault offset of the producing horizon; the existence of high permeability sub-vertical faults that form barriers to lateral migration; the reduction in permeability of fractures due to mineralization; and the natural geometrical clustering of joint and smaller fault networks when matrix permeability is low. In terms of thermal recovery projects, there is an additional type of compartmentalization that is dynamic. Injected steam loses heat to the matrix and condenses. This condensation "front", which may be less of a definable surface than it is a series of fingers reaching out from the well along fracture paths, forms the steam "compartment". Knowledge of the shape and extent of this compartment is crucial to optimizing production. It is a combination of the natural geometrical compartmentalization of the fracture networks, and the ability of the fractures in the networks to exchange heat with the matrix. The geometry of the fracture networks places constraints on the steam compartments; the steam compartments can never be bigger than the networks themselves.

It is usually possible to identify large-scale fault-bounded reservoir compartments from seismic or production histories. It is far more difficult to assess the compartmentalization due to joint network geometry and connectivity, for which seismic is of little use. Fracture network compartmentalization is often suspected when static and dynamic calculations of recoverable oil or gas do not agree, and their is no evidence for fault-offset or others types of fault-related compartmentalization in a fractured reservoir.

For this reason, two approaches have been developed and are being evaluated to address the more general problem of joint network compartmentalization for non-thermal applications, and also to extend the calculation for steam injection applications.

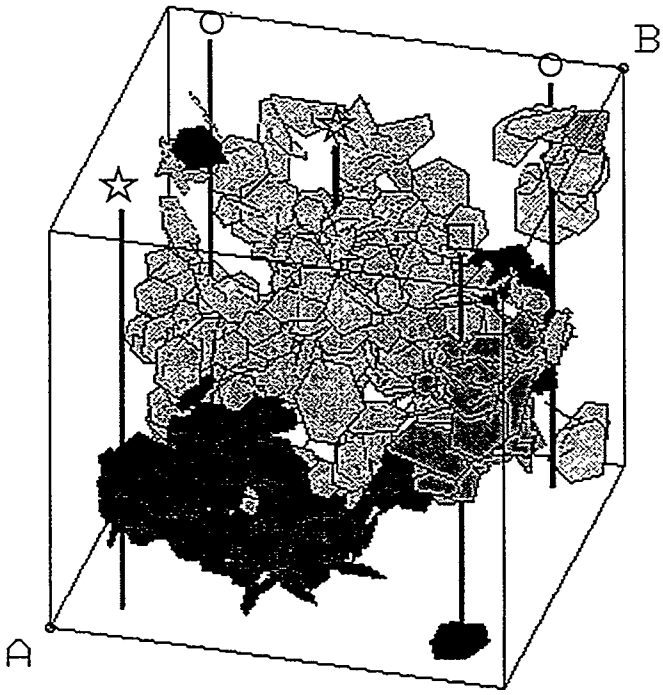

A: (100.0, -100.0, -100.0)
B: (-100.0, 100.0, 100.0)

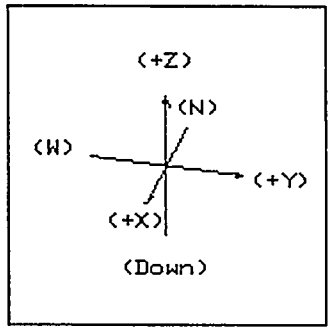

Production

☆ Excellent - major compartments intersected

□ Significant - interference from wells sharing compartment

○ Poor - no major compartments intersected

FIGURE **5-22**
PRODUCTION FROM COMPARTMENTALIZED RESERVOIR
NIPER/FINAL REPORT/WA

Figure 5-23a shows a hypothetical discrete fracture network, with an apparent high density of fracturing. However, not all fractures are interconnected. Rather, the fractures form distinct clusters or compartments, as illustrated in Figure 5-23b. Most of the wells shown in the model intersect a different cluster. In other words, these wells could only communicate with each other through the matrix. If this were a field, it would be important to determine the volumes of these compartments, which ultimately relates to the amount of hydrocarbon that a well can produce, and the horizontal dimensions of these compartments, which relates to optimal well spacings and the efficiency of primary or secondary recovery for a specified well pattern.

5.5.2 Algorithm

The computation of the volume and horizontal extent of joint network compartments is a three-step process:

Step 1. Identify individual fracture networks within the DFN model

Step 2. Compute the bounding surface for each identified network

Step 3. Calculate the volume of the bounding surface and the horizontal extent of the network

The identification of the individual fracture networks is a straightforward process for which robust algorithms have been developed. After the DFN model has been created, the intersections among the fractures are calculated. This leads to a symmetrical matrix of "1"'s and "0"'s, where "1" indicates an intersection, which is represented as an adjacency list or matrix (Figure 5-24). This connectivity matrix is then searched beginning with fracture number 1 in a standard tree search. This search process is repeated for all fractures that do not belong to any previously identified cluster until all fractures in the model have been processed. The results of this first step are saved as a list of fractures belonging to each cluster.

The second step is the calculation of the bounding surface for each cluster. Each network may be irregular. A simple approach for this would be to compute the "bounding box" for a network, and use this box volume and horizontal cross-section as surrogates for compartment volume and horizontal extent (Figure 5-25). However, this would lead to an overestimation in most cases of both volume and cross-section. This in turn would produce overestimates of the ultimate recovery from wells, and suggest greater well spacings and recovery efficiencies than would actually be the case.

To reduce the potential for overestimates, it is necessary to calculate a bounding surface that better approximates the outer limits of the network. A convex hull meets these requirements. Figure 5-26 shows an example three-dimensional convex hull calculated using the QuickHull algorithm and the Qhull software package (Barber et al., 1996). This figure illustrates that the convex hull can frequently be very different (and much more accurate) than a bounding box.

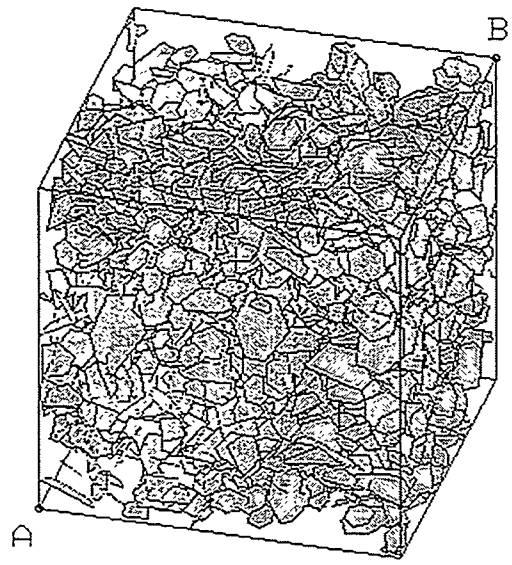

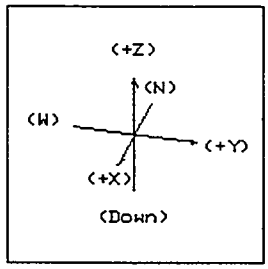

A: (100.0, -100.0, -100.0)
B: (-100.0, 100.0, 100.0)

(a) Fracture Pattern

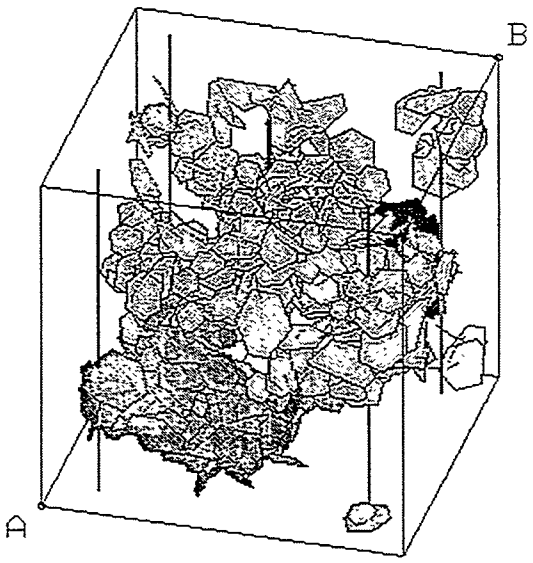

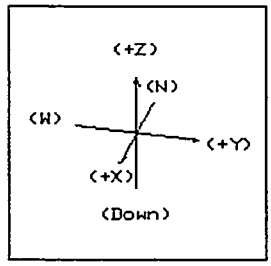

A: (100.0, -100.0, -100.0)
B: (-100.0, 100.0, 100.0)

(b) Compartmentalization

(b) Compartmentalization

FIGURE **5-23**
COMPARTMENTALIZATION OF INTENSITY IN A FRACTURED RESERVOIR
NIPER/FINAL REPORT/WA

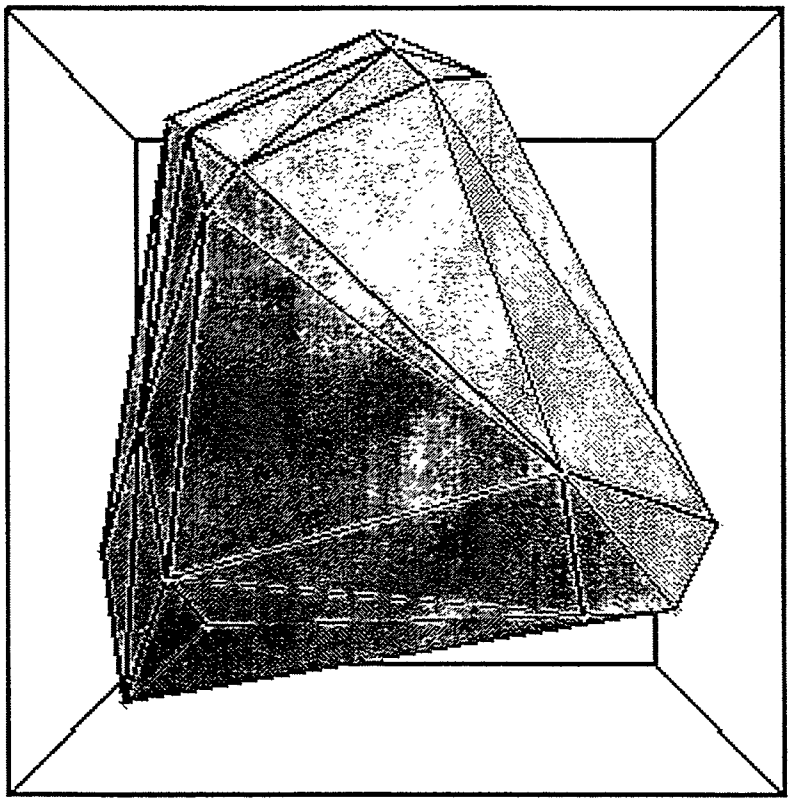

FIGURE **5-26**
CONVEX HULL BY QUICK HULL ALGORITHM
NIPER/FINAL REPORT/WA

PROJECT NO. 963 1357.521 DRAWING NO. 80779 DATE 9/28/98 DRAWN BY EA

Golder Associates

The final step is to compute the volume and cross-sectional area of each hull. This is easily done. First, Qhull contains options to compute the volume of the hull, and to output the coordinates of vertices belonging to the hull. From these vertices, it is possible to compute another convex hull, which represents the horizontal extent (Figure 5-27).

For vertical wells, the probability of whether the well will intersect the cluster (given that the well will be drilled deeply enough to intersect the cluster if the cluster lies under the well) does not depend upon the Z-coordinates of the cluster. The intersection probability is only a function of the X- and Y-coordinates. The shape and area of this horizontal extent is easily determined by calculating the two-dimensional convex hull of the (X,Y) data points belonging to the three-dimensional convex hull that bounds the network cluster. This algorithm can easily be extended to non-vertical wells by projecting the coordinates of the three-dimensional hull onto a plane that is perpendicular to the well trajectory.

Results for the volume and horizontal extent for the hypothetical model are shown in Table 5-3.

Table 5-3 Calculation of Volume and Horizontal Extent for Hypothetical Model

Volume (m^3)	156,789
Horizontal Area (m^2)	4369.0
Bounding Box (m^3)	81.0 x 82.4 x 36.1
Hull/Bounding Box	65%

5.5.3 Compartment Size and Shape

Description of compartment size and shape is important for fractured reservoir engineering because it influences how efficiently a pattern of wells produces a reservoir. For example, if a field is drilled on 160-acre spacings, but the compartments are much smaller (Figure 5-28a), then there may be reservoir compartments which are not accessed by the production wells, reducing field recovery. An infill drilling program will access previously untapped compartments, and may be cost-effective, depending upon the ultimate production per well and the marginal cost of the well. On the other hand, if compartments are considerably larger than the well spacing, then infill drilling may not be cost-effective (Figure 5-28b). Likewise, the efficiency of water or steam floods is affected by reservoir compartmentalization.

Shape is also important, since compartments are rarely equant all directions (for example, see Dershowitz et al., 1996b). This anisotropic shape is due to the fact that fractures in reservoirs typically have two or three preferred orientations. If they are of sufficient size and intensity to create regionally connected networks, then they tend to form networks that are elongated in a predictable fashion (La Pointe et al., 1984). Figure 5-28 shows a hypothetical example in which fracture network compartments are elongated northeast-southwest.

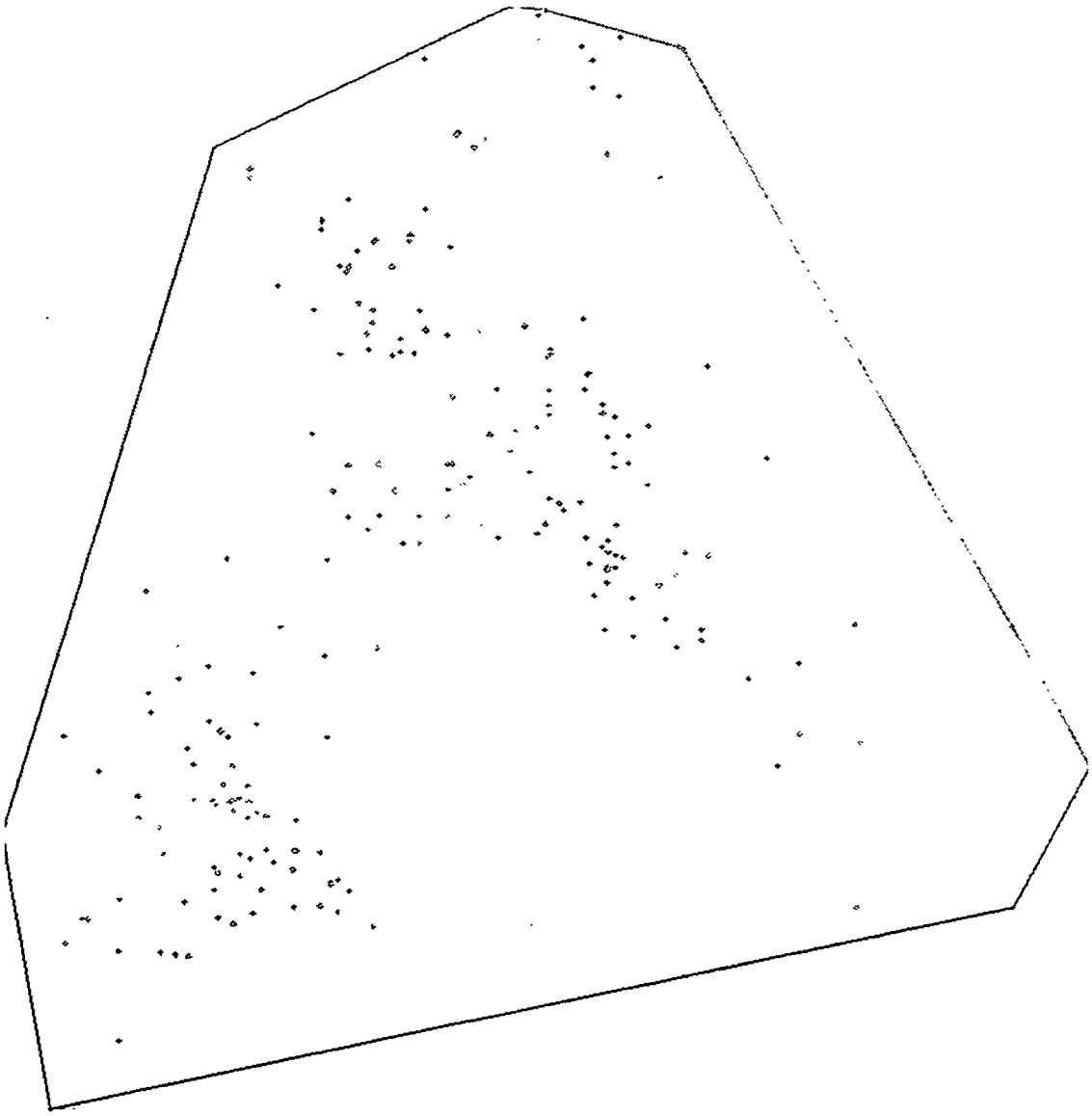

FIGURE **5-27**
HORIZONTAL PLANE PROJECTION OF CONVEX HULL
NIPER/FINAL REPORT/WA

PROJECT NO. 963 1357.521 DRAWING NO. 80780 DATE 9/28/98 DRAWN BY EA

Golder Associates

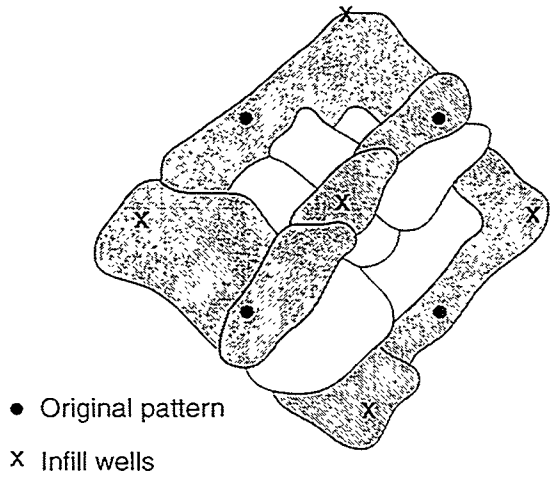

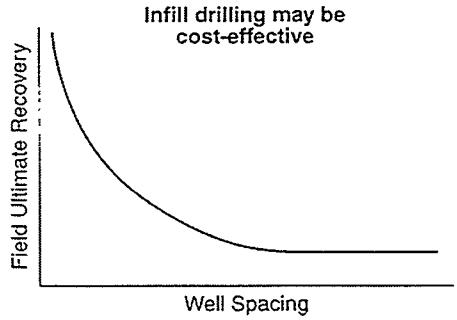

(a) Compartments Smaller than Well Spacing

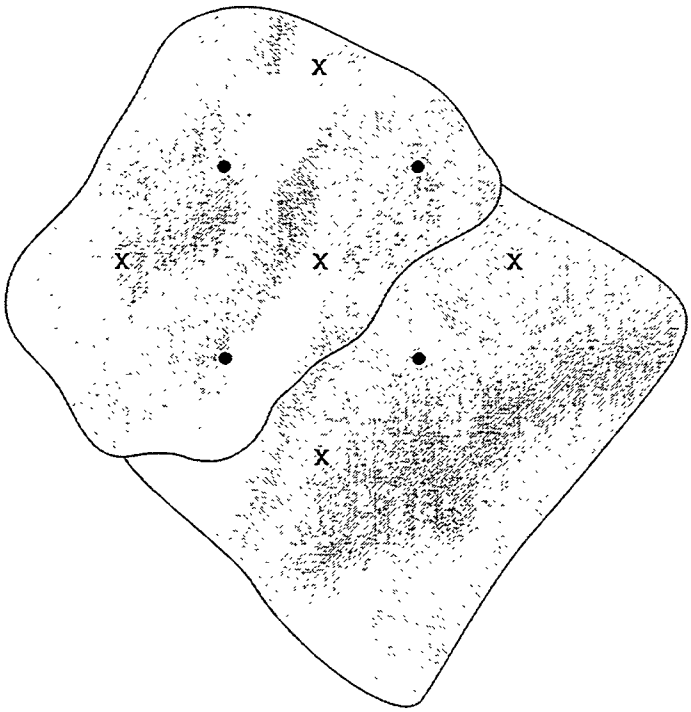

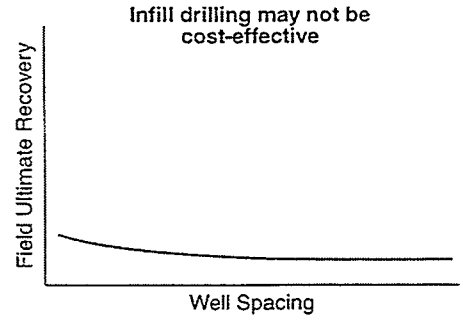

(b) Compartments Larger than Well Spacing

FIGURE **5-28**
IMPORTANCE OF COMPARTMENT SIZE FOR WELL PATTERN OPTIMIZATION
NIPER/FINAL REPORT/WA

Compartment shape and size are described by several different parameters (Figure 5-29):

- compartment volume
- ratio of fracture surface area to matrix volume in each compartment
- compartment cross-sectional area
- compartment cross-sectional shape

Statistics on compartment volume make it possible to estimate what proportion of the reservoir is accessed through the fracture system connected to a specific well pattern. The ratio between fracture surface area and matrix, termed P_{32} (Dershowitz and Herda, 1992), measures how effectively the fractures access the compartment. The higher the ratio, the closer a greater volume of the matrix is to the fracture conduits. In a fractured reservoir with a low-permeability matrix, pressure depletion will mobilize more oil for a higher P_{32}, other parameters being equal.

Compartment cross-sectional area and shape provide information on well pattern efficiency. If the compartment is thought of as the drilling target, then it is beneficial to know the shape and size of that target. Shape is defined by two parameters: aspect ratio and orientation. The aspect ratio is ratio of L_{max} to L_{min}, as shown in Figure 5-29. The minimum and maximum directions need not be orthogonal. The aspect ratio for compartments may be summarized in a rosette diagram like the one shown in Figure 5-29, where aspect ratio is plotted as a function of the orientation of the direction of maximum elongation. The shape is additionally defined by a second rosette which shows the frequency of the direction of maximum elongation as a function of orientation. Together with the area statistics, these three graphs define the compartment cross-sectional shape. The mean area relates to the optimal well spacing. The anisotropy ratio describes whether the wells should be laid out in a square pattern or some other pattern. The elongation frequency rosette indicates what the direction of grid alignment should be.

5.5.4 Verification

Figure 5-30 illustrates a verification case for the compartment size and shape analysis. In this example, a fracture network is defined with a known shape and size based on a hypothetical fracture network. The discrete fracture network model in verification test #1 (Figure 5-30a) consists of 3 elongate fractures with centers at z=1.59, 0, and –1.59 m each with an area of 314 m^2 and an axial ratio of 5:1. These three fractures are linked by 8 small fractures each with an area of 12.6 m^2. The second verification test case (Figure 5-30c) consists of a 25x10x8 m cube filled with 100 fractures each with an area of 28.3 m^2.

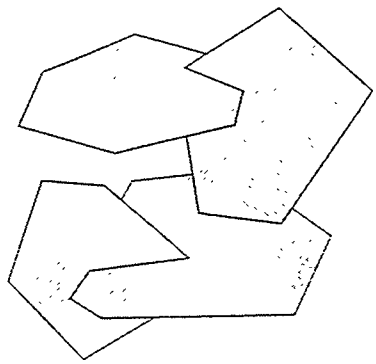

Fracture Network

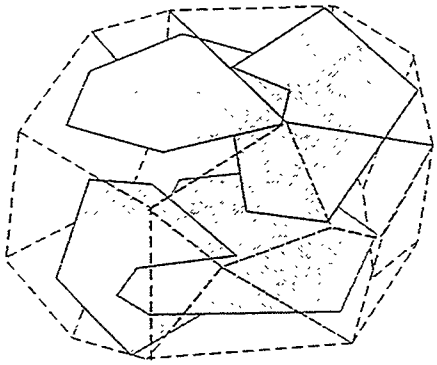

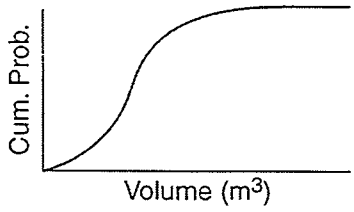

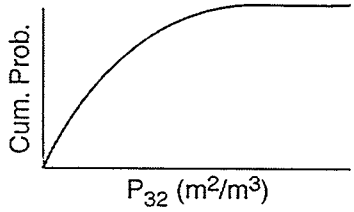

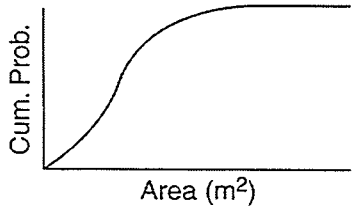

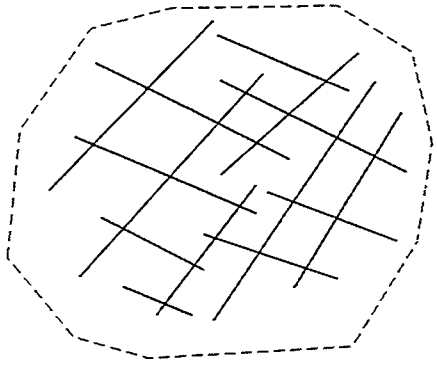

Cross Section of Network

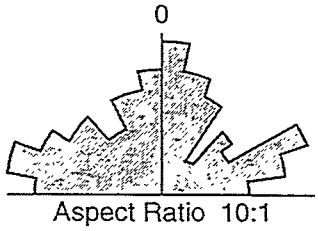

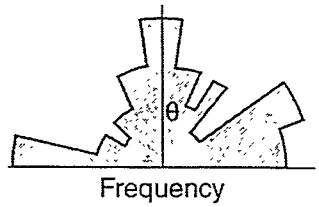

FIGURE **5-29**
COMPARTMENT SHAPE MEASURES
NIPER/FINAL REPORT/WA

PROJECT NO 963 1357.521 DRAWING NO. 80833 DATE 9/29/98 DRAWN BY EA

Golder Associates

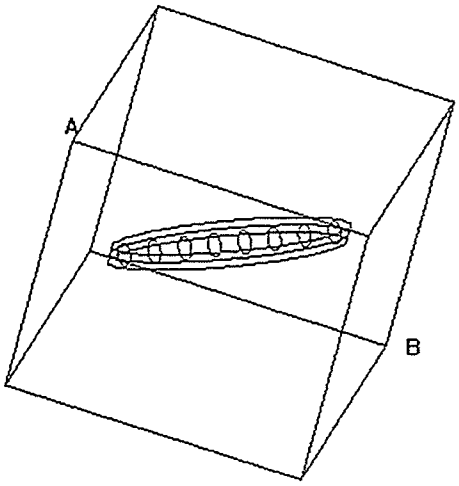

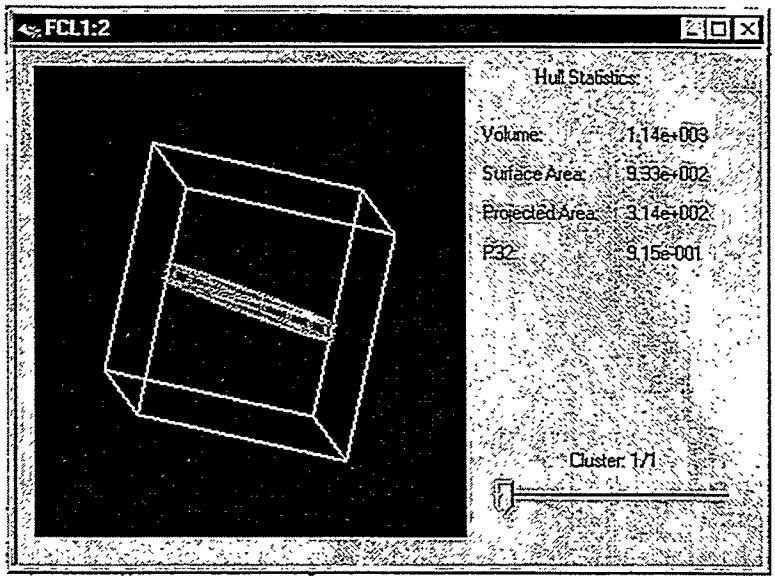

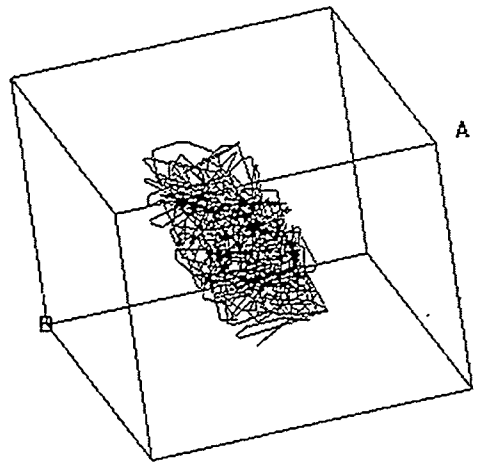

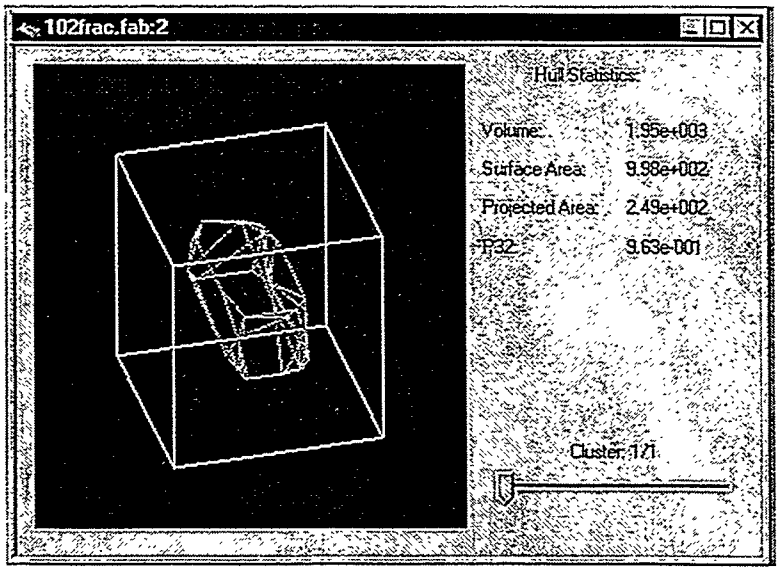

FIGURE **5-30**
FracCluster VERIFICATION
NIPER/FINAL REPORT/WA

Table 5-4 presents a comparison of predicted compartment statistics and the statistics produced by the compartmentalization algorithm of FracCluster.

Table 5-4 Compartmentalization Algorithm Verification

	Compartment 1		Compartment 2	
	Expected Result	Actual Result	Expected Result	Actual Result
Volume (m^3)	314x2x1.59=1000	1140	25x10x8 = 2000	1950
Projected Area (m^2)	314	314	25x10 = 250	249
Surface Area (m^2)	2x314+1.59x115.9 = 996.6	933	250x2+80x2+200x2 = 1060	998
Intensity (P_{32})	(3x314+8x12.6)/1000 = 1.04	0.915	(100x28.3)/2000 = 1.415	0.963

6. TASK 3.1: LINKAGE TO STATIGRAPHIC RESERVOIR MODELS

6.1 Task 3.1.1: Stratagraphic/DFN Model Integration

For discrete feature network models to achieve general acceptance as a valuable tool for reservoir simulation, they must be directly linked to commonly used reservoir stratigraphic models such as GeoFrame, IRAP, GoCAD, and StrataModel. Stratigraphic models use a cell-based approach to define a geographic database of information on reservoir properties, stratigraphy and structure. Faults are often used as boundaries for groups of cells, or as control surfaces for interpolating stratigraphy and lithology. Both large displacement faults and smaller displacement faults can compartmentalize reservoir units There faults influence sweep efficiency, production rates and ultimate recovery.

In this task, the project team developed an approach to link stratigraphic models to discrete feature network models. The prototype linkage between DFN and stratagraphic models has two functions (Figure 6-1):

1. **Discrete Fracture Mapping**: Generate stratigraphic model grid cell values from 3D DFN models by processing fracture intensity, location, and aperture to define fracture porosity, intensity, etc.

2. **Spatial Bootstrapping**: Convert stratigraphic model cellular data into a file format to facilitate direct generation (spatial bootstrapping) of fractures based on stratigraphic model surfaces (e.g., bedding, stratigraphic contacts, faults) and grid cell values (e.g., fracture porosity, stress field, rock type)

6.1.1 Discrete Fracture Mapping

Geo-cellular models such as StrataModel use information on stratigraphy and structure to define the geometry of cells and to assign cell attributes. Faults are often used as boundaries for groups of cells, or as control surfaces for interpolating stratigraphy and lithology. Geo-cellular models frequently incorporate sophisticated algorithms for modeling cells near faults represented as discrete surfaces that die out laterally and vertically.

Geo-cellular model are frequently limited in that they use only deterministic geological interpretations and larger scale features, based on available geophysical data. Thus, for example, a geo-cellular model might contain only the kilometer scale faults identified by geophysics, ignoring smaller faults and discrete features below the resolution of the field characterization efforts.

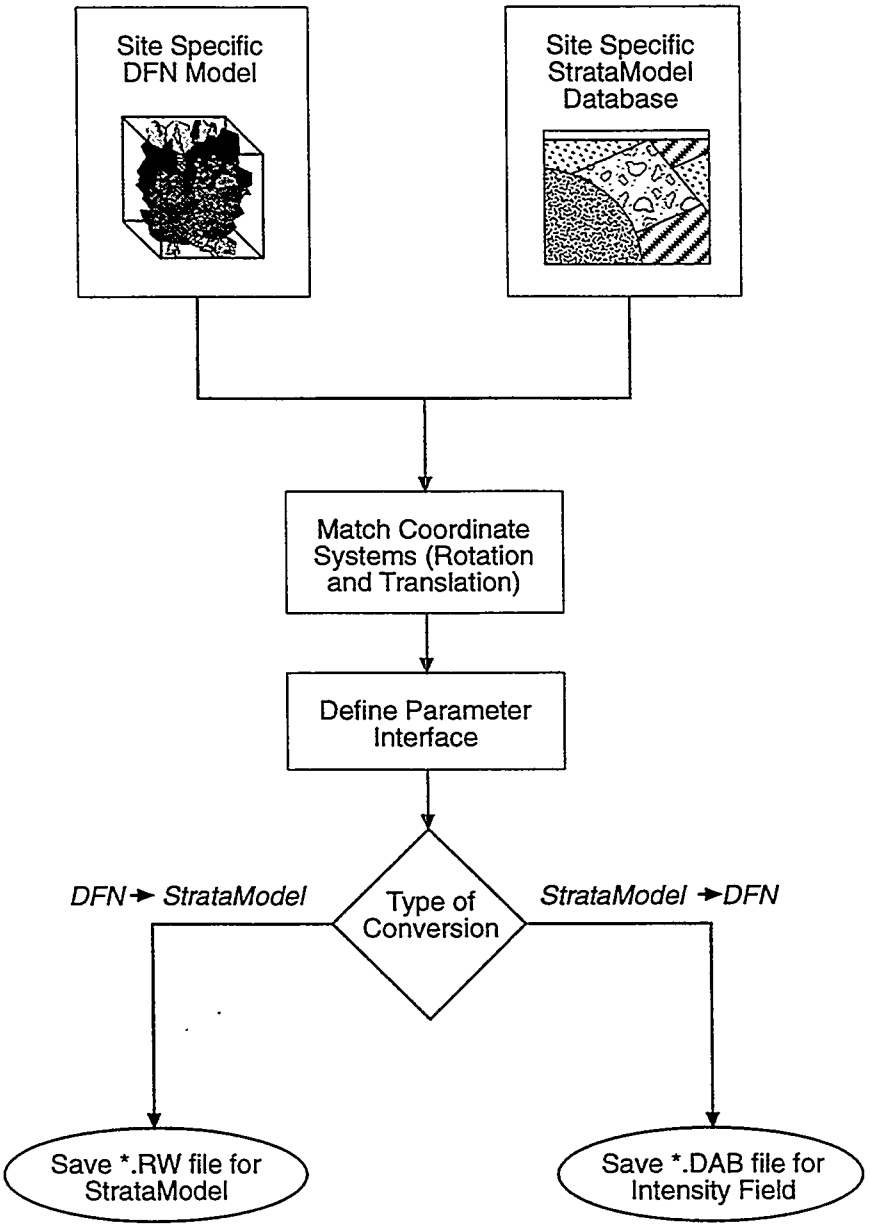

FIGURE **6-1**

LINKING DFN AND GEOCELLULAR FLOW MODELS

NIPER/FINAL REPORT/WA

One of the advantages of discrete feature network modeling is that it provides for generation and specification of discrete features at a full range of scales, including both know (deterministic) and unknown (stochastic or conditioned) features. Discrete fracture mapping was developed as an approach to enhance geo-cellular models using discrete features generated using the DFN approach. The result is a Geo-cellular model that combines basic geological, geophysical, hydraulic, and petrophysical information with cell properties derived by the DFN approach.

For example, DFN models can be used to generate faults using a conditioned deterministic/stochastic approach in which known large displacement faults are combined with stochastically realized smaller displacement faults (Dershowitz and La Pointe, 1995). As an example of conditioning, consider a site where field measurements indicate that a particular set of faults has a statistical distribution of sizes, described by a lognormal distribution with mean 90,000 m^2 and a standard deviation of 50,000 m^2.

Conditional simulation starts with a stochastic DFN realization of this fault population (Figure 6-2). Figure 6-3 illustrates the simulated trace map generated by a horizontal section through this DFN. This can represent either a vertical seismic section or a top of reservoir structure map. These fault traces can then be censored to remove trace lengths less than the smallest one mapped. The remaining traces can then be compared against the actual fault trace length distribution. The mean and standard deviation are adjusted using a grid search until the truncated synthetic trace length distribution approximately matches the observed. In this method, it is assumed that the truncated traces correspond to fractures either lying outside of the seismic grid, or are small enough that they were not intersected by seismic profiles. Thus, it is possible to generate stochastic realizations of the faults using these size parameters. The faults above the truncation threshold are removed and replaced by the actual faults detected through seismic. The faults below the truncation threshold are retained.

Thus, it is possible to generate a better reservoir model than one containing only the faults directly detected by the seismic grid. These stochastic faults are put into the StrataModel reservoir model in the same way that the seismically-detected faults are incorporated. If desired, several stochastic StrataModel realizations can be generated using this procedure, and used to form the basis of reservoir models that more accurately capture faulting in the reservoir and also account for uncertainty in faulting not detected through seismic.

6.1.1.1 Implementation

The algorithm implemented for discrete fracture mapping takes an existing stochastic or conditioned discrete feature network model, and derives cell properties on a pre-defined geo-cellular model grid is as follows (Figure 6-4).

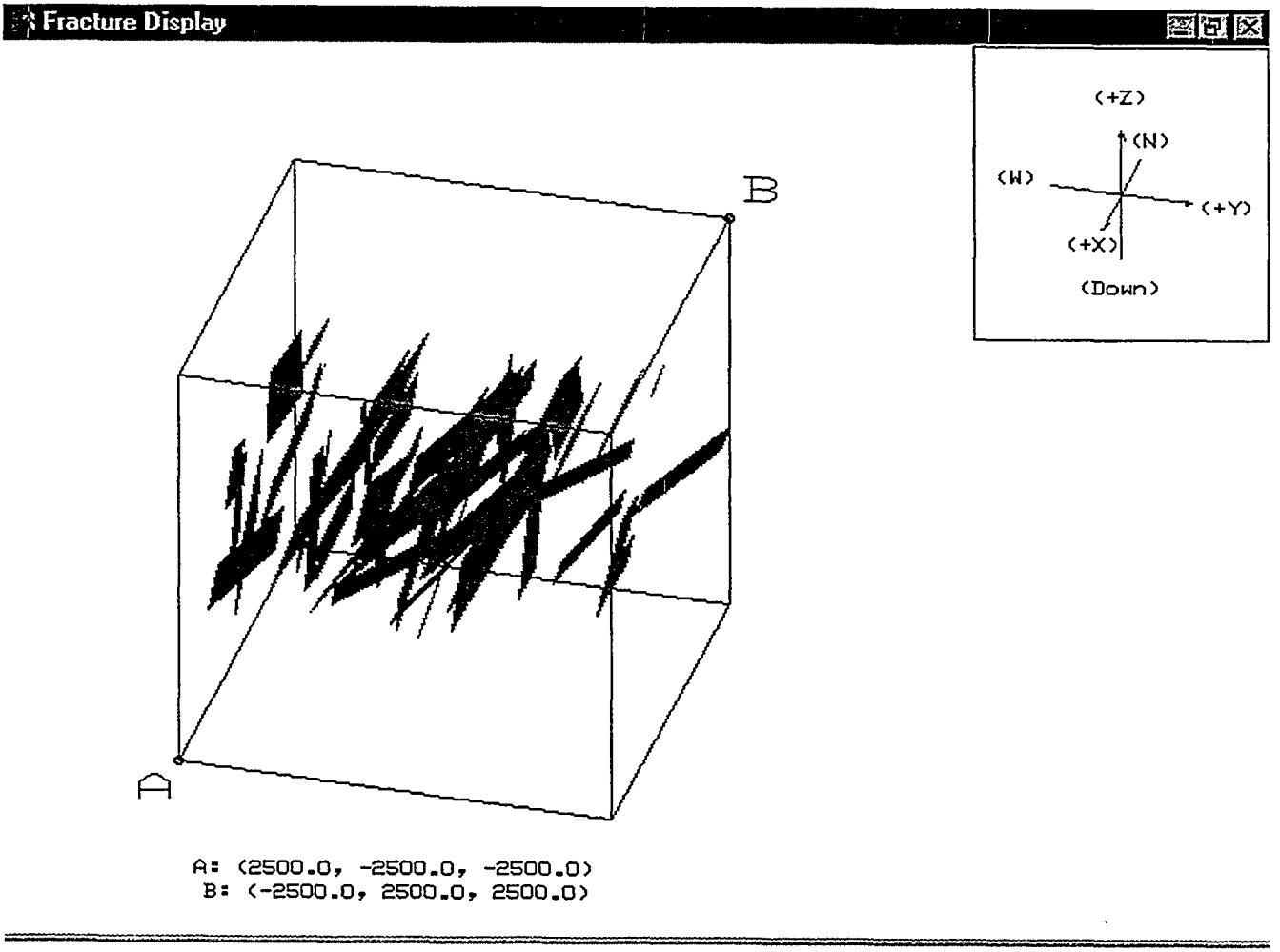

FIGURE **6-2**
EXAMPLE DFN MODEL FOR STRATA MODEL LINKING
NIPER/FINAL REPORT/WA

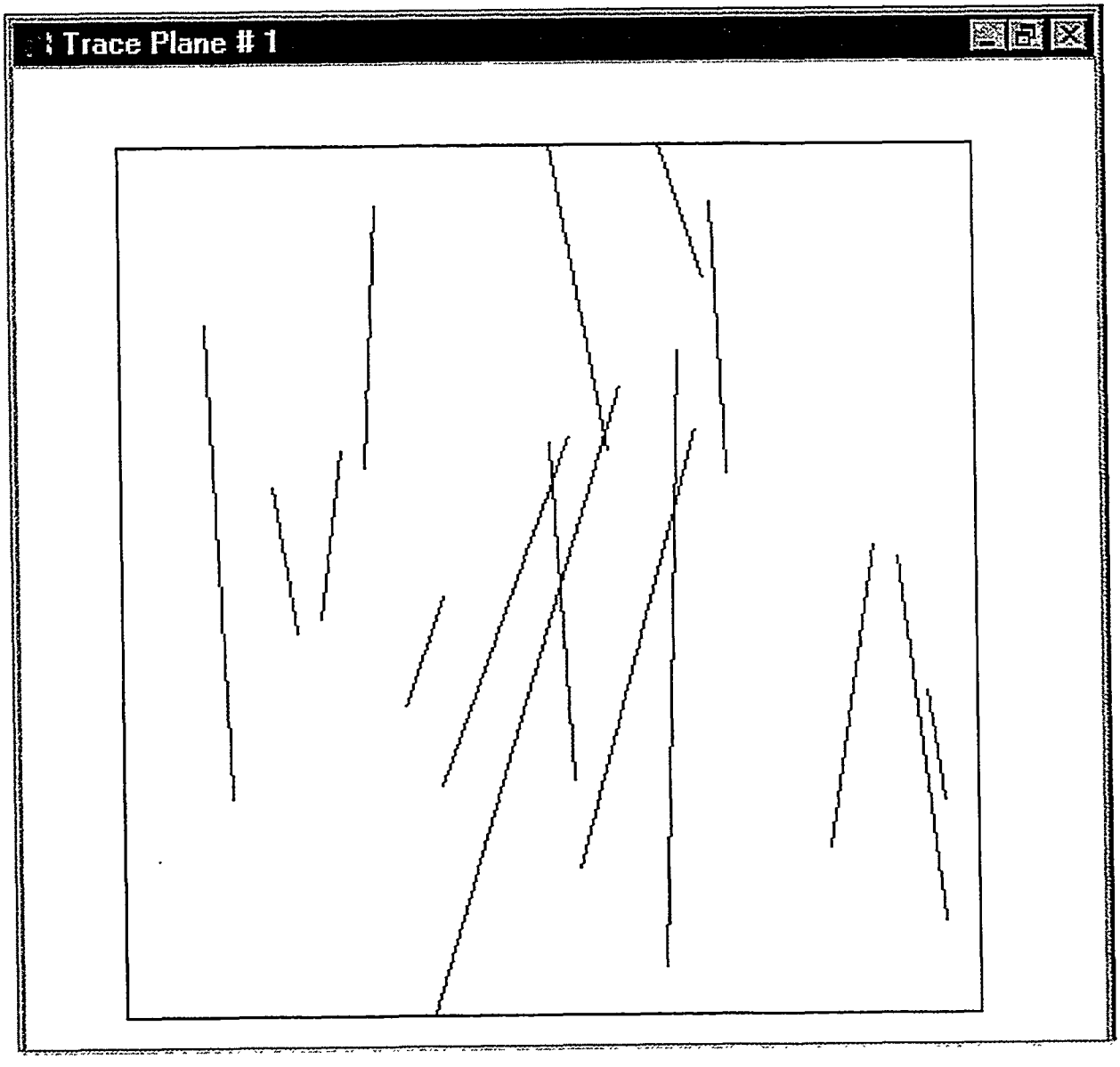

FIGURE **6-3**
SIMULATED HORIZONTAL SECTION
NIPER/FINAL REPORT/WA

PROJECT NO. 963 1357.521 DRAWING NO. 80756 DATE 9/28/98 DRAWN BY EA

Golder Associates

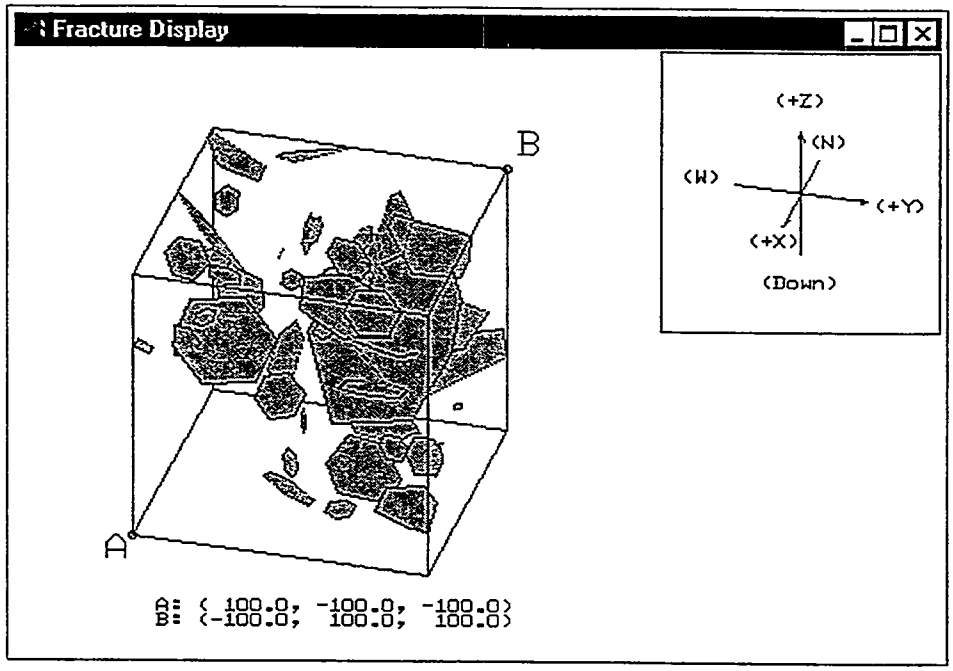

A. Discrete Feature Network

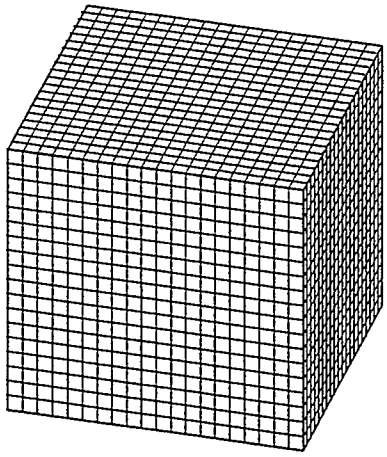

B. Gridded Data

StrataModel

X Coor	Y Coor	elev	Depth	FRAC	NFRAC	P_{21}
2640	39600	-1961	5144	0	0	0
2640	39600	-1962	5145	1	2	0.14
2640	39600	-1963	5146	1	7	1.28

C. StrataModel

FIGURE **6-4**

GRIDDING FOR DFN TO GEOCELLULAR MODEL LINKING

NIPER/FINAL REPORT/WA

1. Implement the discrete fracture network, specifying the geometry and properties of discrete features throughout the region of interest (Figure 6-4a)

2. Specify StrataModel grid for which properties are to be derived from the DFN model (Figure 6-4b)

3. Grid the fracture data using the algorithms for Fractal 1.0 (Figure 6-5a). The selection of a gridding approach depends on the application. Use either :

   a) (0,1) based on whether the grid contains a fracture,

   b) n, the number of features in the cell

   c) Properties such as intensity P_{33} (fracture porosity), P_{32} (fracture area per unit volume), or P_{10} (fractures per grid cell)in the grid cell

   d) Grid cell hydraulic properties based on DFN analysis (Figure 6-6)

4. Format the gridded data for StrataModel (Figure 6-4c).

This is implemented using a simple loop, which visits every fracture in the DFN to build a list of grid cells possibly containing any portion of a fracture. Once this list is built, another loop is made over the cells containing fractures, computing the area and volume of overlap of the fracture within each cell. Once all "possible" cells in the neighborhood of the fracture have been investigated, the next fracture is processed.

Once this processing is done, the filled Stratagrid is serialized to disk to user specifications in a format suitable for the geo-cellular model. Information reported includes; cell number, cell position (center), intensity P_{32} and porosity.

6.1.2 Spatial Bootstrapping

Geo-cellular models such as StrataModel represent complex three-dimensional geology using a cellular data structure. The cellular data structure is often used as a system for building input for reservoir simulators, as well as a reservoir or basin visualization tool. The advantage of a geo-cellular model is that it conditions the properties of each cell to complex internal stratigraphic and structural reservoir architecture, and makes it possible to guide the distribution of reservoir data throughout the model.

One of the primary attractions of the discrete feature network modeling approach is the ability to accurately model geology. However, for many complex fractured reservoirs, this is only possible if one takes into account the type of detailed geologic information that is typically stored in geo-cellular models. Discrete fracture network model can be derived from geo-cellular models using techniques such as "spatial bootstrapping" (LaPointe, 1992). In spatial bootstrapping, fracture properties at every location are linked to the geo-cellular database. For example (Figure 6-6):

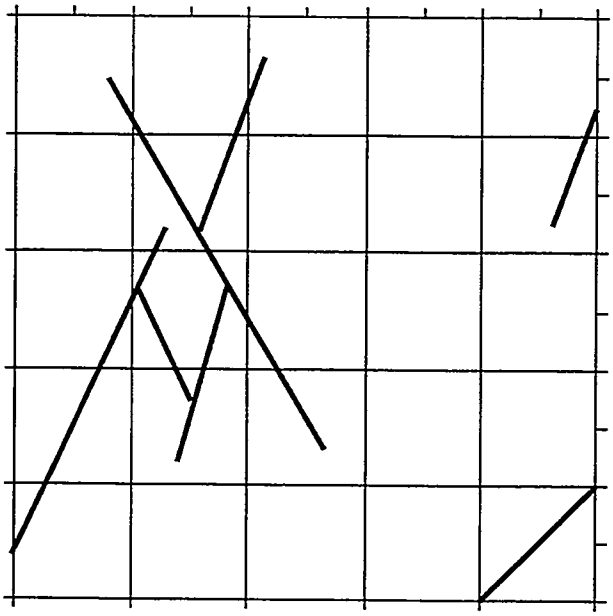

A. DFN Input

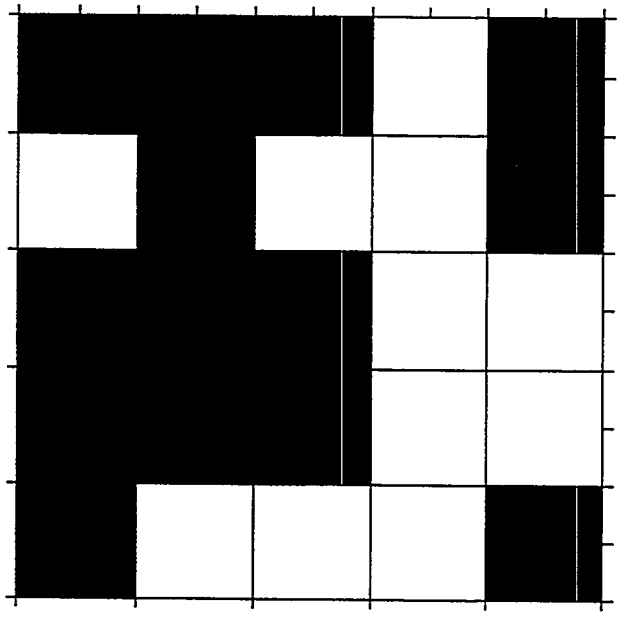

B. Fractured or Unfractured

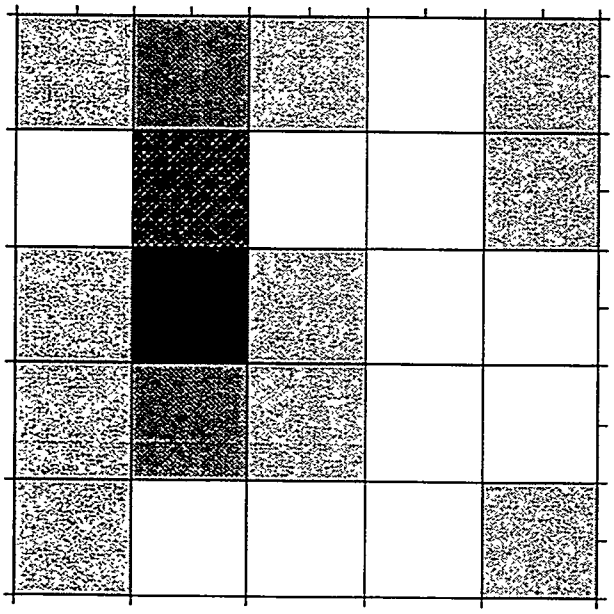

C. Number of Fractures

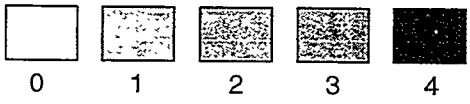

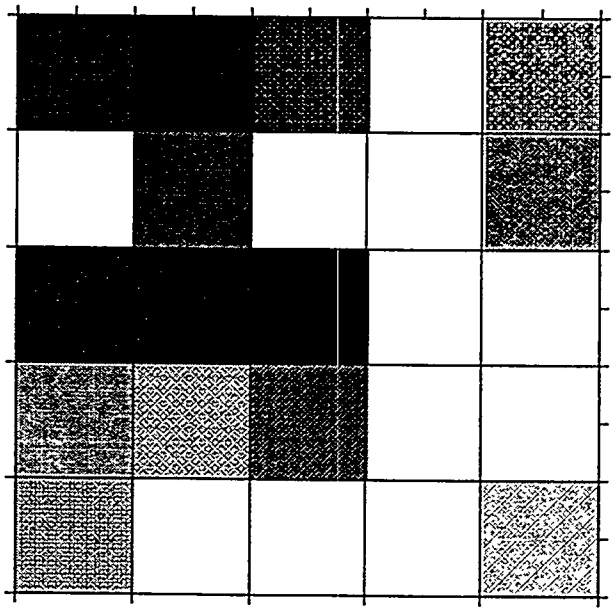

D. Intensity, P21

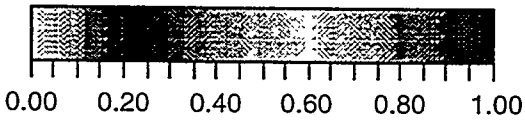

FIGURE **6-5**
GRIDDING ALGORITHMS
NIPER/FINAL REPORT/WA

PROJECT NO. 963 1357.521 DRAWING NO. 80796 DATE 9/28/98 DRAWN BY EA

Golder Associates

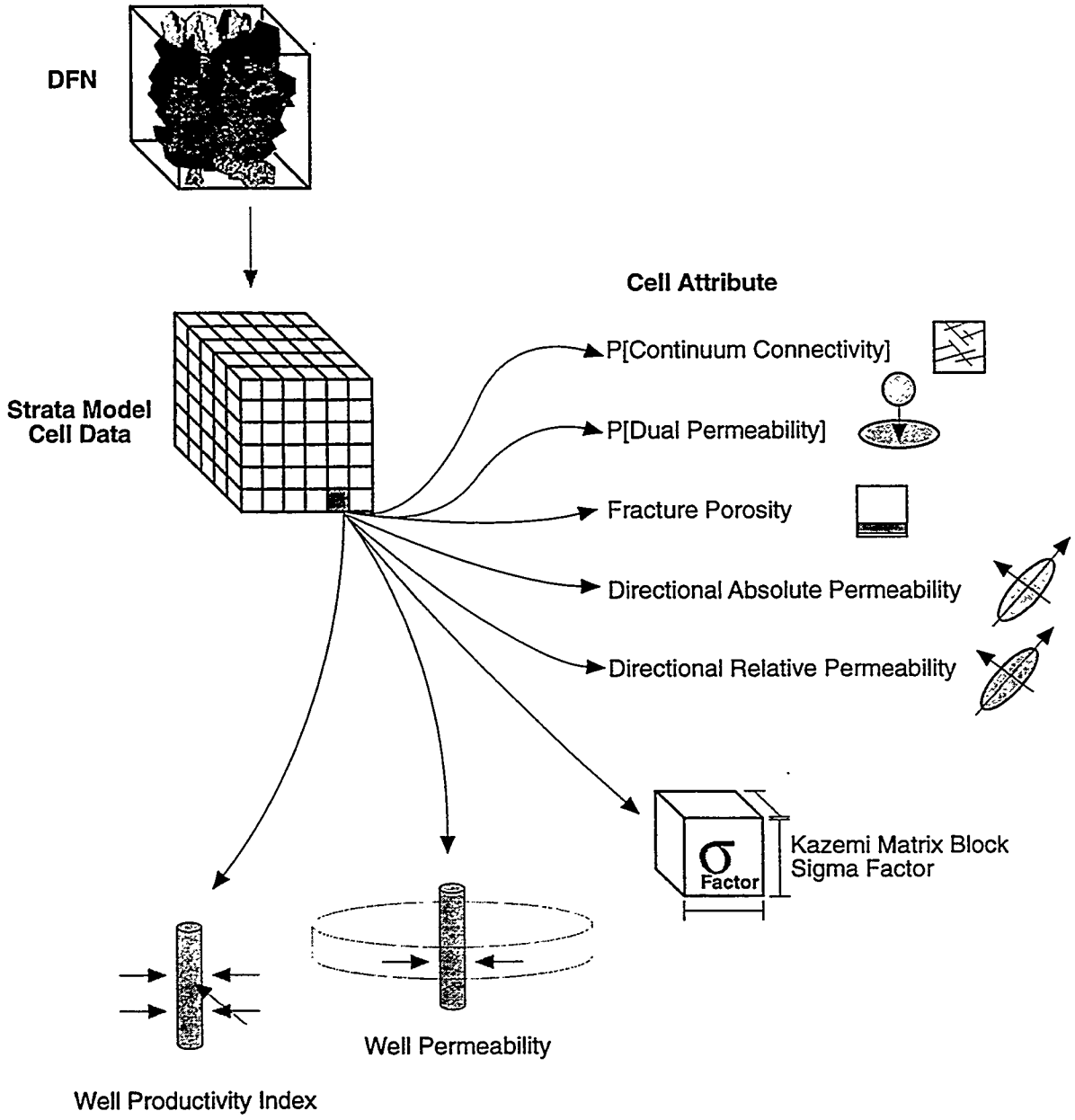

FIGURE **6-6**
STRATA MODEL ↔ DFN LINKING
NIPER/FINAL REPORT/WA

PROJECT NO. 963 1357.521 DRAWING NO. 80757 DATE 9/28/98 DRAWN BY EA

Golder Associates

- fracture intensity P_{32} can be derived based on geo-cellular porosity data,
- mean fracture size R can be derived from geo-cellular stratigraphic information
- mean fracture transmissivity T can be derived from geo-cellular permeability information
- local fracture orientation distribution parameters can be derived from geo-cellular surface orientations

6.1.2.1 Implementation

The process of spatial bootstrapping from geo-cellular data to DFN model parameters is as follows (Figure 6-7):

1. Specify the spatial domain in the DFN model for which geo-cellular data will provide the basis for discrete feature generation
2. Specify the relationship between grid cell parameters and DFN model parameters
3. Specify the relationship between DFN model and geo-cellular model coordinate systems
4. Transform geo-cellular grid cell data to data formats suitable for spatial bootstrapping
5. Generate DFN models by spatial bootstrapping from the transformed geo-cellular data files.

The spatial bootstrap approach requires defining of a mapping from the original geo-cellular coordinate system to DFN coordinate system. Mapping is defined by two parameters: transformation matrix and shift vector. These parameters are calculated based on the following data:

- DFN coordinate system origin
- Trends and plunges of x, y, z directions of DFN coordinate system
- Units of measurement along each coordinate axis in DFN and in geo-cellular systems.

Then a cellular grid in DFN coordinate system is to be constructed. It is possible to achieve it in a few different ways. The user may specify grid coordinate arrays along each of DFN coordinate axis or the user may specify rectangular region in original coordinate system. In the last case the program sets dimensions of the grid in the DFN coordinate system in such a way that the original grid was completely inscribed into the new grid.

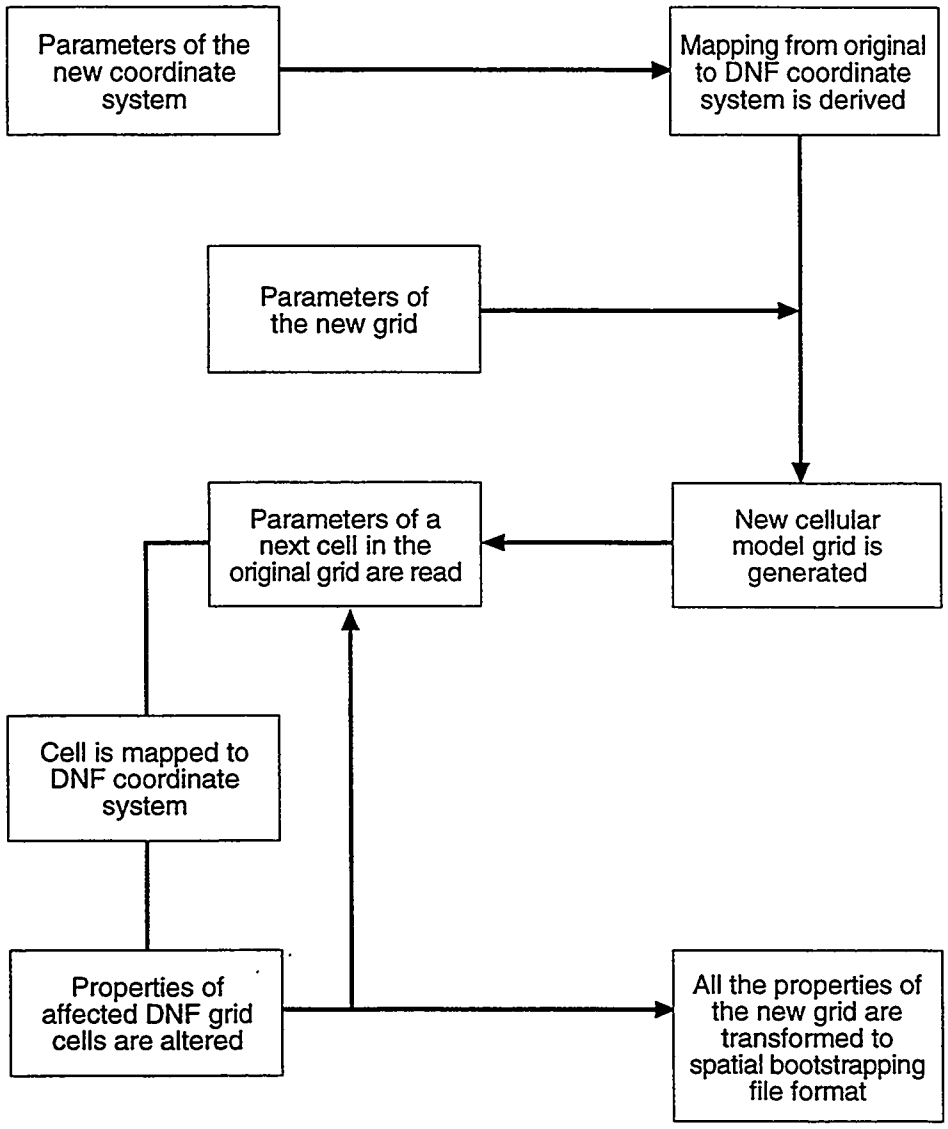

FIGURE **6-7**
SPATIAL BOOTSTRAP INTERFACE ALGORITHM
NIPER/FINAL REPORT/WA

PROJECT NO. 963 1357.521 DRAWING NO. 80266 DATE 9/28/98 DRAWN BY TK

Golder Associates

After the mapping is calculated and the new grid computed the next step is to construct geo-cellular model in the format suitable for spatial bootstrapping . This is done in a few steps:

1. Cells of original grid are mapped to the new grid one by one (Figure 6-8)
2. All the cells of the new grid having intersection with the mapped cell are identified
3. For each such a cell its properties are altered.

It is assumed that all the geo-cellular grid cell properties that are used to characterize fracture properties are described by "weighted average" model. Then the formula for recalculation of geo-cellular model properties is:

$$\mathrm{Pr}operty(new\_cell) = \sum_{old\_cells} \mathrm{Pr}operty(old\_cell) * \frac{Volume(intersection\_of\_new\_and\_old\_cell)}{Volume(new\_cell)}$$

This algorithm is illustrated in Figure 6-9.

The final stage of the program is to transform the data obtained to bootstrapping file format.

6.2 Task 3.1.2: Verification

This section presents example applications of the linkage between geo-cellular (StrataModel) data and discrete feature network models.

6.2.1.1 Discrete Fracture Mapping

Figure 6-10 shows a heterogeneous, 2000' x 2000' x 2000' discrete fracture network (DFN) model. The parameters used to generate this DFN model are provided in Table 6-1. Figures 6-11 and 6-12 provide views of vertical and horizontal cross-sections through the StrataModel interpretation of this DFN, using algorithms (a) through (c).

mapped_cell = Transf_Matrix * (cell - Shift_Vector)

Where:

- "cell" denotes a cell in the original coordinate system
- "mapped_cell" denotes the same cell in the DFN coordinate system
- Shift_Vector is the vector of coordinates of the DFN system origin in the original geo-cellular model coordinate system.
- Transf_Matrix = Scale_Matrix2 * Rotation_Matrix * Scale_Matrix1

  Rotation_Matrix is the orthogonal matrix of rotation from the original to the new coordinate system

  Scale_Matrix1 is a diagonal matrix. It transforms the coordinates of a point in the original coordinate system to the same units of measurement along all coordinate axis.

  Scale_Matrix2 is a diagonal matrix. It transforms coordinates of a point to the units of measurement required in the DFN coordinate system.

FIGURE **6-8**
TRANSFORMATION BETWEEN COORDINATE SYSTEMS
NIPER/FINAL REPORT/WA

PROJECT NO. 963 1357.521 DRAWING NO. 80274 DATE 9/28/98 DRAWN BY TK

Golder Associates

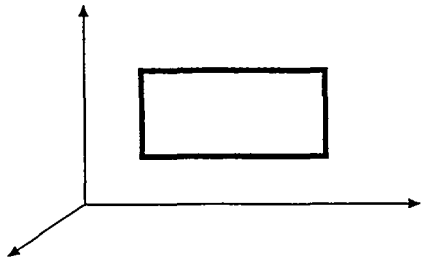

Grid cell in the original coordinate system

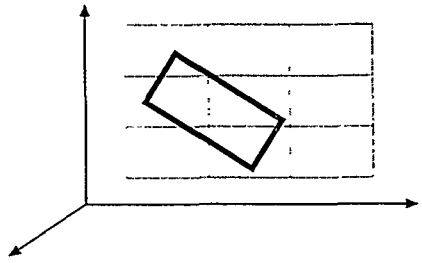

The same cell mapped to the new grid in DFN coordinate system

Formula for property recalculation is derived on example of porosity

$$\text{Porosity (new\_cell)} = \frac{\text{Fracture Volume (cell\_new)}}{\text{Volume (cell\_new)}} =$$

$$= \left(\sum_{\text{cell\_old}} \text{Fracture Volume (cell\_new} \cap \text{cell\_old)/Volume (cell\_new)} \right)$$

$$= \sum_{\text{cell\_old}} \left(\text{Fracture Volume (cell\_old)} \bullet \frac{\text{Volume (cell\_new} \cap \text{cell\_old)}}{\text{Volume (cell\_old)}} \right) / \text{Volume cell\_new} =$$

$$= \sum_{\text{cell\_old}} \frac{\text{Fracture Volume (cell\_old)}}{\text{Volume (cell\_old)}} \bullet \frac{\text{Volume (cell\_new} \cap \text{cell\_old)}}{\text{Volume (cell\_new)}} =$$

$$= \sum_{\text{cell\_old}} \text{Porosity (cell\_old)} \bullet \frac{\text{Volume (cell\_new} \cap \text{cell\_old)}}{\text{Volume (cell\_new)}}$$

Comments:
- cell_old: a cell from original grid
- cell_new: a cell from new grid
- sign "∩" means intersection

FIGURE **6-9**
CELL PROPERTY CALCULATION
NIPER/FINAL REPORT/WA

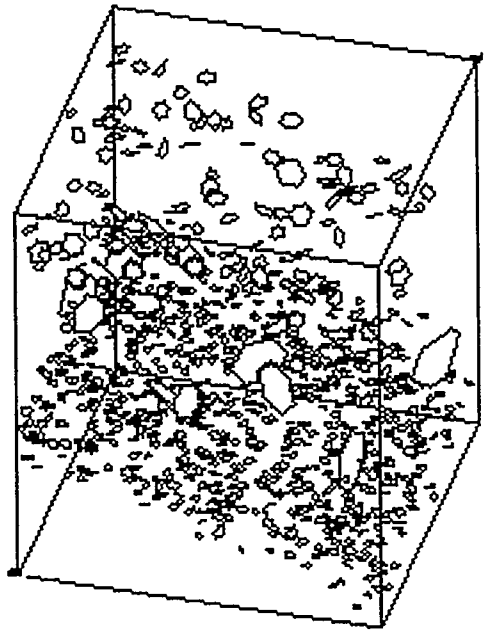

3% Fracs displayed

(A.) 3D view of DFN

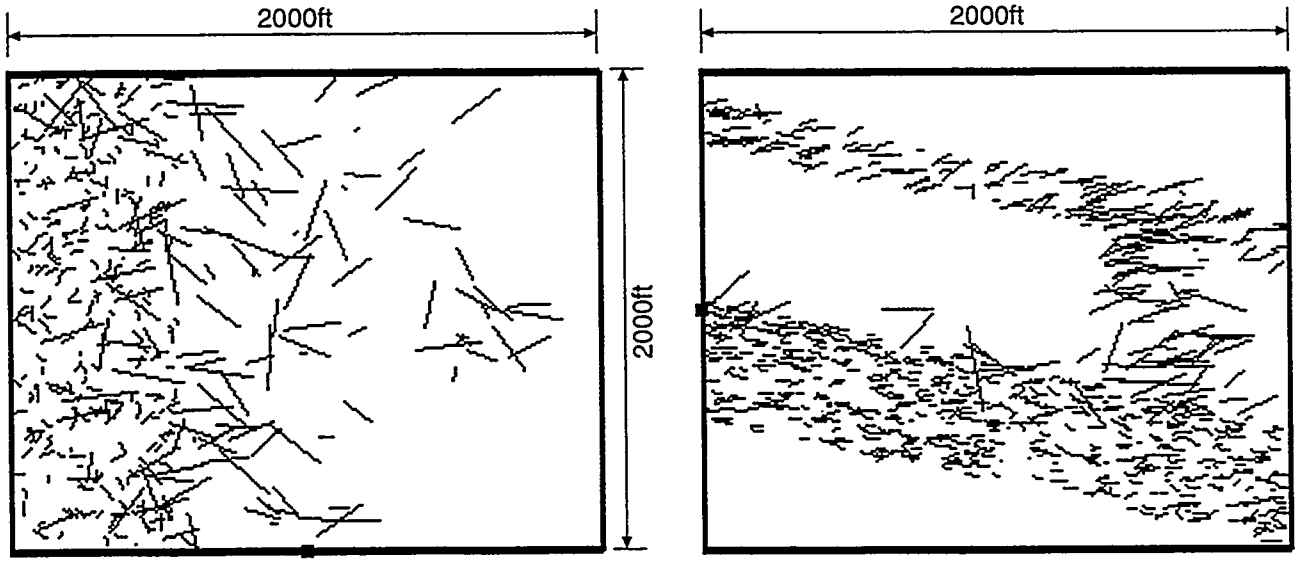

(B.) Trace map of DFN

(C.) Vertical cross section of DFN

FIGURE **6-10**
DFN TO STRATAMODEL DEMONSTRATION CASE
NIPER/FINAL REPORT/W

PROJECT NO. 963 1357.521 DRAWING NO. 80762 DATE 9/28/98 DRAWN BY EA

Golder Associates

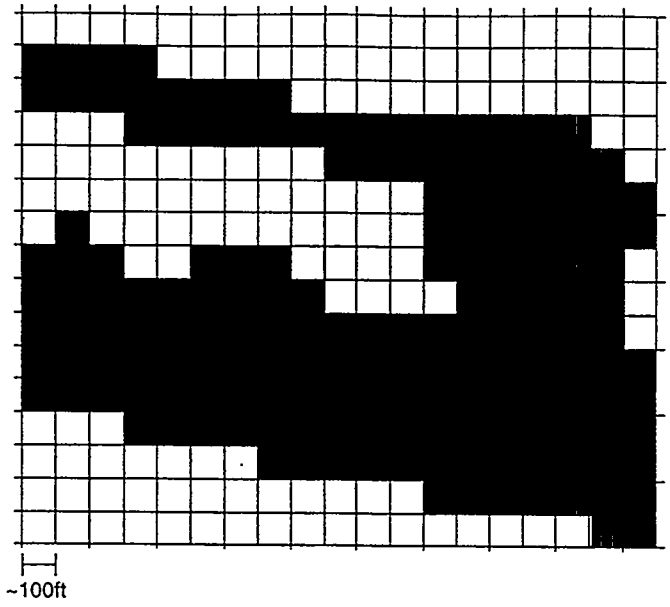

(A.) Fractured blocks

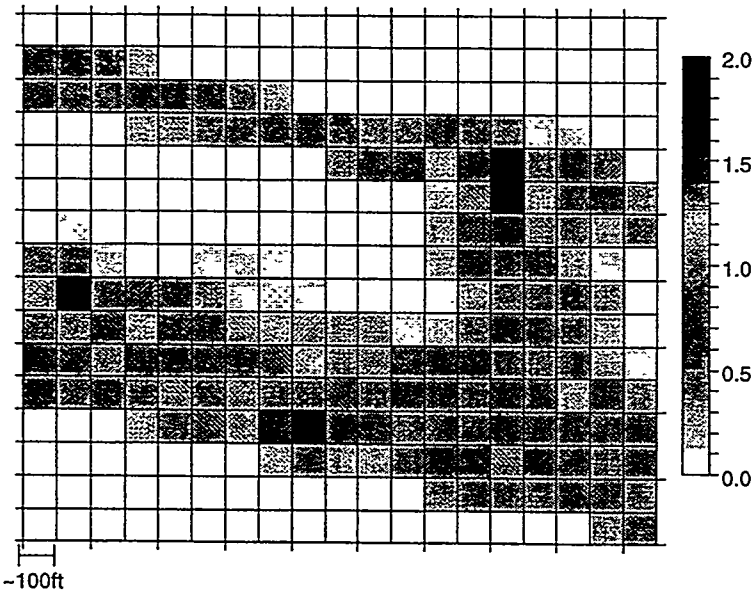

(B.) Number of fractures

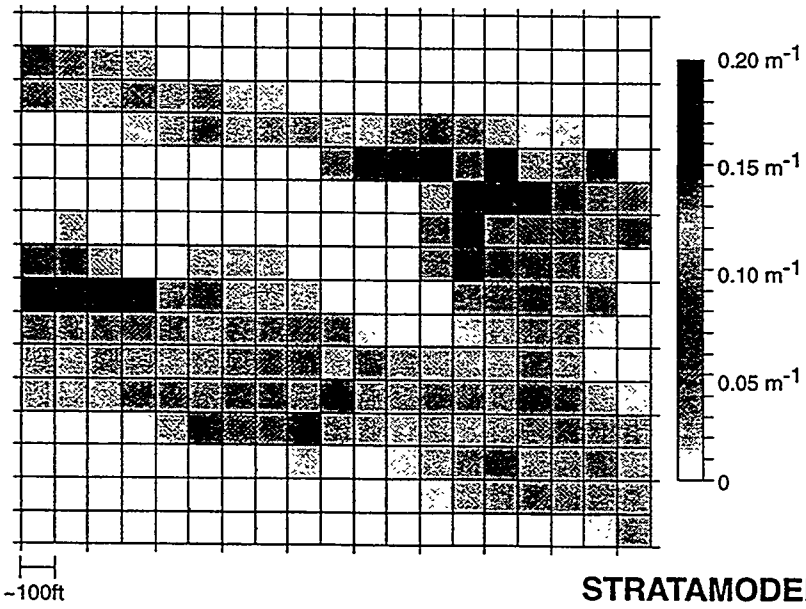

(C.) Fracture intensity, P_{21}

FIGURE **6-11**

STRATAMODEL VERTICAL CROSS-SECTION FOR DFN DEMONSTRATION CASE

NIPER/FINAL REPORT/WA

PROJECT NO. 963 1357.521 DRAWING NO. 80763 DATE 9/28/98 DRAWN BY EA

Golder Associates

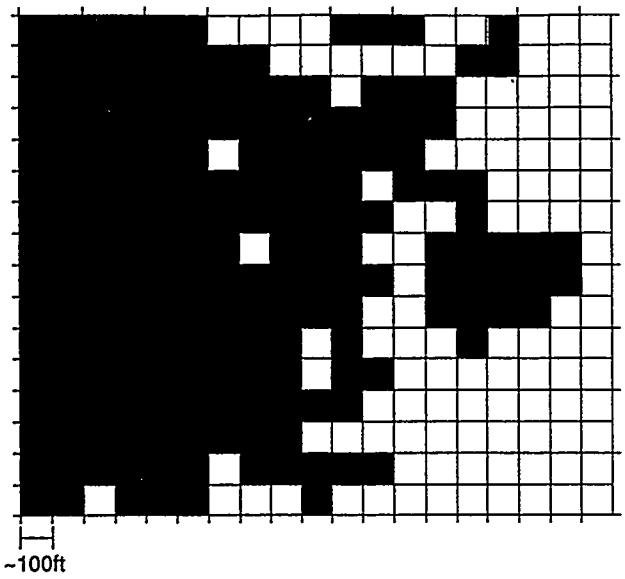

(A.) Fractured blocks

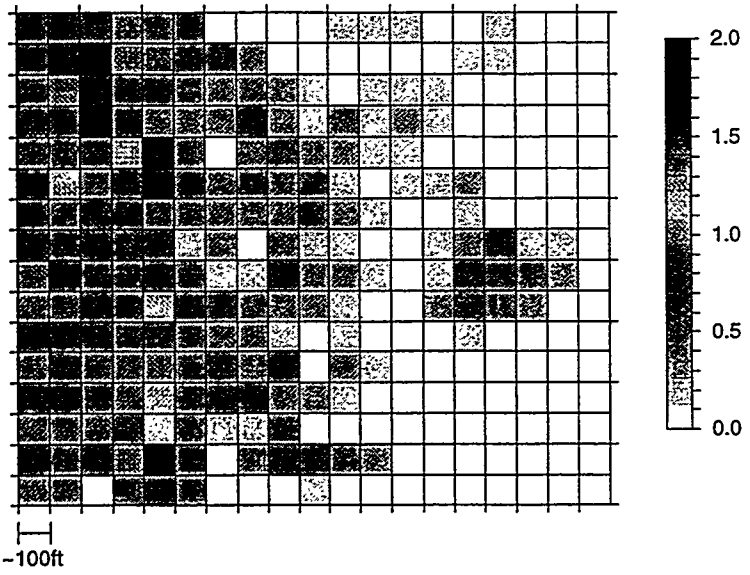

(B.) Number of fractures

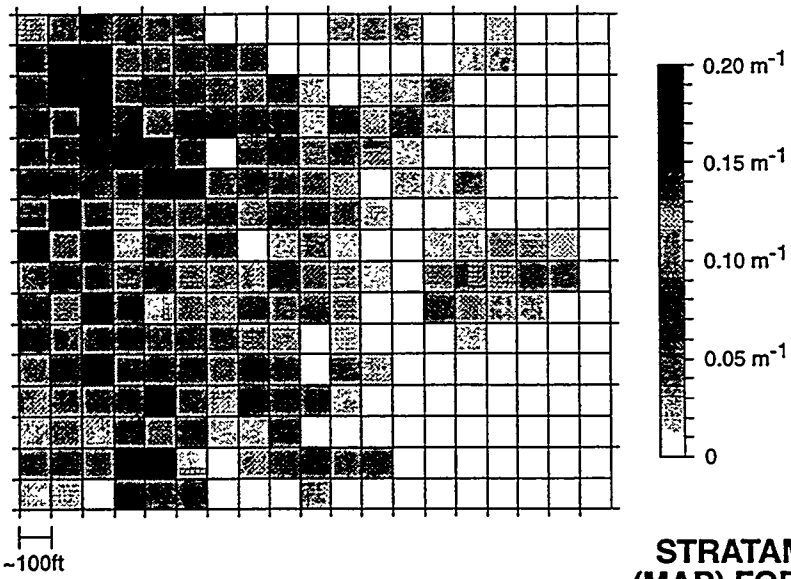

(C.) Fracture intensity

FIGURE **6-12**

STRATAMODEL HORIZONTAL SECTION (MAP) FOR DFN DEMONSTRATION CASE

NIPER/FINAL REPORT/WA

PROJECT NO. 963 1357.521 DRAWING NO. 80764 DATE 9/28/98 DRAWN BY EA

Golder Associates

Table 6-1 DFN Model Parameters

Set #	Initial Point of Feature	Strike, Dip of feature	Region Size	Mean Orient.	Orient. Model	Mean size (ft)	St. dev (ft)	Intensity P_{32} (ft^{-1})
1 slab	(0,-1000, 800)	0,15 E	2000 x 2000 x 200	270,75	Biv. Bing. $K_1=K_2=20$	40	10	0.03
2 slab	(0,-1000,100)	0,15 E	2000 x 2000 x 300	0,0	Fisher K=1	100	25	0.01
3 slab	(0,-200,800)	0,15 E	2000 x 2000 x 500	270,85	Fisher K=10	20	5	0.02
4 cylinder	(100, 500, 500)		r=2000 l=1000	45,75	Fisher K=10	75	25	0.02

6.2.1.2 Spatial Bootstrapping

Spatial bootstrapping test cases were defined using data from the StrataModel geocellular file for the project study site Tract 17 at a depth of 7500 *vara*. The test cases use rectangular grid (6 cells in x and y directions, 1 cell in z direction). Each individual cell is 10 by 10 by 1 *vara*. A *vara* is a Spanish land-grant unit: 1 *vara* = 2.777115 ft = 0.846 m. All the cells in the same row have the same property value and the value is increasing in positive y-direction. The test cases are illustrated in Figures 6-13 and 6-14.

The geo-cellular data used for the test contained data on approximately 7000 cells which were collected from the rectangular region of size (106450, 110550)*(112350, 114850)*(750,780). All the cells have the same size in x and y direction (100*100 meters) and the sizes of the cells in z-direction vary from 0.2 to 4.9 *vara*. Table 6-2 contains part of the original StrataModel file.

The parameters of the new grid were chosen as follows:

- the coordinate system was move approximately to the center of the region - to the point (108500, 113500, 765)
- the sizes on the cells in the new coordinate system were chosen to be 100*100*4.
- the point (106400 , 112300, 753) was chosen as the "lowest" corner of the new grid.
- the number of cells in x direction was set to 41, in y direction to 25, in z-direction to 6.

Figure 6-15 contains a fragment of the spatial bootstrapping file obtained.

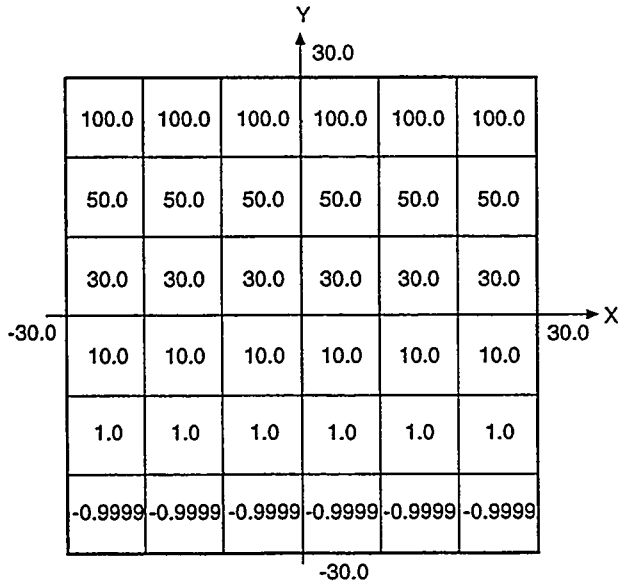

Original geo-cellular grid (property values are indicated inside the cells)

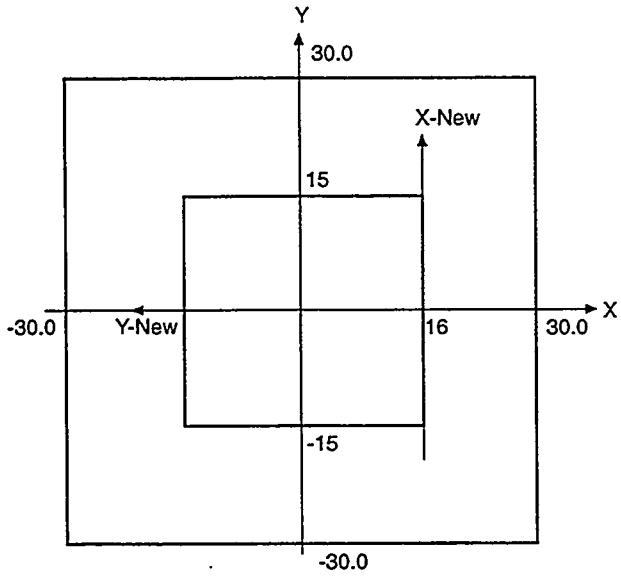

Location of the new grid in the original coordinate system

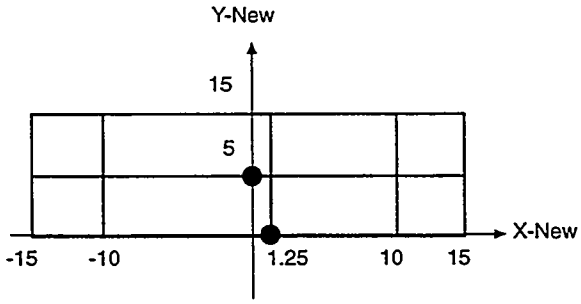

Dimension of the new grid

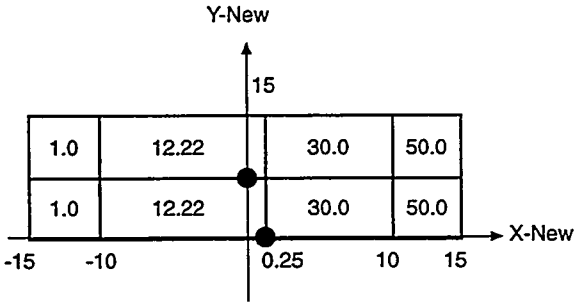

Parameter values for DFN model

FIGURE **6-13**
SPATIAL BOOTSTRAP VERIFICATION CASE 1
NIPER/FINAL REPORT/WA

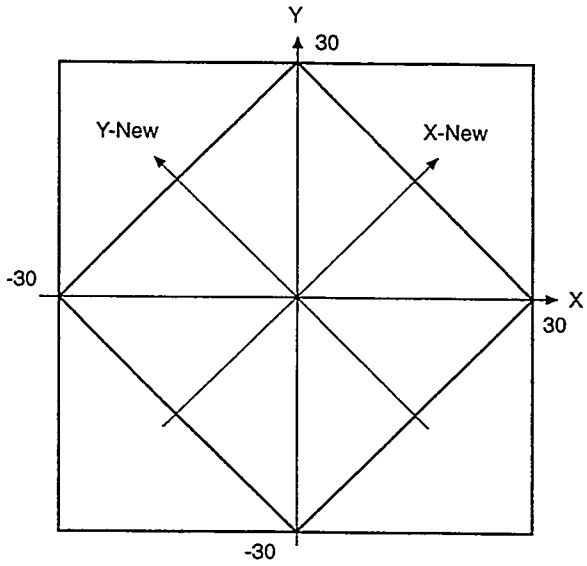

Location of the new grid in the original coordinate system

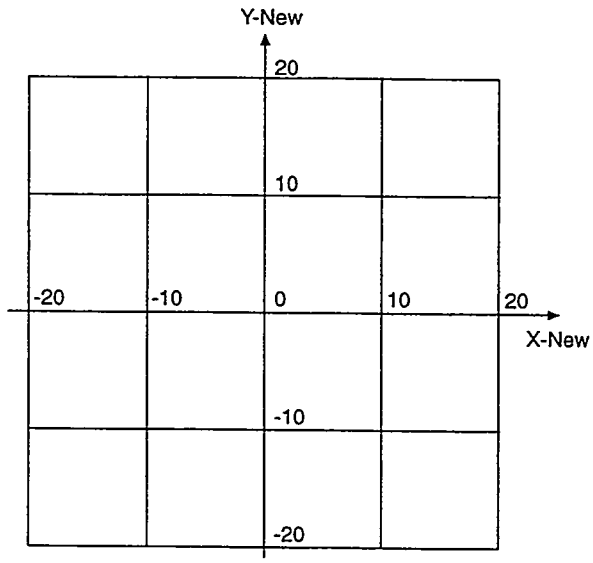

Dimension of the new grid

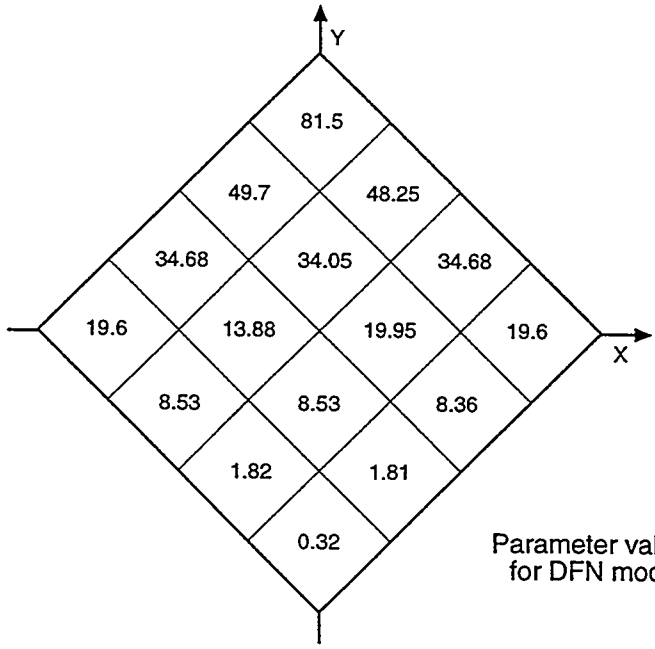

Parameter values for DFN model

FIGURE **6-14**
SPATIAL BOOTSTRAP VERIFICATION CASE 2
NIPER/FINAL REPORT/WA

```
# bootstrapping region created from tract17.rw data file

bootstrap_property_names = Porosity  GammaRay_log_value


BEGIN bootstrap_region
name  = sbsGrid
df_sys = gbl

nodes
#     name        csys              x              y              z
    n0_0_0           D   -2000.000000   -1200.000000     -12.000000
    n0_0_1          DF   -2000.000000   -1200.000000      -8.000000
    n0_0_2          DF   -2000.000000   -1200.000000      -4.000000
    n0_0_3          DF   -2000.000000   -1200.000000       0.000000
    n0_0_4          DF   -2000.000000   -1200.000000       4.000000
    n0_0_5          DF   -2000.000000   -1200.000000       8.000000
    n0_0_6          DF   -2000.000000   -1200.000000      12.000000
    n0_1_0          DF   -2000.000000   -1100.000000     -12.000000
    n0_1_1          DF   -2000.000000   -1100.000000      -8.000000
    n0_1_2          DF   -2000.000000   -1100.000000      -4.000000
    n0_1_3          DF   -2000.000000   -1100.000000       0.000000
    n0_1_4          DF   -2000.000000   -1100.000000       4.000000
    n0_1_5          DF   -2000.000000   -1100.000000       8.000000

      ......        ..   ..............   ............   .........


  n41_25_1          DF    2100.000000    1300.000000      -8.000000
  n41_25_2          DF    2100.000000    1300.000000      -4.000000
  n41_25_3          DF    2100.000000    1300.000000       0.000000
  n41_25_4          DF    2100.000000    1300.000000       4.000000
  n41_25_5          DF    2100.000000    1300.000000       8.000000
  n41_25_6          DF    2100.000000    1300.000000      12.000000


elements

#  Bootstrap Properties      Nodes

        -99999.000000   14.674999   n0_0_0   n1_0_0   n1_1_0   n0_1_0   n0_0_1   n1_0_1   n1_1_1   n0_1_1
        -99999.000000   24.963751   n0_0_1   n1_0_1   n1_1_1   n0_1_1   n0_0_2   n1_0_2   n1_1_2   n0_1_2
        -99999.000000   35.150875   n0_0_2   n1_0_2   n1_1_2   n0_1_2   n0_0_3   n1_0_3   n1_1_3   n0_1_3
              0.080625  38.958374   n0_0_3   n1_0_3   n1_1_3   n0_1_3   n0_0_4   n1_0_4   n1_1_4   n0_1_4
              0.137750  32.947876   n0_0_4   n1_0_4   n1_1_4   n0_1_4   n0_0_5   n1_0_5   n1_1_5   n0_1_5
              0.171750  27.101500   n0_0_5   n1_0_5   n1_1_5   n0_1_5   n0_0_6   n1_0_6   n1_1_6   n0_1_6
        -99999.000000   14.674999   n0_1_0   n1_1_0   n1_2_0   n0_2_0   n0_1_1   n1_1_1   n1_2_1   n0_2_1
        -99999.000000   24.963751   n0_1_1   n1_1_1   n1_2_1   n0_2_1   n0_1_2   n1_1_2   n1_2_2   n0_2_2
        -99999.000000   35.150875   n0_1_2   n1_1_2   n1_2_2   n0_2_2   n0_1_3   n1_1_3   n1_2_3   n0_2_3
              0.080625  38.958374   n0_1_3   n1_1_3   n1_2_3   n0_2_3   n0_1_4   n1_1_4   n1_2_4   n0_2_4
              0.137750  32.947876   n0_1_4   n1_1_4   n1_2_4   n0_2_4   n0_1_5   n1_1_5   n1_2_5   n0_2_5
              0.171750  27.101500   n0_1_5   n1_1_5   n1_2_5   n0_2_5   n0_1_6   n1_1_6   n1_2_6   n0_2_6
        -99999.000000   20.545000   n0_2_0   n1_2_0   n1_3_0   n0_3_0   n0_2_1   n1_2_1   n1_3_1   n0_3_1
        -99999.000000   25.557249   n0_2_1   n1_2_1   n1_3_1   n0_3_1   n0_2_2   n1_2_2   n1_3_2   n0_3_2
        -99999.000000   38.869625   n0_2_2   n1_2_2   n1_3_2

                        .........   .......  .......  .......  .......  .........  .........  .........  .........

              0.187680  17.125340   n40_23_5 n41_23_5 n41_24_5 n40_24_5 n40_23_6  n41_23_6  n41_24_6  n40_24_6
              0.196747  17.334641   n40_24_0 n41_24_0 n41_25_0 n40_25_0 n40_24_1  n41_24_1  n41_25_1  n40_25_1
              0.203471  18.325451   n40_24_1 n41_24_1 n41_25_1 n40_25_1 n40_24_2  n41_24_2  n41_25_2  n40_25_2
              0.199495  16.758488   n40_24_2 n41_24_2 n41_25_2 n40_25_2 n40_24_3  n41_24_3  n41_25_3  n40_25_3
              0.196747  16.655582   n40_24_3 n41_24_3 n41_25_3 n40_25_3 n40_24_4  n41_24_4  n41_25_4  n40_25_4
              0.213134  17.311203   n40_24_4 n41_24_4 n41_25_4 n40_25_4 n40_24_5  n41_24_5  n41_25_5  n40_25_5
              0.111303   8.889457   n40_24_5 n41_24_5 n41_25_5 n40_25_5 n40_24_6  n41_24_6  n41_25_6  n40_25_6

END
```

FIGURE **6-15**
EXAMPLE OUTPUT SPATIAL BOOTSTRAP FILE
NIPER/FINAL REPORT/WA

Table 6-2 Fragment of *.rw Data File from the Yates Field

x-coordinate of the center	y-coordinate of the center	z-coordinate of the bottom	z-thickness	Porosity	Gamma Ray log. value
106450.	112350.	774.310	4.000	0.189	25.375
106450.	112350.	770.310	4.000	0.143	29.979
106450.	112350.	766.310	4.000	0.129	37.896
106450.	112350.	762.310	4.000	-99999.000	40.729
106450.	112350.	758.310	4.000	-99999.000	25.854
106450.	112350.	754.310	4.000	-99999.000	23.480
106450.	112350.	750.310	4.000	-99999.000	-99999.000
106450.	112450.	774.263	4.000	0.189	25.375
106450.	112450.	770.263	4.000	0.143	29.979

7. TASK 3.2: INTEGRATED FRACTURED RESERVOIR DISCRETE FRACTURE MODEL

The project developed a set of tools to integrate discrete feature network (DFN) modeling approaches into fractured reservoir engineering analysis based on the research described in Chapters 2 through 6 above.

7.1 Task 3.2.1: MS Windows 95 Fracture Data Analysis System

This section describes the Windows 95 based data analysis software for fractured reservoir data developed within the project. This software was based on the research conducted in this project.

Quantitative procedures and software implementing those procedures were developed for fracture orientation, spatial structure, flow dimension, and hydraulic parameters. The software developed is summarized as follows:

- **NeurISIS (Fracture Set Analysis):** NeurISIS defines fractures sets based on any combination of fracture characteristics, and fits appropriate fracture orientation distributions. The algorithm is particularly useful for fracture orientations derived from FMI logs, core logs, and outcrop mapping.

- **Spatial (Spatial Location Analysis):** Spatial provides a set of tools to evaluation spatial trends, heterogeneity, and precedence in fracture sets. The analysis is primarily designed for interpretation of large scale lineament maps and outcrop maps, but can also be used to evaluate locations based on FMI logs, core longs, and mud-loss logs.

- **FracDim (Fractional Dimension Type Curve Analysis):** FracDim is an Excel spreadsheet application for fractional dimension analysis of transient pressure response. Flow dimension is a useful index of connectivity and the geometry of pathways which deliver oil, water, and gas to the well bore. FracDim can be applied for single well (DST) test results and multiple-well (interference) test results.

- **Flare (Hydraulic Parameter Analysis):** Flare calculates flow dimension in a simulated fracture network as a function of the variation of conductance or flow area with distance from the well. This is particularly useful for calibrating DFN models to observed DST and multi-well responses, without requiring flow simulation.

- **FraCluster (Compartmentalization Analysis):** FraCluster carries out analyses of fractured reservoir compartmentalization, tributary drainage volume, and block size. The compartmentalization analysis determines the spatial pattern of hydraulic compartments defined by the connected conductive discrete feature networks. The tributary drainage analysis evaluates the volume of compartments drained by specified well geometries, including any combination of vertical and

horizontal wells. Block size analysis calculates the size and shape distribution of matrix blocks defined by fractures and fracture networks.

- **StrataFrac (Linkage of Reservoir and DFN Models):** StrataFrac converts stratigraphic model cellular data into a file format to facilitate direct generation of fractures based on stratigraphic model surfaces (e.g., bedding, stratigraphic contacts, faults) and grid cell values (e.g., fracture porosity, stress field, rock type). In addition, StrataFrac has a capability to generate stratigraphic model grid cell values from 3D DFN models by processing fracture intensity, location, and aperture to define cell properties such as fracture porosity and intensity.

Figure 7-1 illustrates the fracture data analysis components within the context of the data needs for DFN modeling. User documentation for this software is provided in a research report (Dershowitz et al., 1998). FraCluster is described in Section 5.5 above. StrataFrac is described in Chapter 6 above.

7.1.1 NeurISIS Fracture Set Analysis

7.1.1.1 Summary

NeurISIS uses a probabilistic neural network (PNN) for fracture set identification. The algorithm offers the following advantages over conventional approaches:

- It takes advantage of the geologist's ability to define prior assumptions based on visual inspection of the data
- It can define sets based on any combination of fracture attributes
- It allows user control of the relative weightings of different fracture attributes
- It provides reproducible, defensible set classifications
- It provides robust set definitions, even for extensivity overlapping sets

The NeurISIS user interface is illustrated in Figure 7-2.

7.1.1.2 Test Cases

The verification case was defined by generating two overlapping Fisher distributed fracture sets using the statistics given in Table 7-1. The stereoplot before fracture separation by NeurISIS is provided in Figure 7-3. The statistics for the fracture sets following neural network analysis, and the stereoplots for the fractures assigned to the sets are provided in Figure 7-4.

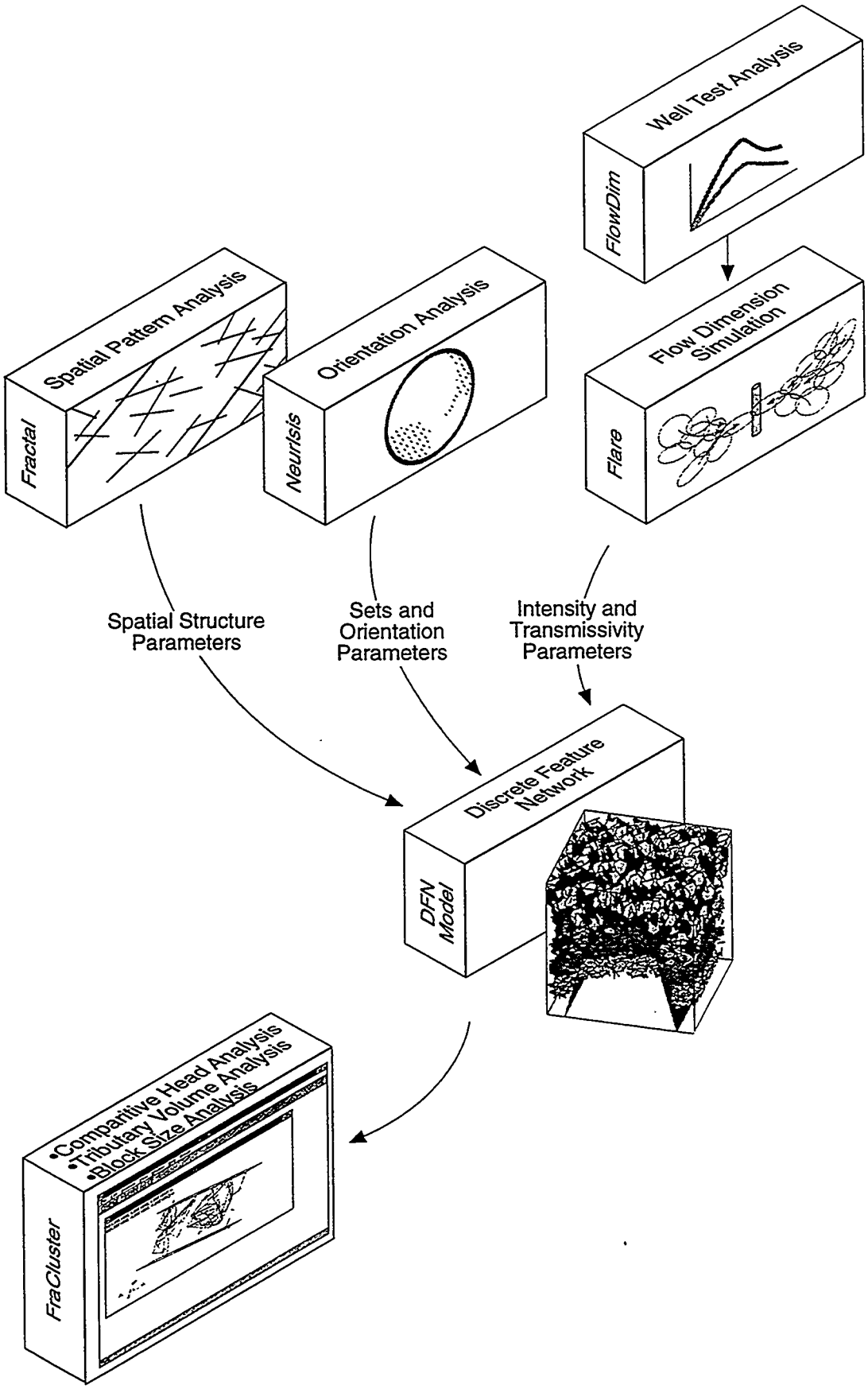

FIGURE **7-1**

FRACTURE DATA ANALYSIS SYSTEM

NIPER/FINAL REPORT/WA

PROJECT NO. 963 1357.521 DRAWING NO. 80758 DATE 9/28/98 DRAWN BY EA

Golder Associates

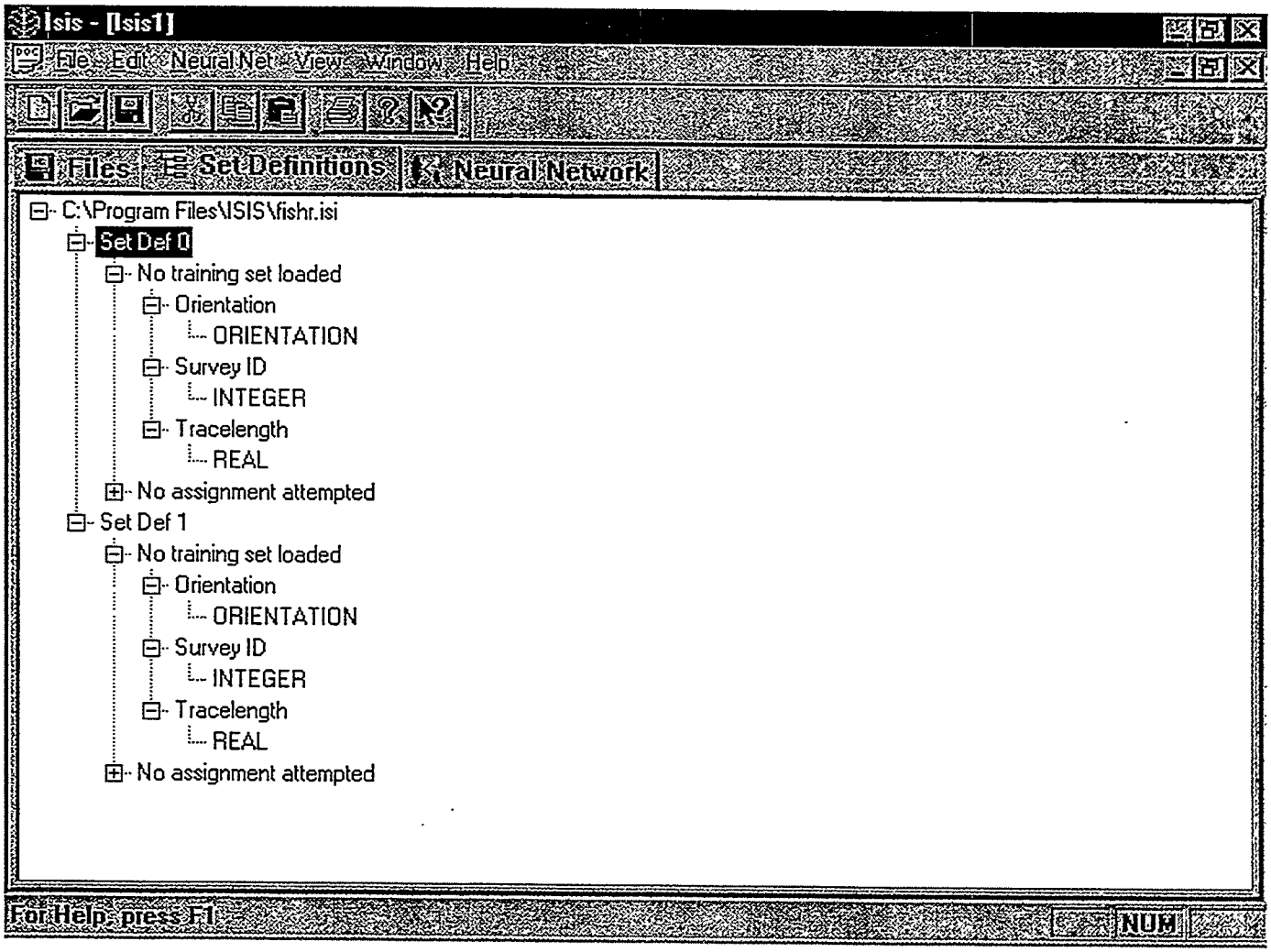

FIGURE **7-2**
NeurISIS USER INTERFACE: OBJECT ORIENTED DATA MODEL
NIPER/FINAL REPORT/WA

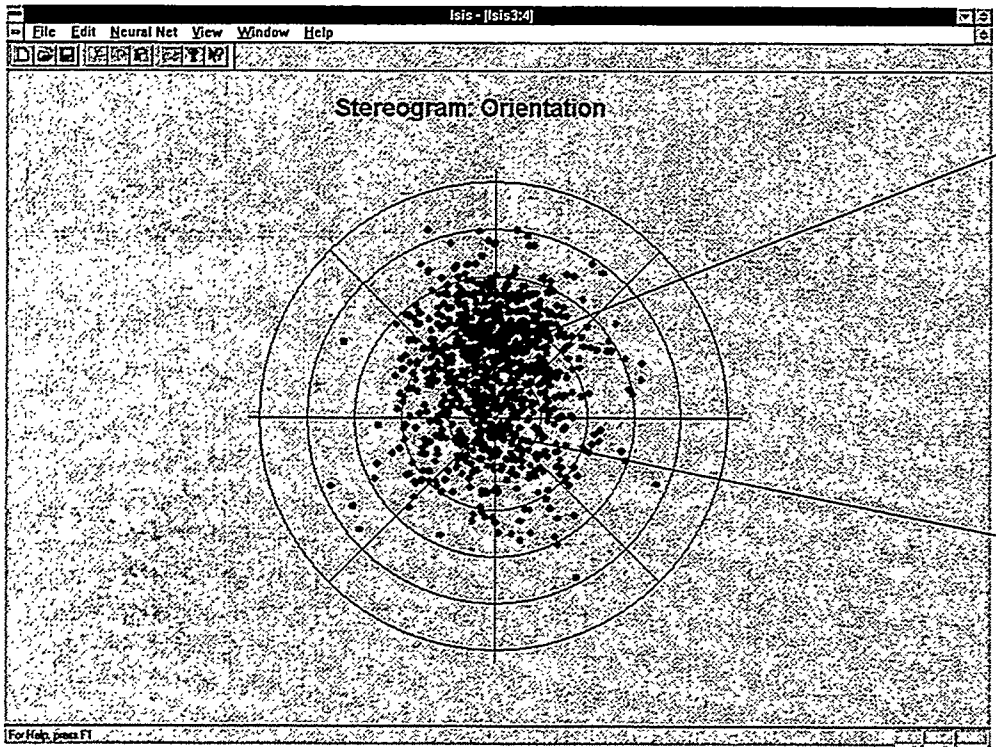

SET #2
Fisher Distribution
Mean Pole Trend $\theta = 0°$
Men Pole Plunge $\phi = 60°$
Dispersion $\kappa = 20$

SET #1
Fisher Distribution
Mean Pole Trend $\theta = 37°$
Men Pole Plunge $\phi = 90°$
Dispersion $\kappa = 10$

FIGURE **7-3**
NeurISIS VERIFICATION CASE
NIPER/FINAL REPORT/WA

PROJECT NO. 963 1357.521 DRAWING NO. 80797 DATE 9/28/98 DRAWN BY EA

Golder Associates

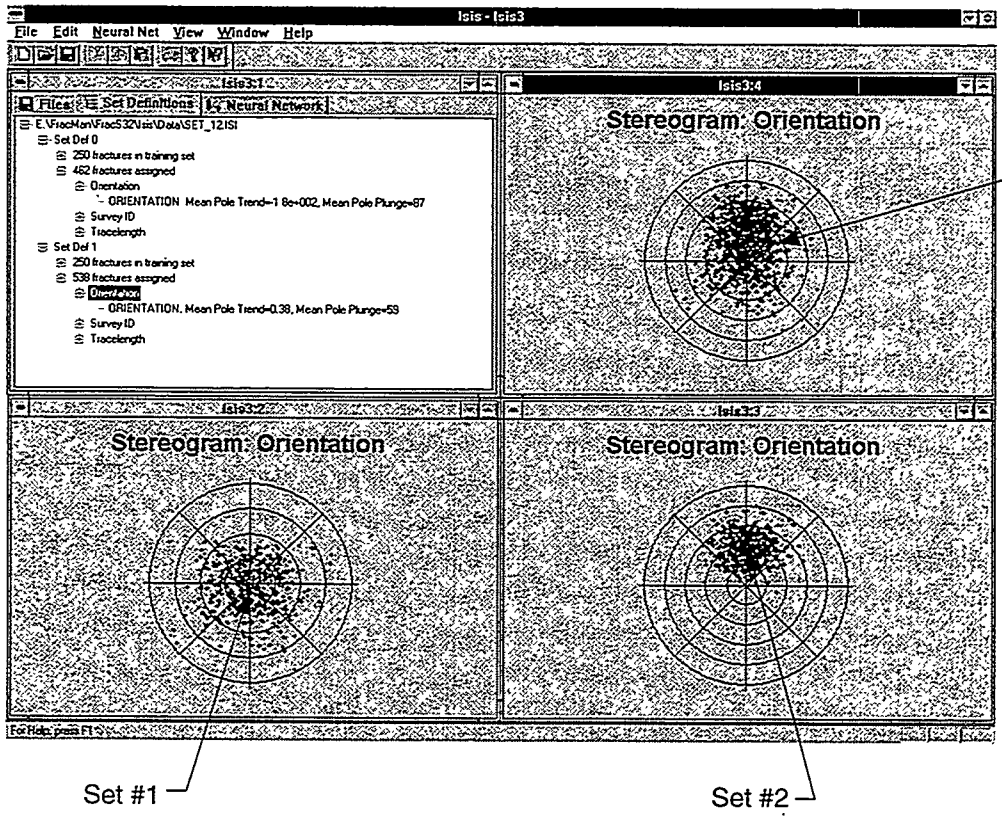

FIGURE **7-4**
VERIFICATION CASE STATISTICS
NIPER/FINAL REPORT/WA

PROJECT NO. 963 1357.521 DRAWING NO. 80798 DATE 9/28/98 DRAWN BY EA

Golder Associates

Table 7-1 NeurISIS Verification Case

Set	Orientation Distribution	Expected Results		NeurISIS 1.0	
		Mean Pole (Trend, Plunge)	Dispersion κ	Mean Pole (Trend, Plunge)	Dispersion κ
1	Fisher	37., 90.	10	180, 87	10
2	Fisher	0., 60.	20	0.38, 59	20

7.1.2 Spatial: Spatial Location Analysis

7.1.2.1 Summary

Spatial analysis of fracture patterns is an essential aspect of the discrete feature network modeling processes. Current spatial analysis methods include geostatistical (Isaaks and Srivastava, 1989), spatial statistics (Ripley, 1988), and fractal (La Pointe and Barton, 1995). Rule-based methods developed within the scope of this project provide an important additional tool for use in defining structural patterns.

The key to spatial fracture analysis of discrete features is the recognition that fracture formation is not a purely stochastic process. Rather, there is a physical, mechanical basis for every fracture's location and geometry. While it is frequently not productive to attempt to understand the entire stress-strain and material property history related to each fracture, the basic rules of fracture formation can be used to derive more realistic DFN model spatial location processes.

Spatial pattern analysis derives correlation structures which can be used to explain the location, size, and orientation of discrete features. A rule-based approach relies on geologically based correlations rather than on purely statistical or stochastic/fractal process based correlations. The geological correlations behind fracture spatial patterns can be expressed quantitatively as (Figure 5-5):

- precedence: the relative order in the sequence of fracture creation
- intensity trends: the variation of fracture intensity with distance from specific types of pre-existing features, or in a specific direction
- orientation trends: the variation of orientation with distance from specific types of pre-existing features, or in a specific direction
- size trends: the variation of orientation with distance from specific types of pre-existing features, or in a specific direction

These correlation structures provide the underlying underpinings for the Hierarchical Fracture Model (Ivanova, 1998). The rule-based spatial analysis approach quantifies

spatial trends and correlations to provide input parameters for hierarchical fracture models.

The user interface for spatial is illustrated in Figures 7-5 and 7-6.

7.1.2.2 Test Cases

Spatial analyses are based on values of intensity P_{21} (m/m^2), fracture length (m), and fracture orientation calculated on a cell-by-cell basis. The center of the cell is used as a spatial reference of each cell value. The cell values are presented in either colored grids or figures. Spatial is therefore verified primarily by checking that the cell values are calculated correctly.

Each of the cells in the Spatial verification case (Figure 7-7) have been assigned a cell number (1 to 16). Figure 7-7a presents a simple fracture pattern in which it is possible to calculate intensity P_{21} (m/m^2), fracture length (m), and fracture orientation manually for comparison to spatial results. The verification of Spatial's correlation features depends on the assignment of fractures to different sets. To evaluate this feature, additional "Set 2" fractures were added to the original "Set 1" fractures, as illustrated in Figure 7-7b.

Figure 7-8 presents the comparison between expected and calculated "Set 1" cell values for the cases illustrated in Figure 7-7a and 7-7b. Spatial results are identical to verification case calculations for both these cases.

The fracture pattern in Figure 7-7a was used to verify Spatial's trend analysis feature, which calculates projected distance along a user specified projection angle Cell No. 10 was selected to verify the projected distance calculation. Figure 7-9 presents comparisons of projected distances to cell No. 10 at angles of 30°, 90° and 135°. For angles of 30° and 90°, the distance is calculated for them low-left corner of the grid. For angles greater than 90°, such as 135°, the projected distance is calculated from the upper-left corner of the grid. The projected distances obtained from Spatial match the expected values for the verification case from hand calculations.

7.1.3 FracDim: Fractional Dimension Type Curve Analysis

7.1.3.1 Summary

Hydraulic pathways through fractured rock are frequently formed by a combination of matrix permeability, flow in planar features such as fractures and fracture zones, and flow through one-dimensional channels such as those formed by selective mineralization, dissolution, and fracture intersection processes (Figure 5-13). This combination of flowing features of different dimensionality is referred to as "fractional dimension response" (Barker, 1988; Doe and Chakrabarty, 1996), as illustrated in Figure 5-14.

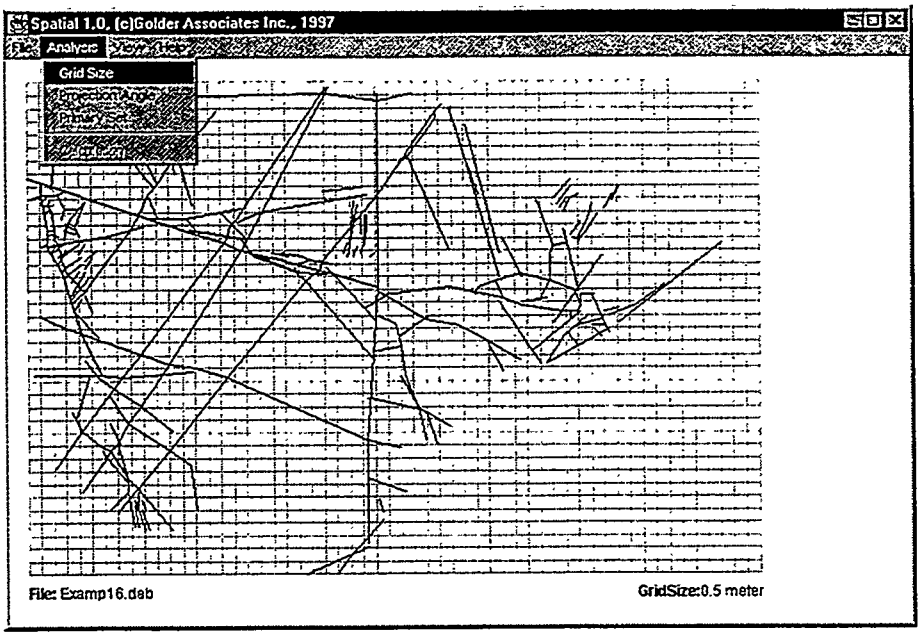

A. Traces.

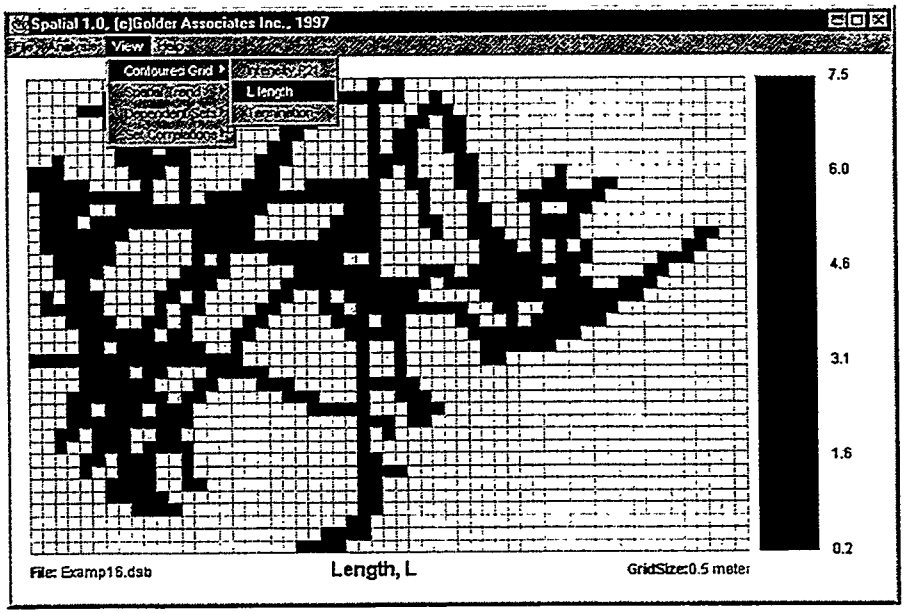

B. Contours.

FIGURE **7-5**
SPATIAL USER INTERFACE
NIPER/FINAL REPORT/WA

PROJECT NO. 963 1357.521 DRAWING NO. 80799 DATE 9/28/98 DRAWN BY EA

Golder Associates

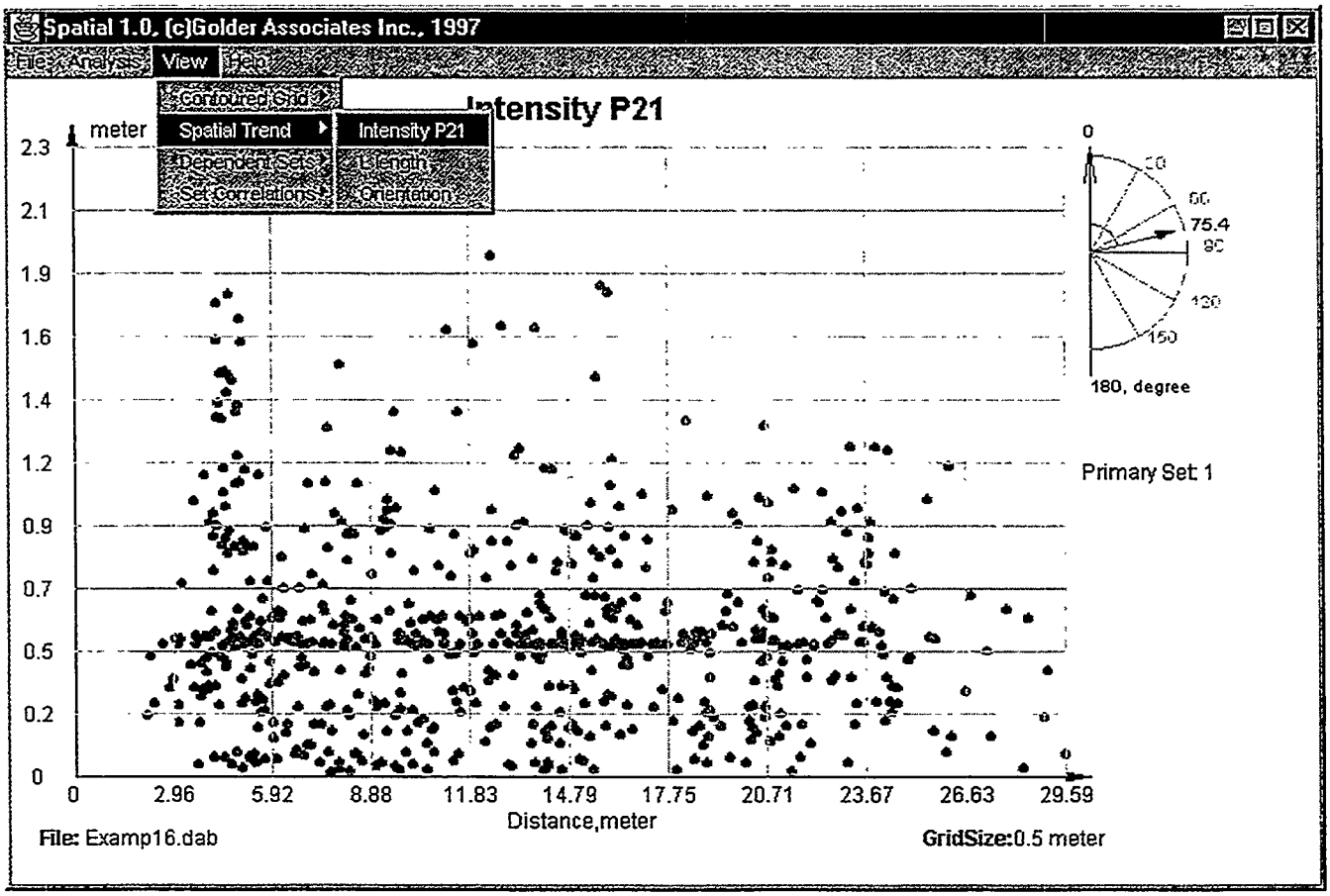

FIGURE **7-6**
SPATIAL USER INTERFACE
NIPER/FINAL REPORT/WA

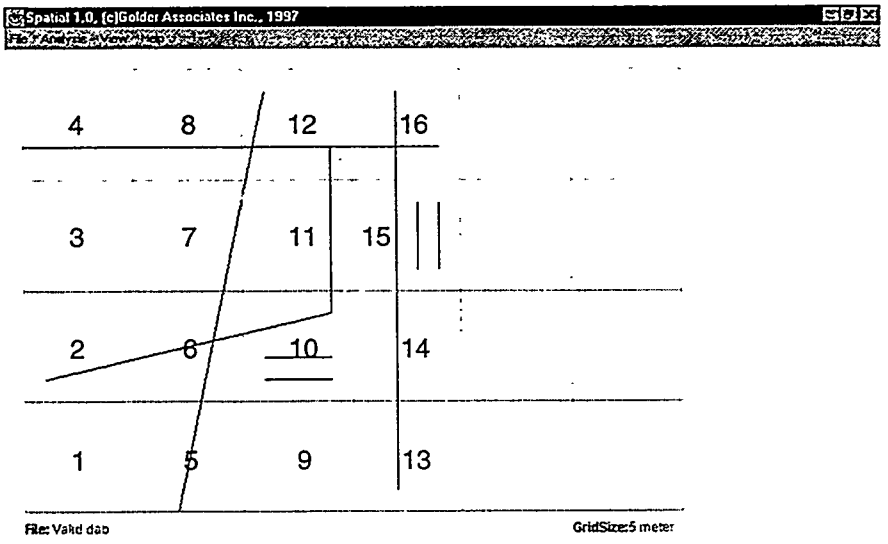

(a) Fractures of Set 1

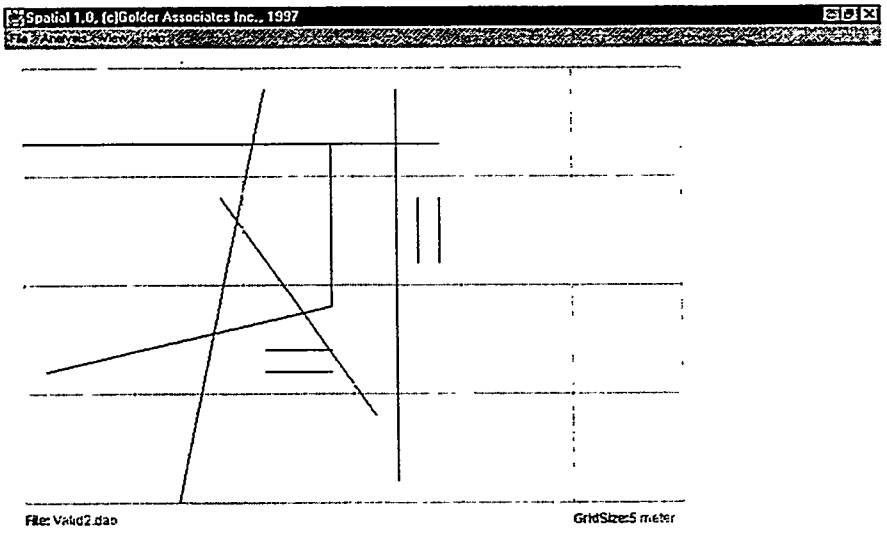

(b) Fractures of Sets 1 and 2

FIGURE **7-7**
SPATIAL VERIFICATION CASE
NIPER/FINAL REPORT/WA

PROJECT NO. 963 1357.521 DRAWING NO. 80801 DATE 9/28/98 DRAWN BY EA

Golder Associates

(a) Cell Intensity P_{21}

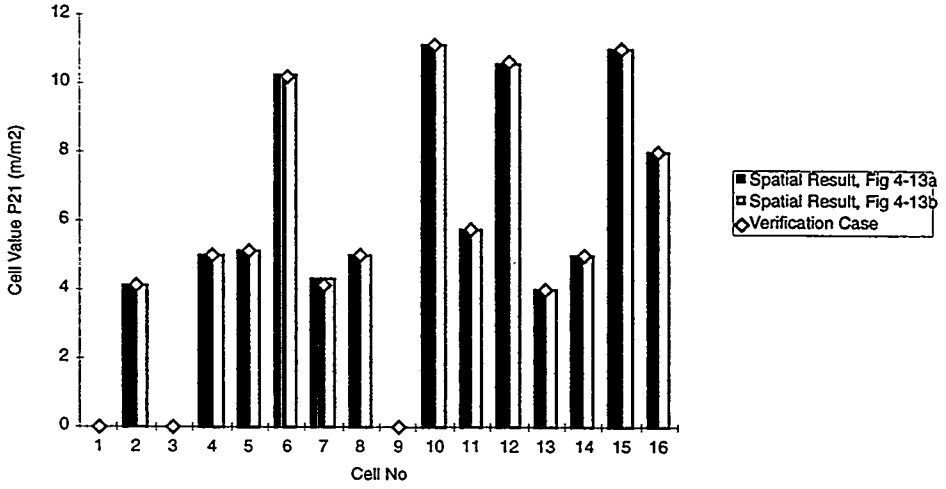

(b) Cell Fracture Length L (m)

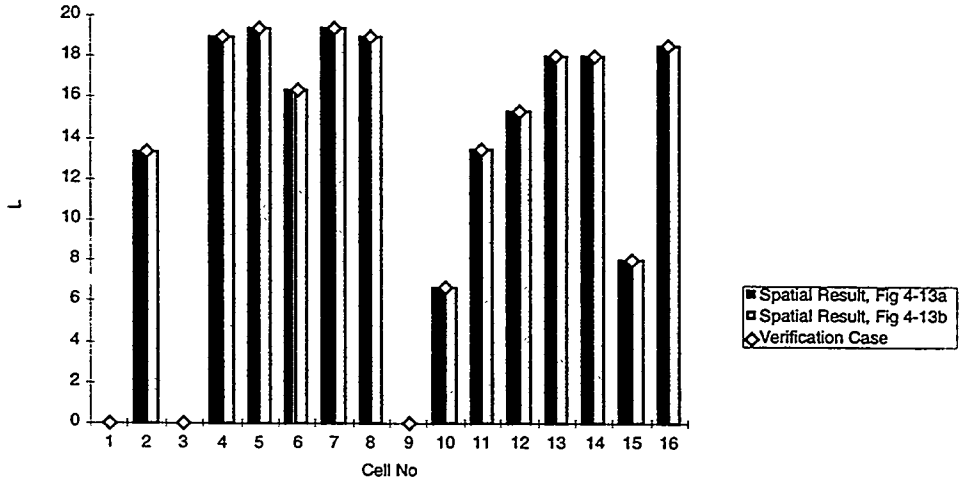

(c) Cell Fracture Orientation

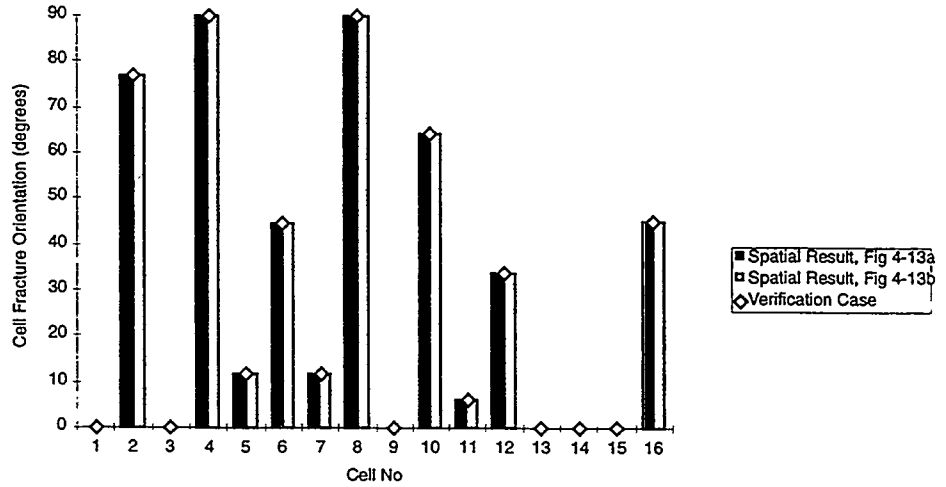

FIGURE **7-8**
SPATIAL VERIFICATION CASE RESULTS
NIPER/FINAL REPORT/WA

PROJECT NO. 963 1357.521 DRAWING NO. 80802 DATE 9/28/98 DRAWN BY EA

Golder Associates

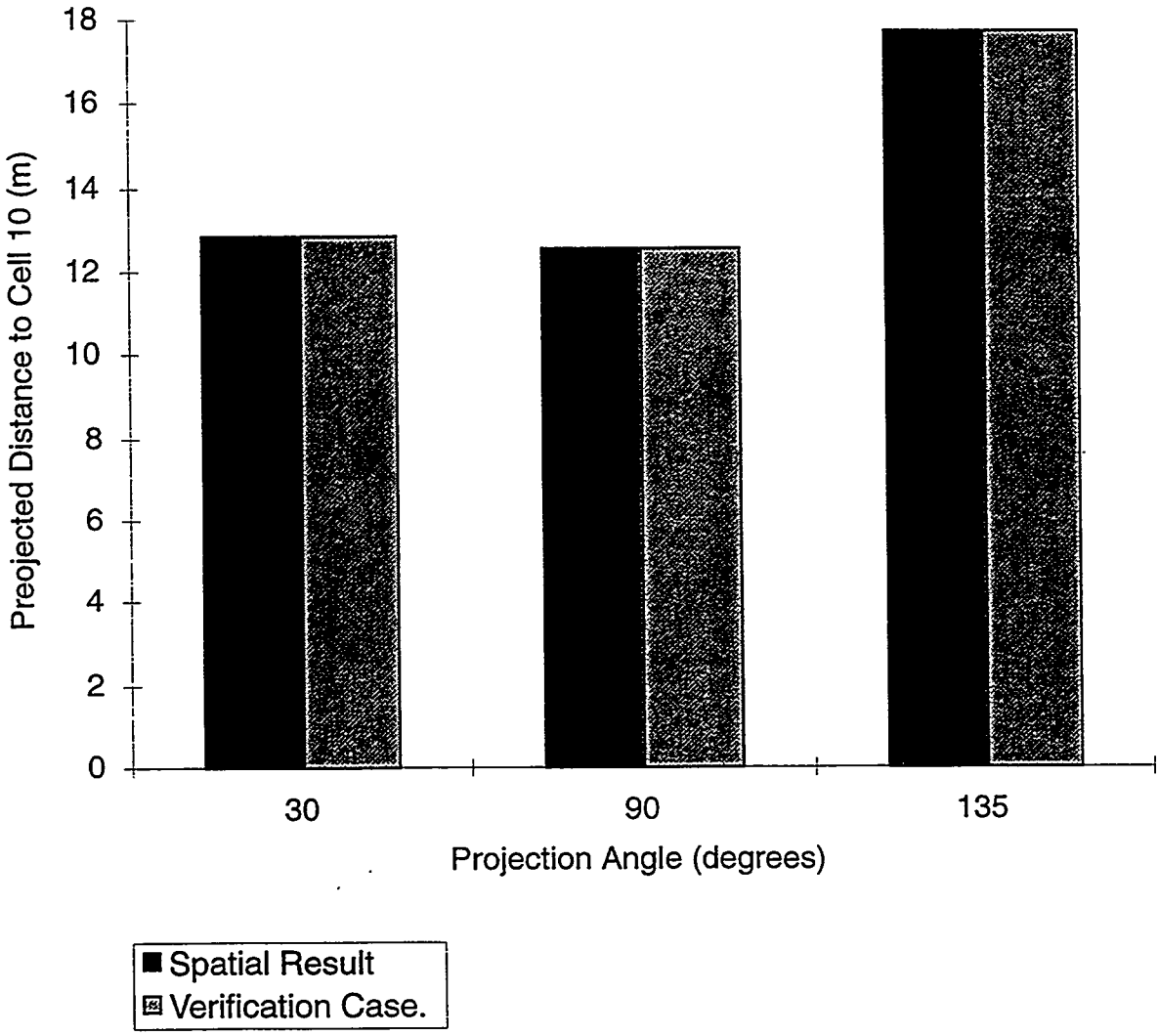

FIGURE **7-9**
SPATIAL VERIFICATION OF PROJECTION ANGLE
NIPER/FINAL REPORT/WA

PROJECT NO. 963 1357.521 DRAWING NO. 80803 DATE 9/28/98 DRAWN BY EA

Golder Associates

An approach was developed for analysis of DFN models to obtain simulated distributions of flow dimension to ensure that the simulated DFN has the same connectivity and heterogeneity structure as the in situ reservoir rock. This method provides an integrated approach to analysis of hydraulic tests in fractured rocks exhibiting this type of "fractional dimension" (Barker, 1988) and heterogeneously connected behavior.

The approach developed combines fractional dimension type curve analysis (Doe and Chakrabarty, 1996) with discrete fracture network simulation (Dershowitz et al, 1996). The FracDim user interface is illustrated in Figure 7-10.

7.1.3.2 Test Cases

FracDim was verified by comparison of type curves produced by FracDim against type curves produced by the FORTRAN code, INCGAM (Doe and Geier, 1991). The verification cases are summarized in Table 7-2. The type curves for both codes are identical, as shown in Figure 7-11.

Table 7-2 FracDim Verification Case

	Case a	Case b	Case c
Dimension (-)	1.00	1.50	2.80
Transmissivity (m^2/s)	10^{-4}	10^{-4}	10^{-4}
Storativity (-)	10^{-3}	10^{-3}	10^{-3}
Pump Rate (m^3/s)	$5x10^{-3}$	$5x10^{-2}$	$5x10^{-3}$

7.1.4 Flare: Hydraulic Parameter Analysis

7.1.4.1 Summary

Just as heterogeneous fractured rock masses are not limited to integer flow dimensions, a series of well tests from different locations in a fracture networks may exhibit a distribution of flow dimensions rather than a single, characteristic flow dimension. This distribution of flow dimensions is thus a valuable measure of rock mass heterogeneity and connectivity. Flow dimension distributions from well test analyses of large data sets from Japan and Sweden (Geier et al., 1992; Winberg et al., 1996) are shown in Figure 5-18. Each of these sites shows a unique distribution of transmission and flow dimension which is indicative of the rock mass heterogeneity and connectivity. The Flare user interface is illustrated in Figure 7-12.

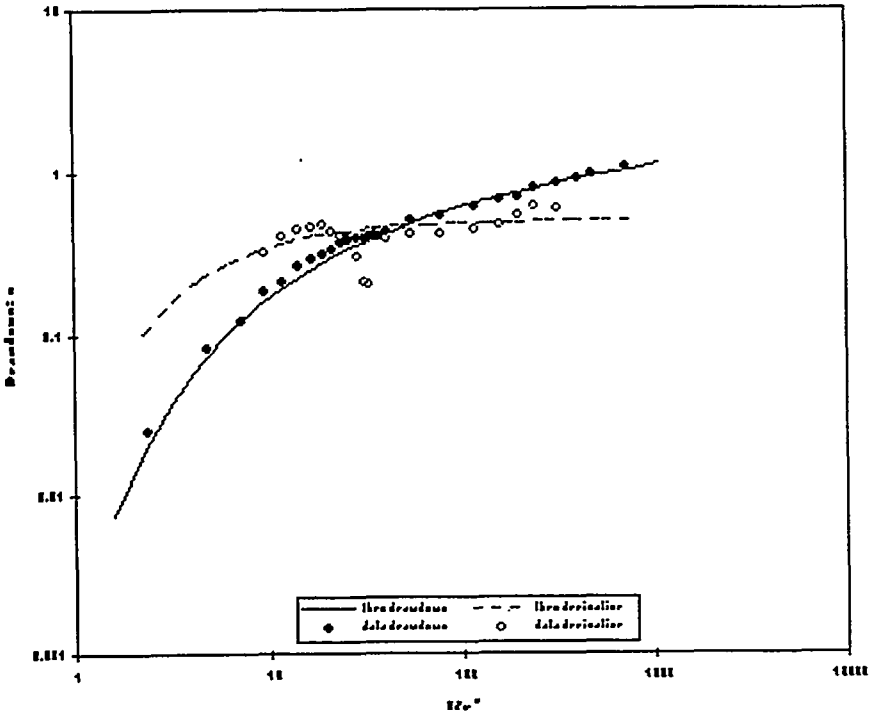

FIGURE **7-10**
FracDim USER INTERFACE
NIPER/FINAL REPORT/WA

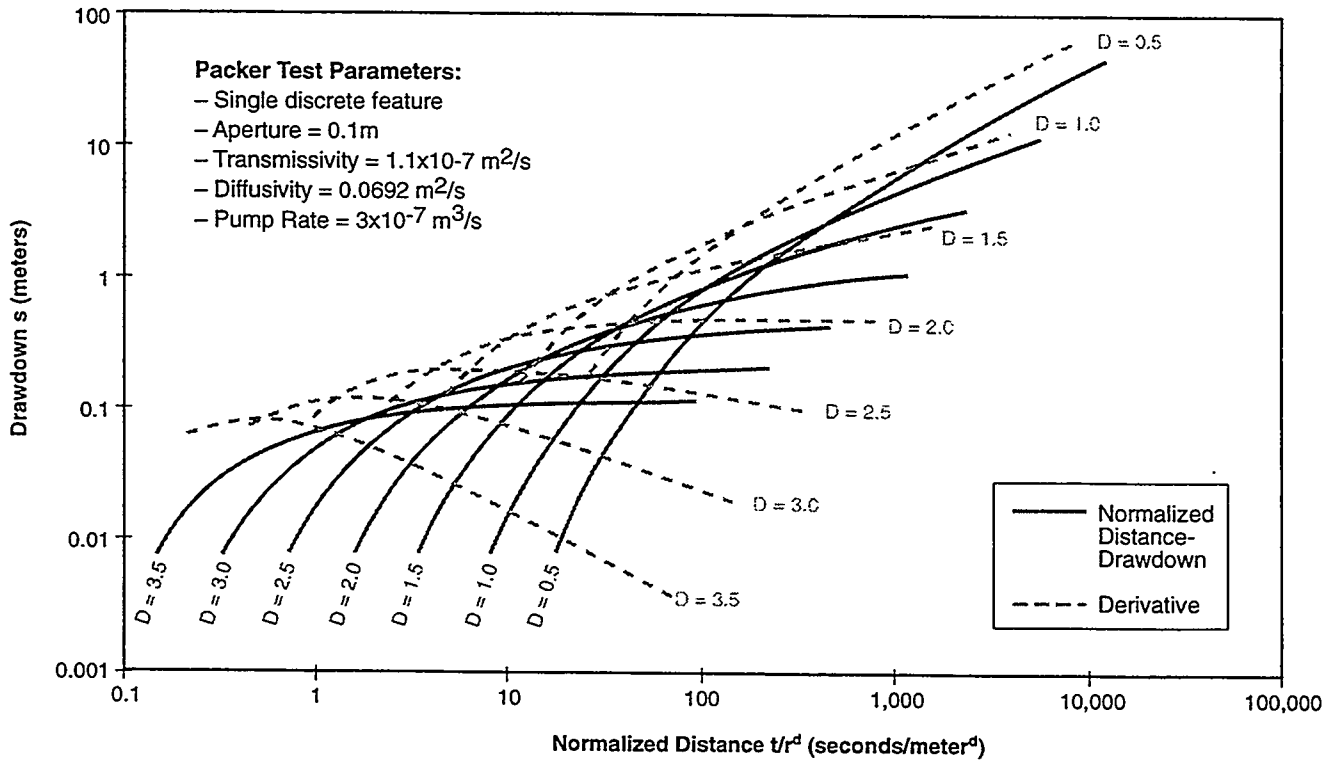

FIGURE **7-11**
FracDim VERIFICATION
NIPER/FINAL REPORT/WA

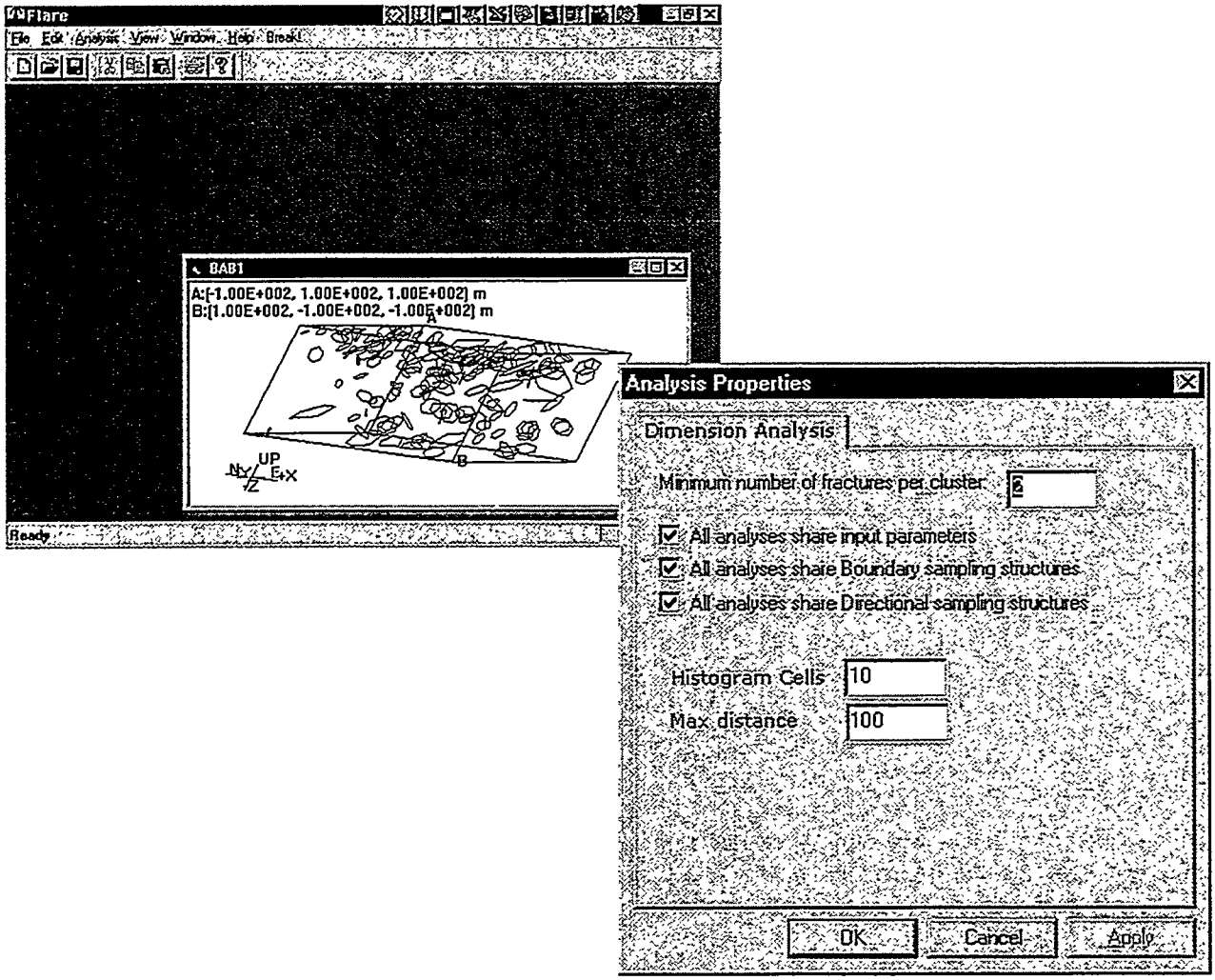

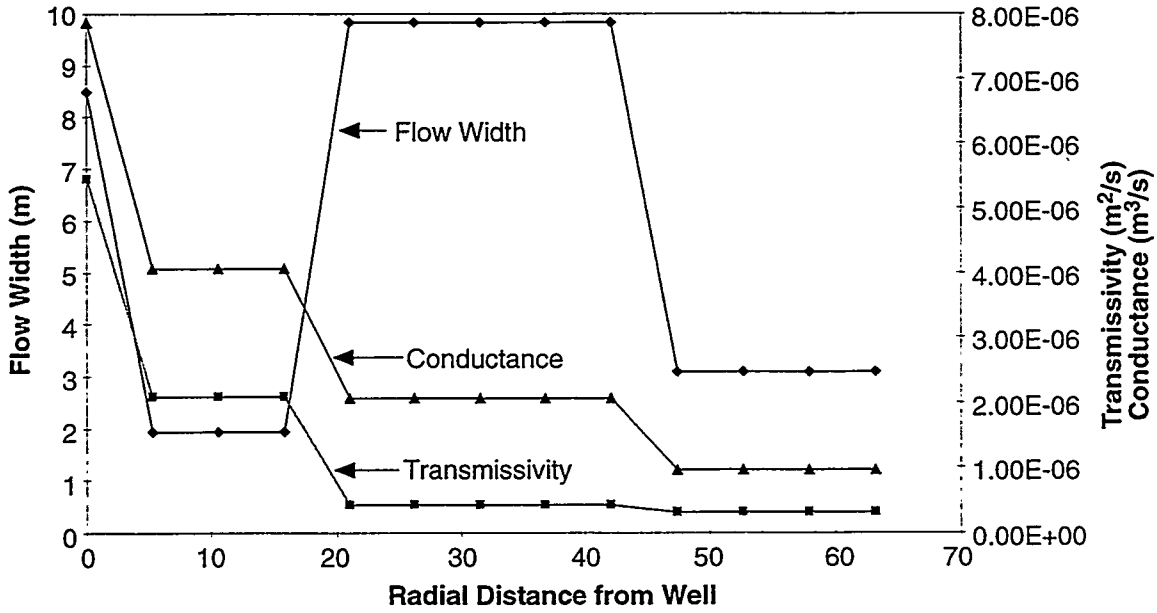

FIGURE **7-12**
FLARE USER INTERFACE
NIPER/FINAL REPORT/WA

PROJECT NO. 963 1357.521 DRAWING NO. 80772 DATE 9/28/98 DRAWN BY EA

Golder Associates

7.1.4.2 Test Cases

Figure 7-13 presents a simple DFN model used to verify Flare. This model consists of a series of 5 fractures, intersecting a well. The fractures have varying size and transmissivity, to produce a variation in both flow area and transmissivity with distance from the well. Figure 7-14 presents the verification results for the comparison of Flare results against the values obtained for this simple fracture network by hand calculations.

7.2 Task 3.2.2: Discrete Fracture Analysis for the TAGS Process

This task included two activities: development of an approach for simulation of the TAGS process within the DFN approach using particle tracking, and DFN analysis of the Yates project study site in support the TAGS process. These are described in Sections 7.2.1 and 7.2.2 respectively. Further applications to the Yates project study site are described in Chapter 9.

7.2.1 DFN Heat Flow Algorithm for Modeling TAGS Processes

Discrete fracture analyses in support of thermally assisted gravity segregation (TAGS) combines the development of a DFN approach to heat transport with the development of the DFN - continuum interface to support continuum modeling of the steam flood process. TAGS is the key to development of the Yates field project study site. The TAGS process being simulated by the DFN approach is illustrated in Figure 7-15.

The TAGS process uses the vertical fracture connectivity to provide a preferential pathway for steam and to serve as a kind of heat-exchanger to the oil in the rock matrix (Figure 7-16). The steam flow direction is parallel to the primary fracture set orientation, forming an elongated zone around each fracture. The light components of the oil (e.g., propane, butane, pentane) will become volatile when heated. In the gas phase it is much easier for these components to leave the matrix. The remaining heavy components will have a decreased viscosity when they are heated. This will increase the ability of the oil to flow within the rock matrix.

There are also other beneficial side effects:

- Heat expansion extends the volume and pressure of the gas cap.
- Light components, which remain gaseous, will also increase the volume of the gas cap.
- Intermediate components will condense and dissolve into the oil remaining in the matrix. The condensate acts like a solvent, thus reducing the oil viscosity.

The TAGS process is directly dependent on the fracture network geometry and connectivity as follows:

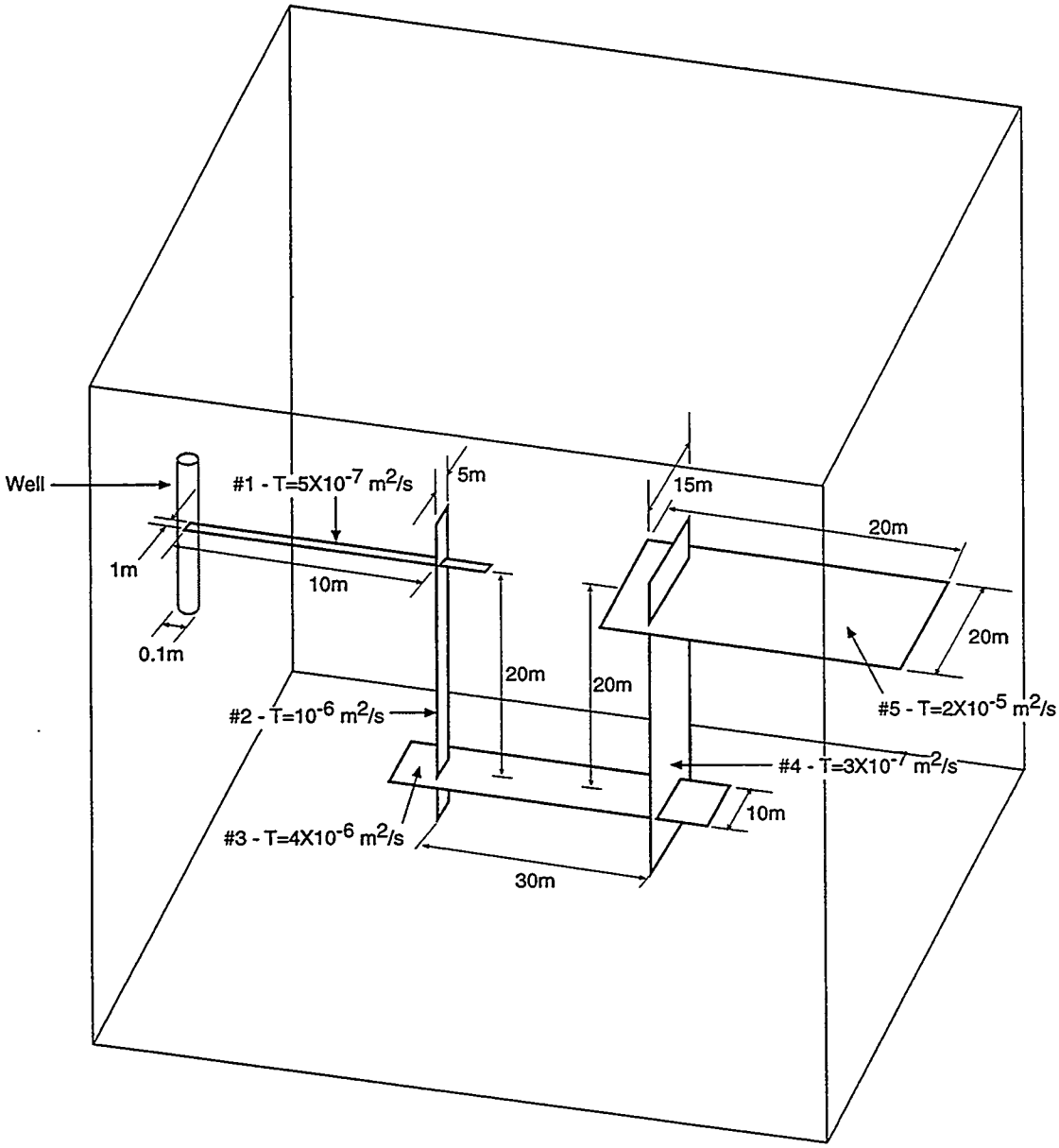

Note: Not to Scale

FIGURE **7-13**
FLARE VERIFICATION CASE
NIPER/FINAL REPORT/WA

PROJECT NO. 963 1357.521 DWG. NO. 80773 DATE 9/28/98 DRAWN EA

Golder Associates

(a) Flow width

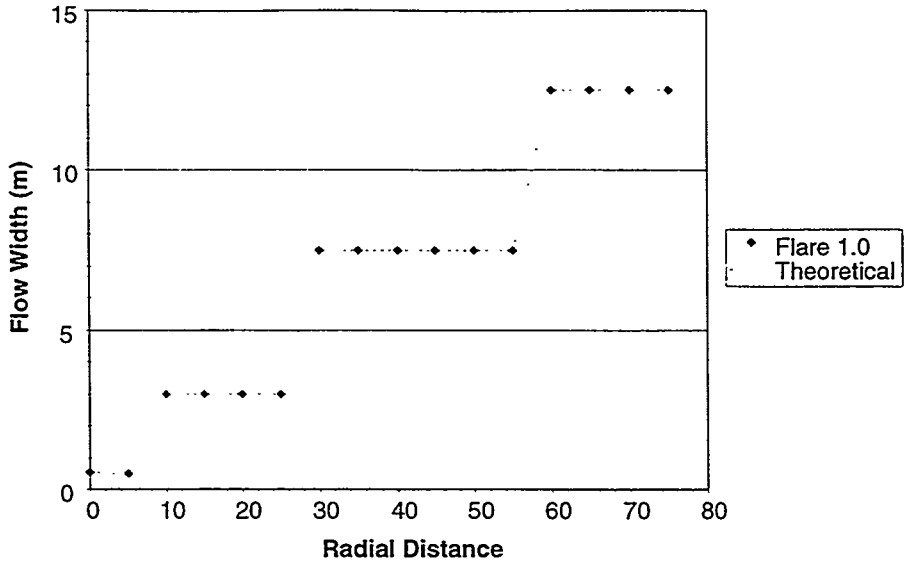

(b) Transmissivity

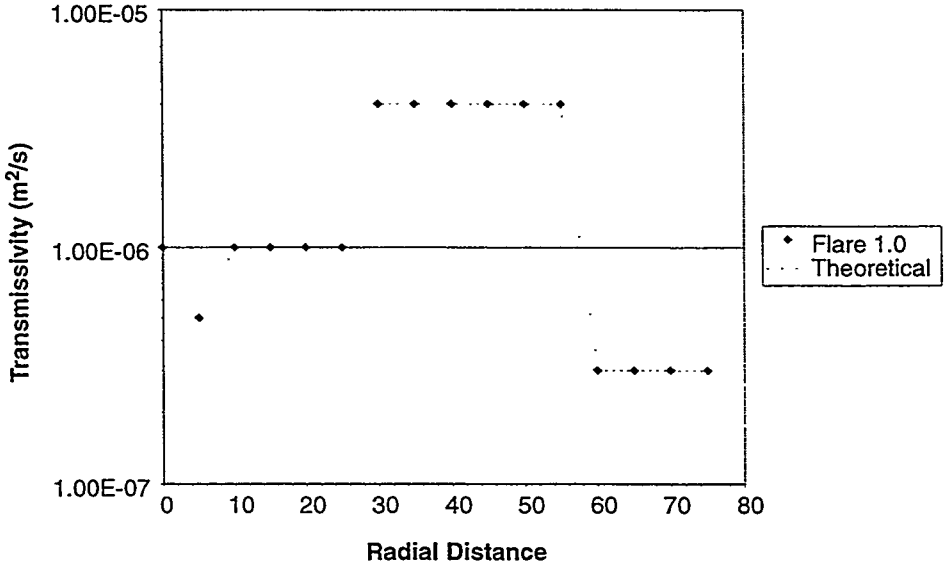

(c) Conductance

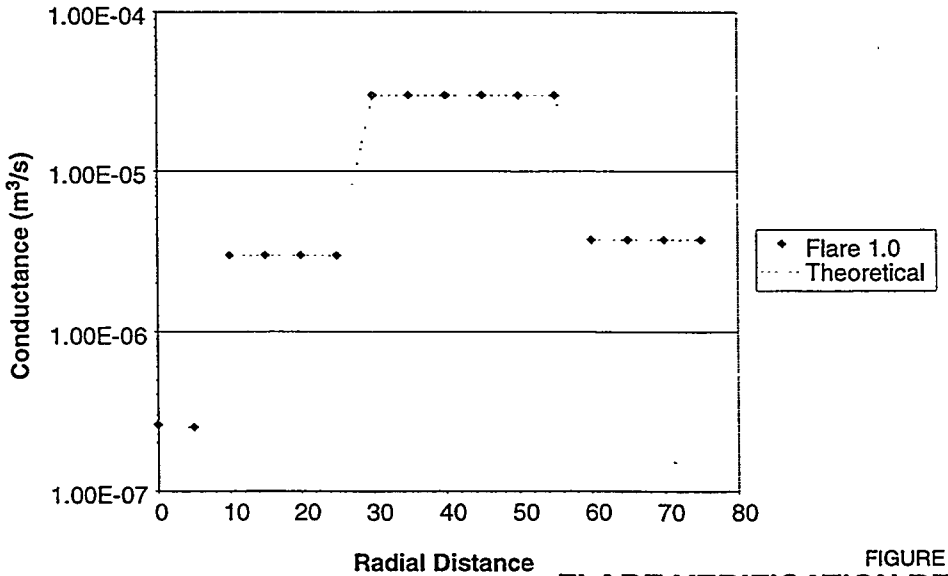

FIGURE **7-14**
FLARE VERIFICATION RESULTS
NIPER/FINAL REPORT/WA

PROJECT NO. 963 1357.521 DWG. NO. 80774 DATE 9/28/98 DRAWN EA

Golder Associates

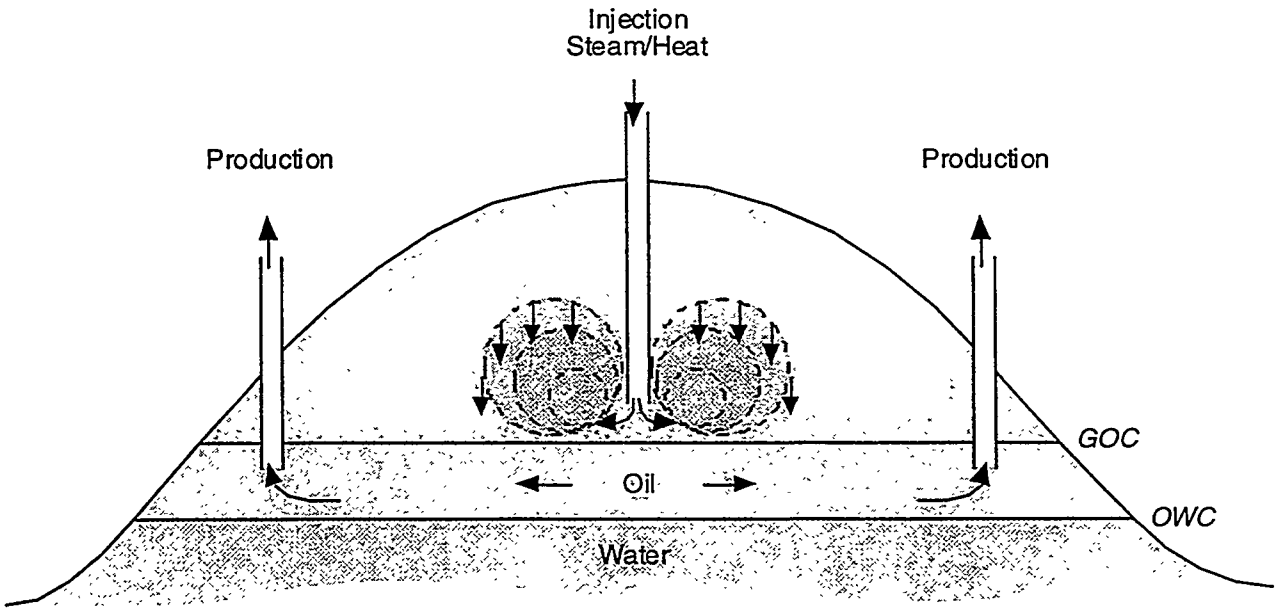

FIGURE **7-15**
TAGS PROCESS SCHEMATIC
NIPER/FINAL REPORT/WA

PROJECT NO. 963 1357.521 DRAWING NO. 80618 DATE 9/24/98 DRAWN BY EA

Golder Associates

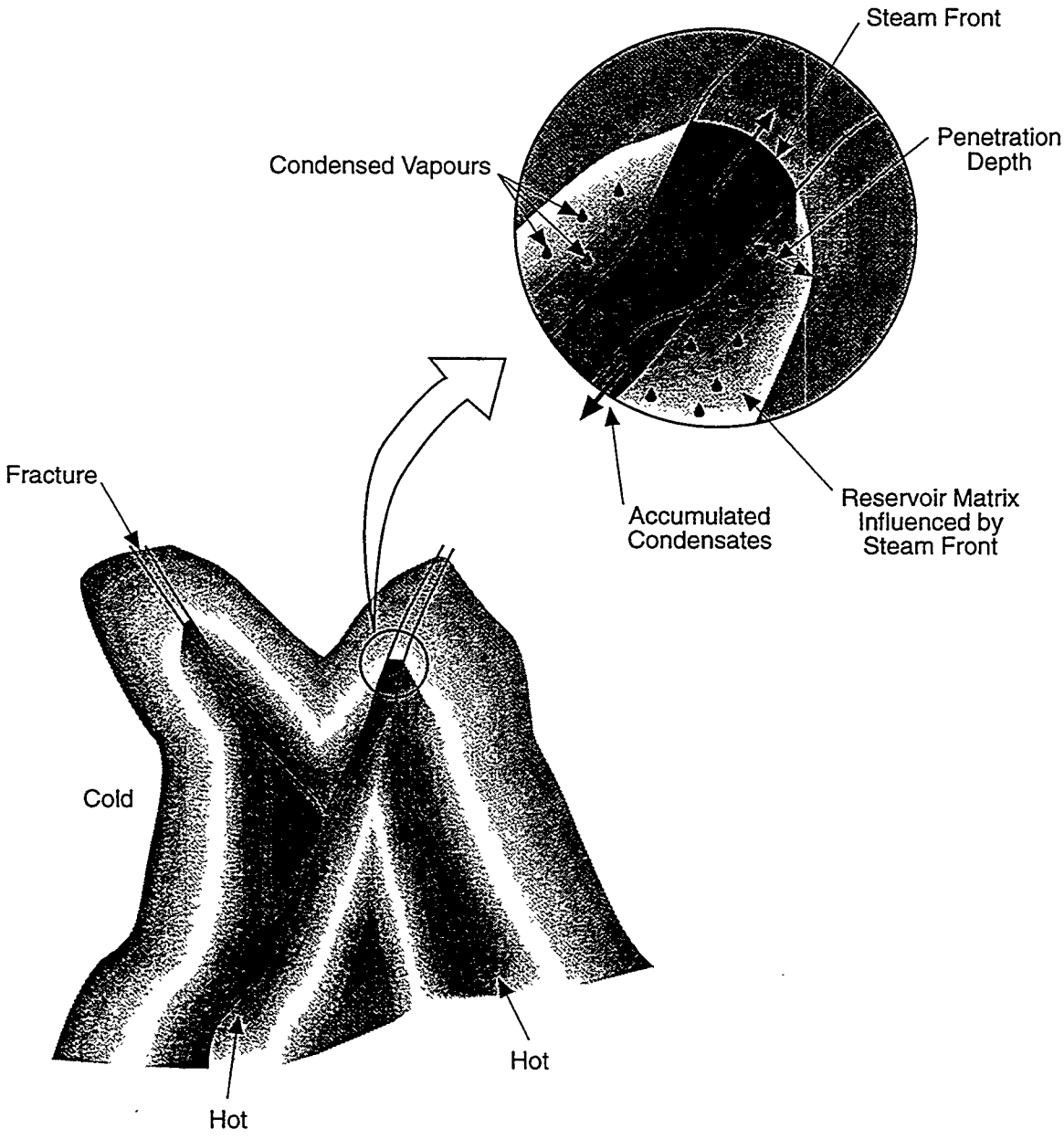

FIGURE **7-16**
HEAT EXCHANGE IN FRACTURE NETWORK
NIPER/FINAL REPORT/WA

- TAGS uses gas-cap inflation to maximize the vertical driving force for segregation of gas and oil while applying heat to reduce the resistance to gravity segregation. Injected gases travel preferentially to the gas-cap through fracture networks (Figure 7-17a).

- TAGS uses heat to segregate hydrocarbon components by steam distilling/boiling the light components of the matrix oil into the adjacent fractures where they are highly mobile (Figure 7-17b).

- TAGS takes advantage of the fracture network preferential orientations to maintain segregation of hot injected fluid from vapors evolving from the matrix blocks (matrix serves as a "semi-osmotic" membrane allowing heat to pass into it but not passing injected fluids through it). In this way injected and produced fluids are both vertically and areally segregated rather than being continuously mixed in a multi-phase horizontal displacement (Figure 7-17c).

The DFN model for support of TAGS must simulate the discrete fracture control of the TAGS process in ways which continuum models cannot. The spatial distribution of heated matrix volume depends mainly on the spatial distribution of the fractures and hence cannot be modeled using averaging continuum model assumptions.

In this project, the DFN approach was extended to model thermal effects. The algorithm is based on a particle tracking approach, except that each particle does not carry a quantum of mass but a quantum of heat (Figure 7-18). The temperature is a function of the number of particles per volume. The particles are released from a source defined by the user (e.g., an injection well). The implemented approach for heat transfer includes two mechanism:

- **Convective Heat Transport**: The hot particles move by convective transport within the fluid flow field, but are assumed not to effect the flow field.

- **Conductive Heat Transport**: Heat transfer between the fluid in the fractures and the rock block is modeled using standard diffusion equations, treating the rock fractures as radiative heat boundaries for the rock blocks. The heat diffusion (conduction) between hot particle and fracture fluid is assumed to be negligible as compared to the convective rate of hot particle and the heat transfer rate to the rock matrix.

The temperature profile in a DFN model depends on the velocity, locations, and paths of the hot particles. The physics of heat transfer from hot particles to the rock and the heat dissipation from the hot rock to the global environment must also be modeled. The equation of energy around the hot particle is

$$\rho_h C_h \frac{dT}{dt} = -\frac{h}{a}(T - T_m) \qquad (7\text{-}1a)$$

$$T = T_h \text{ at } t = 0 \qquad (7\text{-}1b)$$

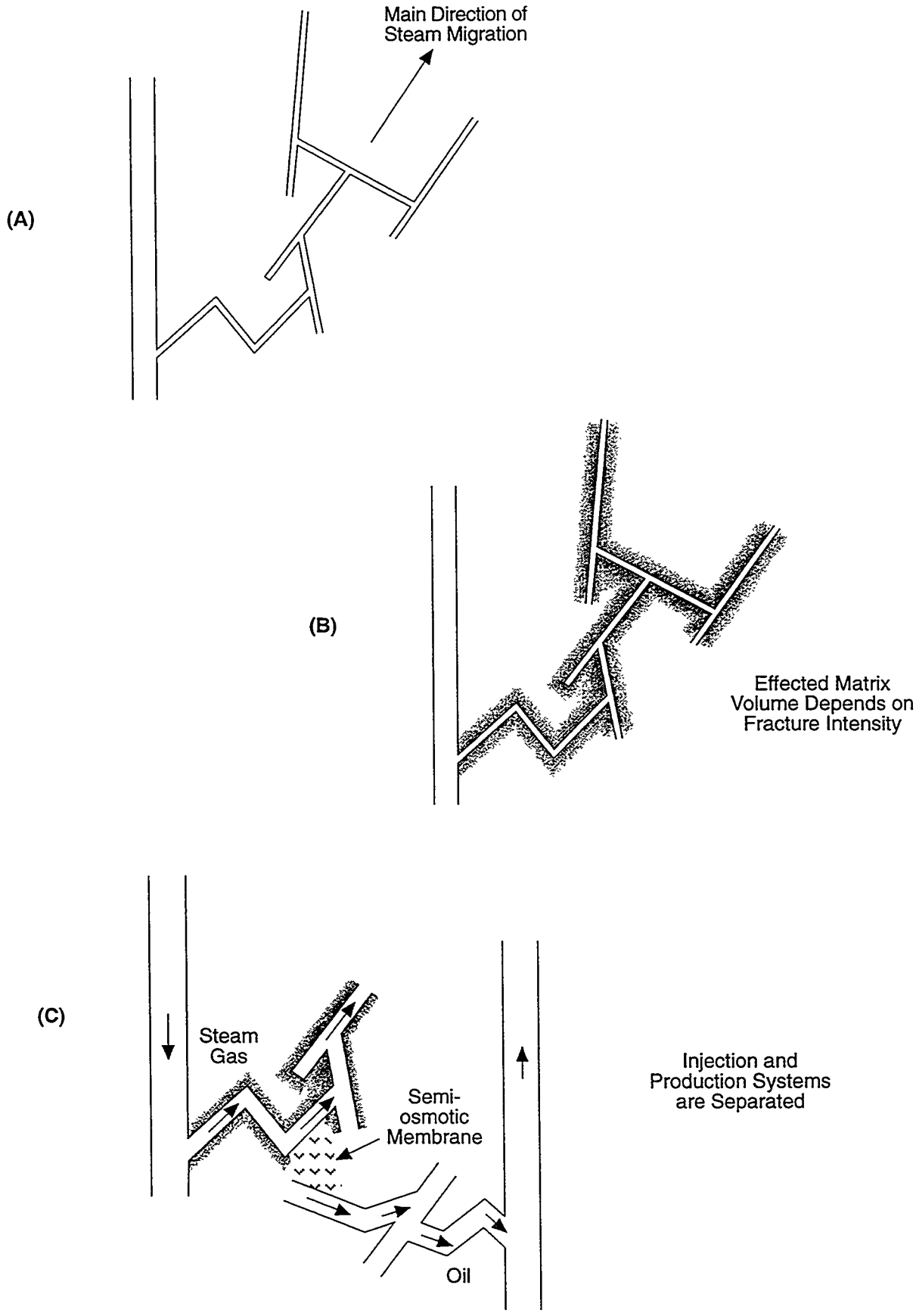

FIGURE **7-17**
ROLE OF FRACTURE GEOMETRY IN TAGS
NIPER/FINAL REPORT/WA

PROJECT NO. 963 1357.521 DRAWING NO. 80767 DATE 9/28/98 DRAWN BY EA

Golder Associates

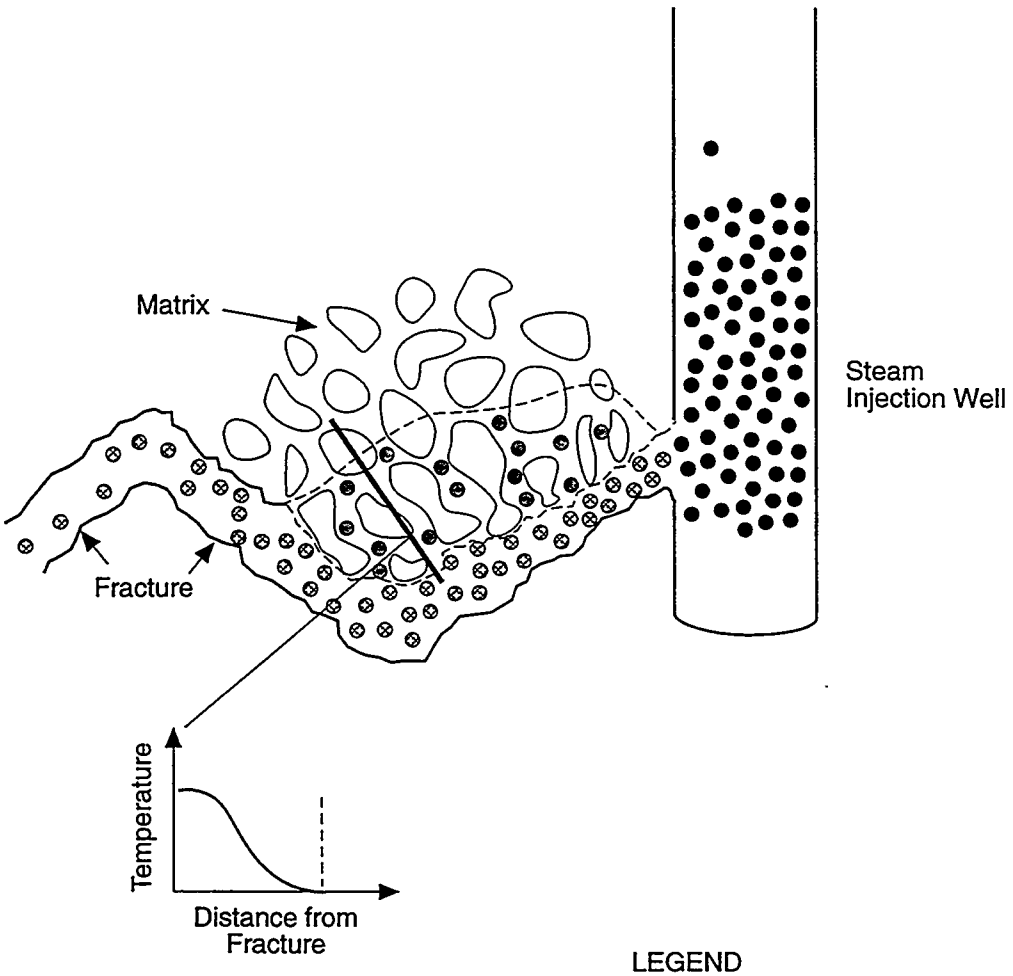

FIGURE **7-18**
DFN HEAT AND PARTICLE TRACKING
NIPER/FINAL REPORT/WA

PROJECT NO. 963 1357.521 DRAWING NO. 80768 DATE 9/28/98 DRAWN BY EA

Golder Associates

where, ρ_h = density of the flowing fluid hot particle, (kg/m^3)
C_h = heat capacity of hot fluid, (kcal/kg°C)
T = temperature of hot fluid or hot particle, (°C)
T_m = temperature of rock, (°C)
T_h = initial temperature of hot fluid, (°C)
h = heat transfer coefficient between hot fluid and rock block, (kcal/m^{2}s°C), and
a = fracture aperture, (m).

Equation 7-1 represents the loss of energy from a hot particle that is completely absorbed by an adjacent rock block. The solution of Equation 7-1 is

$$T(t) = T_m + (T_h - T_m)e^{-Kt} \tag{7-2a}$$

where

$$K = \frac{h}{a\rho_h C_h}. \tag{7-2b}$$

As time passes, the temperature of a hot particle cools to the temperature of the adjacent rock. This cooling is described by a decay rate which is proportional to K.

To apply Equation 7-2 to the discretized fracture elements, the rock volume must be relatively large compared to the fracture medium so that T_m in Equation 7-2 can be treated as constant during heat transfer.

Because T_m varies from fracture element to element, Equation 7-2 is applied to every fracture element that particle travels through where $T_{h,i}$ equals the temperature of particle at the entrance of the element i, $T_{m,i}$ equals the temperature of rock surrounding the fracture element i, and t is the time that a particle takes to traverse the fracture element.

The energy released by a particle to the surrounding rock during the trip across an element is

$$q_i = -\frac{h}{a}\int_0^{t_i} (T(t) - T_m)dt \tag{7-3a}$$

$$q_i = C_h\rho_h h(T_{h,i} - T_{m,i})(1 - e^{-K_i t_i}) \tag{7-3b}$$

where t_i is the residence time of a particle in element i and K_i is the K value defined by Equation 7-2b with a replaced by a_i, the aperture of element i.

The energy, q_i, in Equation 7-3 has units of kcal/m^3. The energy retained by the hot fluid and particle is

$$PE = \Delta V C_h \rho_h (T_h - T_o) \tag{7-4}$$

where, PE = potential energy (relative to T_o) of a particle (kcal);
T_o = initial temperature of the system (fracture + rock media);
ΔV = volume of hot fluid.

Because PE and T_o are provided by the user, ΔV is the only unknown in Equation 7-4.

The total energy released from the hot fluid to a fracture element i is Q_i, which is the volumetric energy, q_i, multiplied by the volume of the hot field:

$$Q_i = \Delta V q_i. \tag{7-5}$$

Equation 7-5 is true if the temperature of rock, $T_{m,i}$, varies little while ΔV passes through element i. The temperature of the hot fluid is assumed uniform.

The energy transferred to rock increases the temperature of rock. Assuming that we are not interested in the heat conduction, and temperature of the rock is uniform (heat conductivity of rock is infinitely large), the temperature of rock can be calculated from:

$$\Delta T_{m,i} = \frac{Q_i}{V_{r,i}\rho_r C_r} \tag{7-6}$$

where, $\Delta T_{m,i}$ = increment of temperature in rock i (°C);
$V_{r,i}$ = rock volume adjacent to fracture element i,
ρ_r = density of rock (kg/m^3);
C_r = heat capacity of rock, (kcal/kg°C).

The rock volume is calculated from fracture area (A_i) and thickness (b) of rock.

$$\begin{aligned} V_{r,i} &= A_i b \\ &= A_i a_i R \end{aligned} \tag{7-7}$$

where, R = b/a_i ratio of rock thickness b to aperture a_i, a user's input value;
A_i = area of fracture triangular element, i.

Overheating occurs when the temperature of the rock ($T_{m,i} + \Delta T_{m,i}$) calculated by Equation 7-2 is greater than the temperature of a hot particle, T_h. In that case, the temperature at equilibrium is calculated from

$$\Delta V \rho_h C_h (T_{h,i} - T_i) = V_{r,i}\rho_r C_r (T_i - T_{m,i}) \tag{7-8a}$$

$$T_i = \frac{T_{h,i} + f T_{m,i}}{1 + f} \tag{7-8b}$$

where

$$f = \frac{V_{r,i}\rho_r C_r}{\Delta V \rho_h C_h}. \tag{7-8c}$$

The temperature, T_i, is the temperature of a hot particle as well as the temperature of the rock. This situation happens when the potential energy of a particle is large, or the related rock volume is small compared to the volume of the fluid ΔV. In either case, the assumption that T_m in Equation 7-2 is constant is not true and Equation 7-2 cannot be used.

The temperature profile in the system can be obtained from Equations 7-2 and 7-6. Temperatures of hot particles or the fracture medium are calculated from Equation 7-2 and temperatures of rock blocks from Equation 7-6. Conservation of heat energy should be checked at every timestep of output:

Total released energy = potential energy of particles still moving (7-9a)
+ potential energy of particles that have moved out of system
+ energy increased in rock blocks

$$N * PE = \sum_{i=1}^{N_{in}} PE_{in,i} + \sum_{i=N_{in}+1}^{N} PE_{out,i} + \sum_{i=1}^{N_e} V_{r,i}\rho_r C_r (T_{m,i} - T_o) \tag{7-9b}$$

where

$$PE_{in,i} = \Delta V C_h \rho_h (T_{h,i} - T_o), \tag{7-9c}$$

$$PE_{out,i} = \Delta V C_h \rho_h (T_{hout,i} - T_o), \tag{7-9d}$$

and, N = total number of particles released;
N_{in} = total number of particles still in the system;
$T_{hout,i}$ = temperature of particle at the outlet of the system;
N_e = total number of fracture elements, this is the same as the total number of rock blocks.

The hot rocks start to cool after all the hot particles have passed through (a "dry" rock). The cooling process is modeled by dissipation of heat to the rocks in the entire simulation region. The user provides the dissipation rate (D in kcal/m^{3}s) and the total volume of rock (V in m^3). This heat transfer process is evaluated at each output timestep, t_k:

$$V\rho_r C_r (T_g - T_{g,k}) = \sum_{i=1}^{N_r} V_{r,i}\rho_r D(t_k - t_{i,k}) \tag{7-10}$$

T_g is the global temperature of rock, $T_{g,k}$ is the global temperature in the previous timestep, N_r is the number of "dry" rocks at time, t_k, and $t_{i,k}$ is the time that the last particle left rock i, or the time of the previous output timestep, whichever is most recent. The solution of Equation 7-10 is

$$T_g = T_{g,k} + \frac{D}{C_r} \sum_{i}^{N_e} \frac{V_{r,i}}{V} (t_k - t_{i,k}) \tag{7-11}$$

The decrement of temperature in the rock i is

$$T_{m,i} = T_{m,i,k} - \frac{V(T_g - T_{g,k})}{V_{r,i}}. \quad (7\text{-}12)$$

Figure 7-19 illustrates an example test case of the DFN approach for support to modeling of the TAGS process. The simulation parameters are provided in Table 7-3. Example simulation results are provided in Figure 7-20. This work will be extended in Section 9.0 using geometries and material properties from the Yates Field.

Table 7-3 Simulation Parameters for Heat Transfer

Property	Value	Units
System and particle properties		
Initial temperature of the system	20.000	°C
Initial temperature of hot particle	120.000	°C
potential Energy of hot particle	150.000	kcal
Hot water properties		
density	1000.00	kg/m^3
heat capacity	1.000	kcal/°C kg
Rock matrix properties		
density	2000.0	kg/m^3
heat capacity	0.200	kcal/°C kg
dissipation rate	1.00E-08	kcal/kg s
total rock volume	1.00E+09	m^3
Heat transfer coef. from hot water to rock	2.00E-03	kcal/s °C m^2
Geometry		
Ratio of Rock Thickness to Aperture	100.00	--

7.2.2 Fracture Zone Model for the Yates Project Study Site

This section presents a demonstration DFN analysis of the Yates project study site, based on a simplified fracture zone model approach. This model does not include the rock matrix or stochastic background fracturing.

The fracture zone DFN model is summarized in Figures 7-21, 7-22, 7-23 and Table 7-4. This model is used to illustrate compartment, tributary and matrix block analyses.

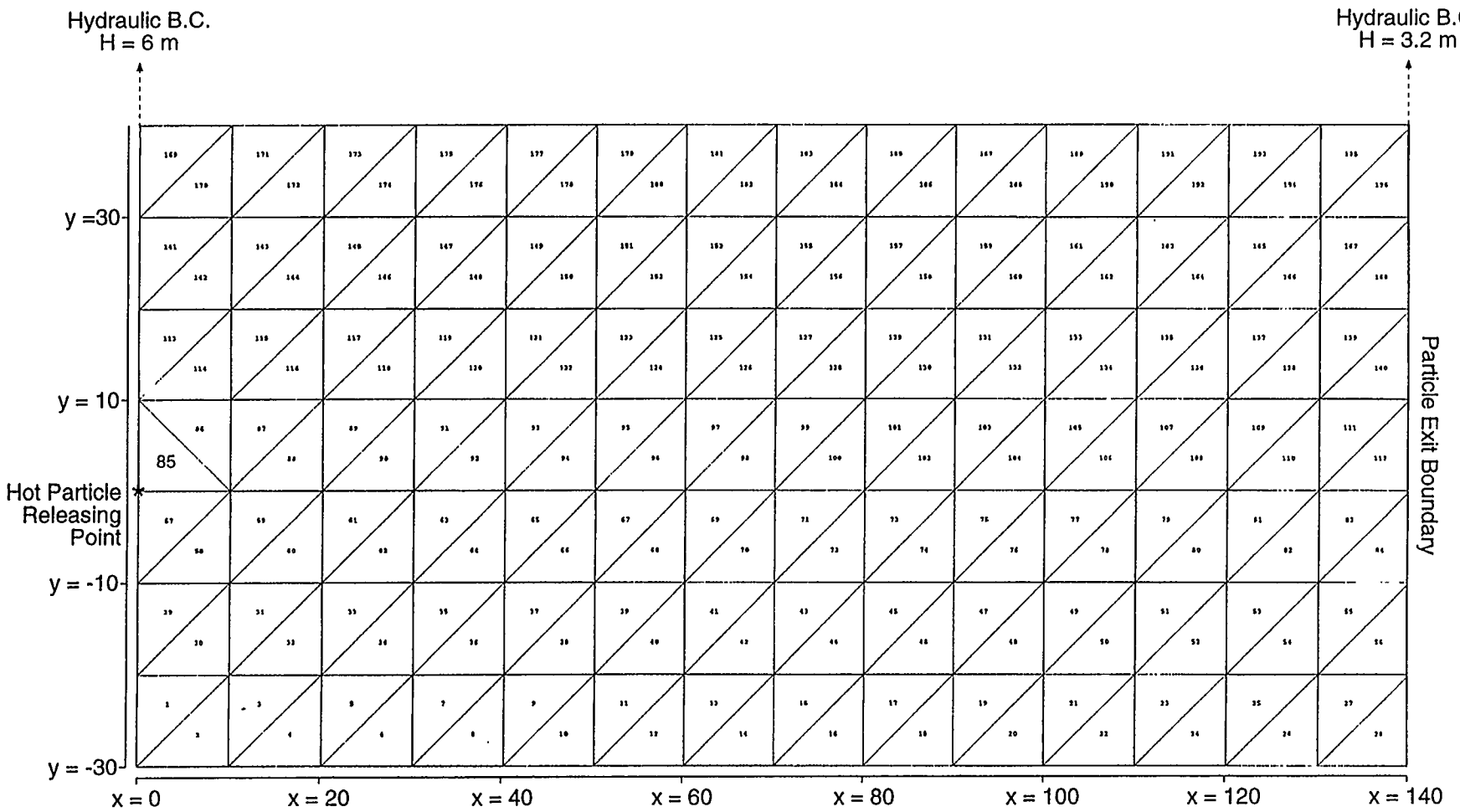

FIGURE **7-19**

TEST CASE OF HEAT MIGRATION ON SINGLE FRACTURE MESHES

NIPER/FINAL REPORT/WA

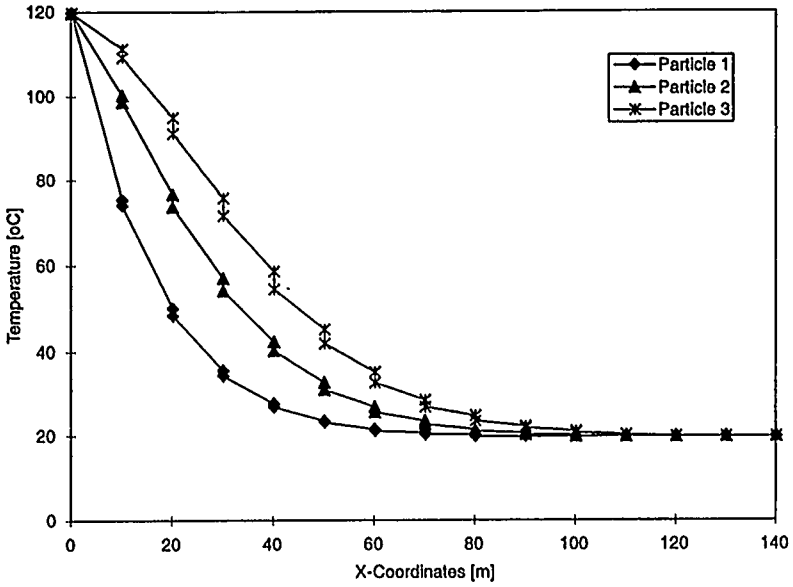

A. Temperature evolution of the first three tracked particles

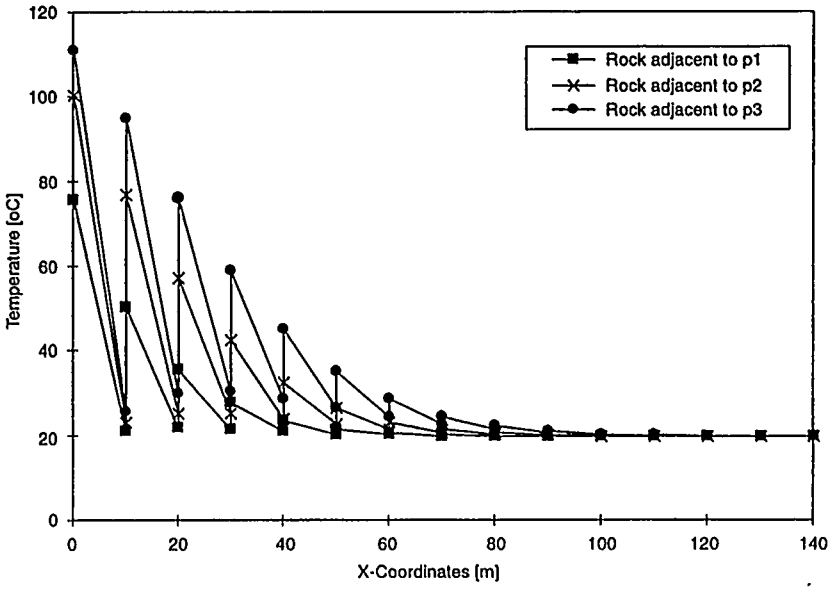

B. Temperature evolution of elements through which first three tracked particles travel

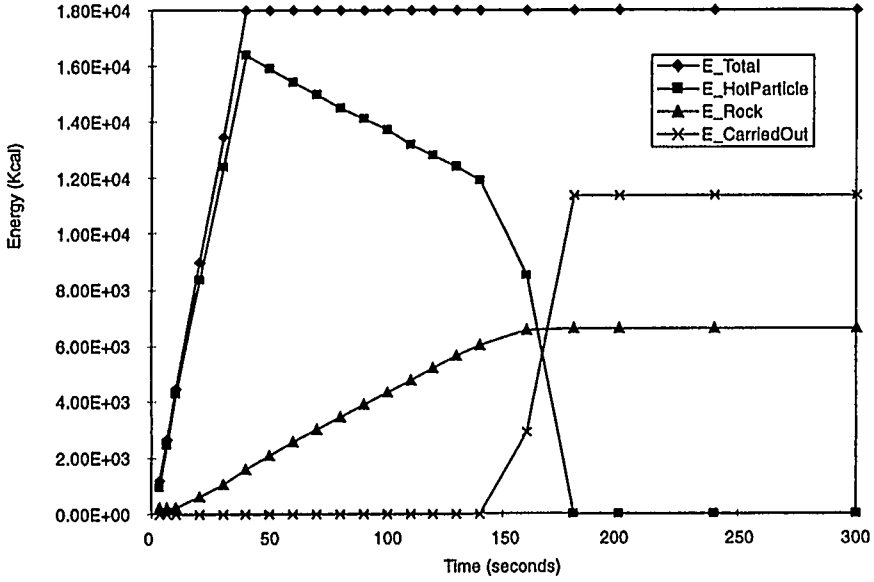

C. Energy migration from hot particles to rock

FIGURE **7-20**
RESULTS OF STEAM TRANSPORT SIMULATIONS
NIPER/FINAL REPORT/WA

PROJECT NO. 963 1357.521 DRAWING NO. 80770 DATE 9/28/98 DRAWN BY EA

Golder Associates

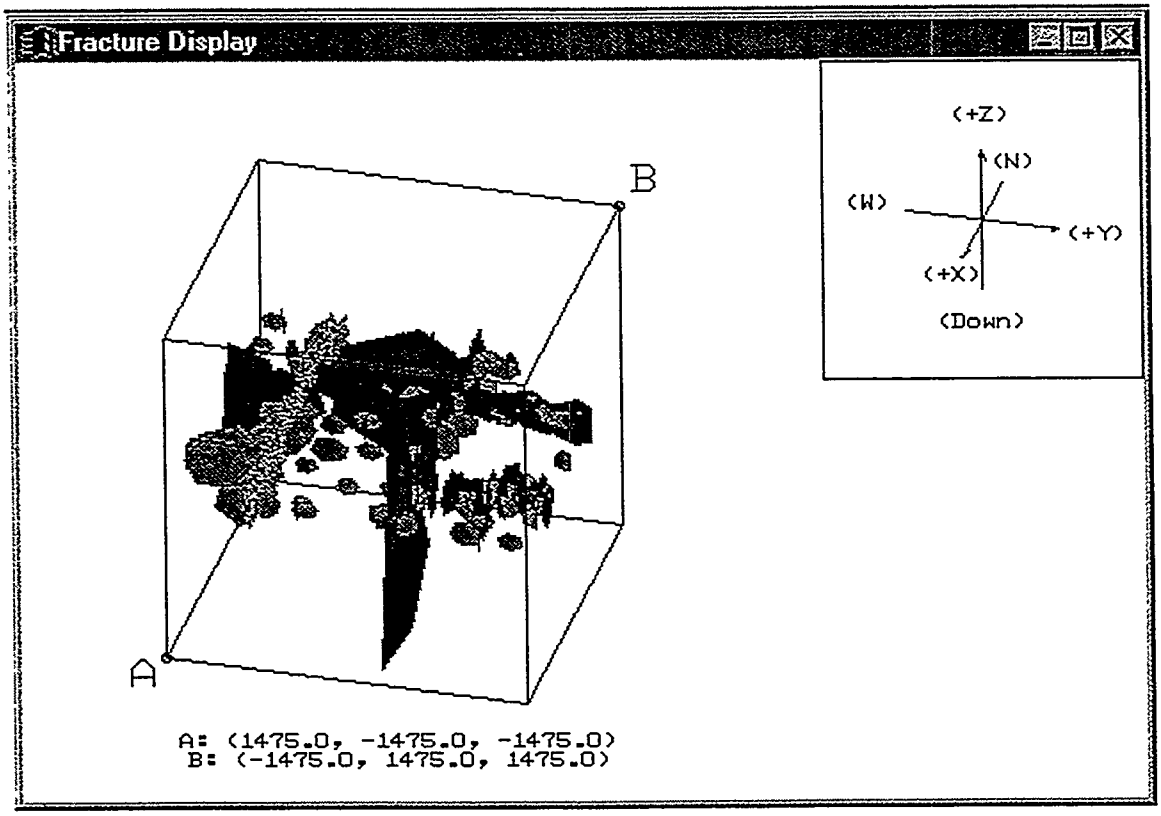

FIGURE **7-21**

YATES DFN FRACTURE ZONE MODEL

NIPER/FINAL REPORT/WA

PROJECT NO. 963 1357.521 DRAWING NO. 80715 DATE 9/28/98 DRAWN BY EA

Golder Associates

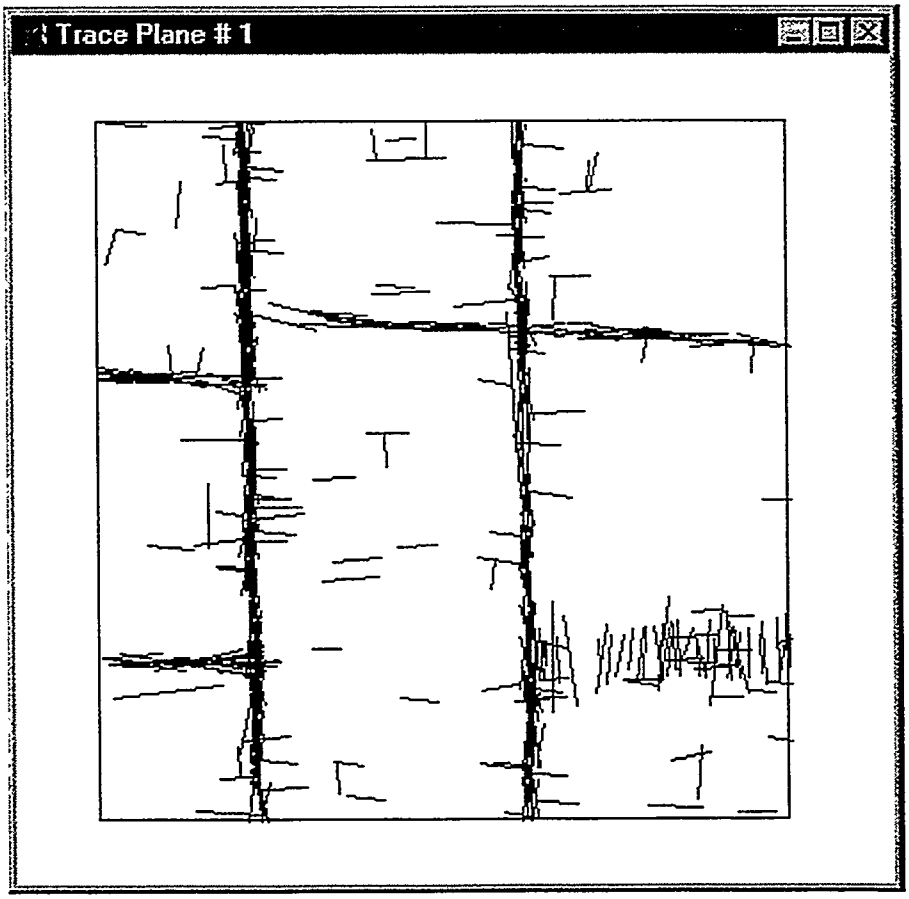

FIGURE **7-22**

2D VIEW, YATES DFN FRACTURE ZONE MODEL

NIPER/FINAL REPORT/WA

PROJECT NO. 963 1357.521 DRAWING NO. 80716 DATE 9/28/98 DRAWN BY EA

Golder Associates

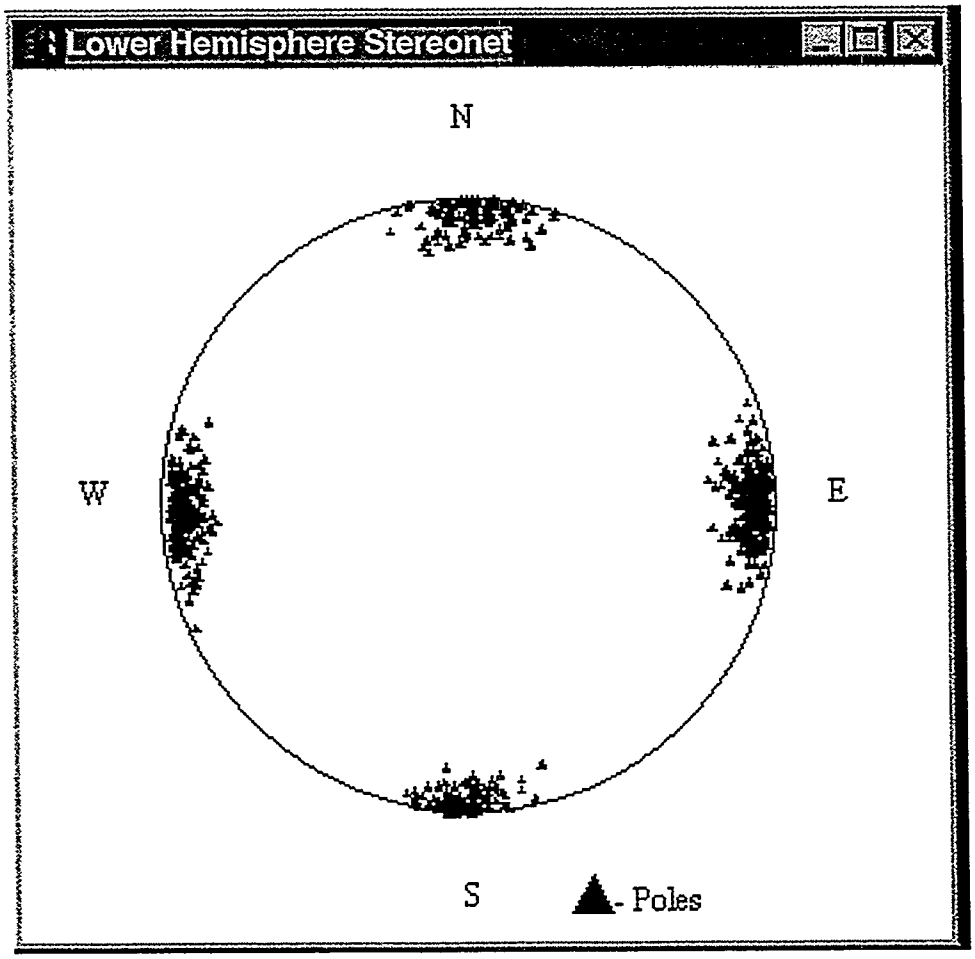

FIGURE **7-23**
STEREOPLOT OF FRACTURES, YATES DFN FRACTURE ZONE MODEL
NIPER/FINAL REPORT/WA

Fracture zone architecture is both variable and complex, and is a subject of much current research worldwide in both petroleum reservoir development and nuclear waste disposal (for example, see Mazurek et al., 1995; Caine et al., 1996). Studies have shown that many fracture zones are composed of thousands of anastamozing discrete fractures. Many of these fractures are on the order of meters or less, and probably do not play a significant role in the regional fault zone permeability (Pusch, 1995). For this reason, the DFN model of the fracture zones only includes the larger fractures and those with a transmissivity above a threshold typical of conductive fractures in fracture zones. The analyses carried out consisted of fractures with radius greater than 75m, which also corresponds to a transmissivity greater than 0.00075 m^2/s.

Table 7-4 Yates Field Reference DFN Fracture Zone Model

		Set 1	Set 2	Set 3	Set 4	Set 5	Set 6	Set 7	Set 8
Slab Region	(L,W,H) (m)	2955, 40 ,150	2955, 40, 150	2324, 40, 50	647, 40, 150	1125, 40, 150	668, 40, 150	2950, 2950, 100	2950, 2950, 101
Slab Orientation	(Trend, Plunge)	179,0	179,0	273,0	93,0	269,0	88,0	0,0	0,1
Slab Origin	(X,Y,Z) (m)	-1475, -856, 0	-1475, 318, 0	-543, 1475 ,0	-415 -1475, 0	759, 1475, 0	818, -1475, 0	1475, 0, 0	1475, 0, 1
Mean Pole	(Trend, Plunge)	269,0	269,0	183,0	183,1	269,0	178,0	0,0	90,0
Dispersion	Fisher Distrib K	70	70	70	70	70	70	85	65
Mean Radius	(m)	100	100	100	100	100	100	40	32
Radius StDev	(m)	45	45	45	45	45	45	23	17
Min Radius	(m)	75	75	75	75	75	75	75	75
Dir of Elong(tr,pl)	Constant	179,0	179,0	273,0	93,0	89,0	88,0	90,0	0,0
Aspect Ratio		1.2	1.2	1.2	1.2	1.2	1.2	1.2	1.2
Termination %		35	35	35	35	35	35	70	85
Intensity P_{32}	(m^2/m^3)	0.5	0.5	0.5	0.5	0.5	0.5	0.00425	0.000877

7.2.2.1 Compartmentalization Analysis

Compartmentalization analysis for the reference DFN are summarized in Table 7-5. Out of a total of approximately 600 fractures in the 2950 ft by 2950 ft by 100 ft reservoir block, FraCluster found 49 networks. The distributions of compartment volume and horizontal plane projection area by the convex hull algorithm are given in Figure 7-24.

Figure 7-24 Compartment Analysis for Yates DFN Fracture Zone Model

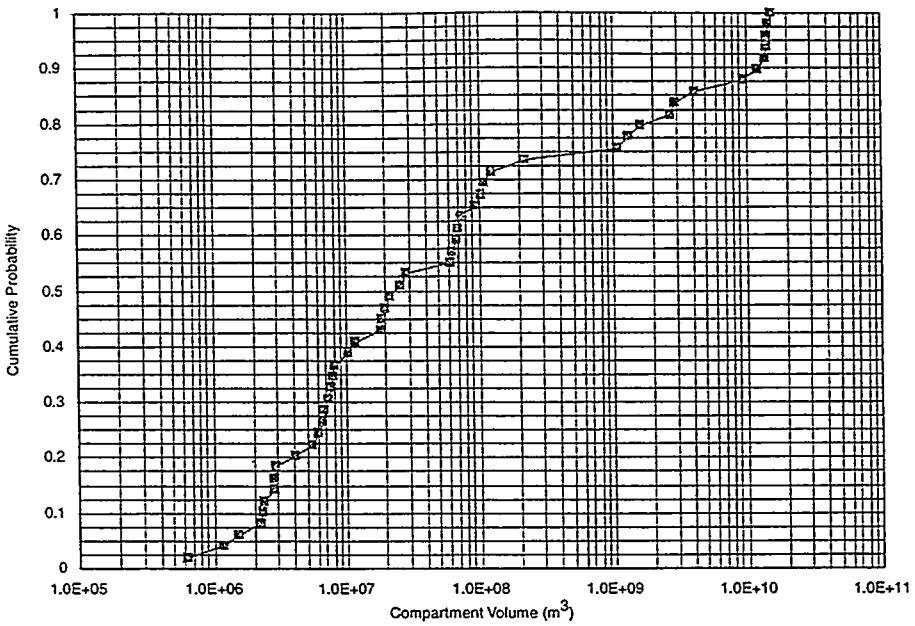

(a) Cumulative Density Function for Compartment Volume

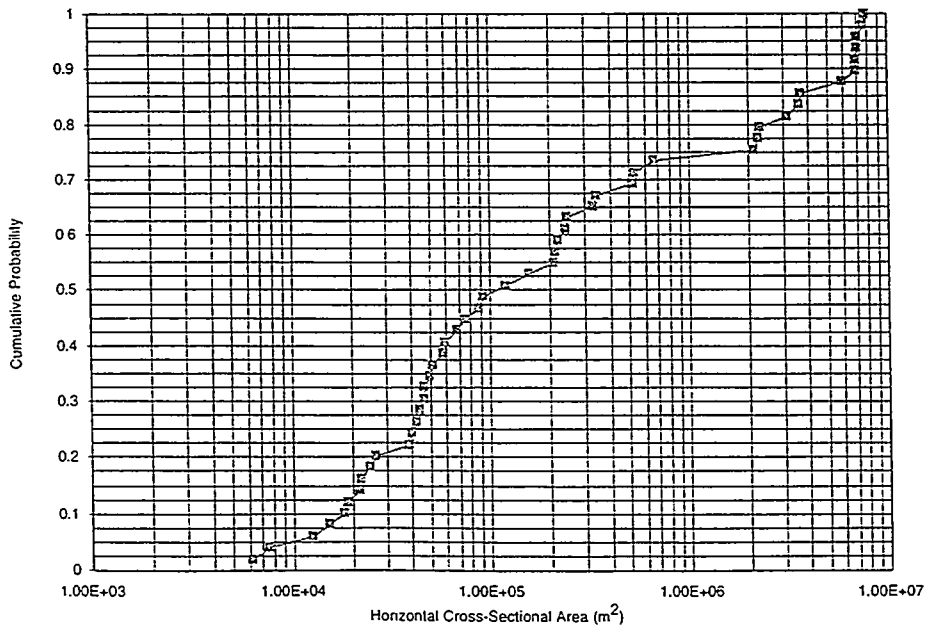

(b) Cumulative Probability Density for Cross Sectional Area

FIGURE **7-24**
COMPARTMENT ANALYSIS FOR YATES DFN FRACTURE ZONE MODEL
NIPER/FINAL REPORT/WA

PROJECT NO 953 1357 521 DRAWING NO. 80718 DATE 9/28/98 DRAWN BY EA

Golder Associates

Table 7-5 Statistics for Reservoir Compartments by Convex Hull Algorithm

	Area (m^2)	Volume (m^3)
Mean	1.44E+06	2.23E+09
Standard Error of Mean	3.54E+05	6.80E+08
95% Confidence Level on Mean	7.11E+05	1.37E+09
Median	1.19E+05	2.60E+07
Standard Deviation	2.48E+06	4.76E+09
Sample Variance	6.13E+12	2.26E+19
Kurtosis	1.29E+00	2.69E+00
Skewness	1.67E+00	2.07E+00
Minimum	6.17E+03	6.23E+05
Maximum	7.66E+06	1.54E+10

7.2.2.2 Drainage Volume Analysis

Drainage volume analysis was performed for a well intersecting the DFN model of the fracture zone. The majority of the fractures were connected to the well directly or through other fractures. Figure 7-25 shows the results of the volume of matrix that could be mobilized for three values of mobilization distance. Such a graph might represent the increasing amount of mobilized matrix through time due to pressure depletion drive. The graph behaves as it should; the volume mobilized does not increase linearly with mobilization distance due to overlap between the polyhedrons.

7.2.2.3 Block Size Analysis

Block size analysis was carried out using both the multi-directional spacing algorithm (MDS) and the convex hull algorithm (CH). The results are summarized in Tables 7-6 and 7-7. The tables indicate that the MDS algorithm estimates mean blocks that are about an order of magnitude bigger than the CH algorithm. The higher standard deviation for the MDS algorithm together with the larger block size estimate suggests that the actual blocks have correlated dimensions. Regression analysis on the dimensions yields a R^2 on the order of 0.25. This suggests that the MDS algorithm will somewhat overestimate matrix block variability, and underestimate the maximum block size. Cumulative probability plots for volume, surface area, sigma factor and Z-dimension are shown for both algorithms in Figures 7-26 through 7-33.

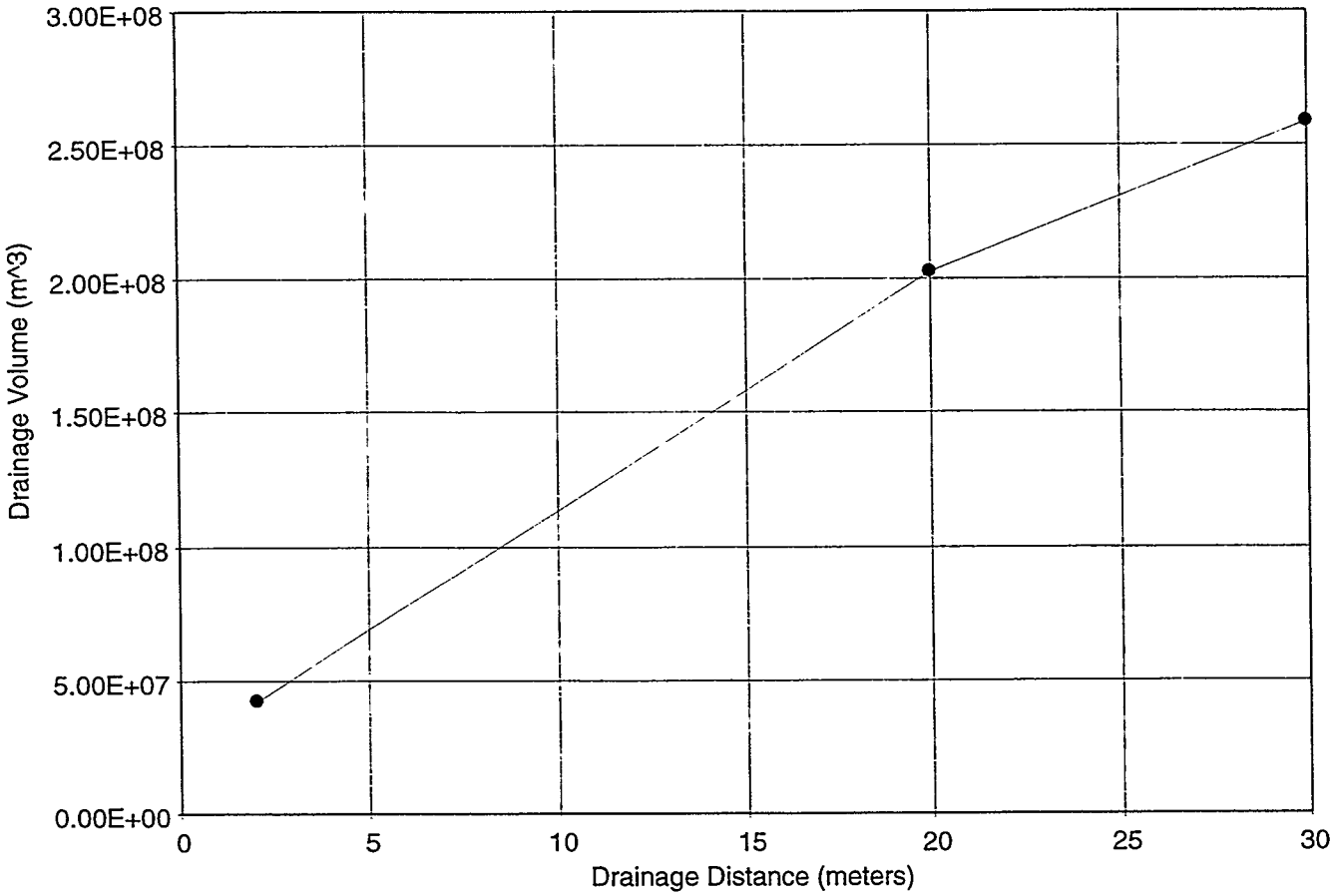

FIGURE **7-25**
ESTIMATED TRIBUTARY VOLUME VS. DRAINAGE DISTANCE
NIPER/FINAL REPORT/WA

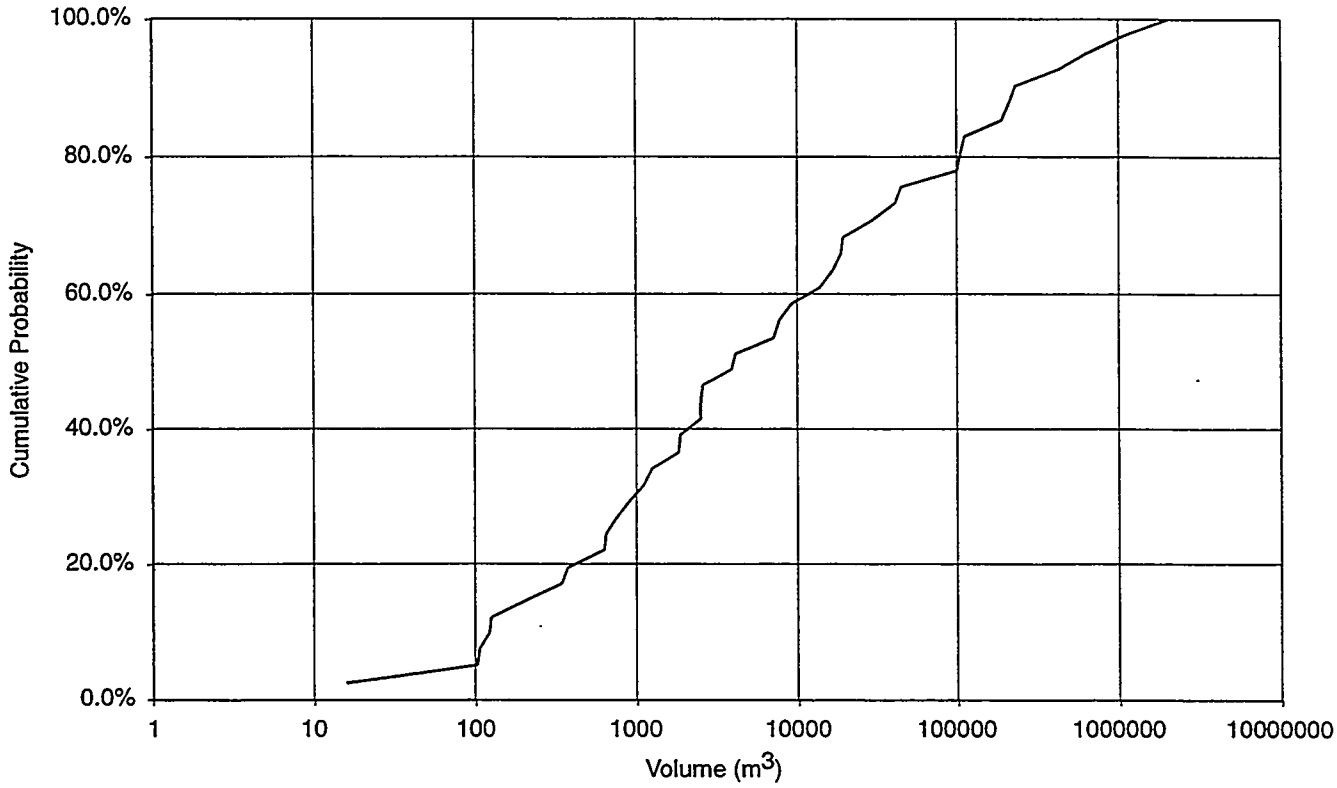

FIGURE **7-26**
DISTRIBUTION OF BLOCK VOLUME, MDS ALGORITHM
NIPER/FINAL REPORT/WA

PROJECT NO. 963 1357.521 DRAWING NO. 80720 DATE 9/28/98 DRAWN BY EA

Golder Associates

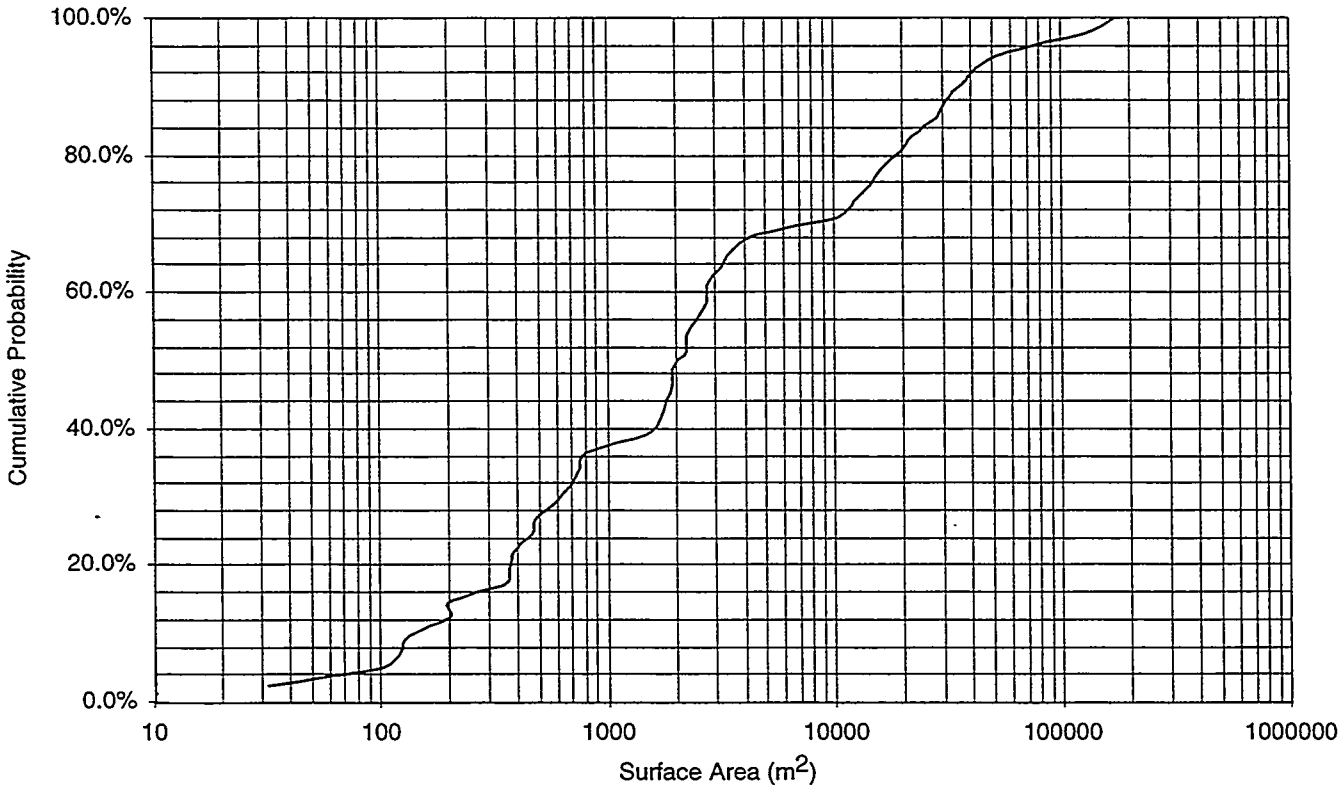

FIGURE **7-27**
DISTRIBUTION OF SURFACE AREA, MDS ALGORITHM
NIPER/FINAL REPORT/WA

PROJECT NO. 963 1357.521 DRAWING NO. 80721 DATE 9/28/98 DRAWN BY EA

Golder Associates

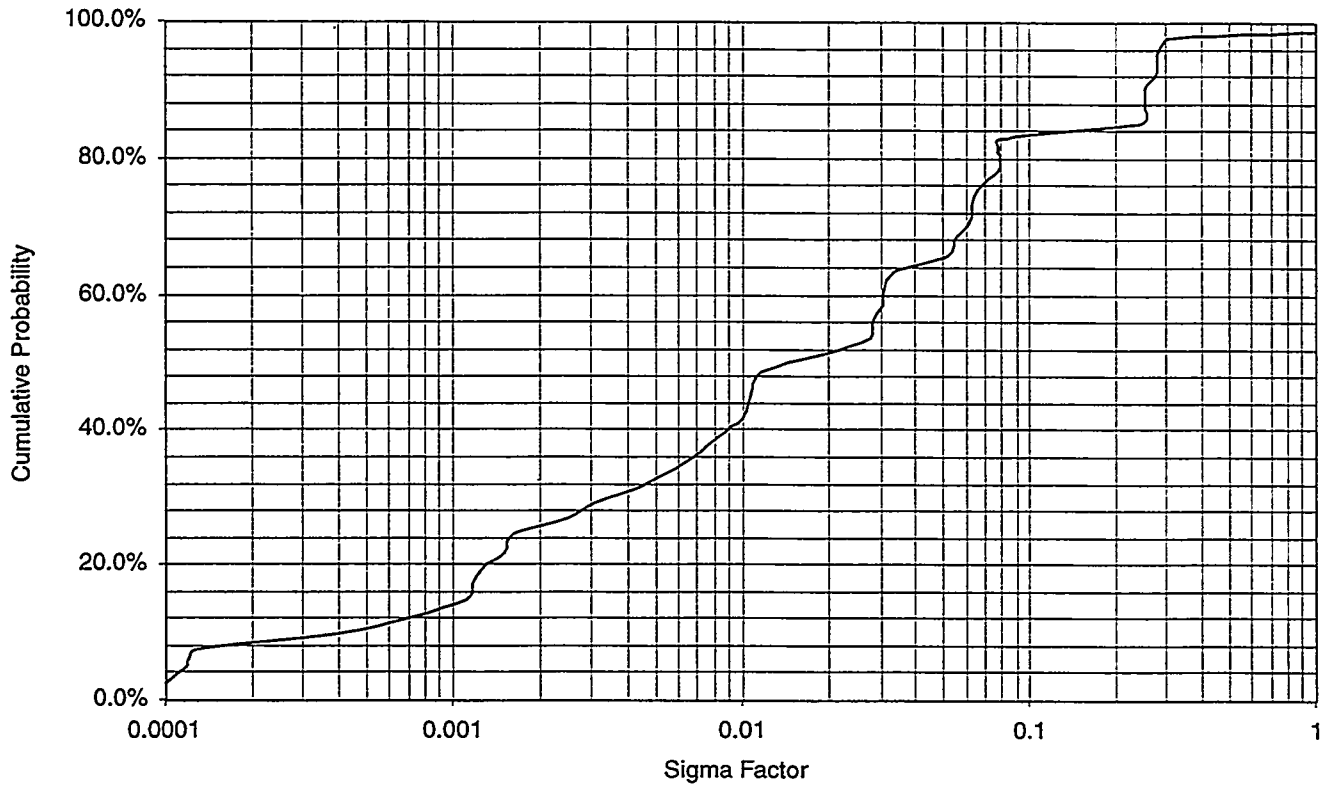

FIGURE **7-28**
DISTRIBUTION OF SIGMA FACTOR, MDS ALGORITHM
NIPER/FINAL REPORT/WA

PROJECT NO. 963 1357.521 DRAWING NO. 80722 DATE 9/28/98 DRAWN BY EA

Golder Associates

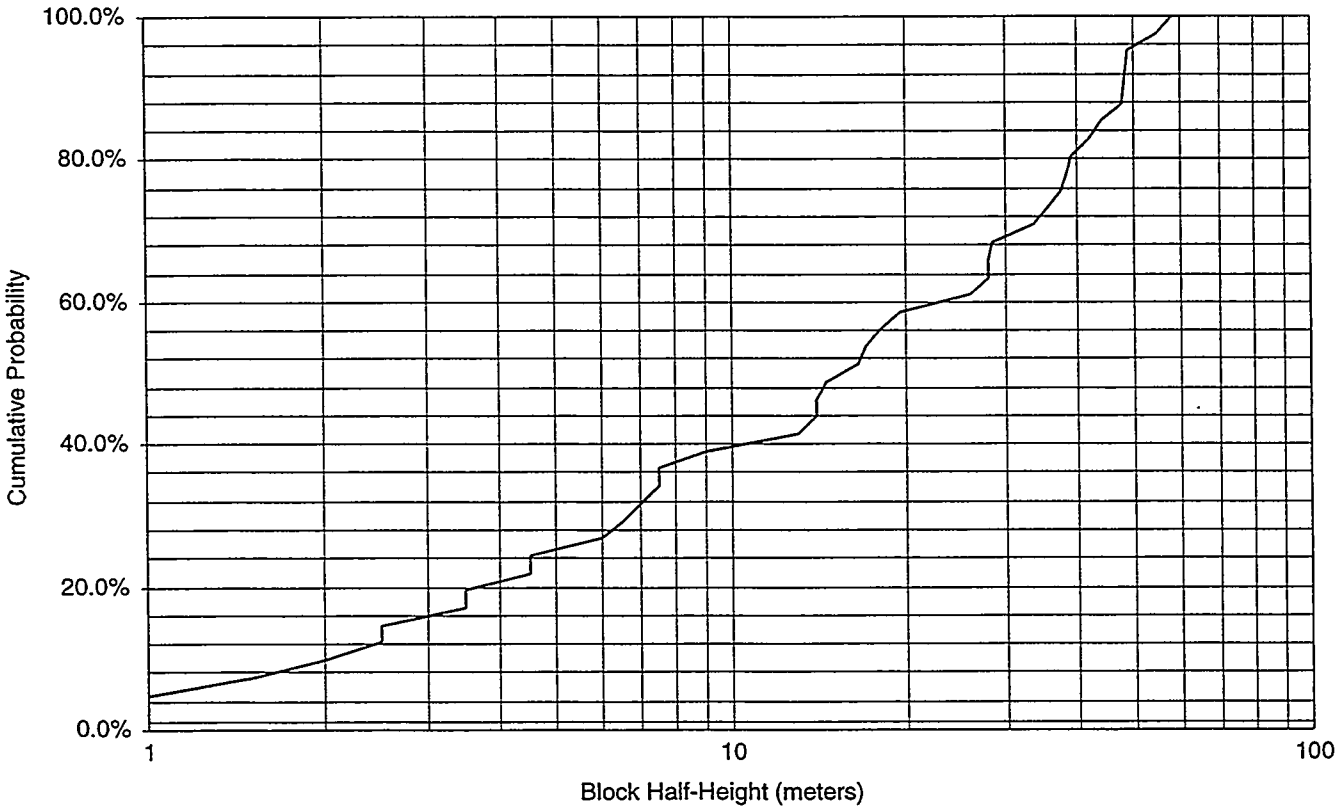

FIGURE **7-29**
DISTRIBUTION OF Z-DIMENSION, MDS ALGORITHM
NIPER/FINAL REPORT/WA

PROJECT NO. 963 1357.521 DRAWING NO. 80723 DATE 9/28/98 DRAWN BY EA

Golder Associates

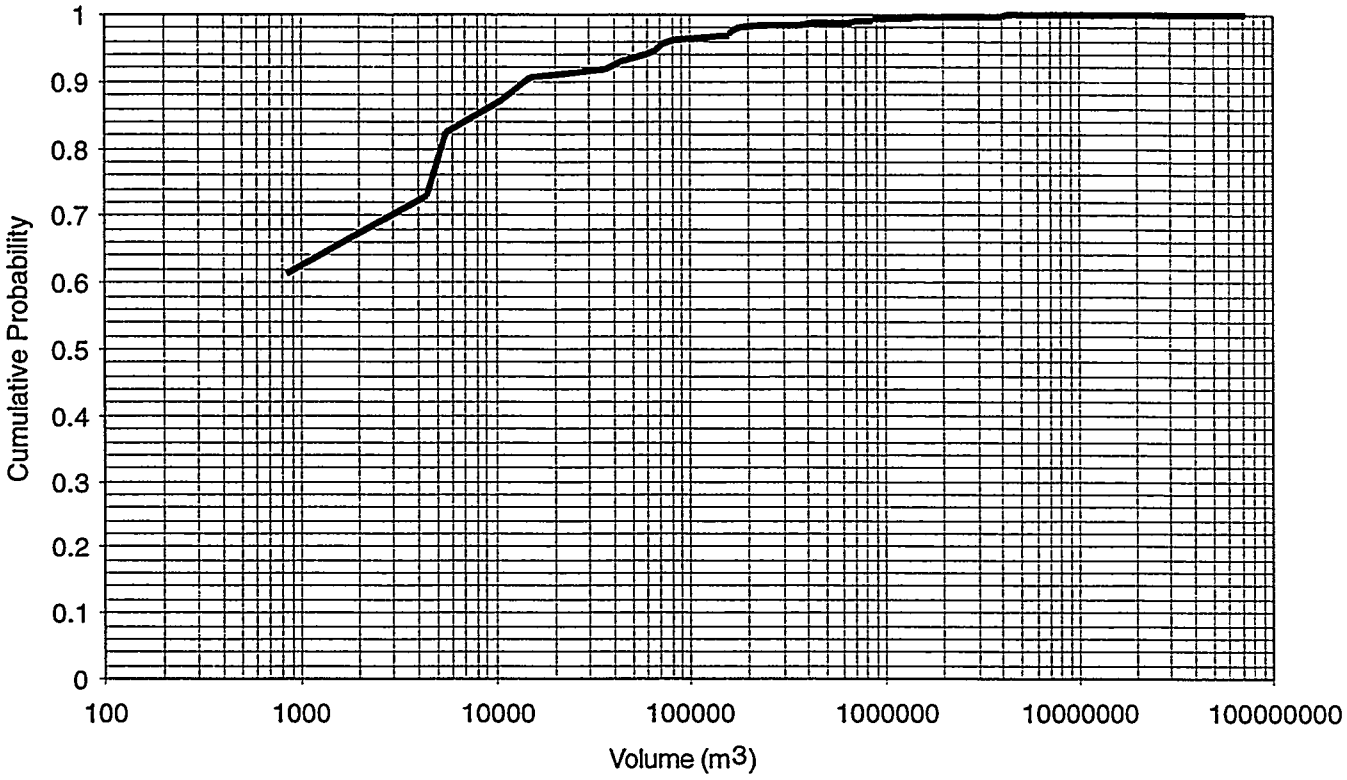

FIGURE **7-30**
DISTRIBUTION OF BLOCK VOLUME-CONVEX HULL ALGORITHM
NIPER/FINAL REPORT/WA

PROJECT NO. 963 1357.521 DRAWING NO. 80724 DATE 9/28/98 DRAWN BY EA

Golder Associates

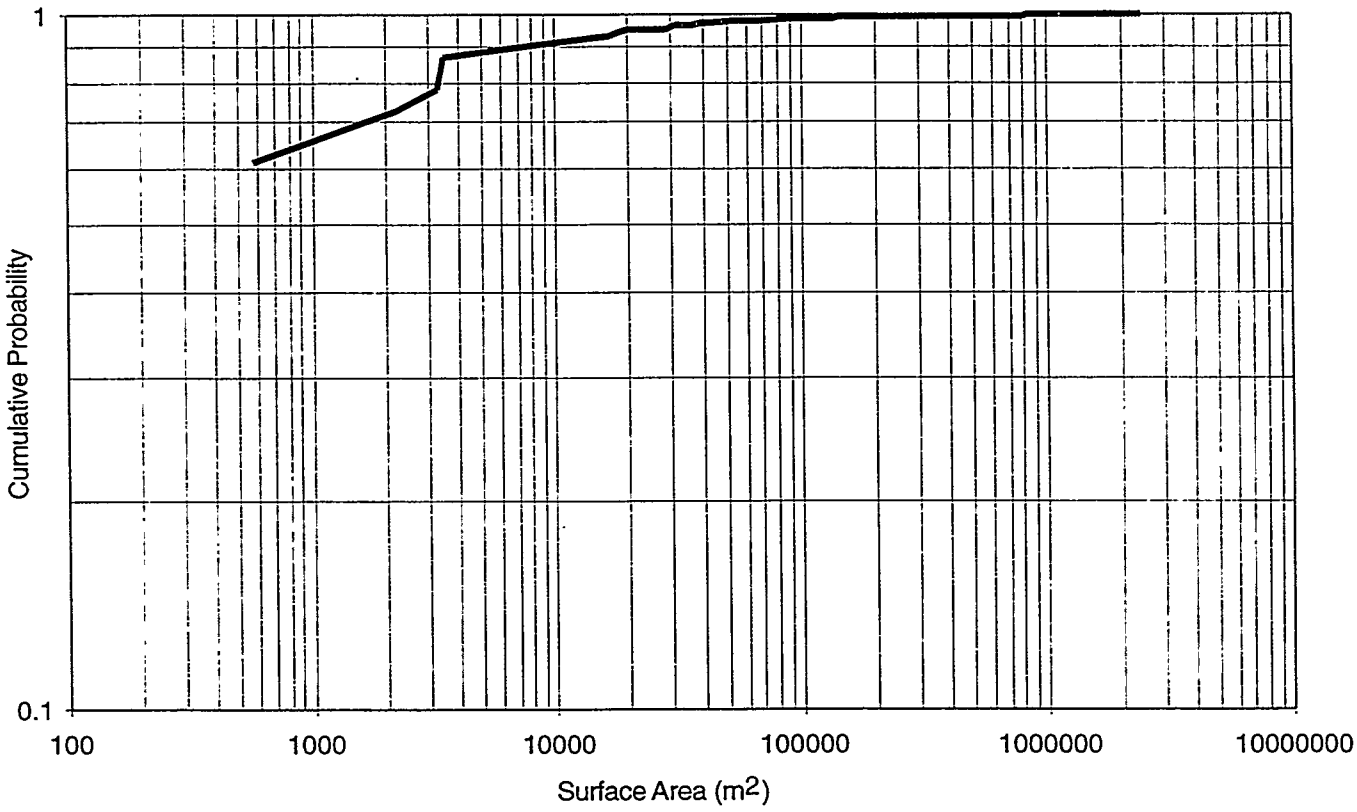

FIGURE **7-31**
DISTRIBUTION OF SURFACE AREA-CONVEX HULL ALGORITHM
NIPER/FINAL REPORT/WA

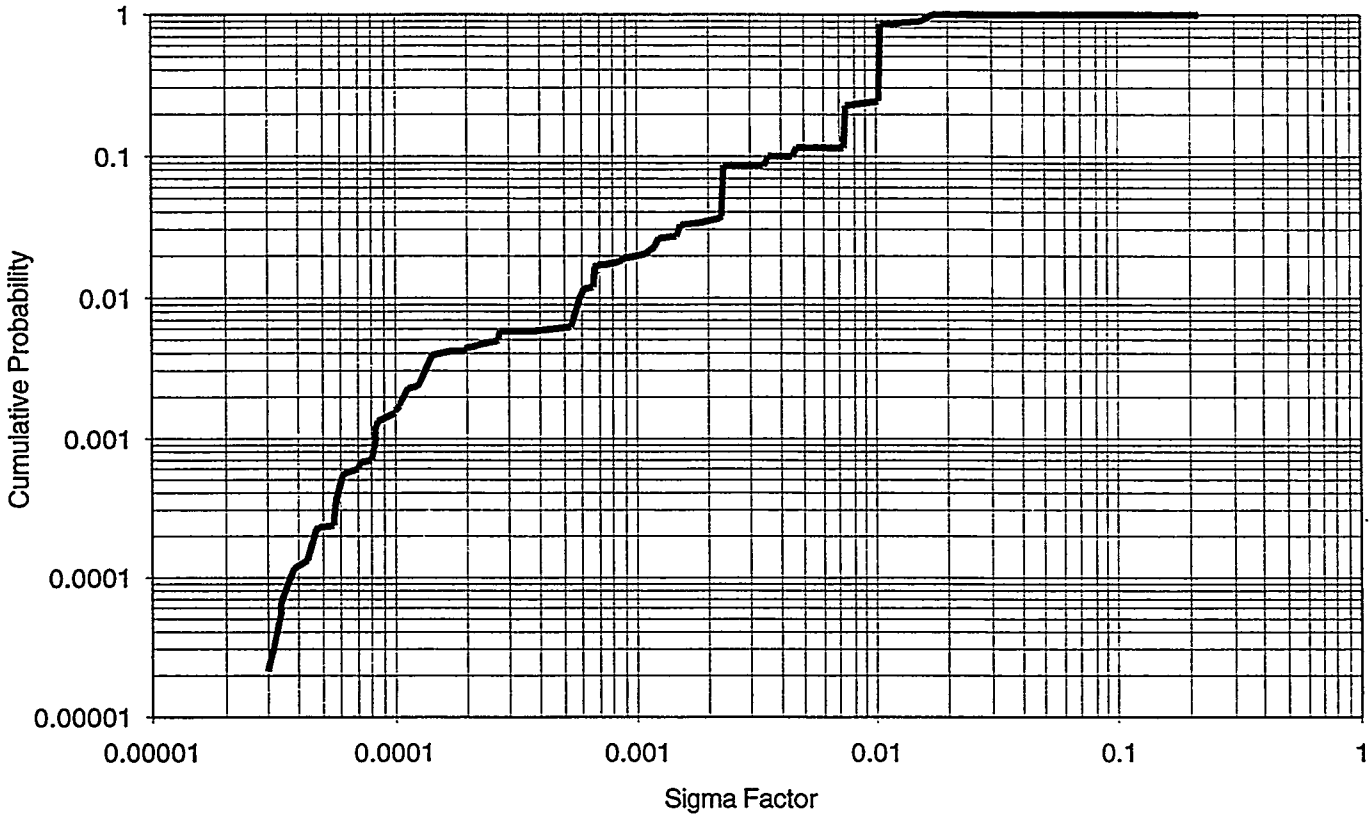

FIGURE **7-32**
DISTRIBUTION OF SIGMA FACTOR-CONVEX HULL ALGORITHM
NIPER/FINAL REPORT/WA

PROJECT NO. 963 1357.521 DRAWING NO. 80726 DATE 9/28/98 DRAWN BY EA

Golder Associates

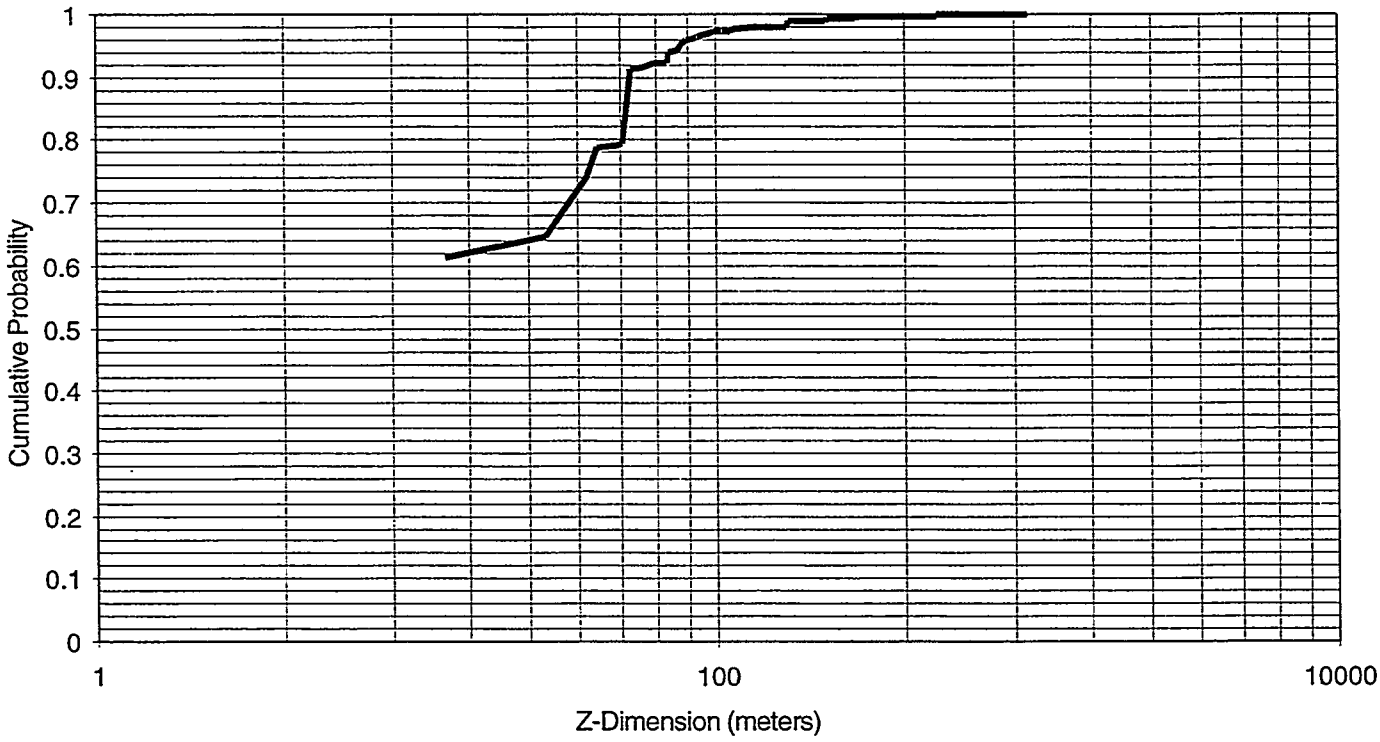

FIGURE **7-33**
DISTRIBUTION OF VERTICAL BLOCK DIMENSIONS-CONVEX HULL ALGORITHM
NIPER/FINAL REPORT/WA

Table 7-6 Block Size Statistics from MDS Algorithm

	Volume	Surface Area	Sigma Factor σ	Z-dimension
Mean	1.32E+05	1.53E+04	0.67	21.52
Median	4.15E+03	2.23E+03	0.02	16.50
Standard Deviation	3.72E+05	3.40E+04	3.90	17.78
Minimum	1.60E+01	3.20E+01	0.0001	1.00
Maximum	2.07E+06	1.73E+05	25.00	58.00

Table 7-7 Block Size Statistics from Convex Hull (CH) Algorithm

	Volume	Surface Area	Sigma Factor σ	Z-dimension
Mean	4.14E+04	7.02E+03	8.95	16.25
Median	1.70E+02*	1.80E+02*	1.29*	3.76*
Standard Deviation	6.54E+04	3.53E+04	22.49	98.46
Minimum	<2.18E+02	<5.66E+02	<0.00016	<0.29
Maximum	1.69E+07	2.42E+06	160.46	661.61

*Estimated by extrapolating cumulative probability curve. Minimum values represent upper bounds.

7.3 Task 3.2.3: Software Linking

Reservoir simulation can be significantly more challenging for fractured reservoirs than it is for conventional porous media reservoirs. Issues of connectivity and heterogeneity which play a key role in fractured reservoirs are generally better addressed by discrete feature network (DFN) approach rather than simplified equivalent porous medium (EPM) approaches. The popular dual porosity (DP) approach for analysis of fractured reservoirs does not address connectivity issues, although it does add a second interacting continuum to reflect storage effects.

Despite the significant simplifications made in DP models regarding the geometry of the fracture network, they are still the leading approach in practice. The project developed algorithms to improve the interface between discrete feature network and DP models, to support the development of DP model which reflect the anisotropy, heterogeneity, and most importantly the scale dependent connectivity structure of DFN approaches. These linkages will allow the DP approach to take advantage of some of the features of the DFN approach, without requiring reservoir engineers to be extensively retrained.

Table 7-8 provides an outline of approaches developed within the project to provide a linkage between DFN and DP approaches. Note that Table 7-8 assumes that the DFN approach is being used primarily as an upscaling tool, to facilitate continuum modeling with codes such as ECLIPSE or THERM/DK. For many reservoirs, continuum modeling will not be practical at reservoir scales due to heterogeneous connectivity and

Table 7-8 Approaches for Linking DFN and ECLIPSE Models

Eclipse Model Parameter	DFN Approach	Comments
cell size	FraCluster: Compute block size distribution from DFN model	Determines the probability for a given cell (size) to contain insufficient fractures to be modeled as a continuum → change cell size or use DFN
active cell	FraCluster: Compute block size distribution from DFN model	Determines the probability for a given cell (size) to contain no fractures (inactive cell) → spatial distribution of inactive cell
fracture porosities	FracWorks: Compute fracture volume in DFN model	Based on fracture aperture distribution
directional absolute permeabilities	PAWorks: Calculate percolation probabilities and effective permeabilities from DFN model MAFIC: Simulate DFN flow in rock blocks and fracture networks connected to wells	Steady state flow through two sides of a cube initiated by constant head boundaries, other four sides are no flow boundaries, k_a is calculated from the resulting flow rate
directional relative permeabilities	PAWorks: Calculate percolation probabilities and effective permeabilities from DFN model including multi-phase effects MAFIC: Simulate multiphase DFN flow in rock blocks and fracture networks connected to wells	Steady state flow through two sides of a cube initiated by constant head boundaries, other four sides are no flow boundaries, function of k_r vs. saturation is calculated from the resulting flow rates for different saturations
matrix-fracture coupling	FraCluster: Compute typical x,y,z dimension of a matrix block, calculate S in DFN model	Based on Kazemi et al., (SPEJ(Dec 1976) 317-326)
well kh	run Oxfilet	Based on fracture intensity distribution and transmissivity distribution
well productivity/ injectivity index	FraCluster: Calculate tributary drainage volumes and compartmentalization in DFN model PAWorks: Calculate effective permeabilities from DFN model including multi-phase effects MAFIC: Simulate DFN flow in rock blocks and fracture networks connected to wells	Based on connected fracture network distribution (tributary drainage volume)

compartmentalization effects. In addition, for sub REV scales (such as a single well) , it is frequently preferable to directly model the reservoir using DFN methods such as MAFIC, PAWorks, and FraCluster.

Algorithms developed by the project to link DFN and DP models are described below for the following DP model parameters:

- optimum grid cell size
- fracture system porosity
- directional fracture system permeabilities
- matrix-fracture interaction factors (spacing, σ-Factor).
- permeability barriers
- marking of active/inactive cells
- well permeability thickness kh,
- well productivity/ injectivity index

7.3.1 Optimum Grid Size

From a discrete fracture network perspective, the optimum grid size would be one at which each grid cell is hydraulically connected to each of its surrounding grid cells. This is illustrated in Figure 7-34. At scales smaller than the optimal grid size, a significant proportion of the grid cells are not connected to their surrounding grid cells. The DP approach assumes connectivity between each grid cell and its six immediate neighbors. As a result, unless the scale is large enough to provide this level of connectivity, the hydraulic behavior of the DFN and DP representations are quite different.

To ensure that the grid cell size in the DP approach is large enough, a series of grid cells systems at a range of sizes must be specified by the user. Graph theory search is then used to determine the number of connected grid cells per grid cell for each discretization. An example of this analysis is presented in Figure 7-35.

Based on this result, the user can chose a grid cell discretization which provides an adequate level of connectivity.

The analysis of grid cell size addresses only one of a number of issues which need to be considered in selecting a grid cell size. Future research is needed to address these issues in grid specification:

- definition of permeability ellipse at grid block scale
- existence of EPM at grid block scale

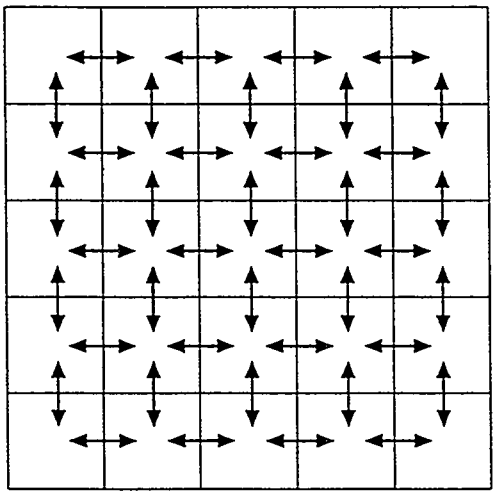

a) Continuum Model: All Neighboring Cells Connected

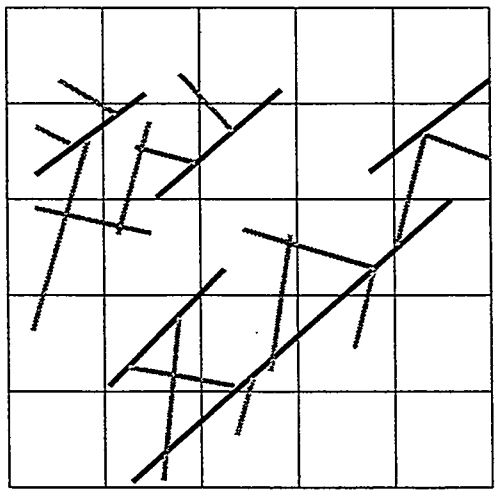

b) DFN Model: Heterogeneous Connectivity

FIGURE **7-34**
GRID CELL CONNECTIVITY
NIPER/FINAL REPORT/WA

PROJECT NO. 963 1357.521 DRAWING NO. 80783 DATE 9/28/98 DRAWN BY EA

Golder Associates

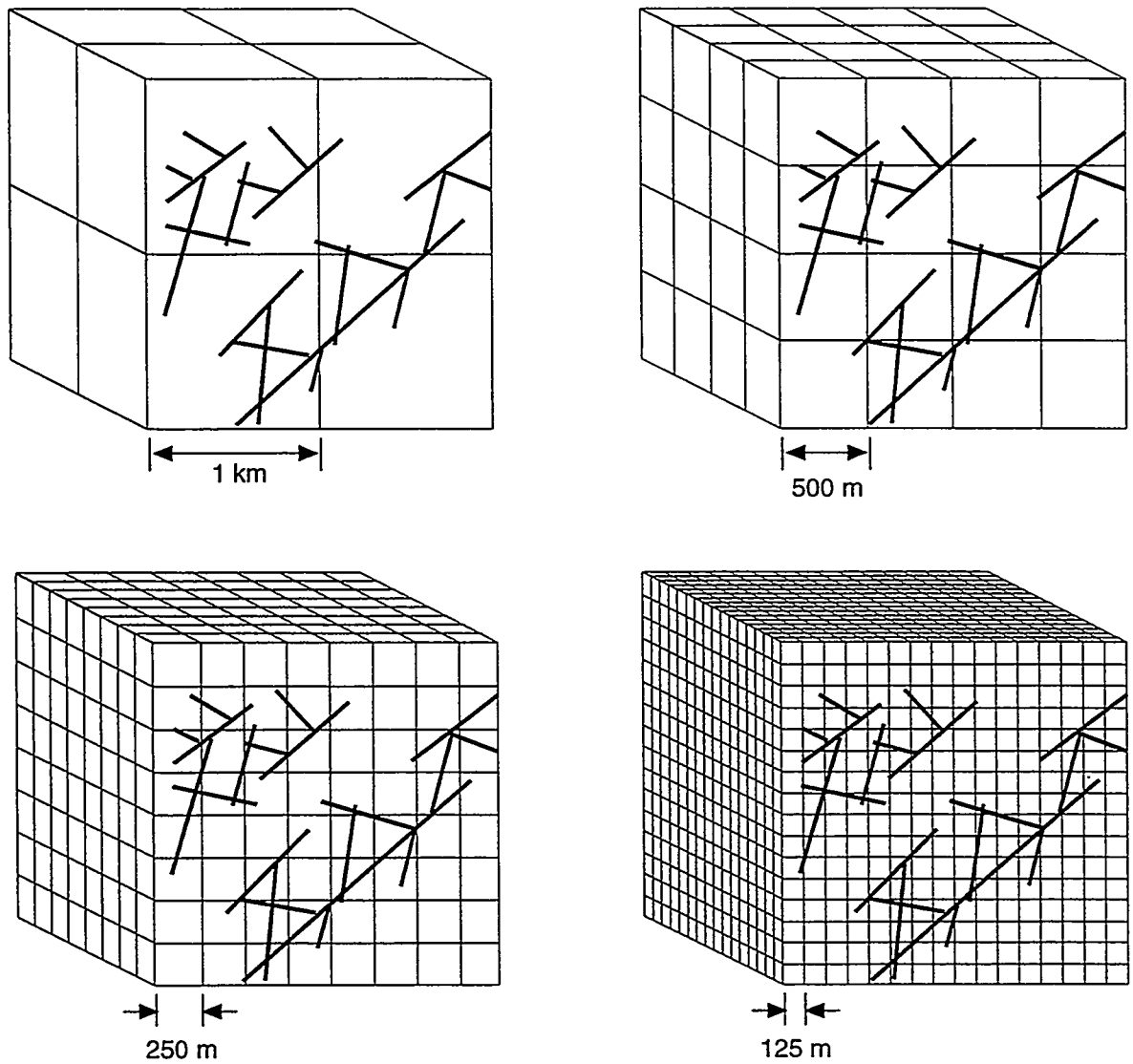

FIGURE **7-35**

GRID CELL CONNECTIVITY ANALYSIS

NIPER/FINAL REPORT/WA

PROJECT NO. 963 1357.521 DRAWING NO. 80784 DATE 9/28/98 DRAWN BY EA

Golder Associates

- stochastic field parameters
- scale dependent permeability
- scale dependent dual porosity behaviors
- compartmentalization

7.3.2 Fracture System Porosity

The fracture system porosity ϕ_F depends solely on the fracture network geometry and can be directly calculated as the product of the fracture intensity expressed as fracture area per unit volume (P_{32}) and the storage aperture of the fractures (e):

$$\phi_F = \frac{V_F}{V_{Cell}} = \frac{\sum (A_F \cdot e)}{V_{Cell}} = P_{32} \cdot e \qquad (7\text{-}13)$$

where:

ϕ_F	=	fracture system porosity
V_F	=	fracture volume, (L^3)
V_{Cell}	=	grid cell volume, (L^3)
A_F	=	fracture area, (L^2)
e	=	fracture storage aperture, (L)
P_{32}	=	fracture intensity as area per unit volume, (L^2/L^3)

No information about the continuum model is necessary to calculate ϕ_F, since it is independent of grid cell size as well as of main grid directions.

Because the fracture system porosity depends on the number of fractures per unit volume, the fracture size and the fracture aperture distribution, a different porosity has to be calculated for every area of the continuum model where these parameters differ. The fracture system porosity can be calculated for each grid cell, based on the fracturing in that cell. The primary issue in definition of fracture porosity from fracture intensity P_{32} is the selection of an appropriate measure for storage aperture e. Possible measures include:

- aperture derived from transient hydraulic response
- mechanical aperture
- aperture derived from fracture permeability or transmissivity ("cubic law")
- aperture derived from geophysical measurements (gamma density, matrix porosity)
- correlations to fracture size and orientation.

The algorithm being implemented in FracLips assumes that fracture storage aperture, *e*, is assigned to fractures primarily based on transient hydraulic response, such that it reflect the storage capacity of the fracture system rather than the mechanical aperture or the ability of the fracture to carry flow.

7.3.3 Directional Fracture System Permeability

The permeability of the fracture system depends on the fracture intensity, the connectivity of the fracture network and the distribution of fracture transmissivities. An approach for approximate solution of the fracture system permeability has been developed by Oda (1984). This approach is illustrated in Figure 7-36. The approach of Oda is as follows (following Doolin and Mauldon, 1995):

Oda (1984) starts with the orientation of each fracture in a grid cell expressed as a unit normal vector **n**. Integrating the fractures over all of the unit normals N, Oda obtained a tensor N_{ij} describing the mass moment of inertia of fracture normals distributed over a unit sphere:

$$N_{ij} = \int_{\Omega/2} n_i n_j E(\mathrm{n})\, d\Omega \tag{7-14}$$

where n_i are the components (direction cosines) of a unit normal to the fracture **n** with respect to orthogonal reference axes x_i.

For a specific grid cell with know fracture areas A_k and transmissivities T_k, an empirical fracture tensor can be obtained by adding the individual fractures weighted by their area and transmissivity:

$$F_{ij} = \frac{1}{V}\sum_{k=1}^{N} A_k T_k n_{ik} n_{jk} \tag{7-15}$$

where V is the grid cell volume and k represents the k^{th} fracture of the N fractures in the grid cell.

Oda's permeability tensor is derived from F_{ij} by assuming that F_{ij} expresses fracture flow as a vector along the fracture's unit normal. Assuming that fractures are impermeable in a direction parallel to their unit normal, F_{ij} must be rotated into the planes of permeability

$$k_{ij} = \frac{1}{12}(F_{kk} S_{ij} - F_{ij}) \tag{7-16}$$

where F_{kk} is trF_{ij}.

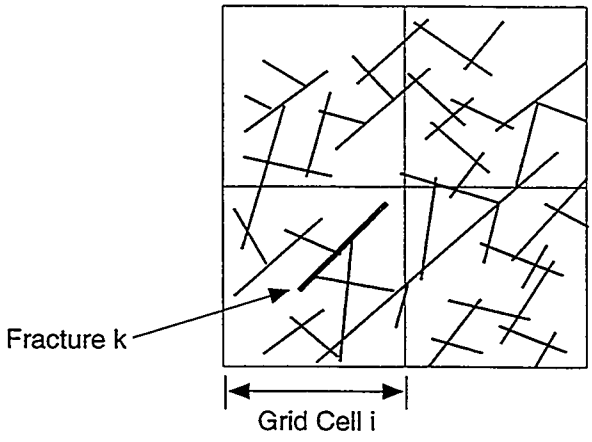

$$\underline{\underline{k}}_i = \frac{i}{V} \sum_{k=1}^{N} A_k \, T_k \, n_{ik} \, n_{jk}$$

all other fractures j in cell i

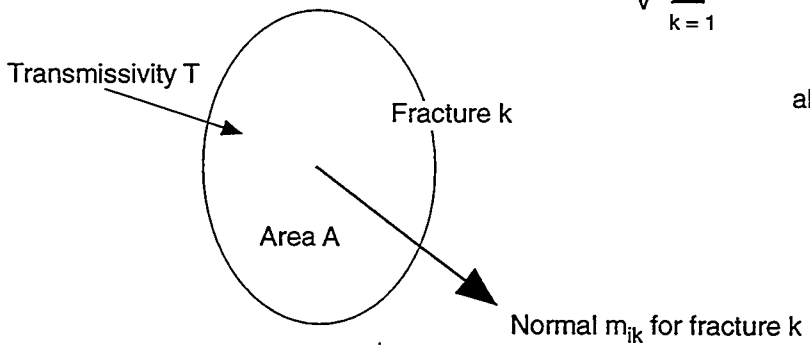

FIGURE **7-36**
ODA (1984) APPROACH FOR GRID CELL PERMEABILITY
NIPER/FINAL REPORT/WA

The Oda (1984) solution has the advantage that it can be calculated without requiring flow simulations. However, it does not take fracture size and connectivity into account, and is therefore limited to well connected fracture networks. Two alternative approaches that could be incorporated:

- pathways analysis: an approximate permeability tensor for a fracture network at a specified grid-cell scale can be obtained by carrying out a graph theory search through the network to identify the most permeable paths and to calculate their effective properties (Dershowitz et al., 1997)

- block scale flow simulation (Figure 7-37): an approximate permeability tensor for a fracture network at a specified grid-cell scale can be obtained by carrying out a series of flow simulations with boundary conditions which define unit gradients in each specified direction (see, e.g., Clemo and Smith, 1997; LaPointe et al., 1996). The key to this approach is the specification of appropriate boundary conditions. The flow solution can be obtained from DFN flow solvers such as MAFIC (Miller et al., 1997).

These approaches could be incorporated into future versions of the software.

7.3.4 Matrix-Fracture Interaction Parameters (Spacing and σ-factor)

The typical fracture spacing describes the average distance between two fractures or expressed in a different way, the average thickness of a matrix block not disturbed by fractures[1]. This parameter gives information about the average distance a fluid has to move before reaching the high permeability fracture system in which it is traveling to (or from) a well. Hence, it is a measure of the accessibility of the matrix system through the fracture system. Kazemi (1976) introduced the σ-factor, which combines average distances in three perpendicular directions to describe this characteristic of fractured reservoirs.

The typical fracture spacing and the resulting σ-factor are calculated in the exact directions of the continuum model grid to be used later. Hence, the main directions of the continuum model grid must be known at the time of this exercise. The fracture spacing is independent of the grid block size.

The average fracture spacing is related to various aspects of the fracture system (e.g., orientation, intensity). Therefore it is important to calculate these parameters for each grid cell. The calculation of fracture spacing and σ-factor is illustrated in Figure 7-38. For more information, see Dershowitz et al. (1997). These calculations will be incorporated into FracLips based on algorithms developed for FraCluster.

[1] Fracture in this context means fracture within the considered size range. The matrix itself may well include micro-fractures which often are responsible for substantial matrix permeability.

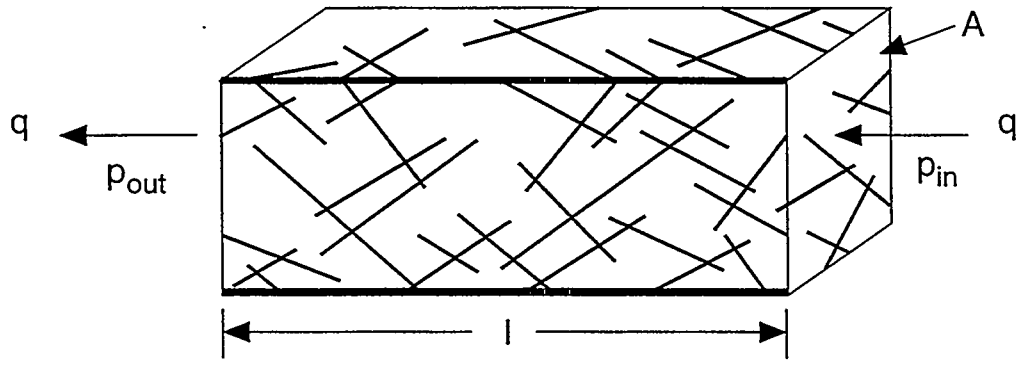

$$\Delta p = p_{in} - p_{out}$$

FIGURE **7-37**
GRID CELL PERMEABILITY BY SIMULATION
NIPER/FINAL REPORT/WA

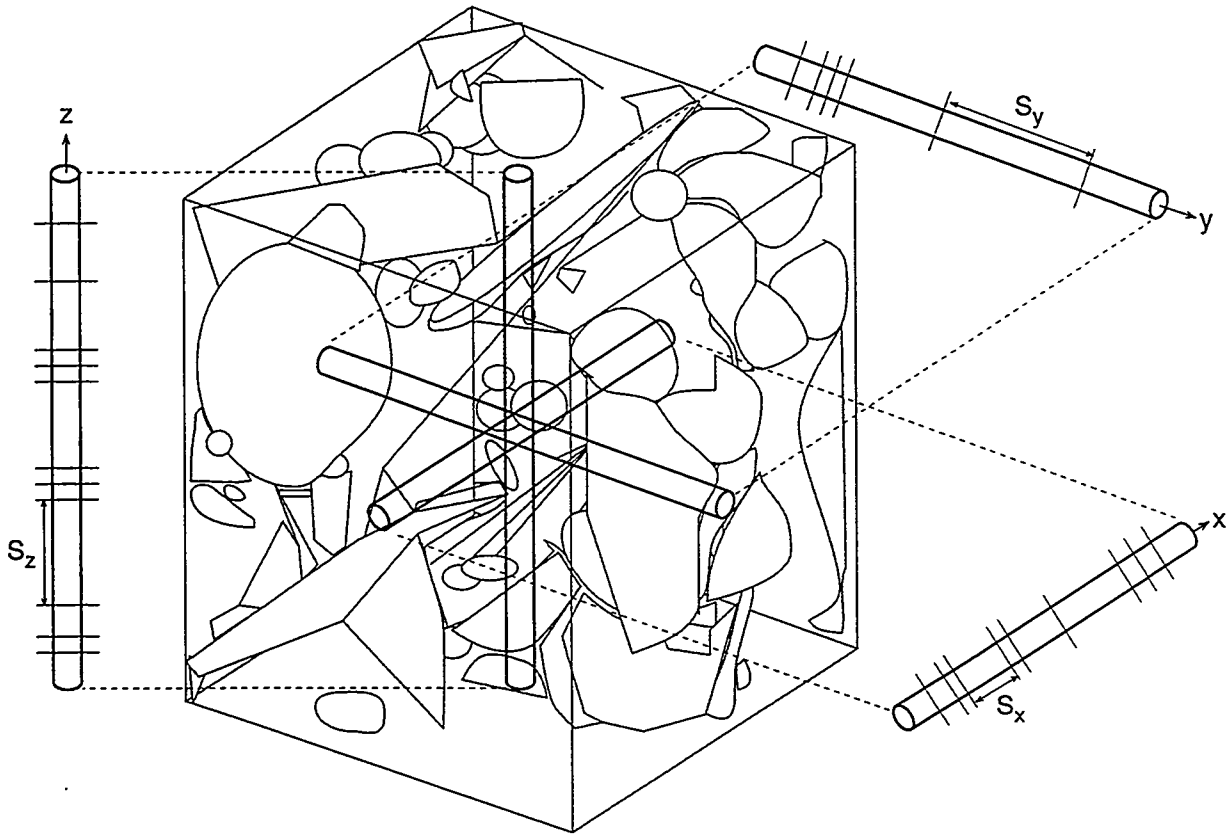

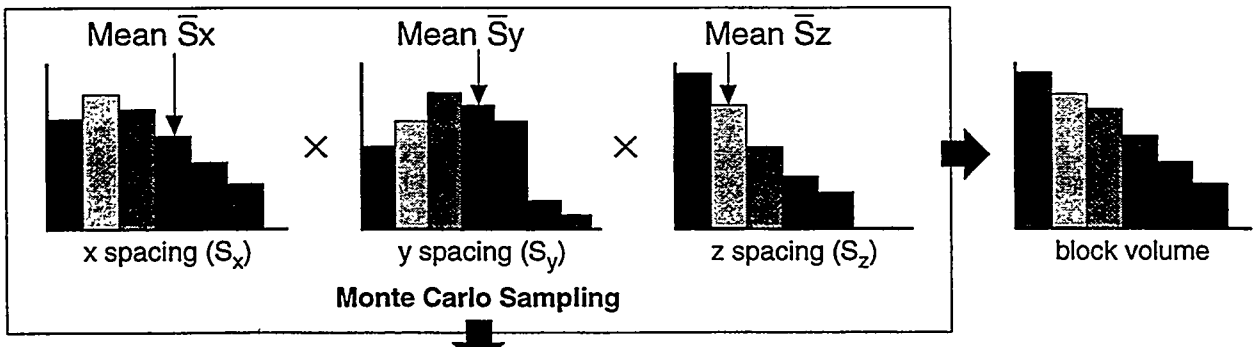

$$\sigma\text{-Factor} = 4\left(\frac{1}{\bar{S}x^2} + \frac{1}{\bar{S}y^2} + \frac{1}{\bar{S}z^2}\right)$$

FIGURE **7-38**
FRACTURE SPACING AND σ FACTOR
NIPER/FINAL REPORT/WA

PROJECT NO. 963 1357.521 DRAWING NO. 80787 DATE 9/29/98 DRAWN BY EA

Golder Associates

7.3.5 Permeability Barriers

Some DP codes, including ECLipse, allow for the effects of heterogeneous connectivity through the definition of permeability barriers. Those barriers exist between cells which are not hydraulically connected to their neighboring cell (Figure 7-39). The use of permeability barriers facilitates the analysis of compartmentalized reservoirs, and provides some of the functionality of DFN model heterogeneous connectivity.

In FracLips, permeability barriers are identified by carrying out graph theory analysis of each grid cell to determine which neighboring cells are not hydraulically connected to this cell. In the ECLipse reservoir model the transmissibility between not connected cells is then set to zero (e.g., using the MULTX keyword).

The location of permeability barriers is dependent on the realization of the discrete fracture network, i.e., in every realization the location of those barriers will be different.

7.3.6 Active/Inactive Cell

Some DP codes, including ECLipse allow for the effects of heterogeneous connectivity through the definition of "inactive" cells. Inactive cells are defined as cells which are not hydraulically connected to any of the six neighboring cells (Figure 7-39). These cells play no role in the reservoir model except to serve as flow barriers. The use of inactive cells facilitates the analysis of compartmentalized reservoirs, and provides some of the functionality of DFN model heterogeneous connectivity.

In FracLips, inactive cells are generated by carrying out graph theory analysis of each grid cell to determine which calls are not hydraulically connected to any neighboring cells. These cells can be marked as inactive for the ECLipse reservoir model.

7.3.7 Well Permeability Thickness K_h

The permeability thickness K_h (Figure 7-40) is one of the key parameter for the determination of well inflow, i.e., the 'quality' of a well connection to the reservoir. For existing wells this parameter is derived from well test analysis.

In a porous media it describes the product of the completion interval thickness and the layer permeability. In fractured reservoirs it describes the sum of fracture transmissivities, i.e., the number of fractures intersecting the well and their transmissivity.

For predictions (i.e., new well locations) this parameter is not known and therefore needs to be calculated from the simulation grid data (i.e., completion data and layer permeability). The use of DFN models allows predicting this parameter also for fractured reservoirs. Furthermore this can be done for different well locations and well directions, thus allowing the modeler to optimize well placement.

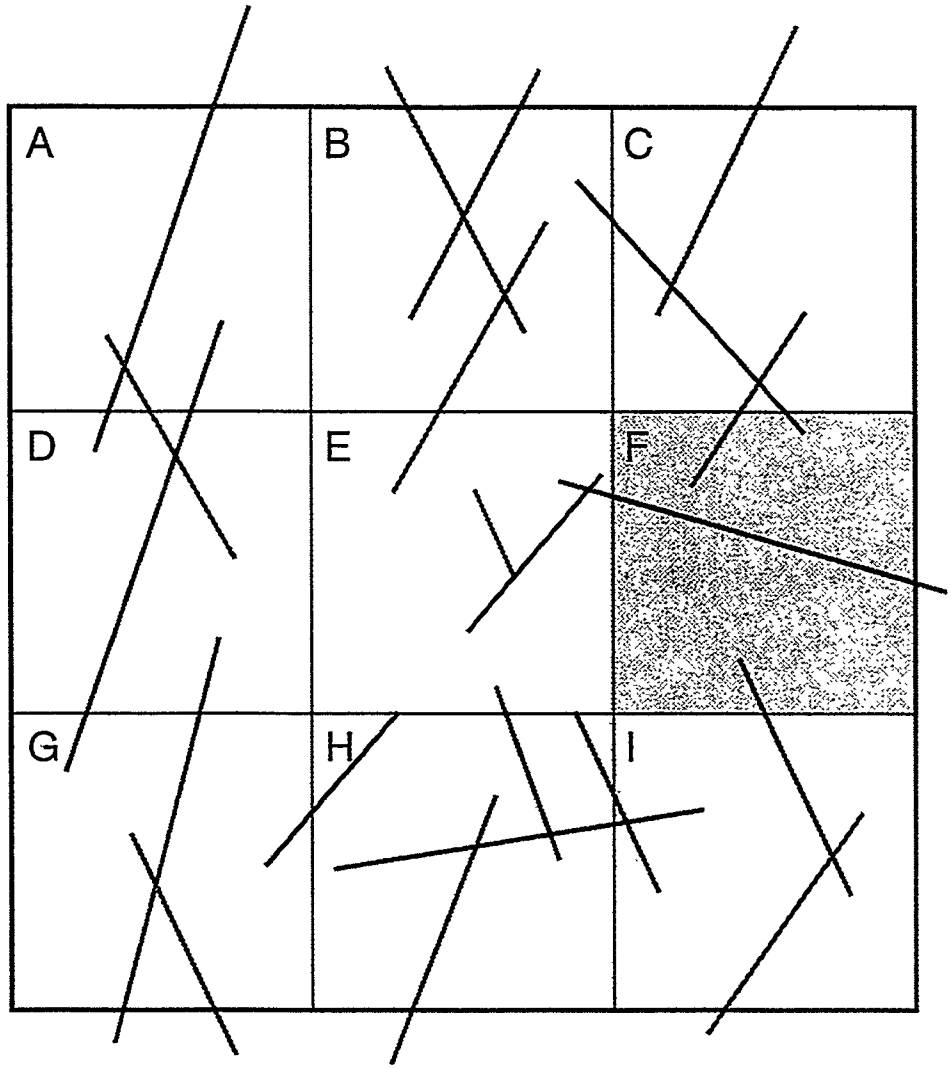

LEGEND

Cell with y-direction permeability

Cell with x-direction permeability

Inactive/permeability barrier cell

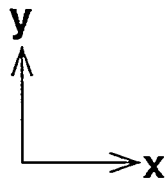

FIGURE **7-39**

INACTIVE CELLS AND PERMEABILITY BARRIERS

NIPER/FINAL REPORT/WA

PROJECT NO. 963 1357.521 DRAWING NO. 80788 DATE 9/28/98 DRAWN BY EA

Golder Associates

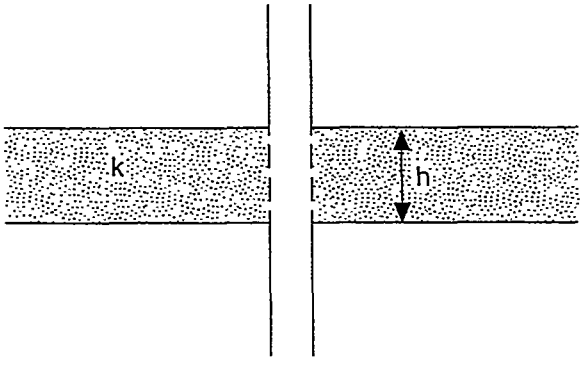

Porous Medium

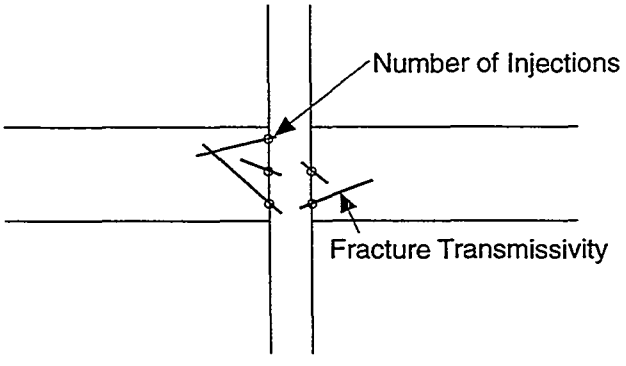

Fractured Reservoir

FIGURE **7-40**
WELL PERMEABILITY THICKNESS
NIPER/FINAL REPORT/WA

For each new well connection the number of fracture intersections is computed by FraClips. The transmissivities of the intersecting fractures is then used to calculate the well K_h. Note that this parameter is derived strictly from geometry, i.e., no flow modeling is carried out. Moreover this parameter does not take into account the connectivity of the fracture network around the well (flow dimension). This can be done by calculating the wells productivity or injectivity index.

7.3.8 Well Productivity/Injectivity Index

The well productivity/injectivity index (Figure 7-41) is used to describe the connection between a well and the reservoir. The steady state index is defined as:

$$J = Q / \Delta p \tag{7-17}$$

where:

Q =production/injection rate
Δp = pressure difference between well and reservoir.

For existing wells this parameter can be measured and it is often used directly in ECLipse to model well performance. For predictions (i.e., new well locations) this parameter is not known and therefore calculated from the existing grid data (e.g., permeability). The use of DFN models allows predicting this parameter for every location and well direction in the model. This is done by simulating steady state production or injection tests with MAFIC.

This approach involves the use of flow simulations and therefore is much more time consuming than calculating the well K_h. It does, however, take the fracture network connected to the well (flow dimension) into account.

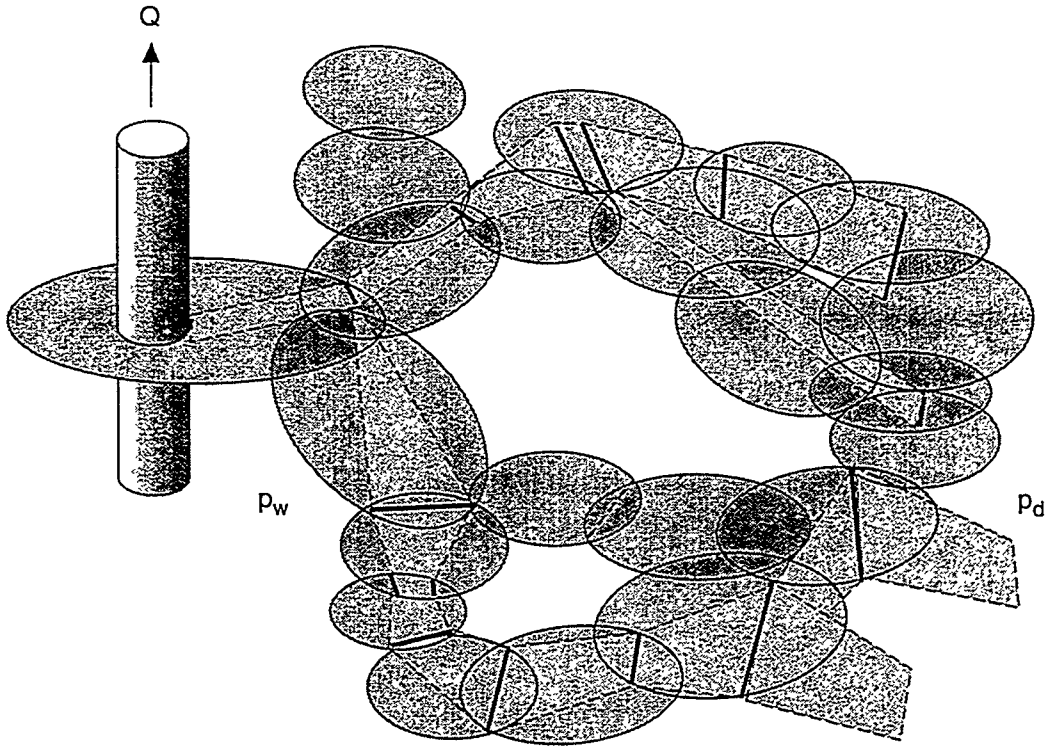

$$\Delta p = p_d - p_w$$

FIGURE **7-41**
WELL PRODUCTIVITY/INJECTIVITY INDEX
NIPER/FINAL REPORT/WA

PROJECT NO. 963 1357.521 DRAWING NO. 80790 DATE 9/28/98 DRAWN BY EA

Golder Associates

8. TASK 4.1: RESERVOIR PERFORMANCE DATA COLLECTION

8.1 Task 4.1.1: Fracture Image Data Acquisition

Throughout the year, Marathon collected and processed fracture image data, and provided the data for posting on the WWW server. Over 30 Megabytes of fracture image data are now available through the project web server. Example fracture image data is illustrated in Figure 2-2.

8.2 Task 4.1.2: Well Testing Data Acquisition

Throughout the year, Marathon collected and processed well test and hydraulic response data, and provided the data for posting on the WWW server. Example well test and hydraulic responses provided by Marathon are illustrated in Figures 8-1 through 8-5.

NEXT STEP THERMAL AREA OBSERVATION WELLS
Water-Oil Contact

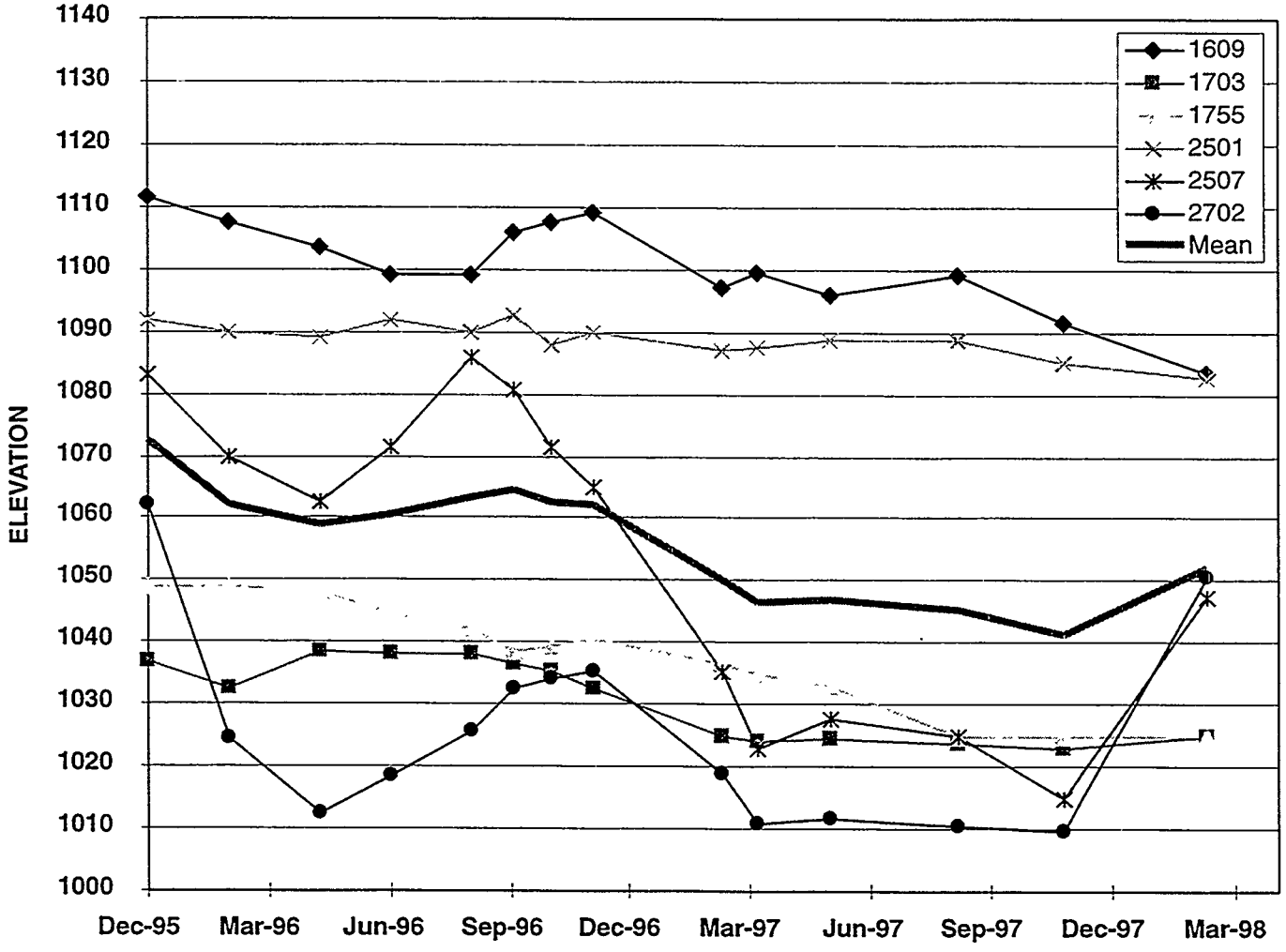

FIGURE **8-1**
WATER-OIL CONTACT
NIPER/FINAL REPORT/WA

PROJECT NO. 963 1357.521 DRAWING NO. 80804 DATE 9/28/98 DRAWN BY EA

Golder Associates

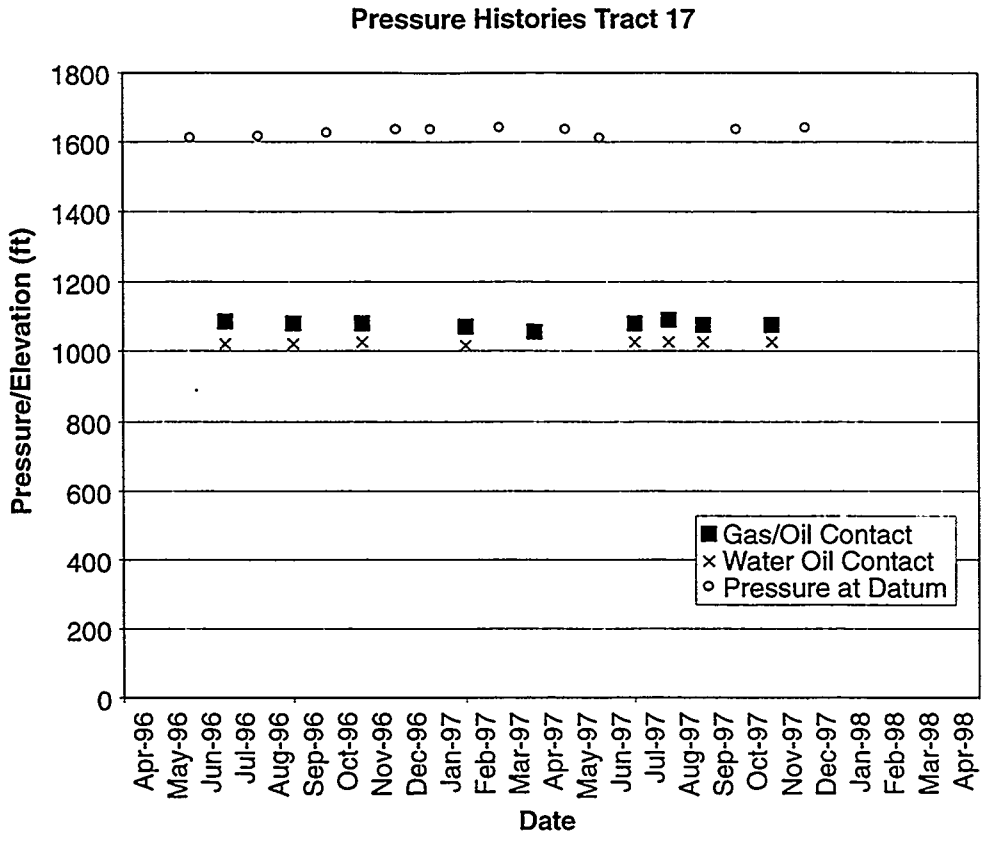

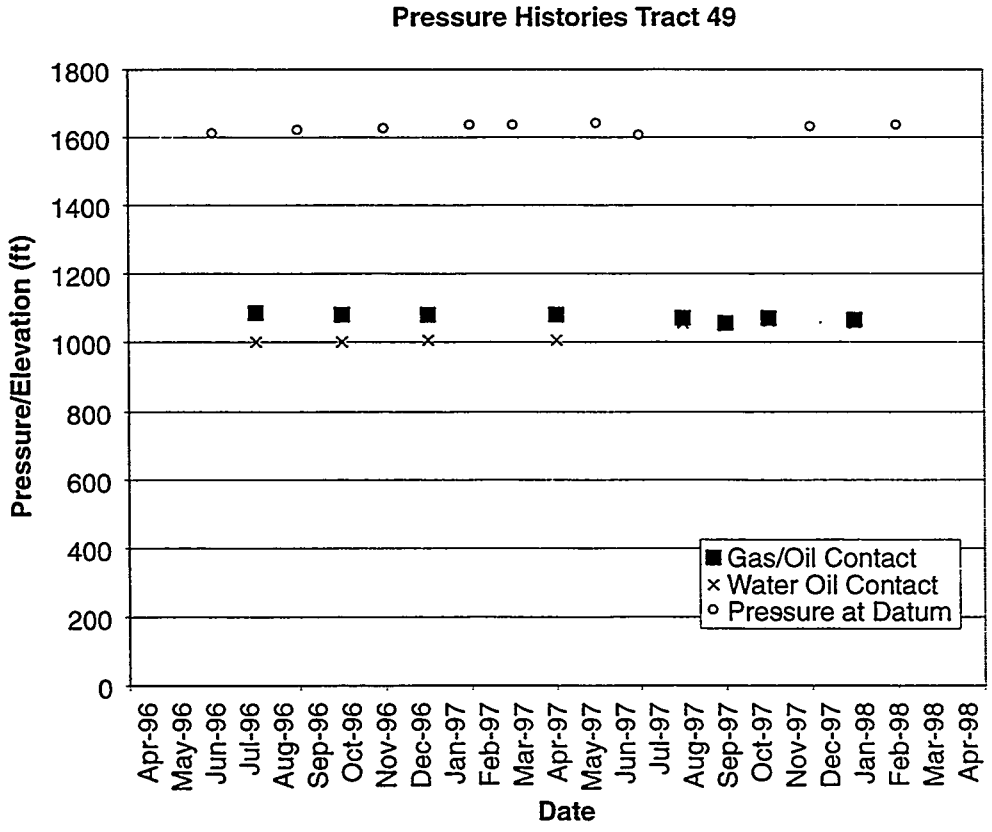

FIGURE **8-2**

TRACT 17 AND 49 WELL RESPONSE

NIPER/FINAL REPORT/WA

PROJECT NO. 963 1357.521 DRAWING NO. 80805 DATE 9/28/98 DRAWN BY EA

Golder Associates

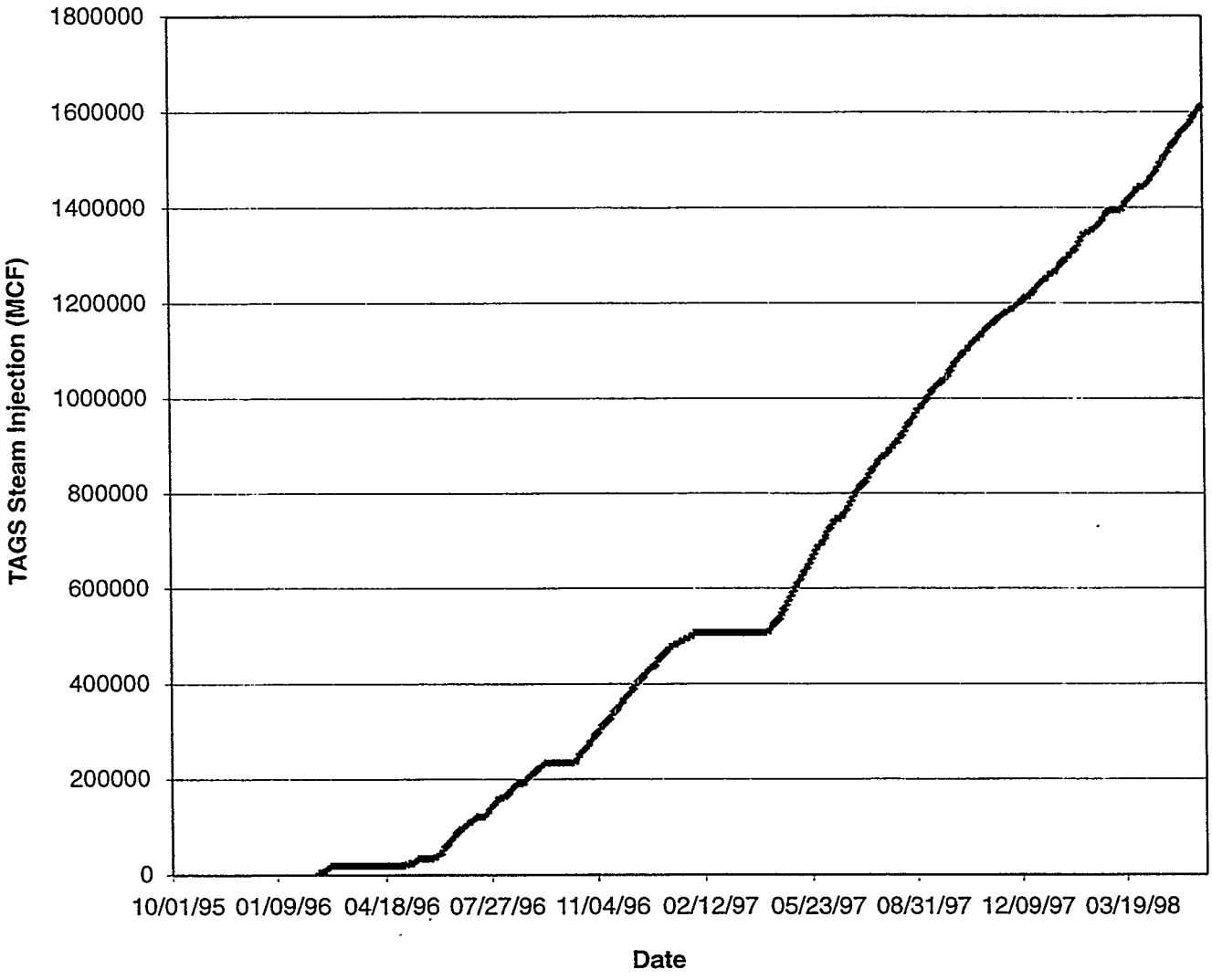

FIGURE **8-3**
CUMULATIVE STEAM INJECTION
NIPER/FINAL REPORT/WA

PROJECT NO. 963 1357.521 DRAWING NO. 80806 DATE 9/28/98 DRAWN BY EA

Golder Associates

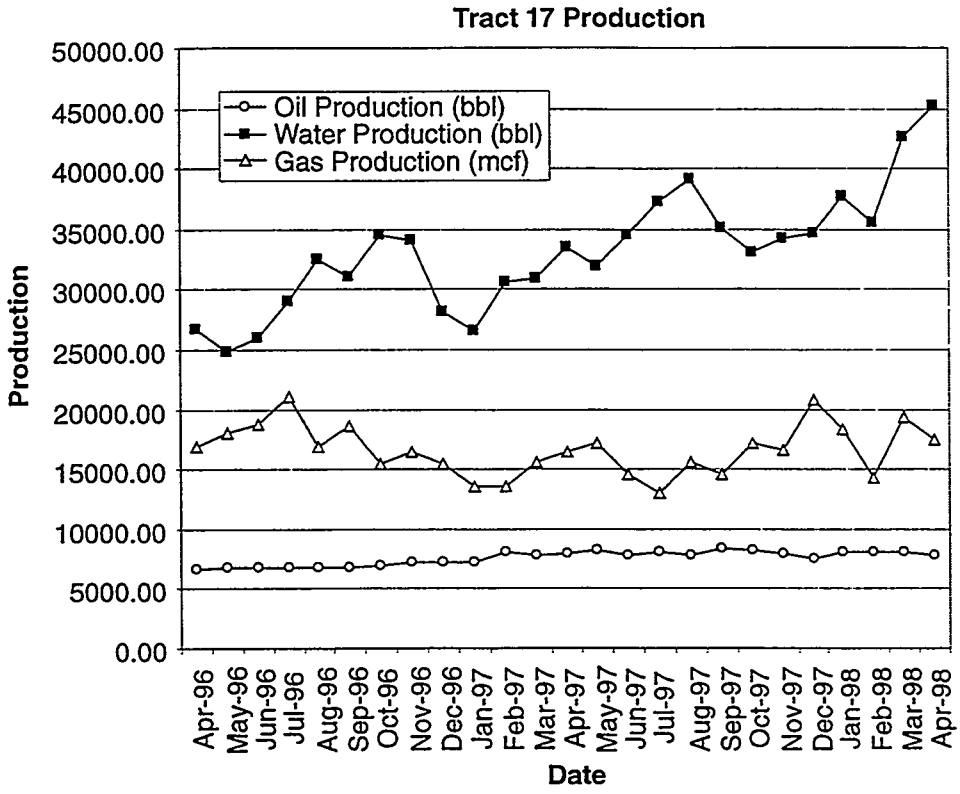

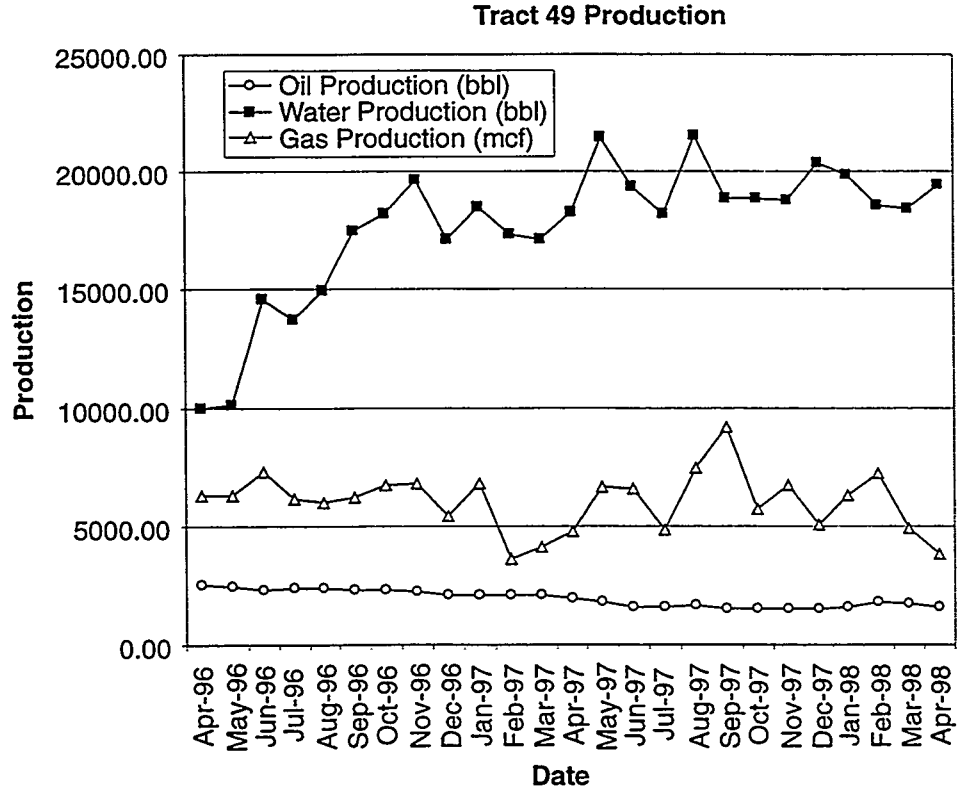

FIGURE **8-4**

TRACT 17 AND 49 PRODUCTION DATA

NIPER/FINAL REPORT/WA

PROJECT NO. 963 1357.521 DRAWING NO. 80807 DATE 9/28/98 DRAWN BY EA

Golder Associates

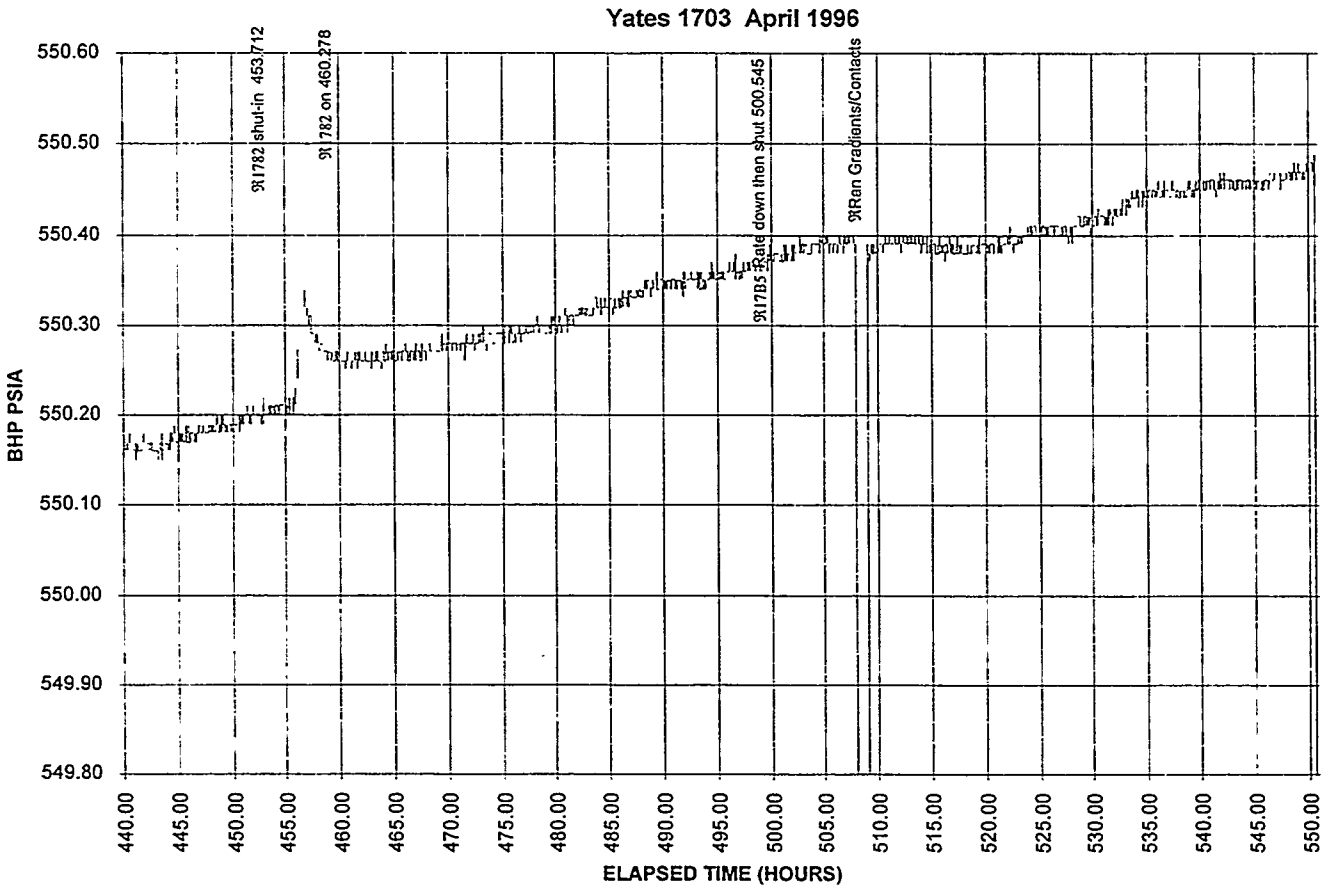

FIGURE **8-5**
TRACER TEST HISTORY
NIPER/FINAL REPORT/WA

PROJECT NO. 963 1357.521 DRAWING NO. 80808 DATE 9/28/98 DRAWN BY EA

Golder Associates

9. TASK 4.2: SIMULATION OF FRACTURED RESERVOIR PRODUCTION

9.1 Task 4.2.1: Reservoir Model Implementation

This section describes the implementation of a conditioned, stochastic DFN model of the Yates field Tract 17. This model provides the basis for Tract 17 reservoir simulations using ECLIPSE and THERM/DK (Section 9.2). The conditioned, stochastic DFN model is linked to StrataModel using the algorithms described in Section 6.1.2 to account for the effects of curvature, shale content and porosity. The model is linked to ECLIPSE using the algorithms developed in Section 7.3.

A typical realization of the conditioned Tract 17 DFN model is shown in Figure 9-1. Figure 9-2 illustrates trace patterns of one extension joint set on horizontal cross-sections through the DFN model. The parameters of the Tract 17 conditioned stochastic DFN model are provided in Table 9-1.

Table 9-1 Conditioned DFN Model for TAGS Support Simulations (Tract 17)

Parameter	Model Assumption
Discrete Features	Large scale deterministic faults located during seismic surveys are modeled deterministically. Fractures representing features located during borehole logging are modeled by conditional simulation with correlation to curvature and shale content.
Orientation Distributions	The deterministic fault orientation is taken from the interpretation of the seismic survey and all faults are assumed to be vertical. The stochastic fracture strike is correlated to curvature, and the dip is assigned using a Fisher distribution with $\kappa=8$.
Size Distribution (Stochastic Fractures)	Power Law distribution D=1.81, minimum radius = 1ft, truncated between 10m and 500 m.
Intensity (Stochastic Fractures)	Intensity of stochastic fractures P_{32} is 0.132 to 0.066 m^2/m^3, depending on shale content and porosity.
Transmissivity	Lognormal distribution, Deterministic Faults are either $5x10^{-2}$ m^2/s or $1x10^{-2}$ m^2/s depending on orientation, while stochastic fractures have log mean = -4.0 and log std.dev. = 0.75 $\log_{10}$ m^2/s.
Aperture	Correlated to fracture transmissivity using the cubic law, such that $a = 0.011T^{0.33}$.
Model Dimensions and Boundary Conditions	Model is 1900 m x 2400 m x 305 m deep. The top and bottom boundaries are defined by StrataModel surfaces at approximately elevations -15 m to 320 m. The model is oriented Northeast-Southwest, with the center at (108, 206.17 *vara* by 113, 835.81 *vara*).

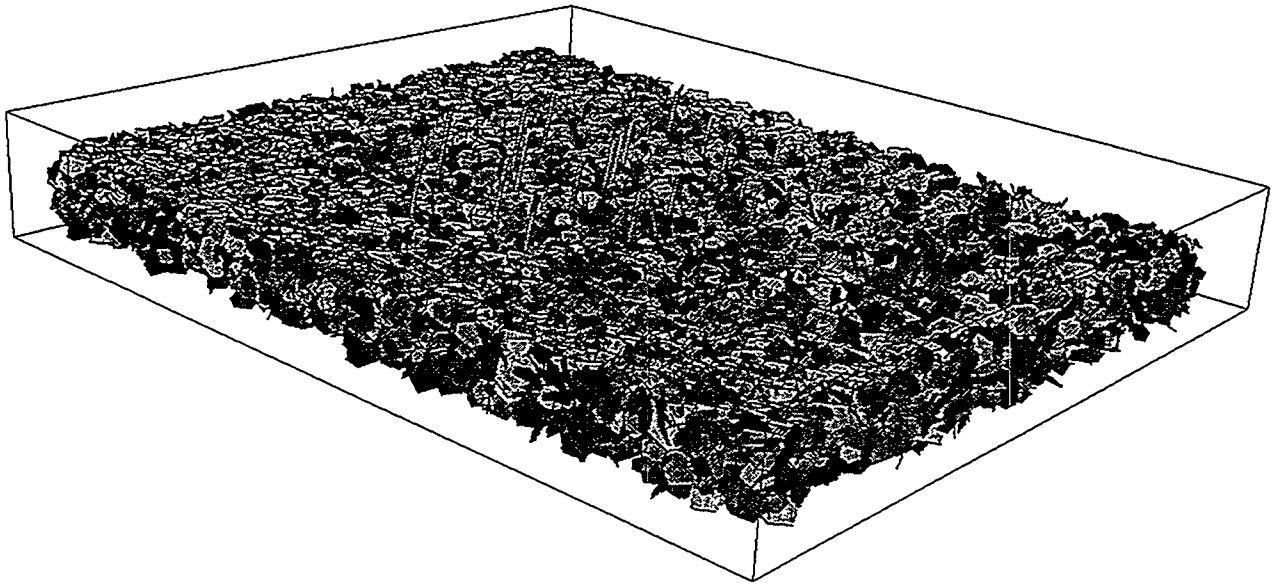

FIGURE **9-1**
TRACT 17 CONDITIONAL DFN MODEL
NIPER/FINAL REPORT/WA

PROJECT NO. 963 1357.521 DRAWING NO. 80824 DATE 9/29/98 DRAWN BY EA

Golder Associates

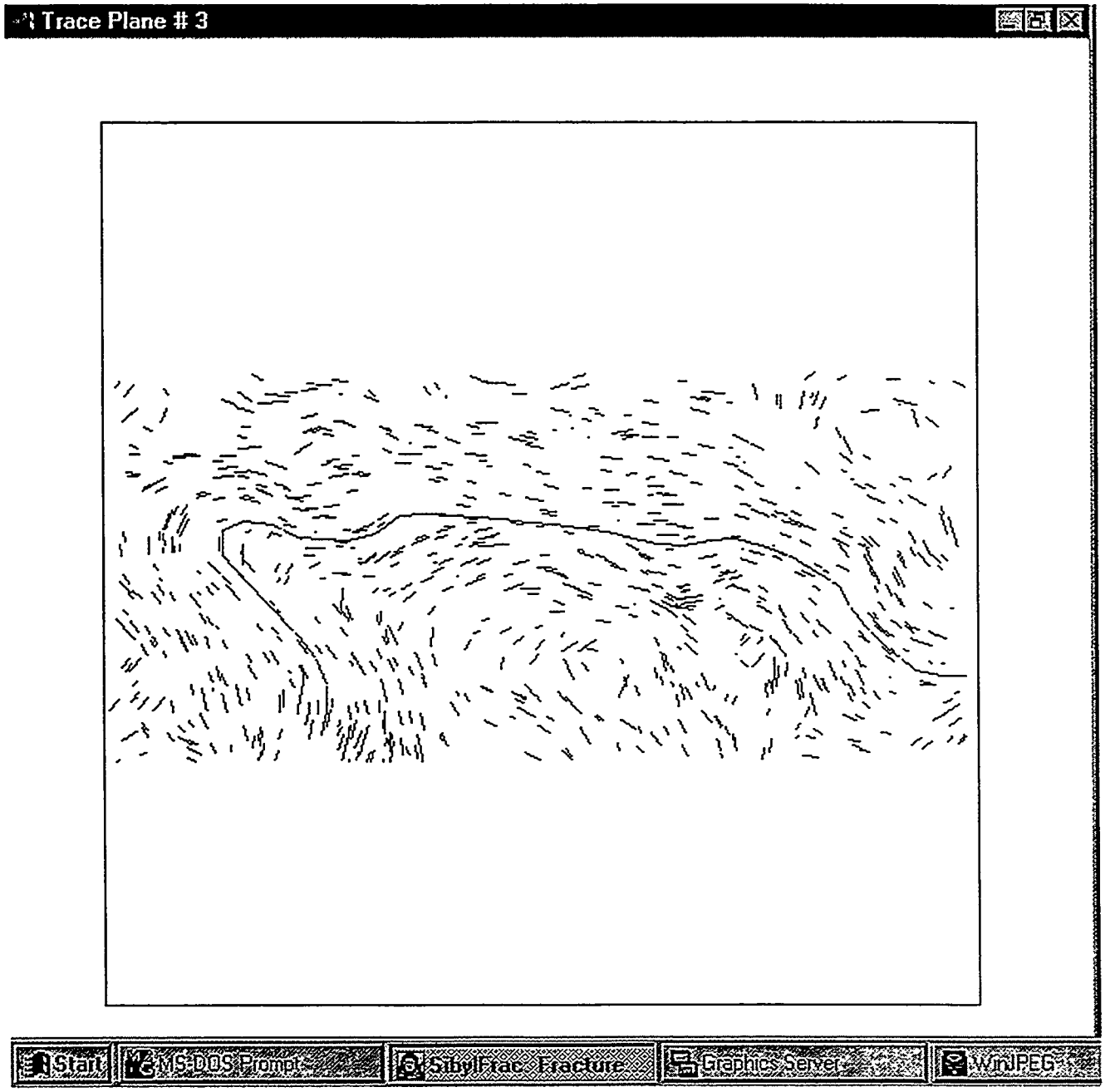

FIGURE **9-2**
CROSS SECTION THROUGH TRACT 17 CONDITIONED DFN MODEL
NIPER/FINAL REPORT/WA

PROJECT NO. 963 1357.521 DRAWING NO. 80825 DATE 9/29/98 DRAWN BY EA

Golder Associates

9.1.1 Deterministic Discrete Features

The reference DFN model for Yates Tract 17 combines deterministic faults with stochastic discrete fractures. Large scale faults are located deterministically based on seismic surveys. Through seismic interpretation, the location of twelve major faults has been determined inside Tract 17. These are large scale features between 400 and 1500 m long, and have a large horizontal to vertical aspect ratio of between 2:1 and 10:1. These faults form two distinct subsets trending NW-SE and NE-SW and are assumed to be vertical. These features are represented deterministically in the fracture network model as their location and geometry is known (Figure 9-3). Deterministic faults were assigned transmissivities of either 10^{-2} m^2/s or $5x10^{-2}$ m^2/s depending on their orientation.

9.1.2 Fracture Orientations

Geological analysis of fracturing in the Yates Field suggests that a major component of the fractures were formed by differential compaction and folding in the Middle and Late Permian. As a result, the orientations of these fractures relate to bedding curvature. The present-day curvature of the San Andres reservoir relates only in part to the drape folding, having been affected by later dissolution. The present-day curvature of the overlying Seven Rivers "M" horizon is thought to be a better representation of the bending-induced stresses that may have produced fractures in the San Andres, since it was less affected by sedimentological processes and dissolution.

Figure 9-4 shows the structural contour maps for the Seven Rivers "M" horizon for the Tract 17 area. This map was produced by contouring picks from wells shown in the respective figures using an algorithm developed by Swain (1976). Orientations of fractures formed due to folding would be systematically related to local bedding orientation. The two most common orientations for joints would be perpendicular to bedding and parallel to bedding strike, and perpendicular to bedding and parallel to bedding dip. Faults should form in conjugate pairs relative to these two orientations of extension joints. They should make a solid angle with the extension joints that depends upon the mechanical properties of the rock, but typically might be from 20 to 40 degrees (Figure 9-5).

Analysis of fractures from the three vertical wells YU1711, YU1755 and YU2511 in the Tract 17 vicinity (Figure 9-6) shows that fractures occur in many different strike orientations. The poles to these fractures define bands that represent fractures that dip about 70 degrees. The least common fractures are those that dip to the northwest.

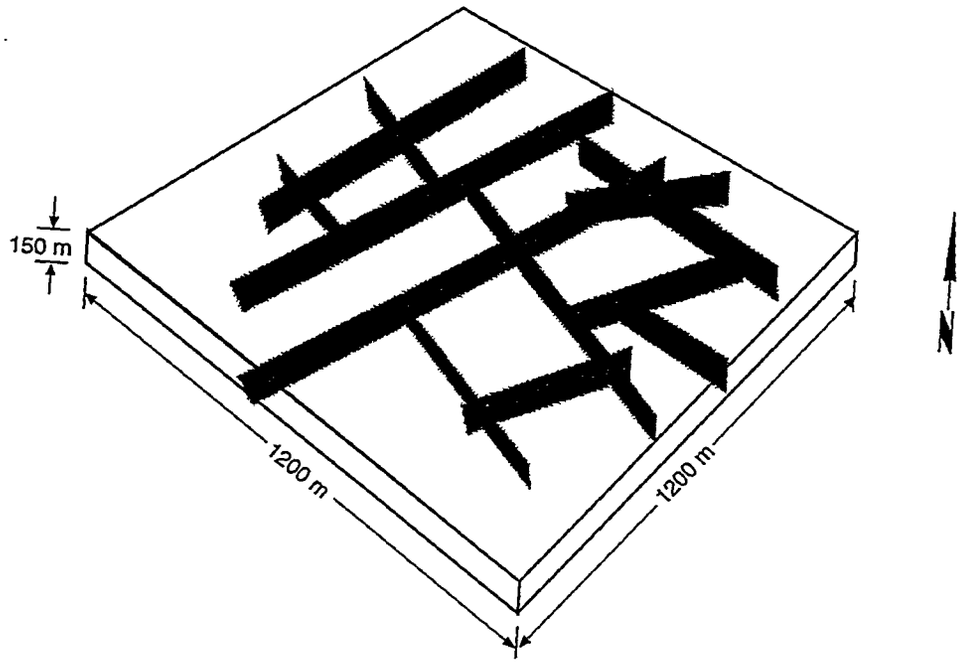

PROJECT NO. 963 1357.521 DRAWING NO. 80812 DATE 9/28/98 DRAWN BY EA

FIGURE **9-3**
DETERMINISTIC FAULTS
NIPER/FINAL REPORT/WA

Golder Associates

RELATIVE ELEVATION OF THE 7 RIVERS "M" HORIZON

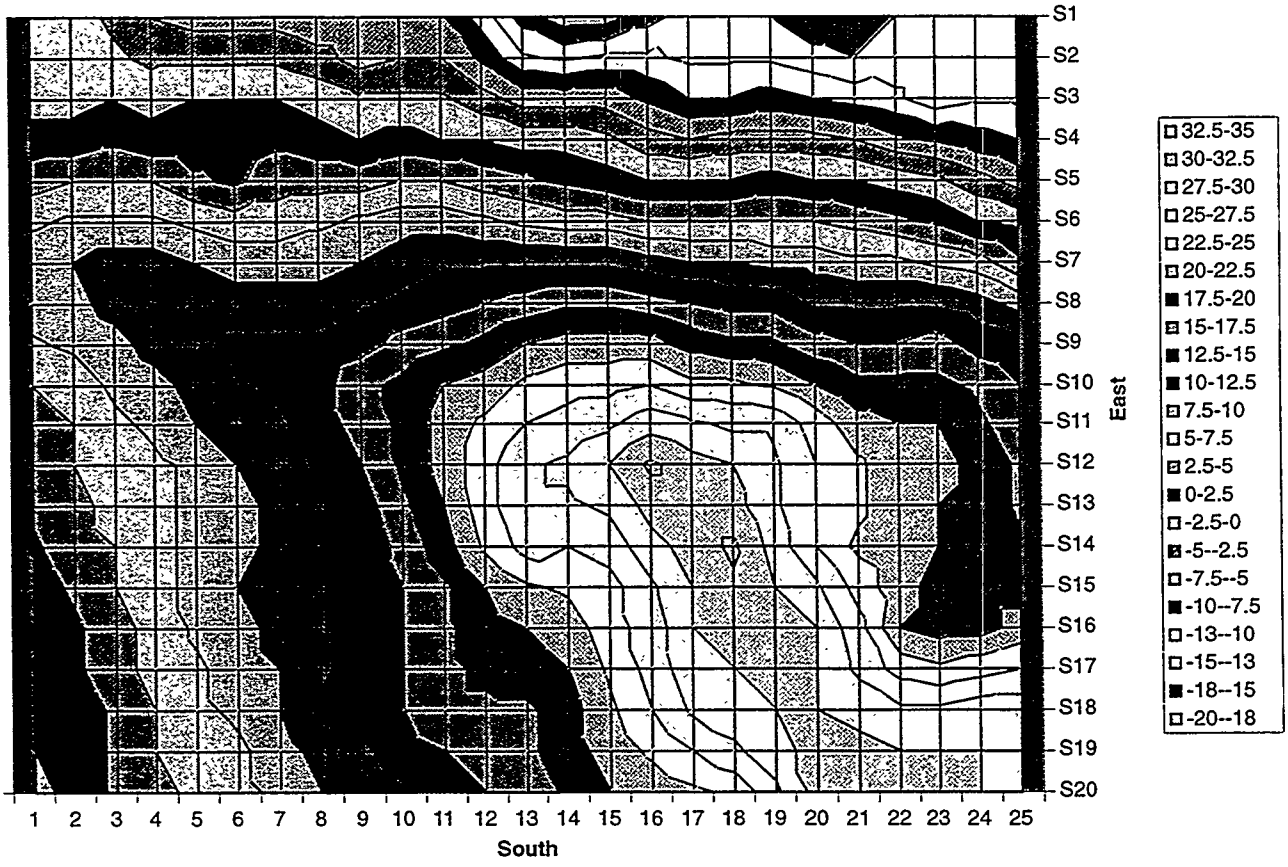

FIGURE **9-4**
SEVEN RIVERS "M" HORIZON
NIPER/FINAL REPORT/WA

PROJECT NO. 963 1357.521 DRAWING NO. 80607 DATE 9/29/98 DRAWN BY EA

Golder Associates

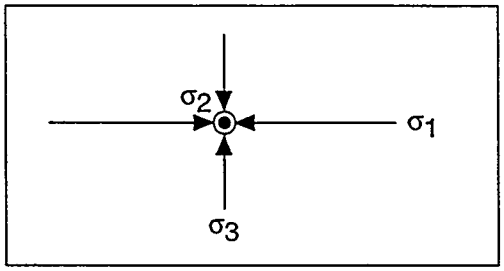

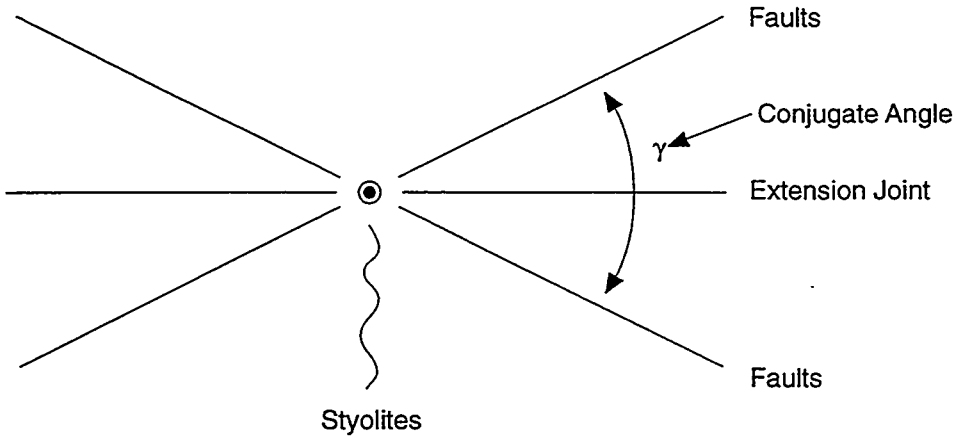

FIGURE **9-5**
RELATION BETWEEN EXTENSION JOINT AND FAULT ORIENTATIONS
NIPER/FINAL REPORT/WA

PROJECT NO. 963 1357.521 DRAWING NO. 80608 DATE 9/29/98 DRAWN BY EA

Golder Associates

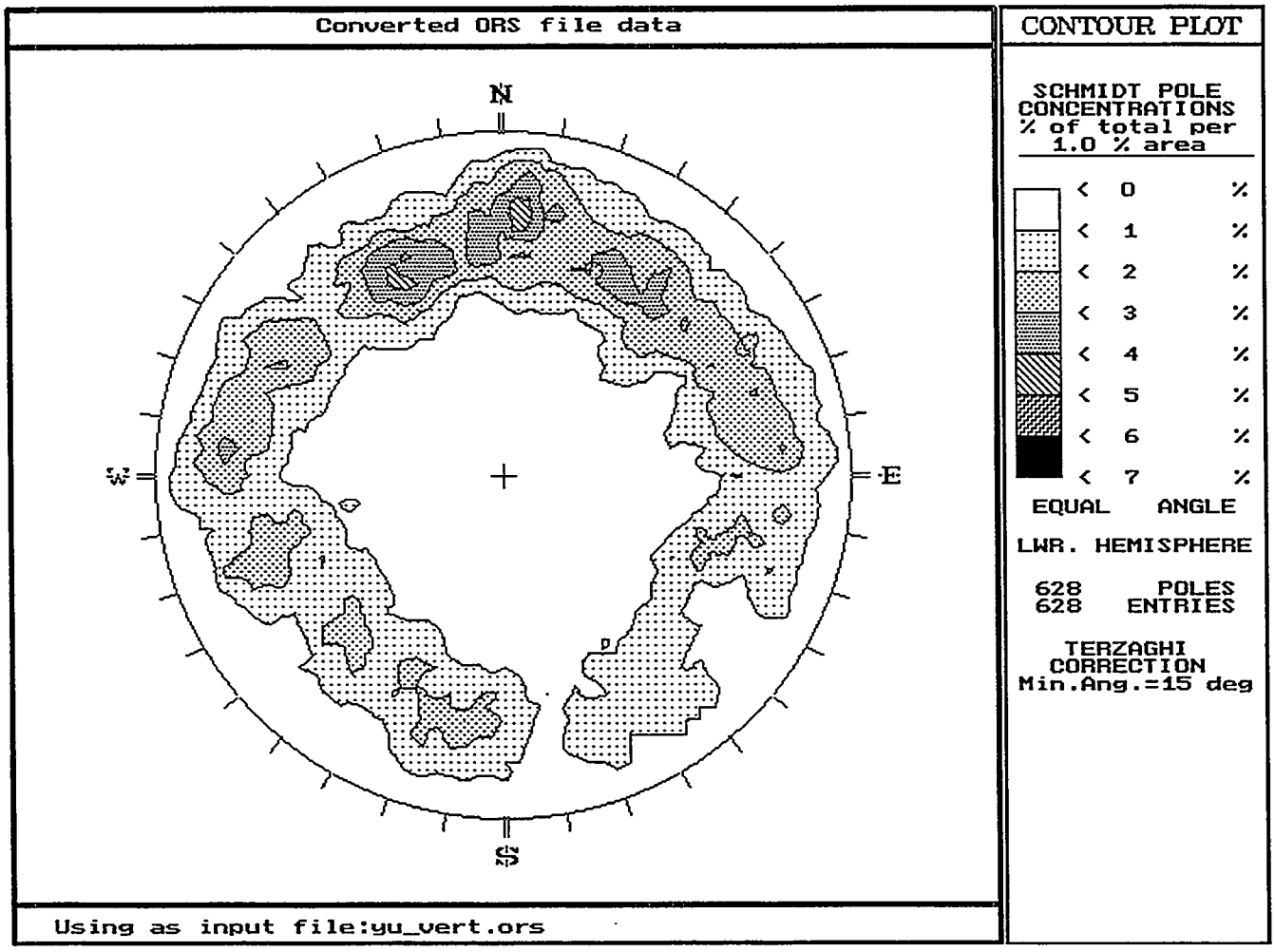

FIGURE **9-6**
STEREOPLOT OF FRACTURES IN TRACT 17 WELLS 1711, 1755, 2511
NIPER/FINAL REPORT/WA

PROJECT NO. 963 1357.521 DRAWING NO. 80609 DATE 9/29/98 DRAWN BY EA

Golder Associates

Interpretation of the FMI and FMS data suggests that most fractures are joints, not faults. Bending-related extension fractures should form perpendicular to bedding, and so those that strike parallel to bedding strike should dip approximately 90 degrees from bedding dip. Histograms of FMS and FMI data for Tracts 17 (Figure 9-7) show that bedding dip is typically in the 5 to 15 degree range, which in turn would suggest that joints should dip between 75 and 85 degrees. Table 9-2 shows the statistics for different types of features detected in the four wells.

Table 9-2 Dip statistics for three vertical and one horizontal well in the Tract 17 test area

Feature	Mean	Standard Deviation
Healed Fractures	64.4	14.9
Open Fractures	71.9	14.1
Bedding	9.4	5.5

Analysis of the structural contour maps for both the San Andres and the Seven Rivers "M" show much shallower slopes than the bedding plane dips determined from FMI and FMS logs. Even in the most steeply dipping portions of the tracts (for example, in the northeast corner of Tract 17), regional dips are only on the order a few degrees at most. Thus, the structural contour maps of these horizons may be useful indicators of bedding strike, but do not accurately reflect dip. In the conditioned DFN models for Tract 17, strike was assigned on the basis of the structural contour map strikes, and dip was assigned as a Fisher distribution with mean dip ϕ of 70 degrees with Fisher dispersion κ of 8. The resulting orientations of fractures generated according to this procedure are shown in Figure 9-8. They show a good correspondence with the fracture orientations inferred from well data (Figure 9-6).

9.1.3 Fracture Size Distribution

A size distribution assumption was derived from the FMS and FMI data in the four wells YU1711, YU1755, YU17D5 and YU2511 using the method of LaPointe et al (1993). La Pointe et al. (1993) showed that the size distribution of a fracture population could be estimated from the relative proportion of fractures detected as a function of the number of pads on which the fracture was imaged (Figure 9-9). For a 4-pad FMS tool, this means that each fracture will be imaged on 1, 2, 3 or 4 pads. The larger the fractures, the greater the probability that they will be imaged on all four pads of the tool. For an 8-pad FMI tool, each fracture will be imaged on from 1 to 8 pads. An eight-pad tool was used for the vertical wells YU1711, YU1755 and YU2511, and a 4-pad tool was used for the horizontal well YU17D5.

In order to compare an 8-pad image log with a 4-pad log, it was necessary to combine adjacent pads on the 8-pad tool. This implies that the number of fractures imaged on 1 or 2 pads are combined, 3 and 4 are combined, 5 and 6 are combined and 7 and 8 are combined. This is not an exact correction, since the azimuthal coverage of a single pad from a 4-pad tool differs from the coverage of two adjacent pads on an 8-pad tool, but it is still useful.

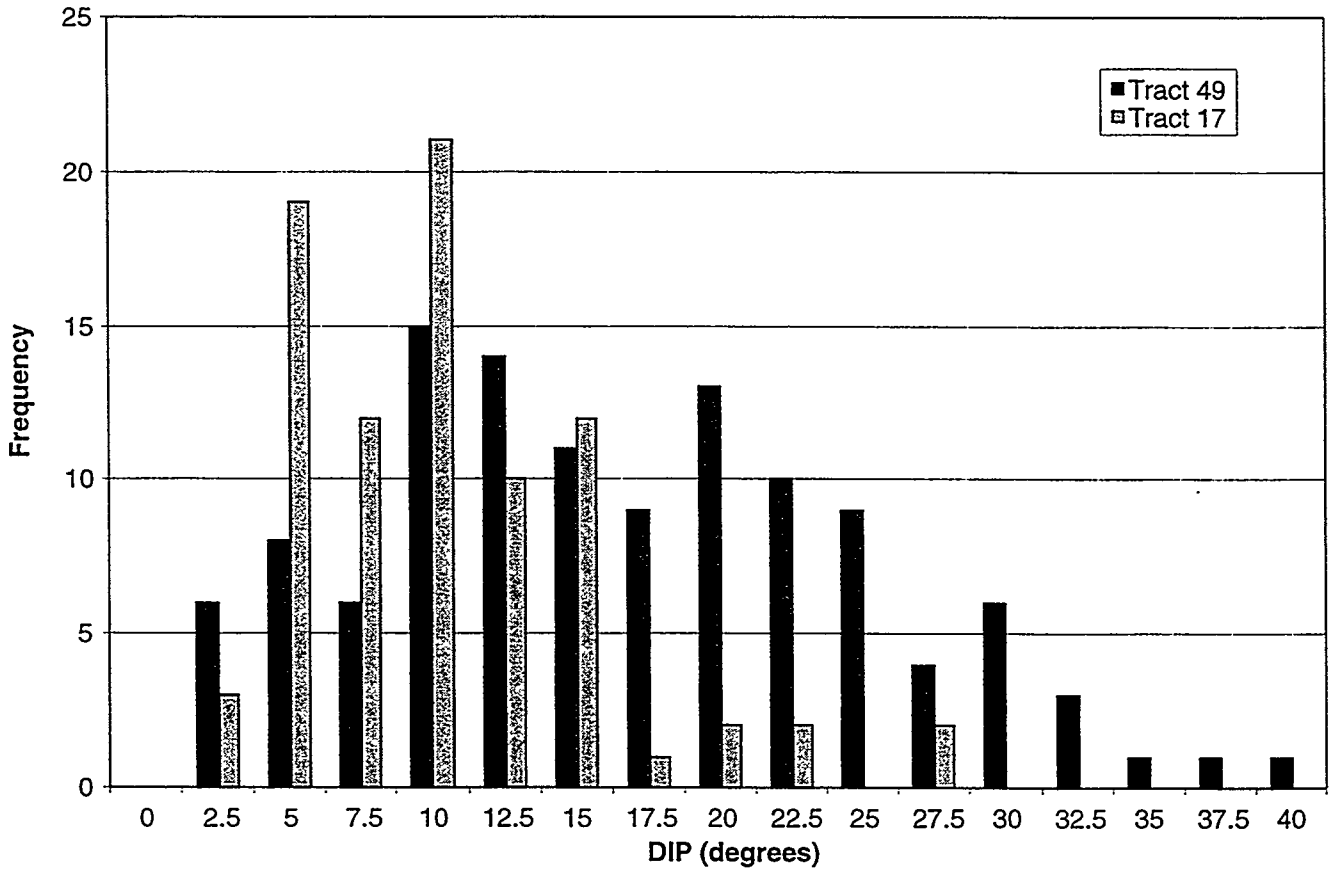

FIGURE **9-7**
BEDDING DIP FROM FMI DATA
TRACT 17
NIPER/FINAL REPORT/WA

PROJECT NO. 963 1357.521 DRAWING NO. 80610 DATE 9/29/98 DRAWN BY EA

Golder Associates

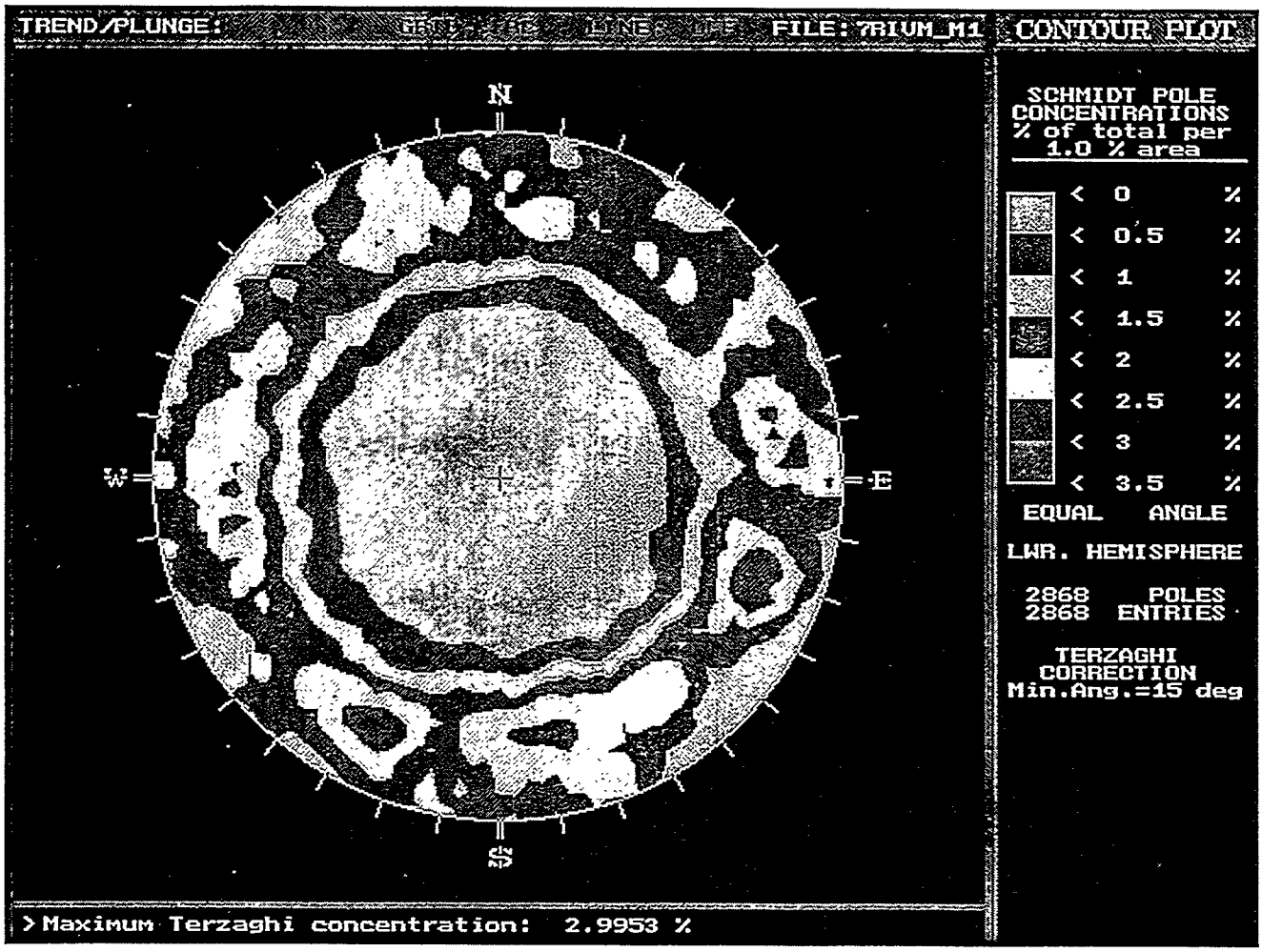

Fracture intersecting simulated wells 1711, 1755 and 2511

FIGURE **9-8**
STEREOPLOT OF FRACTURES IN STOCHASTIC CONDITIONED DFN MODEL
NIPER/FINAL REPORT/WA

PROJECT NO. 963 1357.521 DRAWING NO. 80834 DATE 9/29/98 DRAWN BY EA

Golder Associates

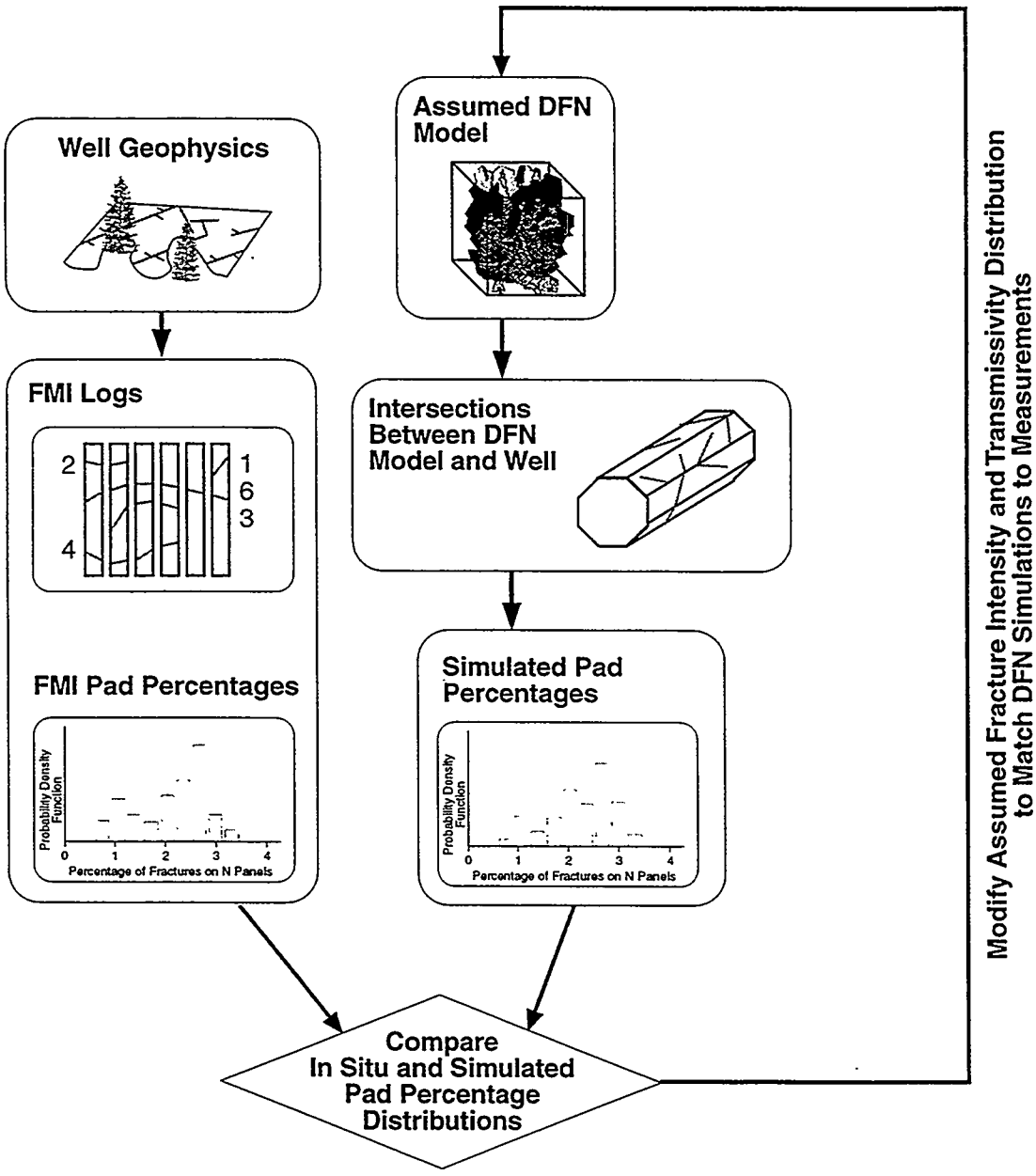

FIGURE **9-9**
PAD PERCENTAGE APPROACH FOR FRACTURE SIZE
NIPER/FINAL REPORT/WA

PROJECT NO. 963 1357.521 DRAWING NO. 80809 DATE 9/28/98 DRAWN BY EA

Golder Associates

Figure 9-10 shows the results for each of the four wells, for the mean and the median of the vertical wells taken together, and for all wells regardless of plunge. All of the intersection percentages as a function of the number of pads are very similar for all well and well groupings with the exception of the horizontal well, YU17D5, which has a higher percentage of 7 & 8 pad fracture images. The pad intersection percentages are summarized in Tables 9-3 and 9-4.

Table 9-3 Pad Percentages for FMI Log Data

Pads Covered	YU1711	YU1755	YU17D5	YU2511
1&2	1.60%	3.01%	1.32%	1.78%
3&4	25.60%	21.05%	8.28%	22.49%
5&6	35.60%	21.05%	21.63%	36.09%
7&8	37.20%	54.89%	68.77%	39.64%

Table 9-4 Pad Percentage Statistics for FMI Log Data

Pads Covered	Average Vert Wells	Average Horz Wells	Average All Wells	Median Vertical Wells	Median All Wells
1&2	2.13%	1.32%	1.93%	1.78%	1.69%
3&4	23.05%	8.28%	19.36%	22.49%	21.77%
5&6	30.92%	21.63%	28.59%	35.60%	28.61%
7&8	43.91%	68.77%	50.13%	39.64%	47.27%

Table 9-3 shows that wells YU1711 and YU2511 are very similar; YU1755 has a greater proportion of fractures that intersect all the pads of the tool. This could be due to:

1. the westerly-striking, subvertical fractures that account for almost all of the fractures imaged in the horizontal well are larger than the other fracture sets;

2. the azimuthal coverage of the 4-pad tool in the horizontal well differs from the azimuthal coverage of the 8-pad tools used in the three vertical wells;

3. fractures in the vicinity of YU17D5 are larger than elsewhere.

Any or all of these factors may explain the difference in intersection percentages. However, considering the variability among the percentages for the three vertical wells, it probably due to spatial variability in the fracture sizes rather than to other causes. For purposes of estimating fracture sizes, the average for all wells was selected as the pad percentages for matching.

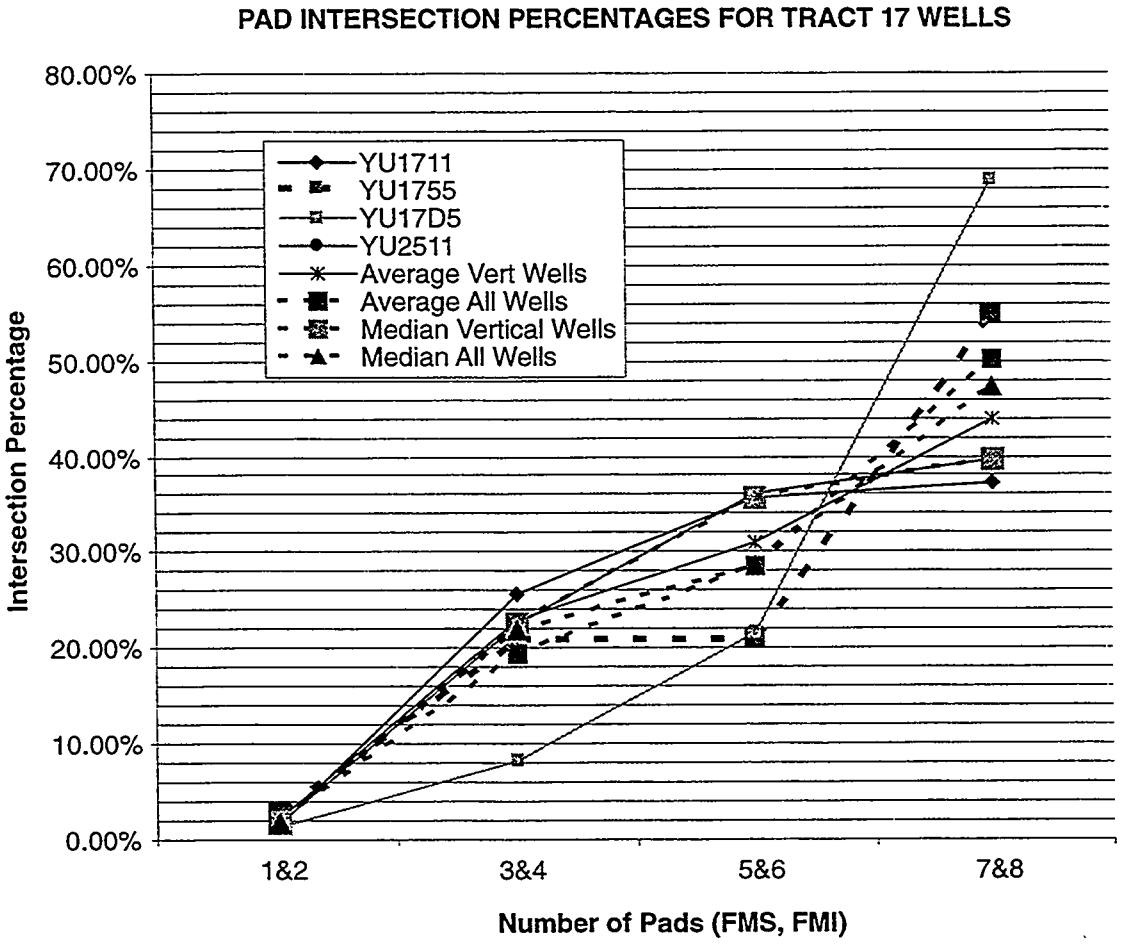

FIGURE **9-10**
TRACT 17 SIZE ANALYSIS
NIPER/FINAL REPORT/WA

PROJECT NO. 963 1357.521 DRAWING NO. 80810 DATE 9/28/98 DRAWN BY EA

Golder Associates

The fracture radius distribution was determined by comparing the measured pad percentage statistics from FMI logs against simulated pad percentages for assumed fracture size distributions (Figure 9-10). Several distributions were tested to see if they could match the observed vertical well pad intersection data. The best match was achieved with a truncated power law distribution with a fractal dimension of 1.81 and a minimum radius R_{min} of 1.0 ft. The distribution parameters and the pad intersection percentages for 25 realizations of the DFN model are shown in Table 9-5.

Table 9-5 Fitted Distribution of Pad Intersections (Power Law, D=1.81, R_{min}=1.0ft)

Number of Pads	Actual Percentages for All Wells	Mean Percentages for DFN Realizations
1&2	1.93%	14.21%
3&4	19.36%	16.99%
5&6	28.59%	10.46%
7&8	50.13%	58.34%

Note that this analysis was carried out for all fractures identifiable in FMI logs. It is likely that the fractures that play a significant role in interwell fracture connectivity represent the largest fractures only; small fractures probably play a very insignificant role at this scale. Thus the size should be adjusted to reflect the fact that the hydraulically significant fractures have a much larger minimum size cutoff. This issue was addressed below.

9.1.4 Fracture Intensity and Transmissivity Distribution

The three dimensional stereological measure of fracture intensity P_{32} is used in DFN modeling. P_{32} is defined as the total fracture surface area per volume of rock containing the fractures. P_{32}. has the units of length^{-1}. For a fracture population with a defined orientation distribution and size distribution, the relation between P_{32} and the number of fractures per unit length that would be intersected by a wellbore of a specific diameter and orientation is a multiplicative constant. This constant can be determined by creating a DFN model with any value of P_{32}, placing wells with the same orientations and diameters as the four Yates wells, and computing the number of fractures intersected per unit length. Table 9-6 summarizes the number of fractures per unit length (P_{10}) for the four wells as a function of the number of pads on which the fracture is seen.

Table 9-6 Fracture Intensity from FMI Data

Pads	YU1711	P_{10}	YU1755	P_{10}	YU17D5	P_{10}	YU2511	P_{10}
1	1	0.004596	0	0	18	0.028911283	0	0
2	3	0.013787	8	0.006777	113	0.18149861	3	0.013561
3	17	0.078125	24	0.02033	295	0.473823805	14	0.063285
4	47	0.215993	32	0.027107	938	1.506599081	24	0.108489
5	39	0.179228	25	0.021177			27	0.12205
6	50	0.229779	31	0.02626			34	0.153693
7	42	0.193015	67	0.056755			41	0.185336
8	51	0.234375	79	0.06692			26	0.11753
All Fractures	250	1.148897	266	0.225326	1364	2.190832778	169	0.763945

Table 9-6 shows that the number of fractures per unit length (P_{10}) varies among the four wells and as a function of how many pads the fracture is imaged on. For all fractures, the number of fractures per foot varies from a low of 0.22 for YU1755 to a high of 2.2 for the horizontal well.

A range of interpretations of fracture intensity P_{10} from Tract 10 data is summarized in Table 9-7. The mean wellbore length-weighted intensity for vertical wells is 0.70 fractures/ft. It is interesting to note that for the vertical wells, approximately half of the overall fracture intensity is made up of the biggest fractures, those that are imaged on 7 or 8 pads. If the conductive fractures are the biggest fractures, then this indicates that the conductive P_{10} should be no greater than 0.35 fractures/ft. Evaluation of static spinner logs from Tracts 17, 49 and neighboring tracts show a spacing of flow anomalies on the order of from 40 ft to 200 ft, corresponding to intensity P_{10} of 0.025 ft^{-1} to .005 ft^{-1}.

Table 9-7 Fracture Intensity from FMI Logs and Spinner Surveys

Basis	Intensity P_{10} (ft^{-1})
All Vertical Wells, adjusted for Well length	0.70
All Vertical Wells, adjusted for Well length, Fractures on 7 or 8 pads	0.35
Spinner log flow anomaly features (maximum 40 ft spacing)	0.025
Spinner log flow anomaly features (minimum 200 ft spacing)	0.005

The linear fracture intensity measure P_{10} can be converted to the volumetric intensity measure P_{32} by calculating the intensity P_{10} (spacing) for a well in a DFN simulation with known P_{32}. Using a bootstrap fracture orientation distribution and a vertical well, the ratio P_{32} / P_{10} was determined to be 2.03. Thus a geological fracture intensity P_{10} of 0.70 ft^{-1} corresponds to P_{32} of 1.42 ft^{-1} .

For reservoir scale simulation, the intensity required is the conductive intensity, rather than the geological intensity. One approach to relate geological and conductive

intensities assumes that fractures below a specified size threshold are non-conductive, and using a truncated radius distribution with the corresponding intensity. The percentage of fractures below the radius truncation limit could then be used to calculate the ratio of conductive fracture intensity to geological fracture intensity.

Figure 9-11 illustrates the relationship between the radius distribution cutoff and the fracture intensity P_{32c} above that cutoff for a power-law radius distribution with dimension D=1.81 and minimum 1 ft. For a radius cutoff of 10m, P_{32} would be reduced by 17.5%, and for a radius cutoff of 100m, P_{32} would be reduced by 41.5%.

For simulation purposes, it is estimated that intensity could adequately be represented by the 50 ft spaced features (P_{10} = 0.020ft^{-1}, P_{32C} = 0.0406 ft^{-1}). This value was independently verified by analysis of flowing features identified in flow logs. This analysis identified conductive structures P_{10}=0.0198 ft^{-1}. This corresponds to P_{32}=0.0402 ft^{-1}, or 0.132 m^{-1}. This is the value assumed for reference case simulations.

The transmissivity distribution derived by analysis of flow logs indicates a lognormal distribution of transmissivity with $\log_{10}$ mean -4, and standard deviation 0.75 $\log_{10}$ m^2/s. This is the transmissivity distribution assumed for reference case simulations.

9.1.5 Influence of Shale Content and Porosity on Fracture Intensity

Tinker and Mruk (1995) discussed the relation between shale content and porosity in the San Andres, and fracture intensity. They showed that fracture intensity begins to decrease as matrix porosity approaches 20%, reducing to roughly half of its peak value for the dolomitic reservoir lithologies.

Shale content influences fracture intensity in two ways. First, as the percentage of shale increases, the rock tends to behave more ductility, reducing the amount of brittle strain. Second, fractures propagating in the dolomites terminate prematurely against the shales, likewise reducing fracture intensity. Tinker and Mruk (1995) showed that the fracture intensity in the more argillaceous units was about half that in the cleaner dolomitic units. Their data suggested that rocks with shale content greater than 10% (corresponding to a gamma ray response of greater than 40 API) should have fracture intensities approximately half that of the less argillaceous units.

The gamma ray profiles for wells in Tract 17 and Tract 49 (Dershowitz et al., 1997) show that the reservoir in Tract 17 have shale-prone areas, while the reservoir in Tract 49 has little shale or argillaceous material.

A total fracture intensity of 0.132 m^{-1} was assumed for this analysis. In the conditioned Tract 17 model, fracture intensities in areas where matrix porosity is greater than 20% or shale content is greater than 10% were reduced by 50% to P_{32} = 0.066 m^{-1}. As a result, the average intensity P_{32} in the model is 7.26x10^{-2} m^{-1}.

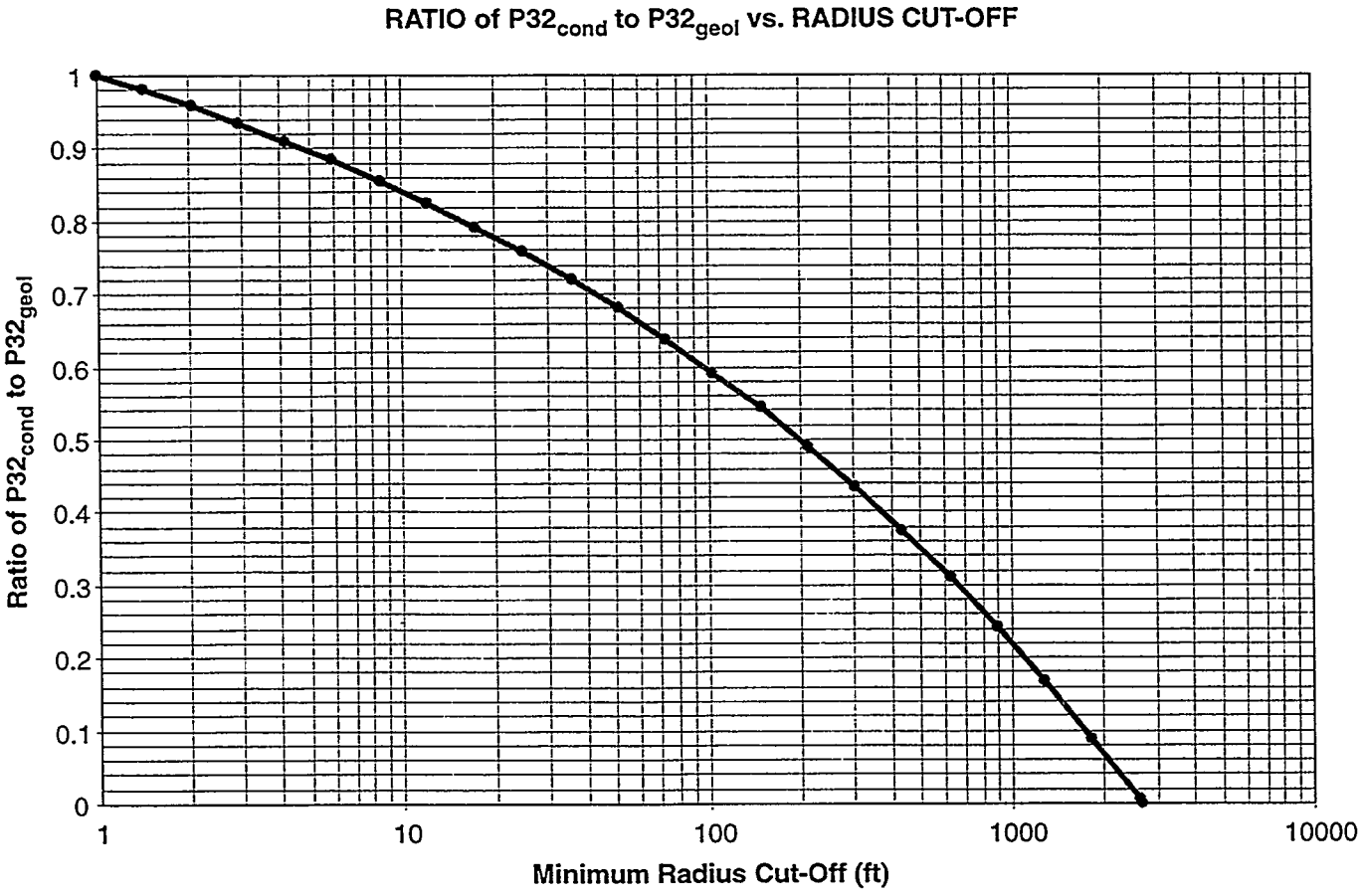

FIGURE **9-11**

POWER LAW DISTRIBUTION INTENSITY CUTOFF

NIPER/FINAL REPORT/WA

PROJECT NO. 963 1357.521 DRAWING NO. 80811 DATE 9/28/98 DRAWN BY EA

Golder Associates

9.2 Task 4.2.2: Reservoir Simulation

The stochastic conditioned Tract 17 DFN model derived in Section 9.1 was used to derive effective properties for heat transport /reservoir simulation of TAGS. This section describes both the derivation of effective properties and reservoir simulations.

The Tract 17 reservoir analysis results are summarized in Table 9-8. All analyses were carried out using the preliminary 11,250 cell THERM/DK and ECLIPSE grid of 12 cells of 71 m (NE-SW) by 12 cells of 71 m (SE-NW) by 24 cells of varying height. MAFIC numerical permeameter simulations were carried out using the model parameters of Table 9-1. The remaining were carried at with an earlier version DFN analyses model using total intensity $P_{32} = 3.85 \times 10^{-2}$ m^2/m^3, fault transmissivity of 5×10^{-3} m^2/s, and lognormal stochastic fracture transmissivity with mean -4.5 and standard deviation of 1.0 $\log_{10}$ m^2/s.

9.2.1 MAFIC Numeric Permeameter Simulations

Block permeability simulations were carried out by dividing the DFN model into 11,250 cells according to a preliminary THERM/DK - ECLIPSE model. A unit gradient was applied in each direction in turn. The boundary conditions for these simulations are provided in Figure 9-12. Effective conductivity was calculated from the block flux as,

$$K_x = Q_x / A_x i_x \qquad (9\text{-}1)$$

$$K_y = Q_y / A_y i_y$$

$$K_z = Q_z / A_z i_z$$

where the subscripts x, y, and z indicate the direction, K is the conductivity (m/s), A is the flow area, and i is the gradient. A gradient i of 1 was used in all simulations. The flow area for x and y directions was 71 m x 30 m = 2130 m^2, and the flow area A for the z direction is 71 m x 71 m = 5041 m^2. The conversion between units of m/s and milliDarcy (mD) units is,

$$K\,(\text{mD}) = K(\text{m/s})\ \mu(\text{Pa·s}) / (\rho_{oil}(\text{kg/m}^3) * g(\text{m/s}^2))/(9.869233*10^{-16})$$

$$\rho_{oil}(\text{kg/m}^3) = \rho_{water}(\text{kg/m}^3)\ 141.5/(131.5+\text{API}) \qquad (9\text{-}2)$$

where μ is the viscosity, ρ is the density, API is the API density in degrees, and g is the gravitational constant. For Yates, the reference density was taken as 30° API, corresponding to 876 kg/m^3, the gravitational constant g was assumed at 9.807 m/s^2, and the viscosity was taken as 7.5 centipoise, corresponding to 0.0075 (Pa·s). As a result, 10^{-5} m/s corresponds to 8.8 D.

Table 9-8 Reservoir Parameter Simulations

Reservoir Parameter	Approach	Values
Distributions for block permeability (K_x, K_y, K_z)	MAFIC Numerical Permeameter	K_x Mean 4.0×10^{-6} m²/s Std Dev 1.4×10^{-5} m²/s K_y Mean 8.0×10^{-5} m²/s Std Dev 4.1×10^{-3} m²/s K_z Mean 5.3×10^{-5} m²/s Std Dev 3.4×10^{-4} m²/s
Distributions for block anisotropy (K_x/K_y, K_z/K_y)	MAFIC Numerical Perimeter	K_x/K_y Mean 11.4 Std Dev 97.2 K_z/K_y Mean 54.0 Std Dev 281.6
Fracture porosity	StrataFrac Calculation	Porosity Mean = 6.0×10^{-4} Std Dev = 4.3×10^{-4}
Active/inactive cell and flow barrier analysis	StrataFrac Calculation	Percent Flow Barrier Cells X Direction: 73% Y Direction: 70% Z Direction: 10%
Spatial structure of block permeability and	MAFIC Numerical Permeameter	Variograms
Compartmentalization	FraCluster	Compartment Size and Shape Distributions
Tributary drainage volume	FraCluster	Tributary Volume Distributions
Block Size Distribution	FraCluster	Mean Volume = 2.5×10^{5} m³* Std Dev Volume = 7.5×10^{5} m³*
Block shape (σ- and Z-factors)	FraCluster	Mean σ-factor = 30* Std Dev σ-factor = 730* Mean Z-factor = 92.8 m* Std Dev Z-factor = 69.7 m*
Well Permeability-Thickness kh	Flare	Median kh = 4.3×10^{-4} m²/s
Exchange Surface Area	FraCluster	Area = 10^{7} m² (for $T_{min} = 10^{-5}$ m²/s)

**At a fracture transmissivity cutoff of 10^{-4} m²/s*

a) Boundary condition flow in X direction

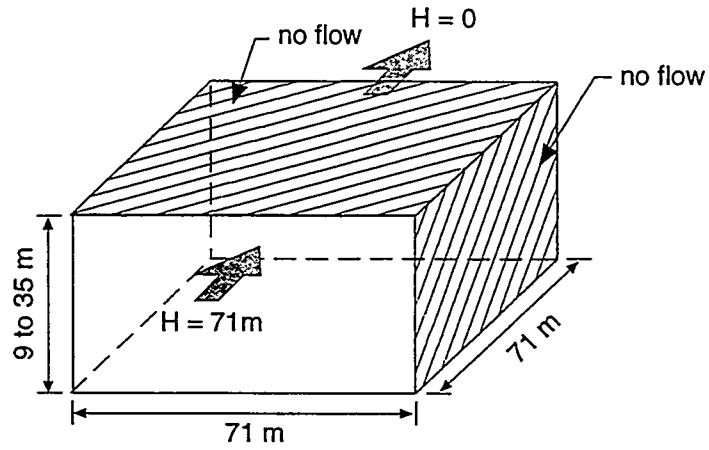

b) Boundary condition flow in Y direction

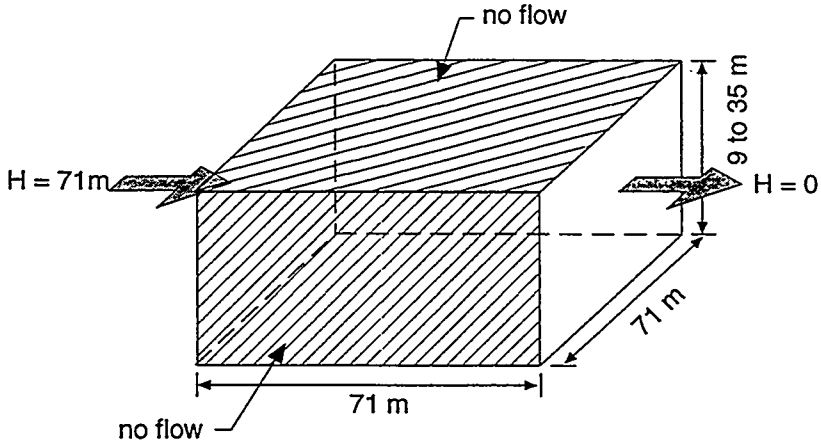

c) Boundary condition flow in Z direction

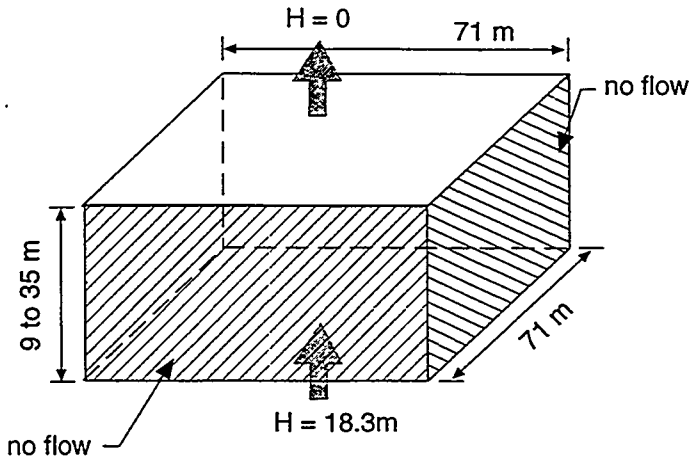

FIGURE **9-12**
BOUNDARY CONDITIONS FOR NUMERIC PERMEAMETER SIMULATIONS
NIPER/FINAL REPORT/WA

The results of MAFIC grid block simulations are provided in Tables 9-9 and 9-10. MAFIC grid block conductivities are illustrated in Figures 9-13 and 9-14.

Table 9-9 Grid Block Conductivity Statistics

	Kx (mD)	*Ky (mD)*
Mean	8723.57	3146.40
Standard Error	759.62	178.13
Median	681.46	945.51
Standard Deviation	20382.83	4779.71
Sample Variance	4.15E+08	2.28E+07
Kurtosis	3.25	0.98
Skewness	2.27	1.64
Range	66210.94	16783.45
Minimum	0.00	0.00
Maximum	66210.94	16783.45
Sum	6280969.57	2265410.84
Count	720	720
Confidence Level(95.0%)	1491.34	349.72

Table 9-10 Grid Block Anisotropy Statistics

	Ky/Kx
Mean	12.06476
Standard Error	2.719152
Median	1.085517
Standard Deviation	71.47803
Sample Variance	5109.108
Kurtosis	330.2975
Skewness	16.38842
Range	1562.13
Minimum	1.61E-17
Maximum	1562.13
Sum	8336.752
Count	691
Confidence Level(95.0%)	5.338805

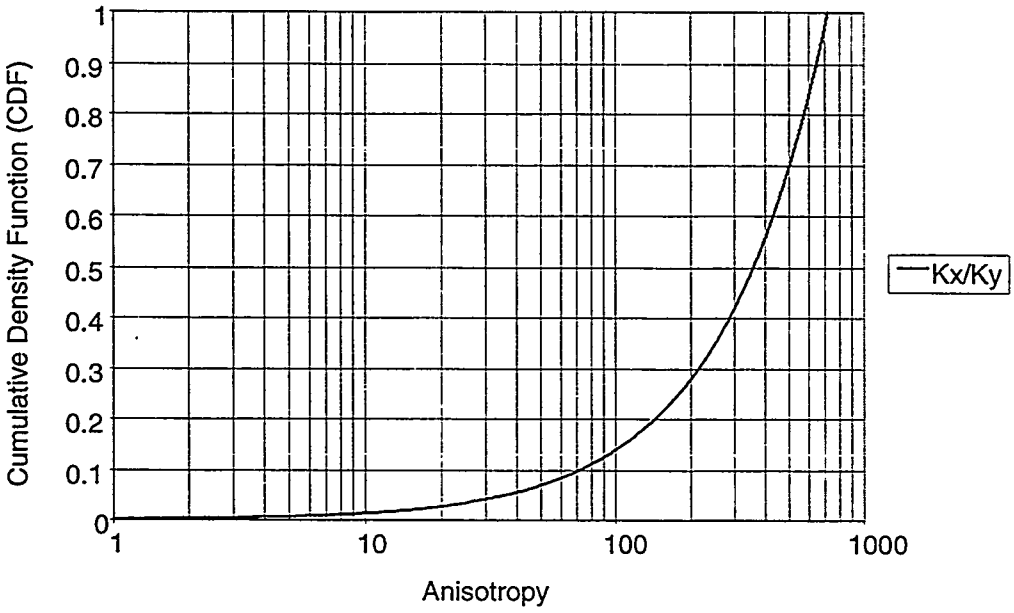

a) Anisotropy

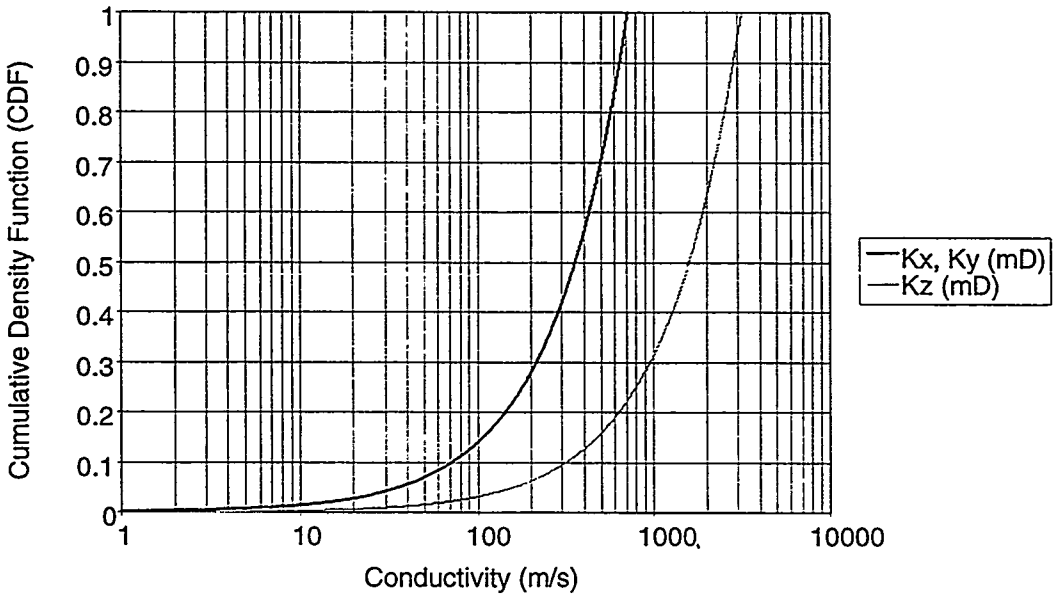

b) Block Conductivity

FIGURE **9-13**
DISTRIBUTION OF GRID BLOCK CONDUCTIVITY
NIPER/FINAL REPORT/WA

PROJECT NO. 963 1357.521 DRAWING NO. 80615 DATE 9/29/98 DRAWN BY EA

Golder Associates

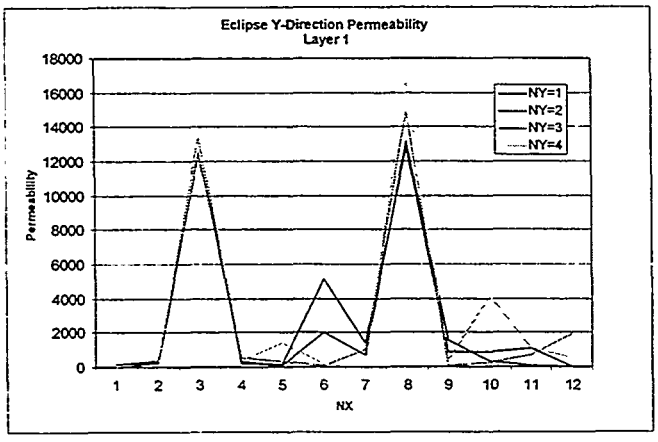

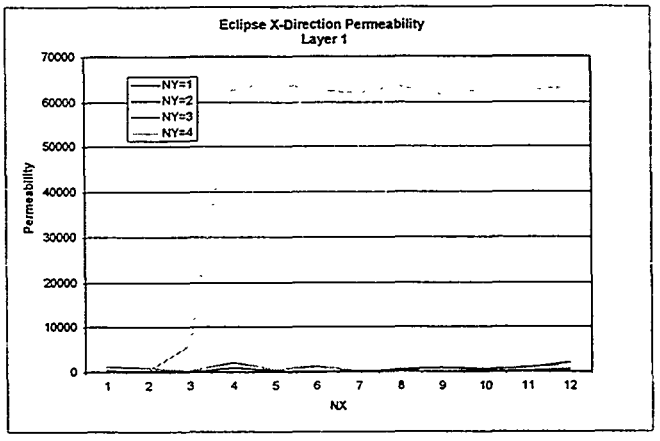

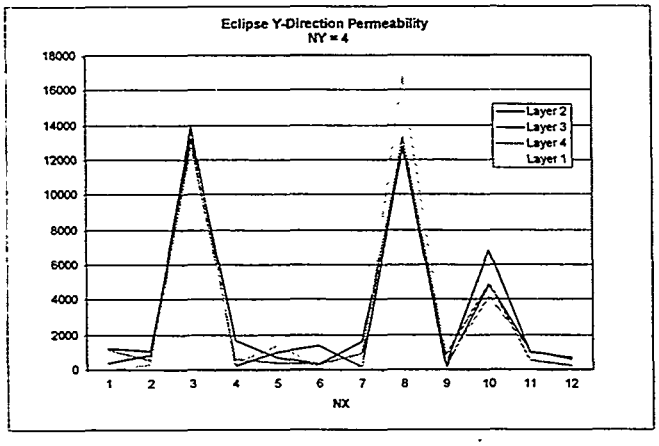

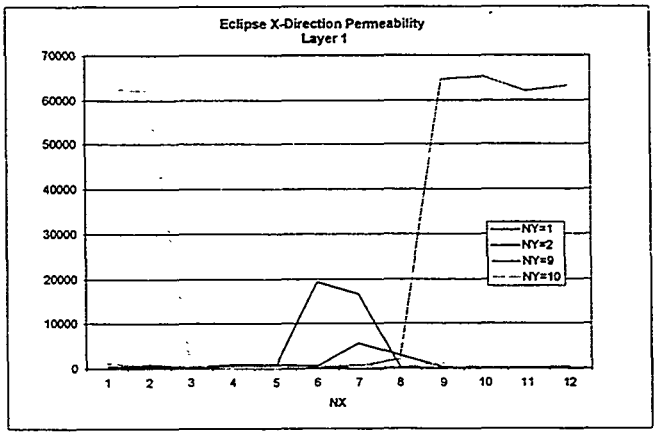

FIGURE **9-14**

SPATIAL PATTERN OF PERMEABILITY

NIPER/FINAL REPORT/WA

PROJECT NO. 963 1357.521 DRAWING NO. 80616 DATE 9/29/98 DRAWN BY EA

Golder Associates

9.2.2 StrataFrac Analysis

StrataFrac was designed to (a) adapt statagraphic (cellular) data for use in DFN model conditioning, and (b) derive cellular values from DFN models. For the present analysis, StrataFrac was used to convert the stochastic conditioned DFN model into a geocellular model using the reference ECLipse grid. Five layers (720 cells) were used for X- and Y-direction flow, while 24 layers (3,456 cells) were used for Z-direction flow. This was necessary because the 24 layer model had insufficient thickness for X- and Y-percolation.

The first StrataFrac analysis addressed the issue of active/inactive cells and flow barrier cells. Inactive cells are cells with no fracture permeability in x, y, or z directions. Of the 720 cells, 716 or 99.2% have permeability greater than 10^{-7} m/s in at least one direction. Thus, 0.8% of the cells can be considered inactive.

Flow barriers are cells in which there is no permeability at least one direction. Based on StrataFrac analysis of the DFN model, flow barrier percentages are as follows:

- X direction: 4.86% of cells have no connectivity for flow in the X direction
- Y direction: 3.33% of cells have no connectivity for flow in the Y direction
- Z direction: 0.06% of cells have no connectivity for flow in the Z direction

This is consistent with the relationship between fracture size and cell size. In the DFN model, the fracture size is generally on the range of 36m to 75 m in diameter, and every grid cell has on the order of 1 to 3 fractures. As a result, very few cells do not have sufficient fracturing to percolate through the 9 to 30 m in the Z direction, on the order of five percent of cells do not have sufficient fracturing to percolate through the 71 m cells in the X and Y directions.

The cell based fracture porosity $n_f(i)$ was calculated by dividing the fracture volume by the cell volume:

$$n_f(i) = \sum A_{ij}\, t_{ij} / V_i \qquad (9\text{-}3)$$

where $n_f(i)$ is the fracture porosity of cell i, A_{ij} is the area of the portion of fracture j in cell i, t_i is the thickness of fracture j in cell i, and V_i is the volume of cell i.

It is important to note that this fracture porosity n_f does not include the porosity of fractures smaller than 10 m in radius or larger than 50 m in radius, and also does not consider fractures which would be considered "non-conductive". As a result, the porosity n_f could be considered the porosity of the flowing fracture network, not including deterministically identified features.

Table 9-11 presents statistics on the fracture porosity and fracture intensity P_{32} on a cell basis from the DFN model. The relationship between fracture intensity P_{32} and porosity n_f is illustrated in Figure 9-15. The spatial variation of fracture porosity is illustrated in Figure 9-16.

Table 9-11 Grid Cell Fracture Porosity and Intensity

	P_{32}	n
Mean	0.06183	0.000595
Standard Error	0.000281	4.52E-06
Median	0.060733	0.000511
Standard Deviation	0.02655	0.000426
Sample Variance	0.000705	1.82E-07
Kurtosis	0.132641	68.84799
Skewness	0.302787	4.278018
Range	0.204352	0.011649
Minimum	0	0
Maximum	0.204352	0.011649
Sum	550.9085	5.301773
Count	8910	8910
Confidence Level(95.0%)	0.000551	8.85E-06

9.2.3 FraCluster Analysis

FraCluster analysis was used to derive dual porosity (matrix block) reservoir parameters, compartmentalization parameters, and tributary drainage volume parameters. FraCluster analyses were carried out directly on a preliminary version of the Tract 17 DFN model.

The matrix block calculation is illustrated in Figure 9-17, and is described in LaPointe et al. (1996). The block volume distribution, sigma factor, and Z-factor are summarized in Table 9-12, Figures 9-18, 9-19, and 9-20.

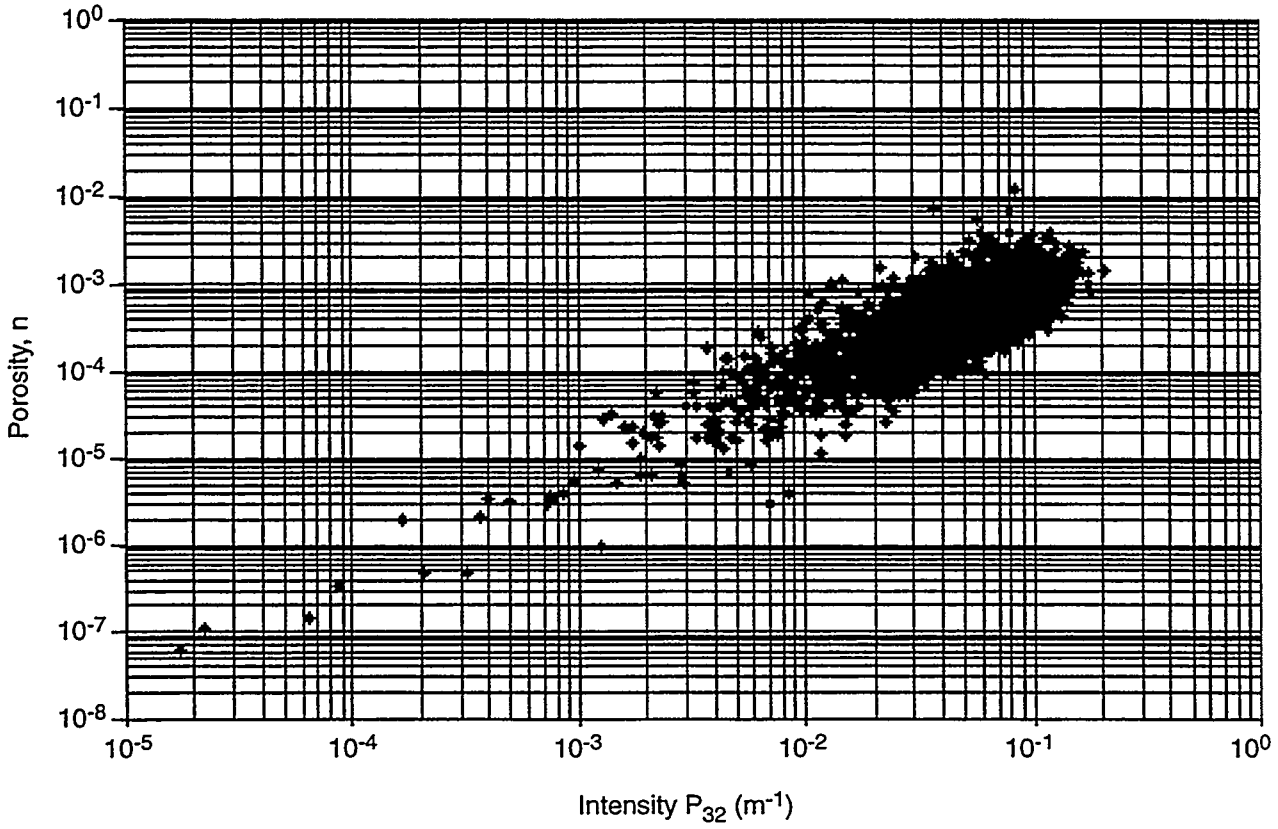

FIGURE **9-15**
GRID BLOCK INTENSITY P_{32} VS. FRACTURE POROSITY
NIPER/FINAL REPORT/WA

PROJECT NO. 963 1357.521 DRAWING NO. 80617 DATE 9/29/98 DRAWN BY EA

Golder Associates

a) X direction log porosity

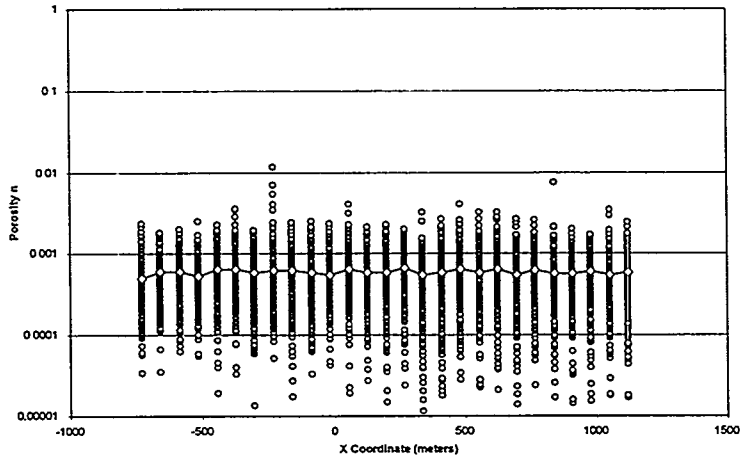

b) Y direction log porosity

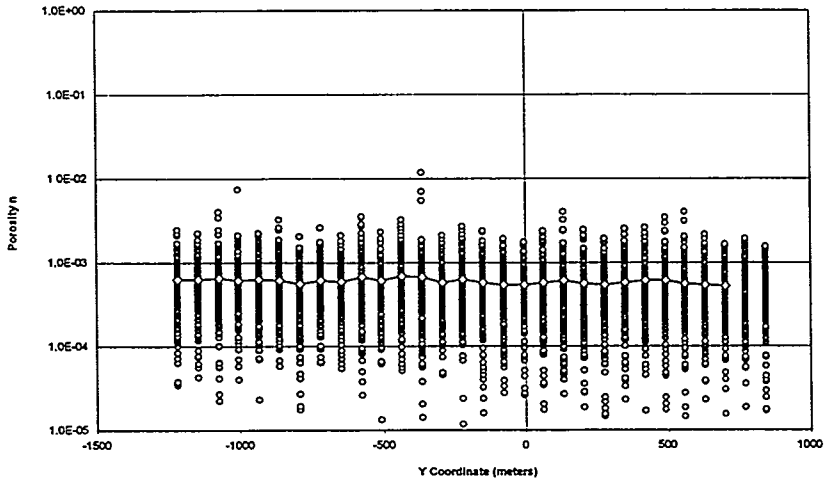

c) Z direction log porosity

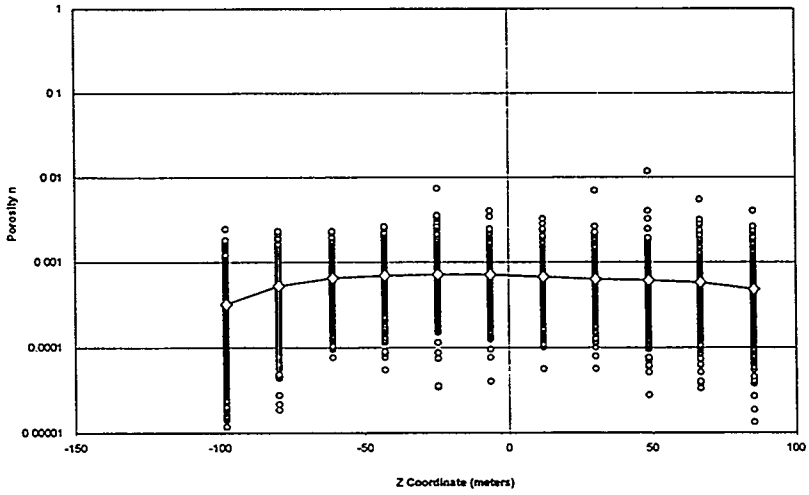

FIGURE **9-16**

SPATIAL PATTERN OF FRACTURE POROSITY

NIPER/FINAL REPORT/WA

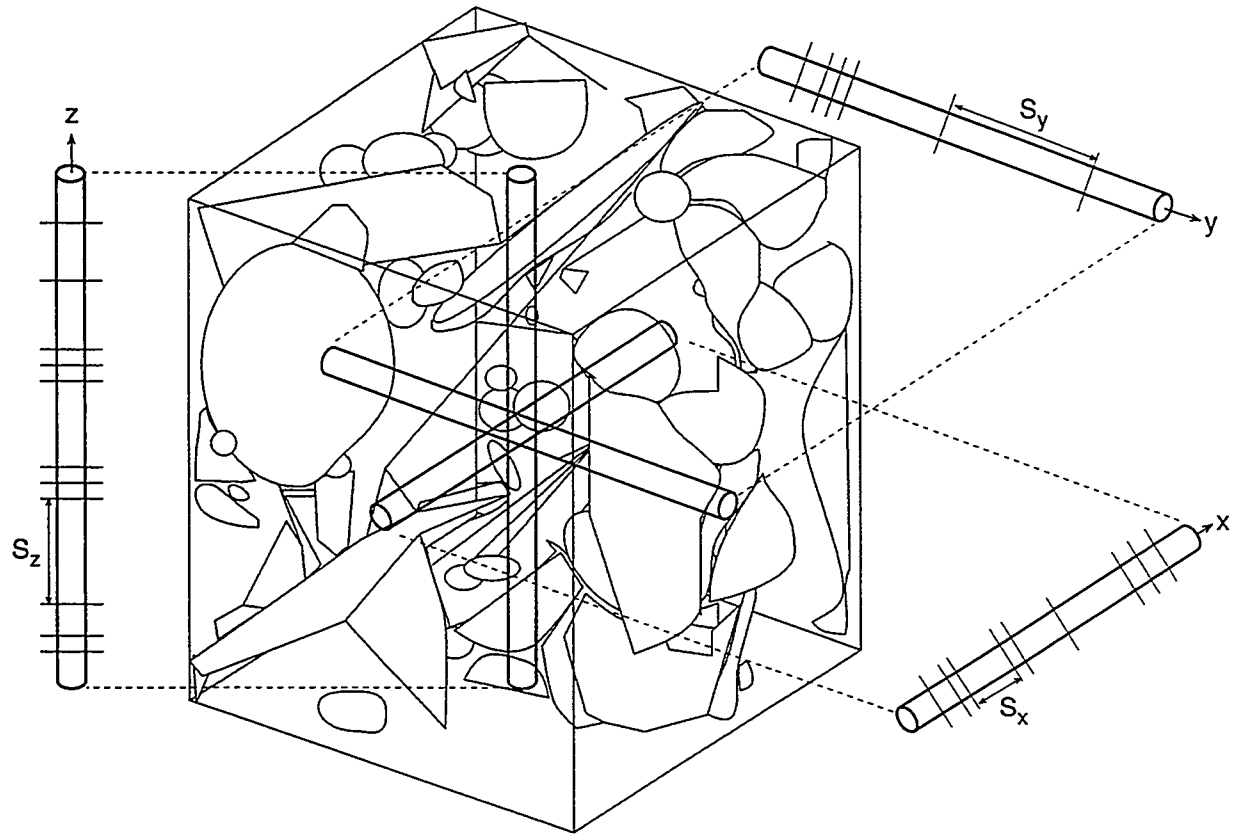

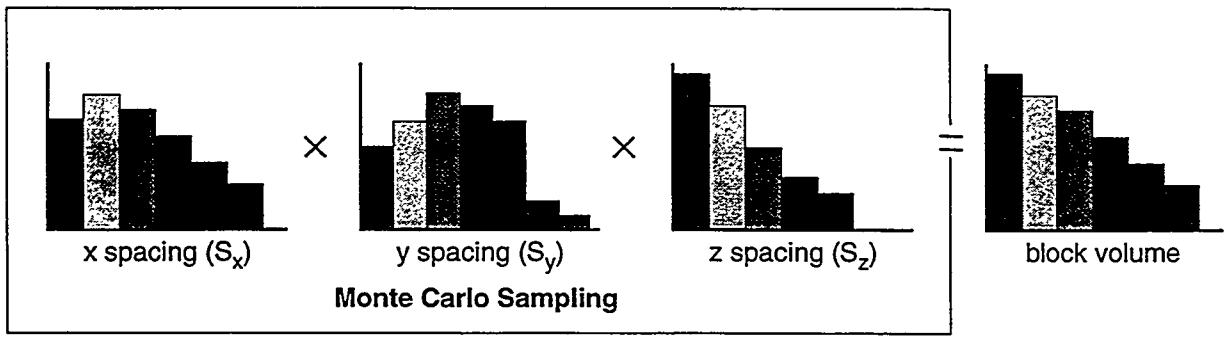

FIGURE **9-17**
MATRIX BLOCK ALGORITHM
NIPER/FINAL REPORT/WA

PROJECT NO. 963 1357.521 DRAWING NO. 80619 DATE 9/29/98 DRAWN BY EA

Golder Associates

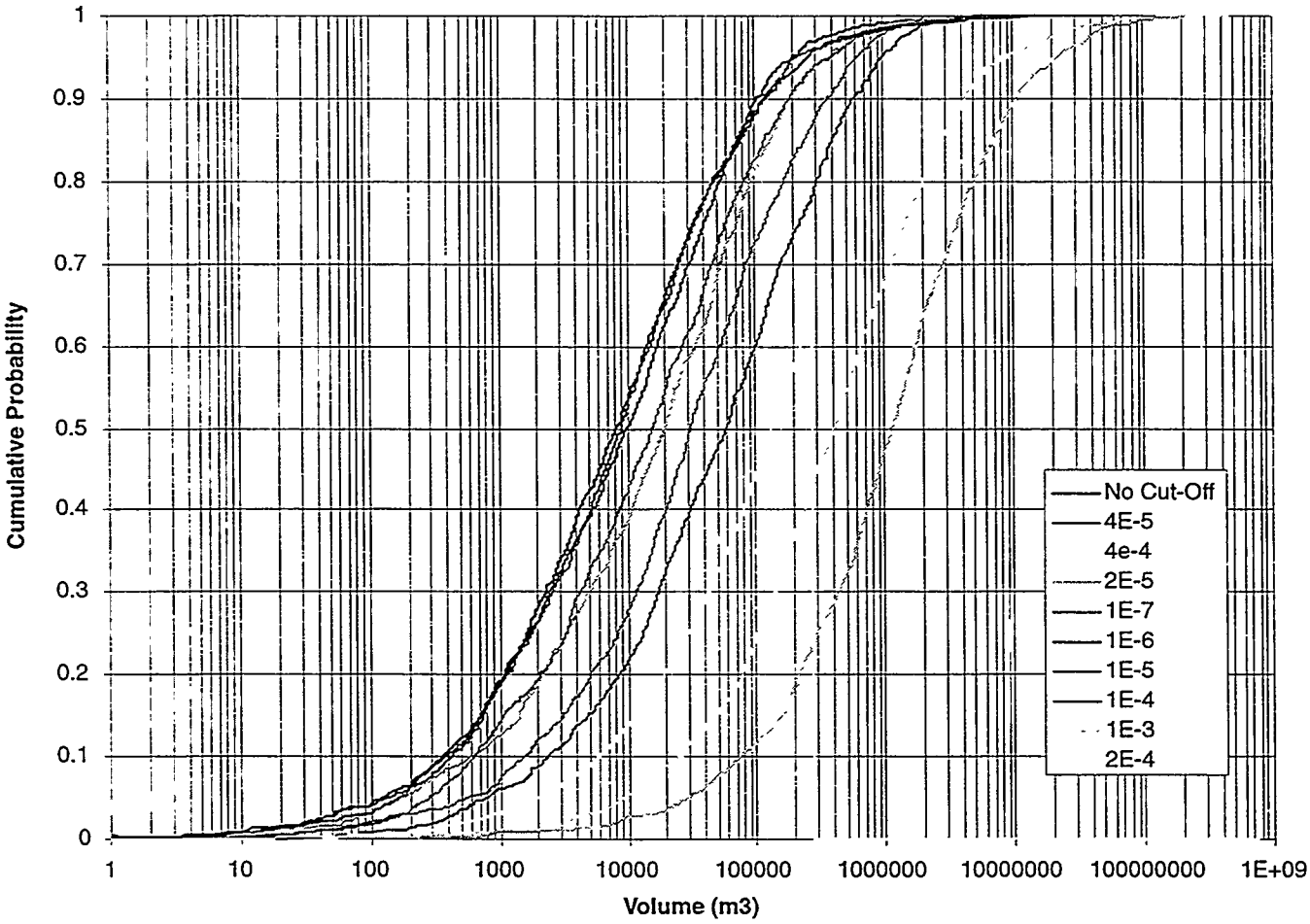

FIGURE **9-18**
CUMULATIVE DISTRIBUTION OF MATRIX BLOCK SIZE
NIPER/FINAL REPORT/WA

PROJECT NO. 963 1357.521 DRAWING NO. 80620 DATE 9/29/98 DRAWN BY EA

Golder Associates

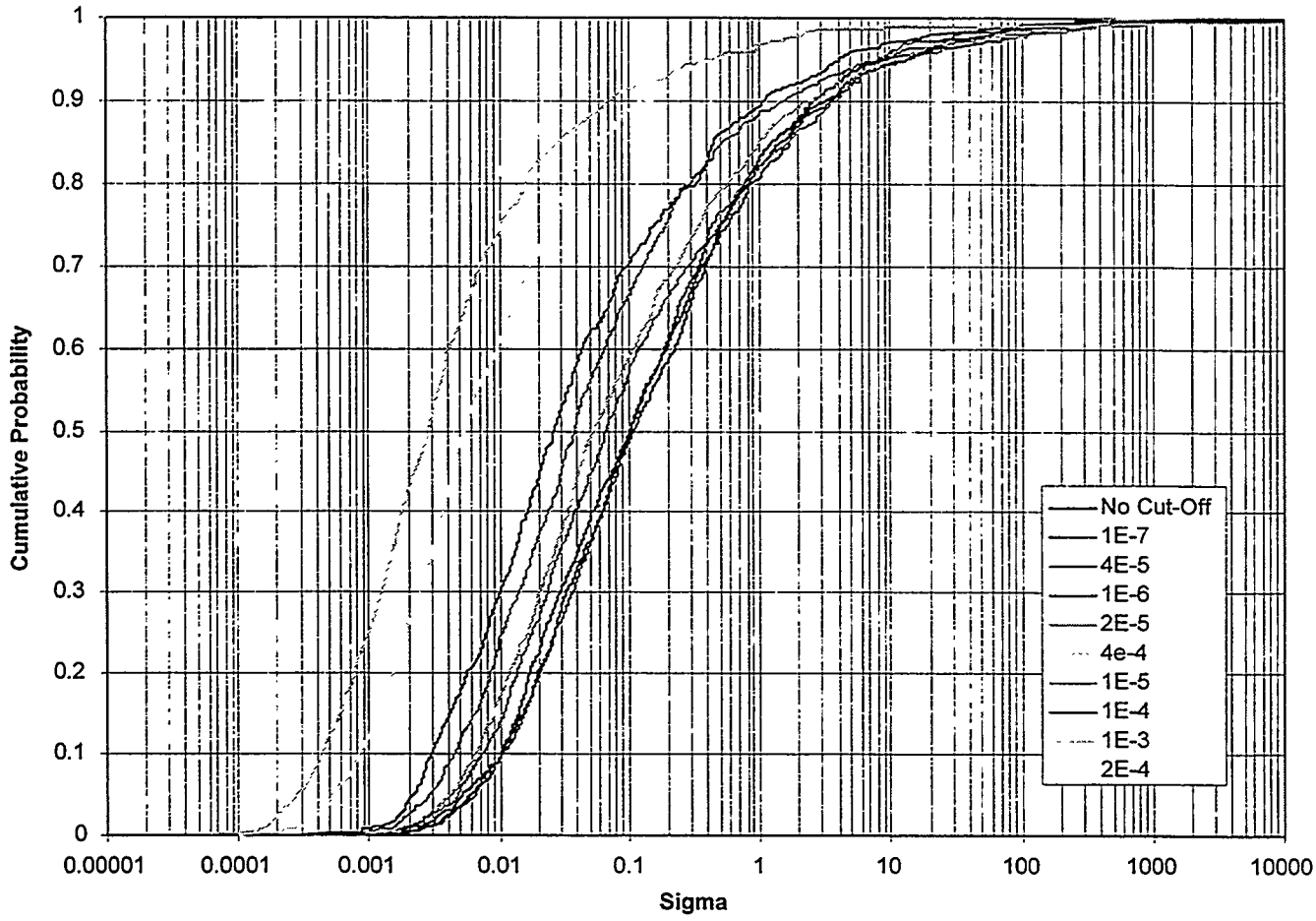

FIGURE **9-19**
CUMULATIVE DISTRIBUTION OF SIGMA FACTOR
NIPER/FINAL REPORT/WA

PROJECT NO. 963 1357.521 DRAWING NO. 80621 DATE 9/29/98 DRAWN BY EA

Golder Associates

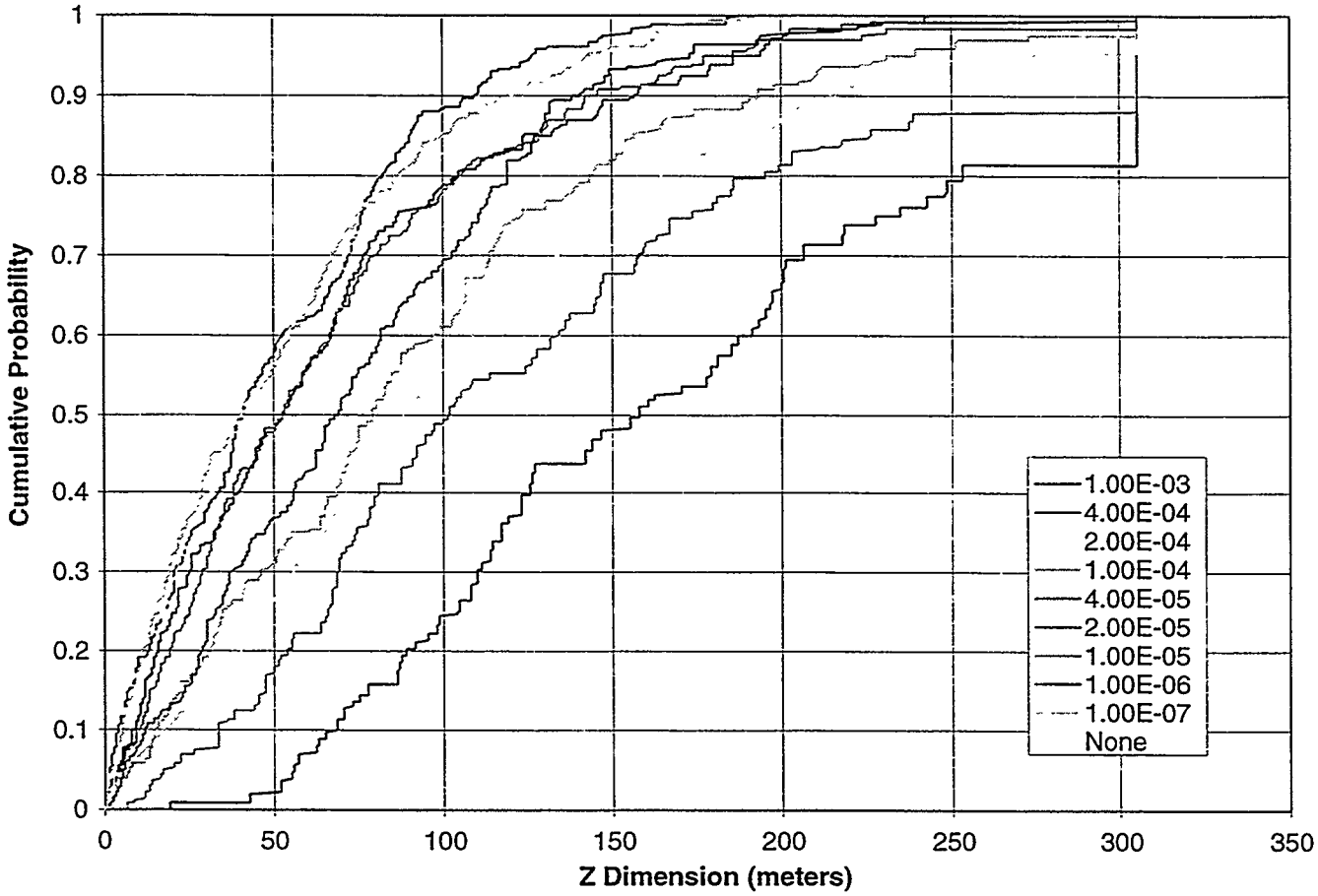

FIGURE **9-20**
CUMULATIVE DISTRIBUTION OF Z FACTOR
NIPER/FINAL REPORT/WA

PROJECT NO. 963 1357.521 DRAWING NO. 80622 DATE 9/29/98 DRAWN BY EA

Golder Associates

Table 9-12 Sigma Factor, Block Volume, and Z-Factor Statistics

Transmissivity Cut-Off	Sigma Factor		Block Volume		Z Factor	
(m^2/s)	Mean (-)	Std Dev (-)	Mean (m^3)	Std Dev (m^3)	Mean (m)	Std Dev (m)
10^{-10}	1476.9	44981.2	7.76E+04	6.94E+05	54.0	45.5
10^{-7}	13.8	188.5	9.43E+04	5.83E+05	52.1	44.7
10^{-6}	181.3	5029.2	1.15E+05	8.91E+05	50.8	40.7
10^{-5}	59.8	1081.4	9.93E+04	4.33E+05	67.6	59.8
$2.x\ 10^{-5}$	132.3	1913.4	1.08E+05	6.24E+05	64.2	55.0
$4.x\ 10^{-5}$	11.2	97.4	2.06E+05	1.90E+06	77.5	54.4
10^{-4}	29.6	729.7	2.47E+05	7.52E+05	92.8	69.7
$2x\ 10^{-4}$	8.1	130.5	9.68E+05	7.60E+06	105.7	76.7
$4x\ 10^{-4}$	3.3	64.5	2.92E+06	1.74E+07	127.6	86.2
10^{-3}	4.1	40.5	5.39E+06	1.79E+07	170.0	84.0

Compartment size in a fractured reservoir is directly dependent on what is considered a "conductive" fracture. Thus, if all features are considered as conductive, the reservoir could be considered a single compartment. Conversely, if only features with a very high transmissivity are considered conductive, compartments would be coincident with these high transmissivity features, and there would be a large number of small compartments. Compartmentalization analysis algorithms are described in LaPointe et al. (1996).

Table 9-13 summarizes the statistics for compartments identified in the conditioned DFN model for different transmissivity cutoffs. Compartmentalization analysis for Tract 17 is illustrated in Figures 9-21 and 9-22.

Table 9-13 Compartmentalization Analysis Summary

Transmissivity Cut-Off	Clusters	Compartment Projected Area (horiz)		Compartment Volume		Compartment Fracture Intensity P_{32}	
(m^2/s)	Number	Mean (m^2)	Std Dev (m^2)	Mean (m^3)	Std Dev (m^3)	Mean (m^{-1})	Std Dev (m^{-1})
10^{-6}	1	4560000	0	1.08E+09	0		0
$4.x\ 10^{-5}$	196	2.82E+04	360258.3	6.08E+06	84022595	1.09E-01	0.082724
10^{-4}	353	1.76E+04	255183.9	3.32E+06	57416335	9.51E-02	0.071003
$2x\ 10^{-4}$	575	1.32E+04	143486.6	2.02E+06	31599001	8.01E-02	0.060299
$4x\ 10^{-4}$	752	8.55E+03	55704.03	9.97E+05	11827738	7.50E-02	0.047796
10^{-3}	549	6.31E+03	46685.51	6.83E+05	10297157	7.67E-02	0.044521
10^{-2}	24	5.53E+03	11649.33	5.86E+05	2015370	7.75E-02	0.029837

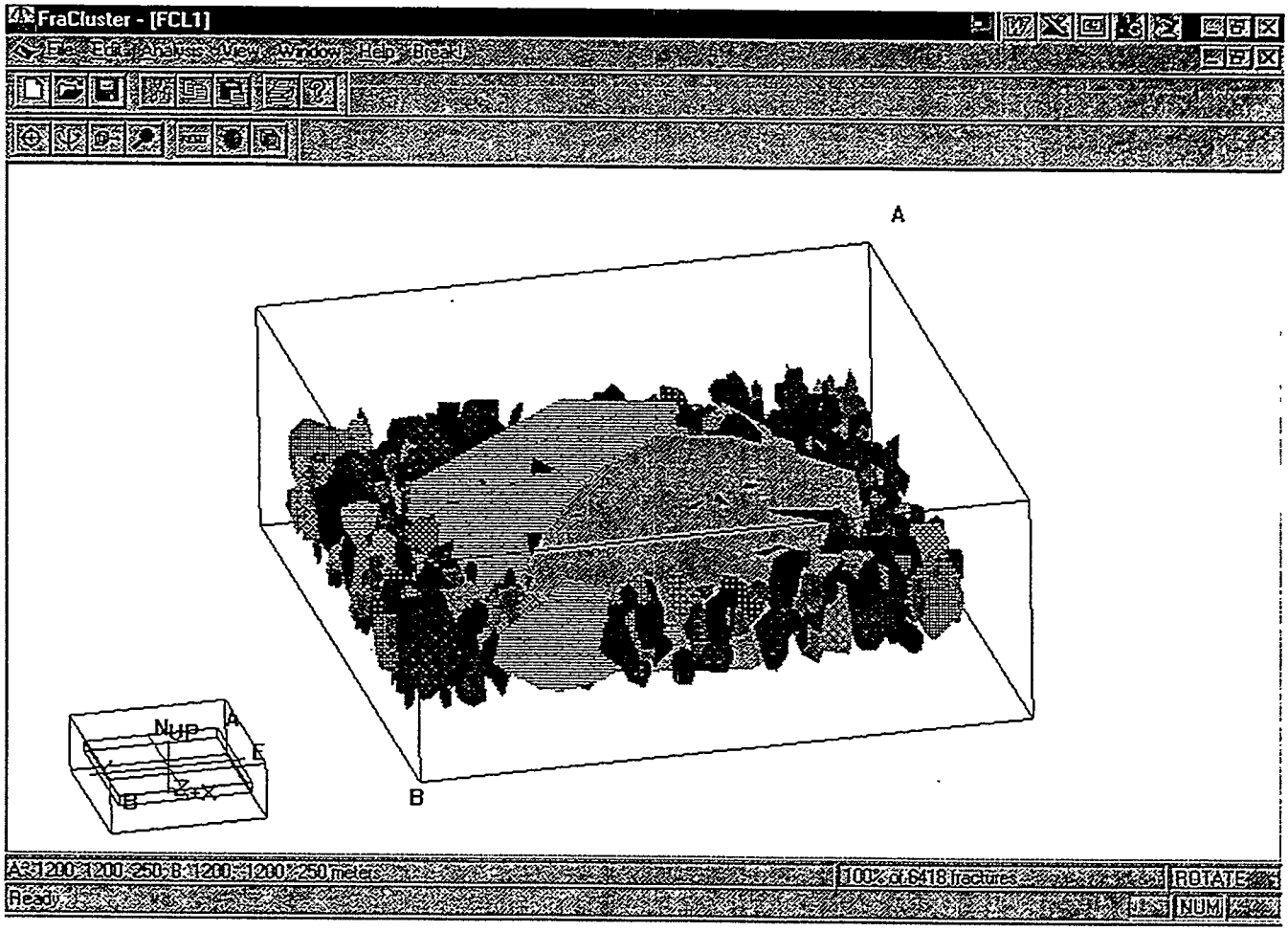

FIGURE **9-21**
TRACT 17 COMPARTMENTALIZATION
NIPER/FINAL REPORT/WA

PROJECT NO. 963 1357.521 DRAWING NO. 80623 DATE 9/29/98 DRAWN BY EA

Golder Associates

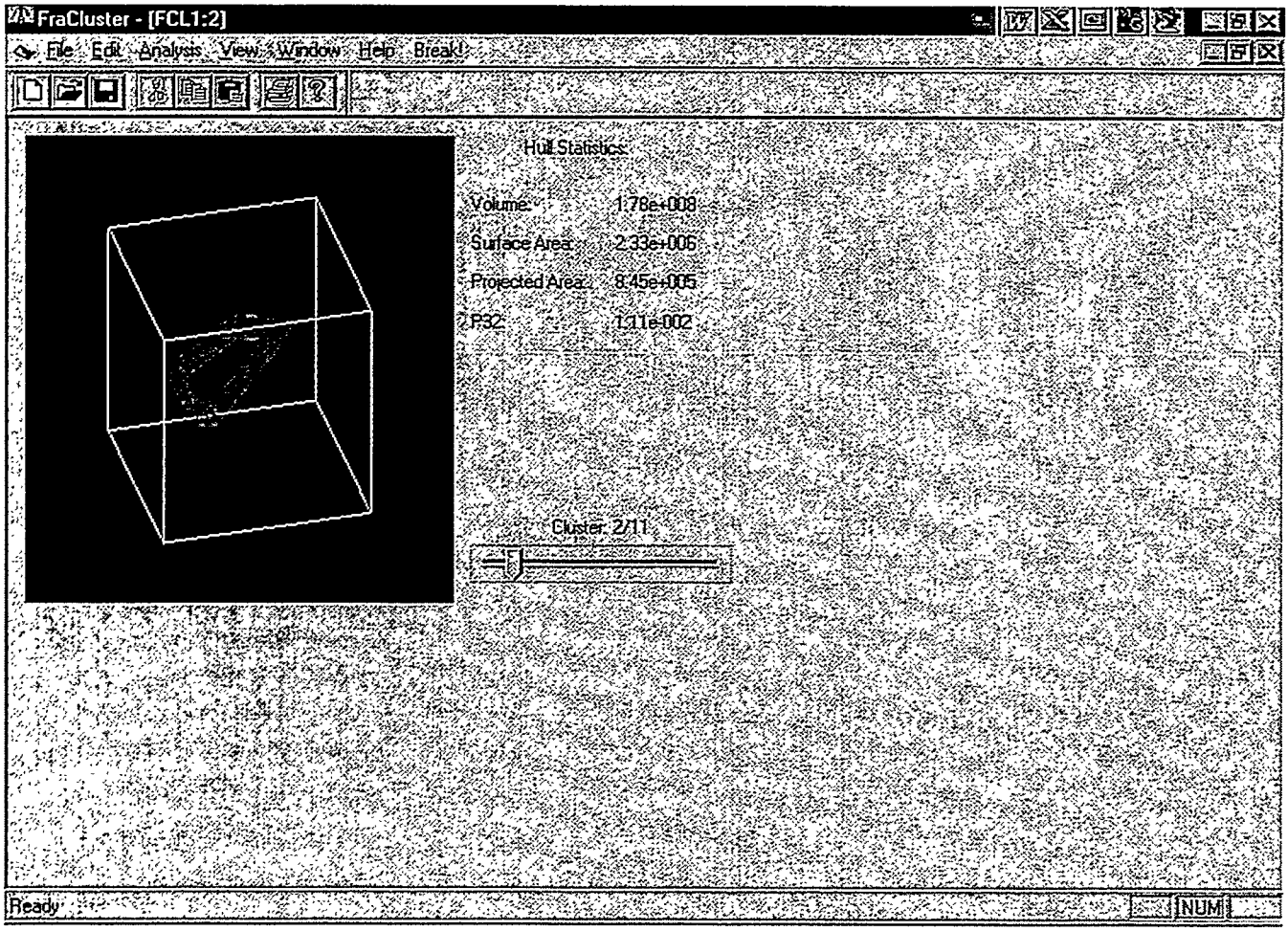

FIGURE **9-22**

TYPICAL TRACT 17 COMPARTMENT

NIPER/FINAL REPORT/WA

PROJECT NO. 963 1357.521 DRAWING NO. 80624 DATE 9/29/98 DRAWN BY EA

Golder Associates

For a given transmissivity cutoff, FraCluster was used to derive the number of compartments, the distribution of compartment projected area, compartment volume, and the intensity of fractures within the compartments. Figure 9-23 illustrates the formation of compartments in the Yates Tract 17 model as a function of the transmissivity, which is used to distinguish between "conductive" and "non-conductive" features. For a transmissivity cutoff of 10^{-6} m^2/s, the entire DFN is connected, resulting in a single network. The maximum number of compartments is formed when a cutoff of approximately $4x\ 10^{-4}$ is used. From there, increases in the transmissivity cutoff decrease the number of compartments dramatically. For Tract 17, a transmissivity on the order of 10^{-4} m^2/s might be considered a reasonable cutoff, such that on the order of 200 hydraulic compartments would be found in the field, connected only by features of less than 10^{-4} m^2/s.

The projected compartment area distribution (Figure 9-24) is the key for the design of infill drilling. From the Tract 17 DFN model, the mean compartment volume at a transmissivity cutoff of 4×10^{-4} m^2/s is approximately 10,000 m^2. The compartment volume distribution is useful for assessing the oil producable for a given compartment (Figure 9-25). The compartment volume varies from on the order of 10^4 m^3 to 10^9 m^3, with a mean on the order of 10^7 to 10^8 m^3. The variability between compartments is much greater than the variability in the mean compartment volume with transmissivity cutoff.

Intensity P_{32}, the fracture area per unit volume in compartments determines the area available for transfer of fluids from matrix storage to the fracture networks which feed well production. As P_{32} increases, the fracture network becomes more efficient for gravity drainage of reservoir matrix storage. As shown in Figure 9-26, the mean compartment P_{32} is fairly constant at 0.07 to 0.12 m^2/m^3. However, very large values of P_{32} can occur, indicating a very effective drainage network, particularly for transmissivity cutoff less than on the order of 10^{-3} m^2/s.

Tributary drainage volume analysis is similar to compartment analysis, except that it focuses on compartments as they intersect specific well fields. The Tract 17 well field analyzed includes all of the currently installed vertical wells (Figure 9-27). Results of this analysis are summarized in Table 9-14.

Table 9-14 Tributary Drainage Volumes

Transmissivity Cut-Off	Producable Volumes	Drainage Volume		Projected Drainage Area (horiz)		Drainage Fracture Intensity P_{32}	
(m^2/s)		Mean (m^3)	Std Dev (m^3)	Mean (m^2)	Std Dev (m^2)	Mean (m^{-1})	Std Dev (m^{-1})
4×10^{-5}	1	1.18E+09		1.15E+07		0.0338	
10^{-4}	1	1.08E+09		1.09E+07		0.0253	
2×10^{-4}	5	1.56E+08	3.35E+08	1.68E+06	3.43E+06	0.0356	0.0219
10^{-3}	13	2.06E+07	6.6322E+07	3.06E+05	8.22E+05	0.0523	0.0460
10^{-2}	1	2.07E+06		1.88E+05		0.0445	

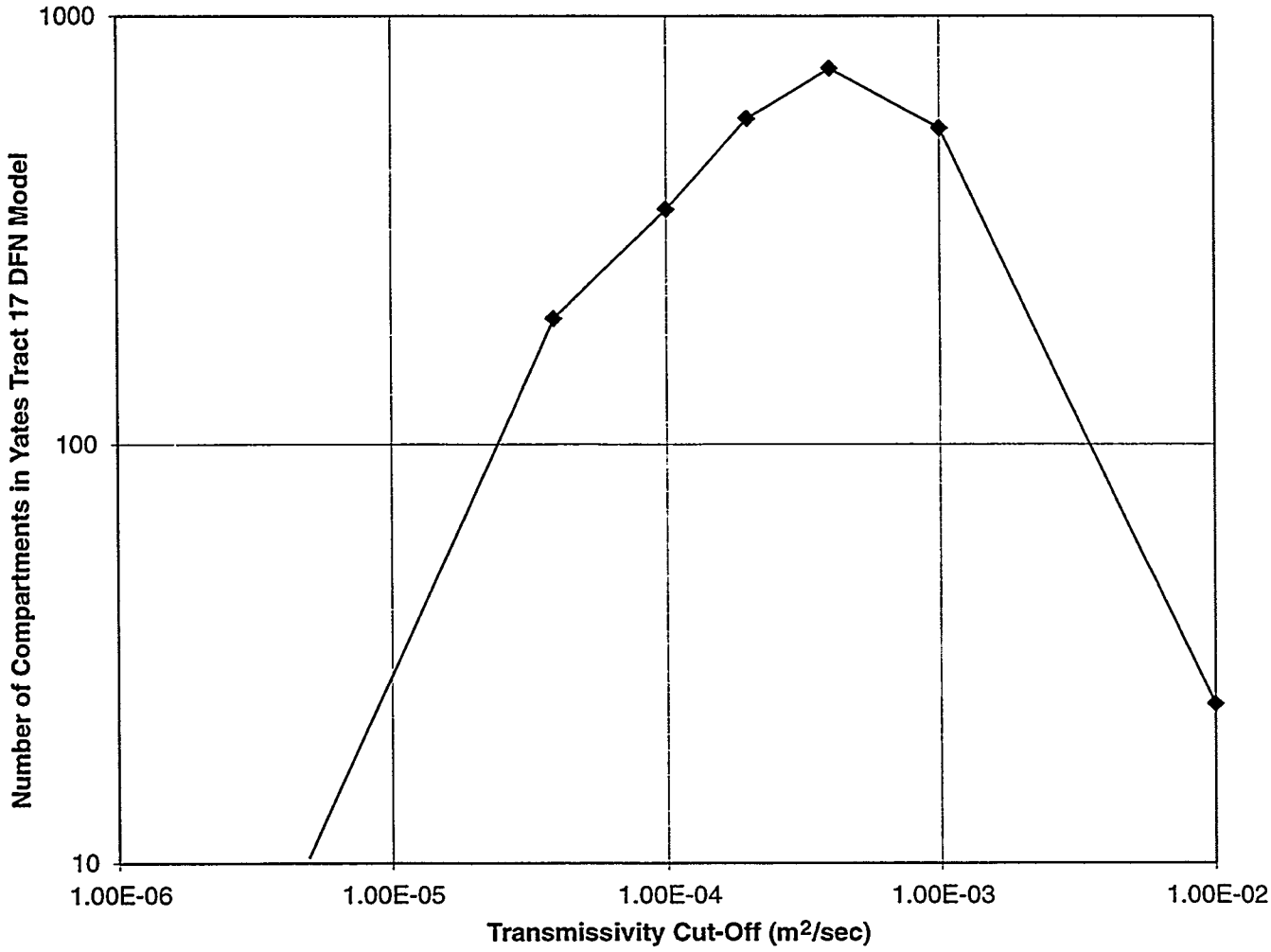

FIGURE **9-23**
TRACT 17 COMPARTMENT FORMATION
NIPER/FINAL REPORT/WA

PROJECT NO. 963 1357.521 DRAWING NO. 80625 DATE 9/29/98 DRAWN BY EA

Golder Associates

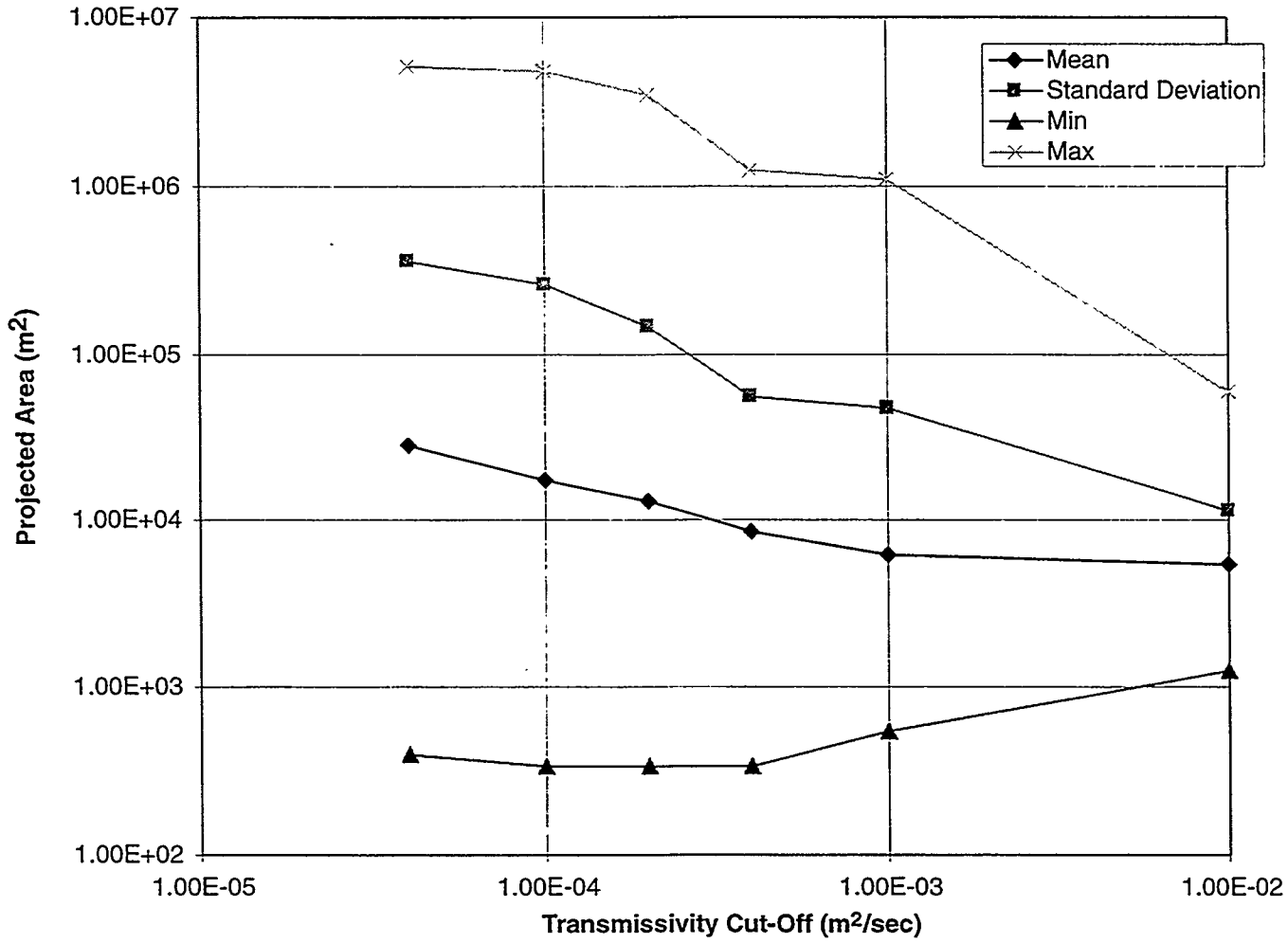

FIGURE **9-24**
PROJECTED COMPARTMENT AREA
NIPER/FINAL REPORT/WA

PROJECT NO. 963 1357.521 DRAWING NO. 80626 DATE 9/29/98 DRAWN BY EA

Golder Associates

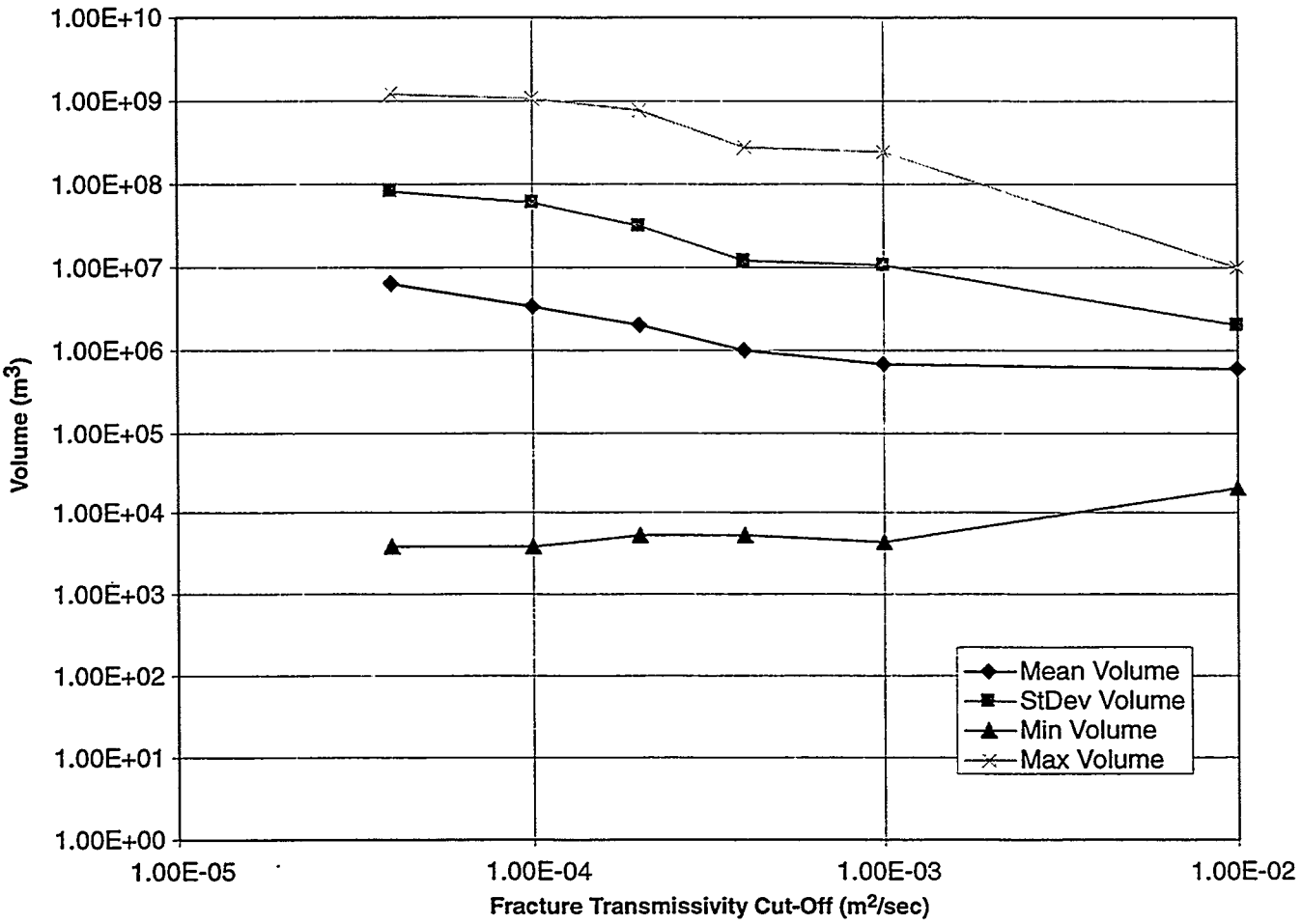

FIGURE **9-25**
COMPARTMENT VOLUME DISTRIBUTION
NIPER/FINAL REPORT/WA

PROJECT NO. 963 1357.521 DRAWING NO. 80627 DATE 9/29/98 DRAWN BY EA

Golder Associates

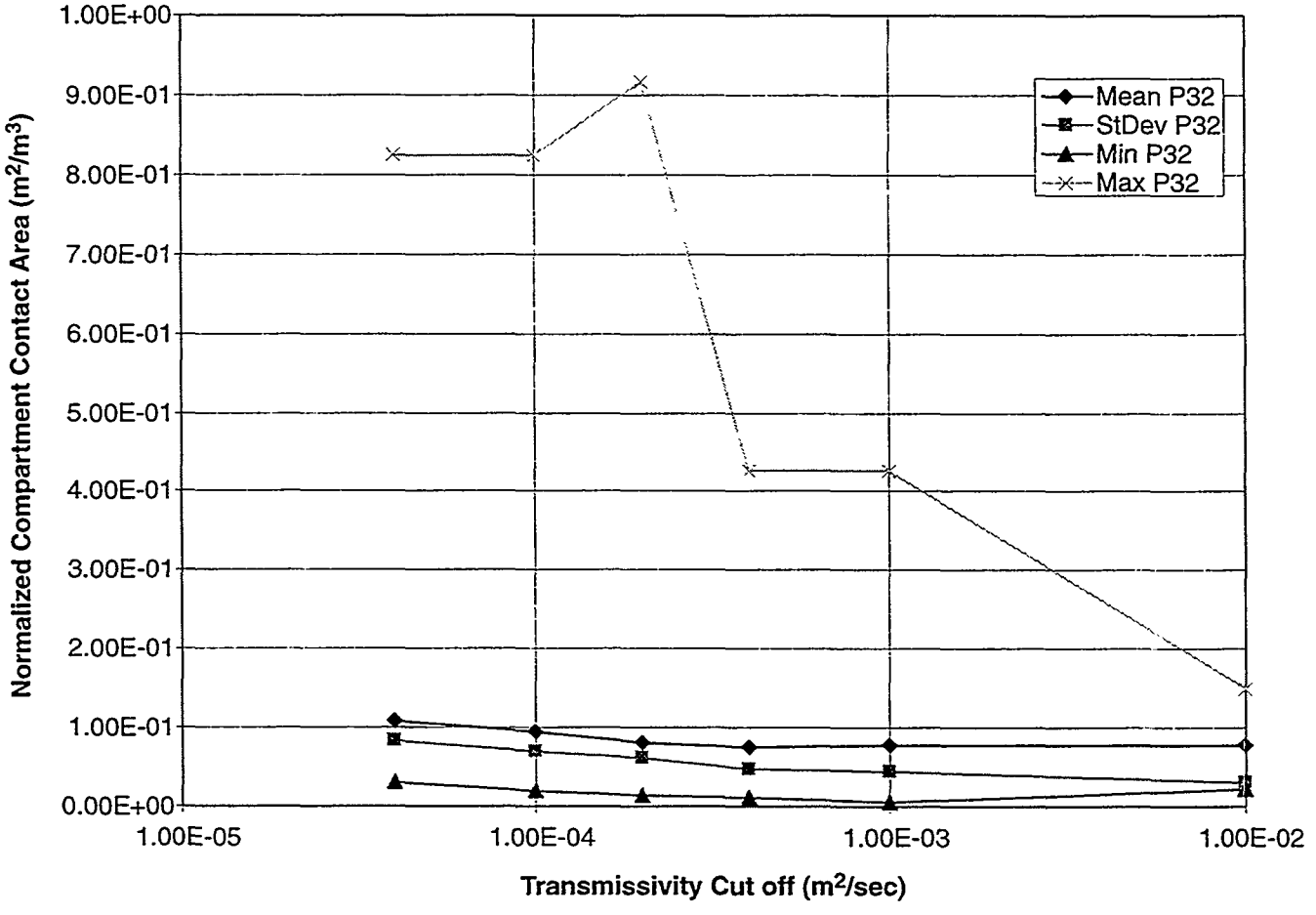

FIGURE **9-26**

COMPARTMENT CONTACT AREA DISTRIBUTION

NIPER/FINAL REPORT/WA

PROJECT NO. 963 1357.521 DRAWING NO. 80628 DATE 9/29/98 DRAWN BY EA

Golder Associates

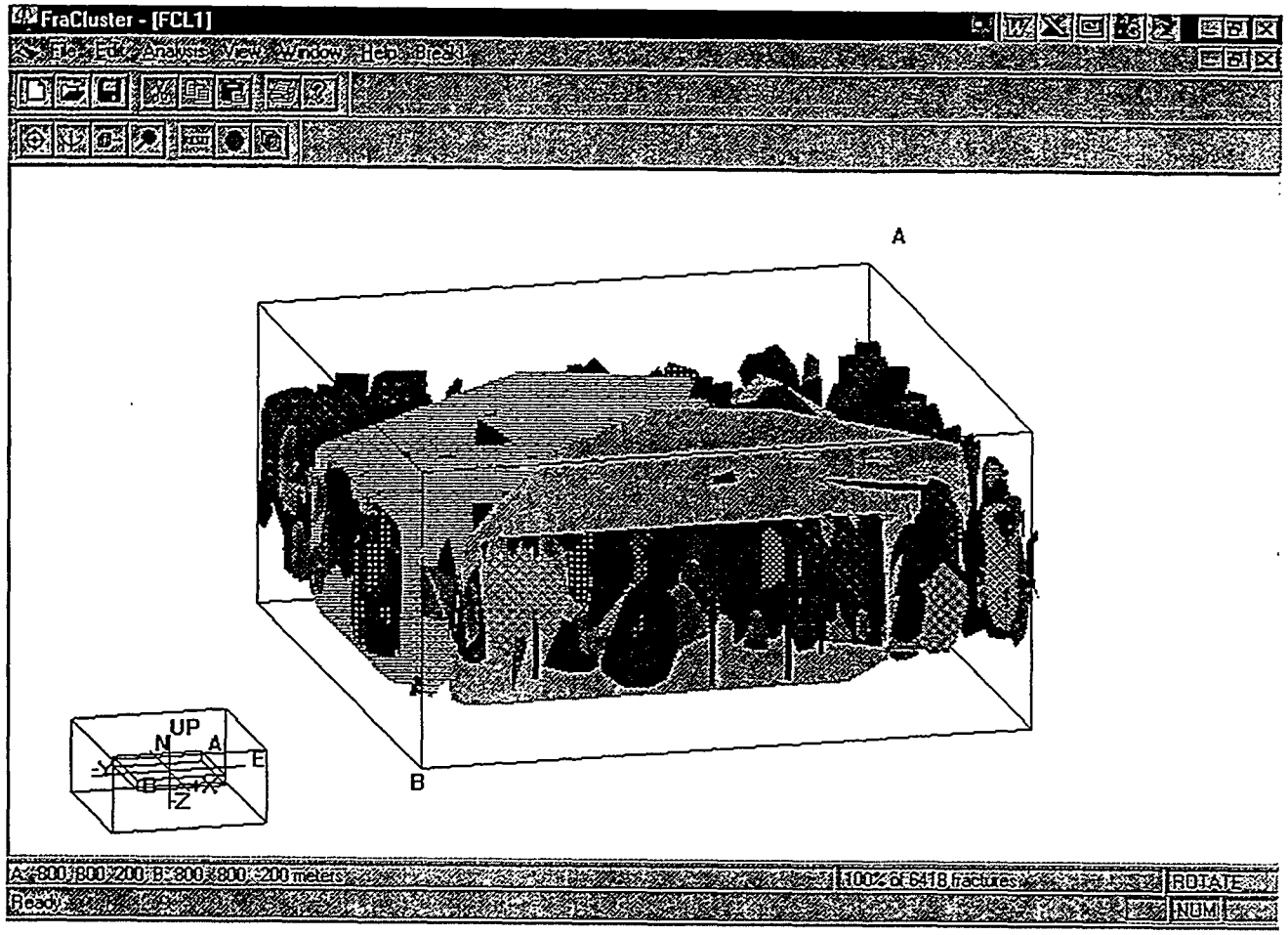

FIGURE **9-27**

TRIBUTARY DRAINAGE VOLUME ANALYSIS

NIPER/FINAL REPORT/WA

PROJECT NO. 963 1357.521 DRAWING NO. 80629 DATE 9/29/98 DRAWN BY EA

Golder Associates

Figure 9-28 illustrates the distribution of tributary drainage volume for the Tract 17 DFN model based on the well field analyzed. A single compartment of on the order of 10^9 m^3 is accessed the wells analyzed within the Tract 17 DFN model region if all fractures above approximately 10^{-5} to 10^{-4} m^2/s are considered conductive. For a transmissivity cutoff greater than 10^{-4}, this compartment is seen as multiple smaller compartments, and therefore more, smaller compartments are identified in the tributary drainage volume calculation.

The exchange surface area for the tributary drainage volumes are shown in Figure 9-29. Figure 9-29a shows the variation in fracture intensity with the transmissivity cutoff. Figure 9-29b shows the total connected fracture surface area available for fluid transfer from matrix storage to the flowing fracture network. An ara on the order of 10^7 m^2 is available for fluid exchange with a transmissivity cutoff of 10^{-5} to 10^{-4} m^2/s.

A typical Tract 17 tributary drainage region is shown in Figure 9-30.

9.2.4 Flare Analysis

Tract 17 reservoir permeability-thickness was calculated from wells simulated into the Tract 17 conditioned DFN model. Permeability thickness K_h was calculated as the total transmissivity from all the fractures seen in a 15 m interval, using a representative sample of 9 of the actual Tract 17 vertical wells.

The cumulative density function for permeability thickness from this analysis is presented in Figure 9-31 for intervals with permeability thickness greater than 10^{-7} m^2/s. Table 9-15 summarizes simulation results statistically for intervals with permeability thickness greater than 10^{-7} m^2/s. Based on this analysis, the median permeability thickness is 4.3×10^{-4} m^2/s, which corresponds to 1.16×10^5 mD-ft. The median permeability is the permeability for which 50% of intervals tested have greater permeability thickness.

Table 9-15 Permeability Thickness (m^2/s) for 15 m Production Intervals

Mean	0.00238
Standard Error	0.001039
Median	0.000431
Standard Deviation	0.004527
Sample Variance	2.05E-05
Kurtosis	5.877014
Skewness	2.538446
Range	0.016437
Minimum	2.34E-05
Maximum	0.01646
Sum	0.045224
Count	19
Confidence Level(95.0%)	0.002182

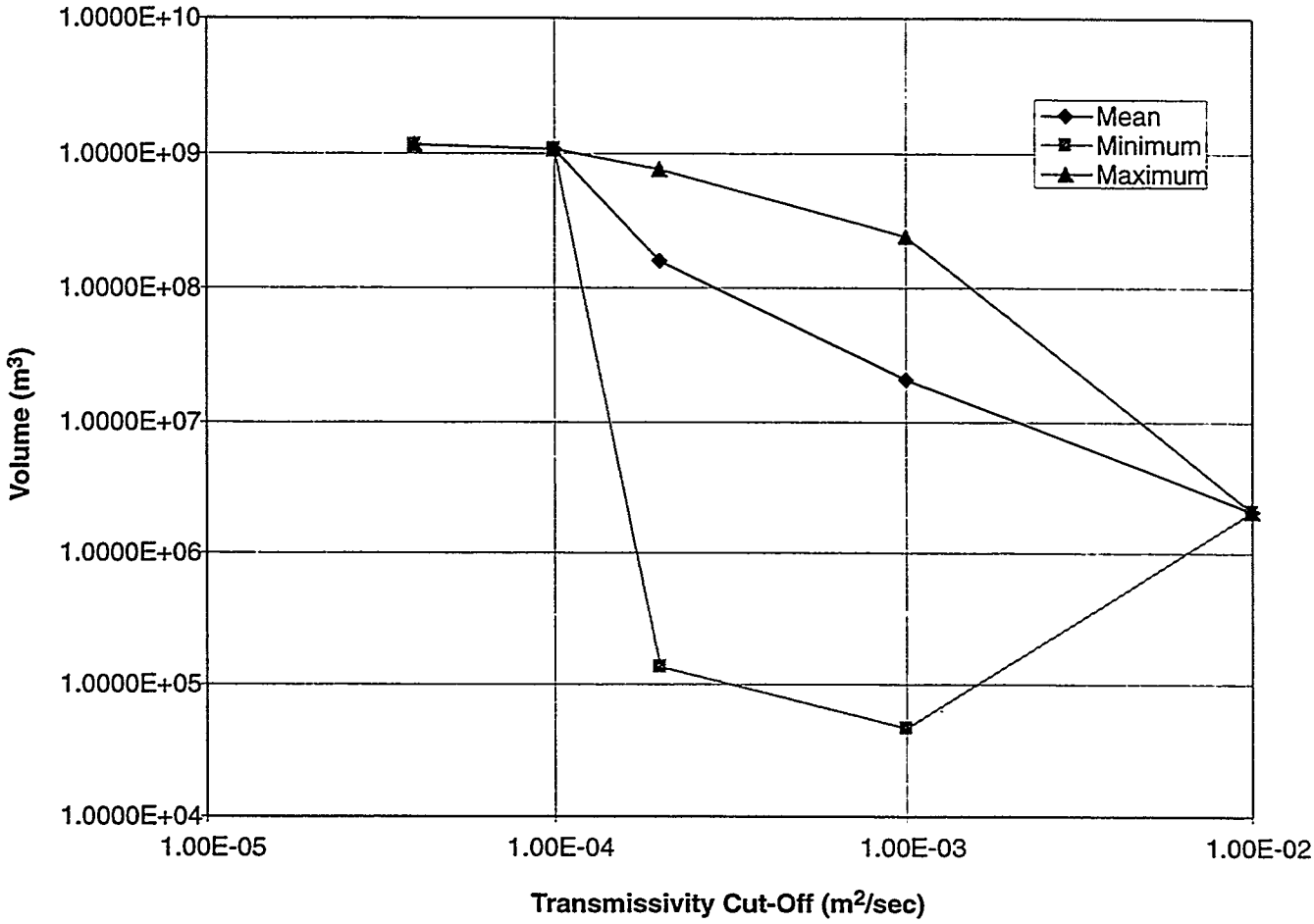

FIGURE **9-28**

TRACT 17 TRIBUTARY DRAINAGE VOLUME

NIPER/FINAL REPORT/WA

PROJECT NO. 963 1357.521 DRAWING NO. 80630 DATE 9/29/98 DRAWN BY EA

Golder Associates

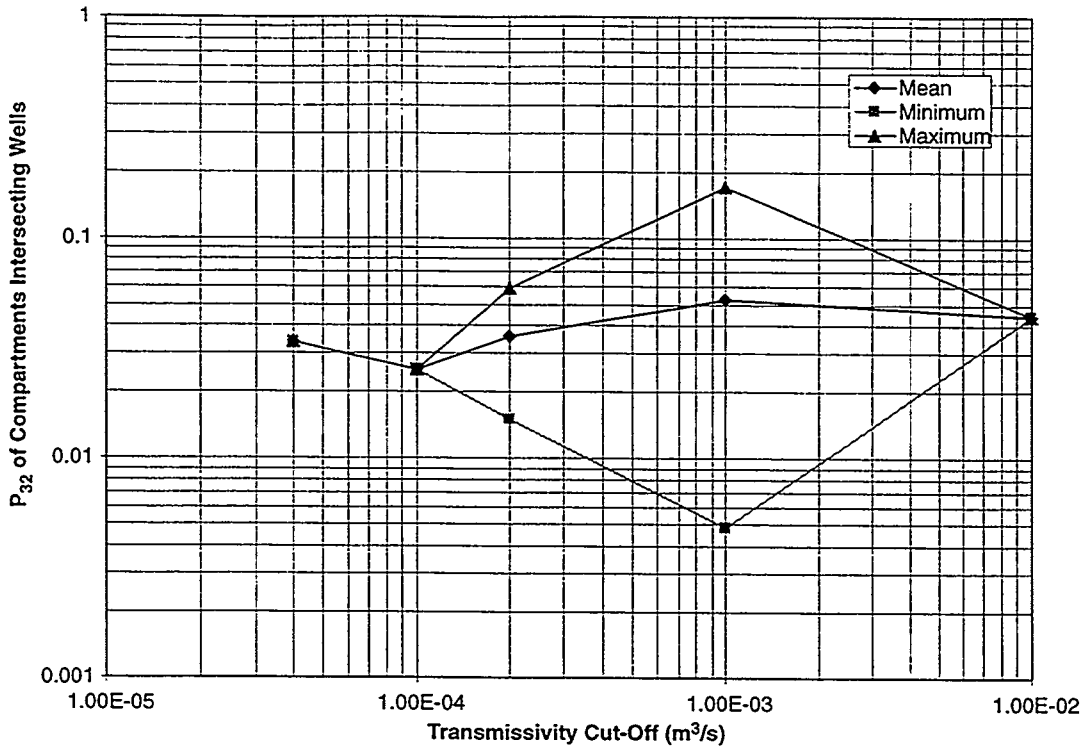

a) Fracture Intensity P_{32} (m^{-1})

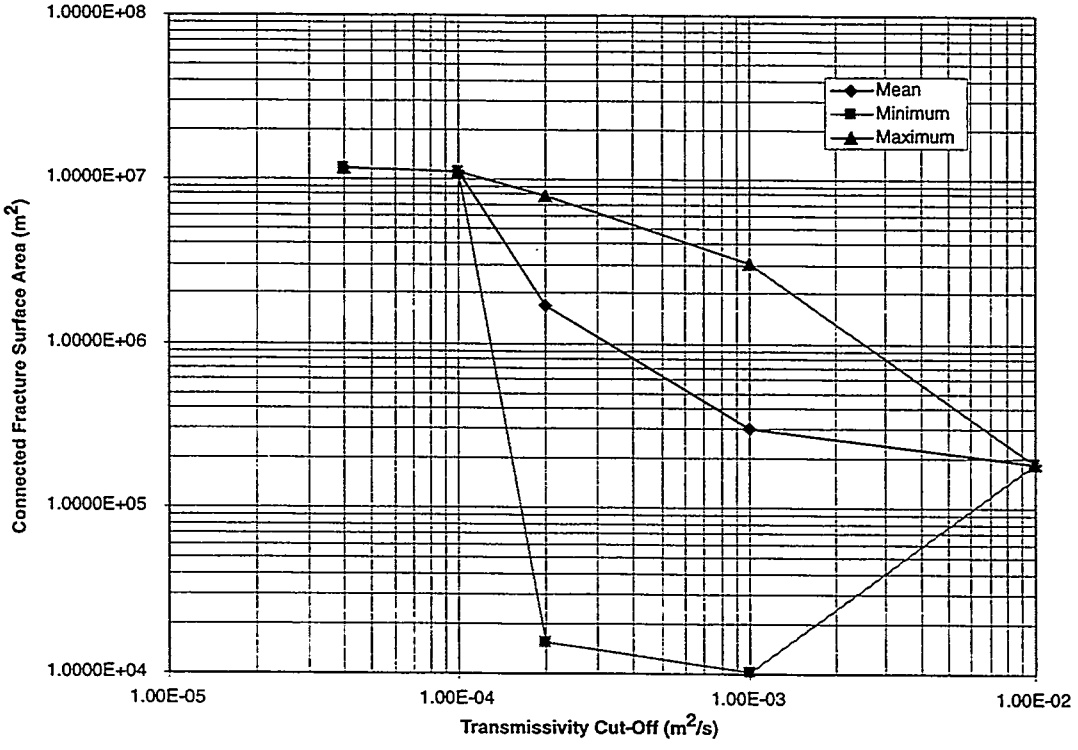

b) Exchange surface area

FIGURE **9-29**
TRACT 17 TRIBUTARY VOLUME FLUID EXCHANGE SURFACE AREA
NIPER/FINAL REPORT/WA

PROJECT NO. 963 1357.521 DRAWING NO. 80631 DATE 9/29/98 DRAWN BY EA

Golder Associates

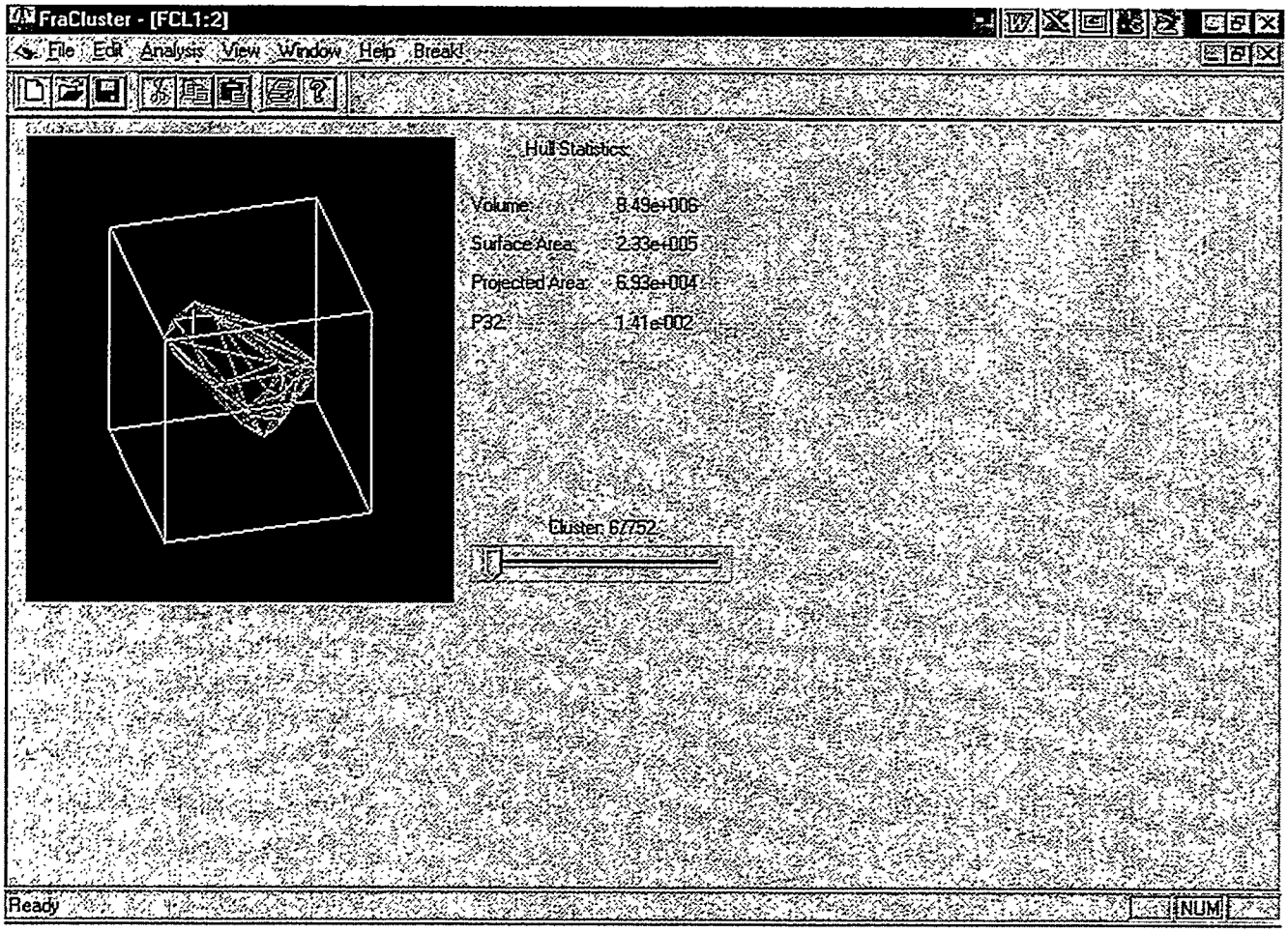

FIGURE **9-30**

TYPICAL TRACT 17 DRAINAGE VOLUME

NIPER/FINAL REPORT/WA

PROJECT NO. 963 1357.521 DRAWING NO. 80632 DATE 9/29/98 DRAWN BY EA

Golder Associates

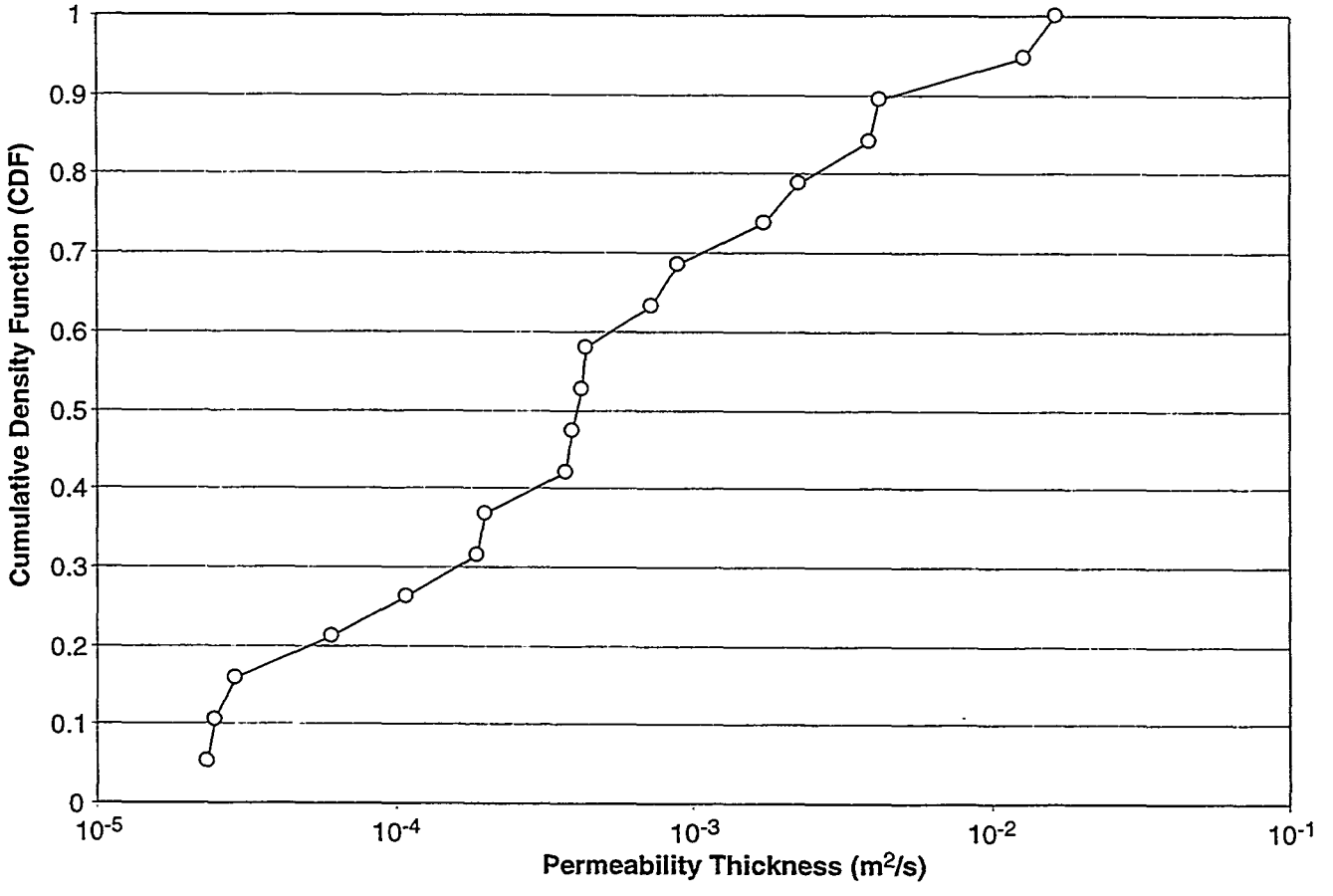

FIGURE **9-31**
PERMEABILITY THICKNESS Kh
NIPER/FINAL REPORT/WA

PROJECT NO. 963 1357.521 DRAWING NO. 80633 DATE 9/29/98 DRAWN BY EA

Golder Associates

9.2.5 ECLIPSE and THERM/DK Simulations

ECLIPSE and THERM/DK reservoir simulations were carried out for Tract 17 to demonstrate the applicability of the discrete fracture network approach for improved production through TAGS. Simulations were carried out based on the DFN model derived in Section 9.1 above using the grid cell K_x, K_y, K_z of Section 9.2.1.

Figure 9-32 shows the location of the ECLIPSE model grid for Tract 17. The model grid is 12 by 12 by 24 grid cells (Figure 9-33), with variations in the number of vertical grid cells to account for local topography. The grid cell K_x,K_y, and K_z permeabilities for the ECLIPSE and THERM/DK models are based on the numerical permeameter study (Section 9.2.1 above). The major geologic structures in the Tract 17 model are shown in Figure 9-34. Figure 9-35 illustrates the variability in permeability in the ECLIPSE grid based on the DFN numerical permeameter simulation results.

Boundary conditions for the ECLIPSE simulations are illustrated in Figure 9-36. The boundary conditions reflect the importance of oil column thickness to maintain connectivity and production. Boundary effects on the model include:

- supply of water to the model from the underlying aquifer
- gas injection to match the downward movement of the oil column as observed since 1992,
- oil injection (at late time) to maintain column thickness.

The ECLIPSE model, based on DFN model parameters, was developed through a series of successively refined DFN models, and therefore the results reflect different stages of model development. As a result, the simulations presented in this section are based on a range of DFN model implementations.

The value of models in the oil industry is frequently judged based on the ability of models to match observed behavior. Figures 9-37 and 9-38 present model matches based on a 1996 DFN model implementation. The fluid contact time histories for Tract 17 based on the ECLIPSE/DFN model are shown in Figure 9-37. In this figure, it can been seen that the DFN model provides a good match to the pattern of movement of the fluid contacts. Figure 9-38 shows a comparable figure for the pressure time history.

The major ECLIPSE/DFN simulations were based on sodium bromide tracer tests carried out in the underlying aquifer during 1996, from deep water injector YU1711. As shown in Figure 9-39a, this tracer test illustrated the anisotropy and heterogenous connectivity which is typical of fractured reservoirs. Figures 9-40 and 9-41 provide more detailed views of the tracer simulations. The tests confirmed the DFN model's major NW-SE directional connectivity, with rapid breakthrough to nearby offset wells and later breakthrough to perimeter wells.

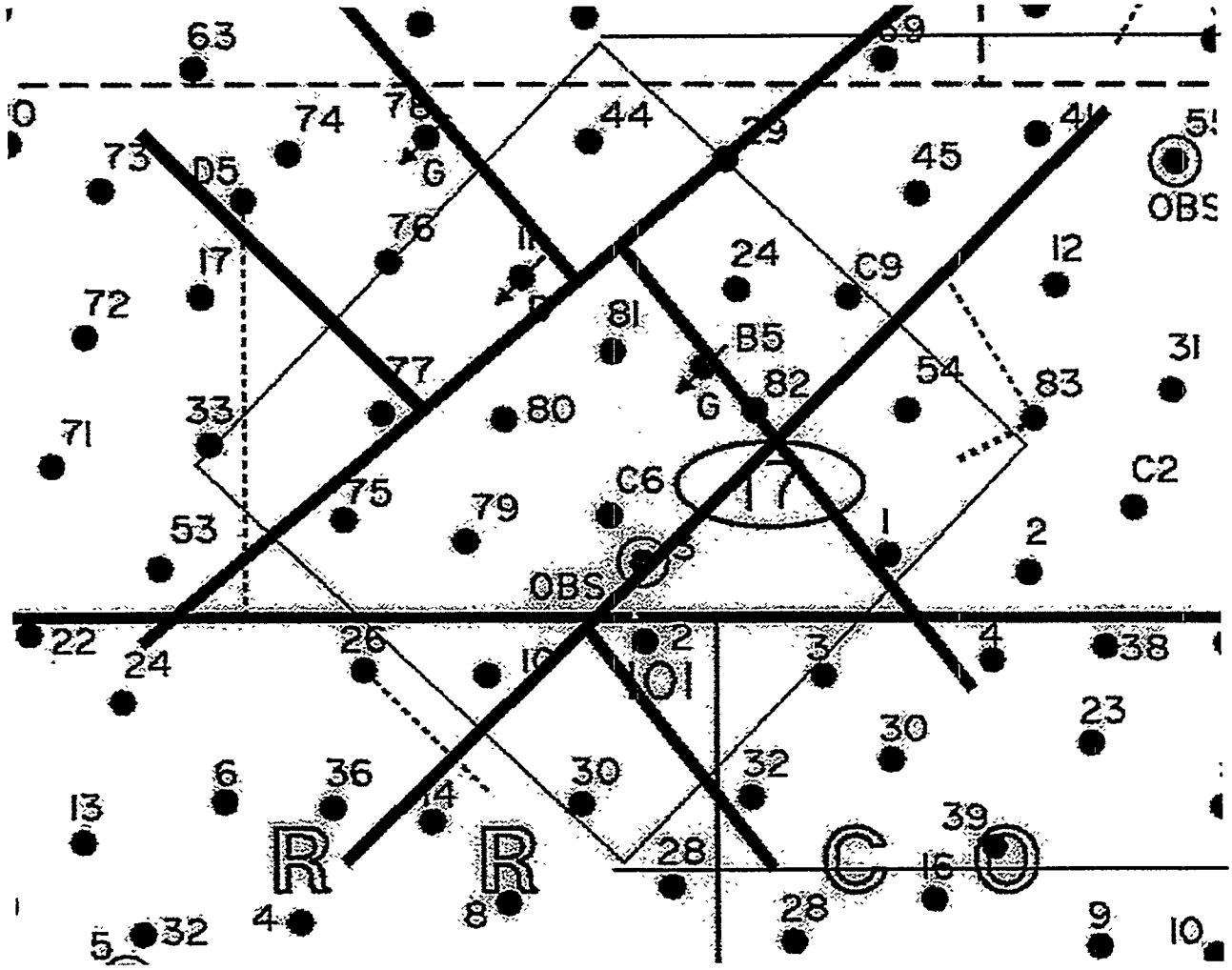

FIGURE **9-32**
TRACT 17 WITH ECLIPSE GRID
NIPER/FINAL REPORT/WA

PROJECT NO. 963 1357.521 DRAWING NO. 80640 DATE 9/29/98 DRAWN BY EA

Golder Associates

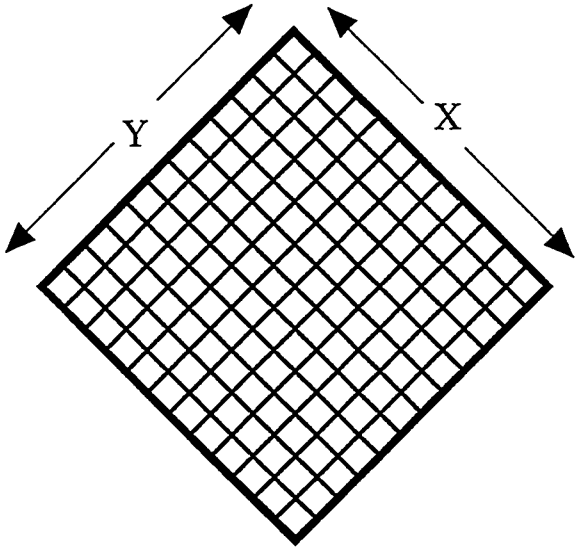

Areal Dimensions 12 X 12
a) Plan

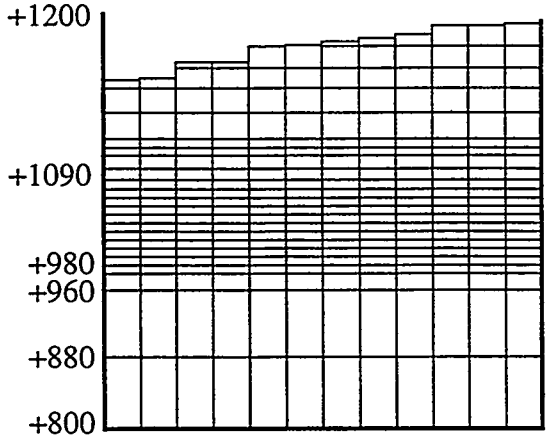

24 Vertical Layers
b) Section

FIGURE **9-33**
ECLIPSE GRID
NIPER/FINAL REPORT/WA

PROJECT NO. 963 1357.521 DRAWING NO. 80641 DATE 9/29/98 DRAWN BY EA

Golder Associates

Step 2: Populate Cells With Porosity and Permeability Data From Stratamodel and Fracman

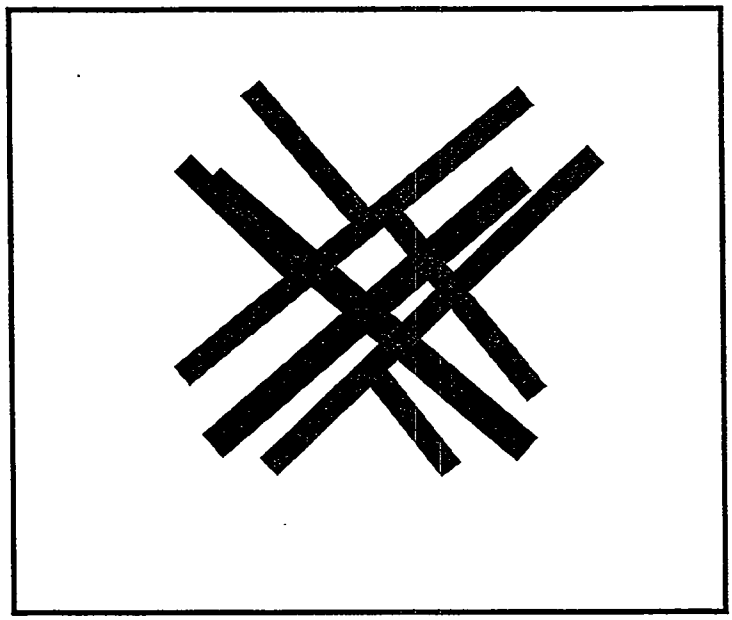

Dominant Fracture Trends From Fracman, Tracer and Pressure Interference Tests

FIGURE **9-34**
MAJOR GEOLOGIC STRUCTURES IN ECLIPSE GRID
NIPER/FINAL REPORT/WA

PROJECT NO. 963 1357.521 DRAWING NO. 80642 DATE 9/29/98 DRAWN BY EA

Golder Associates

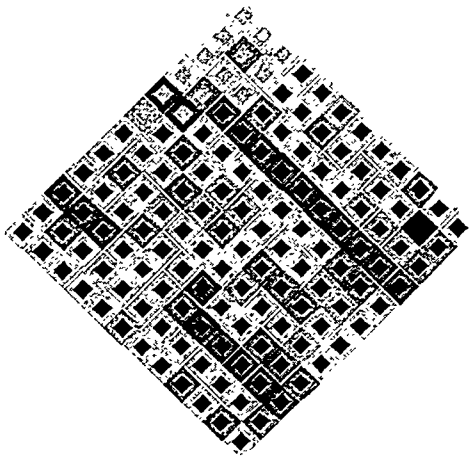

Permeability in "X" Direction
Indicating Modeling of Dominant
Fracture Trends in Layer 15

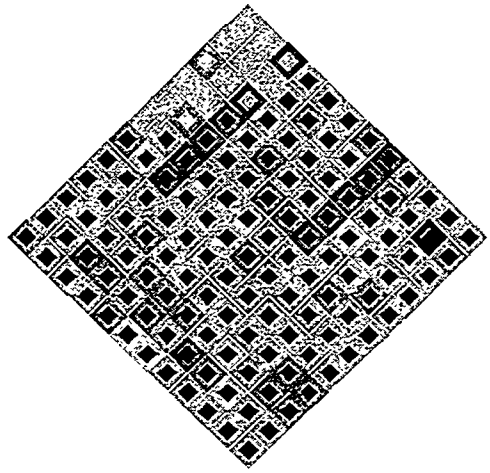

Permeability in "Y" Direction
Indicating Modeling of Dominant
Fracture Trends in Layer 15

FIGURE **9-35**
ECLIPSE MODEL PERMEABILITY
NIPER/FINAL REPORT/WA

PROJECT NO. 963 1357.521 DRAWING NO. 80643 DATE 9/29/98 DRAWN BY EA

Golder Associates

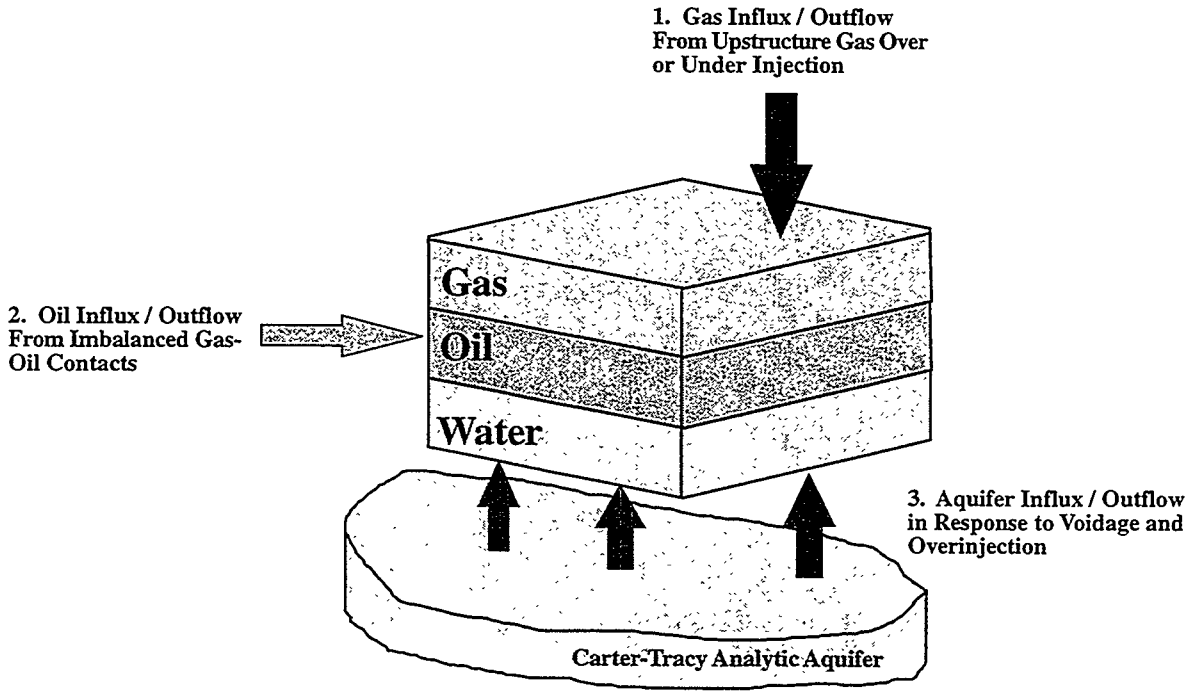

FIGURE **9-36**
BOUNDARY CONDITION ISSUES
NIPER/FINAL REPORT/WA

Tract 17 Model Versus Actual Contact Movement

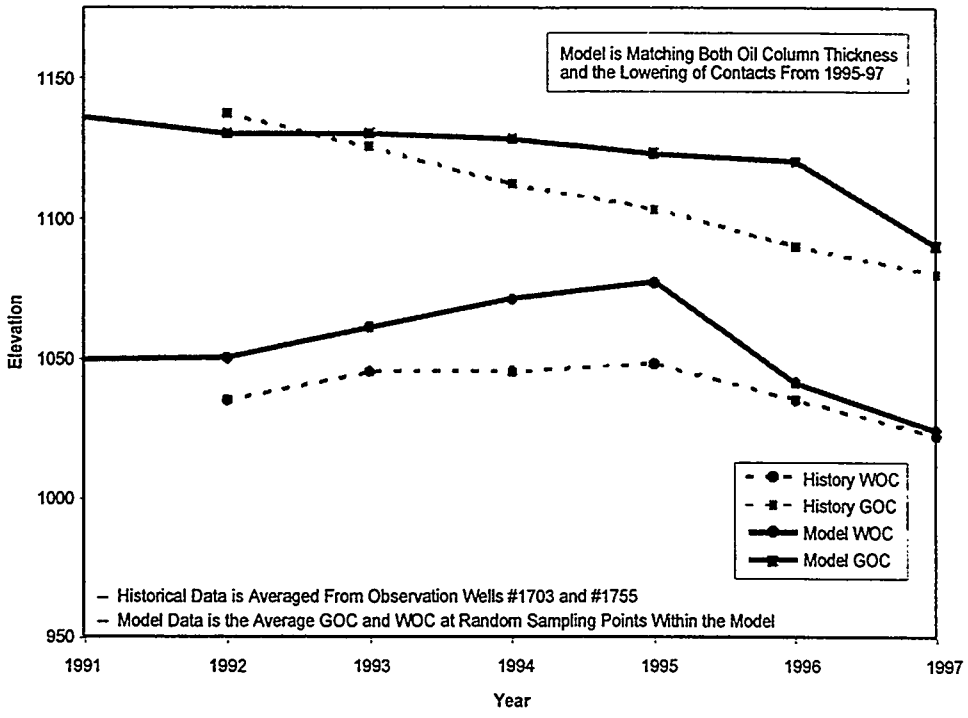

Model Oil Saturation in 1997

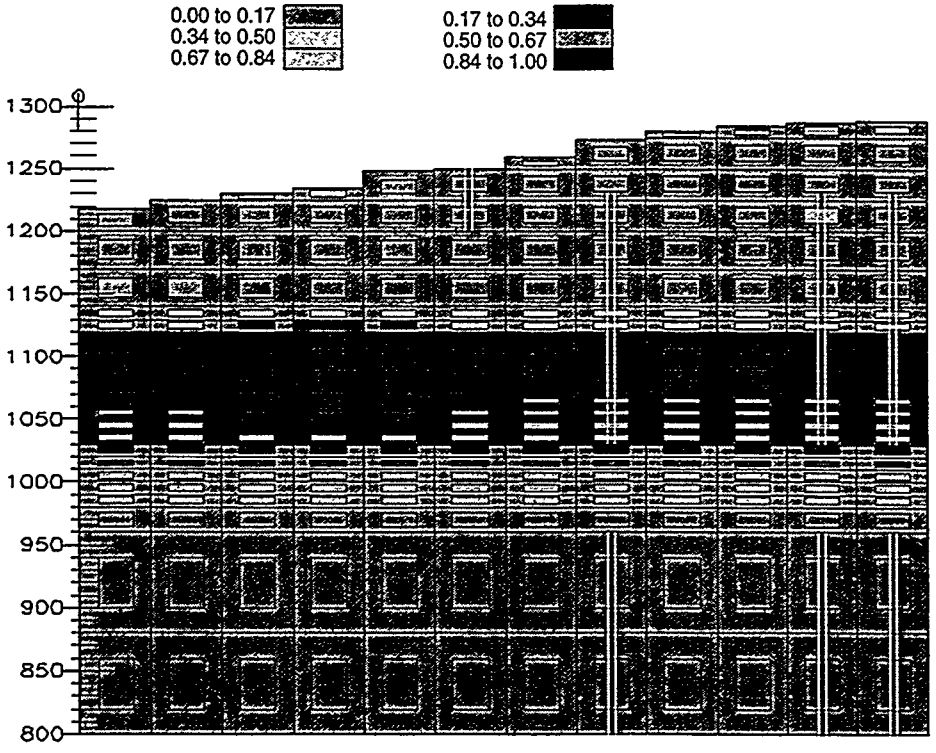

XZ Oil Saturation at Plane 4 (i=4) in 1997

FIGURE **9-37**
WATER-OIL AND GAS-OIL CONTACTS: MEASURED AND SIMULATED
NIPER/FINAL REPORT/WA

PROJECT NO. 963 1357.521 DRAWING NO. 80645 DATE 9/29/98 DRAWN BY EA

Golder Associates

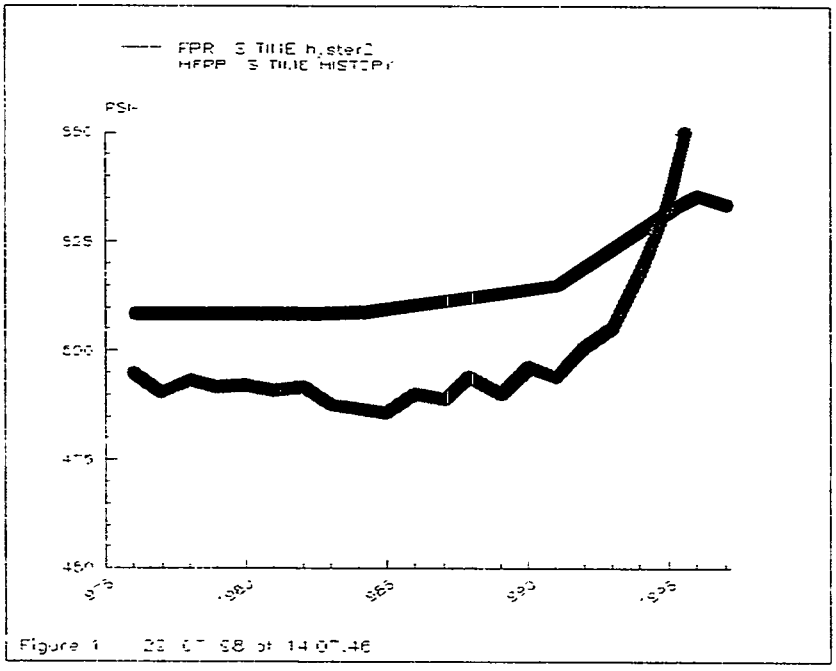

Model Pressure is Close, Although Not a Perfect Match. Improved Runs are Being Made With Increased Gas Injection in 1996-97. This Should Improve the Pressure Match.

FIGURE **9-38**
RESERVOIR PRESSURE: MEASURED AND SIMULATED
NIPER/FINAL REPORT/WA

a) Actual Field Data
1996 NaBr Tracer Tests
Deep Water Injector 1711

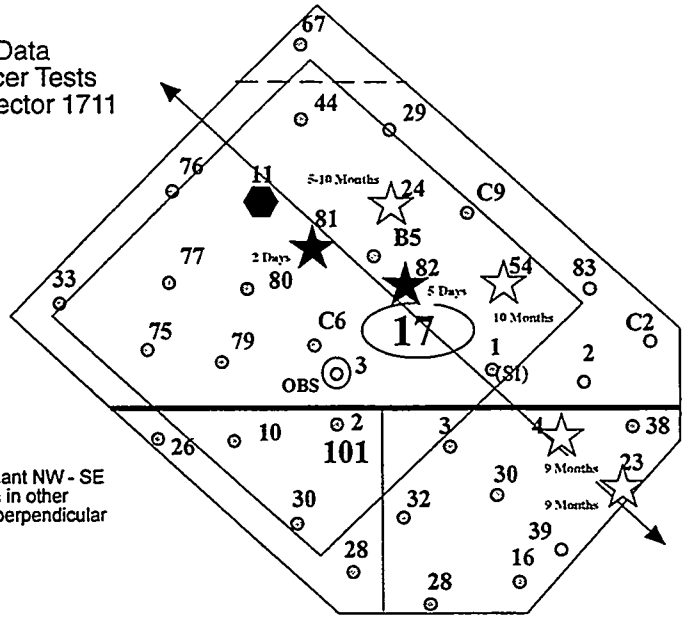

Test confirmed dominant NW - SE directionality, as seen in other evaluations. Slower perpendicular dispersion noted.

b) 1998 Golder Model Results
1996 NaBr Tracer Tests
Deep Water Injector 1711

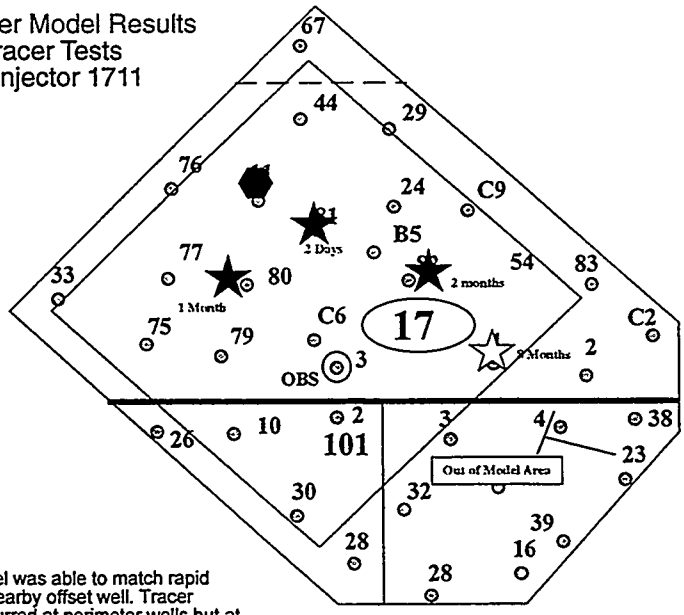

1998 Golder Model was able to match rapid breakthrough in nearby offset well. Tracer breakthrough occurred at perimeter wells but at later times than recorded in field. Model supports NW-SE directionality and lesser perpendicular dispersion. BUT - model could not make historic oil or water rates through history. Lower overall fracture permeabilities allow velocity matches (i.e. tracer test) similiar to higher perm grid but do not support overall fluid rates.

FIGURE **9-39**
TRACER TEST:
MEASURED AND SIMULATED
NIPER/FINAL REPORT/WA

PROJECT NO. 963 1357.521 DRAWING NO. 80636 DATE 9/29/98 DRAWN BY EA

Golder Associates

3-D view of tracer concentration per cell showing immediate vertical and lateral dispersion. (original deterministic discrete fracture grid)

a) Day 1

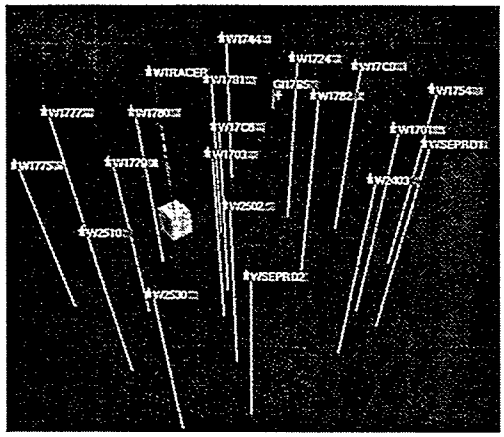

b) 2 Weeks

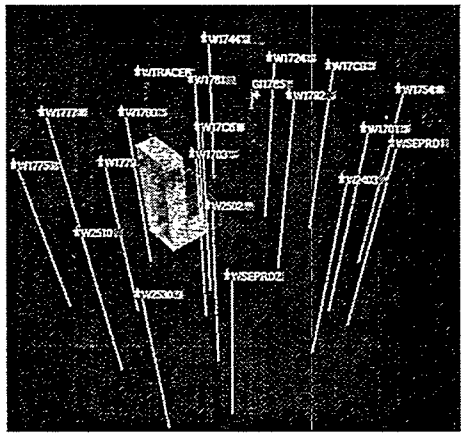

c) 1 Month

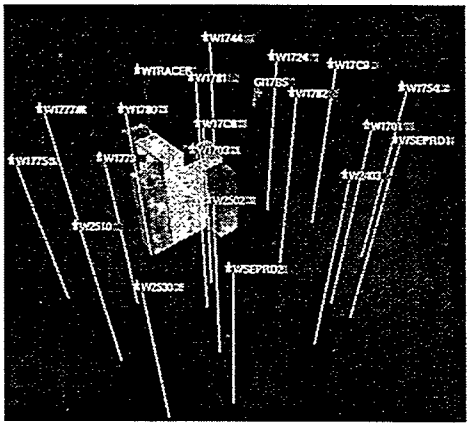

d) 2 Months

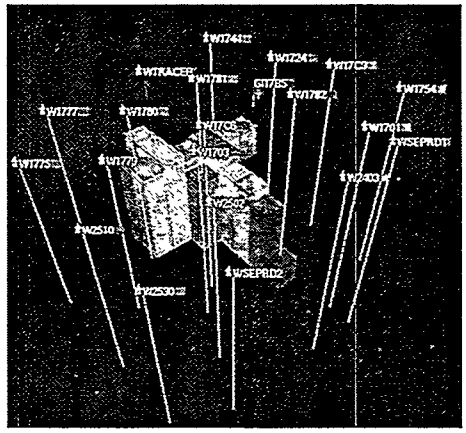

e) 3 Months

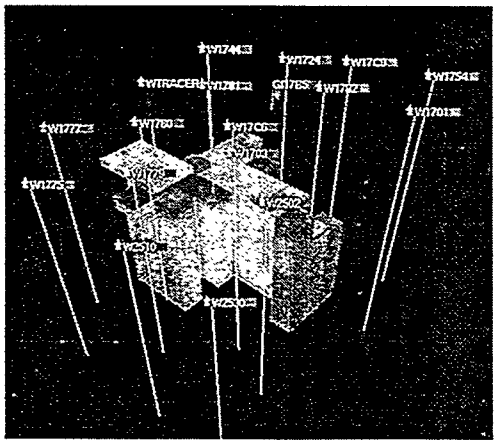

f) 7 Months

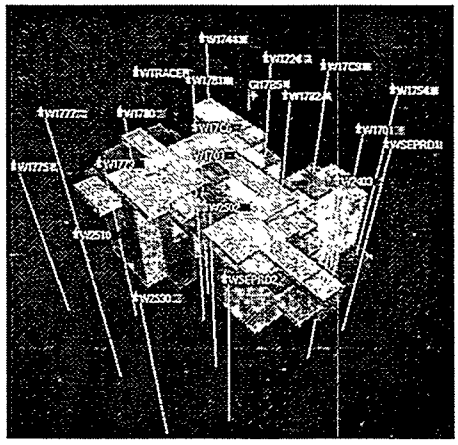

FIGURE **9-40**
3D VIEW OF TRACER SIMULATION
NIPER/FINAL REPORT/WA

Tracer breakthrough results with new Golder conditioned stochastic fracture grid. Tracer breakthrough times and flow direction matched. Major flow features have an order of magnitude lower fracture permeability creating a more "homogeneous" flow network. Tracer results are matched BUT model can not make historic fluid rates with lower fracture perms.

a) Day 1

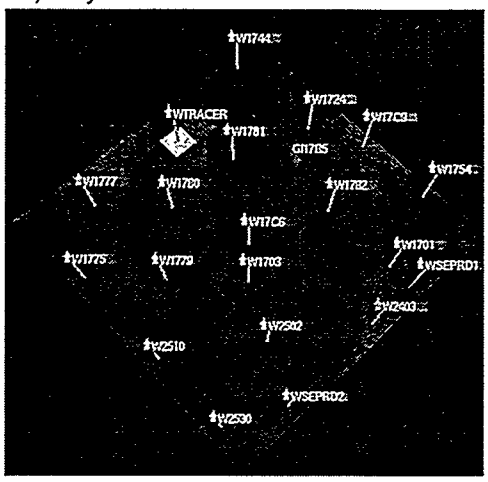

b) 2 Weeks

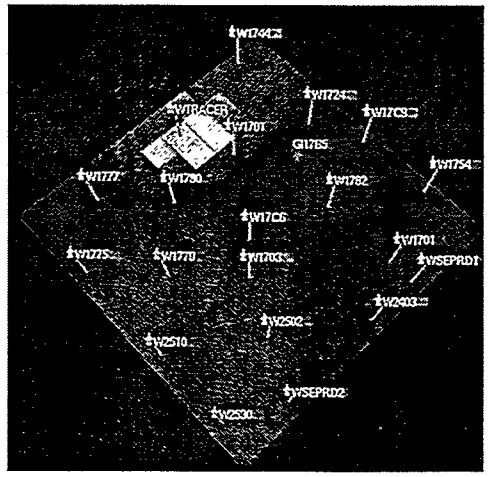

c) 1 Month

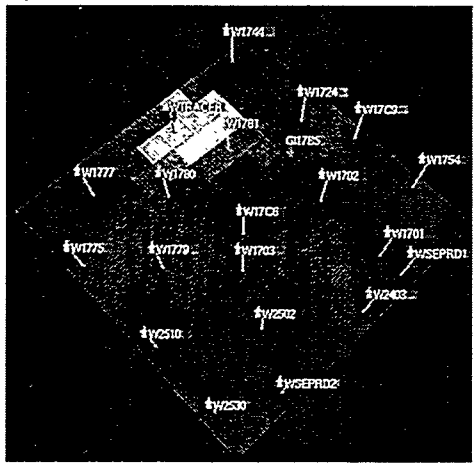

d) 2 Months

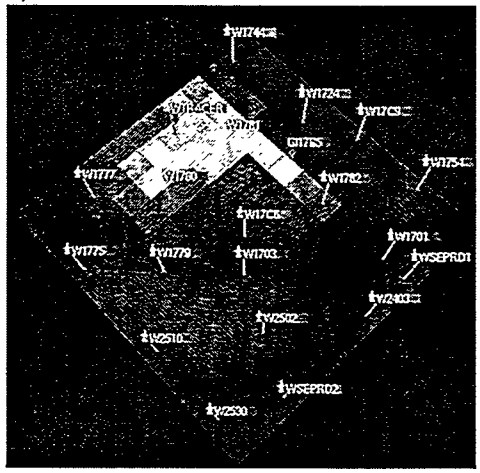

e) 3 months

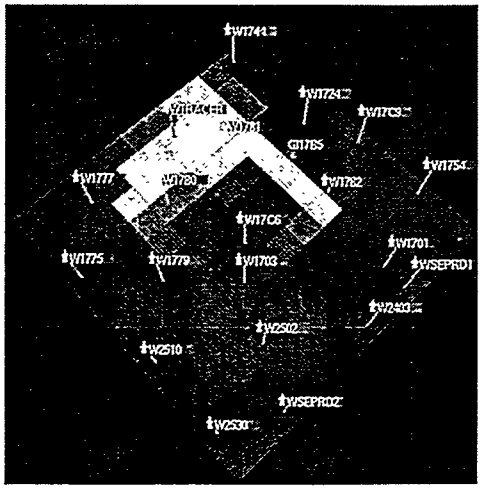

f) 7 Months

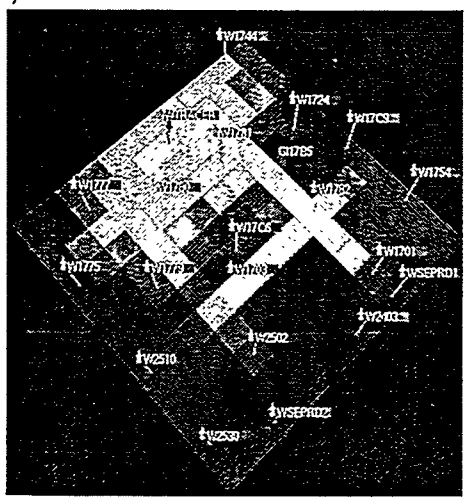

2D View of tracer path. For illustrative purposes tracer is injected continually into Layer 48 (water leg) at W1711

FIGURE **9-41**
2D VIEW OF TRACER SIMULATION
NIPER/FINAL REPORT/WA

PROJECT NO. 963 1357.521 DRAWING NO. 80647 DATE 9/29/98 DRAWN BY EA

Golder Associates

The ECLIPSE/DFN model simulation results provided in Figures 9-39, 9-40 and 9-41 are based on the DFN model described above in Section 9.1. From this simulation it can be seen that the ECLIPSE/DFN model matched the general patter of breakthrough, and particularly the NW-SE directionality. The breakthrough times for this model are comparable to in situ measurement for the nearby wells with strong recovery. However, the breakthrough times are longer than field measurements for the further wells, indicating a need for further refinement of either model properties or boundary condition assumptions.

The ECLIPSE models calibrated to the YU1711 in situ tracer experiment were used as input to THERM/DK for TAGS design simulations. These simulations were carried out to predict the number and geometry of steam injection wells necessary to heat the rock matrix from steam in the fracture network. Figures 9-42, 9-43, and 9-44 illustrate distributions of heat in the rock matrix after one and three years for

- homogeneous fracturing (Figure 9-42)
- the ECLIPSE/DFN model of Section 9.1 (Figure 9-43)
- the ECLIPSE/DFN model of Section 9.1, calibrated to measured fluid production rates (100x K) (Figure 9-44).

The ECLIPSE/DFN model shows that the matrix temperatures will be strongly correlated to the orientation and location of the major faults, regardless of the assumptions concerning background fracturing. The areal extent of high temperatures is improved with the inclusion of heterogeneous and anisotropic cell permeabilities based on the discrete fracture network model of Section 9.1. The most likely distribution of temperatures for the assumed TAGS steam injection configuration is given in Figure 9-44, based on a calibration of the ECLIPSE/DFN model to match the measured field fluid production rates.

Frac Kx=Ky=Kz=2000 md

Matrix Temperature 1 Year

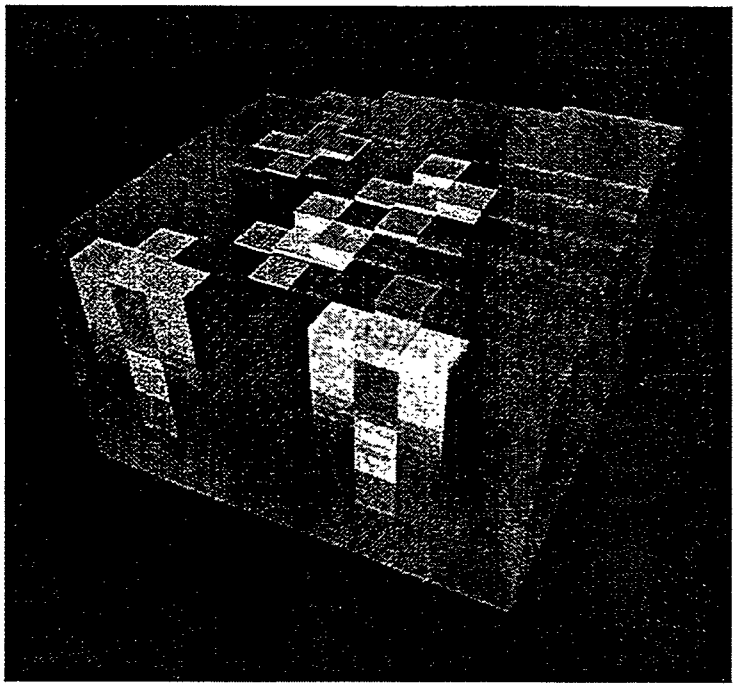

FIGURE **9-42**
TAGS THERMAL SIMULATION: HOMOGENEOUS FRACTURE GRID
NIPER/FINAL REPORT/WA

PROJECT NO. 963 1357.521 DRAWING NO. 80637 DATE 9/29/98 DRAWN BY EA

Golder Associates

Frac Kx & Ky Variable, Kz=2000 md

Matrix Temperature 1 Year

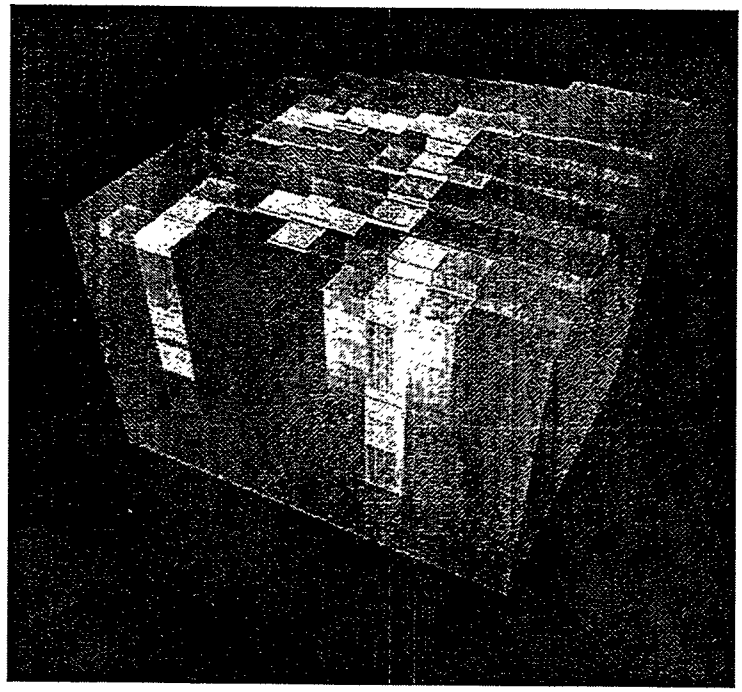

Matrix Temperature 3 Years

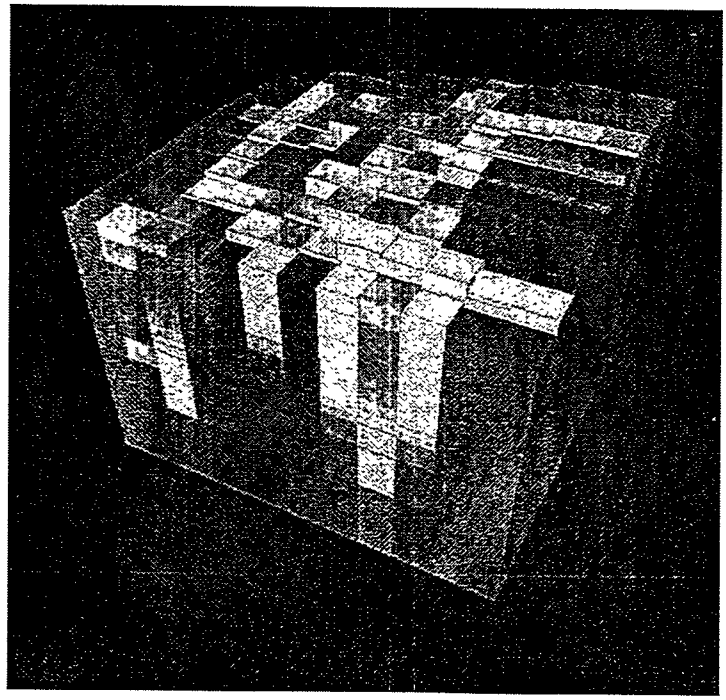

FIGURE **9-43**
TAGS THERMAL SIMULATION:
CONDITIONED STOCHASTIC FRACTURE GRID
NIPER/FINAL REPORT/WA

(Frac Kx & Ky Variable, Kz=2000 md) X 100

Matrix Temperature 1 Year

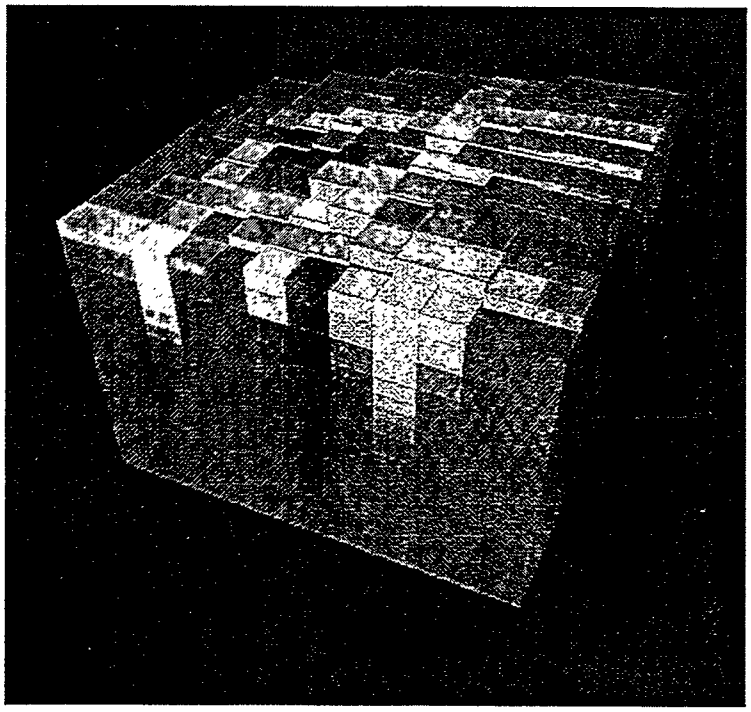

Matrix Temperature 3 Years

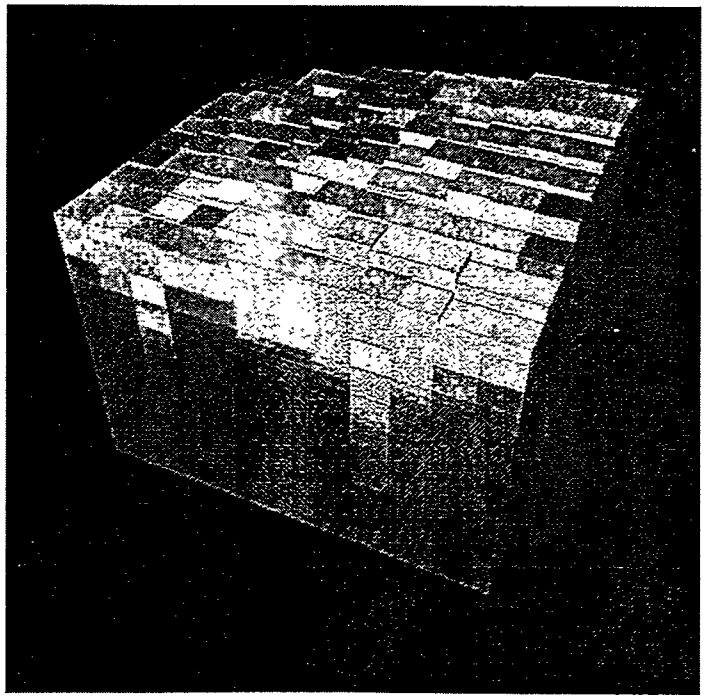

FIGURE **9-44**
TAGS THERMAL SIMULATION:
100X CONDITIONED STOCHASTIC FRACTURE GRID
NIPER/FINAL REPORT/WA

PROJECT NO. 963 1357.521 DRAWING NO. 80639 DATE 9/29/98 DRAWN BY EA

Golder Associates

10. TASK 4.3: TECHNOLOGY EVALUATION

The goal of Task 4.3 was to evaluate the economic value of the discrete fracture approach for fractured reservoirs with reference to the use of thermally assisted gravity segregation (TAGS) at the project study site. Three aspects were evaluated:

- additional site characterization costs associated with discrete feature network (DFN) and TAGS (Task 4.3.1);
- effectiveness of the DFN approach as a tool for support of TAGS tertiary oil recovery (Task 4.3.2); and
- improved reservoir recovery due to DFN and TAGS (Task 4.3.3).

The technology evaluation was carried out with a "cash-flow" perspective, reflecting the need to balance front-end loaded expenditures on site characterization, modeling, and analysis, against production rates and ultimate recovery.

The DFN/TAGS approach evaluation included an operational feasibility test of steam injected into a single well for 2.5 years. Daily injection rates were typically between 2,000 and 3,000 barrels, cold water equivalent (80-quality steam). This operation has reinforced the need for reservoir flow characterization developed independently and prior to heat injection. Heat breakthrough at nearby wells has not been observed. Thermal projects are most efficient when heat stays in the reservoir, so this is a desirable behavior. However, because the steam was not recovered in nearby wells, there is a need to determine:

- where the heat is distributed;
- where should additional heat be injected; and
- where are the best opportunities to produce the thermally mobilized oil; and
- what is an optimum design for completion configuration and operational procedures?

Discrete flow network modeling provides a means of assessing general flow preferences and the statistical probability of intersecting varying quality flow features at target elevations in the rock mass. In general there are three types of wells to design. There are the following:

Steam Injector Completions should intersect highly transmissive flow features in the secondary gas cap where injected steam would, ideally, flow through interconnected fractures across the base of the gas cap. As heat conducts into the matrix, steam in the fractures will condense and gravity segregate downward. Ideal flow conduits have benefited from paleo-fluid-flow solution enhancement and partial mineralization to minimize the probability of thermal closure. The fracture network heat exchange area per rock volume limits the heat dosage and injection well spacing. There is no benefit in

completing additional injectors in already heated portions of the network. Significant cash-flow benefit results from designing a group of steam injectors with maximum injectivity and minimum injection interference.

Oil Producing Completions should intersect highly transmissive flow features in a narrow band under the heating secondary gas cap. Ideally the completions would produce oil from a fracture network having good lateral connectivity to the steam heated reservoir volume. A minimum number of active completions having the capacity to produce the thermally mobilized oil while leaving most of the heat in the reservoir with minimal well-to-well interference is desired (well location designed to fit the discrete feature network).

Static Observation Wells should intersect flow features and porous rock matrix that is being actively heated by steam injection. Observation wells are intended to gather data to assess oil saturation changes as the formation heats. Wells which are completed too far from injected steam flow will remain cold during early years of the project. The distance is the length along a fracture pathway rather than straight-line distance between injection and observation. A fifty-foot offset distance that is not along a fracture flow conduit will require years to warm, while an observation well at the same distance along a flow conduit may heat to steam temperature in a very short time. A steam injector has only one challenge -- intersecting a well connected fracture-flow conduit. An ideal observation well must intersect a flow conduit that is also connected to a nearby steam injector. A minimum number of well-placed wellbores can provide response monitoring in a timely manner only if the fracture network can be adequately characterized.

10.1 Task 4.3.1: Site Characterization Evaluation

Although the DFN approach has extensive data requirements, many of these requirements are satisfied by data which is collected in the course of normal oil field operations and reservoir characterization. The level of effort necessary for the DFN application at the Yates field Tract 17 is estimated in Table 10-1. The total magnitude of field costs allocated for DFN and TAGS design were approximately $80,000. This can be compared to the cost per steam injection well of approximately $500,000.

Table 10-1 DFN/TAGS Data Requirements for Tract 17

	Field Activities	Total Cost (Estimate)	Cost Allocation to DFN, TAGS, and Well Location and Completion
Fracture Spatial Strucure	Outcrop Mapping	5 days at $1000/day	100% DFN
Fracture Orientation Distribution, Fracture Size	BHTV/FMI (9 wells, 1800 ft)	1800 ft at $ 50/ft	20% DFN, 20% TAGS, 60% Completion
Fracture Conductive Intensity, Fracture Transmissivity	Flow Logging (7 wells, 1400 ft)	1400 ft at $7/ft	20% DFN, 20% TAGS, 60% Completion
Network Connectivity	Pressure Interference	$10,000	5% DFN 95% TAGS
Network Connectivity	Tracer Testing	2 tests at $12,000/test	20% DFN, 80% TAGS

10.2 Task 4.3.2: DFN Approach Evaluation

The additional level of effort required to achieve the DFN model analysis results presented above in Section 9 are estimated in Table 10-2. Based on a typical engineering rate of $125/hour, this corresponds to an estimated analysis cost of $105,000. This corresponds to approximately 20% of the cost of a single steam injector well.

Table 10-2 DFN Approach Evaluation

Cost Item	Level of Effort (days)
DFN Data Analysis	20
DFN Model Implementation	20
Numeric Permeameter Studies	10
Compartmentalization Analyses	5
StrataFrac Analyses	5
Block Size Analysis	5
DFN/ECLIPSE Coupling	5
ECLIPSE Modeling	15
THERM/DK Modeling	20

10.3 Task 4.3.3: Recovery Estimation

The improved recovery due to the use of the TAGS process, including the effect of improved TAGS design based on discrete fracture network modeling is estimated as follows. The Yates field is estimated to contain over 4.0 billion barrels of oil. Recovery for the project study site (Tracts 17 and 46) was projected based on:

(a) no tertiary recovery activities; and

(b) TAGS recovery activities, including the use of DFN methods to optimize design.

These analyses are based on projections from observed trends, before and after initiation of TAGS stimulation activities. The TAGS process targets oil recovery from the secondary gas cap, oil column, and water invaded zone (200 ft of 16% average formation porosity at 50% oil saturation).

Based on this analysis, through the year 2015, the volume of oil recovery due to the TAGS process is estimated at 12.2 MMBO per 100 acres, corresponding to 20% ultimate recovery.

Thus, the projected improvement in ultimate recovery balances the front-end loading expenditures in the use of DFN approaches for design analysis of TAGS. As in all thermal stimulation projects, timing of full-field development will be critical for optimum oil price relative to energy prices. This leaves the reduction of operational and process risks as a critical target for technology application.

Alternatively, the benefit of the DFN approach can be quantified by directly estimating the impact of the DFN analysis on the cost of TAGS.

Engineers have therefore evaluated implementation of a TAGS process without guidance from DFN analysis as follows:

1. 50% of the vertical production wells being less efficient than they might be with modified completions (i.e., a horizontal wellbore to intersect a flow conduit);

2. 50% of the steam injection completions not intersecting well-connected flow features in a 60 foot interval immediately above the oil column for greatest thermal efficiency; and

3. 10-25 % of the observation wells being effective (50% will intersect flow conduits, but 50% of those won't be directly connected to a nearby steam injection completion). Time value relationships dictate successful observation wells, 10% of the observation wells may provide early data, building to 25% of the wells providing worthwhile data as the project matures.

The economic value of DFN modeling to improve the efficiency of TAGS development has been demonstrated through:

1. Increases in liquid production capacity of area completions by equipping wells with larger tubing and flow lines to allow increased production from those completions that are efficiently connected.

2. Location of steam injection wells along trends of elevated fracture connectivity with a "designed in" lateral completion for a combined improvement in efficient injection completion probability from 50% to 80% (in a program requiring four

efficient injectors, this has resulted in a three well reduction, from eight to five well).

3. Vertical oil segregation observation of a TAGS process requires vertical wellbores. Strategic location of these observation wells along the targeted steam injection fracture connectivity trends will double the probability of establishing valuable observation wells. The probability will increase to 20-50%, again with a time dependent shift. Five observation wells will adequately provide early results for a five well savings relative to the unbiased 10 observation well requirement to provide early time observation.

Based on the above analyses, it is estimated that the number of steam injectors ($470,000 per well) and observation wells ($325,000 per well) can be decreased by approximately 8 (3 steam injectors and 5 observation wells). This corresponds to a cost savings of in excess of $3 million directly attributable to the use of the DFN method in support of the TAGS process.

11. CONCLUSION

This report describes research carried out for the project, "Fractured Reservoir Discrete Feature Network Technologies," a project of Fundamental Geoscience Research and Development, sponsored by the US Department of Energy National Oil and Related Programs through BDM-OK/NIPER.

This project provided significant advances in discrete feature network analysis technologies for fractured reservoirs. Major conclusions from this research are:

- Discrete fracture network models such as the 3D Hierarchical Fracture Model (HFM) developed by this project are leading to more geologically and hydrologically realistic representations for fractured reservoirs,

- Significant tools have been developed for evaluation of heat flow in fractured reservoirs, reservoir compartmentalization, block size, and tributary drainage volume,

- Significant tools have been developed for analysis of fracture orientation, spatial structure, and flow testing

- The use of the DFN approach and Thermally Assisted Gravity Segregation (TAGS) have been demonstrated to have significant potential economic benefit in tertiary oil recovery, based upon the results of a demonstration analysis from the project study site.

12. REFERENCES

Barber, C. B., D.P. Dobkin, and H.T. Huhdanpaa, 1995. "The Quickhull Algorithm for Convex Hulls", ACM Transactions on Mathematical Software.

Barker, J.A., 1988. A Generalized Radial Flow Model for Pumping Tests in Fractured Rock. Water Resources Research, Vol 24, pp. 1796-1804.

Caine, J.S., J.P. Evans, and C.B. Forster, 1996. Fault Zone Architecture and Permeability Structure. Geology, v. 24, no. 11, p. 1025-1028.

Clemo, T. and L. Smith, 1997. A Hierarchical Model of Solute Transport in Fractured Media. Water Resources Research, Vol. 33, No. 8, pp. 1763-1784.

Dershowitz. W.S., 1979. A probabilistic model for the deformability of jointed rock masses. M.S. Thesis, MIT, Cambridge, MA.

Dershowitz. W.S. 1984. Rock Joint Systems. Ph.D. Thesis, Massachusetts Institute of Technology, Cambridge, MA.

Dershowitz, W.S., and H.H. Herda, 1992. Interpretation of Fracture Spacing and Intensity. Proc. 32nd US Rock Mech. Symp., Santa Fe, NM, p.757-766.

Dershowitz, W. and P. LaPointe, 1995. Discrete Fracture Approaches for Oil and Gas Applications. Proceedings, NARMS '94, Northern American Rock Mechanics Symposium, Austin, TX. Balkema, Rotterdam.

Dershowitz, W. 1997. Research Report, Reservoir Compartmentalization Prepared for contract G4S51728, U. S. Department of Energy, National Oil and Related Programs, BDM-Oklahoma. Golder Associates Inc., Redmond WA.

Dershowitz, W., G. Lee, J. Geier, T. Foxford, P. La Pointe and A. Thomas, 1996. FracMan Interactive Discrete Feature Data Analysis, Geometric Modeling, and Exploration Simulation: User Documentation Version 2.5. Golder Associates Inc., Redmond, WA.

Dershowitz, W., P. LaPointe, H.H. Einstein, and V. Ivanova, 1996, 1997. "Fractured Reservoir Discrete Feature Network Technologies". Quarterly progress reports, prepared for contract G4S51728, U.S. Department of Energy, National Oil and Related Programs, BDM-Oklahoma.

Dershowitz, W., P. LaPointe, H.H. Einstein & V. Ivanova, 1998. Fractured Reservoir Discrete Feature Network Technologies. Seventh quarterly progress report, prepared for contract G4S51728, U.S. Department of Energy, National Oil and Related Programs, BDM-Oklahoma. Golder Associates Inc., Redmond WA.

Diggle, P., 1983. Statistical Analysis of Spatial Point Patterns. Academic Press, London, UK.

Doe, T., 1991. Fractional Dimension Analysis of Constant-Pressure Well Tests. SPE paper 22702, presented at the 66th Annual SPE Technical Conference & Exhibition. SPE, Dallas.

Doe, T. and J. Geier, 1991. Interpretation of Fracture System Geometry Using Well Test Data. OECD/NEA Stripa Project Technical Report TR-91-03. SKB, Stockholm.

Doe T.W. and C. Chakrabarty, 1996. Analysis of Well Tests in Two-Zone Composite Systems with Different Spatial Dimensions. Water Resources Research (in press).

Doolin, D. and M. Mauldon, 1995. Anisotropy and Heterogeneity in Conasauga Group Rocks Near Oak Ridge Reservation, Tennessee. University of Tennessee Technical Report, DOE contract DE-FC05-920R22056. University of Tennessee, Knoxville.

Eberhart, R.C. and R. W. Dobbins, 1990. Neural Network PC Tools. Academic Press, London, 414p.

Ellis, G.W., et al. 1995. "Stress-strain modeling of sands using artificial neural networks" Journal of Geotechnical Engineering Vol. 121, No. 5, pp. 429-435.

Feng, X. 1995. "Neural network approach to comprehensive classification of rock stability, blastability and drillability", International Journal of Surface Mining, Reclamation and Environment Vol. 9, No. 2, pp. 57-62.

Geier, J., C-L Axelsson, A. Hässler, and A. Benabderrahmane, 1992. Discrete Fracture Modeling of the Finnsjön Rock Mass. SKB Technical Report TR 92-07. SKB, Stockholm.

Geier, J., W. Dershowitz, P. Wallmann, and T. Doe, 1995. Discrete Fracture Modeling of In-Situ Hydrologic and Tracer Experiments, in Myer, L.R., N.G.W. Cook, R.E. Goodman, and C.-F. Tsang, eds, Fractured and Jointed Rock Masses. Balkema, Rotterdam.

Goh, Anthony T.C. 1994. "Seismic liquefaction potential assessed by neural networks," Journal of Geotechnical Engineering Vol. 120, No. 9, pp. 1467-1480.

Isaaks, E.H. and R.M. Srivastava, 1985. An Introduction to Applied Geostatistics. Oxford University Press, Oxford.

Ivanova, V., 1995. Three-Dimensional Stochastic Modeling of Rock Fracture Systems. M. Sc. thesis, Massachusetts Institute of Technology, Cambridge, MA, 200 p.

Ivanova, V. et al., 1995. "Development of Stochastic models for Fracture Systems". Proceedings: 35th US Rock Mechanics Symposium, University of Nevada, Reno, June 5-7, 1995, pp. 725-730.

Ivanova, V., 1998. Geologic and Stochastic Modeling of Fracture systems in Rock. Ph.D. Dissertation, Massachusetts Institute of Technology, Cambridge, MA.

Kazemi, H.,1976. Society of Petroleum Engineers Journal, December, pp. 317-326.

La Pointe, P.R., W.C. Belfield and J.A. Helwig, 1984. Analysis of Fracturing and Fluid-Flow Characteristics of the Monterey Formation, Santa Barbara Channel, California: in Proceedings 1984 California Regional Meeting, Society of Petroleum Engineers SPE #12734, 97-106.

La Pointe, P.R., and J. Hudson, 1985. Characterization and Interpretation of Rock Joint Patterns. GSA Special Paper 199. GSA, Denver.

La Pointe, P.R. and C.C. Barton, 1995. Creating Reservoir Simulations with Fractal Characteristics, In Barton, C.C. and P.R. La Pointe, eds., Fractals in Petroleum Geology and Earth Processes. Plenum Press, New York.

La Pointe, P.R., P.C. Wallmann, and S. Follin, 1995. "Estimation of effective block conductivities based on discrete network analyses using data from the Aspo site." SKB Technical Report 95-15, Swedish Nuclear Fuel and Waste Management Co., Stockholm.

LaPointe, P., P. Wallmann, and S. Follin, 1996. Continuum Modelling of Fractured Rock Masses: Is it Useful? Proceedings, Eurock '96, Torino. Balkema, Rotterdam, pp. 343-350.

Lee, C., and R. Sterling, 1992. Identifying probable failure modes for underground openings using a neural network, International Journal of Rock Mechanics, Mining Sciences, and Geomechanics Abstracts, v. 29, n. 1, p. 49-67.

Low, L., 1986. Parametric Study of Rock Fracture Geometry. S.M. Thesis, Massachusetts Institute of Technology, Cambridge, MA.

Masters, T., 1993. Practical Neural Network recipes in C++. Academic Press, NY.

Mazurek, M., P. Bossart, and T. Eliasson, 1995. Classification and Characterization of Water Conducting Fractures at Äspö. SKB Äspö Program Report PR-25-95-03. SKB, Stockholm.

Miles, R.E., 1969. "Poisson Flats in Euclidean Space". Advanced Applied Probability, Vol. 1, p. 211-237.

Miles, R.E., 1973. "The Various Aggregates of Random Polygons Determined by Random Lines in a Plane." Advances in Mathematics, Vol. 10, p. 256-290.

Miller, I., G. Lee, and W. Dershowitz, 1997. MAFIC Matrix/Fracture Interaction Code with Heat and Solute Transport. User Documentation, Version 1.6. Golder Associates Inc., Redmond WA.

Oda, M., 1984. Permeability Tensor for Discontinuous Rock Masses. Geotechnique, Vol. 35, pp. 483-495.

Parzan, E., 1962. On Estimation of a Probability Density Function and Mode. Annals of Mathematical Statistics. Vol. 33, p. 1065-1076.

Pusch, R., 1995. Categorization of Discontinuities in Rock. Clay Technology AB, Lund.

Ripley, B., 1988. Statistical Inference for Spatial Processes. Cambridge University Press, Cambridge, UK.

Specht, D., 1990. Probabilistic Neural Networks. Neural Networks, Vol. 3, pp. 109-118.

Stoyan, D., W. Kendall, and J. Mecke, 1987. Stochastic Geometry and Its Applications. Akademie-Verlag Berlin / John Wiley & Sons, UK.

Swain, C.J., 1976. A FORTRAN IV program for interpolating irregularly spaced data. Computers and Geosciences, 1:221-240.

Thomas, A.L. and P. R. La Pointe, 1995. "Conductive fracture identification using neural networks." Proceedings: 35th U.S. Rock Mechanics Symposium, University of Nevada, Reno, June 5-7, pp. 627-632.

Tinker, S.W. and D.H. Mruk 1995. Reservoir Characterization of a Permian Giant: Yates Field, west Texas, in E. Stoudt and P.M. Harris, eds., Hydrocarbon reservoir characterization, geologic framework and flow-unit modeling: SEPM Short Course 34, pp.51-128.

Tung, A.T., F.S. Wong, and W. Dong, 1994. "Prediction of the spatial distribution of the modified Mercalli intensity using neural networks," Earthquake Engineering and Structural Dynamics, Vol. 23, No. 49, p 62.

Upton, G. and B. Fingleton, 1985. Spatial Data Analysis by Example, Volume I: Point Pattern and Quantitative Data. John Wiley & Sons, Chichester, UK.

Veneziano, D. 1978. Probabilistic modeling of joints in rock. Unpublished manuscript, Massachusetts Institute of Technology, Cambridge.

Winberg, A. (ed), 1996. First TRUE State - Tracer Retention Understanding Experiments. Descriptive Structural-Hydraulic Models on Block and Detailed Scales of the TRUE-1 Site. SKB International Cooperation Report ICR-96-04. SKB, Stockholm.

Xu, Q., et al., 1994. "Artificial neural network methods for spatial prediction of slope stability." in Oliveira, R.(ed.), Proceedings, Congress of the International Association of Engineering Geology; Vol. 7, pp. 4725-4728.